UNCLASSIFIED

AD NUMBER

AD888218

LIMITATION CHANGES

TO:

Approved for public release; distribution is unlimited.

FROM:

Distribution authorized to DoD only; Administrative/Operational Use; SEP 1971. Other requests shall be referred to Office of Naval Research, Arlington, VA 22203.

AUTHORITY

ONR ltr 29 Aug 1973

THIS PAGE IS UNCLASSIFIED

AD888218

UILU-ENG-71-2542

PROCEEDINGS
of the
FOURTH ALLERTON - HOUSE CONFERENCE
on
HF RADIO DIRECTION FINDING AND RADIOLOCATION RESEARCH

2 - 4 JUNE 1971

ROBERT ALLERTON PARK
MONTICELLO, ILLINOIS

RRL PUBLICATION NO. 392

Supported by the
OFFICE OF NAVAL RESEARCH
CONTRACT NO. N00014-71-C-0221

FINAL REPORT

Sponsored by the
RADIOLOCATION RESEARCH LABORATORY
DEPARTMENT OF ELECTRICAL ENGINEERING
ENGINEERING EXPERIMENT STATION
UNIVERSITY OF ILLINOIS
URBANA, ILLINOIS 61801

EACH TRANSMITTAL OF THIS DOCUMENT OUTSIDE OF THE DEPARTMENT OF DEFENSE MUST HAVE PRIOR APPROVAL OF THE OFFICE OF NAVAL RESEARCH (CODE 427), DEPARTMENT OF THE NAVY, ARLINGTON, VIRGINIA 22217.

HF RADIO DIRECTION FINDING AND RADIOLOCATION RESEARCH CONFERENCE

FINAL REPORT

Item A001AD
Contract N00014-71-C-0221
Project 371/167

September 1971

Albert D. Bailey, Editor

RADIOLOCATION RESEARCH LABORATORY
DEPARTMENT OF ELECTRICAL ENGINEERING
UNIVERSITY OF ILLINOIS
URBANA, ILLINOIS 61801

"Reproduction in whole or in part is permitted for any purpose of the United States Government."

DEDICATION

This Conference Proceedings is dedicated to the Office of Naval Research and to those men in the greater Navy who had the vision, foresight, patience and fortitude to encourage the establishment of a radio direction finding research program at the University of Illinois. With their continuous support the program has grown and produced. The fruits of their vision and support can be seen in the research facilities, which are in operation here, and also those that are in operation elsewhere as a direct or indirect result of work done here.

The interactions with other groups and the many voices that will be speaking at this conference are due, in part, to the earlier visions. We hope that, in retrospect, the originators will feel that they built well... even if it didn't come out quite as they expected.

FOREWORD

The purpose of this conference is to promote discussion between Governmental, Educational and Industrial Groups on the "State-of-the-Art" and Science of Radio Direction Finding, Radio Position Finding, Directional Radio Propagation; and to explore, where possible, the future direction of these research efforts, based on user requirements.

The General Theme of this Conference:

"D/F IN THE '70'S"

with subtopics

1. RDF Systems,
2. Radiolocation Systems,
3. Modeling and Simulation Studies,
4. HF Directional Propagation Research,
5. Instrumentation.

ACKNOWLEDGEMENT

The Fourth Allerton House Conference on Radio Direction Finding and Radiolocation Research is due to the encouragement and support of the Office of Naval Research. Dr. Arnold A. Shostak, Dr. Lloyd White and Mr. William Inglis were instrumental in helping us launch the program and their able assistance is hereby acknowledged. We hope that the Conference will achieve the goals that these men had in mind.

The University of Illinois invites your attention to the fact that we are completing our twenty-fifth year of continuous association in research and development with the Office of Naval Research. It has been a rewarding experience for many graduate students and staff who have benefited so much from this program.

We also wish to acknowledge the encouragement and support of Mr. Sterling R. Thrift in the production of the first three Allerton Conferences on RDF. These were held in 1959, 1964 and 1969.

OVERVIEW

Albert D. Bailey
Radiolocation Research Laboratory
Department of Electrical Engineering
University of Illinois
Urbana, Illinois 61801

First off I would like to extend my personal greetings to all of the conference attendees. Radiolocation finder and radiolocation type people are of a very special breed. This common disciplinary bond involves many wonderful people and it is a distinct privilege to have each of you here this morning. There were some who could not make it to the conference. Hopefully, each of you will carry the message back to them and let them read the Proceedings.

The objectives and goals of this conference are many. We called out several interest areas in an earlier letter to you as follows:

RDF IN THE '70's

RDF System
Radiolocation Systems (Short and Long Range)
HF Directional Propagation Research
Active DF
Modeling and Simulation Studies
Instrumentation

Now I certainly don't know all of the goals and objectives that each of you has in mind and this is probably a good thing, but we need a clear day. I would like to propose a common goal to the effect that we leave this conference with a clearer idea of where it is that the radio direction finding and radiolocation disciplines should advance during this decade.

The term CLEAR DAY has been referred to and is used to characterize the closing sessions of this conference. I had several ideas in mind when I originally introduced it. I will use it in several different contexts; the end-point interpretation is common. My original idea was to have two days of paper presentations followed by a closing date that was clear of papers and, hence, a time for feedback from the conferees and a time for impromptu discussions in a cleared atmosphere so that people could talk clearly about that which they clearly see, in order that the rest of us may see more clearly what it is that should be clear.

In another sense I had in mind the theme of a recent B. Streisand motion picture, "On A Clear Day You Can See Forever"; of course, I don't expect that any of us can see that far. But I do hope that the Conference Proceedings will provide insight and inspiration so that we may see to the end of this decade, if only dimly, what it is that should challenge our efforts.

In a third sense I had thought of clear day as time for clearing up any problems or questions that may have been generated by the previous days of formal presentation.

In a fourth sense it has become a day of "clear the decks for action" in the sense of Navy parlance. One of our guests will be speaking here.

In a fifth sense one might even suggest that the closing day is a time for clearing out.

I shall now stand clear of all of this and move into the overview. I shall use slides and transparencies in order to move quickly. Because of the pace, one may need to refer later to the notes. Also, I hope you will make notes in your Proceedings.

The plan for the first-day session of the conference is based upon the classical RDF system concepts and naturally includes the following:

(1) RDF wave collectors and antennas.
(2) Detectors and Receivers.
(3) Indicators and Computers.
(4) Interfacing Systems.

The first slide shows the classical concept of a radio direction finder as it might have been presented to us ca. 1955. In the sense of functional measuring systems it has three essential elements. A wave collector for its "primary element," a radio receiver and directional link for its "intermediate means" and an end device, i.e., an indicator for presenting sensory information. In the intervening years this concept has been modified and redefined, as it should be, because of the impact of all of the research and development that has gone on in the recent period.

The impact of the electronic computer, both analog and digital, is immense. Its capabilities for computation and control are still in the process of being realized, optimized and appreciated.

Following the RDF System, per se, comes the Radiolocation System. Here one is concerned with the following:

(1) Intelligent use of the RDF System, i.e., what can you really measure with it?
(2) The propagation medium and its intelligent exploitation in obtaining a best estimate of the position of the unknown.
(3) Environmental problems, e.g., siting and noise aspects.
(4) Optimum strategies.

The second-day sessions have been organized to provide additional insight into the above aspects of the radiolocation problem. Because of

the nature of this conference, many of these papers may be characterized as being of a research type. It is for this reason that the word "research" appears in the descriptive title of this conference.

The last day sessions are devoted to the immediate future. Hopefully, at that time, each session chairman can summarize the salient points of his session and provide this as feedback and/or feedforward at the last session. Preliminary to this is the Potpourri session scheduled for this evening.

I hope that each of you will become involved in the last session either by providing questions and comments or by serving on a panel which would field the questions and add comments of its own.

The agenda is heavy; accordingly, we have not scheduled extensive visits to the field stations. We will be happy to arrange trips and visits at convenient times. Those of you who have not seen our field stations in operation are urged to take advantage of this opportunity. Thank you.

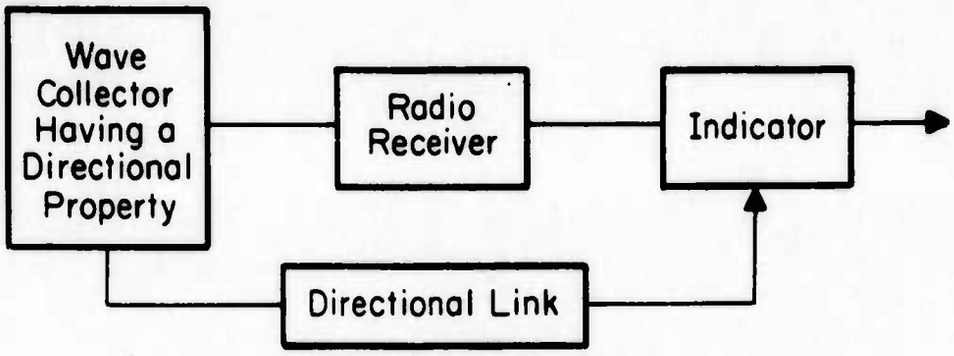

(a) Classical Concept (c a. 1950)

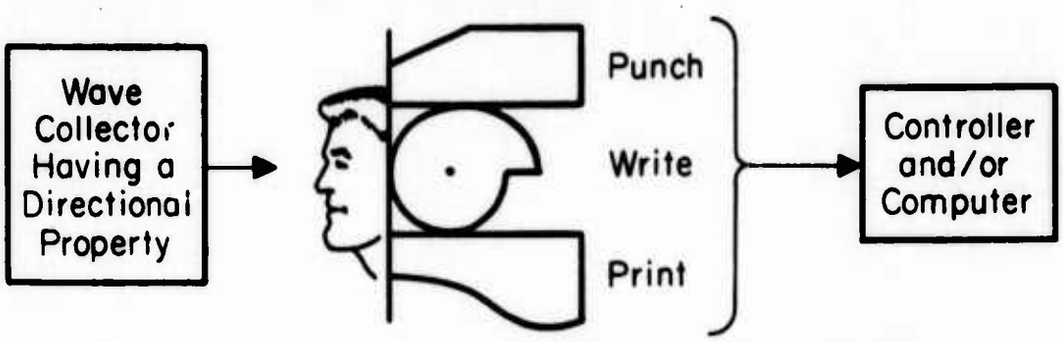

(b) More Recent Concepts (1960-1970)

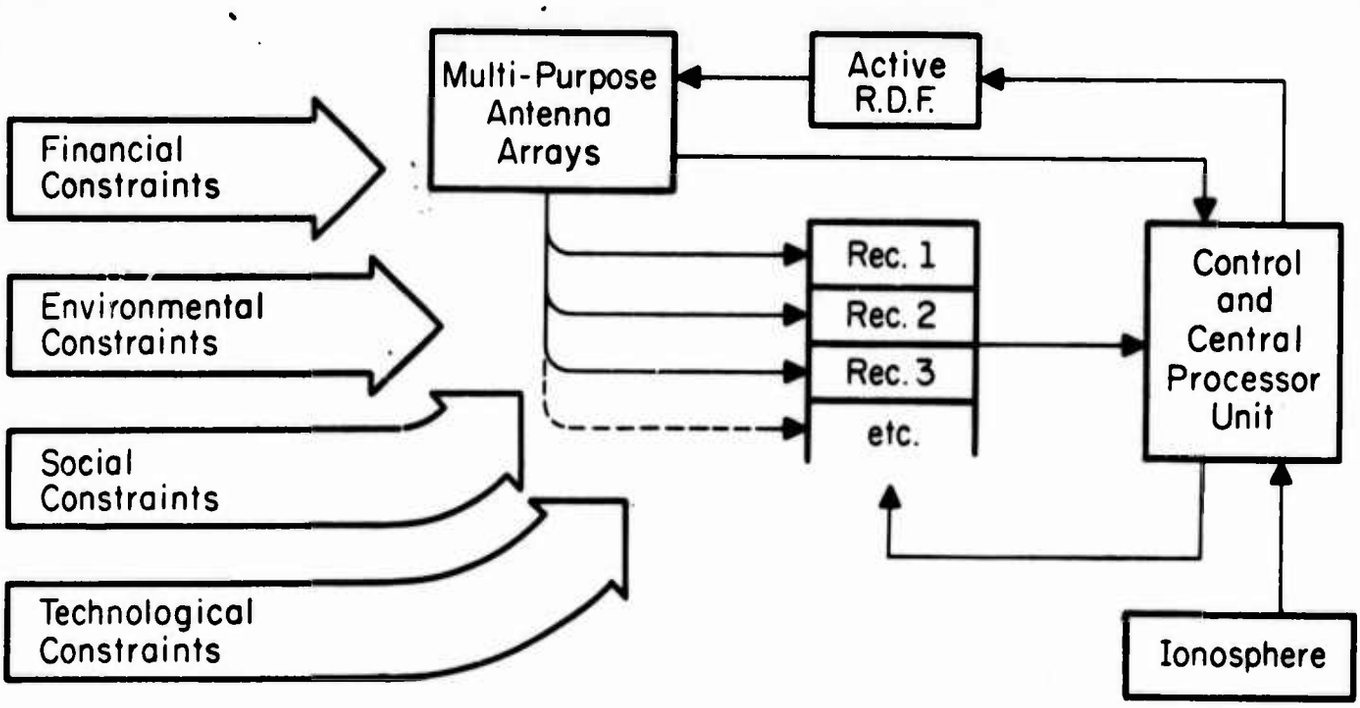

(c) Emerging Concepts (1970-1980)
Striving for an Optimum Solution

Figure 1. Pertinent to the HF/RDF Systems Concept.

FOURTH ALLERTON HOUSE
CONFERENCE ON RADIOLOCATION RESEARCH

Program

TUESDAY, 1 JUNE 1971

1:00 P.M. Begin checking in at the Allerton House, southwest of Monticello, Illinois*, Registration, Procure set of conference notes, Get orientated, Field Station visits.

6:00 P.M. Dinner for early arrivals.

7:00 P.M. Free time, homework, informal meetings, Field Station visits.

10:00 P.M. Late Snack

*(over the heather and through the hedge to Allerton House we go.....)

WEDNESDAY, 2 JUNE 1971

7:00 A.M. Breakfast

8:00 A.M. FORMAL OPENING

WELCOME - E. C. Jordan, Head of Department of Electrical Engineering, University of Illinois, Urbana

INTRODUCTORY REMARKS - W. Inglis, Office of Naval Research, Washington, D.C.

"OVERVIEW" - A. D. Bailey, Radiolocation Research Laboratory, Department of Electrical Engineering, University of Illinois, Urbana

8:30 A.M. FIRST SESSION - ANTENNAS AND RDF WAVE COLLECTORS

Chairman - E. C. Jordan, Head of Department of Electrical Engineering, University of Illinois, Urbana

1.1 "DIRECTION-FINDING APPLICATIONS OF THE MONOPOLE-SLOT--A SMALL, BROADBAND, UNIDIRECTIONAL ANTENNA," P. E. Mayes, University of Illinois, Antenna Lab, Urbana

1.2 "THE APPLICATION OF LINEAR ARRAYS TO DIRECTION-FINDING," J. D. Dyson and A. D. Bailey, Electrical Engineering, University of Illinois, Urbana

1.3 "THE DESIGN OF THE MODERN SPACED-LOOP DF ANTENNA FOR HF AND VHF," J. D. Moore, T. C. Green, M. P. Castles, and J. W. Fogwell, Southwest Research Institute, San Antonio, Texas

10:00 A.M. Coffee Break

10:30 A.M. SECOND SESSION - RDF RECEIVERS AND DETECTION TECHNIQUES

Chairman - H. D. Webb, Department of Electrical Engineering, University of Illinois, Urbana

2.1 "AN APPLICATION OF MATCHED RECEIVER TECHNIQUES TO HF RADIOLOCATION," A. F. L. Rocke, ITT, Columbia, Maryland

2.2 "APPLICATION OF SYNCHRONOUS AND CORRELATION DETECTION TO HF/DF SYSTEMS," R. W. Moss and H. H. Jenkins, Georgia Tech, Atlanta, Georgia

2.3 "ANALYSIS OF CORRELATION DETECTION TECHNIQUE FOR SMALL APERTURE DF SYSTEMS," R. W. Moss, Georgia Tech, Atlanta, Georgia

12:00 NOON Lunch

1:30 P.M. THIRD SESSION - ON-LINE, REAL-TIME COMPUTERS IN RDF

Chairman - W. Inglis, Office of Naval Research, Washington, D.C.

3.1 "REAL-TIME COMPUTER PROGRAMMING TECHNIQUES FOR RADIO-LOCATION PROBLEMS," R. B. Mathews and P. E. Martin, Southwest Research Institute, San Antonio, Texas

3.2 "A CDAA RDF SYSTEM WITH AN ON-LINE COMPUTER," L. C. Cropper and E. W. Ernst, Radiolocation Research Lab, University of Illinois, Urbana

3.3 "AN INTERFEROMETER RDF SYSTEM WITH AN ON-LINE COMPUTER," K. D. Stenzel and E. W. Ernst, Radiolocation Research Lab, University of Illinois, Urbana

3:00 P.M. Coffee Break

3:30 P.M. FOURTH SESSION - RDF SYSTEMS

Chairman - S. R. Thrift, CNO, Washington, D.C.

4.1 "A COMPARISON OF METHODS FOR DETERMINING ANGLE OF ARRIVAL WITH A CDAA," R. E. Hunninghaus and E. W. Ernst, Radiolocation Research Lab, University of Illinois, Urbana

4.2 "THE V-SCAN DIRECTION FINDING TECHNIQUE," J. H. Priedigkeit, Stanford Research Institute, Menlo Park, California

4.3 "RELATIVE PERFORMANCE OF SMALL APERTURE HF/DF SYSTEMS," L. Scott, Electronic Warfare Lab, Ft. Monmouth, N. J.

5:00 P.M. Hospitality Hour

6:00 P.M. Dinner

7:30 P.M. FIFTH SESSION - POTPOURRI

Chairman - C. Clark, Naval Security Engineering Facility, Washington, D.C.

5.1 "THE CHANGING SCOPE OF RDF IN THE NAVY," E. J. Kolb, Naval Security Group, Washington, D.C.

5.2 "THE RADIOLOCATION RESEARCH AND THE PATRON," E. J. Kolb, Naval Security Group, Washington, D.C.

5.3 "MODE ANGULAR WIDTH MEASUREMENT," G. A. Smith, W. M. Sherrill, and W. G. Guion, Southwest Research Institute, San Antonio, Texas

10:00 P.M. Late Snack

THURSDAY, 3 JUNE 1971

7:00 A.M. Breakfast

8:30 A.M. SIXTH SESSION - MEASUREMENTS OF RANGE AND ANGLES OF ARRIVAL IN AZIMUTH AND ELEVATION

Chairman - A. D. Bailey, Radiolocation Research Laboratory, Department of Electrical Engineering, University of Illinois, Urbana

6.1 "MEASUREMENT OF THE VERTICAL ANGLES OF ARRIVAL OF A SKYWAVE SIGNAL IN THE PRESENCE OF MULTIPLE MODES," J. M. Kelso, ITT, Columbia, Maryland

6.2 "RANGE ESTIMATION BASED ON BACKSCATTER MEASUREMENTS," L. H. Tveten, ESSA/ITS, Boulder, Colorado

6.3 "THE EFFECTIVENESS OF SPECTRUM AND AZIMUTH SPREAD MEASUREMENTS IN DETECTING SIDESCATTER," J. C. Blair, ESSA

6.4 "FADE RATE CORRELATION," M. R. Epstein, Page Communication Engineers, Inc., Washington, D.C.

10:00 A.M. Coffee Break

10:30 A.M. SEVENTH SESSION - IONOSPHERIC TILTS AND TRAVELING DISTURBANCES

Chairman - D. G. Detert, AVCO Corporation, Lowell, Massachusetts

7.1 "STUDIES OF TRAVELLING IONOSPHERIC DISTURBANCES WITH A TRIPLE RADIO INTERFEROMETER SYSTEM," E. K. Walton, Radiolocation Research Lab, Department of Electrical Engineering, University of Illinois, Urbana

7.2 "THREE TRANSMITTER EXPERIMENTS IN RADIOLOCATION RESEARCH," A. D. Bailey and E. K. Walton, Radiolocation Research Lab, Department of Electrical Engineering, University of Illinois, Urbana

7.3 "SHORT TIME SCALE IONOSPHERIC TILT MEASUREMENTS FOR LATERAL DEVIATION COMPENSATION," P. E. Martin, R. L. Johnson, and T. C. Green, Southwest Research Institute, San Antonio, Texas

7.4 "THE PREDICTION OF DIURNAL DEVIATION EFFECTS," R. I. Beckwith, Radiolocation Research Lab, University of Illinois, Urbana

12:00 NOON Lunch

1:30 P.M. EIGHTH SESSION - THE IONOSPHERE

Chairman - J. Kelso, ITT, Columbia, Maryland

8.1 "SINGLE-ANTENNA FM/CW VERTICAL INCIDENCE SOUNDING," S. M. Bennett and W. E. Woolhiser, AVCO, Lowell, Massachusetts

8.2 "AMPLITUDE STUDIES OF HF AURORAL BACKSCATTER," F. O. Fahlsing and N. N. Rao, Radiolocation Research Lab, University of Illinois, Urbana

8.3 "OBSERVATION OF DOPPLER COMPONENTS OF HF OBLIQUE PROPAGATION," A. H. Katz and A. S. Weeks, AVCO, Lowell, Massachusetts

3:00 P.M. Coffee Break

3:30 P.M. NINTH SESSION - DIRECTIONAL PROPERTIES OF NOISE

Chairman - M. Clinch, Rome Air Development Center, Rome, N.Y.

9.1 "AZIMUTHAL VARIATION OF MEASURED HF NOISE," L. M. Posa, D. J. Materozzi and N. C. Gerson, Department of Defense

9.2 "UNUSUAL RADIO NOISE SOURCES IN DIRECTION FINDING AND HF RECEIVING SYSTEMS," C. R. Graf, USAF SS, San Antonio, Texas

9.3 "AZIMUTHAL DISTRIBUTION AND CHARACTERISTIC PROPERTIES OF AMBIENT RADIO NOISE AT HF," A. S. Weeks, AVCO, Lowell, Massachusetts

5:00 P.M. Social Hour

6:00 P.M. Dinner

7:00 P.M. FM/CW Ionosonde Demonstration

8:30 P.M. Informal Conference Discussions on RAY TRACING

9:30 P.M. Third A. A. Shostak RDF Hunt - OTH RADAR (over the heather ray detection and ranging)

10:00 P.M. Late Snack

FRIDAY, 4 JUNE 1971

7:00 A.M. Breakfast

8:30 A.M. TENTH SESSION - RDF AND RADIOLOCATION RESEARCH IN THE 70'S

Chairman - J. Kaplan, USA ECOM, Ft. Monmouth, New Jersey

10.1 "THE NAVY'S SATELLITE SOLAR ACTIVITY MONITORING AND FORECASTING SYSTEM," E. W. Peterkin, Naval Research Lab, Washington, D.C.

10.2 "ADVANCED RADIOLOCATION INTERFEROMETRY," W. M. Sherrill, D. R. Travers and P. E. Martin, Southwest Research Institute, San Antonio, Texas

10.3 "FEEDBACK AND FEEDFORWARD," A. D. Bailey, Radiolocation Research Laboratory, Department of Electrical Engineering, University of Illinois, Urbana

9:30 A.M. Coffee Break

10:30 A.M. ELEVENTH SESSION - ON A CLEAR DAY ONE CAN SEE . . . . . ?!

11:55 A.M. Commencement

12:00 NOON Lunch

1:00 P.M. 4th Allerton House Conference on Radiolocation Research Closes.

D/F CONFERENCE ATTENDEES
ROBERT ALLERTON PARK
MONTICELLO, ILLINOIS
2-4 June 1971

AVCO

Sidney H. Bennett
Environmental Science Project Office
201 Lowell Street
Wilmington, Massachusetts 01884
PHONE 617 452 8961
ext. 6388, 6374

Eldon Burkinshaw
Lowell Industrial Park
Lowell, Massachusetts 01851
PHONE 617 453 8961

David Detert
Applied Technology Division
Geophysics Section
Lowell Industrial Park
Lowell, Massachusetts 01851
PHONE 617 452 8961 ext. 6343

David Ovellette
Lowell Industrial Park
Lowell, Massachusetts 01851
PHONE 617 453 8961

Andrew S. Weeks
Systems Division
Lowell Industrial Park
Lowell, Massachusetts 01851
PHONE 617 452 8961

BEUKERS LABORATORIES, INC.

Martin C. Poppe, Jr., Director
Advanced Development
1324 Motor Parkway
Hauppauge, New York 11787
PHONE 516 234 2200

COMMUNICATIONS RES. CENTRE

F. D. Green
Shirley Bay
P. O. Box 490, Terminal "A"
Ottawa 2, Ontario, CANADA
PHONE 613 992 4431

R. W. Herring
Shirley Bay
P. O. Box 490, Station "A"
Ottawa, Ontario K1N8T5, CANADA
PHONE 613 992 4431

D. W. Rice
Shirley Bay
P. O. Box 490, Station "A"
Ottawa, Ontario K1N8T5, CANADA
PHONE 613 992 4431

ESSA

James Blair
Room 3419, Radio Building
ITS/OT
325 South Broadway
Boulder, Colorado 80302
PHONE 303 447 1000

P. L. George
c/o Dr. Kenneth Davies
Boulder, Colorado 80302
PHONE 303 447 1000 ext. 3202

Lowell H. Tveten
Supervisory Physicist
Room 3419, Radio Building
ITS/OT
325 South Broadway
Boulder, Colorado 80302
PHONE 303 447 1000 ext. 3621

F & M SYSTEMS COMPANY

Donald R. Eager
Project Engineer
2525 Walnut Hill Lane
P. O. Box 20778
Dallas, Texas 75220
PHONE 241 4242

GEORGIA TECH

Herndon H. Jenkins
Senior Research Engineer
Engineering Experiment Station
225 North Avenue, N. W.
Atlanta, Georgia 30033
PHONE 404 873 4211

Richard W. Moss
Research Engineer
Engineering Experiment Station
Atlanta, Georgia 30332
PHONE 873 4211 ext. 185

IIT

John M. Kelso
Director of Research
9140 Old Annapolis Road
Columbia, Maryland 21043
PHONE 301 730 1700

A. F. L. Rocke
EPL WC
9140 Old Annapolis Road
Columbia, Maryland 21043
PHONE 301 730 1700

LOWELL TECH. INSTITUTE
RESEARCH FOUNDATION

Klaus Bibl
450 Aiken Street
Lowell, Massachusetts 01851
PHONE 617 458 2501

MAGNAVOX

Norm R. Getzin
Urbana, Illinois 61801
PHONE 217 333 5529

Curtis D. Rugroden
Urbana, Illinois 61801
PHONE 217 333 5022

OFFICE OF NAVAL RESEARCH

W. M. Inglis
Electronics Project Officer
Code 427
Arlington, Virginia 22217
PHONE OX2 4217 (4216)

Lloyd A. White
536 South Clark
Chicago, Illinois 60605
PHONE 175 9 353 6067

PAGE COMMUNICATIONS ENGINEERS

Mark Epstein
3300 Whitehaven Street, N. W.
Washington, D. C. 20007
PHONE 202 337 7600

ROME AIR DEVELOPMENT CENTER

Marvin R. Clinch
ATTN: EMITA
Griffis Air Force Base
New York 13440
PHONE 115 363 3237

SANDERS ASSOCIATES

Walter W. Zandi
Senior Member Technical Staff
Sanders Associates
95 Canal Street
Nashua, New Hampshire 03060
PHONE 603 885 2715

SOUTHWEST RESEARCH INSTITUTE

T. C. Green
8500 Culebra Road
San Antonio, Texas 78228
PHONE 512 694 2963

Richard L. Johnson
8500 Culebra Road
San Antonio, Texas 78228
PHONE 512 684 2000

Richard B. Mathews
8500 Culebra Road
San Antonio, Texas 78228
PHONE OV4 2000

John D. Moore
8500 Culebra Road
San Antonio, Texas 78228
PHONE 684 2000 ext. 469

William Sherrill
Intercept & Direction Finding Research
8500 Culebra Road
San Antonio, Texas 78228
PHONE 512 684 2000

G. A. Smith
8500 Culebra Road
San Antonio, Texas 78228
PHONE 512 684 2000 ext. 472

Douglas Travers
8500 Culebra Road
San Antonio, Texas 78228
PHONE 512 684 2000

STANFORD RESEARCH INSTITUTE

J. H. Priedigkeit
Program Manager
Menlo Park, California 94075
PHONE 415 326 6200 ext. 2730

SYLVANIA ELECTRONIC DEFENSE LAB.

F. W. Smith
Senior Engineering Specialist
P. O. Box 205
Mt. View, California 94040
PHONE 415 966 2748

SYRACUSE UNIVERSITY RESEARCH CORP.

Harvey Schuman
Merrill Land
University Heights
Syracuse, New York 13210
PHONE 446 9372

TEXAS INSTRUMENTS, INC.

Harry A. Currie
Manager, Passive ECM
Texas Instruments, Inc.
P. O. Box 6015 MS 996
Dallas, Texas 75222
PHONE 214 238 2458

UNITED STATES AIR FORCE

Calvin R. Graf
Electronic Engineer
USAF Security Service (DOYGS)
San Antonio, Texas 78243
PHONE 925 2367

UNITED STATES ARMY

Jacob Kaplan
Commanding Officer Electronic Warfare Lab.
Ft. Monmouth, New Jersey 07703
PHONE 201 596 1233

Seth J. Perry
CG USASA
Arlington Hall Station
Arlington, Virginia 22212
ATTN: IARD-C
PHONE 202 692 6885 or 25448

Lawrence Scott
E. W. Laboratory
Code AMSEL/WL-S
Ft. Monmouth, New Jersey 07703
PHONE 201 596 1692

Melvin Weiner
USA ECOM
AMSEL-WL-C
Ft. Monmouth, New Jersey 07703
PHONE 201 596 1654

Harry Wiggins
CG USASA
Arlington Hall Station
Arlington, Virginia 22212
ATTN: IARD-C
PHONE 202-692 5448

U. S. GOVERNMENT

Garth Burleyson, D92
Ft. George G. Meade
Maryland 20755
PHONE 301 688 6406

Robert Clark, Analyst
P. O. Box 1925 Main Station
Washington, D. C. 20013
(5F29 HQ)
PHONE 351 6306

N. C. Gerson
Trapelo Road
Lincoln, Massachusetts 01775
PHONE 617 259 8751

Robert Pipp
Electronic Engineer
Director, National Security Agency
Ft. George G. Meade, Maryland 20755
ATTN: R424
PHONE 301 688 7417

Augustine A. Strejcek
National Security Agency
Ft. George G. Meade, Maryland 20755
ATTN: W62
PHONE 301 677 7130

U. S. MARINE CORPS

Norman Huddy, Jr.
Major
Headquarters, (Code A02F)
Washington, D. C. 20380
PHONE 202 0X4 4369

U. S. NAVY

Raymond Gleason, Electronic Engineer
Naval Research Lab. (5482)
Washington, D. C. 20390
PHONE 202 767 2501

Jack Hortman
Naval Research Lab. (5482B)
Washington, D. C. 20390
PHONE 202 767 2501

Ernest W. Peterkin
Code 7004
Naval Research Lab.
4555 Overlook Avenue, S. W.
Washington, D. C. 20390
PHONE 202 767 3086

Edward J. Kolb
Scientific Staff Physicist
Naval Security Group Command
3801 Nebraska Avenue
Washington, D. C. 20390
PHONE 202 896 0598

Sterling R. Thrift
Technical Advisor
DCNO (D) OP-098T4
Pentagon
Washington, D. C.
PHONE 202 697 9838

UNIVERSITY OF HOUSTON

Thomas N. Whitaker
Prof. of Electrical Engineering
3801 Cullen
Houston, Texas 77004
PHONE RI 84380

VICTORIA UNIVERSITY

Norman Barber
P. O. Box 196
Wellington, NEW ZEALAND

UNIVERSITY OF ILLINOIS

Eric Anderson
Urbana, Illinois 61801

Albert D. Bailey
Urbana, Illinois 61801

Roy Beckwith
Urbana, Illinois 61801

Leigh Cropper
Urbana, Illinois 61801

John Dyson
Urbana, Illinois 61801

Edward W. Ernst
Urbana, Illinois 61801

Fred Fahlsing
Urbana, Illinois 61801

John Huff
Urbana, Illinois 61801

Roy Hunninghaus
Urbana, Illinois 61801

Larry Jones
Urbana, Illinois 61801

Edward C. Jordan
Urbana, Illinois 61801

Harold Lawler
Urbana, Illinois 61801

William Little
Urbana, Illinois 61801

Frank Luksander
Urbana, Illinois 61801

Helen Mackey
Urbana, Illinois 61801

Ross Martin
Urbana, Illinois 61801

Paul Mayes
Urbana, Illinois 61801

Jack Miller
Urbana, Illinois 61801

Tom Mueller
Urbana, Illinois 61801

Genny Polizzotti
Urbana, Illinois 61801

N. Rao
Urbana, Illinois 61801

Keith Stenzel
Urbana, Illinois 61801

Eric Walton
Urbana, Illinois 61801

Harold Webb
Urbana, Illinois 61801

Walter W. Wood
Urbana, Illinois 61801

TABLE OF CONTENTS

DD FORM 1473

TITLE PAGE

DEDICATION

FOREWORD

ACKNOWLEDGMENT

OVERVIEW by A. D. Bailey

PROGRAM

LIST OF ATTENDEES

TABLE OF CONTENTS

1. ANTENNAS AND RDF WAVE COLLECTORS

   1.1 "DIRECTION-FINDING APPLICATIONS OF THE MONOPOLE-SLOT--A SMALL, BROADBAND, UNIDIRECTIONAL ANTENNA" by P. E. Mayes

   1.2 "THE APPLICATION OF LINEAR ARRAYS TO DIRECTION-FINDING" by J. D. Dyson and A. D. Bailey

   1.3 "THE DESIGN OF THE MODERN SPACED-LOOP DF ANTENNA FOR HF AND VHF" by J. D. Moore, T. C. Green, M. P. Castles, and J. W. Fogwell

2. RDF RECEIVERS AND DETECTION TECHNIQUES

   2.1 "AN APPLICATION OF MATCHED RECEIVER TECHNIQUES TO HF RADIOLOCATION" by A. F. L. Rocke

   2.2 "APPLICATION OF SYNCHRONOUS AND CORRELATION DETECTION TO HF/DF SYSTEMS" by R. W. Moss and H. H. Jenkins

   2.3 "ANALYSIS OF CORRELATION DETECTION TECHNIQUE FOR SMALL APERTURE DF SYSTEMS" by R. W. Moss

3. ON-LINE, REAL-TIME COMPUTERS IN RDF

   3.1 "REAL-TIME COMPUTER PROGRAMMING TECHNIQUES FOR RADIOLOCATION PROBLEMS" by R. B. Mathews and P. E. Martin

   3.2 "A CDAA RDF SYSTEM WITH AN ON-LINE COMPUTER" by L. C. Cropper and E. W. Ernst

   3.3 "AN INTERFEROMETER RDF SYSTEM WITH AN ON-LINE COMPUTER" by K. D. Stenzel and E. W. Ernst

4. RDF SYSTEMS

   4.1 "A COMPARISON OF METHODS FOR DETERMINING ANGLE OF ARRIVAL WITH A CDAA" by R. E. Hunninghaus and E. W. Ernst

4.2 "THE V-SCAN DIRECTION FINDING TECHNIQUES" by J. H. Priedigkeit

4.3 "RELATIVE PERFORMANCE OF SMALL-APERTURE HF/DF SYSTEMS" by L. Scott

5. POTPOURRI

5.1 "THE CHANGING SCOPE OF RDF IN THE NAVY" by E. J. Kolb

5.2 "THE RADIOLOCATION RESEARCH AND THE PATRON" by E. J. Kolb

5.3 "MODE ANGULAR WIDTH MEASUREMENTS" by G. A. Smith, W. M. Sherrill, and W. G. Guion

6. MEASUREMENTS OF RANGE AND ANGLES OF ARRIVAL IN AZIMUTH AND ELEVATION

6.1 "MEASUREMENT OF THE VERTICAL ANGLES OF ARRIVAL OF A SKYWAVE SIGNAL IN THE PRESENCE OF MULTIPLE MODES" by J. M. Kelso

6.2 "RANGE ESTIMATION BASED ON BACKSCATTER MEASUREMENTS" by L. H. Tveten

6.3 "THE EFFECTIVENESS OF SPECTRUM AND AZIMUTH SPREAD MEASUREMENTS IN DETECTING SIDESCATTER" by J. C. Blair

6.4 "FADE RATE CORRELATION" by M. R. Epstein

7. IONOSPHERIC TILTS AND TRAVELING DISTURBANCES

7.1 "STUDIES OF TRAVELLING IONOSPHERIC DISTURBANCES WITH A TRIPLE RADIO INTERFEROMETER SYSTEM" by E. K. Walton

7.2 "THREE TRANSMITTER EXPERIMENTS IN RADIOLOCATION RESEARCH" by A. D. Bailey and E. K. Walton

7.3 "SHORT TIME SCALE IONOSPHERIC TILT MEASUREMENTS FOR LATERAL DEVIATION COMPENSATION" by R. L. Johnson, P. E. Martin, and T. C. Green

7.4 "THE PREDICTION OF DIURNAL DEVIATION EFFECTS" by R. I. Beckwith

8. THE IONOSPHERE

8.1 "SINGLE-ANTENNA FM/CW VERTICAL INCIDENCE SOUNDING" by S. M. Bennett and W. E. Woolhiser

8.2 "AMPLITUDE STUDIES OF HF AURORAL BACKSCATTER" by F. O. Fahlsing and N. N. Rao

8.3 "OBSERVATION OF DOPPLER COMPONENTS OF HF OBLIQUE PROPAGATION" by A. H. Katz and A. S. Weeks

9. DIRECTIONAL PROPERTIES OF NOISE

9.1 "AZIMUTHAL VARIATION OF MEASURED HF NOISE" by L. M. Posa, D. J. Materozzi, and N. C. Gerson

9.2 "UNUSUAL RADIO NOISE SOURCES IN DIRECTION FINDING AND HF RECEIVING SYSTEMS" by C. R. Graf

9.3 "AZIMUTHAL DISTRIBUTION AND CHARACTERISTIC PROPERTIES OF AMBIENT RADIO NOISE AT HF" by A. S. Weeks

10. RDF AND RADIOLOCATION RESEARCH IN THE 70'S

10.1 "THE NAVY'S SATELLITE SOLAR ACTIVITY MONITORING AND FORECASTING SYSTEM" by E. W. Peterkin

10.2 "ADVANCED RADIOLOCATION INTERFEROMETRY" by W. M. Sherrill, D. R. Travers, and P. E. Martin

10.3 "FEEDBACK AND FEEDFORWARD" by A. D. Bailey

DISTRIBUTION LIST

Direction-Finding Applications of the Monopole-Slot - A Small, Broadband, Unidirectional Antenna

Paul E. Mayes

Antenna Laboratory
Electrical Engineering Department
University of Illinois
Urbana, Illinois 61801

I. Introduction

The monopole-slot is a new antenna element which has unique properties that appear to be particularly suited in radio direction-finding. The element consists of a conical monopole and a cavity-backed slot which are simultaneously excited from the same feeder. The element has unidirectional beam patterns and nearly constant input impedance over broad (greater than 10 to 1) frequency bands. The broadband impedance is obtained by combining a series element (slot) and a shunt element (monopole) which have impedances that are complementary. The bandwidth is limited on the low frequency side by either pattern or efficiency, depending upon the frequency range of application.

The monopole-slot is a two-port antenna and has two cardioid patterns, one associated with each port. The patterns are related by reflection through the line of symmetry of the element, thus providing an amplitude comparison DF element in a single structure. Of course, a single cardioid pattern can be obtained by simply terminating one port in a matched load. In this form the antenna is well suited for use as an element in large-aperture, circularly-disposed DF arrays. Since the element pattern is unidirectional, no reflecting screen would be required. Over a major

portion of the pattern band, the antenna is electrically small so that construction for operation in the HF band does not present severe mechanical problems. Since a ground mat is generally required at these frequencies anyway, the addition of a slot and shallow cavity below the ground screen is not difficult to achieve.

A sketch of a UHF embodiment of the monopole-slot antenna is shown in Figure 1. A narrow rectangular slot is cut in a ground plane which is several wavelengths in dimension. The slot is backed by a shallow cavity with a width several times the slot width and a length slightly larger than the slot length. The slot is excited by the ground-plane currents produced when a voltage is applied to a microstrip conductor which passes over the slot. The microstrip is supported by a thin dielectric sheet which is not shown in the figure. Provision is made to connect the microstrip to coaxial cable at each end. A monopole which is perpendicular to the ground plane is connected to the top side of the microstrip at a location corresponding to the center of the slot.

II. Theory of Operation

The monopole-slot is a passive, two-port network. There are many ways of representing such two-ports and each one has its particular applications. The classical A B C D matrix defined in (1) relates input voltage and current to the same output quantities and is useful when networks are to be cascaded. However, at higher frequencies, it is more convenient to measure incident and reflected wave amplitudes than to measure voltage and current. A transformation converts the A B C D representation to one involving wave amplitudes A_1, B_1, A_2 and B_2, propagation factors γ_1 and γ_2 and image impedances Z_{i1} and Z_{i2} as given in (2).

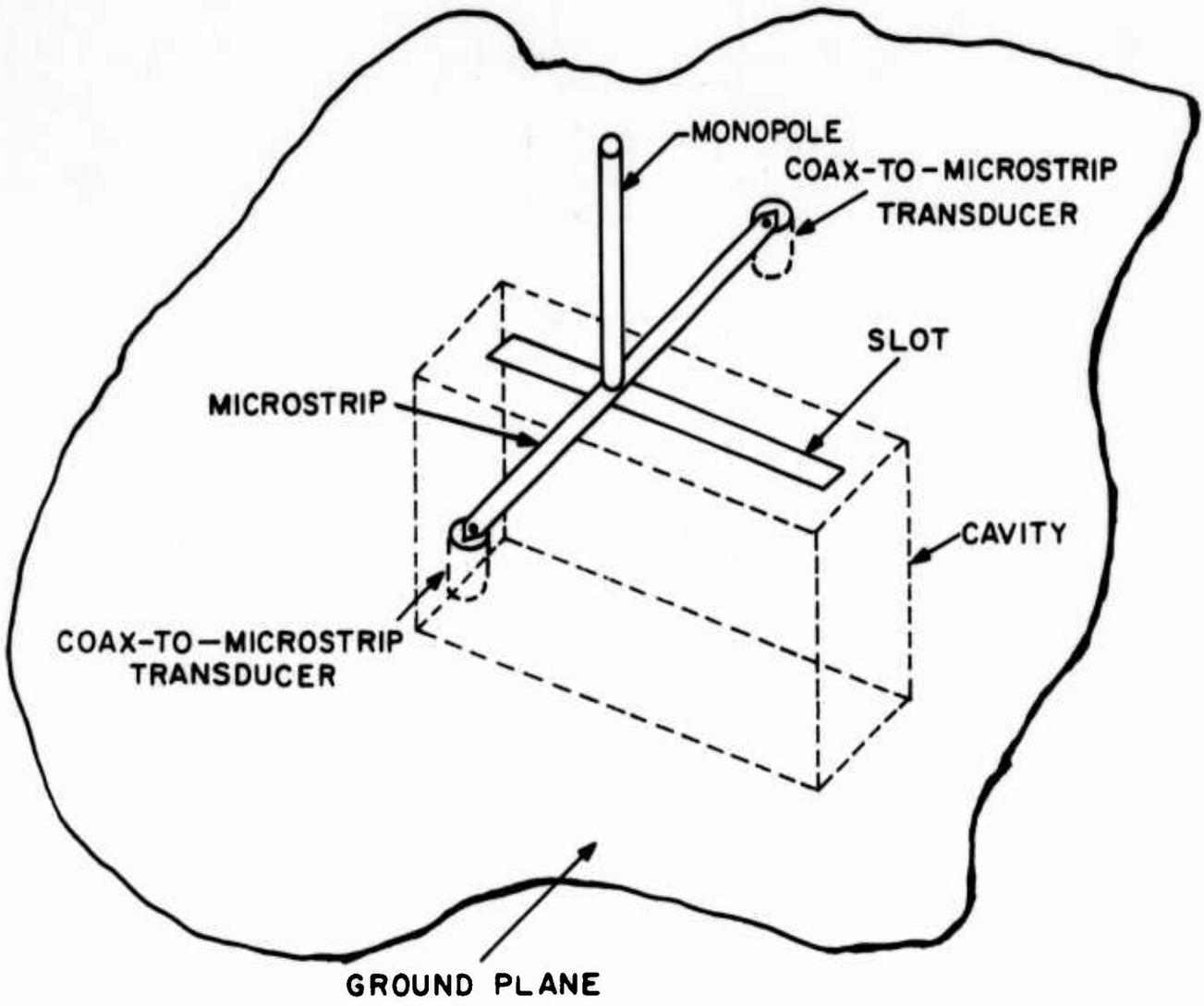

Figure 1. Monopole-slot antenna.

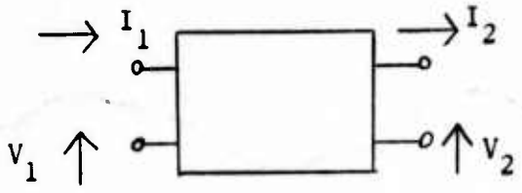

$$\begin{bmatrix} V_1 \\ I_1 \end{bmatrix} = \begin{bmatrix} A & B \\ C & D \end{bmatrix} \begin{bmatrix} V_2 \\ I_2 \end{bmatrix} \tag{1}$$

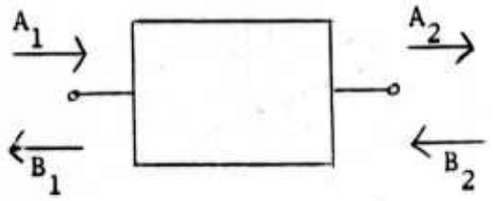

$$\begin{bmatrix} A_1 \\ B_1 \end{bmatrix} = \begin{bmatrix} e^{\gamma_1} & 0 \\ 0 & e^{\gamma_2} \end{bmatrix} \begin{bmatrix} A_2 \\ B_2 \end{bmatrix} \tag{2}$$

$$A = \frac{\sqrt{R_{i2}}}{2Z_{i2}} \quad (V + Z_{i2}\, I)$$

$$B = \frac{\sqrt{R_{i1}}}{2Z_{i1}} \quad (V - Z_{i1}\, I)$$

For convenience in measurements, the scattering parameters have been used as defined in (3).

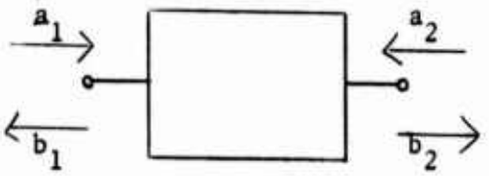

$$\begin{bmatrix} b_1 \\ b_2 \end{bmatrix} = \begin{bmatrix} S_{11} & S_{12} \\ S_{21} & S_{22} \end{bmatrix} \begin{bmatrix} a_1 \\ a_2 \end{bmatrix} \tag{3}$$

$$a_{\substack{1 \\ 2}} = \frac{1}{2\sqrt{R_o}} \left(V \pm R_o I\right)$$

$$b_{\substack{1 \\ 2}} = \frac{1}{2\sqrt{R_o}} \left(V \mp R_o I\right).$$

In the case of the monopole-slot, the structure is reciprocal and symmetrical and the following simplifications result:

Reciprocal	Symmetrical
$AD - BC = 1$	$A = D$
$Y_1 = Y_2$	$Z_{i1} = Z_{i2}$
$S_{21} = S_{12}$	$S_{11} = S_{22}$

Finally, equivalent network representations are also useful. For example, the A B C D matrix of a T network is given by

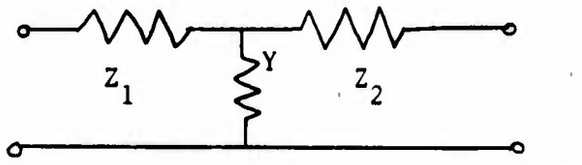

$$\begin{bmatrix} 1 + Z_1 Y & Z_1(1 + Z_2 Y) + Z_2 \\ Y & 1 + Z_2 Y \end{bmatrix} \tag{4}$$

Note that when Y = 0 this matrix becomes

$$\begin{bmatrix} 1 & Z_1 + Z_2 \\ 0 & 1 \end{bmatrix} \tag{5}$$

and when $Z_1 = 0$, $Z_2 = 0$ it becomes

$$\begin{bmatrix} 1 & 0 \\ Y & 1 \end{bmatrix} \tag{6}$$

Hence, inspection of the A B C D matrix indicates how well a given two-port can be represented by a single series or shunt element.

The scattering parameters measured for the slot and monopole individually, when converted to A B C D matrix form, indicate that the slot is predominantly a series load; the monopole, a shunt load, as is expected. Furthermore, since each is a multiply-resonant device, it can be represented approximately by a lossless transmission line stub with appropriate termination and a resistance which is added to simulate the effect of the radiation. Hence, an approximate equivalent circuit for the monopole-slot antenna is as shown in Figure 2. The series arm has been divided into two parts to maintain the symmetry of the circuit. When $R_s/R_o = G_s/G_o$ (condition of complementarity), the image impedance of this two port network is given by

$$Z_i = \sqrt{\frac{B}{C}} = \left[\frac{R_o}{G_o} \left[2 + (R_o G_o)^{-1} \left(\frac{R_s}{R_o} - j \operatorname{ctn} \theta \right)^{-2} \right] \right]^{\frac{1}{2}} \tag{7}$$

and the propagation factor is

$$\gamma = \ell n \left\{ 1 + ZY + \sqrt{ZY(2 + ZY)} \right\} \tag{8}$$

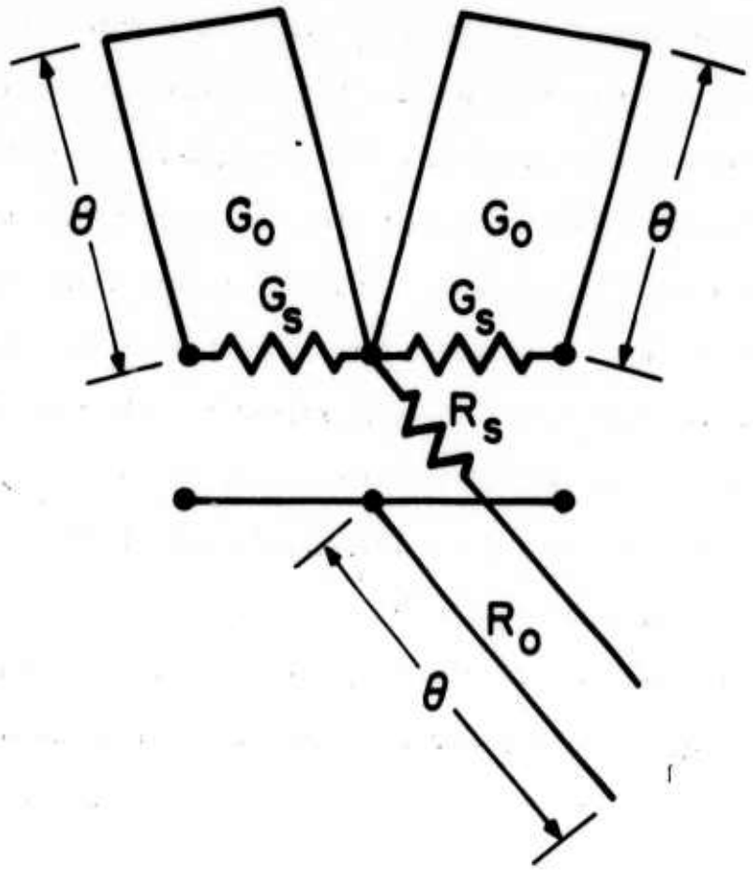

Figure 2. Approximate equivalent circuit for monopole-slot antenna.

where

$$Z = (G_s + jG_o \text{ ctn } \theta)^{-1}$$

$$Y = (R_s + jR_o \text{ ctn } \theta)^{-1}.$$

Figures 3 and 4 show computed plots of Z_i and γ for a particular set of parameters for the circuit of Figure 2. It is observed that the image impedance behavior resembles that of a lossy low-pass filter, the image impedance remaining relatively constant with frequency below the first resonance of the stubs. Hence, when terminated in the image impedance, the input impedance should remain relatively constant also. Thus, the problem of impedance stability is largely solved by this type of network, as has long been recognized in filter design. However, the present application calls for maximizing the loss (radiation) in the two-port rather than minimizing it as in the filter application. It is thus important that the real part of γ be large to prevent low efficiency in the transmitting case (due to power delivered to the termination). Assuming a matched system ($S_{11} = 0$), the efficiency is given by

$$\varepsilon = 1 - e^{-2\alpha} = 1 - |S_{21}|^2. \qquad \gamma = \alpha + j\beta \tag{9}$$

Concentric circles on the Smith Chart are constant efficiency contours with regard to the S_{21} data.

III. Experimental Results

A. Impedance Characteristics

In terms of scattering parameters, the condition of complementarity is

$$S_{11}(\text{monopole}) = -S_{11}(\text{slot}) \tag{10}$$

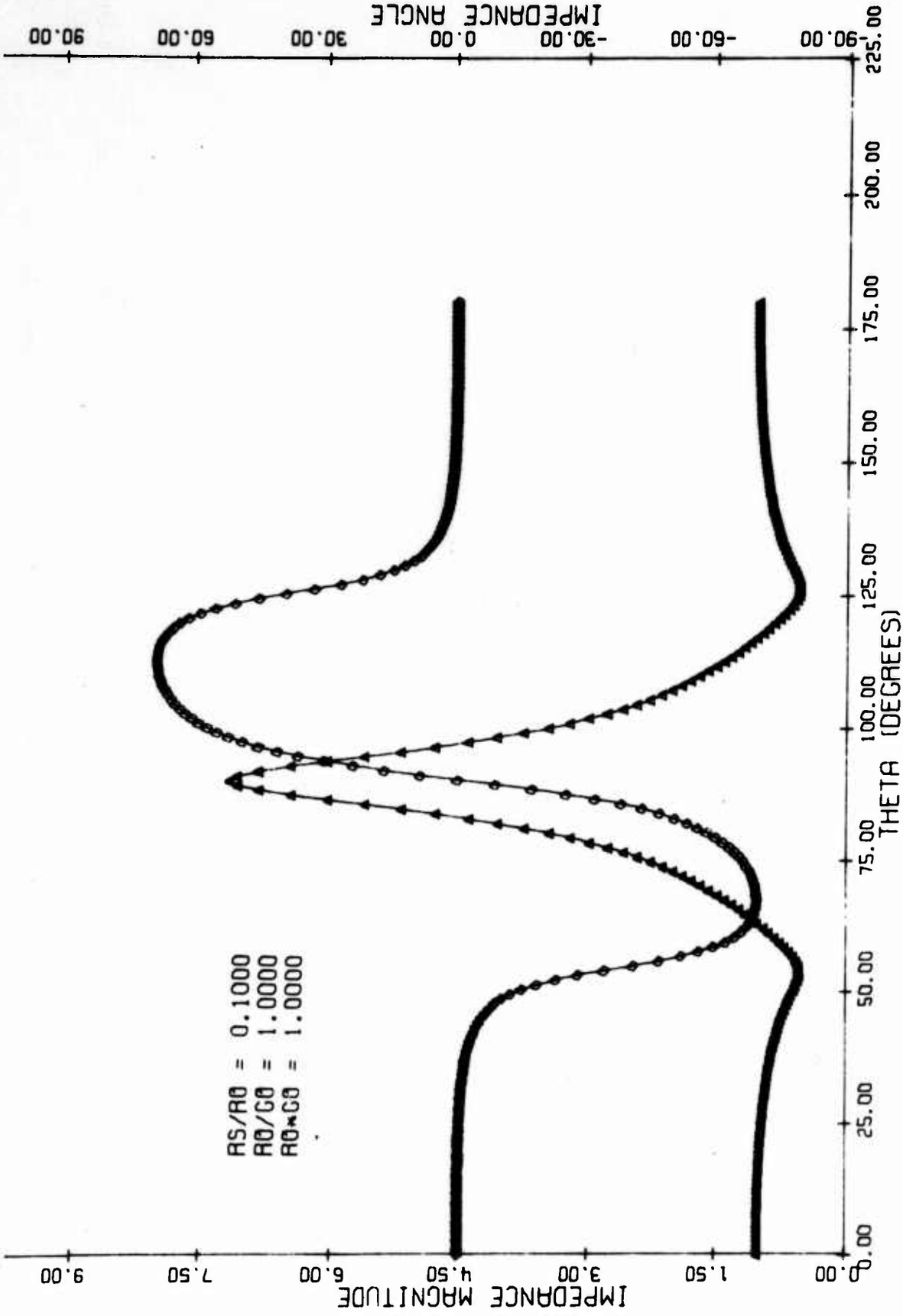

Figure 3. Computed image impedance versus frequency for circuit of Figure B.15.

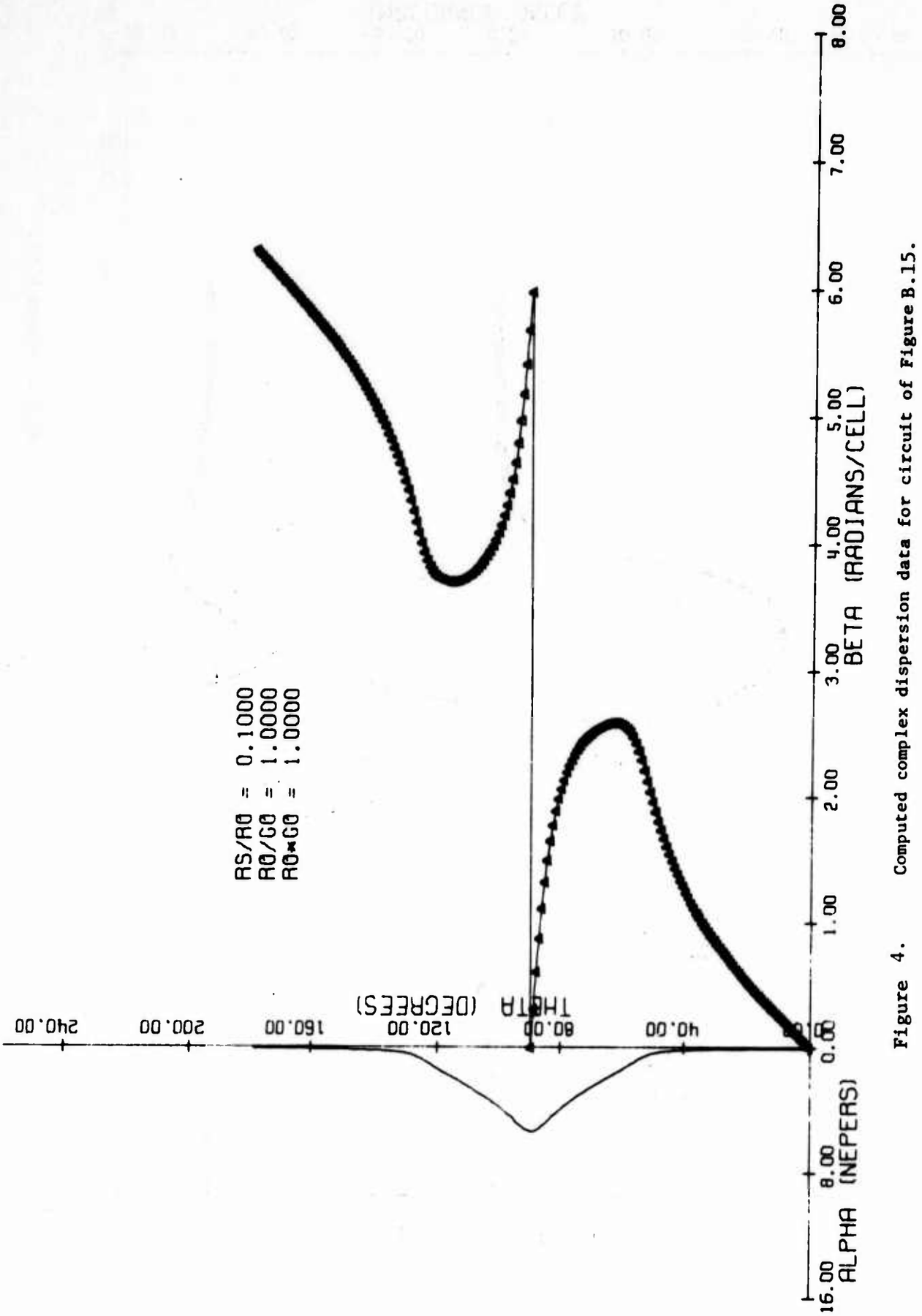

Figure 4. Computed complex dispersion data for circuit of Figure B.15.

Figure 5 shows how the individual series and shunt arms of the network of Figure 2 satisfy this condition. It is desirable that the two arms be complementary with respect to 50-ohms for connection to external circuitry having that impedance. Hence, the measurements have consistently been made in a 50-ohm system and are represented as such on all Smith Charts shown.

Figure 6 shows the S_{11} versus frequency of a cavity-backed slot with microstrip feed as shown in Figure 1, but with no monopole. The principal effect of the cavity is a shift in resonant frequency which is typical of tuning by means of a shorted stub across the slot. The slot length corresponds to a half-wavelength at about 845 MHz. A cavity depth of one-quarter guide wavelength ($\lambda g/4$) would affect the slot resonance to a minimum degree since the short-circuit is transformed to a high impedance across the slot. This is found to be in close agreement with the measured S_{11} which displays zero phase at 845 MHz when the cavity is $\lambda g/4$ deep. However, the result of more practical interest is that the depth of the cavity can be made very much smaller without appreciably altering the impedance level (related to magnitude of S_{11}) at resonance. The principal effect of reducing the cavity depth is a shift in resonant frequency as shown in Figure 7. The minimum depth of 1.5 cm was fixed by the dimensions of finger stock on the adjustable cavity bottom. Even at this small depth the slot creates a significant discontinuity on the stripline, the slot resistance at resonance remaining approximately 400 ohms. These results are considered significant since they indicate the possibility of constructing low-silhouette antennas which are very thin and therefore do not protrude excessively on either side of the ground plane.

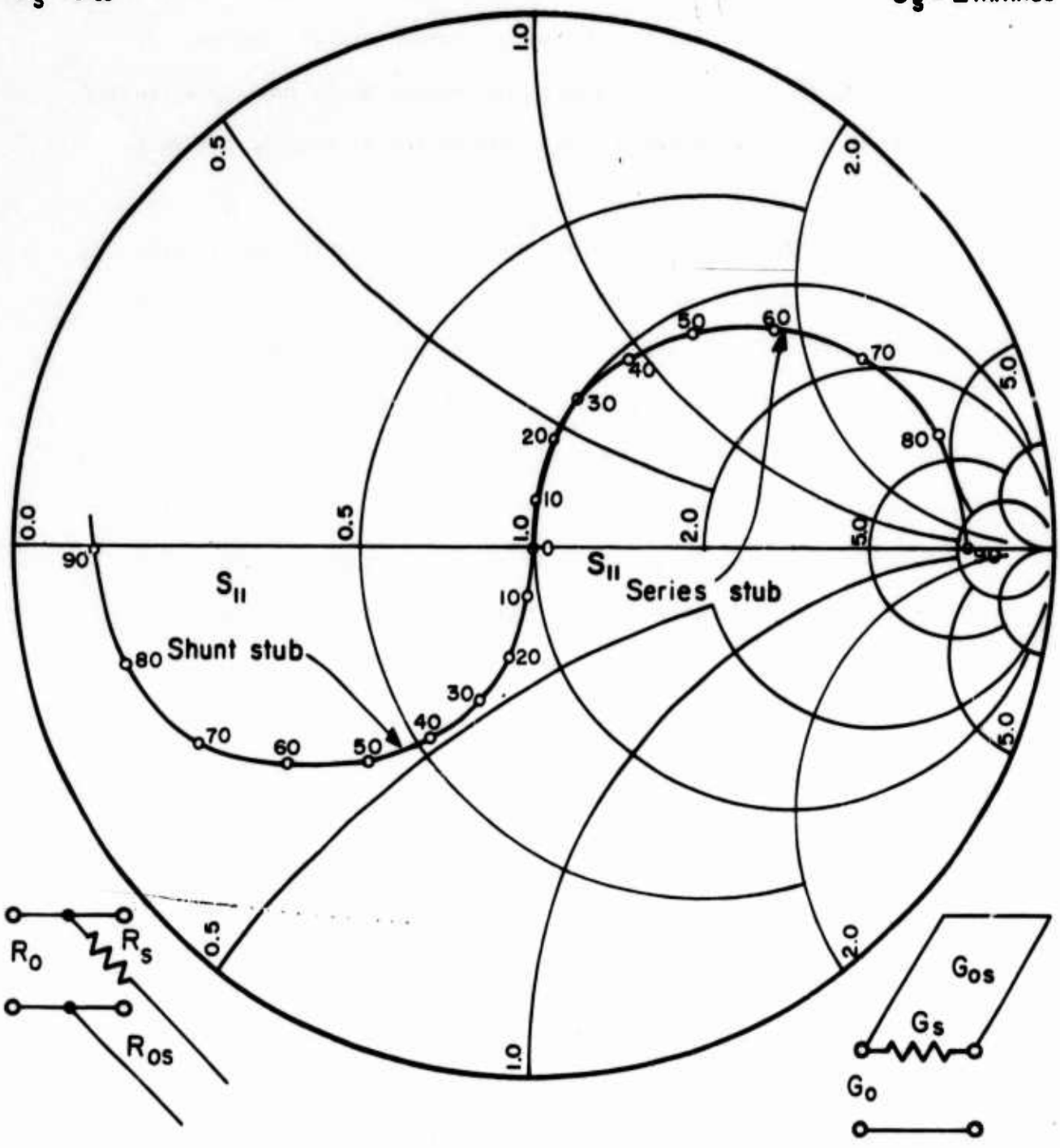

Figure 5. S_{11} versus electrical length (degrees) for a series shorted stub and shunt open stub.

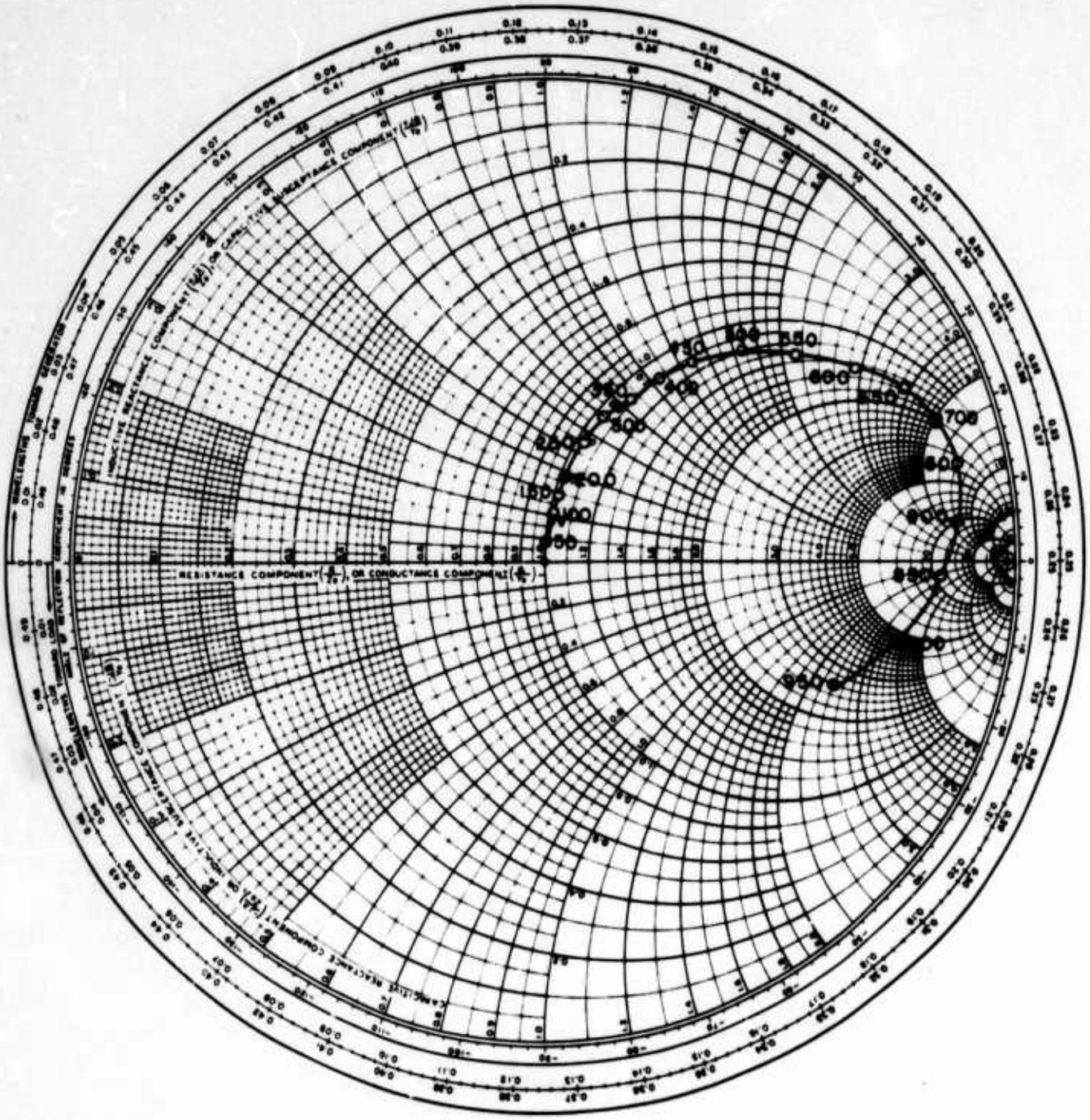

Figure 6. S_{11} versus frequency (MHz) for slot backed with cavity 11.8 cm deep.

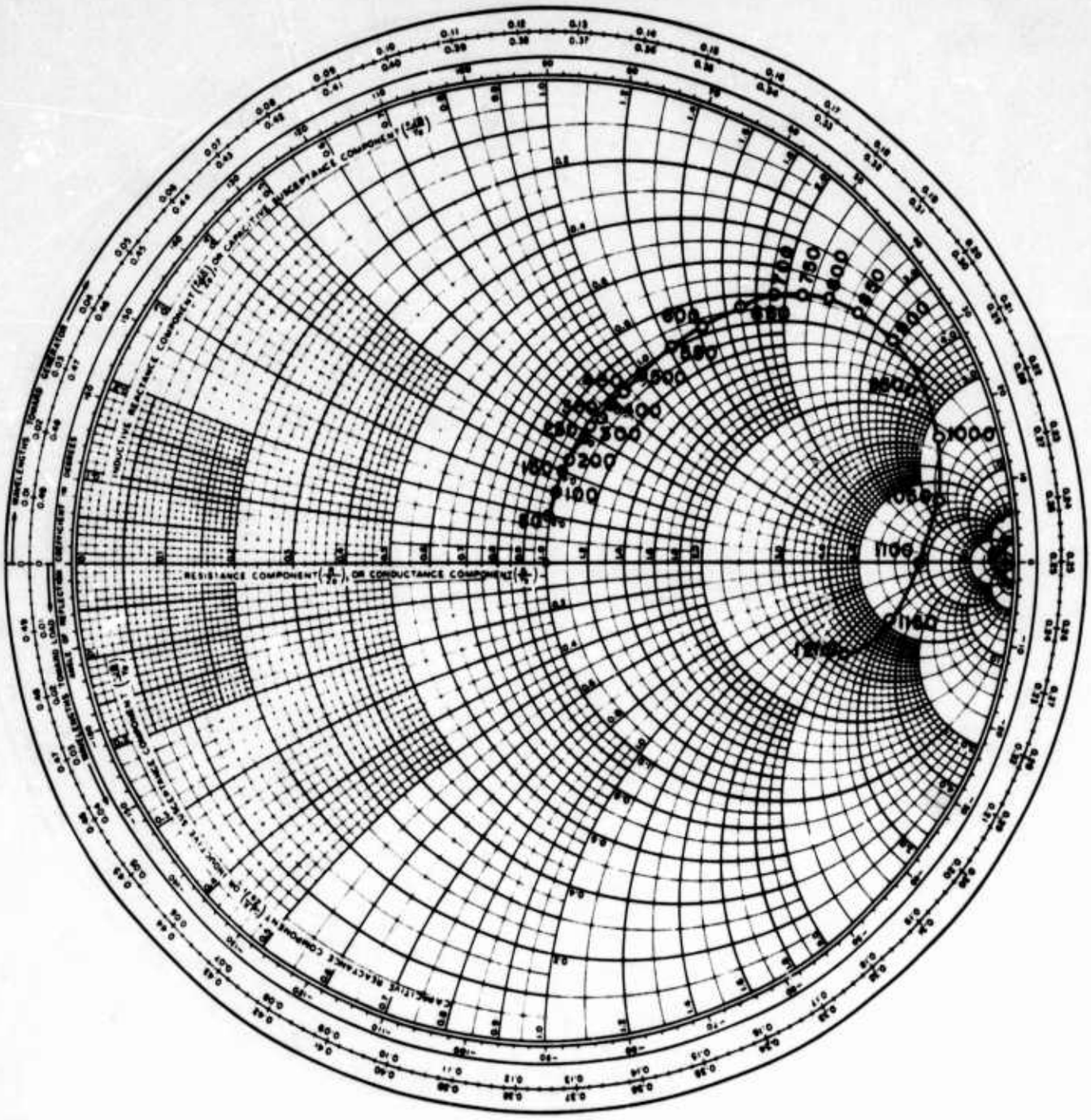

Figure 7. S_{11} versus frequency (MHz) for slot backed with cavity 1.5 cm deep.

It was apparent from measured data for linear monopoles that Equation (10) could not be satisfied over a wide band of frequencies by combining such monopoles with the previously measured shallow-cavity slots. The monopole reactance is much higher than the slot reactance at the lower frequencies (below 700 MHz) and the slot resistance near resonance is greater than 50 ohms by a larger factor than the monopole resistance at resonance is less than 50 ohms.

It thus appears that linear monopoles alone cannot be made to track, in a complementary impedance sense, the cavity-backed slot. The principal difficulty with the linear monopole is the high reactance at low frequencies. Various alternate antenna configurations were investigated with the view toward reducing the reactance and the resistance at resonance. The best results have been obtained with conical monopoles. Figure 8 shows the measured S_{11} data for a 90° conical monopole 3.8 cm high. Note that the low-frequency reactance has been reduced to the point where the S_{11} locus is off the center of the chart at 100 MHz and the resonant frequency is about 900 MHz. Furthermore, the resistance at resonance has been reduced to approximately 15 ohms. This particular monopole would therefore apparently satisfy very well the complementary condition with the cavity-backed slot, even one which has a small cavity depth. The measured S_{11} data for the conical monopole-slot are shown in Figure 9 and indicate that a good match to 50 ohms is indeed obtained from very low frequencies (all the way down to $\omega = 0$ even) up through 2000 MHz. Hence, it has been demonstrated that it is possible to design an antenna with very broadband impedance by using the complementary principle applied to a monopole-slot. However, no attempt was made tc minimize the power delivered to the matched

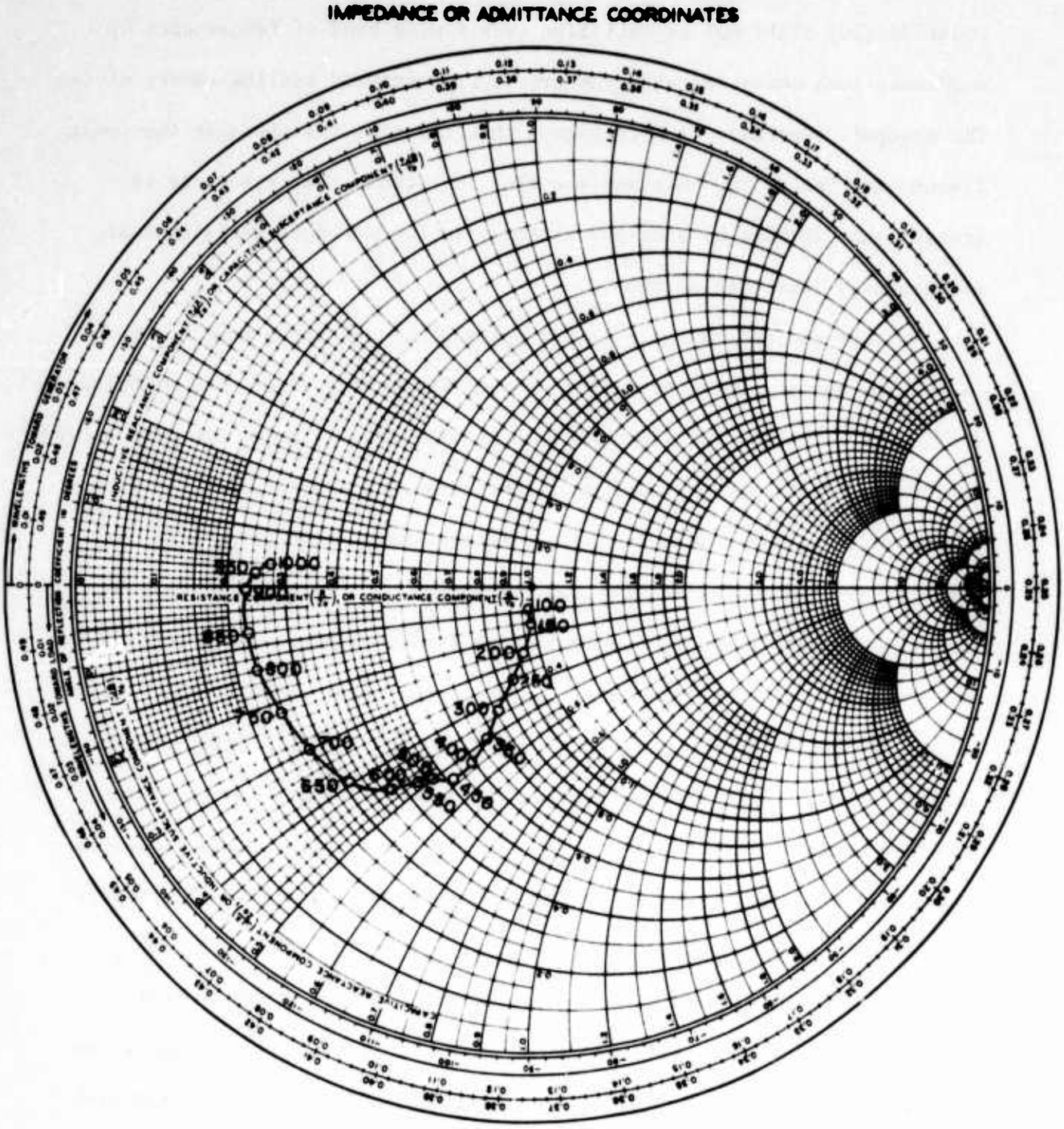

Figure 8. S_{11} versus frequency (MHz) for 90° conical monopole 3.8 cm high.

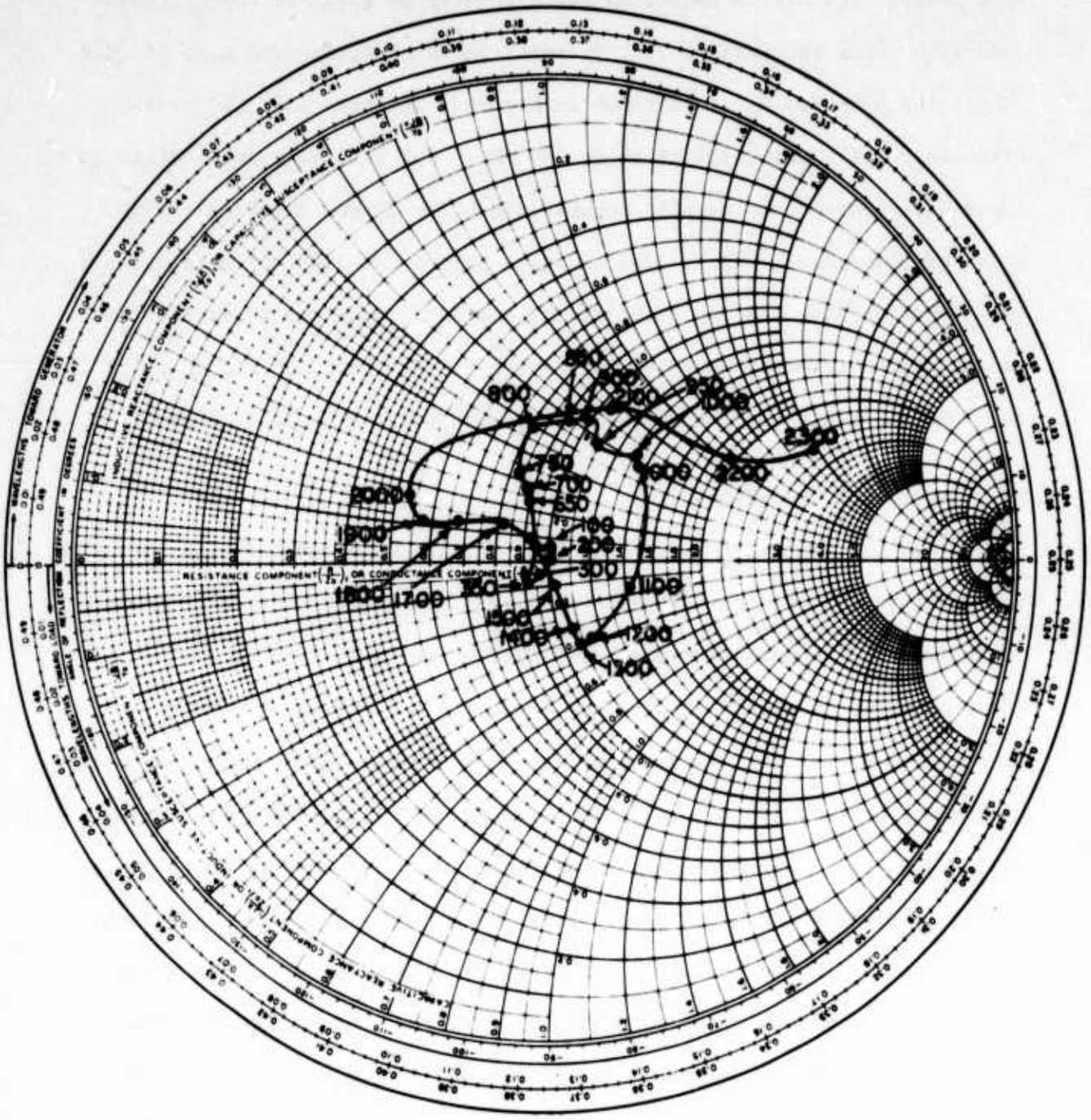

Figure 9. S_{11} versus frequency (MHz) for combination of 90° conical monopole (3.8 cm high) and 17.8 cm slot with 1.9 cm depth of cavity.

load in this antenna. Hence, it is not likely that the maximum efficiency will remain high over a bandwidth anywhere near as great as the impedance bandwidth since the antenna is very small in wavelengths over most of that band. The measured S_{21} data shown in Figure 10 indicate that the maximum efficiency falls below 10% at about 600 MHz. For receiving applications, lower efficiencies are usually permissible below 30 MHz due to the high level of atmospheric noise. The two data points for 1000 MHz in Figures 9 and 10 demonstrate the repeatability of the data. One point for 1000 MHz and those for lower frequencies were taken at one time; the second point for 1000 and those for frequencies above were taken at a later time.

B. Directional Properties

Since the radiation pattern of the slot in the azimuthal plane is a figure-eight with two out-of-phase lobes and the pattern of the monopole in that plane is omnidirectional, the possibility exists of combining these patterns to obtain a cardioid. Thus, the monopole-slot may have appreciable directivity in spite of its small size. Furthermore, exciting one port of the monopole-slot will produce a cardioid with maximum in one direction whereas exciting the other port will produce the same pattern reflected through a plane of symmetry of the antenna. That such performance is indeed obtainable is shown in Figure 11 where an azimuthal pattern in the ground plane is shown for excitation of each port. The application to amplitude-comparison DF systems is obvious. Ordinarily achieving such directivity over a wide band is associated with radiators which are much larger in size than the monopole-slot antenna. The frequency stability of the radiation pattern for the conical monopole-slot is illustrated in Figure 12. The unidirectional pattern is shown to be maintained from 200 to 2000 MHz, a 10:1 band.

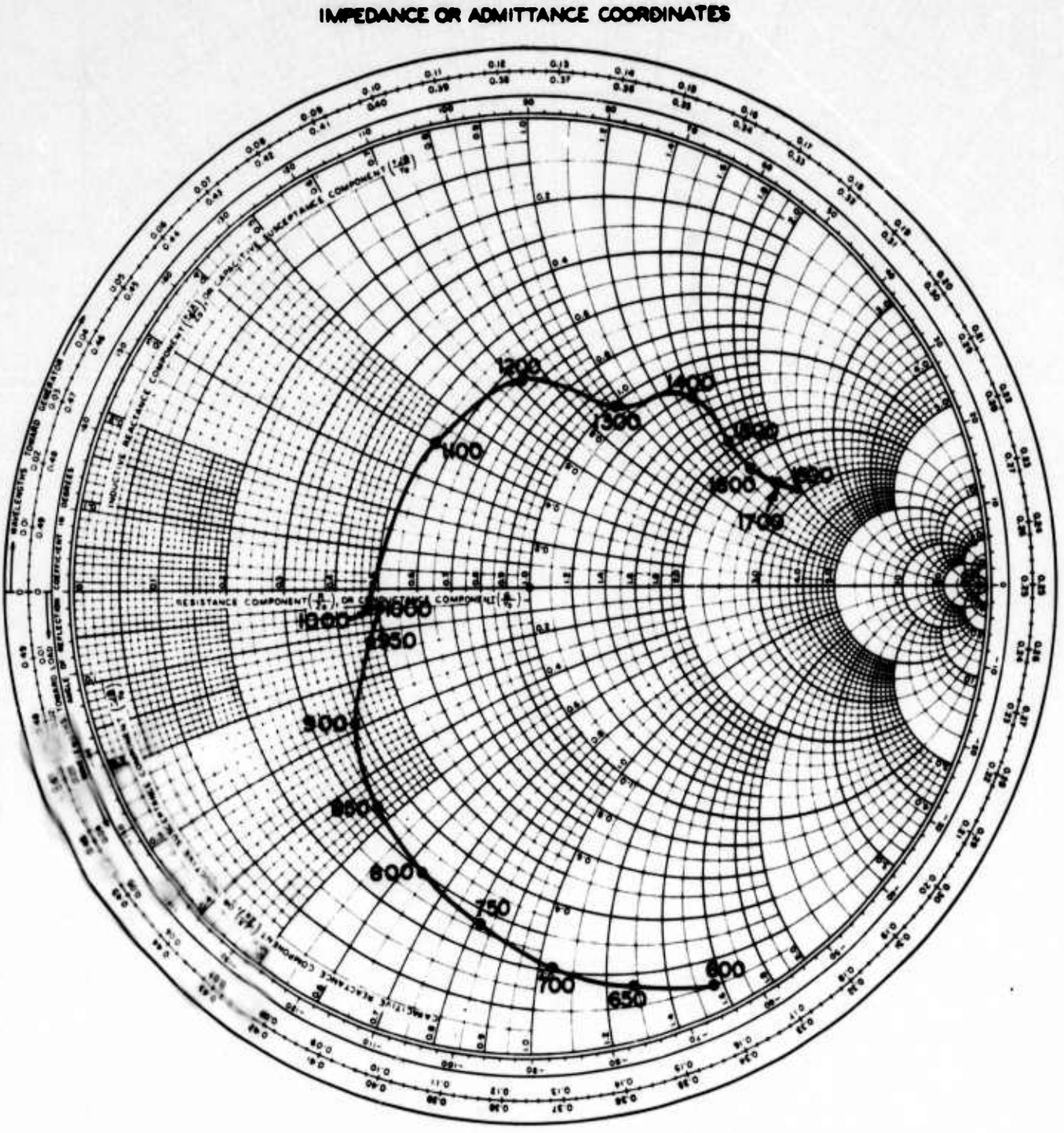

Figure 10. S_{21} versus frequency (MHz) for combination of 90° conical monopole (3.8 cm high) and 17.8 cm slot with 1.9 cm depth of cavity.

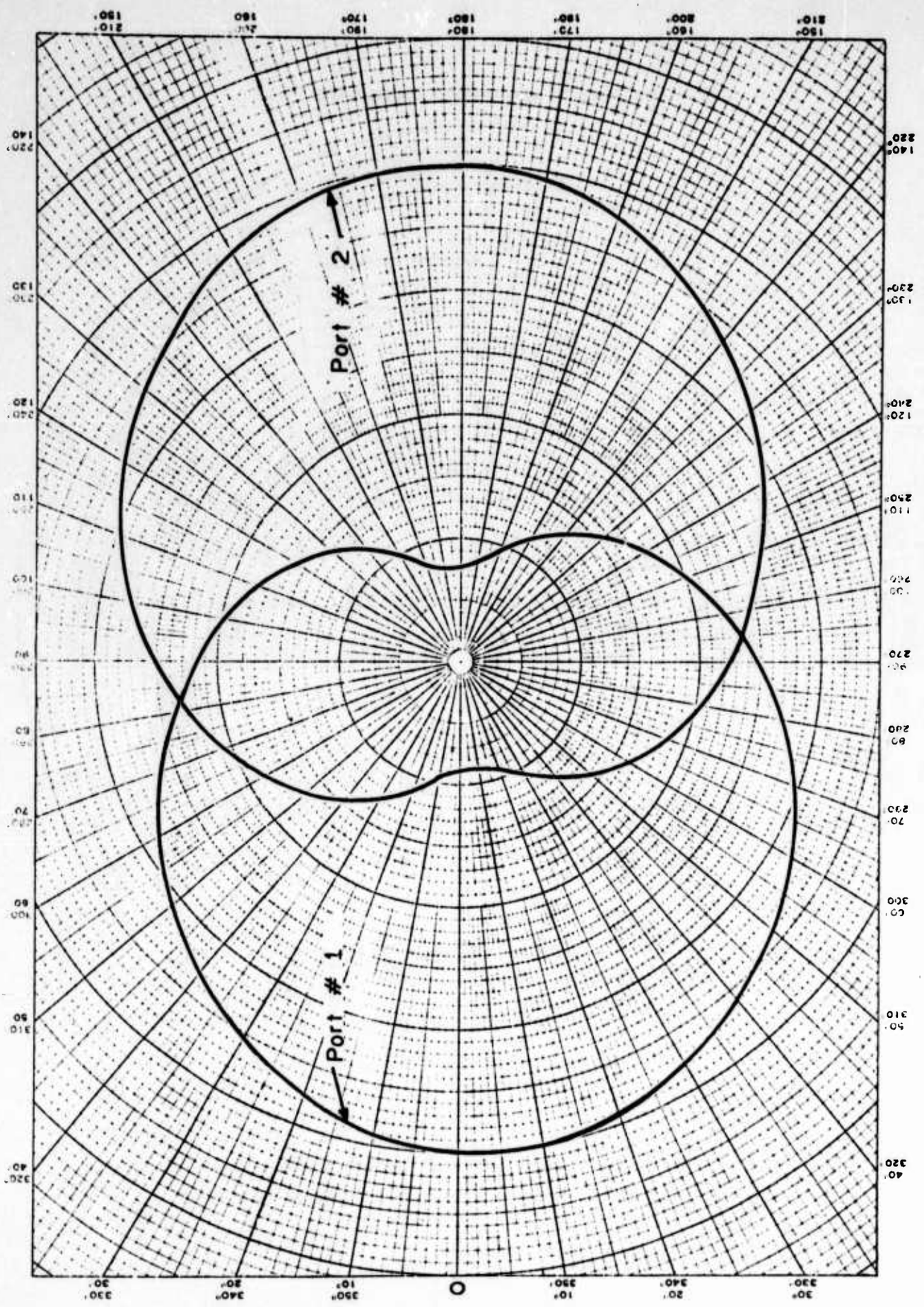

Figure 11. Radiation patterns in azimuthal (ground) plane of a monopole slot antenna.

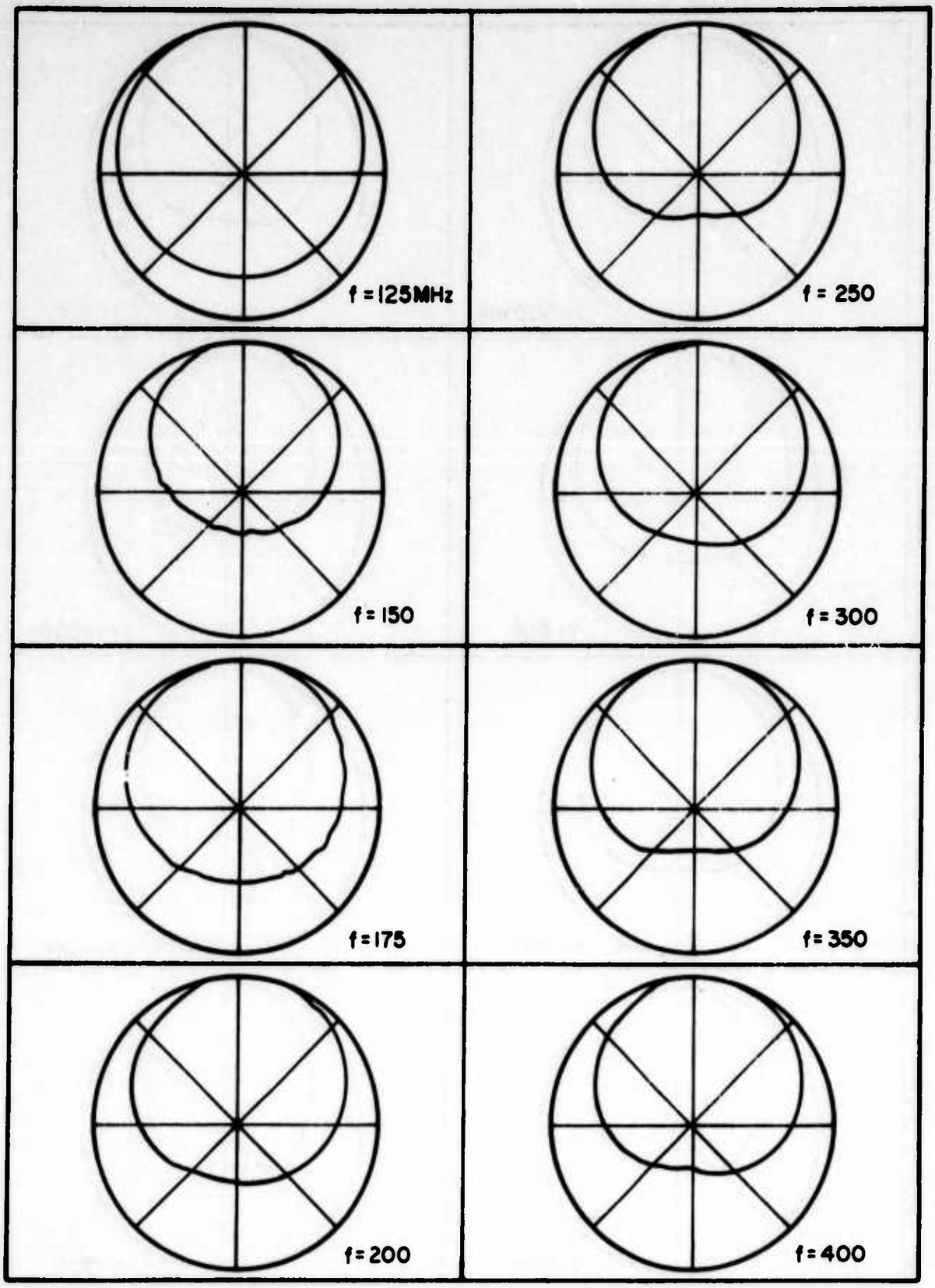

Figure 12 (a). Azimuthal (H-plane) patterns of monopole-slot antenna of Figures B.31 and B.32.

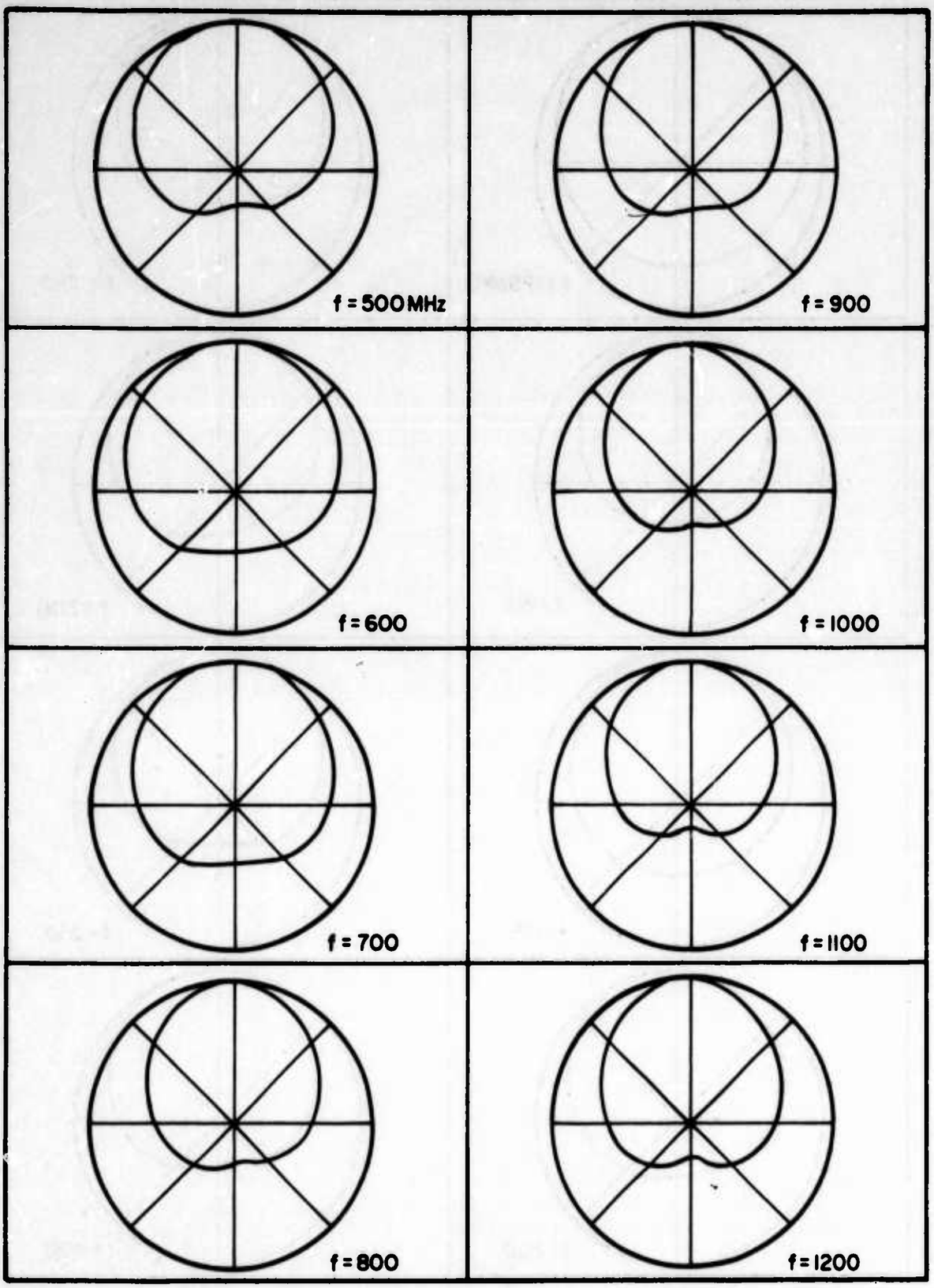

Figure 12 (b). Azimuthal (H-plane) patterns of monopole-slot antenna of Figures B.31 and B.32.

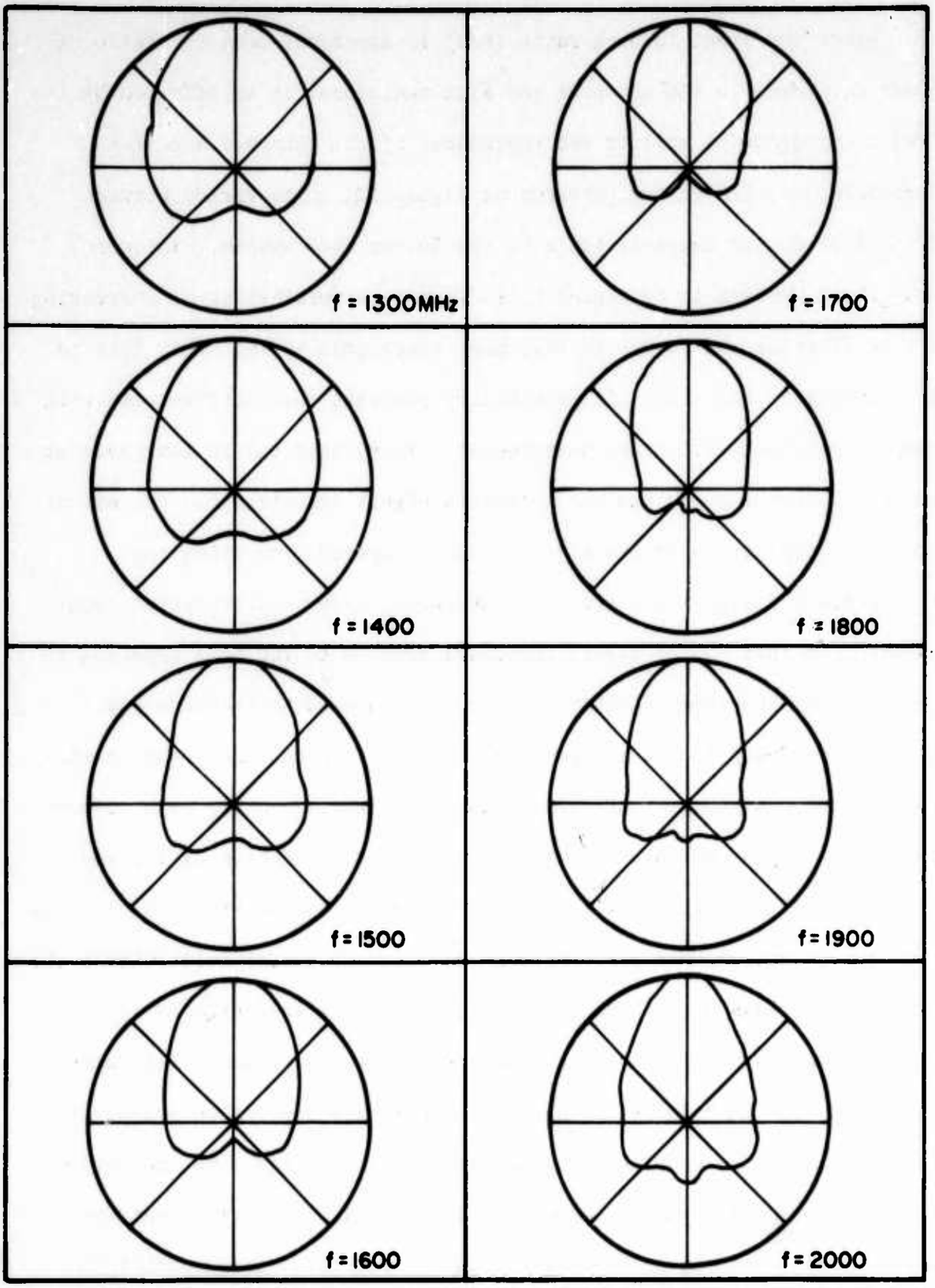

Figure 12(c). Azimuthal (H-plane) patterns of monopole-slot antenna of Figures B.31 and B.32.

Since the front-to-back ratio (F/B) is dependent upon the ratio of power delivered to the monopole and slot radiators, it is affected by the feeder impedance as well as the impedances of the monopole and slot. Therefore, the F/B of the patterns of Figure 12, which varies between 7.5 and 25 db, is characteristic of the 50-ohm feed system. The monopole field appears to be dominant, indicating a possibility of increasing F/B by altering the feeder so that more power goes to the slot, less to the monopole. Checking this possibility presents some difficulties with respect to construction and measurement. To prevent the 50-ohm level at input and output ports and yet provide a higher impedance for the microstrip as it passes over the slot, a double-tapered line using the Klopfenstein design was carefully constructed using photo-etching techniques. An increase of feeder impedance from 50 to 100 ohms appeared to be practical and representative of the value needed to increase F/B. However, once the feeder impedance has been increased, the monopole-slot combination previously used will no longer be complementary with respect to the new impedance level. This then requires a redesign of the radiating elements so the Equation (10) continues to be satisfied, since this also has an effect upon F/B. Because of these practical difficulties the matter of increasing F/B has not been exhaustively investigated at this time. However, two models have been constructed using the cavity with 1.9 cm depth. In both cases, 30-degree conical monopoles were found to better satisfy the complementary condition. In one case, the monopole height was made 4.0 cm; in the other, 4.9 cm. The results of pattern measurements on these antennas are shown in Figure 13 along with F/B data for the original monopole-slot. It is seen that F/B greater than

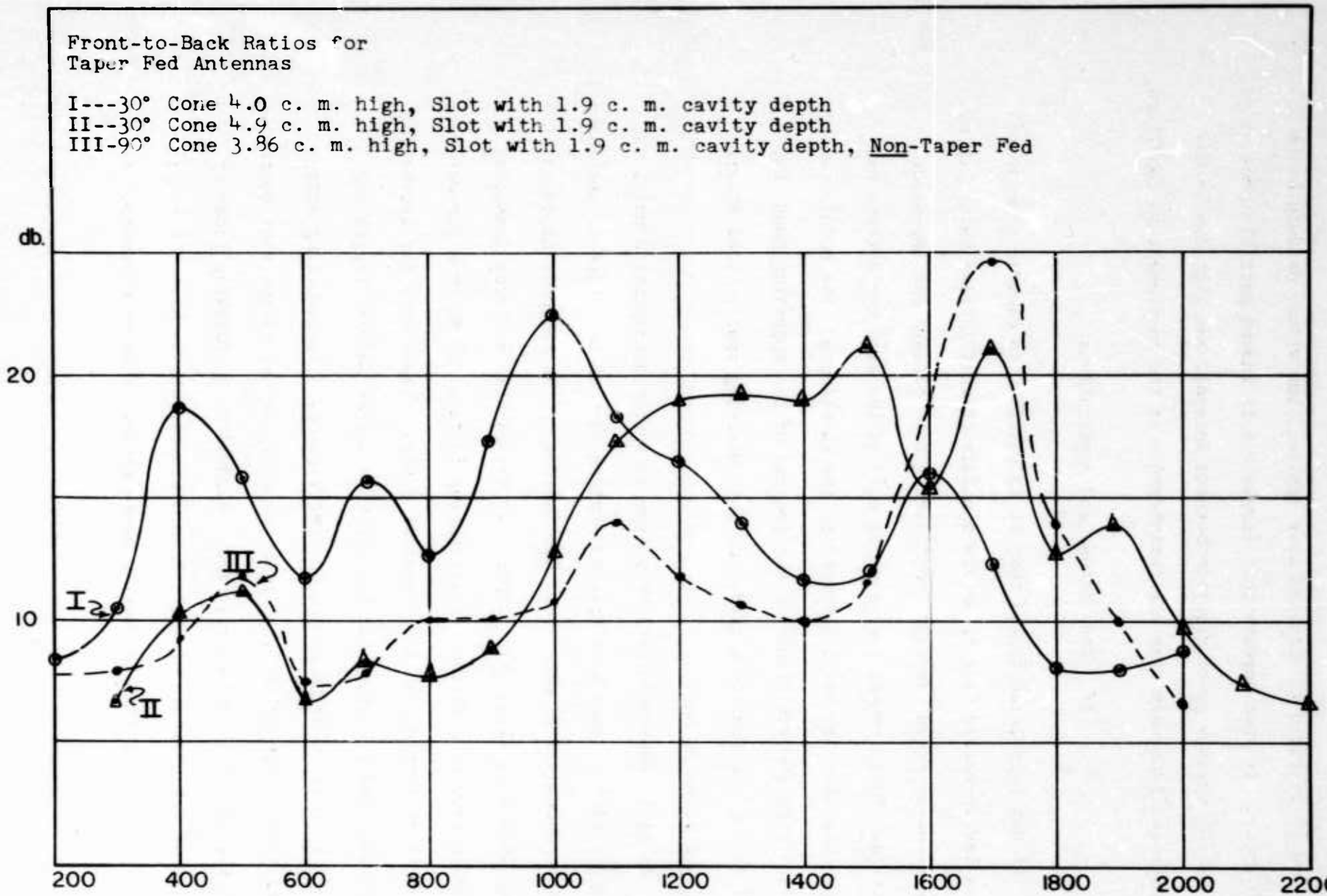

Figure 13: Front-to-back ratios for several conical-monopole/slot antennas.

previously observed is obtained over limited, but wider, bandwidths in both cases. It thus appears that larger F/B is indeed possible providing the optimum power division between monopole and slot can be obtained simultaneously with the satisfaction of the complementary condition.

IV. Conclusions and Applications

It has been demonstrated that it is possible to combine a monopole and a cavity-backed slot to obtain a unidirectional antenna which has an exceptionally broad bandwidth considering both pattern and impedance criteria. Furthermore, over a major part of the band the antenna has dimensions that are small compared to the wavelength. The models tested to date have low efficiency at the low end of the operating band, but this is not necessarily a hindrance for receiving applications at frequencies below 30 MHz.

An amplitude-comparison DF system is easily accomplished using the monopole-slot antenna by simply connecting each of the ports to one channel of a twin-channel DF receiver. Utilization of the monopole-slots in large-aperture, circularly-disposed arrays is also believed feasible, although requiring further investigation in terms of optimum parameters for best performance in an economical design. Techniques for increasing efficiency and F/B even when the cavities are of reduced length and extremely shallow depth should be investigated. The resulting arrays would have a form quite like those currently in use except that no reflecting screen should be required. Bandwidths approaching those of arrays of log-periodic elements should be possible without the complications resulting from the moving phase center of those elements. It

seems unlikely that the high efficiency which is possible with log-periodics will ever be realized across comparable operating bands. However, for receiving applications in the HF band, this is not necessarily a requirement for a successful system.

ERRATA

1. ANTENNAS

In Paper 1.2 "The Application of Linear Arrays to Direction-Finding"

by

J. D. Dyson and A. D. Bailey

Department of Electrical Engineering
University of Illinois
Urbana, Illinois 61801

page 20 is page 21, and page 21 is page 20.

The Application of Linear Arrays to Direction-Finding*

J. D. Dyson and A. D. Bailey

Department of Electrical Engineering
University of Illinois
Urbana, Illinois 61801

I. Introduction

The successful application of large antenna arrays in the field of radio astronomy suggests that similar systems might be used for HF radio direction finding when the direction of arrival of signals in the vicinity of the zenith is of concern. Any practical size array will result in less resolution at H.F. than that now achievable in radio astronomy applications, however, an order of magnitude or more change in resolution would still provide performance which is consistent with present direction finding requirements.

Under a contract with the Army Material Corps, the University of Illinois has been studying some of the characteristics and limitations of moderate size arrays when used for the determination of arrival information on high angle waves in the H.F. range of frequencies. We have chosen as a model for study, a cross configuration of two linear arrays of a length such that they would form the diagonals of a square forty-acre field, i.e., a length of 570 meters. This is equivalent in size to many present day Wullenweber arrays.

It is of interest to consider some basic array theory as applied to the arrays of this size when used from 2 to 32 MHz.

II. Uniform Linear Arrays

The cross array is shown in Figure 1 with its associated coordinate system. The individual elements are represented by circles. We assume

*Presented at the 4th Allerton Conference on Radiolocation Research, Allerton Park, Monticello, Illinois, June 2-4, 1971.

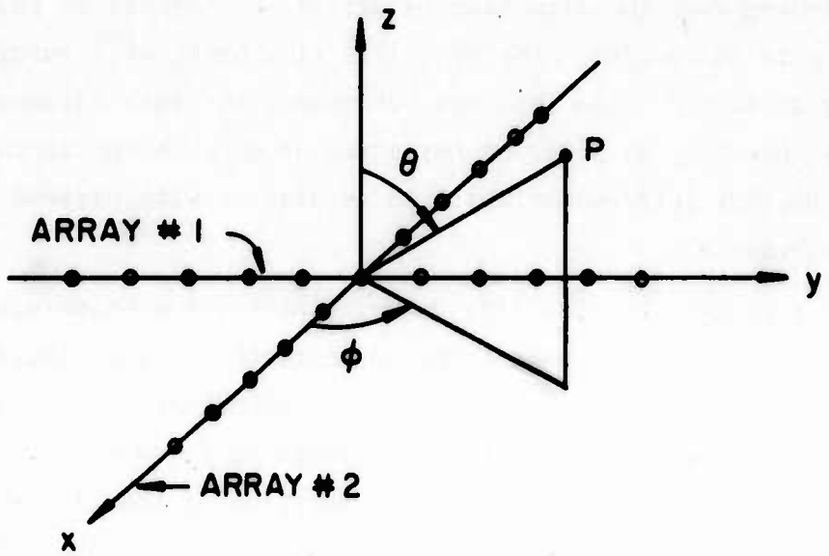

Figure 1. Cross antenna imbedded in associated coordinate system.

that each linear broadside array has a fan beam voltage pattern of several coaxial cones with a plane as the limiting case. The main beam lies in a plane when steered to the zenith, but is a cone for all other declinations.

There are various methods of processing the information which would be available from such a cross-array system. One of the first that comes to mind is the successful phase-switching technique used for array multiplication, as developed by Ryle in 1952[1] and applied to cross arrays in radio astronomy by Mills in 1953.[2] However, it can readily be shown that this technique depends upon the incoherent, uncorrelated nature of radio astronomical signals.[3] For direction finding, the sources are not necessarily uncorrelated, since it is frequently necessary to identify two or more signals arriving from the same source via multi-path propagation. Hence for the present purpose we must look for another data processing scheme.

If we again consider the two beams of these arrays, we note, as shown in Figure 2(a), that the intersection of these beams forms a "pencil beam." This intersection is shown at the zenith in Figure 2(a) and at an angle off the zenith in Figure 2(b). By an appropriate phasing of these two arrays this pencil or intersection beam can be scanned over a major portion of the upper hemisphere. One approach to the determination of the direction of arrival of an incident wave would simply be to determine the orientation of this pencil beam for a maximum response. The resolution of such a technique is a function of the angular width of this intersection beam, and this width is, in turn, a function of the spherical coordinates defining the position of the beam in the hemisphere, and of the wavelength of operation.

To illustrate the change in this intersection beam as a function of orientation, it is possible to calculate the radiation pattern of the two arrays and then plot on a unit hemisphere the null, and the half-power contours of the intersection beam. The null beamwidth is defined to be the angular width between the first nulls on each side of each of the fan beams. In theory this forms a square when the two fan beams are at the zenith. The half-power beamwidth is the angular width at the half-power points of the main beams.

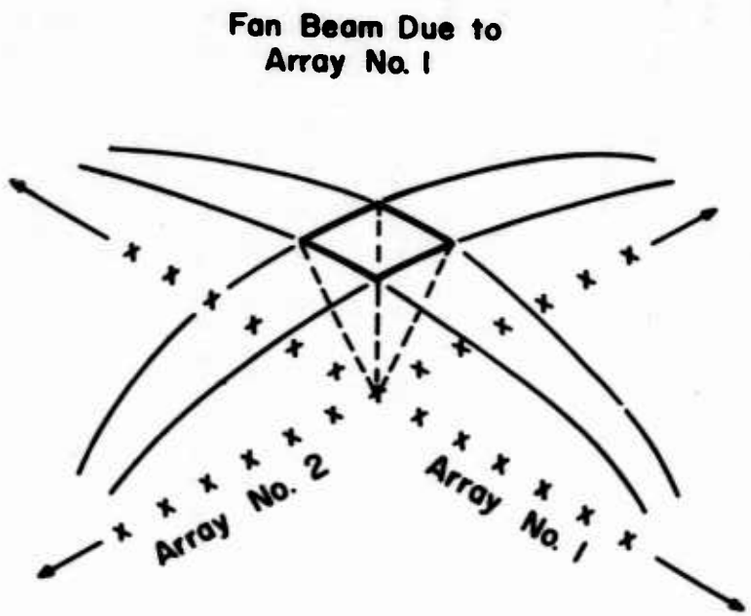

(a) Pertinent to the Unique Intersection of Two Orthogonal Fan Beams.

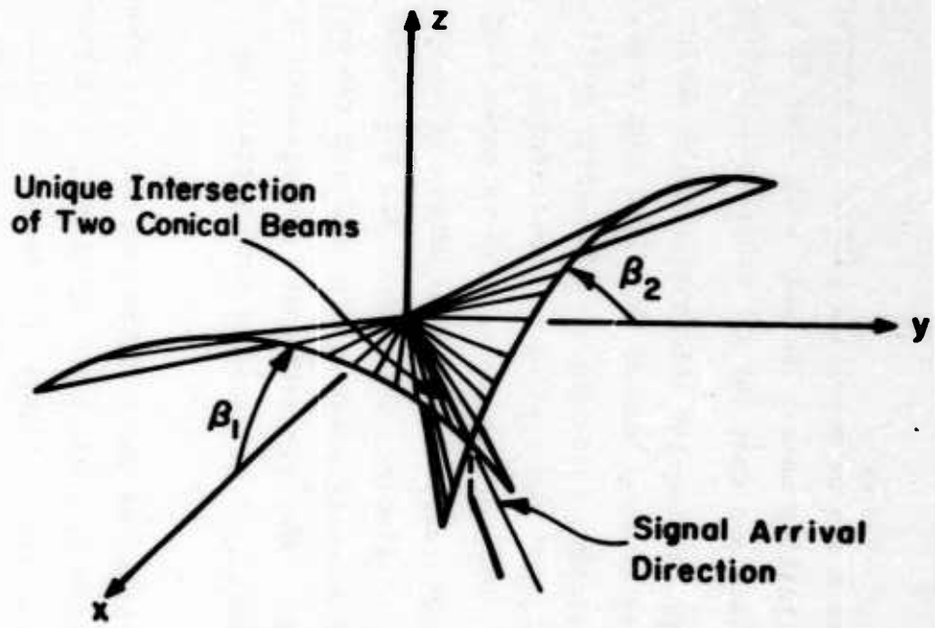

(b) Pertinent to the Unique Intersection of Two Orthogonal Conical Beams.

Figure 2. The cross array geometry.

Assume as an example, 570 meter uniform arrays of isotropic elements, with these elements spaced one-half wavelength apart, which are operated at 6 MHz. The relative size and shape of the intersection beam at seven different orientations is shown in Figure 3.

We note that as the beam is scanned away from the zenith, and in particular as it is scanned away from the plane of the two arrays, the shape of the beam becomes distorted. Thus if the resolution in the determination of the direction of arrival is a function of the beamwidth, this change in pattern shape will place a bound on the maximum permissible angle of scan. Since the pattern shape is a function of the length of the arrays in wavelengths, this bound will also be a function of the frequency of operation. This is dramatically shown in Figures 4 and 5 where the beams for the same example which was considered in Figure 3, are replotted when the arrays are operated at 4 and 2 MHz respectively.

The change in beamwidth of our 570 meter arrays with angle of scan and frequency of operation is shown in Figures 6 and 7.

Several interesting conclusions can be drawn from an inspection of Figures 3 through 7.

1. As frequency increases, both beamwidths decrease.
2. The shape of both contours repeats at ϕ_m = 0°, 90°, 270° and 360°.
3. The contours lose symmetry at any angle other than ϕ_m = 0°, 45°, 90°, 135°, etc.
4. The vertical beamwidths (measured in θ direction) increase with scan angle off the zenith.
5. The beamwidth contours are not centered about the maximum in the θ direction, this asymmetry becoming worse as the angle of incidence increased.
6. For very low frequencies and very large angles of incidence, there is a point where the pattern may not reach a null (c.f. Figure 4).

It should be noted that these figures show the worst cases, since they are for operation at very long wavelengths for this size array, and operation at frequencies above 6 MHz will bring substantial improvement.

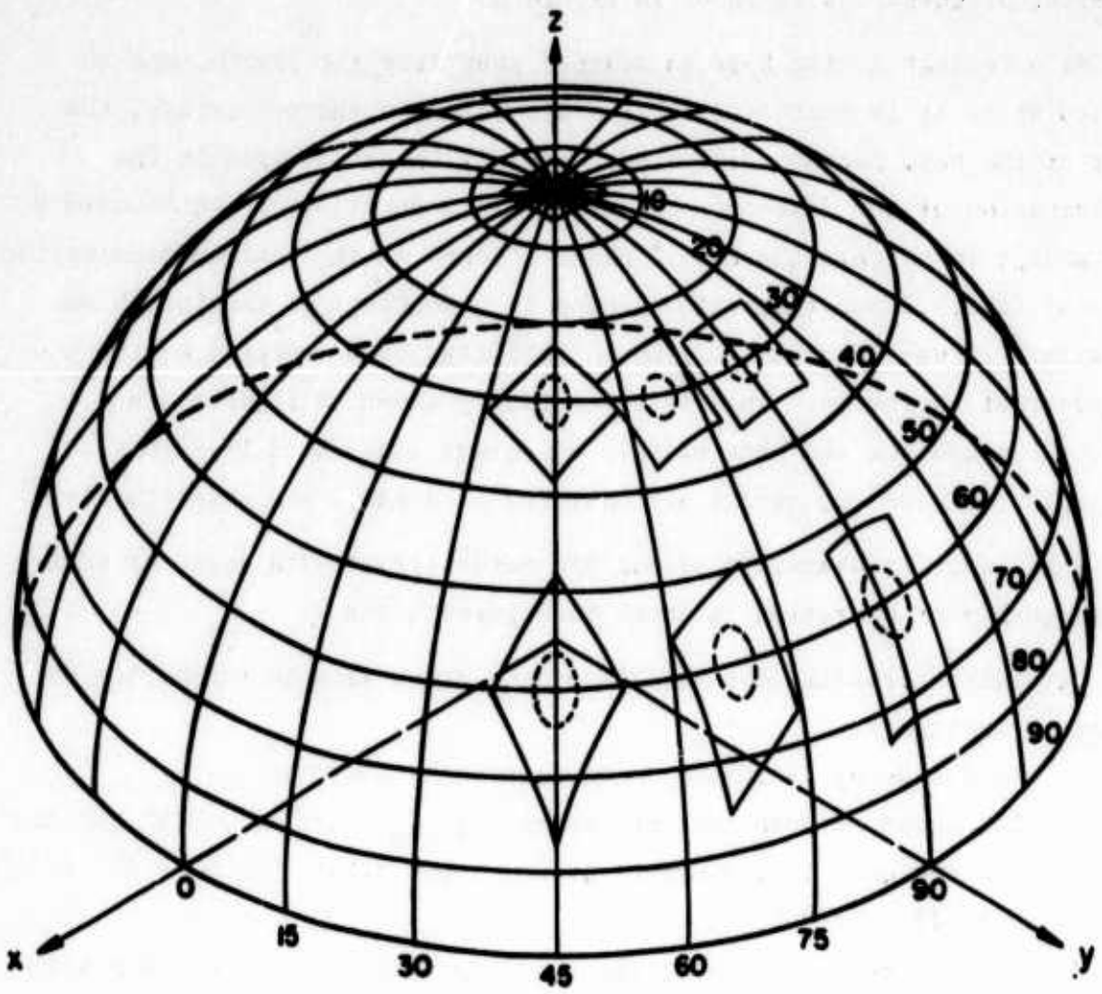

--- Half power contours

—— Null contours

Figure 3. Projection of Half-Power and Null-Beamwidths on the Unit Sphere F = 6 Mc, L = 570 meters

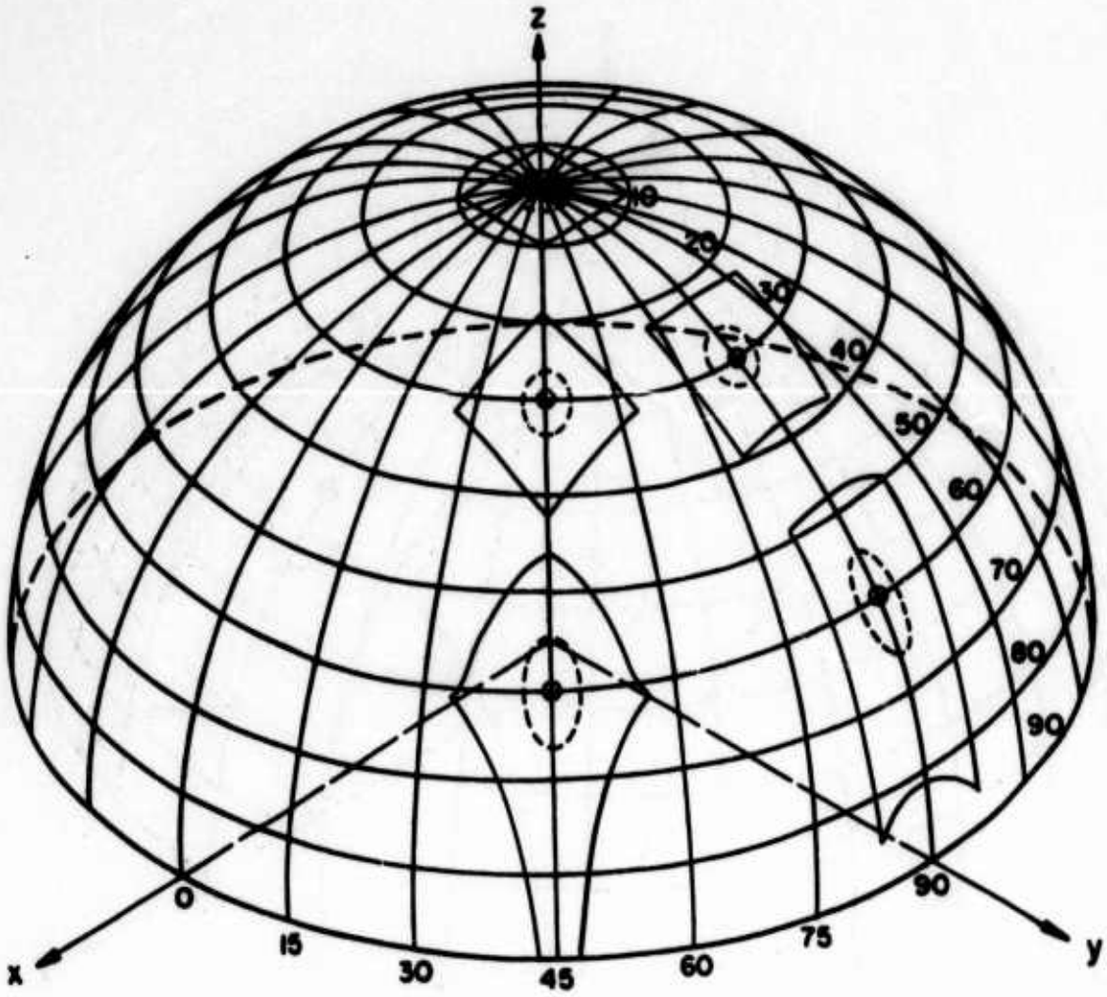

--- 3db contours
——— Null contours

Figure 4. Projection of Half-Power and Null-Beamwidths on the Unit Sphere F = 4 Mc, L = 570 meters

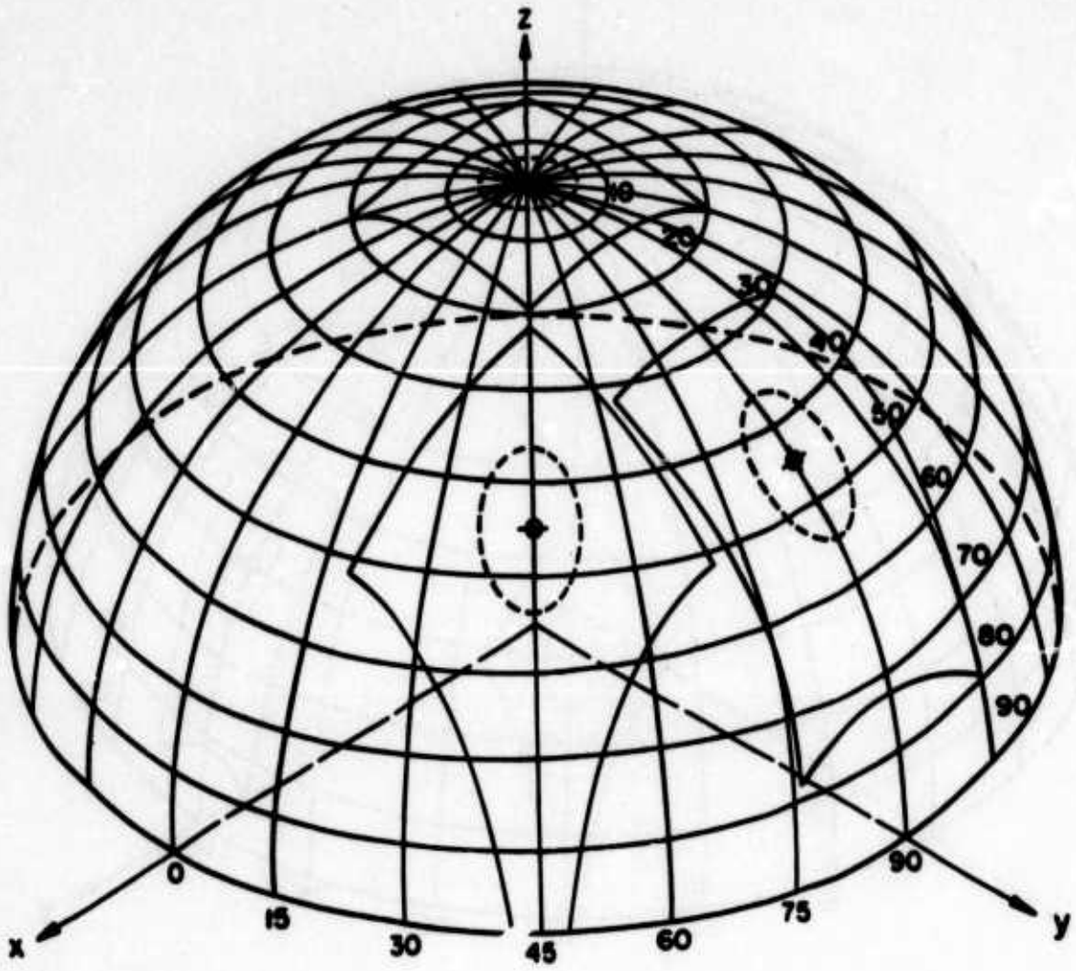

--- 3db contours
—— Null contours

Figure 5. Projection of Half-Power and Null-Beamwidths upon the Unit Sphere F = 2 Mc, L = 570 meters

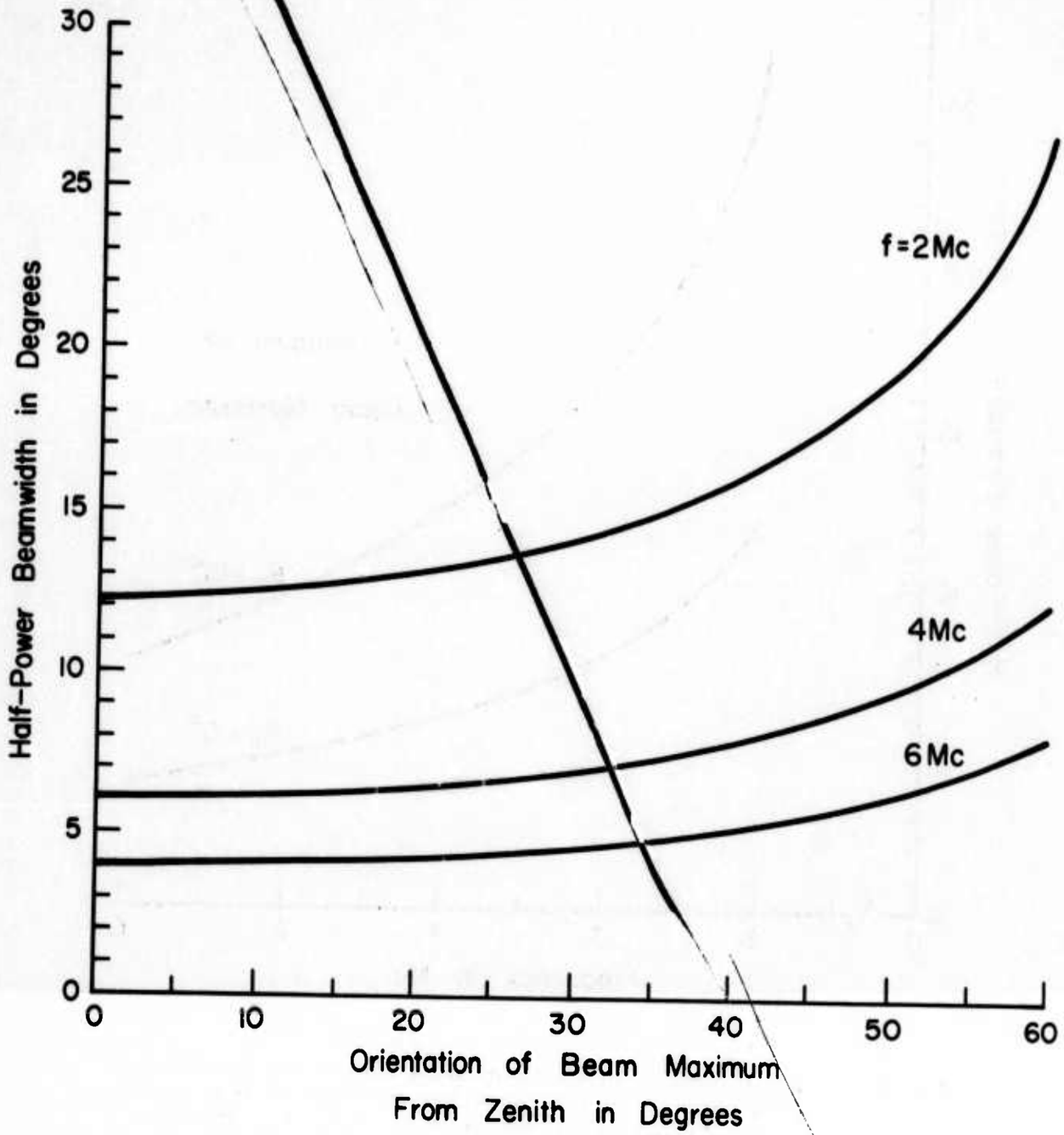

Figure 6. H-P Beamwidth of Given Antenna as a Function of Orientation of the Beam Maximum (Scan Angle) in One of the Principal Planes of the Array for Three Frequencies of Operation. L = 570 meters

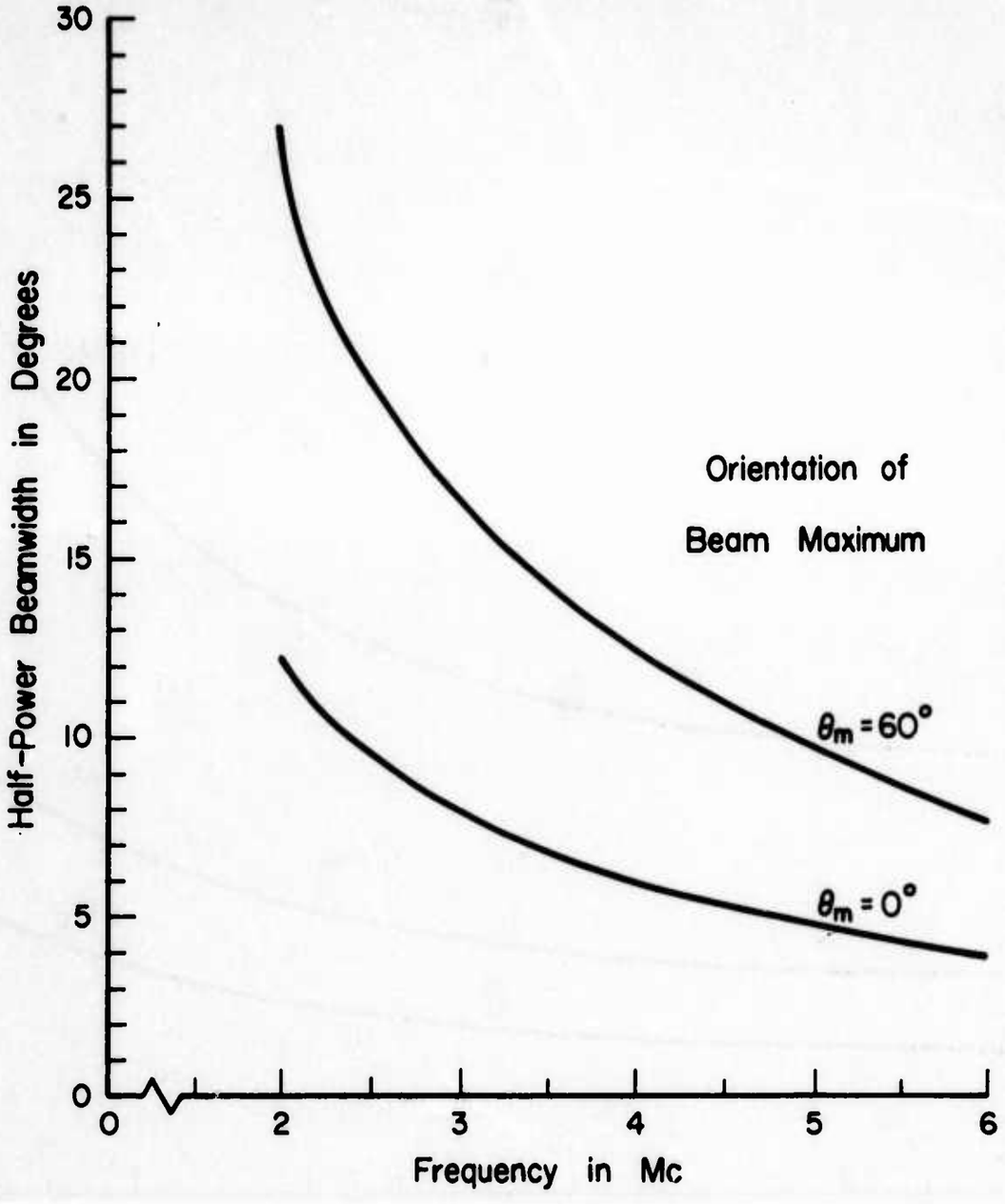

Figure 7. H-P Beamwidth of Given Antenna Array as a Function of Frequency for Two Orientations of Beam Maximum in one of the Principal Planes of the Array. L = 570 meters

Thus far we have considered arrays with elements spaced one-half wavelength ($\lambda/2$) apart, and only one main beam associated with each array. If the spacing (d) between elements in a uniform array becomes greater than $\lambda/2$, a second main beam will appear as the first beam is scanned down toward the horizon. Thus to limit the radiation pattern of the array to a single main beam we must choose

$$\frac{d}{\lambda} < \frac{1}{1 + \cos(\gamma_{max})} \tag{1}$$

where

$$\gamma = \frac{\pi}{2} - \beta$$

and γ_{max} is the maximum angle of scan. In Figure 8, the number of elements required to form a 570 meter uniform linear array is plotted as a function of the maximum usable frequency of operation, and angle of scan.

III. The Determination of Directional Information

As indicated above, we have assumed that the linear arrays have conical main beams that may be scanned over the hemisphere. The wave arrival direction corresponds to a unique orientation of the conical beam for each array. The orientations of these conical beams form a unique hemispherical intersection as shown in Figure 2. This intersection is a pencil beam which corresponds to the wave arrival direction. The angle of beam maximum with respect to each array axis, called the conical beam angle, and the corresponding wave arrival direction are related by

$$\cos \beta_1 = \cos \phi \sin \theta \tag{2}$$

and

$$\cos \beta_2 = \sin \phi \sin \theta, \tag{3}$$

where β_1 and β_2 are the conical beam angles for the first and second arrays, respectively.

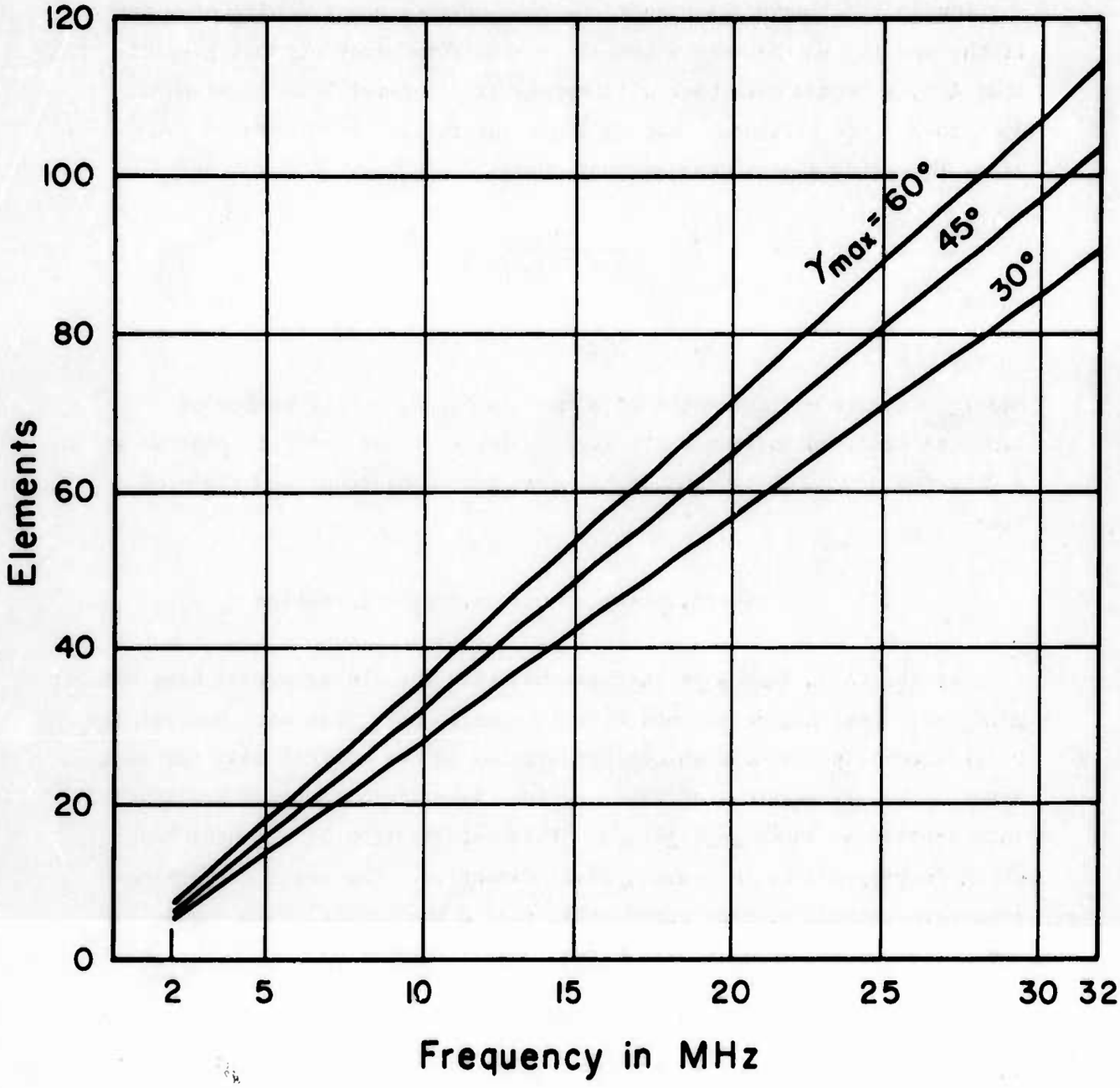

Figure 8. Number of elements required to form a 570 meter uniform linear array to insure a single main beam for the maximum indicated scan angles.

In theory, one need only scan the array responses of both arrays over the hemisphere to determine the values of β_1 and β_2, which are the angles corresponding to the maximum array responses of the two arrays. The angles may then be used along with Equations 2 and 3 to determine the direction of arrival. In actual practice this procedure would not provide sufficient accuracy because of the slowly varying nature of the array amplitude function in the neighborhood of the beam maximum.

This study has been based upon the premise that it might be desirable to keep the antenna system transportable and rather easily set up, but of necessity, the associated electronics would be sophisticated if its full capabilities were to be realized. Thus, it has been assumed that a small computer would be incorporated into the system at the receiving site.

To take advantage of the presence of a small on-line computer, Davis has shown that it is possible to improve the accuracy of determination, if we take a weighted mean of the beam angles.[4] The weighting factors for such a mean would be the corresponding amplitude responses of the arrays. The resultant means would be considered to be the true conical beam angles. They would be combined as described above to determine the true direction of arrival.

In order to proceed with the formulation of such a mean, it is necessary to again review some basic array concepts and mathematical notation. We assume all the elements of the cross array to be identical, with the same orientation, and the received amplitude at each element to have the form

$$A = P(\theta,\phi)A_a, \tag{4}$$

where

A = received amplitude at element,

$P(\theta,\phi)$ = amplitude modification of wave due to pattern and polarization properties of element,

A_a = amplitude of wave incident from (θ,ϕ) direction.

Thus, the resolution of a wave of amplitude A_a incident on an array with element patterns given by $P(\theta,\phi)$ is equivalent to the resolution

of a wave of amplitude A incident on an array of isotropic elements. Therefore, we may work with the received amplitude A to resolve the wave direction. After the direction of arrival has been determined, the wave amplitude may be computed from Equation 4.

If we consider the uniform linear array of N elements in Figure 9, with a wave oriented at angle β_0 from the axis of the array, and we choose the r^{th} element to be the reference with a response of A, then the response at each element n is

$$E'_n = Ae^{-j2\pi(n-r)\frac{d\cos\beta_0}{\lambda}} \tag{5}$$

where

d = element spacing,

λ = signal wavelength.

The $e^{j\omega t}$ time convention is assumed.

To form the array response for the main beam directed in the β direction, we shift each element response by

$$e^{j2\pi(n-r)\frac{d\cos\beta}{\lambda}} \tag{6}$$

and add the shifted responses. The resultant array response for a wave incident at an angle β_0 is

$$y'(\beta) = \sum_{n=1}^{N} Ae^{-j2\pi(n-r)\frac{d}{\lambda}(\cos\beta_0 - \cos\beta)} \tag{7}$$

Since the amplitude is the variable to be maximized with respect to the array angle, it is reasonable to use the magnitude of the array response as the weighting factor for a weighted mean.

If we choose β for the mean variable, we find that the weighted mean results in an angle closer to the array axis than the angle of maximum amplitude. This result is due to the asymmetry of the array function for the main beam when it is positioned at angles far from the zenith.

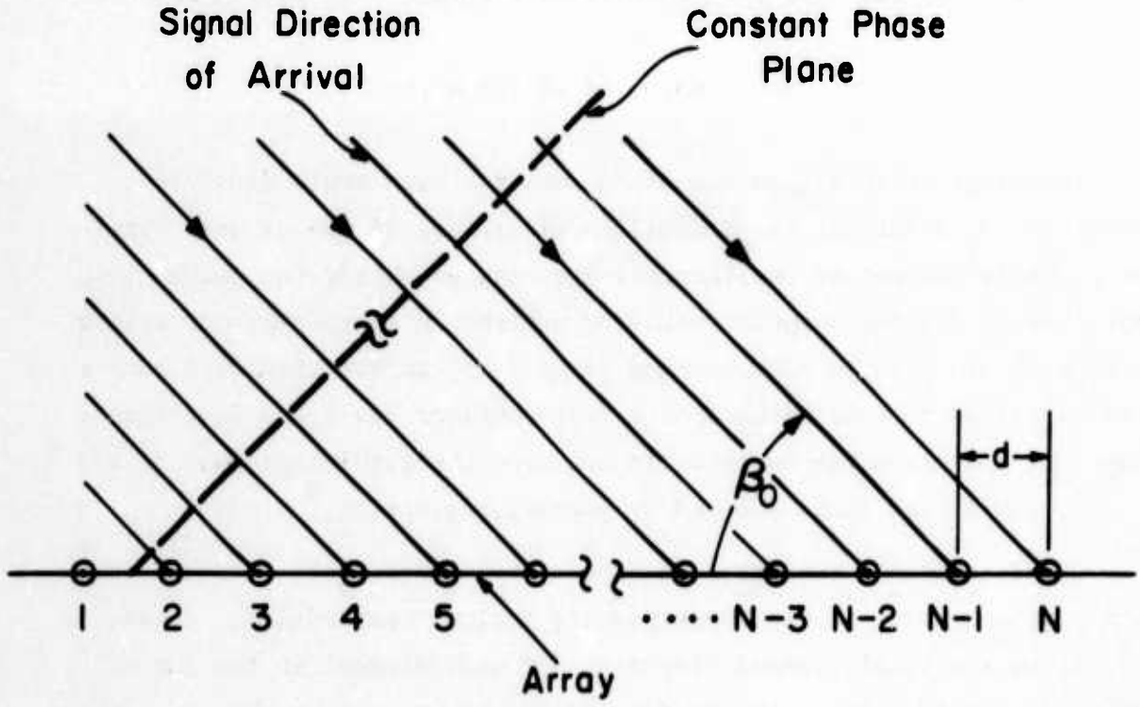

Figure 9. The geometry pertinent to a conical beam and associated linear antenna array.

It is easily observed in Figure 10 that the array factor, the orthogonal projection of the array function onto the array axis, is a symmetrical function, as needed.[5] If we define the projection variable* (or projected angle) as

$$x = 1 - \cos \beta, \tag{8}$$

then the array response is a symmetrical function of x about x_0, and thus a useful weighted mean may be calculated using x as the mean variable. Scanning the main beam results in a simple translation of y(x).

IV. The Resolution of the Arrays

If arrays of this type are to be used for high angle D.F., the capability of resolving the directions of arrival of two or more closely spaced waves becomes of considerable importance. Using the assumption that a small digital computer would be on line in an operational system, a computer was used to simulate and process the information from such a system. Again to take advantage of this computer Davis has developed a technique for using the computer to increase the resolving power of a given array to the limit imposed by geometrical optics.[4]

Let us consider two waves of amplitudes A_1 and A_2 to be incident upon a linear array at the corresponding conical beam angles, β_1 and β_2. Since the total element response for each element is the sum of the responses to both waves, we can obtain the expression for the element response phasor. The array response Y is the sum of Y_1 and Y_2, the response phasors for the two waves.

In general, we have no information about the phasor elements of Y_1 or Y_2, but can determine the values of the phasor Y. Since we know the form of the array response phasors for the two signals, it is possible to determine Y_1 and Y_2 by an iterative process using a sophisticated curve fitting routine.

---

*Instead of using the conventional ψ as the space factor variable, we have used x. For a main beam located at x_0, x and ψ are related by $\psi = 2\pi d\ (x_0 - x)/\lambda$.

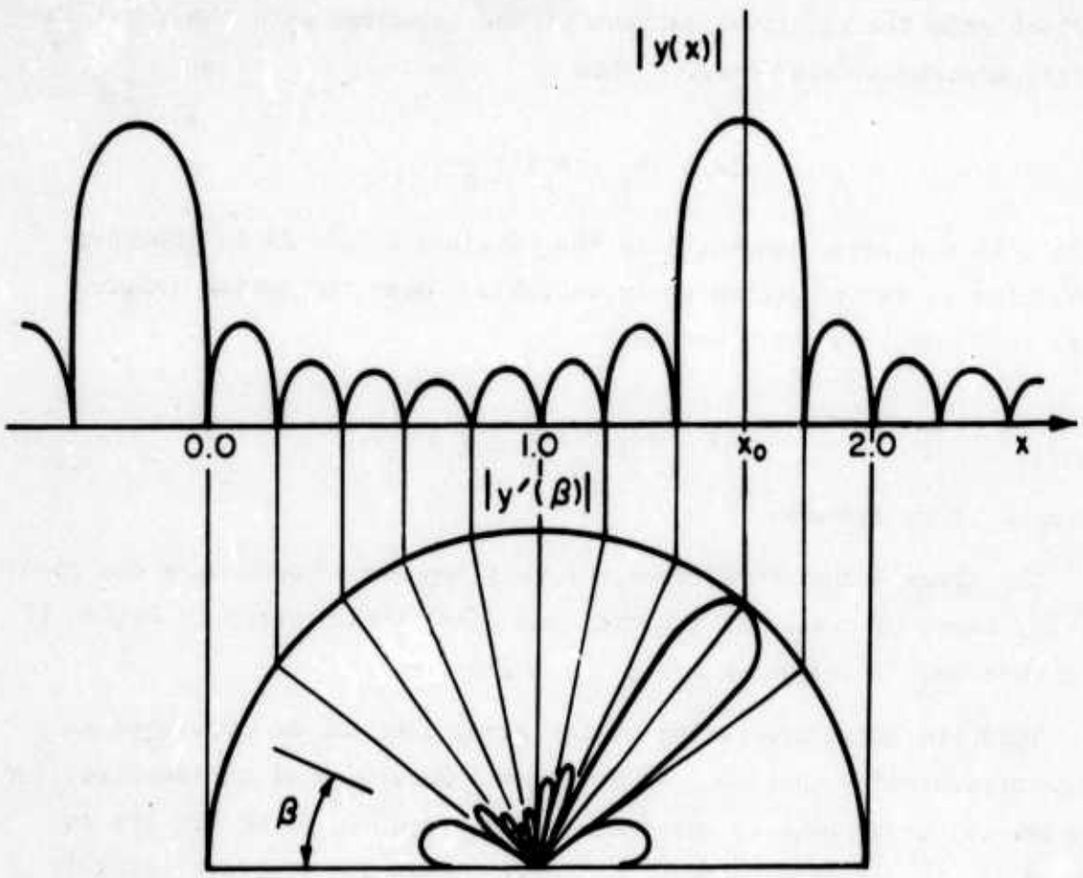

Figure 10. The general form of the array function, $|y'(\beta)|$, and the array factor, $|y(x)|$. The region of x between 0.0 and 2.0 is called the visible region of the array factor.

A necessary criterion for resolution of such an iterative process can be found from the use of physical optics criteria. The Rayleigh criterion is that two components of equal intensity should be considered to be just resolved when the principal maximum of one coincides with the first intensity minimum of the other.[6] Thus

$$\Delta x = |x_1 - x_2| \geq \frac{\lambda}{b} ,$$

where b is the array length, λ is the wavelength, and Δx is the wave separation in the projected array variable. Near the zenith (angles close to 90 degrees) this becomes

$$\Delta\beta = |\beta_1 - \beta_2| \geq \frac{\lambda}{b} ,$$

where $\Delta\beta$ is in radians.

The array length in wavelengths thus imposes a bound upon the resolving power of the array and this bound has been plotted in Figure 11 as a function of frequency for a 570 meter array.

This iterative processing of the array data can be described as a "reconstruction" technique. It utilizes a knowledge of an idealized (or a measured) array pattern (or response) for a given array in its environment, to a single incident wave, to obtain and separate, closely spaced incident waves. The technique is applied to each broadside array of the cross array, the results being combined to obtain the actual direction of arrival information. Briefly this "reconstruction" is accomplished by measuring the complex (amplitude and phase) signals received by the array as it is scanned in space.

Initially, samples are taken of the phase and magnitude of the array response across the chosen portion of the hemisphere. The sampled magnitudes are scanned for a maximum which is assumed to be the location of the primary wave and is designated as such. (This assumption may be in error, but will be corrected by iteration.) This sampled response is separated into real and imaginary parts. About the location of the maximum of the sampled primary, the response of the array to a single wave

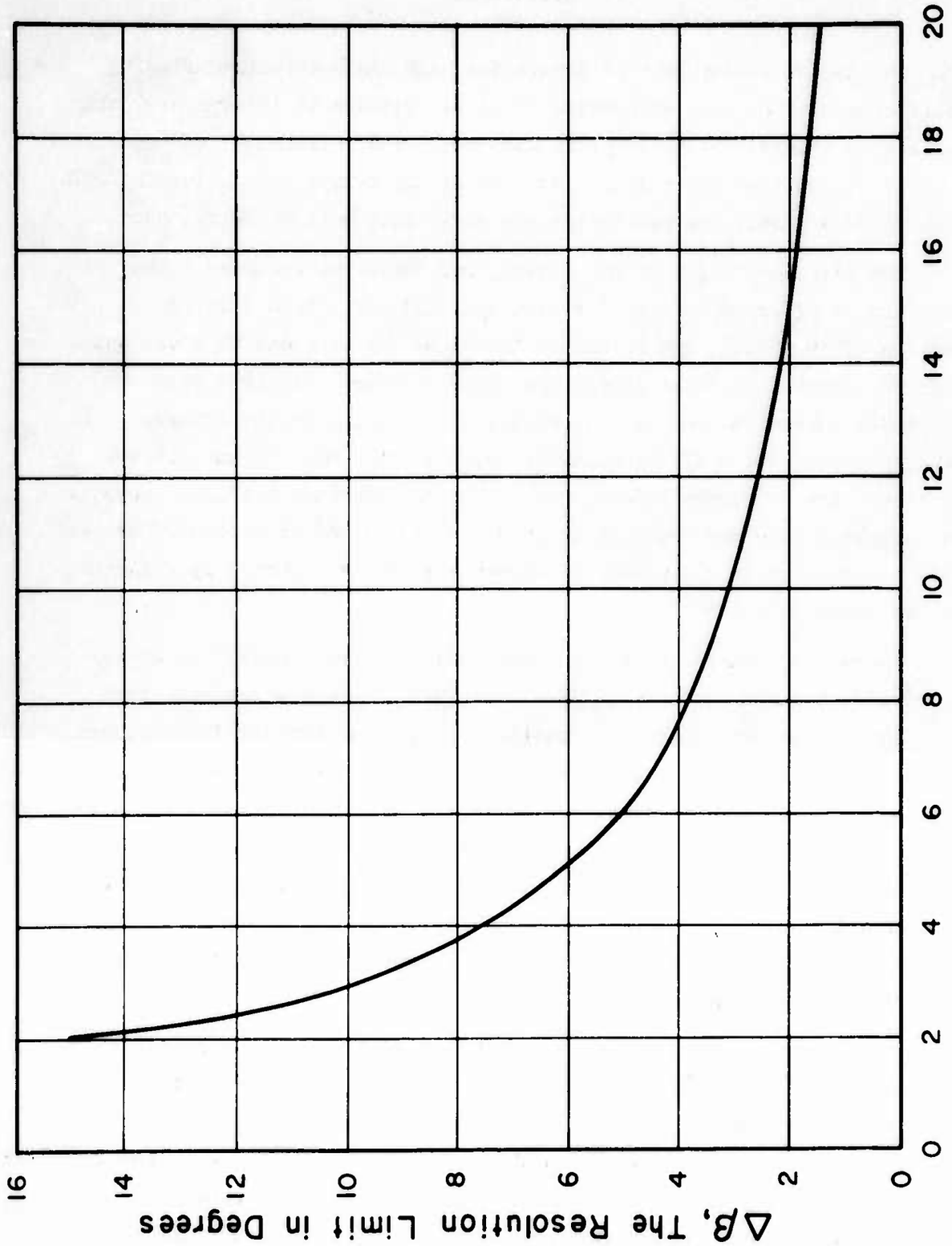

Figure 11. Limit of the resolving power of a linear 570 meter array as a function of the frequency of operation.

V. Discussion

The use of linear crossed arrays for high angle direction finding would appear to be very attractive if it is possible to incorporate into the system a small on-line digital computer. The performance of the arrays however are unalterably tied to the size of the arrays in wavelengths. To gain added accuracy and resolution the array size must be increased.

The size, or length of the arrays, and hence the required number of elements is of prime concern for many applications. In a limited extension of this work, the iteration technique was extended to cover space tapered arrays. In these arrays the spacing between adjacent elements increases toward the ends of the aperture.[7] Using a cosine squared density taper, for a 570 meter array operated at 6 MHz, it was possible to reduce the 22 elements down to 13 elements with only a slight increase in computing time and uncertainty in determination of direction of arrival. Thus a reduction in the number of elements shown in Figure 8 by a factor of two seems possible.

There are several receiving system-computer trade-offs. An electronically scanned system that provides a single complex response from each of the two arrays at each position of scan is straight forward, but requires adequate electronic phase-shifters to scan the beams. An alternate system, and the one simulated in this study, would consist of an individual receiver for each element, or a scanning sampler that connects the elements in turn to one more receivers capable of recording the magnitude and relative phase of the output of each array element. These complex signals are then combined in the computer to form the radiation beam of the total array.

The computational techniques which have been considered permit a determination of the direction of arrival of each of two waves to within an angular uncertainty substantially less than 1 degree, if there is 5% or more difference in their amplitudes and they are separated by the resolution limit of the array. For the crossed arrays this uncertainty may increase to 2.5 degrees (at 6 MHz with 570 meter arrays) when the orientation of the incident waves are such that the separation of the waves is closer than the resolution limit for one array but not for the other.

of that amplitude is constructed. The real and imaginary parts of the constructed response are subtracted from the measured response. The remainder is combined to give an assumed secondary response, i.e. a "reconstructed" secondary.

The magnitude of the reconstructed secondary, is scanned to obtain a tentative secondary bearing. As was done for the primary bearings, an array response is constructed about this secondary bearing and subtracted from the original sampled response. This new response is referred to as the reconstructed primary.

The indicated bearings are then calculated by applying the center of gravity calculations to the main beams (response between the first nulls on each side of the maximum) of the reconstructed responses.

These new estimates of direction of arrival are now used to repeat the reconstruction process just described. This routine is iterated until the estimates converge to constant values.

Applying this technique to the broadside arrays of the cross, the results will be conical beam bearings. The true bearings are at the intersections of these conical beams and can easily be calculated. There are some fundamental limitations on such a process. For example, two waves of the same frequency may be separated if they satisfy an array limit criterion for each array and the optical resolution criterion for at least one array. The array limit criterion requires that the main beam of the array factor be completely contained in the visible region of the array factor for beam orientations in the directions of both waves.[5] The optical resolution criterion requires that one half of the main beam width of one array be less than the wave separation.

This iterative technique may easily be extended to separation of more than two waves. This would require additional initial values for the iterative routine and an extension of the criteria presented above.

The process converged when Gaussian noise was added to the response of each element such that standard deviation of the noise was as great as 0.7 of the magnitude of the strongest of the two waves. The presence of this noise caused the uncertainty of determination to rise to slightly more than 1 degree for a single array.

V. Conclusions

Moderately sized linear arrays are well suited for the determination of the direction of arrival of high-angle incident waves. If the receiving system can incorporate a small on-line computer, data processing techniques are available that make such antenna-receiving systems competative with any of the low-angle receiving systems.

References

1. Ryle, M., "A new radio interferometer and its application to the observation of weak radio stars," Proc. Roy, Soc., 211, p. 351, 1952.

2. Mills, B. Y. and A. G. Little, "A high resolution aerial system of a new type," Australian J. Phys., Vol. 6, p. 272, 1953.

3. Bailey, A. D., J. D. Dyson and E. W. Ernst, "HF/DF system studies and directional propagation research," T.R. ECOM-0097-4, Contract DAAB-07-69-C-0097, Dept. of Elect. Engr., University of Illinois, Urbana, Illinois, April 1970.

4. Davis, W. A., "Wave separation with crossed linear antenna arrays," M.S. Thesis, Dept. of Elect. Engr., University of Illinois, Urbana, Illinois, June 1970, (also published as Appendix A to T.R. ECOM-0097-7, Contract DAAB-07-69-C-0097, July 1970.

5. Bach, H. and J. E. Hansen, "Uniformly spaced array," Chapter 5 in Antenna Theory, Ed. by R. E. Collin and F. J. Zucker, McGraw-Hill, Pub. Co., 1969.

6. Born, M. and E. Wolf, Principles of Optics, 2nd ed., McMillan, New York, pp. 333, 401-406, 416, 1964.

7. Lo, Y. T. and S. W. Lee, "A study of space tapered arrays," IEEE Transactions, Vol. AP-14, pp. 22-30, January 1966.

J. D. MOORE, T. C. GREEN, M. P. CASTLES, J. W. FOGWELL

Southwest Research Institute, San Antonio, Texas

THE DESIGN OF THE MODERN SPACED-LOOP DF ANTENNA FOR HF AND VHF

ABSTRACT

HF and VHF coaxial spaced loop antenna designs are reviewed for various applications. Bearing accuracy, polarization response, sensitivity, response time, sensing methods and other performance characteristics are reviewed.

I. INTRODUCTION

Coaxial spaced loop antennas in a variety of designs can be used to satisfy direction finding requirements in the HF-VHF range. These applications include ground based, airborne, and shipboard siting and involve various types of DF processing. The purpose of this paper is to examine several types of spaced loop direction finders and describe the general performance characteristics.

II. ANTENNA PATTERNS

The coaxial spaced loop antenna pattern is obtained by differentially connecting simple loop antennas as shown in Figure 1. Coaxial spaced loop antenna* azimuth patterns for vertical, horizontal, and elliptical polarization are shown in the Figure 2. Note that the spaced or interferometer nulls remain fixed in azimuth independent of the incident polarization. The elevation patterns are given in Figure 3 where a maximum for vertical polarization occurs at horizontal incidence and a maximum for horizontal polarization occurs at a 45° elevation angle.

III. SPACED LOOP ANTENNA TYPES

We categorize spaced loop antennas into three distinct configurations: (1) the rotating single spaced loop element, (2) the 8-loop fixed

* The term spaced loop will be used for the coaxial spaced loop antenna throughout.

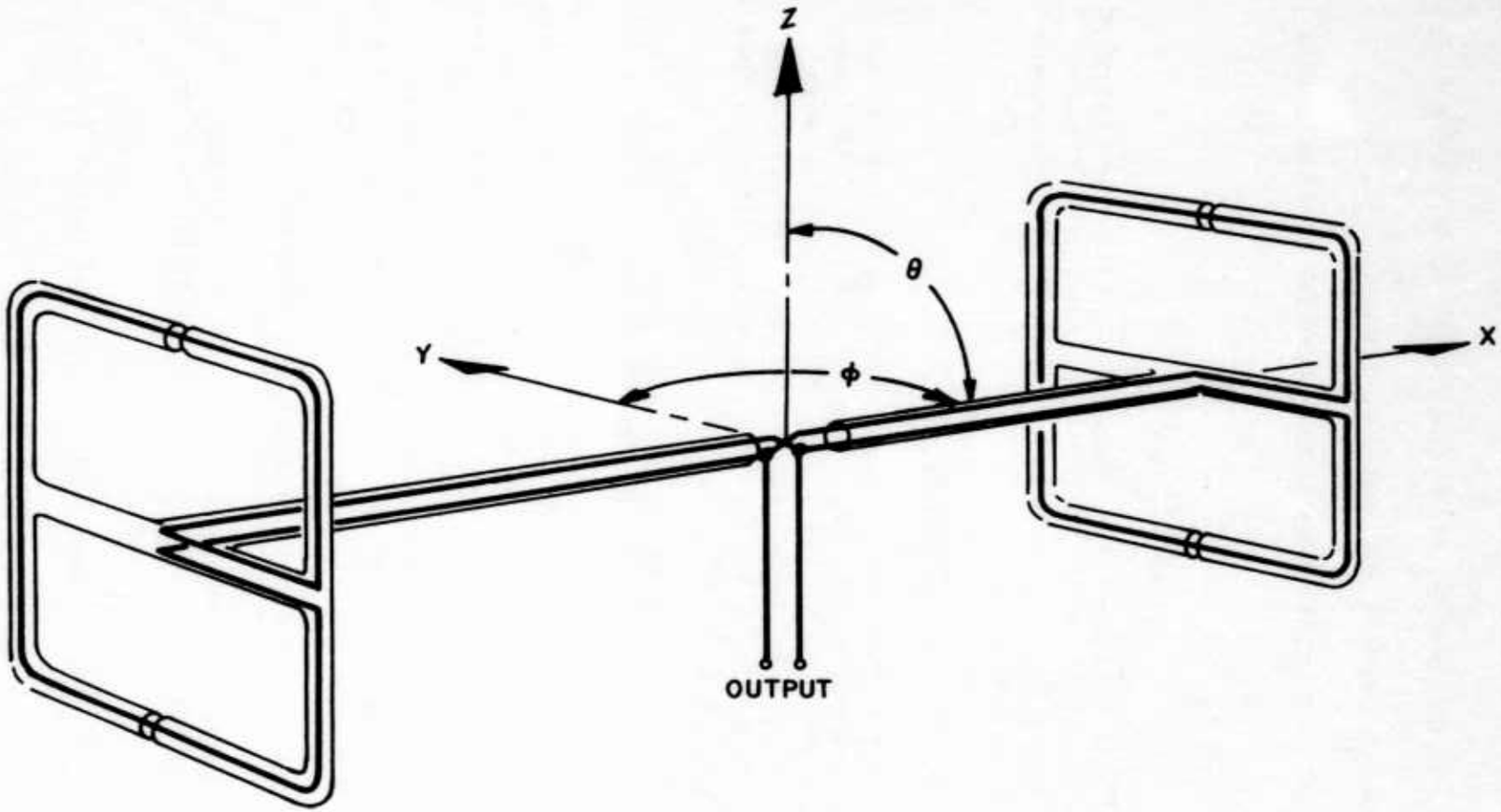

FIGURE 1. COAXIAL SPACED LOOP ANTENNA WITH BALANCED GAP LOOPS

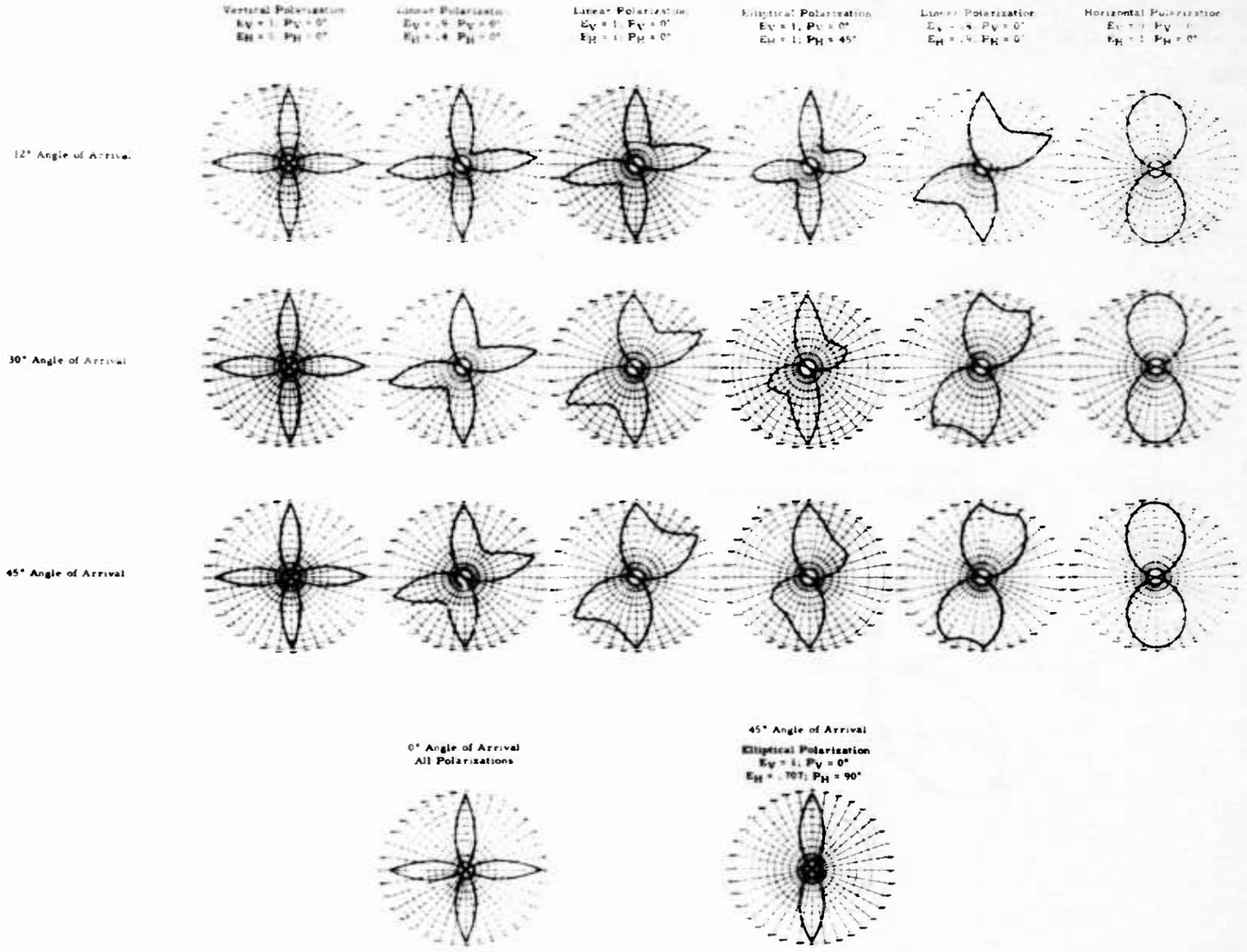

FIGURE 2. COAXIAL SPACED LOOP PATTERNS AS A FUNCTION OF SIGNA POLARIZATION AND ANGLE OF ARRIVAL

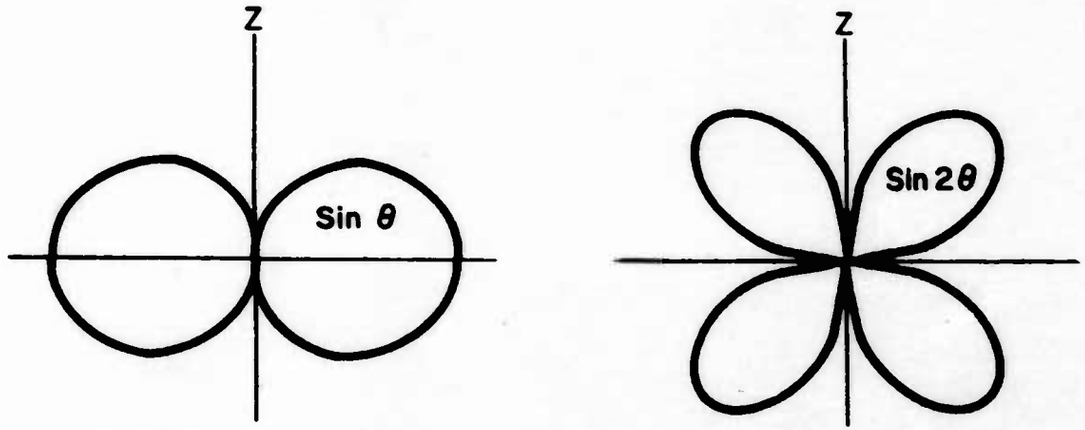

FIGURE 3. NORMALIZED ELEVATION PATTERNS FOR THE COAXIAL SPACED LOOP ANTENNA

crossed spaced loop array, and (3) the fixed single spaced loop element.

In each case the antenna pattern is used to obtain the direction finding information. The primary differences between these configurations is in the method of DF processing which is adapted to the specific application and requirements.

A. Rotating Antenna

Figure 4 shows a typical rotating spaced loop antenna designed to meet a portable HF multipolarization direction finding requirement. The rotating spaced loop element develops the antenna pattern which is displayed on a CRT display. Sense is obtained by unbalancing the simple loop outputs to provide the necessary dipole mode injection. The rotating antenna provides multipolarization direction finding by the interferometer null measurement on the CRT (spaced loop antenna axis broadside to the plane of incidence). Typical CRT displays for signals of various polarization on an antenna range including sense injection are shown in Figure 5. Typical CRT patterns for sky wave signals are shown in Figure 6. The various designs of this basic configuration are adaptible for mobile, portable, man-pack, and airborne requirements.

B. Fixed Crossed Spaced Loop Antenna

The 8-loop crossed spaced loop antenna has conventionally been applied to groundwave, vertical polarization signals. Through appropriate digital processing techniques multipolarization response can be obtained. A multibay fixed crossed spaced loop antenna designed for the HF-VHF range is shown in Figure 7.

DF processing can be performed with either single or multichannel receiver techniques as illustrated in Figure 8. Single channel receivers are used with goniometer scanning to provide the familiar CRT propeller display. The phase and gain matched twin channel receiver provides an alternate DF processing technique generating the bearing ellipse. Sense information is normally obtained from crossed simple loops located symmetrically with the fixed spaced loop array. In a broadband application, the upper bay spaced loop antennas can be connected in simple loop mode to provide sense for the lower bay spaced loop array.

The fixed crossed spaced loop with a multichannel receiver is ideally adaptable to digital processing techniques including both DF and sense computation. Digital sense logic can be performed without computer computation to aid in a manual CRT display system as shown in Figure 9.

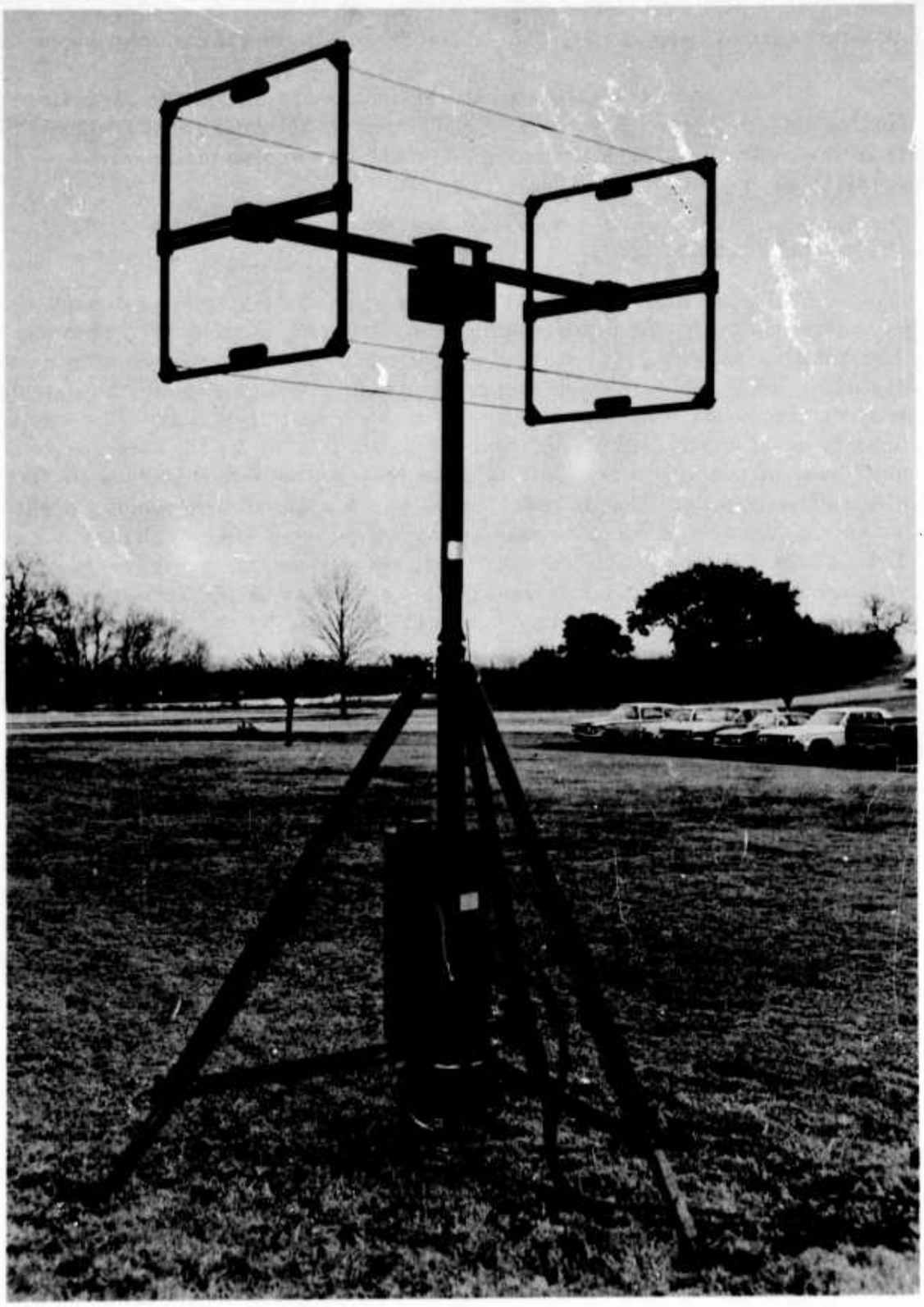

FIGURE 4. TUNED ROTATING SPACED LOOP ANTENNA

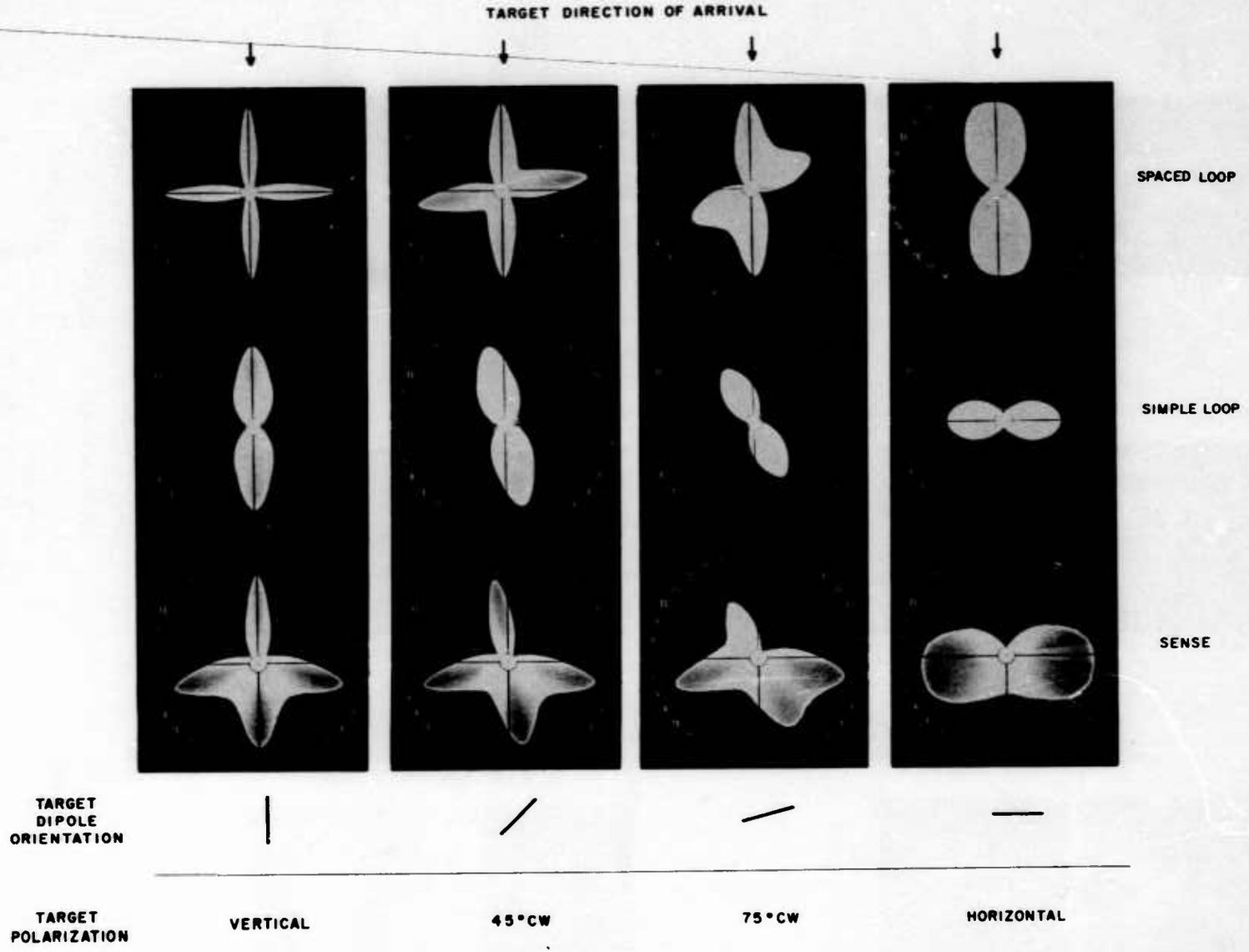

FIGURE 5. TYPICAL SPACED LOOP, SIMPLE LOOP, AND SENSE PATTERNS AT VARIOUS POLARIZATIONS AS DISPLAYED ON THE AZIMUTH INDICATOR FOR A SPACED LOOP DIRECTION FINDER

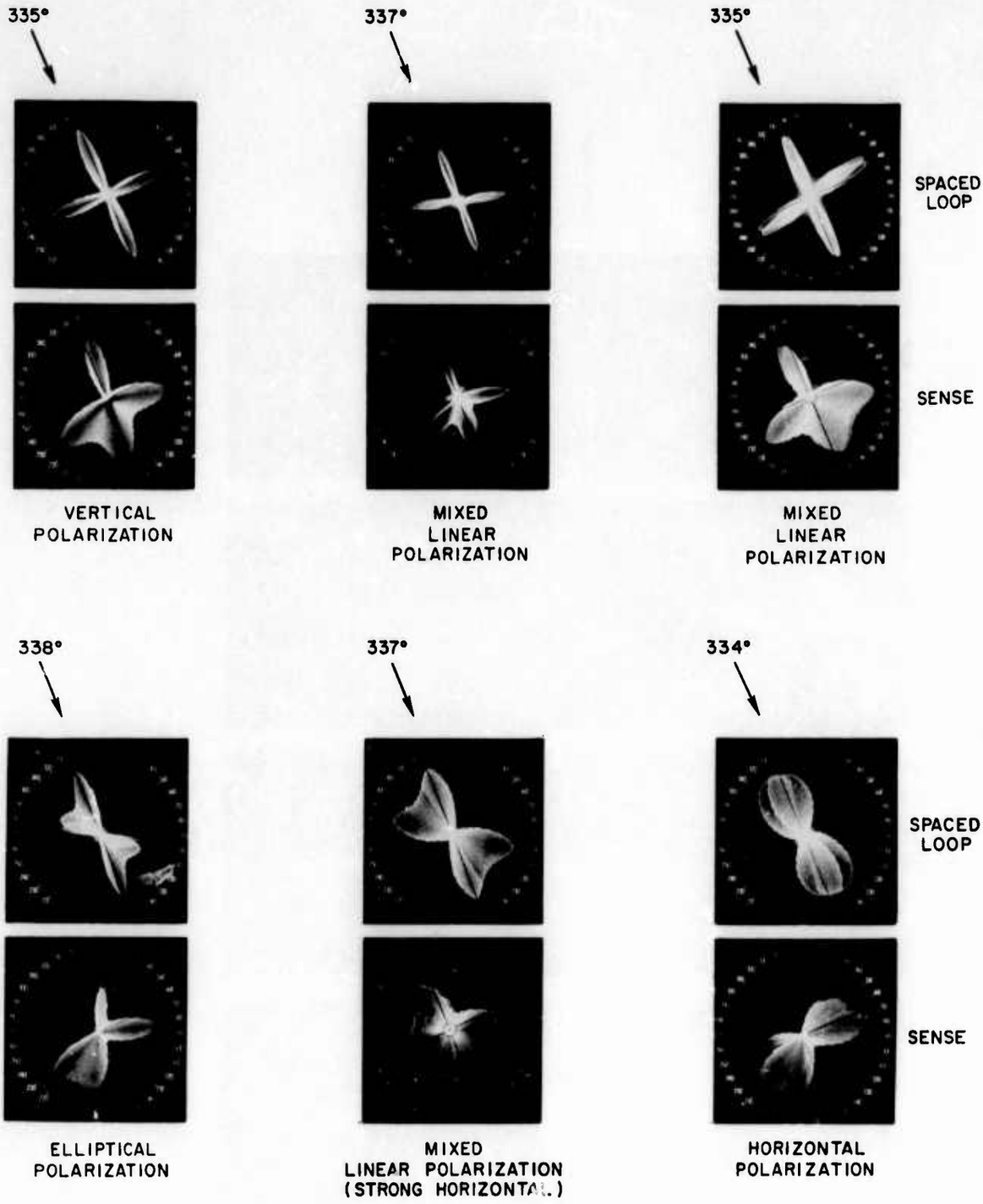

STATION	: WWV	TRUE BEARING	: 336.7°
FREQUENCY	: 10 MHz	LOCATION	: FT. COLLINS, COLO.
EMISSION	: AØ AND A2	DISTANCE	: 857 MILES
		ANTENNA ROTATION	: 150 RPM

FIGURE 6. TYPICAL SKYWAVE SPACED LOOP AND SENSE PATTERNS FOR A ROTATING SPACED LOOP DIRECTION FINDER

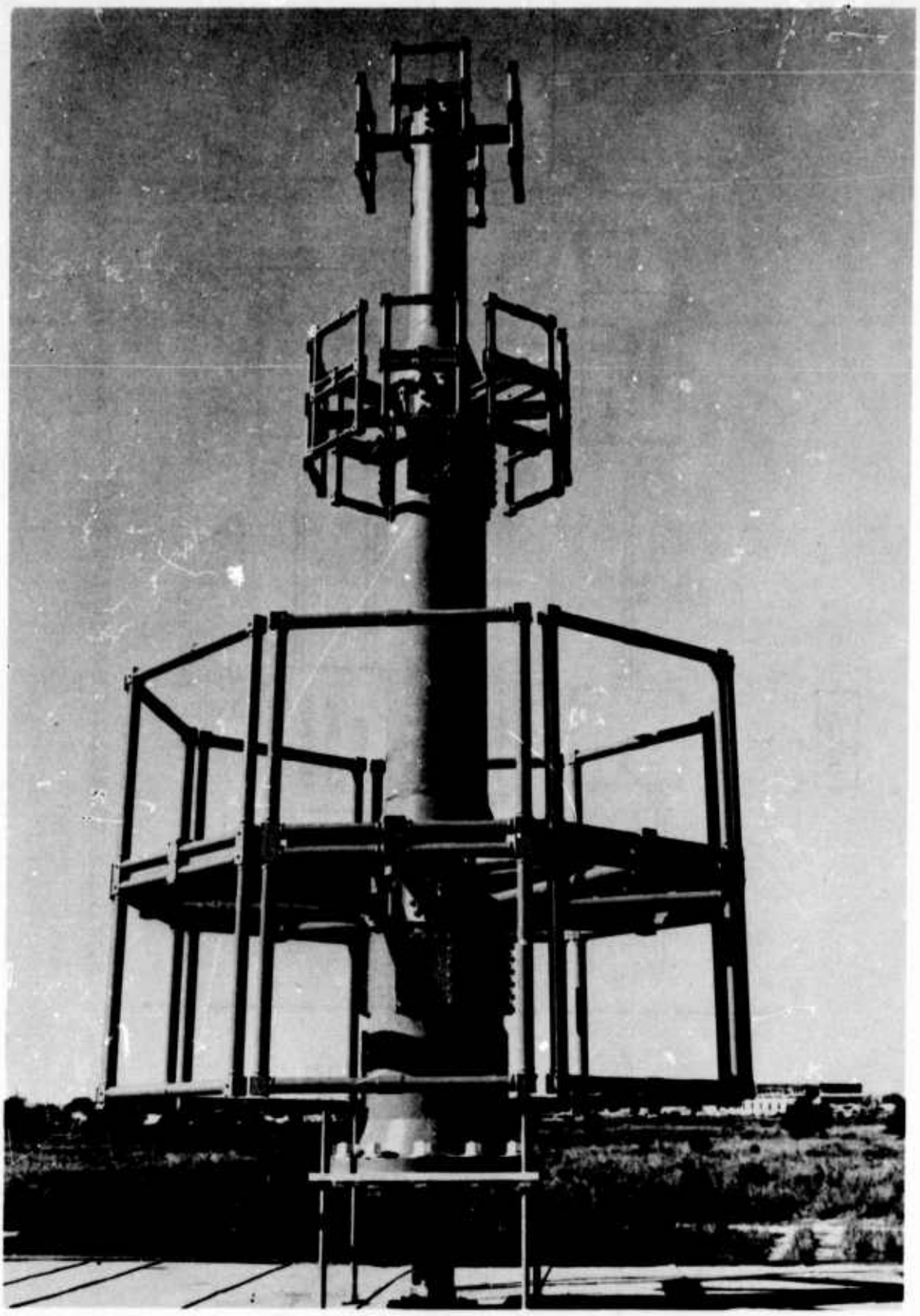

FIGURE 7. FIXED CROSSED SPACED LOOP ANTENNA (HF-VHF)

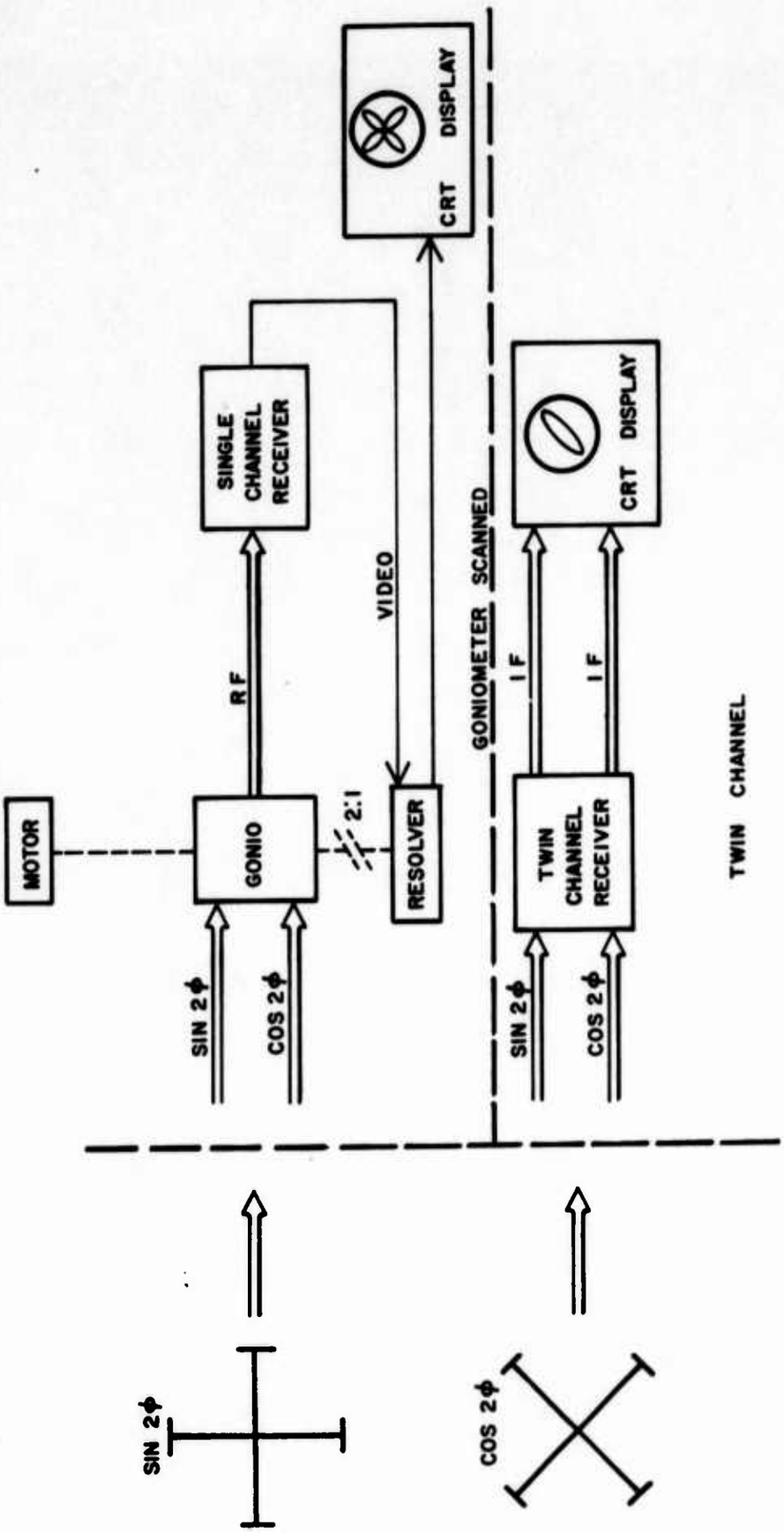

FIGURE 8. SINGLE AND MULTICHANNEL RECEIVER SPACED LOOP DF

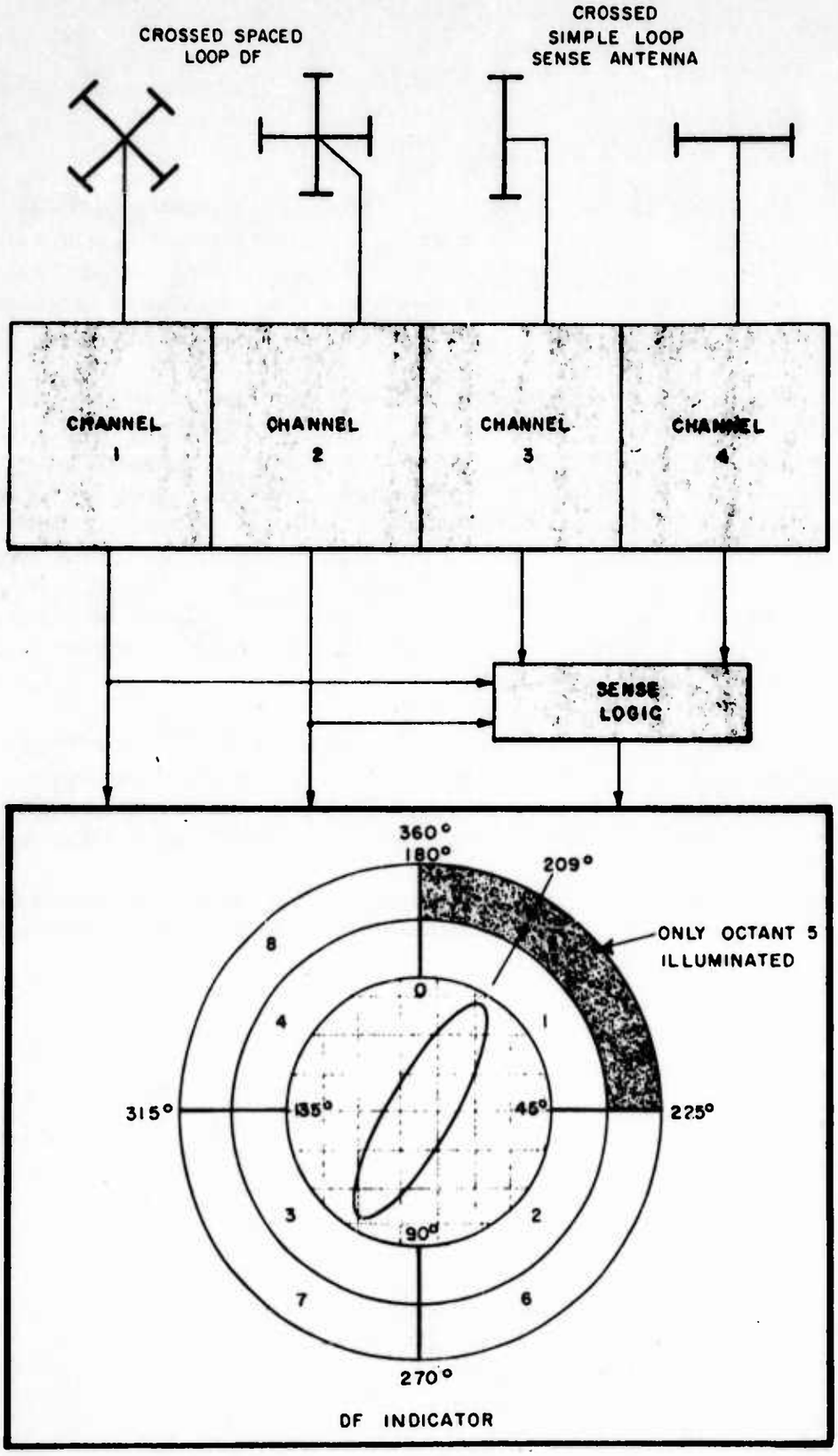

FIGURE 9. DIGITAL SENSE DISPLAY

C. Fixed Single Spaced Loop Element

The fixed single spaced loop element on airborne platforms provides the same type of response as a rotating element since the platform is normally moved to develop the antenna pattern for the multipolarized signal. An example of this type of antenna is shown in Figure 10.

The DF processing techniques with the fixed element and relatively slow moving platform are based on presentation of left, right and boresight readouts. Figure 11 shows the patterns possible with the antenna for vertical polarization with the exception of Fig. 11(c) which is the normal sense pattern for a rotating spaced loop with CRT display. The CW and CCW sense patterns are equal with opposite slopes at the position of the spaced loop nulls and one pattern is always larger than the other in 180° sector. While the patterns of Figure 11 are for vertical polarization, the condition has been demonstrated to hold for all signal polarizations.

Readouts in the basic left-right systems include meters, recorders, and oscilloscope displays. Sufficient information is available to resolve the forward bearing from the reciprocal bearing. The basic output of this left-right system can easily be digitized.

A combination of the basic left-right system with similar variation of the sense pattern will yield a technique for scanning a 60° sector with a fixed antenna.

IV. SENSITIVITY

The effective height of the spaced antenna in meters is given by

$$he = \frac{\pi^2 NV}{\lambda^2}$$

where

V= volume in cubic meters
N= number of turns in the loops
λ= wave length in meters
μ= relative permeability

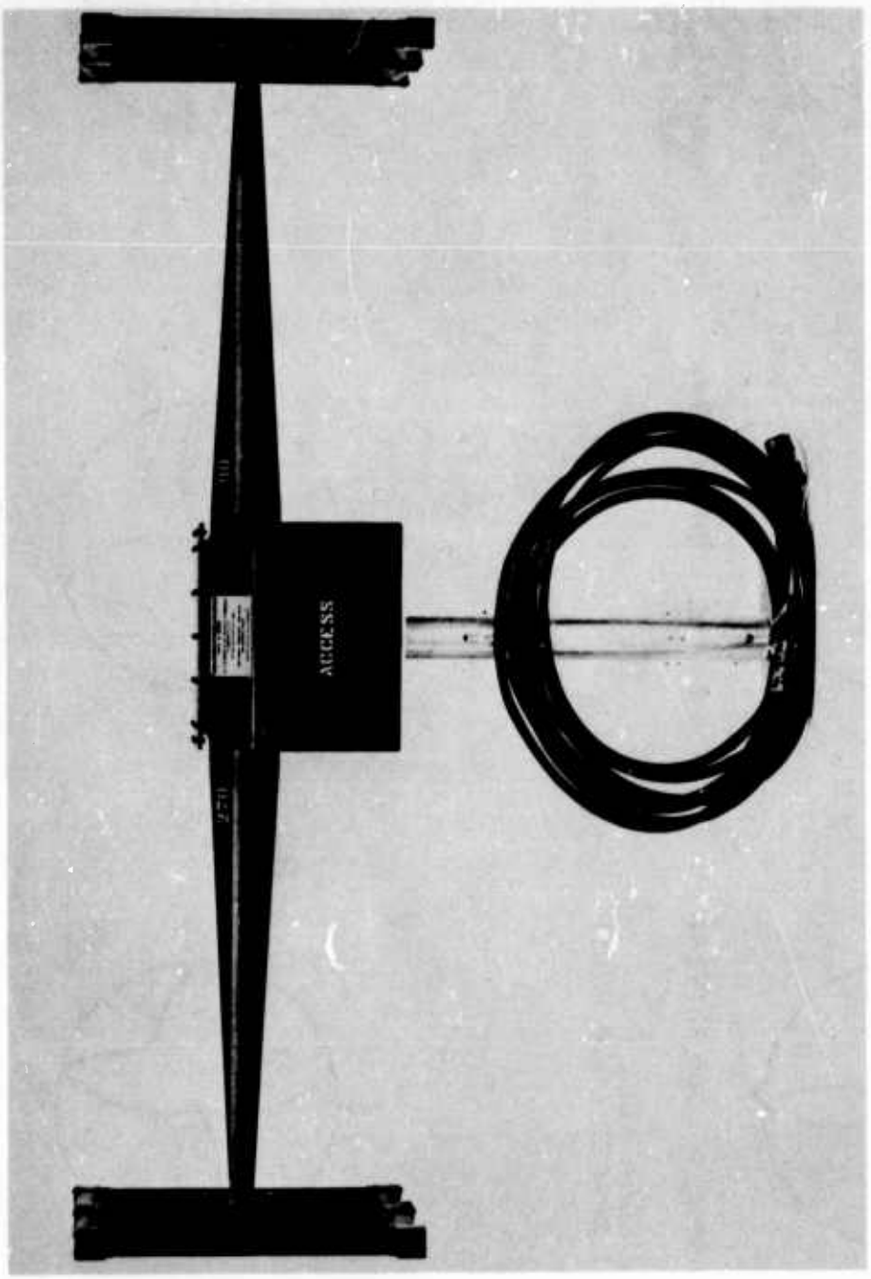

FIGURE 10. TUNED SINGLE FIXED ELEMENT SPACED LOOP

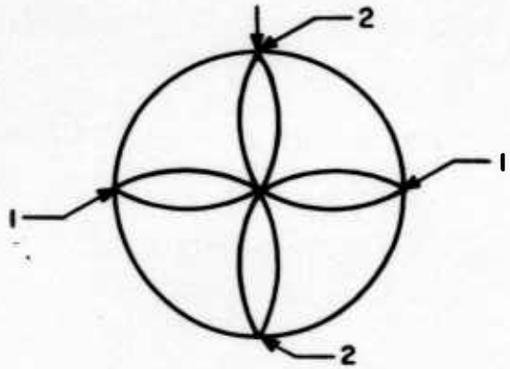

a. SPACED LOOP PATTERN

1. LOOP NULL
2. SPACED LOOP NULL

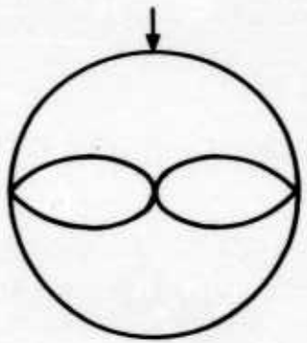

b. SIMPLE LOOP PATTERN

c. SENSE PATTERN (ROTATED 90°)

d. CW SENSE

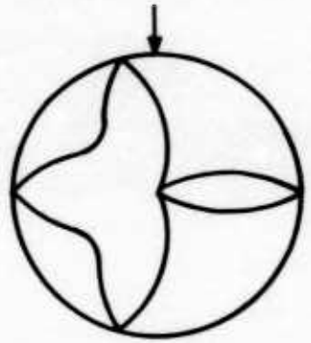

e. CCW SENSE

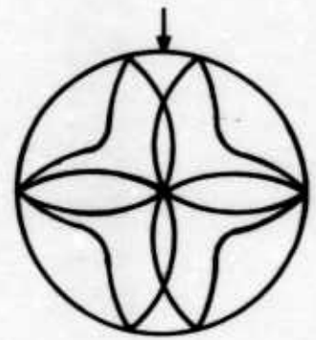

f. CROSSOVER

FIGURE 11. TYPICAL PATTERNS FOR VERTICAL POLARIZATION

The inherent aperiodic sensitivity of the antenna is directly proportional to antenna volume, the number of turns and the permeability of the core medium and is inversely proportional to the frequency squared.

The spaced loop antenna element is readily tuned providing significantly increased sensitivity compared to the aperiodic mode for equivalent antenna size. Additional techniques for sensitivity improvement include (1) multiturn antenna elements, (2) ferrite core antennas, and (3) use of shunt capacitors across the electrostatic shield gaps to provide an effective increase in antenna inductance. These techniques affect the intrinsic antenna sensitivity. Not treated are the processing techniques such as synchronous and correlation detection which increase sensitivity with some tradeoff in dynamic range, response time and system bandwidth response.

Typical CW sensitivities obtained with tuned spaced loop antennas are shown in the sensitivity curves of Figure 12. Sensitivities range from 15 μv/m at 2 MHz to 2 μv/m at 40 MHz. Receiver bandwidth was 3 kHz below 20 MHz and 16 MHz above 20 MHz.

A sensitivity curve for an untuned (aperiodic) fixed crossed spaced loop antenna is also shown in Figure 12. This antenna was designed for groundwave vertically polarized intercept.

V. SIZES AND WEIGHTS

The weight and size of a spaced loop direction finder is determined primarily by (1) sensitivity and bandwidth, (2) application (portable or fixed), and (3) type of construction.

Air core loops are normally constructed from aluminum tubing to provide an integral electrostatic shield. The physical size of the antenna is determined by the loop spacing and number of elements. Weight is nominally established by the application. That is, an HF man-pack antenna or airborne obviously must satisfy commensurate size and weight requirements while a fixed HF-VHF shipboard spaced loop antenna (See Figure 7) must be designed to withstand severe shock and vibration requirements at the top of a free standing mast with significant increases in weight.

VI. MULTIPATH ERROR

The spaced loop direction finder provides a 2 to 1 error reduction compared to a simple loop antenna when subjected to a two-component

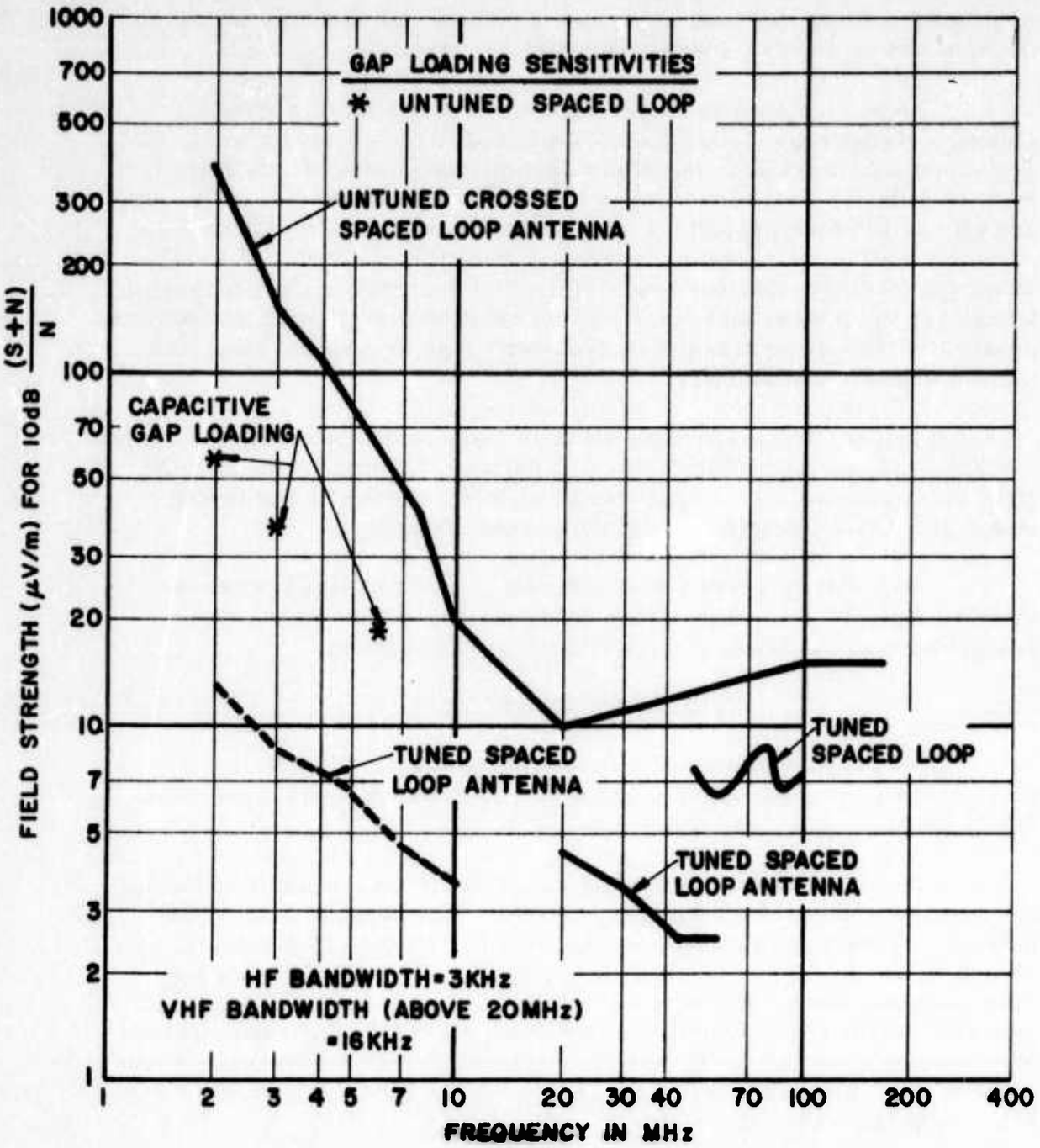

FIGURE 12. SPACED LOOP DIRECTION FINDER SENSITIVITIES

vertically polarized field. In addition, the simple loop antenna has extensive polarization error while the spaced loop is polarization independent. The bearing accuracy of a typical ground based rotating spaced loop direction finder for skywave signals is shown in Figure 13. The bearing error histogram is developed for 415 intercepts and shows a 3.23° standard deviation about a $-.68^{\circ}$ mean error over the 2-10 MHz frequency range.

For shipboard applications the accuracy of the spaced loop direction finder is measured in terms of the quality and repeatability of the DF calibration curves obtained. DF calibration curves to be usable over 360° must be single valued and continuous. In addition, the general shape of the calibration curves as a function of frequency determine the minimum number of DF calibration curves over a specified bandwidth. Repeatability of shipboard DF calibration curves obtained in a semi-automatic continuous mode show a $\pm 2^{\circ}$ standard deviation as shown in Figure 14.

VII. POLARIZATION ERRORS

Figure 15 shows the bearing error histogram obtained for 245 DF cuts on horizontally polarized skywave signals. Note that the standard deviation of 2.8° about a mean error of $+.4^{\circ}$ agrees closely with the previously shown mixed polarization data (Figure 13).

VIII. DYNAMIC RANGE AND SIGNAL FIDELITY

The dynamic range of the spaced loop direction finder is primarily determined by (1) inherent antenna sensitivity, (2) dynamic range of the active terminating network, and (3) circuit components in antenna switch assemblies.

For example, a typical tuned airborne HF spaced loop antenna with an inherent 10 dB signal-to-noise ratio sensitivity of 40 μv/m at 4 MHz requires 3 μv/m incident upon the antenna to produce a 1 dB compression in the output signals. This represents a 100 dB dynamic range. With the improved state-of-the-art capabilities of FET circuits and off-the-shelf commercial amplifiers, spaced loop antennas both tuned and aperiodic can be operated linearly in field strengths of the order of 10 v/m. In addition, incident signals of 100 v/m or more can be sustained without permanent active circuit damage.

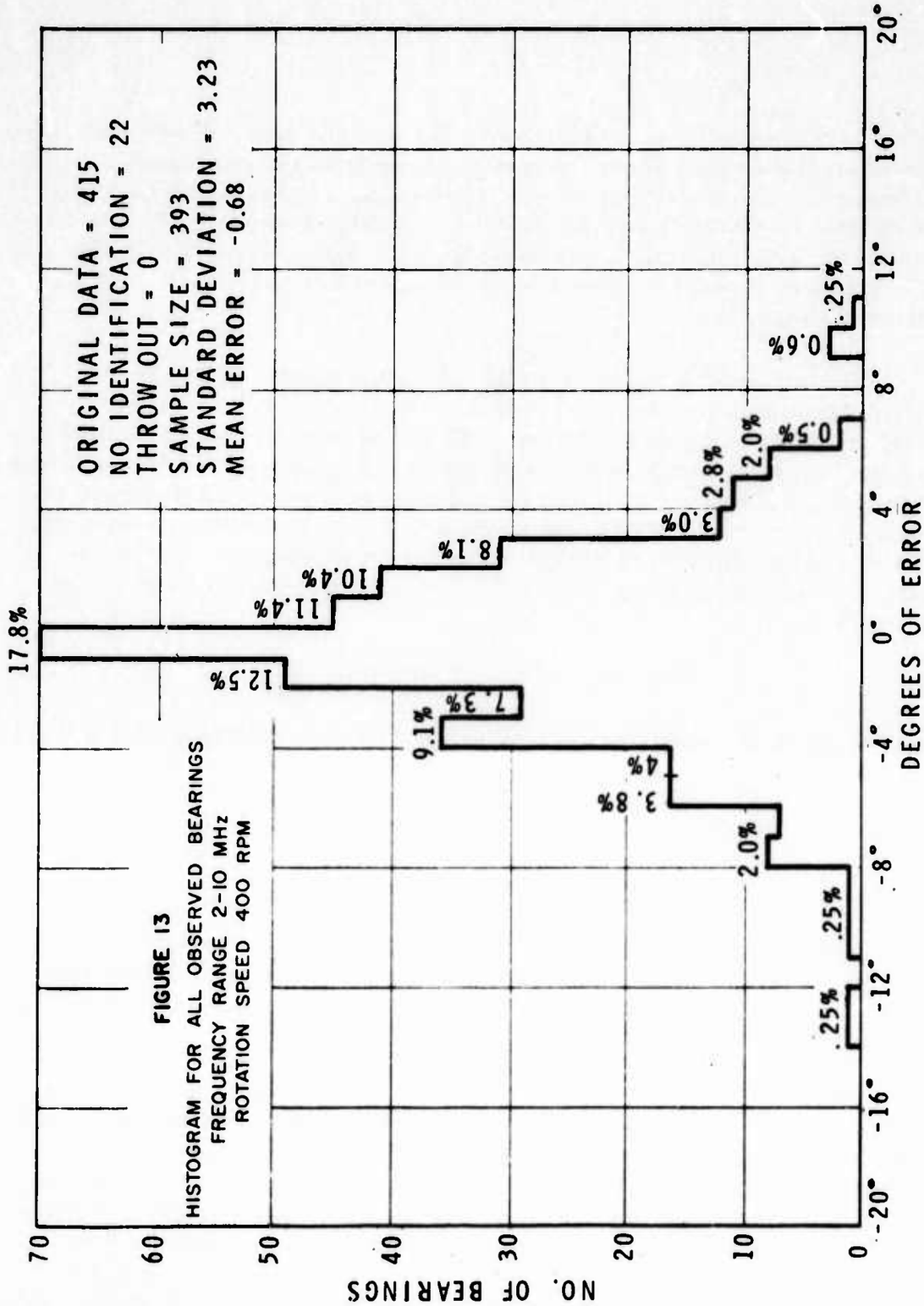

FIGURE 13. HISTOGRAM FOR ALL OBSERVED BEARINGS

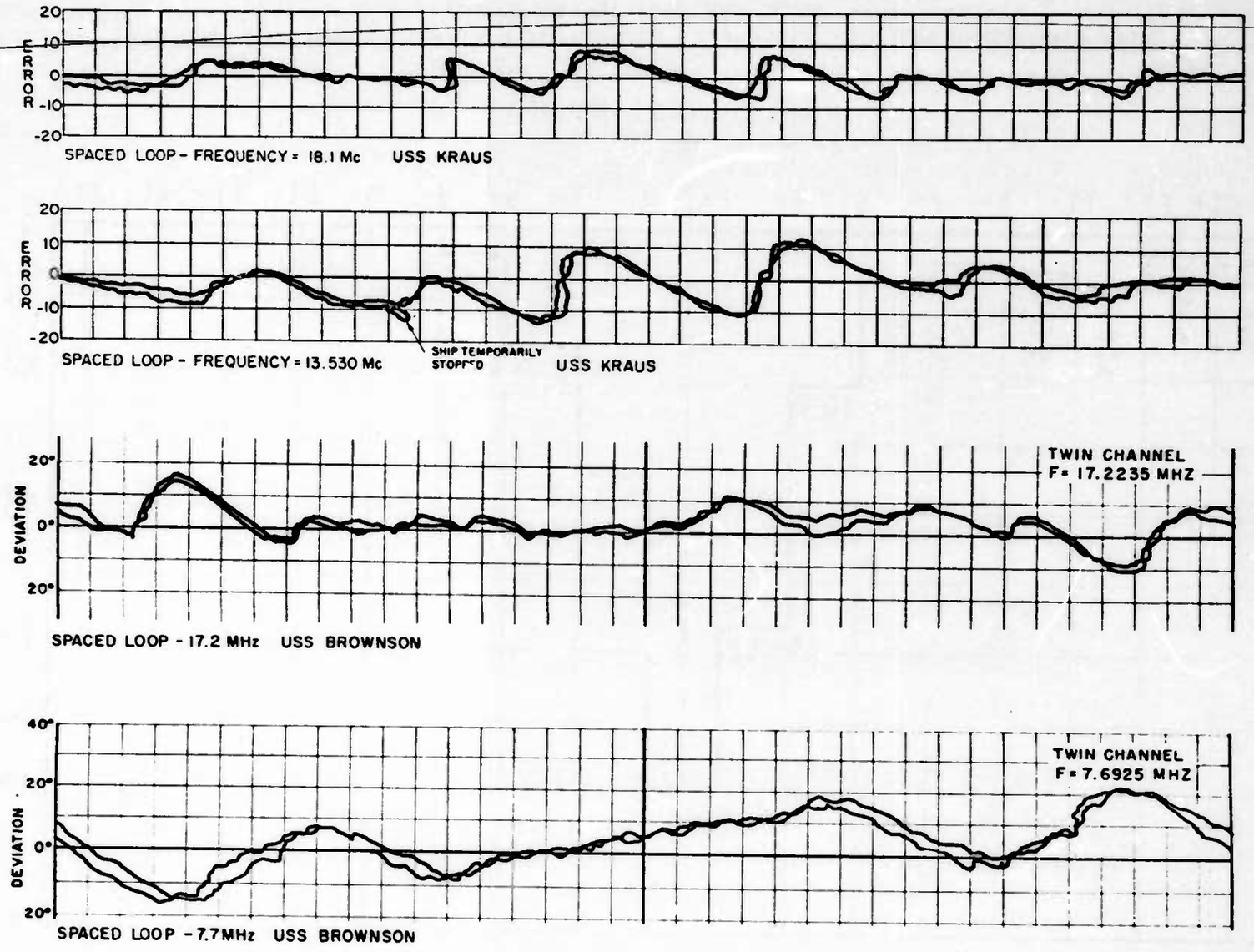

FIGURE 14. REPEATABILITY CURVES FOR SPACED LOOPS ON TWO SHIPS

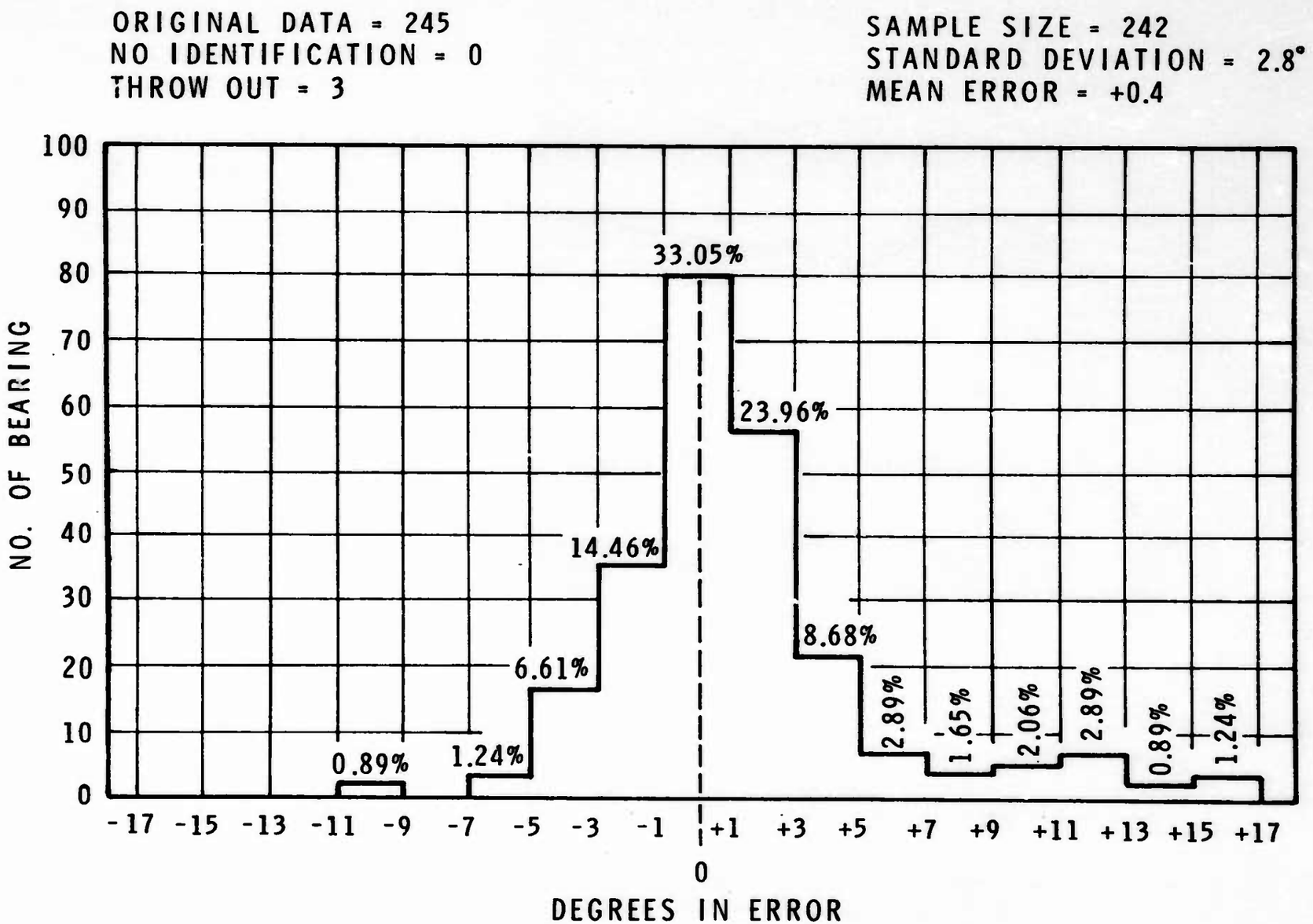

FIGURE 15. HISTOGRAM OF HORIZONTAL POLARIZATION BEARINGS FOR A ROTATING SPACED LOOP

Spaced loop antennas typically have a dynamic range 20 dB greater than the tuned dynamic range outside the tuned frequency region. Intermodulation and spurious response performance is determined by the susceptibility of the antenna preamplifiers and the antenna terminal voltage. For example an untuned crossed spaced loop antenna at 2.00 MHz has a 130 dB dynamic range using state-of-the-art commercial preamplifiers.

IX. RESPONSE TIMES

The response time of the spaced loop antenna is determined to a large extent by the basic antenna configuration. Rotating spaced loop antennas for example have a minimum response time of 1/2 the rotation rate or 1/2 the period of rotation. Typical rotation rates for previously developed rotating spaced loop antennas are in the order of 30 to 1200 rpm, thereby providing response time on the order of 1000 to 25 ms. Conversely, the 8-loop cross spaced loop antenna has response times limited primarily by the receiver bandwidth. Therefore, response time of the crossed fixed spaced loop antenna using solid state switching circuits and including digital DF and sense processing is in the order of 1 to 5 milliseconds. Alternatively, fixed crossed spaced loop antennas utilizing reed relay switching circuits would typically have DF and sense digital response times in the order of 50 milliseconds.

X. SUMMARY

The coaxial spaced loop antenna has significant advantages for local site wave interference error. In addition, it is the smallest polarization error free antenna for HF and low VHF. Sensitivities are good when the small size is considered. Significant improvements in the spaced loop intrinsic sensitivity can be obtained where requirements exist. The spaced loop configuration should be chosen in terms of the compatibility with the DF processing system based on the DF requirements.

AN APPLICATION OF MATCHED RECEIVER TECHNIQUES TO HF RADIOLOCATION

Prepared by:

L. Rocke
Principal Staff Engineer

Date: 25 May 1970
Revised: 29 June 1970

ABSTRACT

Using receivers matched for gain and phase, and a vertically disposed array of two element, Wilkins and Minnis have shown that the vertical angle of arrival of horizontally polarized HF radio waves can be measured. In this paper it is shown that matched receivers used with an array of three elements, or of multiple elements combined into three groups, permit measurement whatever the polarization.

The arrival angles of double or triple mode signals are derived from Lissajous figures.

Some results computed from observations of signals in a horizontally polarized array are shown.

INTRODUCTION

A. D. Bailey pointed out[1,2] that if elevation angle, in addition to azimuth, was measured, the application of ray-retracing techniques would allow the position of a radio transmitter to be found. He was funded by the U.S. Army to demonstrate this, using the direction finding facilities at the University of Illinois, and the successful results were reported to the Army[3] in 1964. Bailey used, and extended, the techniques that were developed by Ross, Bramley and Ashwell[4] in Britain. These were based on matched receiver principles introduced by Watson-Watt and Herd[5] in 1926 and developed by the British Admiralty[6] and the University of Illinois[7]. Treharne[8], in Australia had the same idea of single station position finding and introduced the principle of calibrating the ionosphere by observing the elevation angle of arrival of waves from a known transmitter in the target area.

All these studies employed horizontal arrays which were correct for the short ranges involved but now, to perform the same function at greater ranges, lower elevation angle coverage is required and there is no alternative to the extension of the DF array into the vertical plane.

The fading reduction that results from selecting a single mode by means of vertical directivity or, at least, by rejecting a major interferring mode by generating a null in the

vertical response, has been known for 36 years[9, 10, 11] but radiolocation circles have failed to take advantage of the corresponding increase in bearing stability and have gone to extremely complex processes to extract the wanted answer from the phase front that is the resultant of all possible modes. Indeed, care has been taken to ensure that DF systems respond to all modes so that none shall be missed. With the new interest in measurement of low elevation angles, the possibility exists to derive azimuth, with much simpler systems and greater precision, by using arrays extending in both the vertical and horizontal planes and favoring a wanted mode by vertical directivity.

The practical limitations in vertical aperture limit the perfection of mode selection by beam steering and a major difficulty remains in the interference between modes in signals that are not suited to time gating. In this paper it is shown that this interference results, in time, in a Lissajous figure in which the sides contain the necessary information of the elevation angles and relative magnitudes of all modes within the beamwidth and it is argued that matched receiver techniques are the proper approach to the measurement of these properties. The corresponding application of these techniques to the measurement of azimuth, and the techniques of ray-retracing, are considered to be well known and so the paper deals mainly with the measurement of elevation angles.

Practical HF systems should cover at least three octaves, from 4-32 Mc/s or, ideally, four octaves covering 2-32 Mc/s, yet typical elevation direction finders cover one octave defined by the lowest frequency at which adequate angular discrimination is available, to the high frequency at which ambiguous solutions of the display equation cannot be resolved. It has been

shown[20] that a preferred system of $3 \times 2^{N-1}$ vertically disposed elements can cover N octaves and that corresponding frequencies in each octave have the same calibration (Display angle as a function of elevation angle). In the proposed system the display angle is independent of polarization of the wave.

Since very little information is available on the subject of the distribution of noise power in the vertical plane, this paper attempts a forecast of its character and influence upon a proposed elevation direction finder.

PART 1. THE ANTENNA

Elevation Direction Finding Systems Using Vertical Arrays

For many years[12, 13, 14, 15, 16] the two element system of elevation direction finding that was introduced by Wilkins and Minnis before World War II and reported[17] in 1956 has been a standard when lower elevation angles were to be measured. (Down to 1° in references 13, 14, 16).

This system is polarization sensitive and any response to vertically polarized waves will introduce an error. The upper frequency limit is determined by ambiguities in the display equation solution that depend upon the height of the lower element. The height of the upper element has an influence upon the low frequency limit and upon the display calibration.[18]

In this paper we propose an alternative system that employs three elements and the following analysis is intended to show that the display calibration is independent of mean height although mean height and spacing of elements still control directivity. It will also be shown that the display is the same for vertical or horizontal polarization, providing that the ground plane is ideal, and it is therefore useful on any polarization, including circular, even though there will be a 90° phase difference between the responses to the two polarizations.

The Three-Element Elevation Direction Finder

The electric field above a perfect groundplane[19] for horizontal polarization is

$$E_{z_\perp} = 2j\, E_i \sin \beta_z\, Z\, e^{-j\beta_y Y} \sin \omega t$$

where Z is height above the groundplane and Y is horizontal distance in the direction of propagation.

$\beta_z = \frac{2\pi \sin \Delta}{\lambda}$ = the phase-shift constant in the Z direction

and

$\beta_y = \frac{2\pi \cos \Delta}{\lambda}$ = the phase-shift in the Y direction

In considering a system disposed only in the Z dimension, we can ignore Y and t and $E_{z_\perp} = 2j\, E_i \sin \left(2\pi \frac{h}{\lambda} \sin \Delta\right)$

where $h = Z$ = the height of an antenna element.

For vertical polarization

$$E_{z_\parallel} = 2\eta \cos \Delta\, H_i \cos \beta_z\, Z\, e^{-j\beta_y Y} \sin \omega t$$

$\eta = \frac{E_i}{H_i}$ so $E_{z_\parallel} = 2E_i \cos \Delta \cos \beta_z\, Z\, e^{-j\beta_y Y} \sin \omega t$

and, again ignoring Y and t,

$$E_{z_\parallel} = 2\, E_i \cos \Delta \cos \left(2\pi \frac{h}{\lambda} \sin \Delta\right)$$

Now, for three antenna elements at heights $h - \frac{d}{2}$, h and $h + \frac{d}{2}$ we have voltages V_1, V_2, and V_3 and we propose to display the ratio $\frac{V_2}{V_1 + V_3}$ in an XY scope to obtain a deflection $\tan^{-1} \frac{V_2}{V_1 + V_3}$

For horizontal polarization

$$V_{3_\perp} = 2j\,E_1 \sin\left(2\pi \frac{h}{\lambda} \sin\Delta + \pi \frac{d}{\lambda} \sin\Delta\right)$$

$$V_{2_\perp} = 2j\,E_1 \sin\left(2\pi \frac{h}{\lambda} \sin\Delta\right)$$

$$V_{1_\perp} = 2j\,E_1 \sin\left(2\pi \frac{h}{\lambda} \sin\Delta - \pi \frac{d}{\lambda} \sin\Delta\right)$$

$$V_{1_\perp} + V_{3_\perp} = 4j\,E_1 \sin\left(2\pi \frac{h}{\lambda} \sin\Delta\right) \cos\left(\pi \frac{d}{\lambda} \sin\Delta\right)$$

$$\frac{V_{2_\perp}}{V_{1_\perp} + V_{3_\perp}} = \frac{1}{2\cos\left(\pi \frac{d}{\lambda} \sin\Delta\right)}$$

Similarly, for vertical polarization

$$V_{3_\parallel} = 2\,E_1 \cos\Delta \cos\left(2\pi \frac{h}{\lambda} \sin\Delta + \pi \frac{d}{\lambda} \sin\Delta\right)$$

$$V_{2_\parallel} = 2\,E_1 \cos\Delta \cos\left(2\pi \frac{h}{\lambda} \sin\Delta\right)$$

$$V_{1_\parallel} = 2\,E_1 \cos\Delta \cos\left(2\pi \frac{h}{\lambda} \sin\Delta - \pi \frac{d}{\lambda} \sin\Delta\right)$$

$$V_{1_\parallel} + V_{3_\parallel} = 4\,E_1 \cos\Delta \cos\left(2\pi \frac{h}{\lambda} \sin\Delta\right) \cos\left(\pi \frac{d}{\lambda} \sin\Delta\right)$$

$$\frac{V_{2_\parallel}}{V_{1_\parallel} + V_{3_\parallel}} = \frac{1}{2\cos\left(\pi \frac{d}{\lambda} \sin\Delta\right)}$$

The resulting display angles are identical for each polarization and, consequently, mixtures of the two can be tolerated and so the directions of ordinary and extra-ordinary components of an ionospherically propagated wave can be seen separately

by employing circularly polarized antennas of the correct sense. This capability removes the fading that rotation of polarization causes in antennas that respond to a single polarization.

Wave Range of Three Element Array

The proposed display, Figure 1, becomes ambiguous in Δ when $\frac{d}{\lambda} > 1$ and this sets a high frequency limit that can only be ignored when the ambiguity can be resolved by other information. (When a low elevation angle is observed using the dimensions of Figure 1, it can be read to greater precision, Figure 2, if $\frac{d}{\lambda}$ is increased, yet there should be no confusion of the ambiguous solutions). The low frequency limit is reached when the change of display angle is much less than the change of elevation angle and this occurs at important elevation angles when $\frac{d}{\lambda} < 0.5$ so that, as with other systems, the normal unambiguous working range is of the order of one octave. In addition, wave-range is a function of sensitivity and this, for a given elevation angle and frequency, is determined by mean height and spacing of the elements.

If polarization versatility is to be provided by the use of composite elements such as crossed dipoles or crossed loops, and if all responses are to be within a few db of the maximum, the sine and cosine height functions of the two polarizations require the mean height to be $\frac{N\lambda}{8 \sin\Delta}$ (N is odd) where the two responses are equal but 3 db below their respective maxima. When N = 1, the wave range is from $\frac{\lambda}{6.58 \sin \Delta}$ to $\frac{\lambda}{10.23 \sin \Delta} = 1.555{:}1$ where the two responses are within 3 db of each other. (When N = 3 the wave range will be 1.157:1 and it will decrease rapidly as N is increased.)

On the other hand, if the whole system could be moved up or down continuously, or in small enough steps, the ratio of the responses, and the gain, could be kept constant. In this case it would be more ideal if the vertical and

horizontal elements alternated in height and were spaced $\frac{\lambda}{4 \sin \Delta}$. (In practice, the elements would be identical but switched in polarization as required.)

When a single polarization system is required, the response to horizontal polarization can be within 3 db of the optimum over the 3:1 height range $\frac{\lambda}{8 \sin \Delta}$ via $\frac{\lambda}{4 \sin \Delta}$ (= Optimum) to $\frac{3 \lambda}{8 \sin \Delta}$. The corresponding height range for vertical polarization would be 1.67:1 or $\frac{3 \lambda}{8 \sin \Delta}$ via $\frac{\lambda}{2 \sin \Delta}$ (= optimum) to $\frac{5 \lambda}{8 \sin \Delta}$. Optimum spacing is discussed under the heading of gain.

Gain of Three Element EDF

The magnitude of the response of a three element EDF is

$$\sqrt{V_2^2 + (V_1 + V_3)^2}$$

When simple horizontal loops are employed, this equals

$$2jEi \cos \Delta \sin \left(2\pi \frac{h}{\lambda} \sin \Delta\right) \sqrt{1 + 4 \cos^2 \left(\pi \frac{d}{\lambda} \sin \Delta\right)}$$

and is a maximum when $\frac{h}{\lambda}$ and $\frac{d}{\lambda}$ are optimum.

$\frac{h}{\lambda}$ is optimum when $\sin \left(2\pi \frac{h}{\lambda} \sin \Delta\right) = 1$

$$2\pi \frac{h}{\lambda} \sin \Delta = \frac{M\pi}{2} \qquad M \text{ is odd.}$$

$$\frac{h}{\lambda} = \frac{M}{4 \sin \Delta}$$

These heights are plotted in Figure 3.

$\frac{d}{\lambda}$ is optimum when $\sqrt{1 + 4 \cos^2 (\pi \frac{d}{\lambda} \sin \Delta)}$ is a maximum.

This occurs when $\pi \frac{d}{\lambda} \sin \Delta = N\pi$ N is any integer.

$$\frac{d}{\lambda} = \frac{N}{\sin \Delta}$$

This is plotted in Figure 4.

When these two dimensions are optimum, the voltage gain, including the image in the ground is $2\sqrt{5}$. Since the voltage gain is the ratio of the antenna response in free space to its response near the ground, involving an impedance ratio of 2, the maximum power gain is $\frac{(2\sqrt{5})^2}{2} = 10 = 10$ db. With the worst value of $\frac{d}{\lambda}$ the gain is only 3 db.

The first derivatives of the display calibration (Figures 1 and 2) maximize at certain combinations of $\frac{d}{\lambda}$ and Δ and it would be ideal if the gain maximized at the same combinations. It can be shown that $\frac{d}{d\Delta} \tan^{-1} \frac{1}{2} \sec (\pi \frac{d}{\lambda} \sin \Delta)$ is a maximum when $\frac{d}{\lambda} = \frac{L}{2 \sin \Delta}$, where L is odd. This, also, is plotted in figure 4 and it will be seen that the spacing requirements for optimum scale shape and optimum gain are incompatible. Intermediate spacings must be chosen if only three elements are employed but, with a filled array, the ideal can be approached. Figure 5 shows vertical polar patterns of three element systems with dimensions that optimize (a) sensitivity at a chosen angle of 14.58°, (b) best angular discrimination at 14.58°, and (c) a compromise. (14.58° was chosen only because $\tan 14.58^\circ = 1/4$).

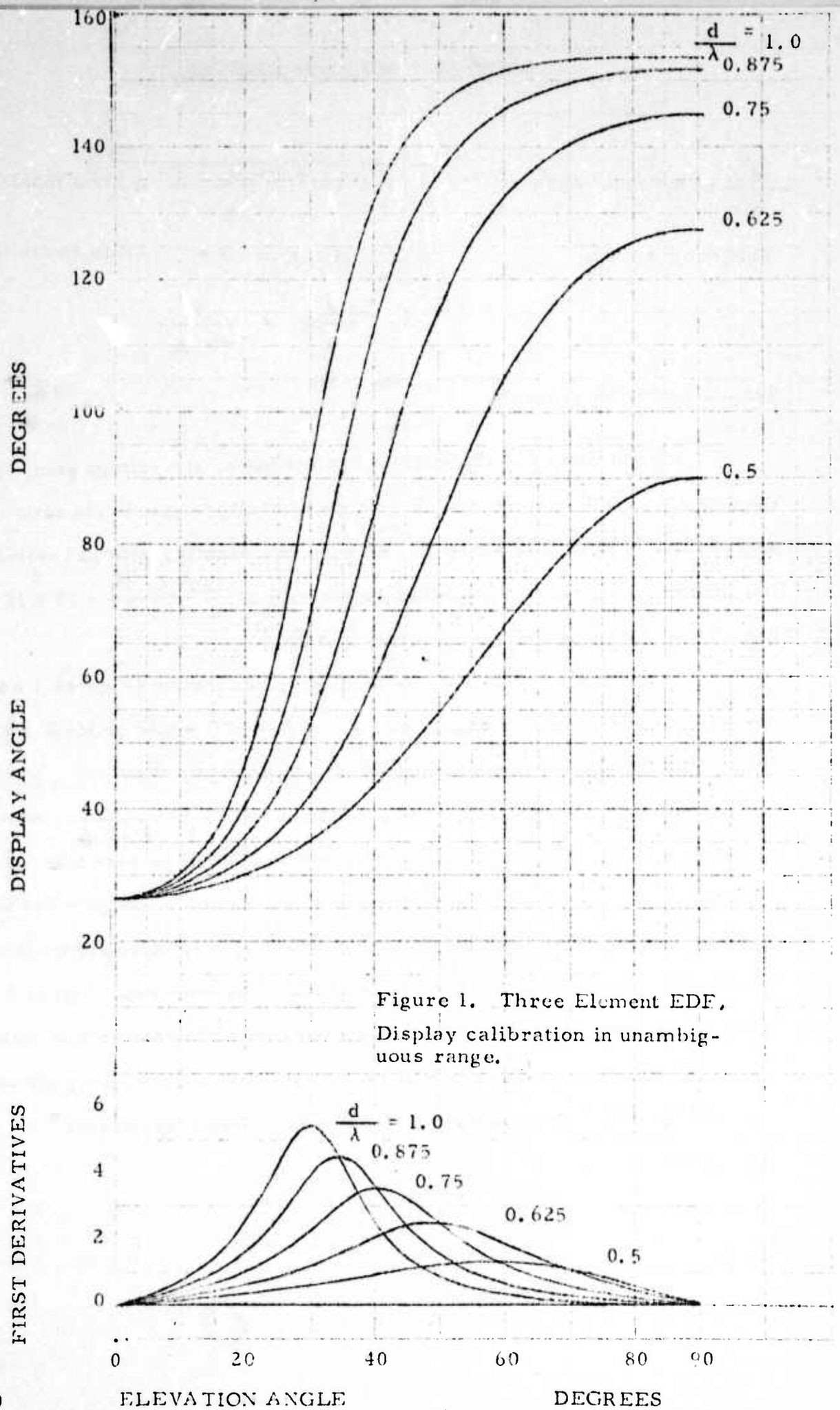

Figure 1. Three Element EDF, Display calibration in unambiguous range.

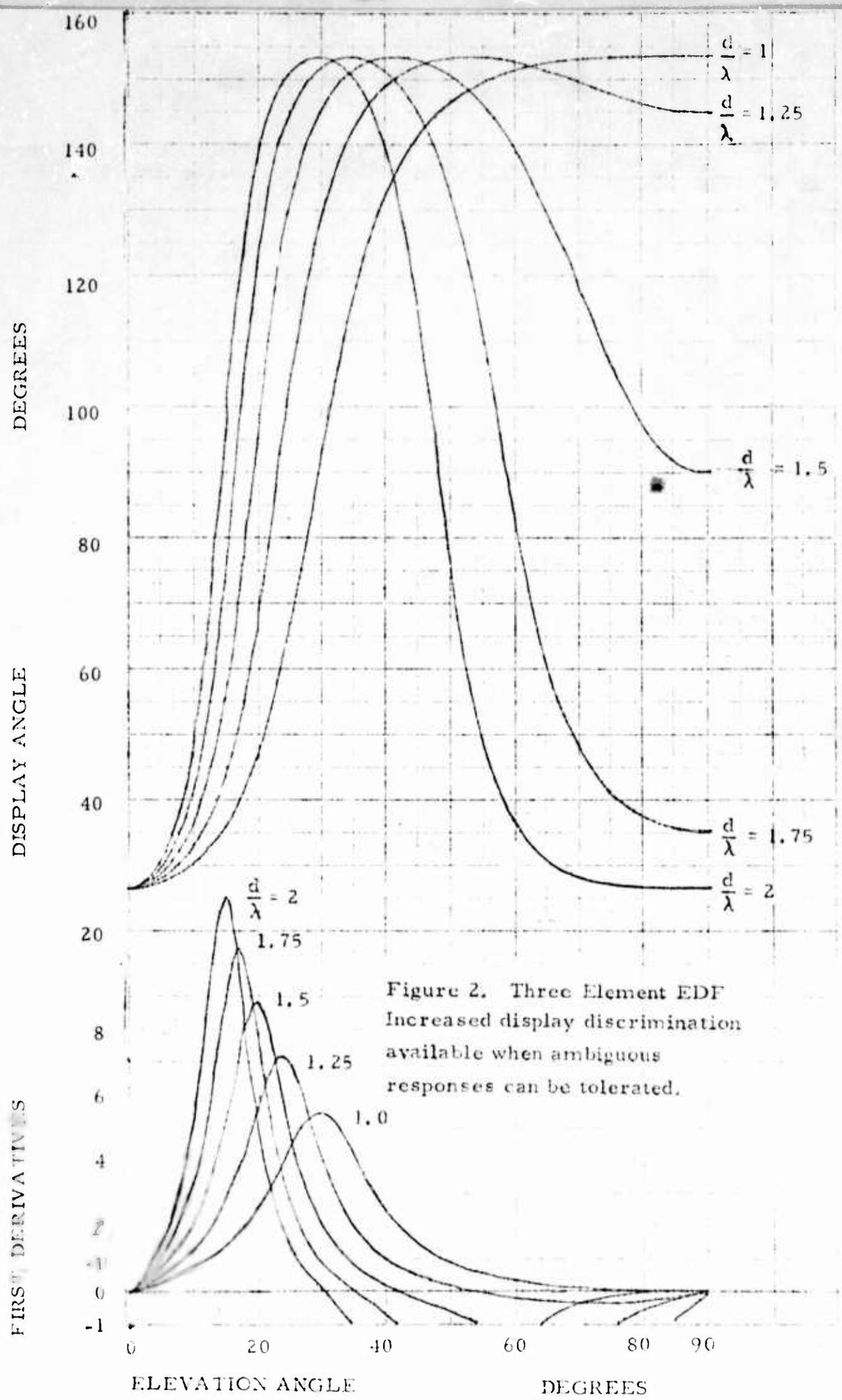

Figure 2. Three Element EDF
Increased display discrimination available when ambiguous responses can be tolerated.

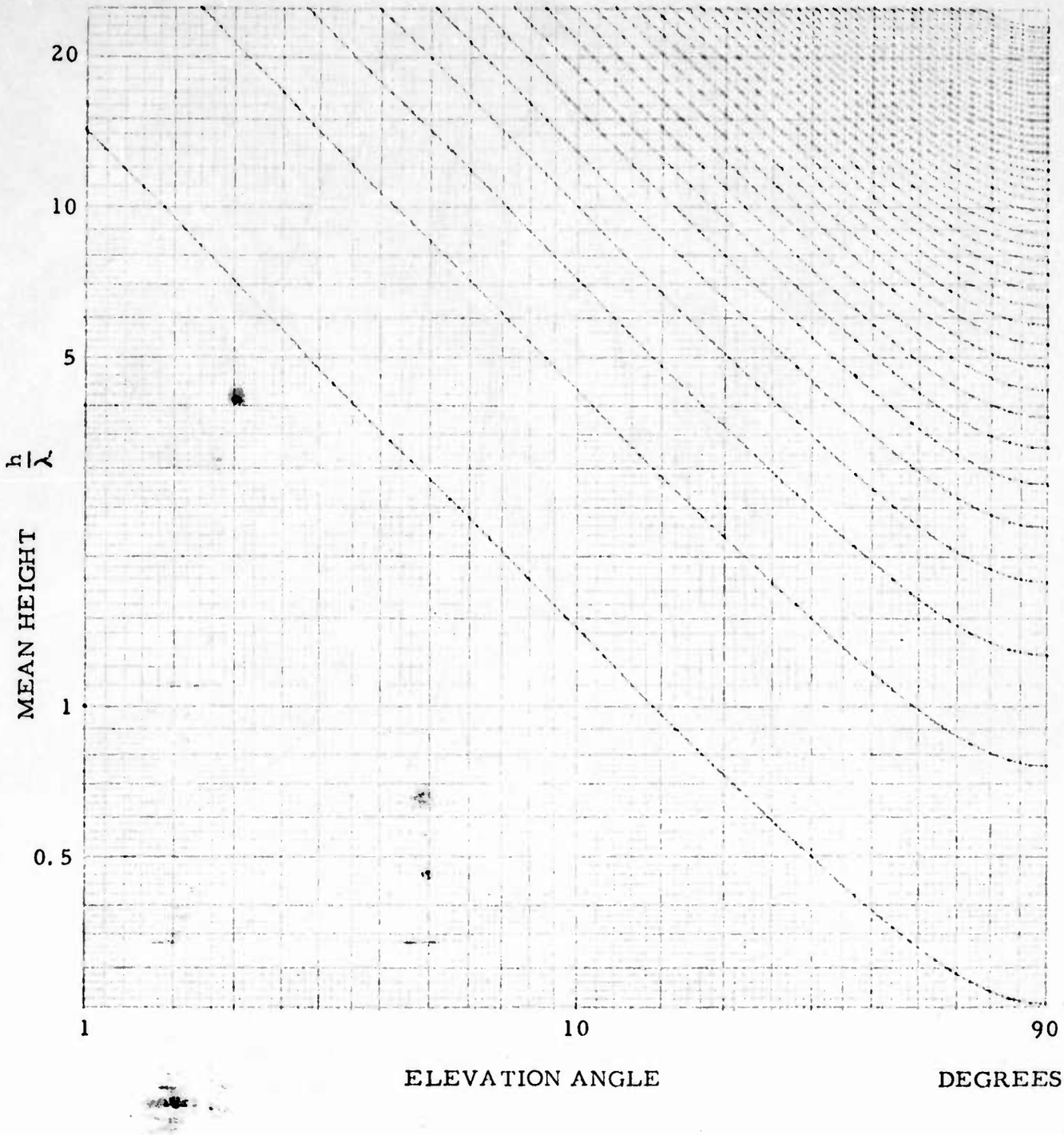

Figure 3. Optimum mean heights of a horizontally polarized three element EDF. For vertically polarized systems, the intermediate heights are optimum.

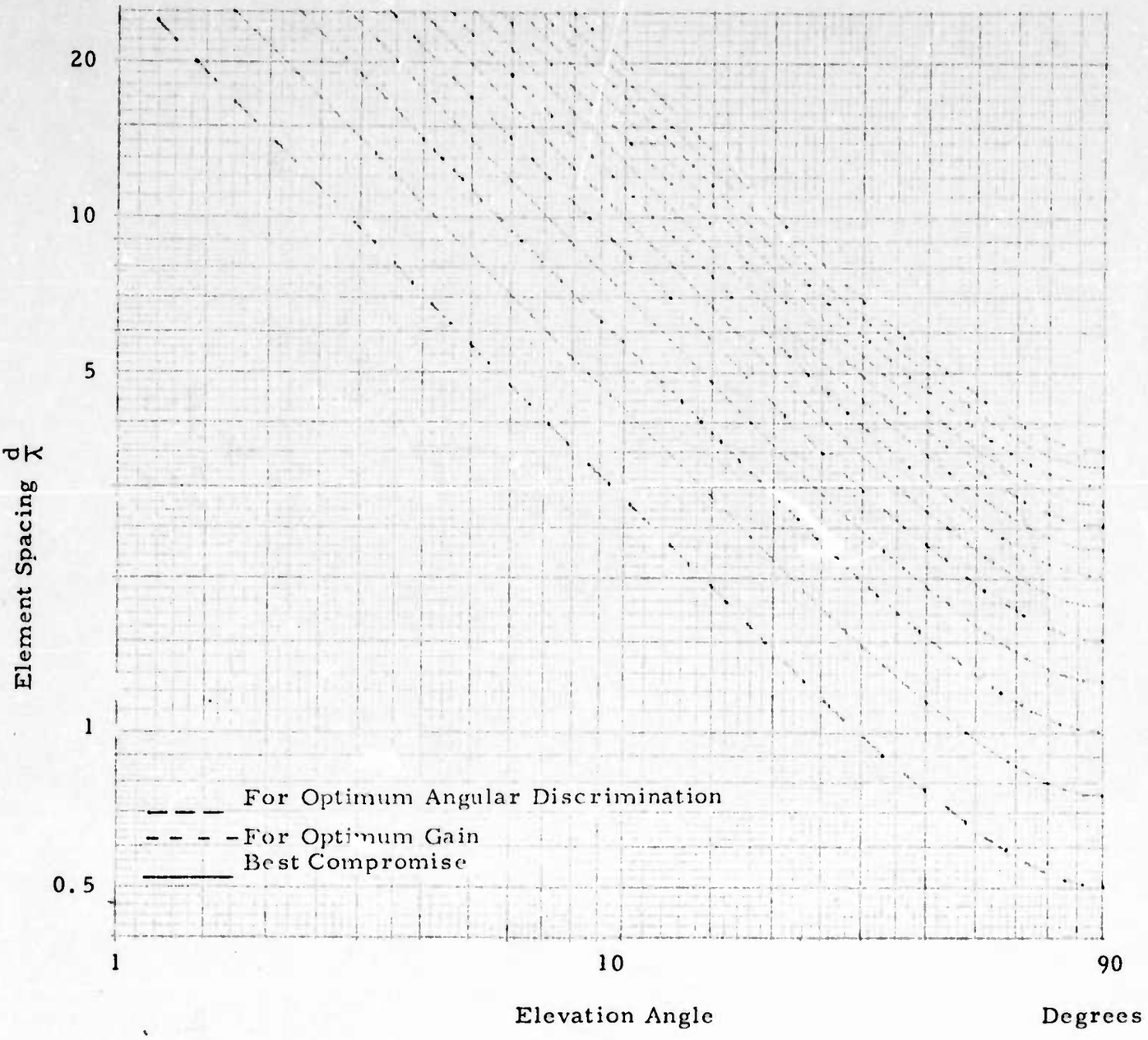

Figure 4. Optimum Element Spacings for Three Element EDF.

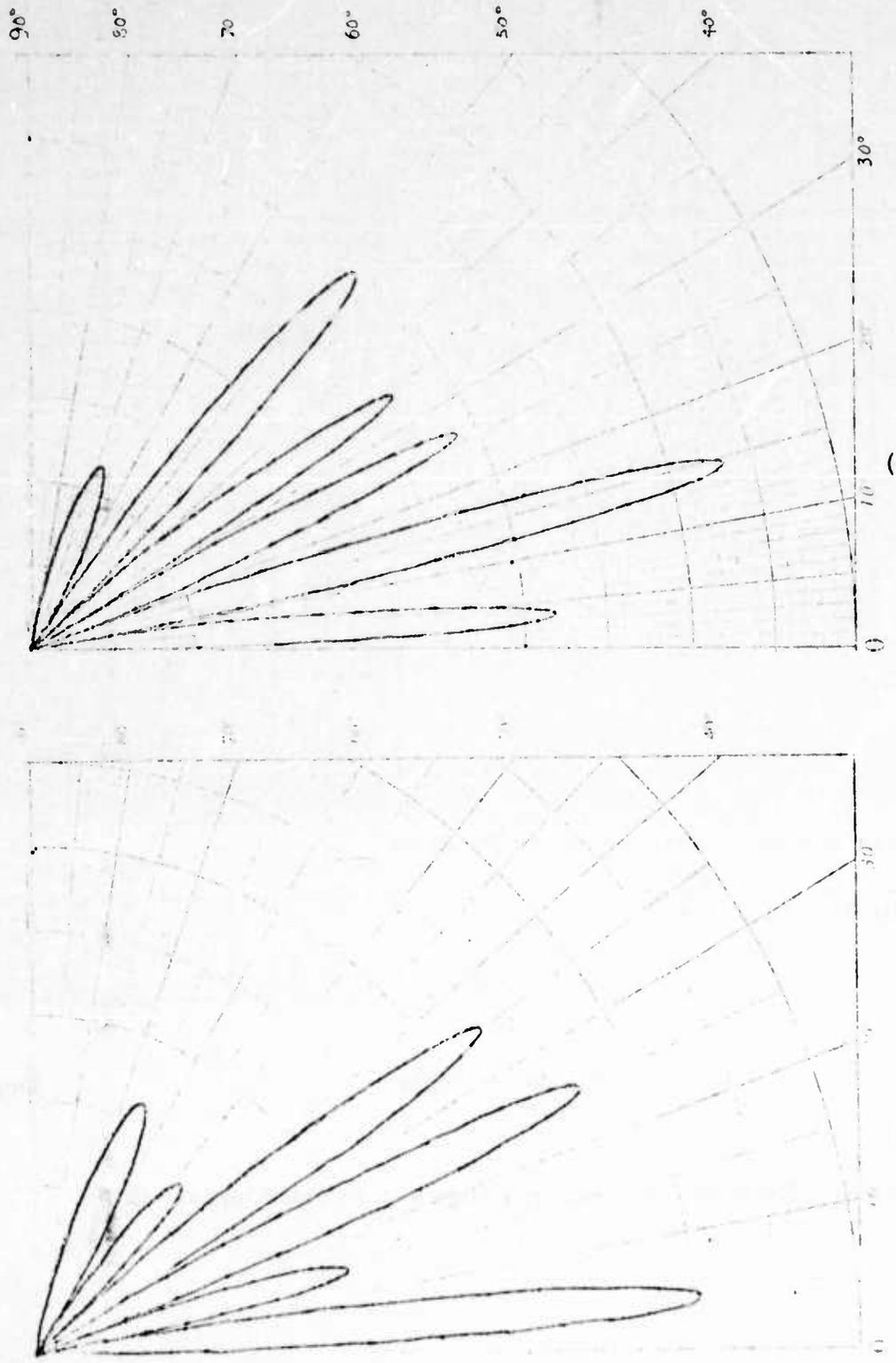

Figure 5. Vertical Polar Diagrams of Three Element EDF at optimum height for 14.48°

(a) Elements spaced for best sensitivity Voltage gain = $2\sqrt{5}\cos\Delta$

(b) Elements spaced for best angular discrimination Voltage gain = $2\cos\Delta$

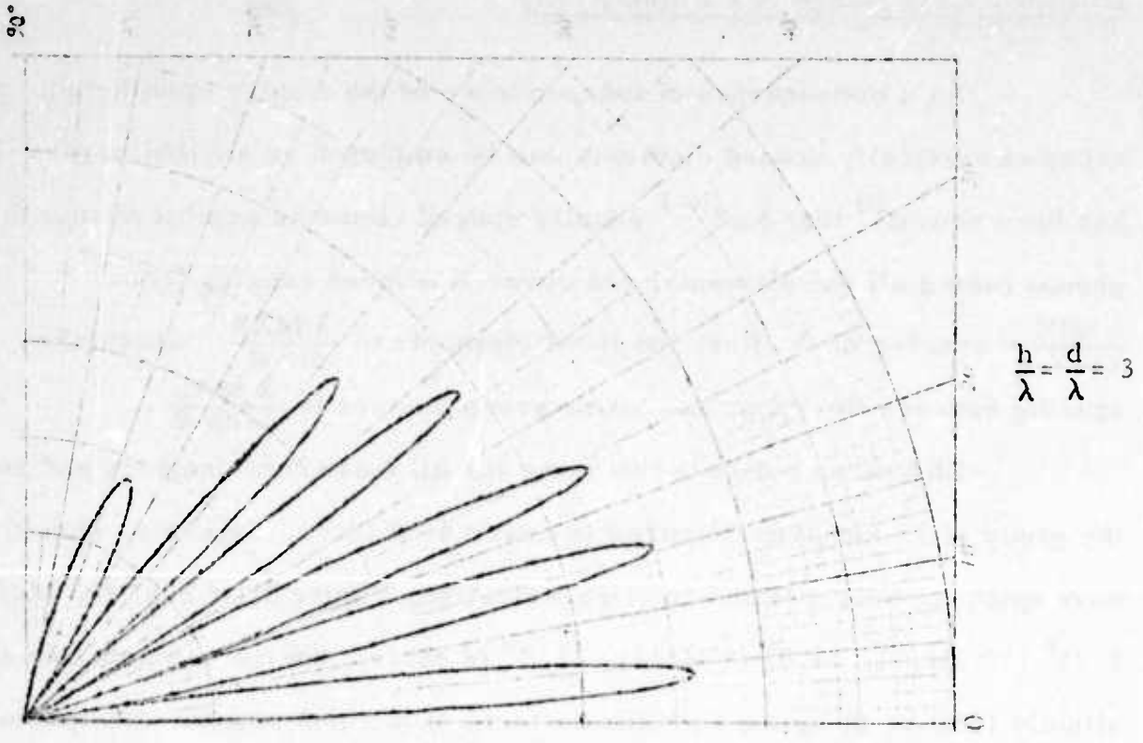

Figure 5 (c) Vertical Polar Diagram of Three Element EDF at optimum height for 14.48°.

Elements spaced for compromise between best gain and best angular discrimination. Voltage gain = 3.65 cos Δ

Extended Wave Range of a Filled Array

As a consequence of independence of the display upon height, an array of vertically spaced elements can be employed as a filled array. It has been shown[20] that $3 \times 2^{N-1}$ equally spaced elements combined into three groups (using all the elements) can cover N octaves ranging from $\frac{\lambda \text{ MIN}}{\text{Sin } \Delta}$ = spacing of the first and third elements to $\frac{\lambda \text{ MAX}}{\text{Sin } \Delta}$, where the spacing between the upper and lower group centers is $\frac{\lambda \text{ MAX}}{2 \text{ Sin } \Delta}$.

The mean height is the same for all these combinations and so the group of 12 antennas required to cover 4-32 Mc/s, Figure 6, should have optimum height (Horizontal Polarization, Figure 3) at 2.6° (32 Mc/s), 5.25° (16 Mc/s), 10.5° (8 Mc/s), 21.5° (4 Mc/s), but the maxima are shifted slightly (Figure 8) by the combined effects of element pattern and spacing. Twenty-four elements with the same spacing, on a 500 foot tower, could cover 2-32 Mc/s and there would be a choice of optimum gain angles to be either the same as, or half, the above values.

This spacing is insufficient for wideband circularly polarized elements but there is plenty of room for horizontal log periodic dipoles or for horizontal or crossed loops to be used. The horizontal loop arrangements is omnidirectional.

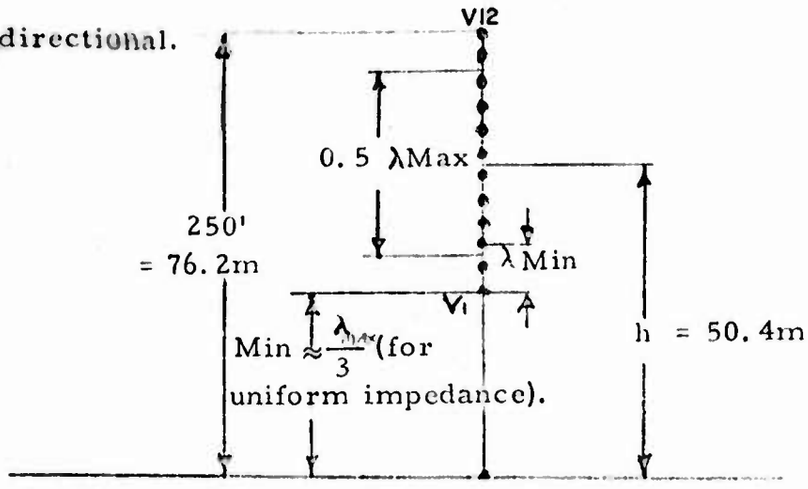

Figure 6. 12-Element Elevation Direction Finder for 4-32 Mc/s

Gain of 12 Element EDF

The magnitude of the response of a 12 element EDF is,[20] in the lowest octave, $\sqrt{(V_1 + V_{12} + V_2 + V_{11} + V_3 + V_{10} + V_4 + V_9)^2 + (V_5+V_8+V_6+V_7)^2}$

This, with simple horizontal loops equals

$2j\ Ei \cos\Delta \sin(2\pi\frac{h}{\lambda} \sin\Delta)(\cos 3\varphi + \cos\varphi)\sqrt{1 + 4\cos^2 8\varphi}$ where

$\varphi = \pi \frac{d}{\lambda} \sin\Delta$

In the middle octave, the magnitude is

$$\sqrt{(V_1+V_{12}+V_2+V_{11}+V_5+V_8+V_6+V_7)^2 + (V_3+V_{10}+V_4+V_9)^2}$$
$$- 2j\ Ei \cos\Delta \sin(2\pi\frac{h}{\lambda} \sin\Delta)(\cos 7\varphi + \cos 5\varphi)\sqrt{1+4\cos^2 4\varphi}$$

In the highest octave, the magnitude is

$$\sqrt{(V_1+V_{12}+V_3+V_{10}+V_4+V_9+V_6+V_7)^2 + (V_2+V_{11}+V_5+V_8)^2}$$
$$= 2j\ Ei \cos\Delta \sin(2\pi\frac{h}{\lambda} \sin\Delta)(\cos 9\varphi + \cos 3\varphi)\sqrt{1+4\cos^2 2\varphi}$$

The dependence on height is the same as in Figure 3 but the dependence upon $\frac{d}{\lambda}$ is more complicated and is illustrated in Figure 7. The scale shapes are those of Figures 1 and 2 except that the effective spacing is $K\frac{d}{\lambda}$ where K = 8 in the lowest octave, 4 in the middle and 2 in the highest octave.

Figures 8 (a), (b), and (c) show vertical polar patterns of a 12 element EDF at the low and high ends of each octave. The voltage scale has been reduced by a factor 2 and the maximum voltage gain is $4\sqrt{5}$. The maximum power gain is 16 db when impedance is taken into account. This is 6 db more than the equivalent 3 element system.

Steerable Nulls:

There will be nulls in the 3 or 12 element system responses to a signal component at a particular height, wavelength and elevation angle. Zero will occur when $\frac{h}{\lambda} = \frac{N}{2 \sin\Delta}$ for horizontal polarization.

(N = any integer). For vertical polarization the nulls occur when $\frac{h}{\lambda} = \frac{M}{4 \sin \Delta}$ (M = any odd integer.) A circularly polarized system will only have nulls when the wave is not circularly polarized or when the wrong sense is selected. In a system that has choice of polarization and mean height, the response to an unwanted mode of a 2 mode case can be greatly reduced by selecting a single polarization and the correct mean system height. In the proposed three or twelve element systems, because the display equation is independent of height, the angular information will be unaffected by this action; only the relative magnitudes will change, one going to zero.

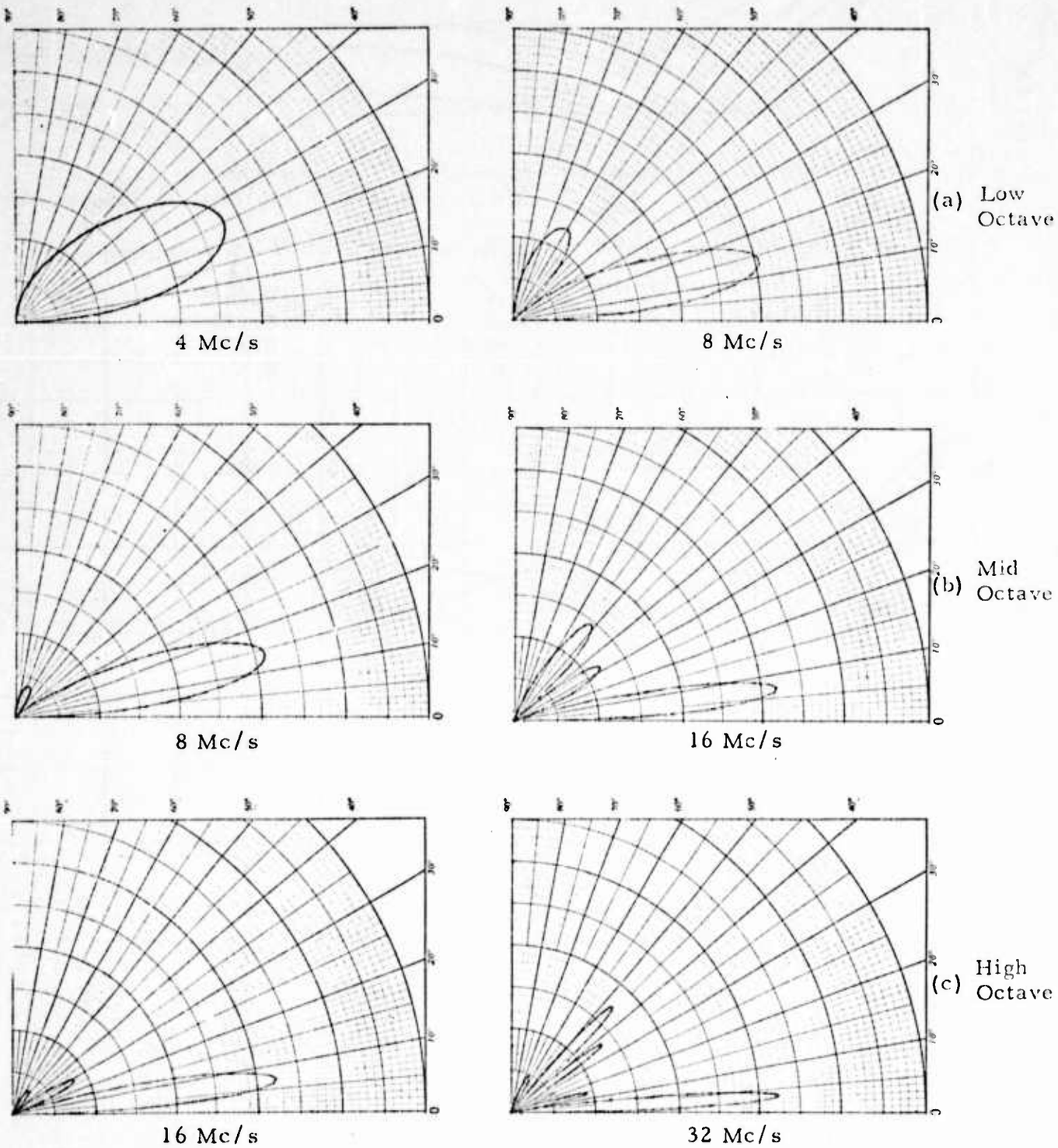

Figure 8. 12 Element EDF as in Figure 6. Vertical Polar Patterns. Voltage gain scale 0-10.

Figure 7. 12 Element EDF as in Figure 6. Dependence of voltage gain upon frequency, element spacing and elevation angle.

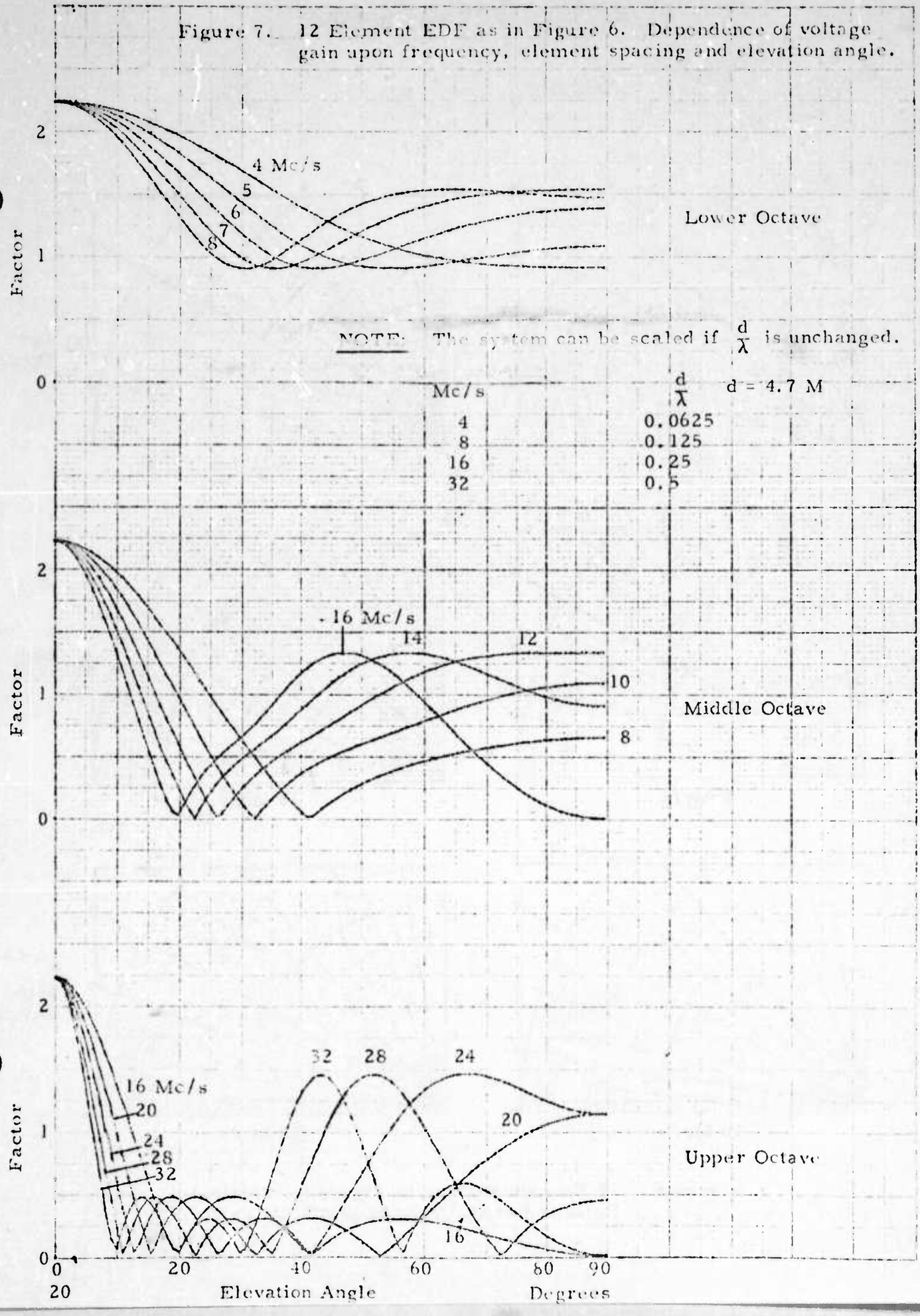

PART II THE RECEIVER

The instantaneous direction finding system introduced by Watson-Watt and Herd[5] (1926) was a natural marriage of the sine and cosine directional patterns of crossed spaced antenna systems, and the sine and cosine input requirements of an XY cathode ray tube. With this system, assuming sufficient field strength and some frequency selection, the direction of arrival of a wave relative to the reference antenna base line would be indicated directly on the tube, relative to the corresponding deflection system, with bandwidth and phosphor response the only time limitations. The field inside the deflection system, in fact, would be an exact replica of the field around the antenna and the display for a single plane wave would be a straight line of direction $\tan^{-1} \frac{\text{Sin } \theta}{\text{Cos } \theta}$, where θ is the azimuth: the length of the trace would be directly proportional to the field strength. The 180° ambiguity of this display can be resolved by deriving a non directional reference (S for sense) either from $\sin \theta + j \cos \theta$ or from a separate, non-directional, antenna. In either case, the phase of S must be adjusted to equal the phase at the center of the DF system for the preferred direction so that it will be of opposite phase in the reciprocal direction. Then the reference signal can be used to brighten or black out one end of the CRT trace by grid modulation. Such a system is ideal for the observation of direction and relative amplitudes of short-time signals such as pulses but it requires the X, Y and S components of the signal to be amplified without change of relative amplitude or phase. This is the matched receiver requirement

which is particularly difficult to meet when narrow bandwidths or rapid changes of signal strength are involved.

Note:

The design of such receivers is a very specialized subject that was given impetus by the urgent need to locate U-Boats in World War II or, at least, to make them so afraid of using radio that their efficiency was impaired. The Germans reacted by shortening their signals and, at the end of the war, were almost ready to introduce a system in which a U-Boat message was compressed into one third of a second. Fortunately their test signals were intercepted and a network of matched receiver systems,[6] capable of being triggered by the U-Boat signals and of storing the direction, was installed and waiting in England. This system relied on the pre-knowledge of the U-Boat frequencies, which we had acquired, but which could have been changed, and it lacked an effective automatic gain control and so was liable to miss a signal by the gain being pre-set at too high or too low a level.

It was not until 1953 that a suitable AGC system for matched receivers was invented (by T. R. O'Meara[7] in the University of Illinois). O'Meara attempted to match the conversion efficiency of typical mixer tubes over a wide range of local oscillator voltage but his system required tube selection and was burdened by the high effective noise resistance of low GM multi-element tubes. Anyone attempting to apply his method, and to have a good noise figure, had to employ a lot of RF gain. The dynamic

range was thereby reduced (because it extends only from the lowest signal at which acceptable signal to noise ratio exists to the signal level at which the conversion conductance departs from a constant.)

Guided by knowledge of O'Meara's approach, the author introduced an alternative that proved to be a complete solution of this problem. This was incorporated in a triple channel receiver made by Intercept Research Incorporated (Model IR-3).* The IR 3 System uses low noise square law mixers and is as follows:[21, 22]

Let the signal voltage be $E_s \cos \omega_s t$

and the oscillator voltage be $E_o \cos (\omega_o t + \theta)$

then the input $e = E_s \cos \omega_s t + E_o \cos (\omega_o t + \theta)$

and the output $e^2 = \frac{Es^2}{2} + \frac{Es^2}{2} \cos 2\omega_s t + \frac{E_o^2}{2} + \frac{E_o^2}{2} \cos 2(\omega_o t + \theta) \cdot$

$$+ E_s E_o \cos \left[(\omega_o + \omega_s)t + \theta\right] + E_s E_o \cos \left[(\omega_o - \omega_s)t - \theta\right]$$

If the last term is selected by the receiver IF filter, it is obvious that the output is directly proportional to the magnitude (and phase) of the local oscillator voltage so long as the law applies. Thus, any number of receiver channels can be controlled for gain by controlling the common local oscillator voltage. Inequalities of conversion conductances of the mixers are a constant factor and are corrected by a constant ratio introduced in the relative gains.

By using very low noise triodes in a balanced mixer circuit the harmonic output was greatly reduced and the need for high RF gain was avoided. The dynamic range of this circuit can be extended until the noise cannot be further reduced or until the stray coupling of local oscillator voltage becomes comparable with the very low level of intended feed. 70 db control with no measurable difference between two channels was easily attained in a system in which 0.01 db gain difference could be detected. The extension to 100 db range was a matter of attention to detail.

*Details of the circuits are proprietary since the receiver was developed entirely on private capital.

The availability of this AGC circuit permitted the use of linear amplifiers in all other stages and intermodulation was limited to the natural effects of a square law mixer. Most of the common causes of intermodulation were removed by RF selectivity and, in principle, when the receiver forms part of a radar system, the clutter will set the gain level so that the display system is not overloaded, while the echoes remain at their correct relative level. There should be no confusion with intermodulation products because they are of even lower level.

The fact that only one set of time constants are involved in the AGC permits the use of very high loop gain before the instability level is reached. This results in extremely constant output in spite of very large changes in signal level, as shown in Figure 9.[23]

The IR-3 also benefitted from studies of matched multi-pole filters carried out by R. F. Donnelly[24] at the University of Illinois. Since Intercept Research, Inc. were interested in displaying pulses, special care was taken to develop multi-pole filters similar to Donnelly's but with maximally uniform phase change between the 6 db limits of the passband. The filter characteristics are shown in Figure 10[23] and it was possible to detune to the 50 db points before differences between pairs of filters could be detected.

Such a receiver, fitted with a cathode ray tube with persistent screen, is ideal for use in the present application, especially when mode interference is experienced, and the rest of this report assumes its use.

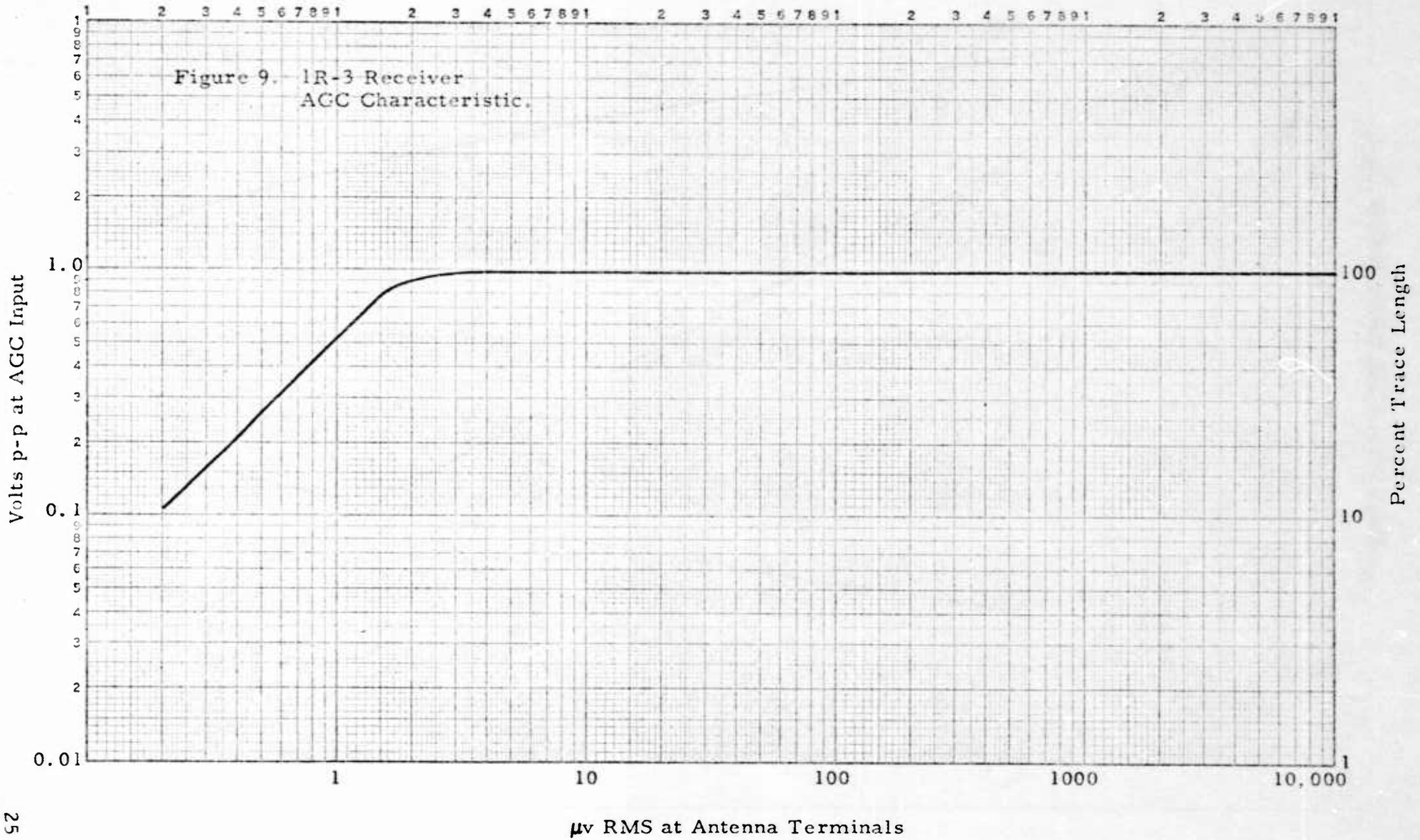

Figure 9. 1R-3 Receiver AGC Characteristic.

Figure 10. IR-3 Receiver

IF Filter Characteristics

Nominal Bandwidth	1 kc	5 kc
Envelope Delay*	1.015 ms	182 μs
Measured 60 db BW	4.6 kc	25.4 kc
Measured 6 db BW	1.26 kc	6.6 kc
Measured 3 db BW	1.0	5.0 kc
Figure of Merit	3.65	3.85

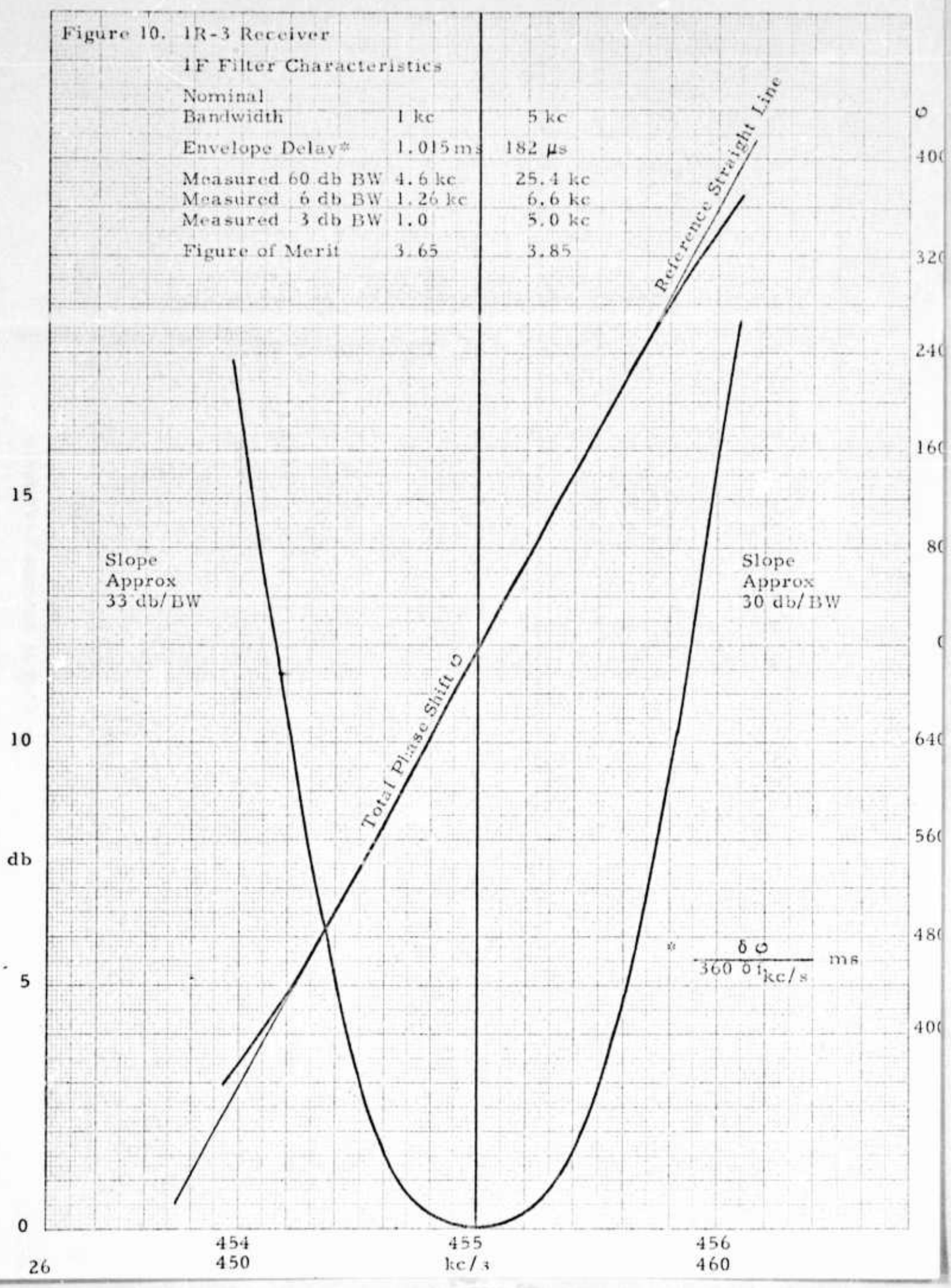

Multiple Mode Performance of Instantaneous Elevation Direction Finders.

When the signal consists of short enough pulses, the two or three element EDF systems indicate each ionospherically propagated mode separately. However, when the pulses overlap, or if the signal is CW, the mutual instabilities of the signal paths cause the resultants of the X and Y inputs to vary, in direction and magnitude, with time. If the fading rate in each mode is slow compared to $\frac{1}{2f_d}$, where f_d is the Doppler difference between the mode frequencies, the tips of the trace in an XY scope will lie on the envelope of a Lissajous figure, Figure 11. If the XY scope has a persistent screen, and the signal to noise ratio is adequate, the Lissajous figure can be observed directly and the direction and relative magnitudes of up to two major modes can be read. When there are more than two major modes, height selection can place a null on one mode so that observations can be made in the presence of three major modes.* If there are more modes of comparable strength the system is no longer capable of direct reading and a computer display must be substituted. This is discussed under the heading of signal to noise performance.

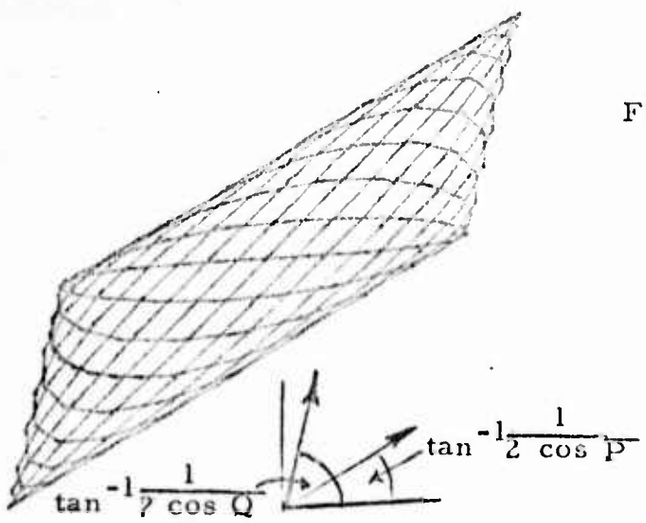

Figure 11. Lissajous Figure Resulting from Interference Between Two CW Modes in a Three Element I. E. D. F.

*Note: This rejection of a mode is employed, within the limits of the two element system, by Gething et al.[15] But it is of special value when the three element system is employed, because the display angles are independent of height.

Derivation of Lissajous Figure. Two Modes.

Assuming three antenna elements, as before, at heights $h - \frac{d}{2}$, h and $h + \frac{d}{2}$ and two modes at angles Δ_1 and Δ_2 and frequencies ω_1 and ω_2, the voltage at each antenna would be V_1, V_2, and V_3.

$$V_1 = \text{Sin}\left(2\pi \frac{h - \frac{d}{2}}{\lambda} \text{ Sin } \Delta_1\right) \text{Sin } \omega_1 t + A \text{ Sin}\left(2\pi \frac{h - \frac{d}{2}}{\lambda} \text{ Sin } \Delta_2\right) \text{Sin } \omega_2 (t + \delta t)$$

$$V_2 = \text{Sin}\left(2\pi \frac{h}{\lambda} \text{ Sin } \Delta_1\right) \text{Sin } \omega_1 t + A \text{ Sin}\left(2\pi \frac{h}{\lambda} \text{ Sin } \Delta_2\right) \text{Sin } \omega_2 (t + \delta t)$$

$$V_3 = \text{Sin}\left(2\pi \frac{h + \frac{d}{2}}{\lambda} \text{ Sin } \Delta_1\right) \text{Sin } \omega_1 t + A \text{ Sin}\left(2\pi \frac{h + \frac{d}{2}}{\lambda} \text{ Sin } \Delta_2\right) \text{Sin } \omega_2 (t + \delta t)$$

δt = constant A = another constant

Let $2\pi \frac{h}{\lambda} \text{ Sin } \Delta_1 = L$ $\pi \frac{d}{\lambda} \text{ Sin } \Delta_1 = P$ $\omega_1 t = R$

$2\pi \frac{h}{\lambda} \text{ Sin } \Delta_2 = M$ $\pi \frac{d}{\lambda} \text{ Sin } \Delta_2 = Q$ $\omega_2 (t + \delta t) = S$

then $V_1 = \text{Sin } (L - P) \text{ Sin } R + A \text{ Sin } (M - Q) \text{ Sin } S$

$V_2 = \text{Sin } L \text{ Sin } R + A \text{ Sin } M \text{ Sin } S$

$V_3 = \text{Sin } (L + P) \text{ Sin } R + A \text{ Sin } (M + Q) \text{ Sin } S$

Taking the first terms of V_1 and V_2 for example,

$$\text{Sin } (L \pm P) \text{ Sin } R = \text{Sin } L \text{ Cos } P \text{ Sin } R \pm \text{Cos } L \text{ Sin } P \text{ Sin } R$$

so, taking both terms, $V_1 + V_3 = 2 \text{ Sin } L \text{ Cos } P \text{ Sin } R + 2A \text{ Sin } M \text{ Cos } Q \text{ Sin } S$

In this system we display $\frac{V_2}{V_1 + V_3}$

$$= \frac{\text{Sin } L \text{ Sin } R + A \text{ Sin } M \text{ Sin } S}{2 \text{ Sin } L \text{ Cos } P \text{ Sin } R + 2 A \text{ Sin } M \text{ Cos } Q \text{ Sin } S}$$

$$= \frac{1}{2 \cos P + \frac{2 A \text{ Sin } M \text{ Cos } Q \text{ Sin } S}{\text{Sin } L \text{ Sin } R}} + \frac{1}{2 \cos Q + \frac{2 \text{ Sin } L \text{ Cos } P \text{ Sin } R}{A \text{ Sin } M \text{ Sin } S}}$$

sin R and sin S are functions of time and second terms in the denominators become 0 or ∞ as sin R or sin S = 0. If the condition sin R = 0 was maintained the display would be a straight line of direction $\tan^{-1} \frac{1}{2 \cos Q}$ but in practice the display is a spot at the position

$$-Y = \sqrt{V_2^2 + (V_1 + V_3)^2} \cos \varphi_1 \qquad X = \sqrt{V_2^2 + (V_1 + V_3)^2} \sin \varphi_1$$

and $\varphi_1 = \tan^{-1} \frac{1}{2 \cos Q}$

Similarly, when sin S=0, the spot has a position $-Y = \sqrt{V_2^2 + (V_1 + V_3)^2} \cos \varphi_2$

$X = \sqrt{V_2^2 + (V_1 + V_3)^2} \sin \varphi_2$ where $\varphi_2 = \tan^{-1} \frac{1}{2 \cos P}$

This happens twice per cycle of ω_1 and of ω_2. At other times the spot takes up a position that is the resultant of both terms and the locus of the spot is a Lissajous figure.

Further, the magnitude of the first term goes to zero when sin L= 0 and the second term goes to zero when sin M= 0

sin L and sin M are of the form $\sin (2\pi \frac{h}{\lambda} \sin \Delta)$ and equal zero when

$$2\pi \frac{h}{\lambda} \sin \Delta = (n-1)\pi$$

$$h = \frac{(n-1)\lambda}{2 \sin \Delta}$$

So there are heights at which the first or second terms can be observed alone for all times at which λ and Δ are constant. This is illustrated in Figure 12(a) which shows the field above a groundplane at the time when two modes are in phase. Lissajous figures have been plotted at heights at which one or other mode goes through zero net field, as well as at intermediate points. The important fact to be observed is the constancy of direction of the sides of the figure which is a demonstration of the independence of the display angle upon height.

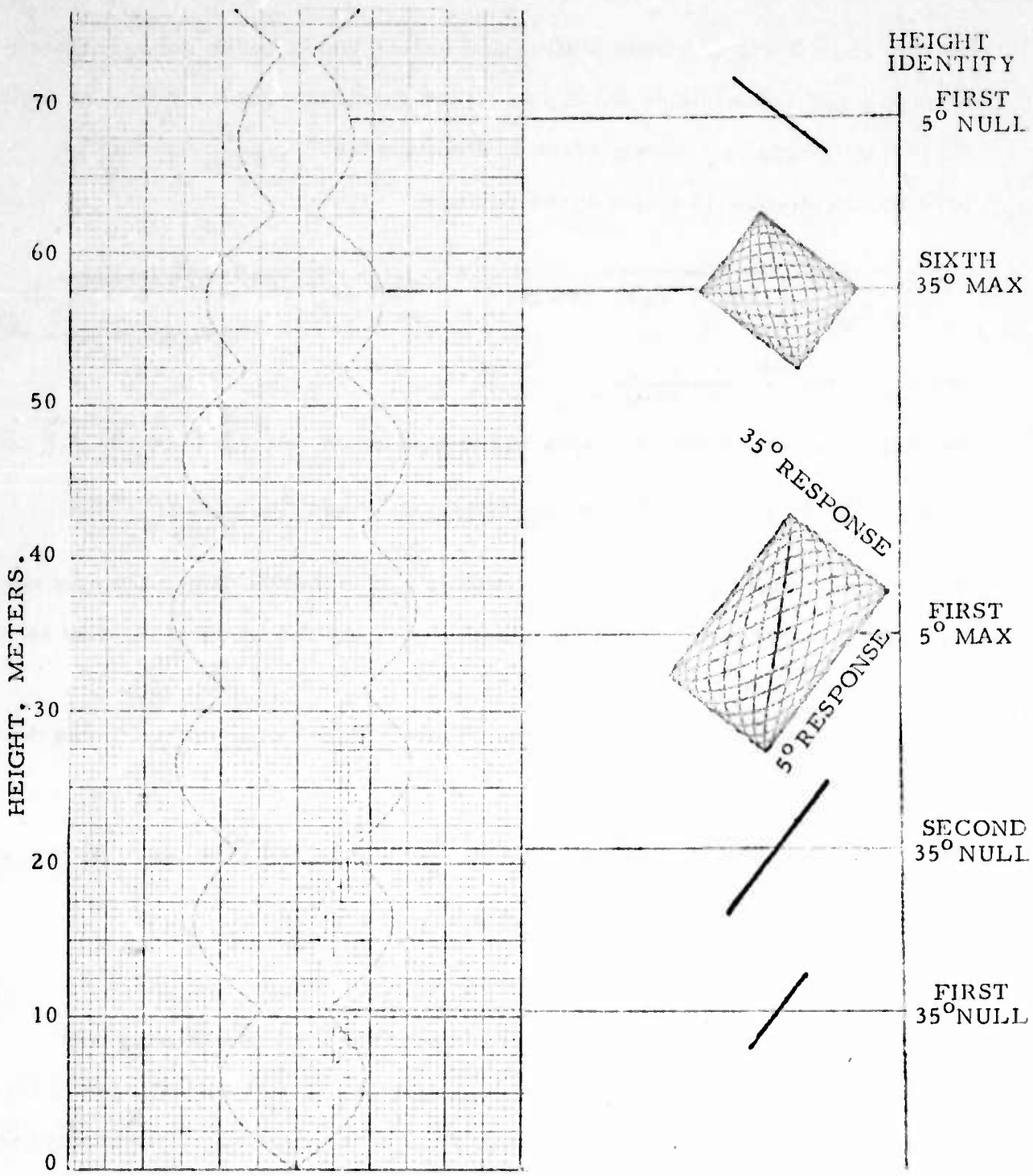

Figure 12. (a) Horizontally Polarized Field above a flat groundplane, due to two modes: Δ = 5° Magnitude = 1

Δ = 35° Magnitude = 0.8

(b) Consequent dependence of 3 element EDF display upon height.

NOTE: Tower height 76 M. f = 25 Mc/s

Another important fact is that the higher elevation angle goes through 7 nulls in the specified height (at 25 Mc/s) where the 5^{o} wave field strength only goes to zero near the top of the tower. At a slightly lower frequency there would be no nulls for a 5^{o} elevation angle. Thus steering to a magnitude null in a practical system permits the observations of lower angle modes. (It was pointed out by Bramley[25] that the azimuthal variance of a two hop mode can be as much as 12 times the variance of a one hop mode. The variance of the corresponding elevation angles should also favor the one hop, low angle, mode, so the locating of the transmitter should be more accurate in this case too). If the signal is frequency modulated, or if height is scanned, the magnitude of each mode response will be a function of time, going to zero in accordance with this expression. The display of a wideband signal will be a fan with a sharp null at the angle and frequency that satisfy this equation. The frequency can be identified by superimposing a reference signal and observing beats. If the equation is not satisfied by any part of the signal spectrum, the height must be increased. If λ, n and mean height are accurately known, an accurate value of Δ can be derived. Of course, a wideband signal is accompanied by all the other signals in the passband and identification by its fan shape may be difficult. However, if the receiver bandwidth is reduced and its center frequency is scanned over the signal spectrum, the correlation with the fan display should be observed. If the signal occupies a narrow spectrum, a very narrow band receiver can be used because the bandwidth need pass only the Doppler modulations. However, if height is scanned, the bandwidth should be adjusted to admit this new modulation.

HF Noise Field Above a Perfect Groundplane

As stated earlier, interference between the direct and ground reflected waves of a horizontally polarized signal, arriving at an elevation angle Δ degrees above a perfect groundplane, leads to a standing wave in the vertical plane of magnitude $2jE_1 \sin(2\pi \frac{h}{\lambda} \sin \Delta)$, the time phase being independent of height and of elevation angle.

Direct and ground reflected noise impulses arriving in the same manner also add coherently and assume the same distribution.

Similarly, vertically polarized signals and noise impulses produce standing waves of the form $2E_1 \cos \Delta \cos (2\pi \frac{h}{\lambda} \sin \Delta)$ and retain their initial relative time phases.

Thus, as far as signals are concerned, there are heights,* depending upon frequency, angle of arrival and polarization, at which the signal strength is a maximum. These maxima are the result of perfect ground reflection and so contain the full image gain.

Components of signal frequency in the spectrum of a noise source near the site of the transmitter will be propagated in the same way and will have a similar height dependence. In this special case, there may be no signal to noise advantage in selecting a particular height except in the presence of interfering signals. In practice, especially if the system is omnidirectional, there will be sensitivity to noise sources that are distributed in range and direction and therefore in elevation angle and propagation characteristics. Since these are also random in magnitude and time, it

*Figure 3

seems reasonable to assume that there will be ranges of heights, depending upon polarization, at which a selected frequency in the spectrum of a storm at a given mean distance will produce maximum fields. Storms in the immediate vicinity of the receiver will arrive as space waves of high elevation angle. Slightly more distant storms will tend to arrive as vertically polarized ground waves. Storms at greater distances will cause interference only if their fields can be propagated by the ionosphere and so, as with signal propagation, there will be a skip zone in which storms cause no interference. The angle of arrival of waves originating beyond the skip zone is a function of range and height of reflection, and so also of frequency, season, time of day, direction, etc.

Thus, the noise fields just above a perfect ground plane might be expected to be impulsive and vertically polarized and due to sources at groundwave range or to the vertically polarized components of ionospherically propagated waves of any angle. These are the noises that are sampled by conventional HF direction finders. Up higher, they may be expected to be horizontally polarized and impulsive and due to high angle local sources, or due to sources just beyond the skip zone.

The longer range noises that resemble white noise because they are the sum of a great number of sources might be expected to be randomly polarized and to arrive at low elevation angles and so to reach their first horizontally polarized maximum field strength at the greater heights, their first vertically polarized maximum being near ground level. Vertically polarized antennas at ground level are, therefore, subjected to noise fields from all ranges whereas horizontally polarized antennas at the lower heights

are subjected to high angle noise sources only. Higher up, the horizontally polarized antennas are subjected to long range low angle fields whereas vertically polarized antennas are sampling higher angle, shorter range sources. Thus a study of noise levels above a perfect ground plane should select polarization, frequency, height, direction, angle of arrival and ionosphere data and be correlated with information concerning storms; the outcome might allow a proposed system design to be optimized. On the other hand, if the new system can be versatile in choice of polarization, height, and, perhaps, direction it might be adjusted to suit each new situation and avoid the need for accumulation of statistics.

Signal to Noise Ratio

It is evident that each noise impulse is correlated at each antenna (because the ground reflection is assumed to be perfect and to lead to a standing wave in the vertical plane), therefore the direction and relative magnitude of each noise impulse will be indicated correctly in the three or twelve element system. The cathode ray display will show the ratio of the resultant of the Y components of signal plus noise to the resultant of the X components at each instant, and this will cause momentary variations in the direction and magnitude of the trace. The total effect can be stored in a persistent screen and may be expected to have the mean direction of the signal, when the signal to noise ratio is large enough, as described by de Walden and Swallow[26] in a study of the equivalent azimuthal display problem.

REFERENCES

1. A. D. Bailey and W. C. McClurg "A Sum and Difference Interferometer System for H.F. Radio Direction Finding" IEEE Transactions ANE-10 Number 1, March 1963, pp. 65-72.

2. University of Illinois. "Studies and Investigations Leading to the Design of a Radio Direction Finder System for the MF, HF and VHF Range". Contract DA 36-039 SC 84525. Final Report 31 July 1961 p. 25.

3. University of Illinois. "Studies and Investigations Leading to the Design of a Radio Direction Finder System for the MF, HF, and VHF Range". U. S. Army Contract DA 36-039 AMC 03720(E) Final Report 31 July 1964, particularly pp. 121-177.

4. W. Ross, E. N. Bramley and G. E. Ashwell. "A Phase-Comparison Method of Measuring the Direction of Arrival of Ionospheric Radio Waves" Proc IEE 1951 Vol 98, Part III pp. 294-302

5. R. A. Watson-Watt and J. F. Herd "An Instantaneous Direct-Reading Radiogoniometer". JIEE 1926 Vol 64, p. 611

6. S. deWalden, A.F.L. Rocke, J.O.G. Barrett and W.J. Pitts. "The development of a High-Frequency Cathode-Ray Direction-Finder for Naval Use". JIEE Vol 94, Part III a No. 15 1947 pp. 823-837.

7. University of Illinois. ONR Project 076-161 Task XV Particularly Technical Report 17, April 1953, and ONR Project 1834-02 Technical Report 5 1-25-57.

8. R. F. Treharne "Vertical Triangulation Using Skywaves" Proc IREE Australia Nov 1967 pp. 419-424

9. H. T. Friis, C. B. Feldman and W. M. Sharpless "The Determination of the Direction of Arrival of Short Radio Waves". Proc IRE Vol 22, No. 1 Jan 1934 p. p. 47-78, particularly pp. 62-76

10. E. Bruce and A. C. Beck "Experiments with Directivity Steering for Fading Reduction" Proc IRE Vol 23, No. 1, April 1935 pp. 357-371.

11. H. T. Friis & C. B. Feldman "A Multiple Unit Steerable Antenna for Short Wave Reception" Proc IRE Vol 25, No 7 1937 pp. 841-917

12. For instance in the British CH Radar during World War II. See J. A. Ratcliffe "Aerials for Radar Equipment" JIEE Part IIIa 1946 Vol 93 p. 22

13. A. F. Wilkins "Characteristics of HF Signals" Electronic & Radio Engineer Sept 1957 pp. 335-341

14. A. T. Low & B.V. Harris "Vertical Wave-Arrival Measurements of HF Transmissions During the Period Dec 1960 to July 1961" IEE HF Convention 1963 pp. 52-60

15. P.J.D. Gething, J.G. Morris, E.G. Shepherd and D.V. Tibble "Measurement of Elevation Angles of HF Waves" Proc IEE Vol 116, No. 2 Feb 1969 pp. 185-193

16. F. Kift, P.A. Bradley, L.T.J. Martin and E.N. Bramley "HF Oblique Sounding Measurements over a 6,700 km Temperate Latitude Path" Proc IEE Vol 116, No. 12, Dec 1969 pp. 1985-1991

17. A. F. Wilkins and C.M. Minnis "Arrival Angle of HF Waves". Wireless Eng. Feb 1956 p. 47-53

18. Internal Memorandum Lyle Rocke to W. T. Whelan "Analysis of a GCHQ Type Elevation Direction Finder". 22 May 1970

19. E. C. Jordan & K. G. Balmain "Electromagnetic Waves and Radiating Systems" pp. 139-143

20. Internal Memorandum L. Rocke to W. T. Whelan "Filled Aperture Wide Frequency-Range Instantaneous Elevation Direction Finder". Revised 23 March 1970.

21. J. G. Brainerd, G. Koehler, H. J. Reich and L. F. Woodruff, "Ultra-High-Frequency Techniques" p. 238.

22. Intercept Research Inc. Design Notes 1963.

23. Intercept Research Inc. Design Notes 1965

24. R. F. Donnelly "Narrow Band Matched Channel I. F. Amplifiers" Parts 1 x 2 Contract 1836 (02) ONR Project 371-161 Tech Reports 16 (11. 30. 61) and 20 (9. 19. 63).

25. E. N. Bramley "Some Comparative Measurements on Short Radio Waves over Different Transmission Paths" Proc IEE Part B July 1955 Vol. 102 No. 4 pp. 544-549

26. S. de Walden and J. C. Swallow "The Relative Merits of Presentation of Bearings by Aural-Null and Twin-Channel Cathode-Ray Direction-Finders" Proc IEE 96 PartIII No. 42 July 1949

APPLICATION OF SYNCHRONOUS AND CORRELATION DETECTION TO HF/DF SYSTEMS

R. W. Moss and H. H. Jenkins
Communications Branch
Electronics Division
Engineering Experiment Station
Georgia Institute of Technology
Atlanta, Georgia

and

W. S. Hayden
Department of the Army

May 1971

ABSTRACT

The application of synchronous and correlation detection to small-aperture, HF/DF systems has resulted in significantly improved performance. Sensitivity can be increased and bearing error and dispersion reduced. These detection techniques also provide additional performance improvements such as instantaneous sensing, increased bearing display quality, and modulation tolerance.

Synchronous and correlation detection have been implemented and used in rotating interferometer systems. Field test results indicate that sensitivity using synchronous and correlation detection is some 10 dB and 27 dB better, respectively, than envelope detection. Also, correlation detection can reduce bearing dispersion by as much as 3:1 and is especially useful under weak signal and severe groundwave/skywave interference conditions. Other improved performance characteristics were also verified by the field tests.

APPLICATION OF SYNCHRONOUS AND CORRELATION DETECTION TO HF/DF SYSTEMS

Introduction

Synchronous and correlation detection have been extensively used in communications and radar systems to lower the detection threshold and increase the post-detection signal-to-noise ratio. However, the application of these detection techniques to radiolocation and direction-finding systems has not been as widespread, even though significant improvements can be made in system performance. This paper describes the application of synchronous and correlation detection to small-aperture HF/DF systems and shows that not only is sensitivity improved but also other performance characteristics such as instantaneous sense, modulation tolerance, and increased bearing accuracy can be obtained.

The basic operating principles of synchronous detection as applied to HF/DF systems using small-aperture arrays are presented. Small-aperture arrays considered are rotating interferometers (both spaced coaxial loops and spaced vertical dipoles) and the simple loop. Improvements obtained in sensitivity, detection dynamic range, and bearing display quality are described, and the technique of instantaneous sensing using the synchronous detection output is explained.

A post-synchronous detection correlation technique called orthogonal correlation is described. It is shown how quadrature sinusoidal and cosinusoidal replicas of the antenna array scan rate can be multiplied by the synchronous detection output, low-pass filtered, and time averaged by integration to acquire a significant increase in sensitivity. It is also shown how bearing error and dispersion reduction are obtained by orthogonal correlation.

Complete dual-channel HF/DF systems designed especially for synchronous and correlation detection have been fabricated and field tested. The systems are short baseline rotating interferometers using both spaced vertical dipoles and spaced coaxial loops. Field tests under a variety of signal and propagation conditions have verified the improvements afforded by synchronous and correlation detection.

The work summarized in this paper was performed under Contract DAAB07-68-C0072 with the U. S. Army Electronics Command.

Synchronous Detection - Basic Principles

Figure 1 depicts a rotating interferometer array with identical antenna elements separated by a baseline distance d. The baseline is horizontal and rotated about the vertical axis at a rate of ω_s. For tactical HF usage, the baseline must be electrically short and the antenna elements must be electrically small in order to maintain a physically small form factor consistent with operational requirements. For example, the baseline and effective element heights may not exceed 0.2 λ at the highest frequency of interest.

Both of these factors combine to decrease the sensitivity of a short-baseline interferometer relative to a larger interferometer (e.g., $d/\lambda = 0.5$) with resonant antenna elements. One basic approach to improving sensitivity is the use of synchronous rather than envelope detection. Synchronous detection requires two input signals for proper demodulation -- one with the bearing information and another phase reference signal without the bearing information. This requirement is satisfied by using a broadband RF hybrid at the interferometer output to obtain sum (Σ) and difference (Δ) signals. The Δ signal contains the bearing information; the Σ signal does not. The Δ signal is applied to one channel of a dual-channel receiver; the Σ signal is applied to the other channel. It is important to note that the dual-channel approach described does not require amplitude and phase matching in the dual-channel receiver. The IF outputs are used as the synchronous detector input signals.

For a single frequency received component, the antenna element output voltages referenced to a common phase center can be represented by

$$E_1 = G(\lambda, \psi, \Phi, \theta) \cos\left[\omega_c t - \frac{\pi d}{\lambda} \cos \Phi \sin (\omega_s t - \theta)\right] \qquad (1)$$

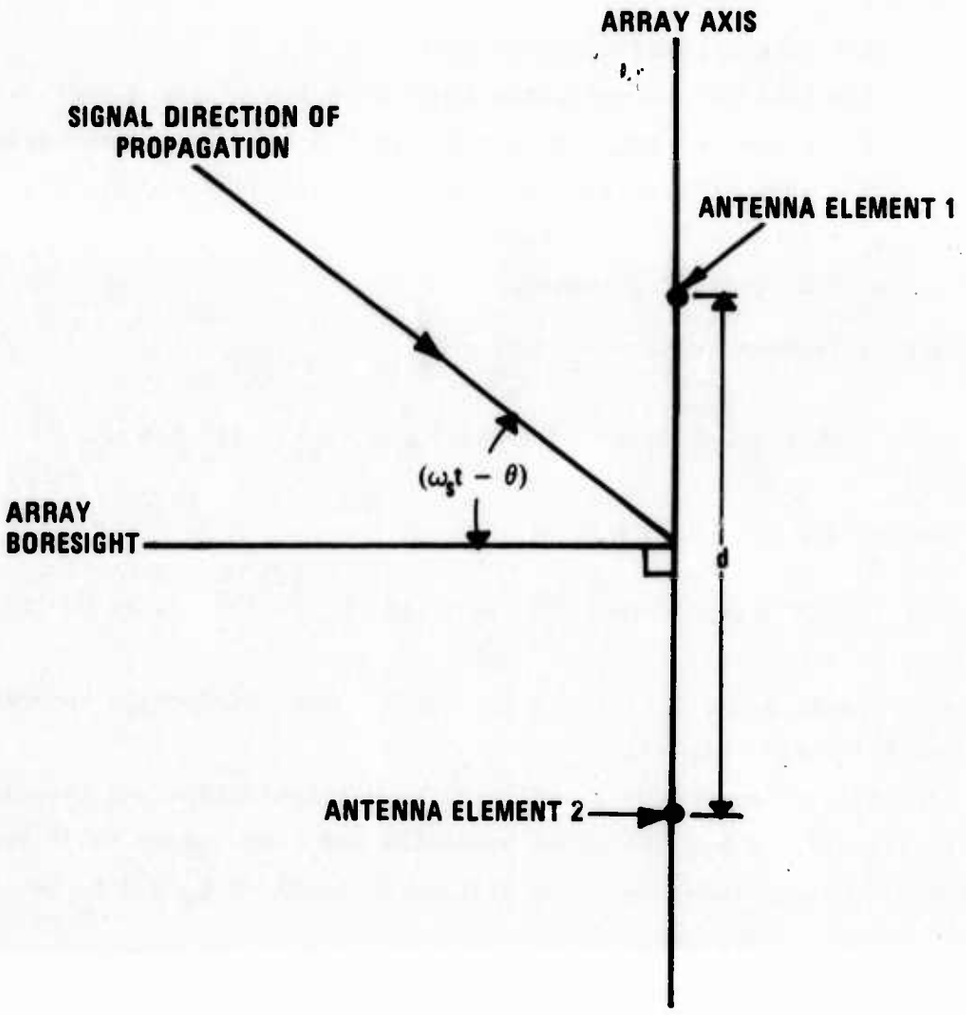

Figure 1. Interferometer - Top View.

and

$$E_2 = G(\lambda,\psi,\Phi,\theta) \cos\left[\omega_c t + \frac{\pi d}{\lambda} \cos\Phi \sin(\omega_s t - \theta)\right], \qquad (2)$$

where $G(\lambda,\psi,\Phi,\theta)$ describes the antenna response pattern associated with each element and,

λ = incident wavelength,

ψ = incident polarization angle with $\psi = 0^\circ$ for a vertical signal,

Φ = elevation angle of arrival with $\Phi = 0^\circ$ for a groundwave signal,

θ = azimuth direction of arrival of incident signal,

ω_s = antenna rotation rate, and

ω_c = RF carrier frequency.

The difference voltage $E_\Delta = E_1 - E_2$

$$= 2G(\lambda,\psi,\Phi,\theta) \sin\left[\frac{\pi d}{\lambda} \cos\Phi \sin(\omega_s t - \theta)\right] \sin\omega_c t. \qquad (3)$$

The sum voltage $E_\Sigma = E_1 + E_2$

$$= 2G(\lambda,\psi,\Phi,\theta) \cos\left[\frac{\pi d}{\lambda} \cos\Phi \sin(\omega_s t - \theta)\right] \cos(\omega_c t + \delta), \qquad (4)$$

where the phase angle δ accounts for any RF phase difference between the sum and difference signals.

Synchronous detection is achieved by multiplication and lowpass filtering of signals (3) and (4) after reception and translation to IF frequency in a dual-channel receiver. The filtered product of E_Δ and E_Σ is

$$E_S = E_\Delta E_\Sigma$$

$$= -G^2(\lambda,\psi,\Phi,\theta) \sin\delta' \sin\left[\frac{2\pi d}{\lambda} \cos\Phi \sin(\omega_s t - \theta)\right], \qquad (5)$$

where the phase angle δ' accounts for both the RF and IF phase differences. It may be noted that δ' has no effect on bearing measurement in that it only affects the amplitude of E_s.

For all of the antenna systems considered, the baseline d is much

less than a wavelength so that the simplifying assumption

$$d/\lambda << 1 \qquad (6)$$

can be made. Two basic interferometer configurations are considered: coaxially spaced loops and spaced vertical dipoles. For the loop elements the loop circumference is considerably less than a wavelength so that the loop antenna pattern function becomes

$$G(\lambda,\psi,\Phi,\theta) = K\left\{\cos\psi\cos(\omega_s t - \theta) + \sin\psi\sin\Phi\sin(\omega_s t - \theta)\right\}, \qquad (7)$$

where K is a constant related to loop area and frequency. The loop interferometer difference voltage is

$$E_{\Delta L} = 2K\left\{\cos\psi\cos(\omega_s t - \theta) + \sin\psi\sin\Phi\sin(\omega_s t - \theta)\right\}$$
$$\left\{\frac{\pi d}{\lambda}\cos\Phi\sin(\omega_s t - \theta)\right\}\sin\omega_c t. \qquad (8)$$

Equation (8) represents the conventional output voltage that is obtained from a rotating spaced loop antenna. The sum voltage from (4) is

$$E_{\Sigma L} = 2K\left\{\cos\psi\cos(\omega_s t - \theta) + \sin\psi\sin\Phi\sin(\omega_s t - \theta)\right\}$$
$$\left\{\cos(\omega_c t + \delta)\right\}. \qquad (9)$$

The synchronously detected scan pattern obtained from (5) is

$$E_{SL} = -K^2\left\{\cos\psi\cos(\omega_s t - \theta) + \sin\psi\sin\Phi\sin(\omega_s t - \theta)\right\}^2$$
$$\left\{\sin\delta' \cdot \frac{2\pi d}{\lambda}\cos\Phi\sin(\omega_s t - \theta)\right\}. \qquad (10)$$

For the spaced vertical dipole interferometer the antenna elements are electrically short so that the antenna pattern function for a single dipole is

$$G(\lambda,\psi,\Phi,\theta) = C \cos\psi \cos\Phi, \tag{11}$$

where C is a constant related to the effective height of the element. The vertical dipole interferometer difference voltage is

$$E_{\Delta D} = 2C \cos\psi \cos^2\Phi\left\{\frac{\pi d}{\lambda} \sin(\omega_s t - \theta)\right\} \sin\omega_c t, \tag{12}$$

and the corresponding sum voltage is

$$E_{\Sigma D} = 2C \cos\psi \cos\Phi \cos(\omega_c t + \delta) . \tag{13}$$

The synchronous detector output is the filtered product of (12) and (13) or

$$E_{SD} = -C^2 \cos^2\psi \cos^3\Phi \sin\delta' \left\{\frac{2\pi d}{\lambda} \sin(\omega_s t - \theta)\right\} . \tag{14}$$

Table I summarizes all of the basic equations which describe interferometer sum and difference outputs and the synchronously detected scan patterns. Also included in Table I are the equations which result when a simple rotating loop is used to provide the difference signal and a short vertical probe antenna is used to provide the sum signal. An analysis of Table I will show that the desired bearing information is contained in the zero crossings of E_S and is therefore an inherently narrowband process affording considerably smaller bandwidth post-detection filtering than conventional envelope detection. Single channel rotating DF systems frequently use simple envelope detection of the magnitude of the different signals shown in Table I leading to the well known full-wave rectified waveform with amplitude nulls indicating the bearing locations. A waveform of this type is inherently wideband requiring a post-detection bandwidth considerably larger than the basic scan rate; heavy filtering to improve the signal-to-noise ratio results in reduction in bearing accuracy and display sharpness and readability. In practice it has been found that 10-15 dB improvement in sensitivity can be realized with synchronous detection by use of narrow post-detection filters. An additional advantage of

TABLE I

Basic Interferometer Equations

	Difference Signal E_Δ	Sum Signal E_Σ	Synchronously Detected Signal E_S
General Case - Interferometer $G(\lambda,\psi,\phi,\theta)$ = element pattern	$E_\Delta = 2G(\lambda,\psi,\phi,\theta) \times \sin\left\{\frac{\pi d}{\lambda}\cos\phi\sin(\omega_s t - \theta)\right\} \times \sin\omega_c t$.	$E_\Sigma = 2G(\lambda,\psi,\phi,\theta) \times \cos\left\{\frac{\pi d}{\lambda}\cos\phi\sin(\omega_s t - \theta)\right\} \times \cos(\omega_c t + \delta)$.	$E_S = -G^2(\lambda,\psi,\phi,\theta)\sin\delta \times \sin\left\{\frac{2\pi d}{\lambda}\cos\phi\sin(\omega_s t - \theta)\right\}$.
Spaced Loops - $d/\lambda \ll 1$ Circumference $\ll \lambda$	$E_{\Delta L} = 2K\left\{\cos\psi\cos(\omega_s t - \theta) + \sin\psi\sin\phi\sin(\omega_s t-\theta)\right\} \times \left\{\frac{\pi d}{\lambda}\cos\phi\sin(\omega_s t - \theta)\right\} \times \sin\omega_c t$.	$E_{\Sigma L} = 2K\left\{\cos\psi\cos(\omega_s t - \theta) + \sin\psi\sin\phi\sin(\omega_s t-\theta)\right\} \times \cos(\omega_c t + \delta)$.	$E_{SL} = -K^2\left\{\cos\psi\cos(\omega_s t - \theta)+\sin\psi\sin\phi\sin(\omega_s t - \theta)\right\}^2 \times \left\{\sin\delta\frac{2\pi d}{\lambda}\cos\phi\sin(\omega_s t-\theta)\right\}$.
Spaced Dipoles $d/\lambda \ll 1$ $\ell \ll \lambda$	$E_{\Delta D} = 2C\cos\psi\cos^2\phi \times \left\{\frac{\pi d}{\lambda}\sin(\omega_s t - \theta)\right\} \times \sin\omega_c t$.	$E_{\Sigma D} = 2C\cos\psi\cos\phi \times \cos(\omega_c t + \delta)$.	$E_{SD} = -C^2\cos^2\psi\cos^3\phi\sin\delta \times \left\{\frac{2\pi d}{\lambda}\sin(\omega_s t - \theta)\right\}$.
Simple Loop with Short Vertical Probe Circumference $\ll \lambda$ $\ell \ll \lambda$	$E = K\left\{\cos\psi\sin(\omega_s t - \theta) - \sin\psi\sin\phi\cos(\omega_s - \theta)\right\} \times \sin\omega_c t$.	$E = C\cos\psi\cos\phi \times \cos(\omega_c t + \delta)$.	$E_S = -\frac{KC}{2}\sin\delta\cos\psi\cos\phi \times \left\{\cos\psi\sin(\omega_s t - \theta) - \sin\psi\sin\phi\cos(\omega_s t - \theta)\right\}$.

synchronous detection is that the azimuthal information is contained in a waveform zero crossing rather than a simple minimum value. This feature of synchronous detection gives rise to improved dynamic range of the bearing display and enhanced pattern sharpness and readability. Also, quadrature noise rejection is achieved by use of synchronous demodulation contributing to improved post-detection signal-to-noise ratio.

Figure 2 illustrates normalized envelopes of the IF sum and difference signals and the resultant synchronously detected scan patterns for the two basic interferometers and the simple loop/vertical probe system. Conditions are depicted for $\psi \equiv 0^{o}$. It may be noted that in all cases the desired bearing information (occurring at π and 2π) is contained in a zero-crossing rather than in a signal null. Therefore the bearing information is inherently narrowband since it is contained in a simple zero-crossing (low harmonic content) at the basic antenna scan rate. Also sense determination (bearing ambiguity removal) is inherent in all of the synchronously detected scan patterns. In every instance, the waveform zero crossings have opposite slopes for the two bearing null positions. This fact has been exploited in the Georgia Tech dual-channel approach by providing the capability for determining instantaneous sense on a single scan of the DF antenna.

The photographs in Figure 3 demonstrate the sense capability that can be achieved with synchronous detection. Display patterns obtained with the spaced dipole interferometer and the spaced loop interferometer are shown. It may be noted that the spaced loop display contains four possible null locations. These figures show bearing display patterns obtained when a portion of the synchronously detected signal is used to provide sense "lobes" on the display. For the spaced dipole interferometer, the correct null is indicated by the null which is preceded by the sense lobe when viewing the compass rose in a clockwise sense. Similarly, the correct null for the spaced loop display is indicated by the null which is preceded by, but not followed by, the sense lobe. Note that the bearing displays are not degraded by the addition of the sense information. It is particularly significant to note that only one antenna scan is required for a complete determination of bearing. This fact is important

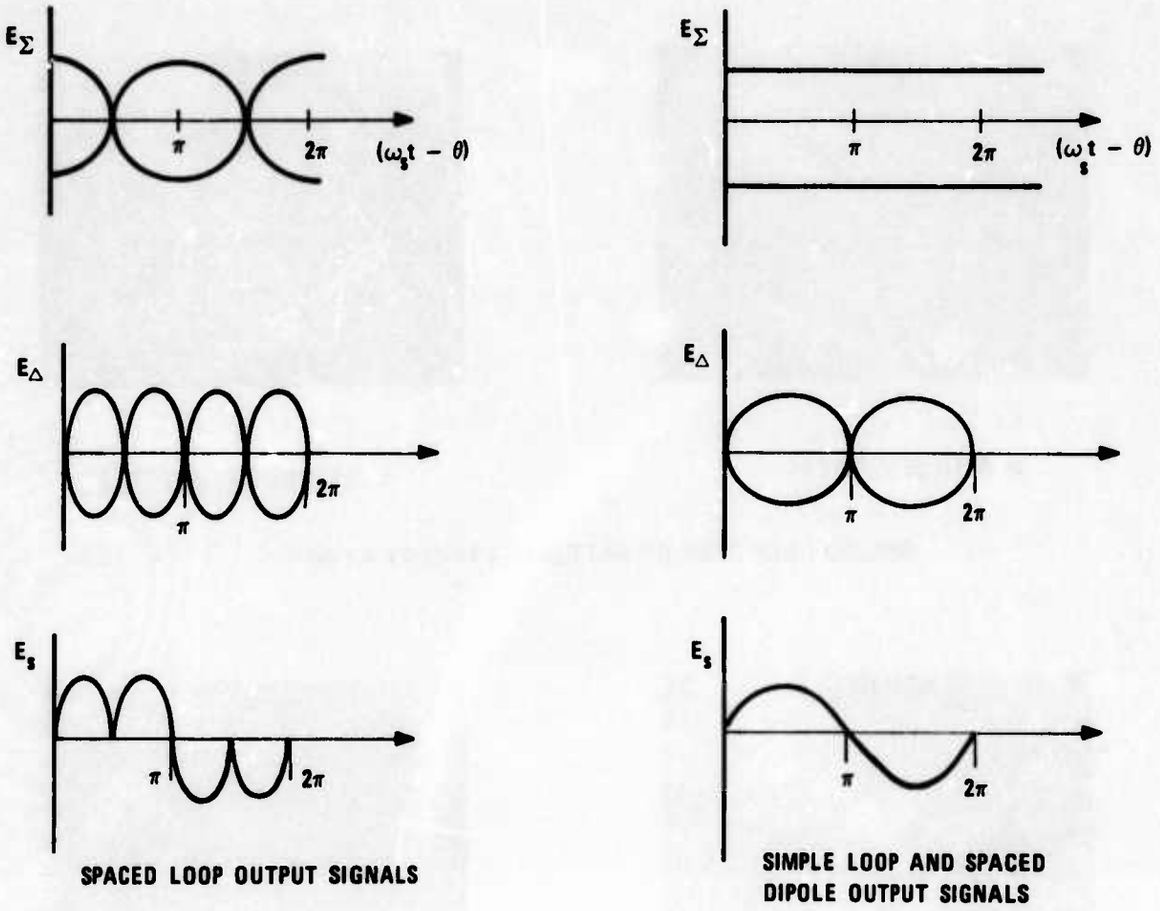

Figure 2. Sum, Difference, and Synchronous Detection Signals.

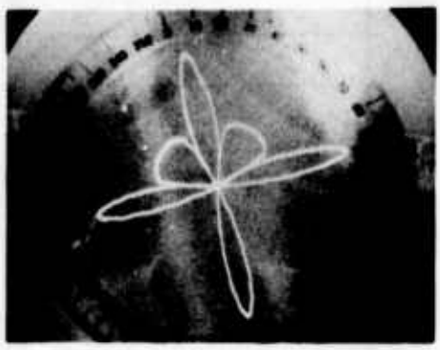

a. WITH SENSE LOBE

b. WITHOUT SENSE LOBE

SPACED LOOP DISPLAY PATTERNS (TARGET AT 94°)

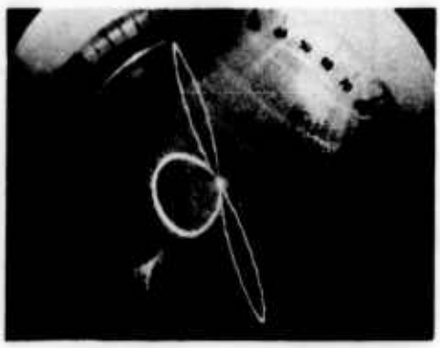

c. WITH SENSE LOBE

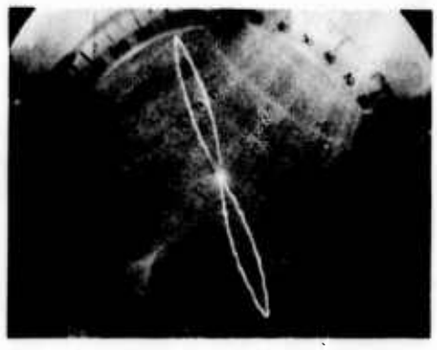

d. WITHOUT SENSE LOBE

SPACED DIPOLE PATTERNS (TARGET AT 0°)

Figure 3. Bearing Displays Depicting Sense Patterns.

when it is recognized that pattern time history is normally required for most conventional small-aperture direction finders.

Synchronous detection has a considerably larger dynamic range than envelope detection again due to the use of zero-crossing (phase) rather than amplitude information. With synchronous detection the increased dynamic range tends to stabilize the bearing display, i.e., the null depths indicated on the display do not vary as the signal amplitude changes due to fading.

To summarize, synchronous detection results in (1) increased sensitivity, (2) improved bearing display sharpness and reliability, (3) increased dynamic range, and (4) instantaneous sensing.

Orthogonal Correlation - Basic Principles

The basic form of the synchronous detection output makes it possible to obtain even larger sensitivity improvement by use of an orthogonal correlation technique depicted in Figure 4. The basic function of orthogonal correlation is to perform a cross correlation of the synchronous detector output with quadrature (orthogonal) sinusoidal components of the antenna scan rate. Since a crosscorrelator provides a measure of the coherence between two waveforms, the two parallel crosscorrelators in Figure 4 produce sin θ and cos θ outputs where θ is the bearing angle as contained in the zero-crossings (i.e., phase) of the synchronous detector output. Also, a crosscorrelator acts as a form of matched filter providing the ultimate in linear filtering that leads to the highest possible signal-to-noise ratio at the filter output. In addition to sensitivity improvement, orthogonal correlation provides bearing error and dispersion reduction, modulation tolerance, reduction of antenna array unbalance effects, easily read bearing displays, inherent sense, and output signals compatible with a digital readout.

In Table I when noise and time variable bearing errors are included, the synchronously detected output signals are all of the form

$$E_S = K' a(t) \sin\left[\omega_s t - \theta + \epsilon(t)\right], \qquad (15)$$

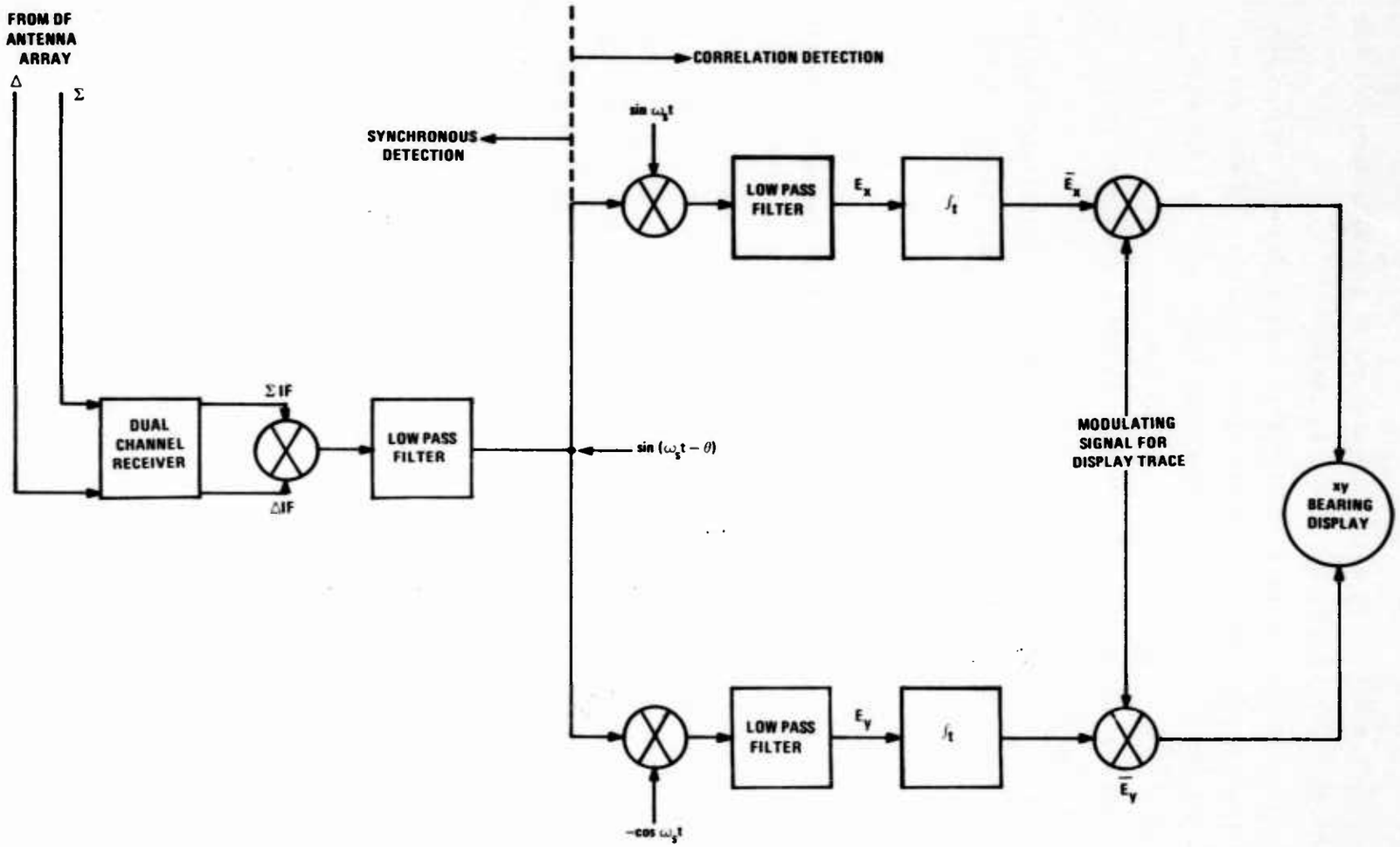

Figure 4. Basic Functional Diagram of Synchronous Detection and Orthogonal Correlation.

where K' = a constant related to the antenna element gain factor, Φ,Ψ,δ', and d/λ,

$a(t)$ = a time variable amplitude that is a function of modulation, noise, fading, etc.,

ω_s = the antenna scan rate,

θ = azimuth angle of arrival, and

$\epsilon(t)$ = a time variable bearing error created by noise, polarization changes (simple loop), and ionospheric effects such as multiple wave propagation and path deviation.

Fortunately, the function described by Equation (15) is of a form that can be efficiently time cross correlated with orthogonal sinusoidal representations of the antenna scan rate in order to recover the bearing information.

In Figure 4, E_s of Equation (15) is multiplied by $\sin \omega_s t$ and $\cos \omega_s t$ in parallel paths and lowpass filtered to remove the double frequency terms ($2\omega_s$). The outputs from the two correlation detectors prior to the integrators are of the form

$$E_x = K'' b(t) \cos \left[\theta - \epsilon(t)\right]$$

$$= K'' b(t) \left[\cos \theta \cos \epsilon(t) + \sin \theta \sin \epsilon(t)\right] \text{ and} \qquad (16)$$

$$E_y = K'' b(t) \sin \left[\theta - \epsilon(t)\right]$$

$$= K'' b(t) \left[\sin \theta \cos \epsilon(t) - \cos \theta \sin \epsilon(t)\right], \qquad (17)$$

where K'' is a constant and b(t) is a time variable amplitude resulting from the multiplication/filtering process.

It will now be assumed that $\epsilon(t)$ is an ergodic, stochastic process confined to the range $|\epsilon(t)| < \frac{\pi}{2}$ with a time average of zero. This basically assumes that the probability density function $p(\epsilon)$ of $\epsilon(t)$ is symmetrical about $\epsilon = 0$. A considerable amount of empirical data acquired by many investigators strongly indicates that, in general, the time-average value of DF bearing errors is zero implying a symmetrical function with zero mean.

It may be noted that E_x and E_y are time-variables due to $\epsilon(t)$. After integration the expected values are

$$\bar{E}_x = K'' \overline{b(t)} \left[\cos\theta \int_{\text{all } \epsilon} \cos\epsilon \, p(\epsilon) d\epsilon + \sin\theta \int_{\text{all } \epsilon} \sin\epsilon \, p(\epsilon) d\epsilon \right] \quad (18)$$

$$\bar{E}_y = K'' \overline{b(t)} \left[\sin\theta \int_{\text{all } \epsilon} \cos\epsilon \, p(\epsilon) d\epsilon - \cos\theta \int_{\text{all } \epsilon} \sin\epsilon \, p(\epsilon) d\epsilon \right]. \quad (19)$$

Note also that the amplitude terms have been time averaged, providing the modulation tolerance feature.

Assuming $p(\epsilon)$ is a symmetrical (even) function about $\epsilon = 0$, Equations (18) and (19) simplify to

$$\bar{E}_x = K'' \overline{b(t)} \cos\theta \int_{\text{all } \epsilon} \cos\epsilon \, p(\epsilon) d\epsilon \quad , \text{ and} \quad (20)$$

$$\bar{E}_y = K'' \overline{b(t)} \sin\theta \int_{\text{all } \epsilon} \cos\epsilon \, p(\epsilon) d\epsilon \quad . \quad (21)$$

When $\bar{E}_x$ and $\bar{E}_y$ are applied to an XY oscilloscope display, the resultant displayed bearing angle is

$$\theta_d = \tan^{-1} \left[\frac{\bar{E}_y}{\bar{E}_x} \right] = \theta \quad , \quad (22)$$

which is the desired information with all error producing and modulation effects removed. Sense is inherent in the display, which is simply a straight line pointing to θ —after trace/retrace modulation is applied to the integrator outputs. Also inherent in the orthogonal correlation technique is reduced susceptibility to antenna unbalance effects. At the synchronous detector output antenna unbalance is manifested by a DC offset voltage; however, this voltage when crosscorrelated with the quadrature scan signals has a time average value of zero. Hence, antenna unbalance effects are reduced.

The combination of correlation, lowpass filtering, and time averaging acts to remove a very large portion of the noise present at the synchronous detector output greatly improving the sensitivity. (In theory, if a noise-free sum signal is available, any signal periodic with respect to the scan rate can be extracted from noise by use of the described correlation technique regardless of the input signal-to-noise ratio.) In practice, some 20-30 dB improvement relative to envelope detection has been obtained.

The integrator outputs are slowly varying DC levels representing sin θ and cos θ. Therefore, it has been possible to convert these outputs to a digital bearing readout. The sin θ/cos θ outputs are applied to a sine/cosine-to-BCD angle converter which drives a decoder/driver/Nixie readout.

To summarize, orthogonal correlation provides the following advantages:

(1) Sensitivity improvement

(2) Bearing error and dispersion reduction

(3) Inherent sense

(4) Modulation tolerance, i.e., modulations such as OOK and SSB do not clutter the bearing display

(5) Reduction of antenna unbalance effects

(6) Simple, easily read displays

(7) Adaptable to digital readout

(8) Can be applied to most, if not all, small aperture DF systems

(9) Can be used on-line with conventional bearing displays.

Practical Implementation - Systems Description

Synchronous and correlation detection have been used with several types of rotating interferometer systems. One system (Figure 5) uses 1.8 m vertical dipoles spaced on a 1.8 m baseline. Another (Figure 6) uses 0.3 m diameter loops spaced on a 1.8 m baseline. Both the dipoles and loops arrays are untuned and applied directly to a broadband hybrid to obtain the RF sum and difference signals. The coaxial transmission lines from the elements to the hybrid are loaded with spaced ferrite toroids to reduce undesired horizontal polarization pickup and environmental coupling. The 1.5 m transmission line between the hybrid output (in the antenna rotator base) and the dual-channel receiver input is twisted balanced coax. Antenna scan rate is 30 rpm.

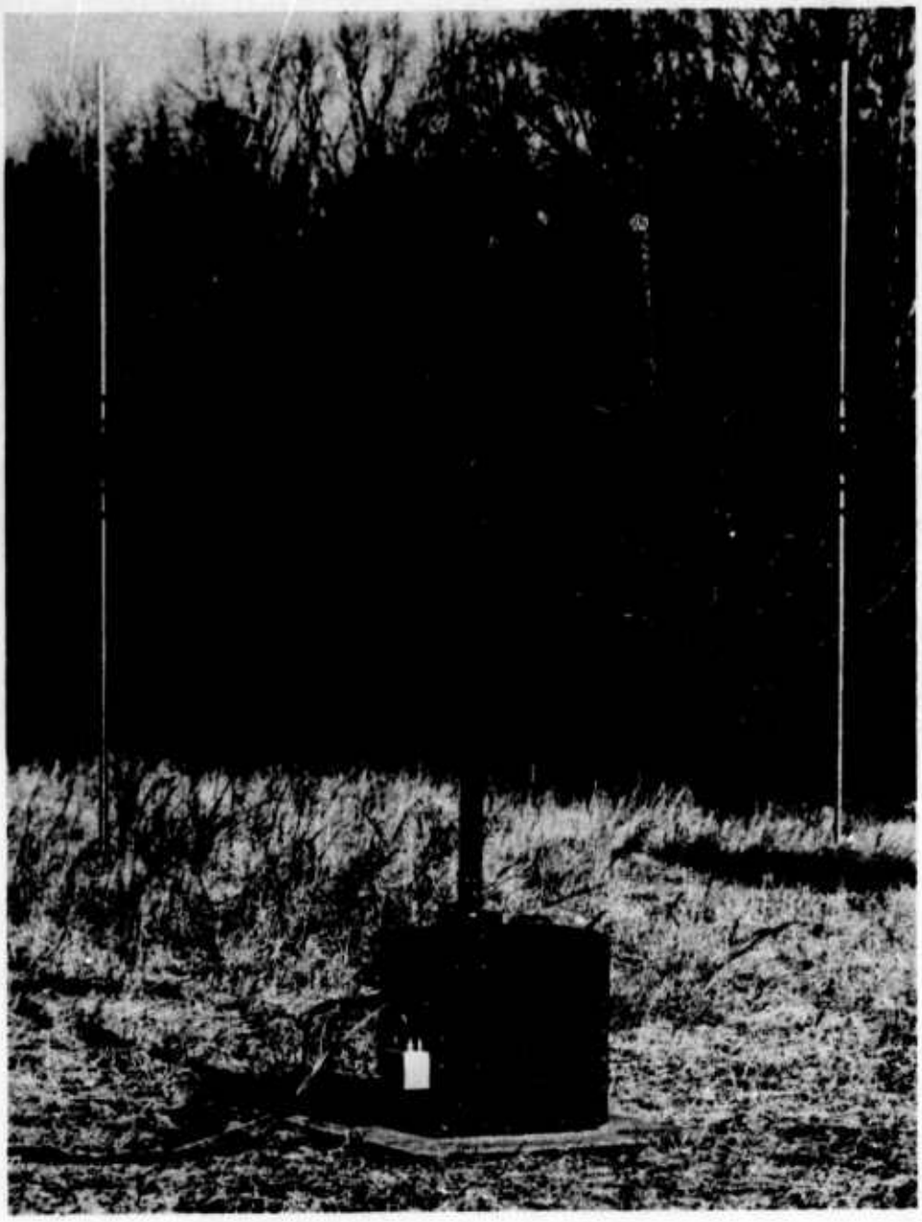

Figure 5. Six-Foot Baseline Rotating Interferometer with Spaced Dipoles.

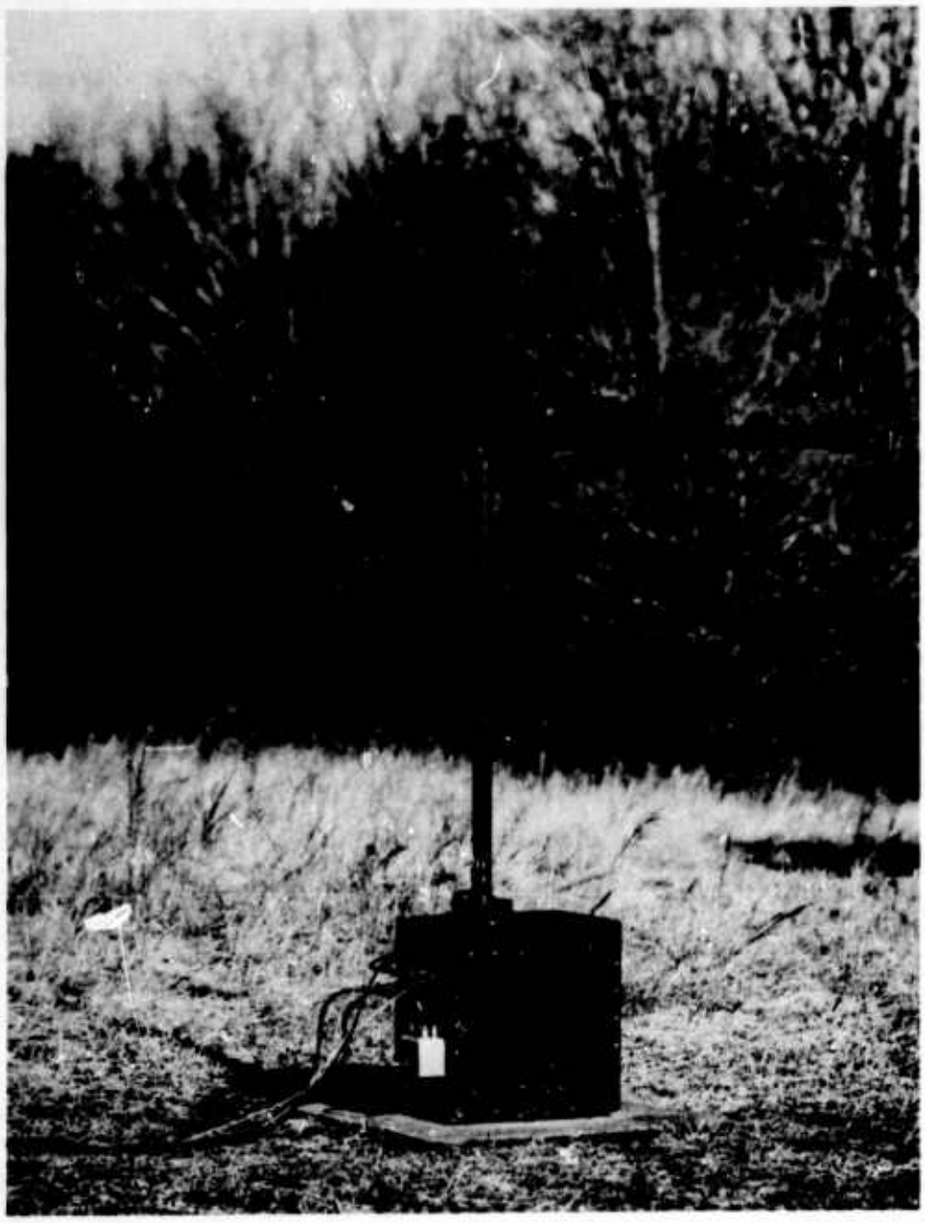

Figure 6. Six-Foot Baseline Rotating Interferometer with Spaced Loops.

Figure 7 depicts a simplified functional block diagram of the post-IF circuitry.

The interferometer RF Δ output, which contains the bearing information, is converted to IF in one channel of the dual-channel receiver. The IF Δ can then be applied to either an envelope or a synchronous detector. Either detector can be selected for display. The instantaneous sense, which is derived from the synchronous detector, may be used with either the synchronous or envelope detector displays. After shaping, positive and negative representations of the scan (bearing) information are applied to a sine/cosine potentiometer rotating in synchronism with the loop. The sine/cosine potentiometer, which may be viewed as a rectangular-to-polar conversion device, converts the scan modulation to the proper form for display on an XY scope.

The synchronous detector also supplies an input to the orthogonal correlator which operates as previously described. When orthogonal correlation is used the sine/cosine potentiometer functions as the multipliers for correlation detection.

The IF Σ, which does not contain the scan modulation, is applied to a sense band adjust circuit. This circuit is a continuously variable phase-shifter used to adjust the IF Σ phase to compensate for major differential phase shifts between receiver channels and hence insure that sense is correct over the entire 2-20 MHz range. This control also peaks the synchronous detector output level.

Operational Field Evaluation - Test Results

Field tests consisted of two major phases. The first phase was directed toward measuring both the absolute and relative sensitivities of envelope, synchronous, and correlation detection using a local signal source to establish known field strengths. The second phase evaluated bearing accuracy and dispersion using cooperative test transmissions at distances of 3.1, 8, and 22 km and uncooperative transmissions from distances exceeding several hundred kilometers. This second phase was devoted to evaluating the performance of the spaced dipole interferometer and emphasized testing over the 8 and 22 km paths which provided groundwave/skywave interference

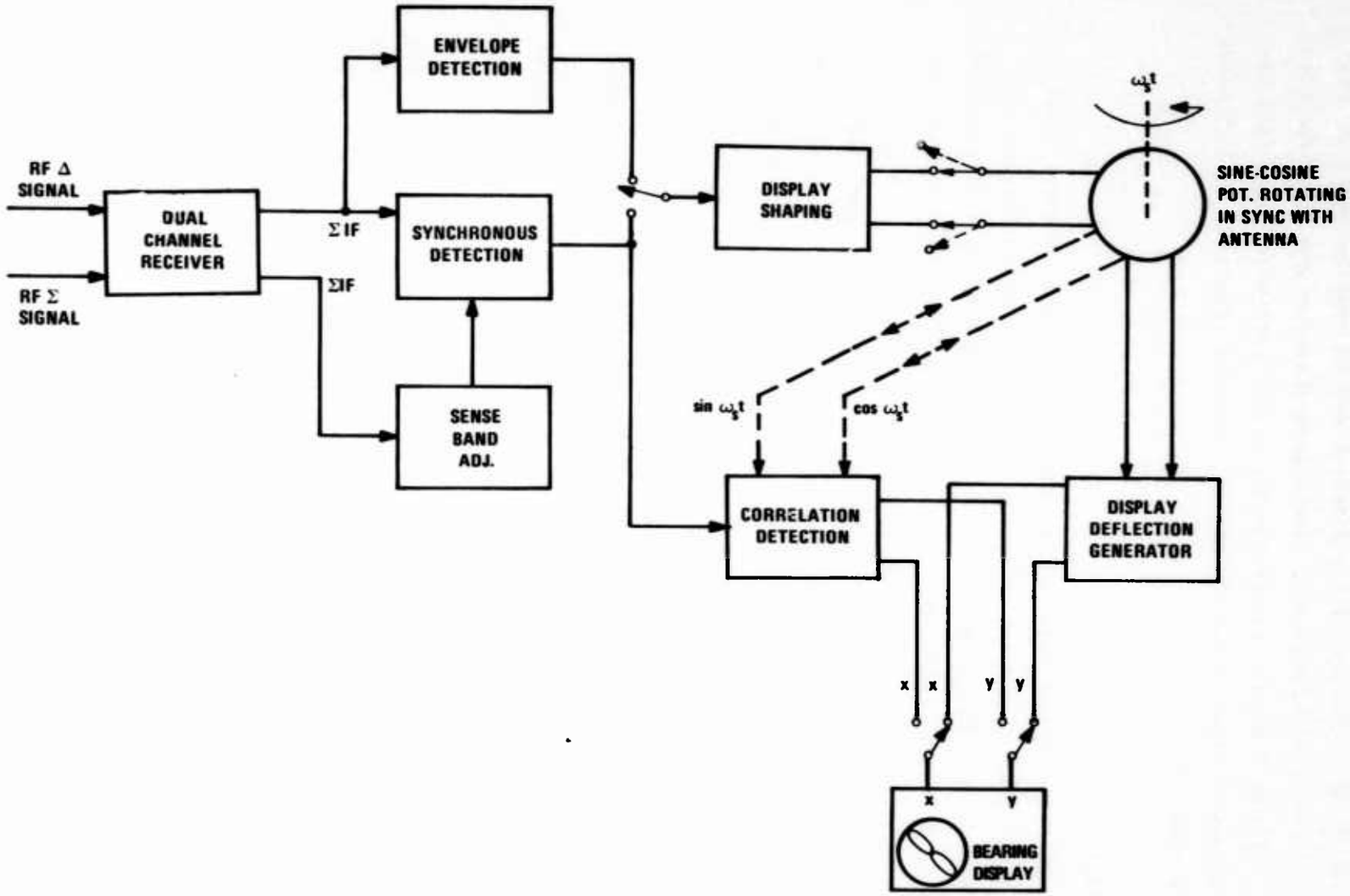

Figure 7. Functional Block Diagram of Post-IF Circuitry.

effects. (A major objective of the research was to develop improved techniques for direction finding under severe groundwave/skywave interference effects. The spaced dipole interferometer using synchronous detection has a $\cos^3 \Phi$ elevation plane response implying improved rejection to high elevation angle skywaves.)

Sensitivity

Sensitivity was measured by reducing the field strength until a minimum usable bearing display occurred. DF visual bearing sensitivity criteria were used. Measurements were taken with the sense band adjustment positioned for maximum synchronous detector output. Figure 8 depicts the measured sensitivity for the spaced dipoles (1.8 m lengths) on a 1.8 m baseline; sensitivity of the 1.8 m baseline spaced loop is approximately 20 dB less, i.e., 20 dB should be added to the dB/μv/m values in Figure 8. Figure 8 shows that synchronous detection improves sensitivity by approximately 10 dB relative to envelope detection. Orthogonal correlation is some 17 dB more sensitive than synchronous detection, and hence about 27 dB more sensitive than envelope detection. The correlation sensitivity levels presented in Figure 8 could be acquired within 5-10 seconds after signal acquisition.

It may be noted from Equation (5) that the synchronous detector output is multiplied by the term sin δ' where δ' corresponds to the phase difference between the two IF outputs. The factor sin δ' is set very close to unity by use of a phase shifter at the sum channel IF output, providing both maximum sensitivity and unambiguous sensing. An objective of the field tests was to determine how broadband the sin δ' or sense band adjustment is with respect to operating frequency.

Tests showed that the sense band adjust setting for maximum synchronous detector output and proper sense proved to be relatively insensitive to operating frequency. In fact, for the dipole interferometer, a single setting could be used over the entire 2-20 MHz range.

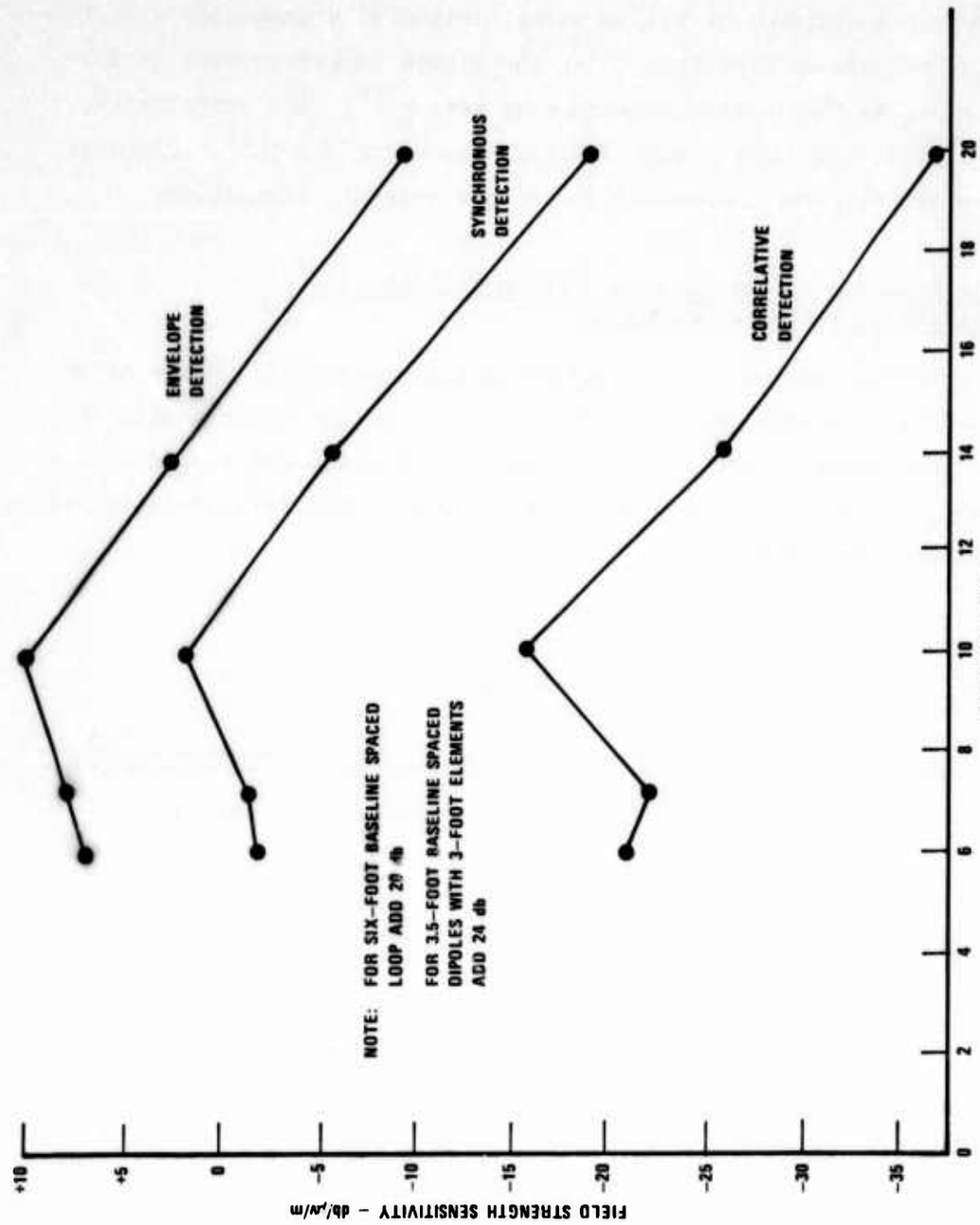

Figure 8. Sensitivity Data for Various Detection Techniques.

Bearing Accuracy and Dispersion - Groundwave

Slight skywave interference was noted on 80 watt 7.310 and 4.010 MHz transmissions at a distance of 3.1 km using horizontal transmitter polarization. Using synchronous detection, with the dipole interferometer, bearing fluctuations due to the skywave interference were $\pm 2^{\circ}$; with correlation, no bearing fluctuations were noted, and the mean error was 0.5°. Envelope detection sensitivity was inadequate for usable bearing information.

Bearing Accuracy and Dispersion - Groundwave/Skywave Combination (Groundwave Dominant)

7.310 MHz, 80-watt transmissions on a long wire at a distance of 8 km produced considerable groundwave/skywave interaction under conditions of dominant groundwaves. Table II presents results using the spaced dipole interferometer. (In Table II and subsequent figures, the term instantaneous refers to synchronous detection.)

TABLE II

Test Results: 8 km Path
With Groundwave/Skywave Interference

Display	No. Bearings	Mean Error	Standard Deviation	Spread
Correlation	214	0.8°	1°	3.1°
Instantaneous	263	0.5°	2.7°	11.9°

In comparing the correlation results with the instantaneous data, the difference of 0.3° between the bearing errors should not be considered significant because both values are well within calibration accuracy. The large reductions in standard deviation and spread afforded by correlation are the significant factors.

Bearing Accuracy and Dispersion -
Severe Groundwave/Skywave Interaction

Severe groundwave/skywave interference was acquired over a 22 km path at 7.310 MHz using a vertical monopole transmitting antenna. Indications were that the groundwave and skywave were of comparable level on the average.

A relatively large amount of data were collected under these conditions due to the severe signal conditions which furnished an excellent test of the spaced dipole interferometer performance.

Figures 9 and 10 present histograms of the data obtained. Figure 9 presents data acquired using the instantaneous bearing information (synchronous detection); Figure 10 data were obtained by using the correlation bearing display.

The data in Figures 9 and 10 conclusively demonstrate that a short-baseline interferometer using electrically small dipole elements can obtain reliable bearing information under severe groundwave/skywave conditions. The data also indicate that both bearing error and dispersion are significantly reduced by orthogonal correlation.

The most dramatic demonstration of the advantages of orthogonal correlation was observed during the ionospheric transitional periods when the skywave scatter mode became quite evident. For example, on 7.310 MHz, the transitional period occurred between 2200 and 2400 hours (local sunset). Fade characteristics became very erratic and fade rates increased; fade rates of one per second were typical. The instantaneous bearing display became very difficult to read; bearings occurred over 360^{o} due to scatter effects. However, reliable bearing information could be obtained using correlation. Table III illustrates typical results obtained from continuous observation during a period with heavy intermittent scatter effects. Data were taken during the periods of scatter. Interspersed among the scatter periods were intervals of relatively steady, obviously groundwave, signals. Correlated bearings were also taken during these non-scatter periods and produced means of about $+1^{o}$ to -2^{o} and standard deviations of approximately 2^{o} - 4^{o}. Instantaneous bearings were also reliable during the non-scatter intervals with typical means of -1^{o} to -4^{o} and standard deviations of 4^{o} - 5^{o}.

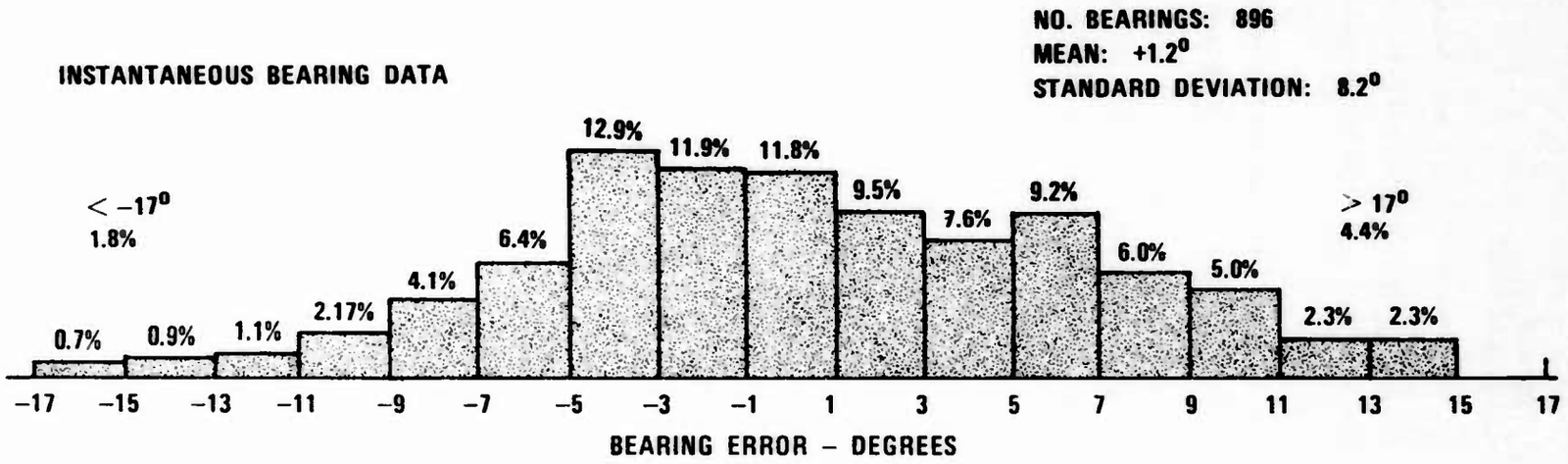

Figure 9. Histogram for 22km Path. 7.310 MHz. 400 Watt Transmissions on Monopole. Instantaneous Bearing Data.

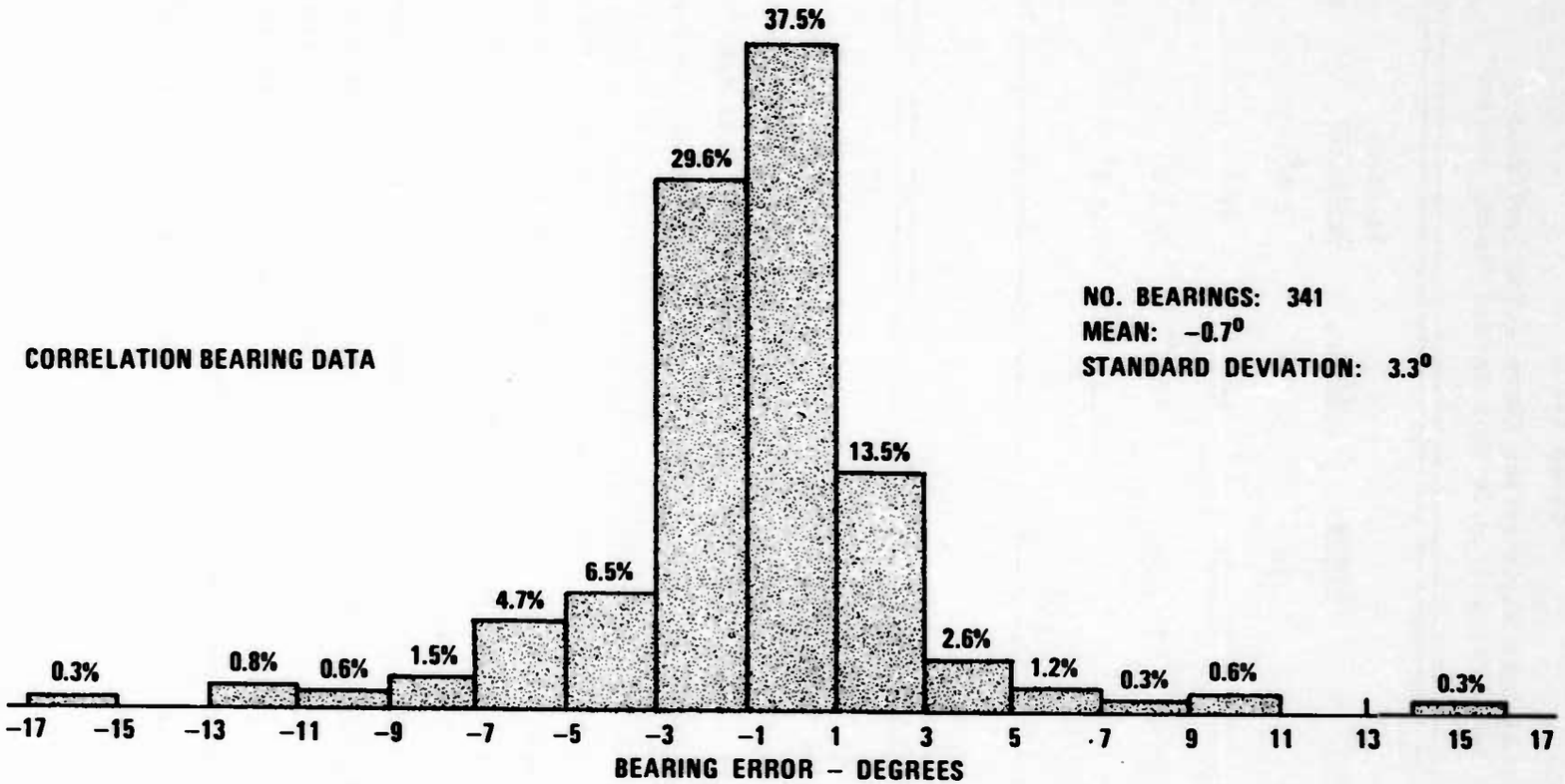

Figure 10. Histogram for 22km Path. 7.310 MHz. 400 Watt Transmissions on Monopole. Correlation Bearing Data.

TABLE III

Typical Data Illustrating Correlation Performance
During Ionospheric Transitional Period (Heavy Scatter)

Time Period (U.T.)	Number	Mean	Standard Deviation	Spread
2300-2305*	10	-1.3°	2.5°	7°
2310-2315	10	-5°	0°	0°
2330-2335	10	-1.2°	3.0°	8°
2335-2425	22	-6.4°	8.3°	29°

*1700-1705 Local Time.

A series of tests was performed to evaluate performance for very small groundwave/skywave ratios. A horizontal dipole transmitting antenna was used to greatly reduce the groundwave/skywave ratio. Fade rate and depth increased significantly; bearing dispersion and spread also increased relative to the vertical monopole.

Data were obtained by performing a sequence of monopole-dipole tests using the 80 watt transmitter. The relatively low transmitted power required that correlation be used to obtain reliable bearing information. Figures 11 and 12 present histograms of the results.

The most noticeable difference between the monopole and dipole data is the bearing dispersion; the mean errors are not significantly different. The horizontal dipole standard deviation and spread are approximately ten times greater and indicate the performance that could be expected with little or no groundwave and a relatively large amount of skywave scatter.

Tests were also performed on 4.010 MHz using the dipole transmitting antenna and similar results were noted.

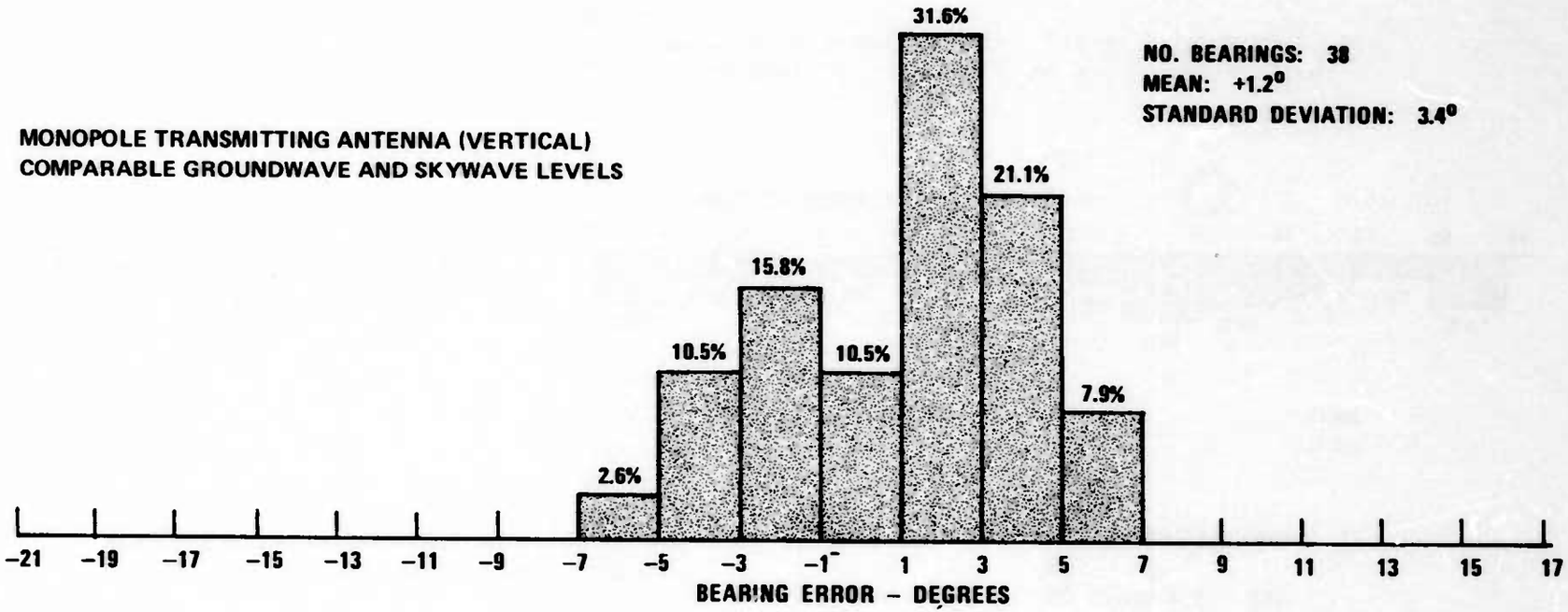

Figure 11. Histogram for 22km Path. 7.310 MHz. 80 Watt Transmissions on Monopole. Correlation Bearing Data. Six-Foot Baseline Spaced Dipoles.

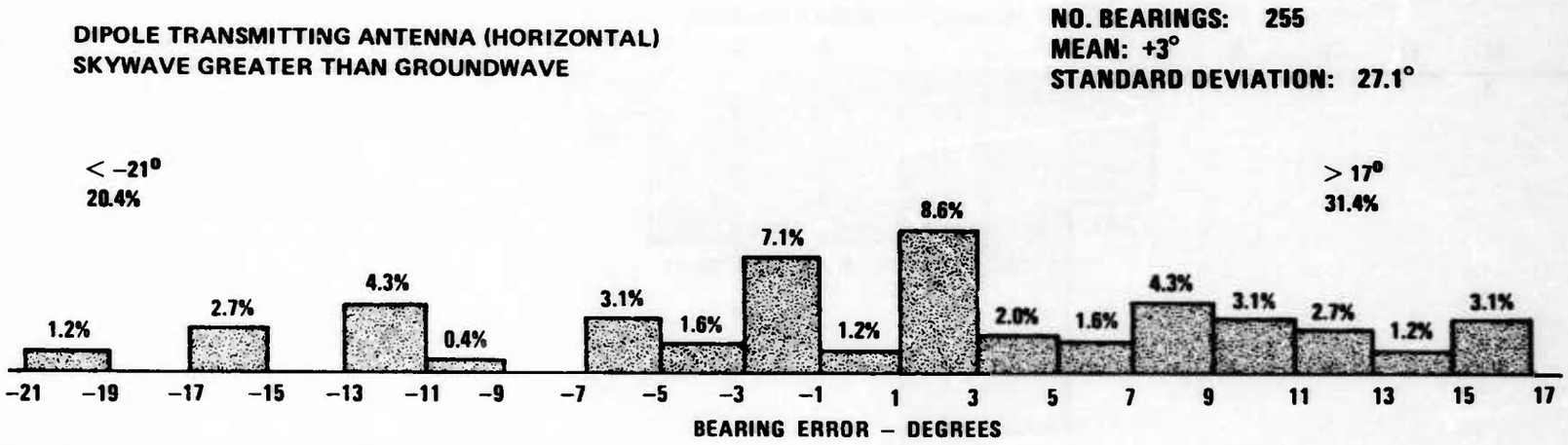

Figure 12. Histogram for 22km Path. 7.310 MHz. 80 Watt Transmissions on Dipole. Correlation Bearing Data. Six-Foot Baseline Spaced Dipoles.

Bearing Accuracy and Dispersion - Long Distance, Low Elevation Angle Transmissions

Twenty-seven tests on seven long-range (distance greater than several hundred kilometers) transmissions produced mean errors within $\pm 1^{o}$ and standard deviations of 5^{o} (synchronous detection) and 4^{o} (correlation).

Other Performance Characteristics

The operational field tests also verified the qualitative aspects of the improved performance of synchronous and correlation detection. Synchronous detection bearing displays were of consistently higher quality (sharpness, readability, and dynamic range) than envelope detection. Instantaneous sensing proved completely reliable under all signal conditions. Also, the inherent sense and modulation tolerance of correlation detection were thoroughly verified. The steady (or slowly varying) correlation detection display proved to be quite readable and was considered to be a significant improvement over the conventional displays.

Conclusions

The inclusion of synchronous and correlation detection in dual-channel, small-aperture HF/DF systems significantly improves performance. Sensitivity can be increased by tens of dB relative to envelope detection. Instantaneous sensing is inherent in both detection modes. Correlation detection can reduce bearing dispersions by as much as 3:1 and, in some cases, relatively reliable bearings can be obtained using correlation when other detection methods fail. Display characteristics such as bearing readability and dynamic range are enhanced by both synchronous and correlation detection. Correlation detection possesses the additional major advantage of modulation tolerance.

The practical application of synchronous and correlation detection to short baseline, dual-channel, rotating interferometer systems has been demonstrated and operationally verified by field tests performed under a wide variety of signal and propagation conditions. Correlation detection proved to be especially useful under weak signal and severe groundwave/skywave conditions.

Acknowledgement

The authors gratefully acknowledge the assistance and encouragement of D. W. Robertson, Head of the Communications Branch of the Georgia Tech Electronics Division, and Mr. L. Scott of the U. S. Army Electronics Command.

Analysis of Correlation Detection Technique for Small Aperture DF Systems

Richard W. Moss
Georgia Institute of Technology
Electronics Division
Atlanta, Georgia

I. Introduction

Small aperture direction finders continue to find application where tactical constraints such as size, weight, and portability prohibit the use of large aperture systems. With ionospherically propagated signals, most small aperture direction finders display a bearing indication which is time variable. The variation in indication is semi-random and depends largely on the instantaneous phase front of the incident signal. Due to the smallness of the antenna array, small aperture systems have two basic disadvantages: the sensitivity is severely limited, and the antenna system provides little or no phase front averaging. Thus, improved techniques for sensitivity improvement and bearing estimate variance reduction are highly desired.

Since most small aperture DF systems use multiple periodic scans of the antenna array for direction of arrival observations, a logical technique for improving performance is the use of correlation to improve the results with each additional antenna scan. In principle, an improvement can be achieved provided undesirable variations become uncorrelated as time progresses. Based on this general approach, a number of signal processing techniques have been investigated. One of these techniques, termed "orthogonal correlation," is the subject of this paper. This technique is based on the use of correlation detection for improving sensitivity and reducing variance. Although completely general in concept, the performance of orthogonal correlation will be evaluated specifically for small aperture, rotating, coaxial spaced loop and spaced vertical dipole DF systems. The technique has been successfully applied to simple loop, spaced loop, and spaced vertical dipole DF systems.

II. Basic Correlation Detection

The basic form of the orthogonal correlator is shown in Figure 1. The input signal, $e_i(t)$, is a simple sinusoid whose average phase is related directly to the direction of arrival. The input is

$$e_i(t) = a(t) \sin[\omega_s t - \theta + \epsilon(t)] , \tag{1}$$

where ω_s is the antenna scan rate, θ is the azimuthal arrival angle, $a(t)$ with mean greater than zero is a time variable amplitude due to modulation, noise, fading, etc., and $\epsilon(t)$ is time variable bearing error due to noise, polarization changes, and ionospheric variations. The phase error is assumed to be confined to the range $|\epsilon(t)| < \frac{\pi}{2}$. The signal $e_i(t)$ can be multiplied with orthogonal reference signals derived from the antenna scan rate. After lowpass filtering to remove the double frequency terms, we have

$$e_x(t) = \frac{b(t)}{2} \cos[\theta - \epsilon(t)]$$

$$= \frac{b(t)}{2} \cos\theta \cos\epsilon(t) + \frac{b(t)}{2} \sin\theta \sin\epsilon(t) , \tag{2}$$

and

$$e_y(t) = \frac{b(t)}{2} \sin[\theta - \epsilon(t)]$$

$$= \frac{b(t)}{2} \sin\theta \cos\epsilon(t) - \frac{b(t)}{2} \cos\theta \sin\epsilon(t) , \tag{3}$$

where $b(t)$ represents the amplitude after filtering. After integration the two output signals are of the form

$$E_{xo} = \frac{1}{2} \cos\theta \, \overline{b(t) \cos\epsilon(t)} + \frac{1}{2} \sin\theta \, \overline{b(t) \sin\epsilon(t)} \tag{4}$$

and

$$E_{yo} = \frac{1}{2} \sin\theta \, \overline{b(t) \cos\epsilon(t)} - \frac{1}{2} \cos\theta \, \overline{b(t) \sin\epsilon(t)} , \tag{5}$$

where the overhead bar indicates time averaging. With $\epsilon(t)$ ergodic and stationary, and $\overline{\epsilon(t)} = 0$,

$$E\left(\overline{b(t)\ \sin\ \epsilon(t)}\right) = 0 \tag{6}$$

and

$$E\left(\overline{b(t)\ \cos\ \epsilon(t)}\right) = C,\ C > 0\ , \tag{7}$$

where E( ) is the expectation operator. Therefore,

$$E(E_{xo}) = \frac{C}{2} \cos\ \theta \tag{8}$$

and

$$E(E_{yo}) = \frac{C}{2} \sin\ \theta\ , \tag{9}$$

so that

$$\theta = \tan^{-1} \frac{E(E_{yo})}{E(E_{xo})}\ . \tag{10}$$

The steps above are equivalent to time cross-correlation between the input signal and orthogonal scan waveforms, i.e., for example,

$$R_{xs}(0) = \lim_{T \to \infty} \frac{1}{T} \int_0^T a(t) \sin\ \omega_s t \sin[(\omega_s t - \theta + \epsilon(t)]dt \tag{11}$$

$$= \lim_{T \to \infty} \frac{1}{T} \int_0^T \frac{a(t)}{2} \left\{\cos\ [\theta - \epsilon(t)]\right.$$

$$\left. - \cos\ [2\omega_s t - \theta + \epsilon(t)]\right\} dt \tag{12}$$

$$= \frac{\cos\ \theta}{2} \lim_{T \to \infty} \frac{1}{T} \int_0^T a(t) \cos\ \epsilon(t)dt$$

$$+ \frac{\sin\ \theta}{2} \lim_{T \to \infty} \frac{1}{T} \int_0^T a(t) \sin\ \epsilon(t)dt$$

$$- \lim_{T \to \infty} \frac{1}{T} \int_0^T \cos\ [2\omega_s t - \theta + \epsilon(t)]dt \tag{13}$$

$$= \frac{C}{2} \cos\ \theta\ . \tag{14}$$

It may be noted that the correlation process tends to reduce the time variable bearing error and also reduces the effects of signal amplitude variations. As will be shown in the following discussion, orthogonal correlation also significantly improves the SNR.

The correlator outputs (8) and (9) can be used to generate a display of the bearing estimate. When modulated and applied to an XY oscilloscope, the display is in the form of a line which indicates azimuth. Direct digital readout is possibly by use of a synchro to digital converter.

III. Receiver Models

It was seen above that the correlation technique requires an input sinusoid whose phase is related to the direction of arrival. In this section, the antenna and receiver configurations to meet this requirement will be described.

Antenna Output: For a rotating spaced-element antenna system in its normal operating mode, the individual element voltages are subtracted to yield

$$E_\Delta = E_1 - E_2$$

$$= G(\lambda,\psi,\Phi,\theta)\cos\left[\omega_c t - \frac{\pi d}{\lambda}\cos\Phi\sin(\omega_s t - \theta)\right]$$

$$-G(\lambda,\psi,\Phi,\theta)\cos\left[\omega_c t + \frac{\pi d}{\lambda}\cos\Phi\sin(\omega_s t - \theta)\right] \qquad (15)$$

$$= 2G(\lambda,\psi,\Phi,\theta)\sin\left[\frac{\pi d}{\lambda}\cos\Phi\sin(\omega_s t - \theta)\right]\sin\omega_c t\,, \qquad (16)$$

where G = element response which in general is a function of frequency and spatial parameters,

ψ = polarization angle of the incident signal,

ω_s = antenna scan rate,

Φ = elevation angle above horizontal of the incident signal,

θ = azimuthal direction of arrival,

d = array baseline,

λ = wavelength, and

ω_c = IF or RF carrier frequency.

The element voltages can also be summed to yield,

$$E_\Sigma = E_1 + E_2$$

$$= 2G(\lambda,\psi,\Phi,\theta) \cos\left[\frac{\pi d}{\lambda} \cos\Phi \sin(\omega_s t - \theta)\right] \cos\omega_c t \ . \qquad (17)$$

For the small aperture case, $d/\lambda << 1$, we note that E_Σ is equivalent to a single element placed at the center of the rotating array.

For a coaxial spaced loop DF system, loops are used as array elements so that the element response becomes

$$G_L(\lambda,\psi,\Phi,\theta) = \cos\psi \cos(\omega_s t - \theta) + \sin\psi \sin\Phi \sin(\omega_s t - \theta) \ , \qquad (18)$$

where the λ dependence has been suppressed and the loop response normalized for analytical convenience.

For a spaced dipole system, vertical dipole elements are used so that the normalized element response becomes

$$G_d(\lambda,\psi,\Phi,\theta) = \cos\psi \cos\Phi \ . \qquad (19)$$

Dual Channel Receiver: We first consider the use of a dual channel receiver where the sum and difference signals can be processed as illustrated in Figure 2. From equations (16) and (17) the product detector output can be written as

$$E_{s1} = 2G(\lambda,\psi,\Phi,\theta) \sin\left[\frac{\pi d}{\lambda} \cos\Phi \sin(\omega_s t - \theta)\right] \sin\omega_c t$$

$$\cdot 2G(\lambda,\psi,\Phi,\theta) \cos\left[\frac{\pi d}{\lambda} \cos\Phi \sin(\omega_s t - \theta)\right] \cos(\omega_c t + \zeta) \qquad (20)$$

$$= -G^2(\lambda,\psi,\Phi,\theta) \sin\zeta \sin\left[\frac{2\pi d}{\lambda} \cos\Phi \sin(\omega_s t - \theta)\right] \ , \qquad (21)$$

where ζ is the IF phase shift produced by the adjustable phase shifter.

Noting that the loop element voltage (18) can be written as

$$G_L(\lambda,\psi,\Phi,\theta) = \sqrt{\cos^2\psi + \sin^2\psi \sin^2\Phi}\ \cos[\omega_s t - \theta - \alpha] , \tag{22}$$

with $$\alpha = \tan^{-1}\left[\frac{\sin\psi \sin\Phi}{\cos\psi}\right] , \tag{23}$$

and using the short baseline assumption

$$d/\lambda << 1 , \tag{24}$$

(20) reduces to

$$E_{s1} = -\frac{1}{2}\left(\cos^2\psi + \sin^2\psi \sin^2\Phi\right) \sin\zeta\left(\frac{2\pi d}{\lambda}\right) \cos\Phi$$
$$\cdot\left\{\sin(\omega_s t - \theta) + \frac{1}{2}\sin(3\omega_s t - 3\theta - 2\alpha)\right.$$
$$\left.-\frac{1}{2}\sin(\omega_s t - \theta - 2\alpha)\right\} , \tag{25}$$

where the double frequency terms $2\omega_c t$ have been removed by filtering.

Ignoring the third harmonic term and letting $\zeta = \pi/2$, (25) reduces to

$$E_s = -\frac{1}{2}\left(\cos^2\psi + \sin^2\psi \sin^2\Phi\right)\left(\frac{2\pi d}{\lambda}\right) \cos\Phi$$
$$\cdot\left\{\sin(\omega_s t - \theta) - \frac{1}{2}\sin(\omega_s t - \theta - 2\alpha)\right\} . \tag{26}$$

The synchronous detector output for spaced loop elements can also be expressed in the alternate form

$$E_s = -\frac{2\pi d}{\lambda} \cos\Phi$$
$$\cdot\left\{\left[\frac{1}{4}\cos^2\psi + \frac{3}{4}\sin^2\Phi \sin^2\psi\right] \sin(\omega_s t - \theta)\right.$$
$$\left.+\frac{1}{4}\sin\Phi \sin 2\psi \cos(\omega_s t - \theta)\right\} . \tag{27}$$

For spaced vertical dipole elements and using the short baseline assumption (24), the product detector output would be

$$E_{s1} = -\frac{2\pi d}{\lambda} \cos^2 \psi \cos^3 \Phi \sin(\omega_s t - \theta) , \tag{28}$$

where again $\zeta = \frac{\pi}{2}$.

Single Channel Receiver: For many applications, it is desirable to use a single channel receiver to simplify the RF requirements. Figure 3 illustrates a model where single channel processing is used to generate a correlator drive signal. Noting the fixed $\pi/2$ phase shifter and using (16), (17) and (24), the receiver IF output becomes

$$E_i = 2G(\lambda,\psi,\Phi,\theta) \cdot \frac{\pi d}{\lambda} \cos \Phi \sin(\omega_s t - \theta) \sin \omega_c t$$

$$+ KG(\lambda,\psi,\Phi,\theta) \sin \omega_c t , \tag{29}$$

where K is an amplitude coefficient for E_Σ. The envelope detector output becomes

$$E_{D1} = |E_i|$$

$$= |2G(\lambda,\psi,\Phi,\theta) \cdot \beta \sin(\omega_s t - \theta) + KG(\lambda,\psi,\Phi,\theta)| , \tag{30}$$

where $\beta = \frac{\pi d}{\lambda} \cos \Phi$. (31)

Equation (30) can be written as

$$E_{D1} = |G(\lambda,\psi,\Phi,\theta)| \; |2\beta \sin(\omega_s t - \theta) + K| . \tag{32}$$

Using standard Fourier series analysis, it can be shown that

$$|2\beta \sin(\omega_s t - \theta) + K| = -K + \frac{2K\theta_1}{\pi} + \frac{4\beta}{\pi} \sin\theta_1$$

$$+ \frac{2}{\pi}\left\{2K \sin\theta_1 + \beta \sin 2\theta_1 + 2\beta\theta_1 - \beta\pi\right\} \sin(\omega_s t - \theta)$$

$$+ \frac{4}{\pi} \sum_{n=2}^{\infty} \left\{ \frac{K}{n} \sin\theta_1 + \frac{\beta}{n+1} \sin(n+1)\theta_1 + \frac{\beta}{n-1} \sin(n-1)\theta_1 \right\}$$

$$\cos n(\omega_s t - \theta - \frac{\pi}{2}) , \qquad (33)$$

where $K + 2\beta \cos\theta_1 = 0$ defines θ_1.

For a spaced loop array it can also be shown that

$$|G_L(\lambda, \psi, \Phi, \theta)| = \sqrt{\cos^2\psi + \sin^2\psi \sin^2\Phi}$$

$$\cdot\left\{\frac{2}{\pi} + \frac{2}{\pi} \sum_{n=1}^{\infty} (-1)^n \left[\frac{1}{2n+1} - \frac{1}{2n-1}\right] \cos 2n(\omega_s t - \theta - \alpha)\right\} . \qquad (34)$$

The product of (33) and (34) produces a complete expression for a spaced loop array used with the single channel receiver model; however, only the fundamental component is of interest so that harmonic terms can be dropped. In general, the amplitude of the fundamental term itself depends on higher order harmonic mixing so that in order to simplify the results, only the significant fundamental term will be retained. Thus, it is found that

$$E_D \approx \left(\frac{2}{\pi}\right)^2 \left(2\beta\,\theta_1 - \beta \sin 2\theta_1 - \beta\pi\right)$$

$$\cdot\left\{\left[\sqrt{\cos^2\psi + \sin^2\psi \sin^2\Phi} - \frac{1}{3}\left(\frac{\cos^2\psi - \sin^2\Phi \sin^2\psi}{\sqrt{\cos^2\psi + \sin^2\psi \sin^2\Phi}}\right)\right]\right.$$

$$\cdot \sin(\omega_s t - \theta)$$

$$\left. + \frac{1}{3}\left(\frac{\sin\Phi \sin 2\psi}{\sqrt{\cos^2\psi + \sin^2\psi \sin^2\Phi}}\right) \cos(\omega_s t - \theta)\right\} . \qquad (35)$$

For a spaced vertical dipole array,

$$|G_d(\lambda,\psi,\Phi,\theta)| = \cos\Phi\ |\cos\psi| \ , \tag{36}$$

so that the product of (33) and (36) produces a complete expression for a spaced vertical dipole array used with the single channel receiver model. The fundamental component which is of interest would be

$$E_D = \frac{2}{\pi}\cos\Phi\ |\cos\psi|\ \left\{2K\sin\theta_1 + \beta\sin 2\theta_1 + 2\beta\theta_1 - \beta\pi\right\}\sin(\omega_s t - \theta) \ . \tag{37}$$

IV. Polarization Dependence

For most ionospherically propagated signals, the properties of the received signal depend on the signal amplitude, polarization, elevation angle, and array parameters. Of the time variable factors, signal polarization has the most significant effect on small aperture DF performance. From the results of the preceding section, it is apparent that the polarization parameter ψ, in general, affects the phase and amplitude of the correlator drive signals. As shown in Section II, the amplitude variations do not influence the bearing estimate; however, phase variations in the correlator drive signal can produce error. In this section, errors due to polarization dependence are considered.

From equations (26) and (35) it is apparent that the phase of the correlator drive signals for a spaced loop array not only depends on the azimuthal direction of arrival, but also depends on the polarization characteristics of the incident signal. This dependence results from the fact that the loop antenna responses for the array elements are a function of the signal polarization. This dependence is apparent in equation (18) and can produce errors in the estimate of the bearing angle. As can be seen from (28) and (37) a spaced vertical dipole system is not subject to polarization error, and can be used to prevent polarization dependence. For the

coaxial spaced loop array, the effects of signal polarization will depend primarily on the polarization time dependence. It should be noted that an instantaneous display of the envelope of the signal in (16) results in a pair of antenna nulls which are independent of polarization and a pair of nulls which are dependent on polarization. This method of display is conventionally used with a rotating spaced loop DF system. The correlator receiver models combine the antenna responses to produce a single correlator drive signal.

Dealing first with <u>static</u> polarization error, ϵ_p, for the spaced loop array when ψ is constant, it is straightforward to show from equations (26) and (35) that

$$|\epsilon_p|_{\Phi=0} = |\epsilon_p|_{\psi=0} = |\epsilon_p|_{\psi=\pi/2} = 0. \tag{38}$$

The maximum polarization error occurs when $\Phi = \pi/2$ and $\psi = \pi/4$ and can be shown to be about 26.5° for the dual channel receiver model and about 18.5° for the single channel receiver model. It is evident from equations (28) and (37) that aside from amplitude variations, static values of ψ do not produce errors in the spaced dipole array.

In order to describe the effects of time variable polarization, a model must be assumed for the distribution of ψ. For many cases of interest, it has been found that ψ is approximately uniformly distributed 0 to 2π degrees. This model will be used to illustrate the correlator performance for time variable polarization.

Consider first the spaced loop array. Since E_s and E_D display similar dependence, only the single channel receiver model will be evaluated. With reference to equation (35) and the correlator of Figure 1, the correlator outputs can be shown to be

$$E_{xo} = \cos\theta \left[\int_{\psi} \sqrt{\cos^2\psi + \sin^2\psi \sin^2\Phi}\ d\psi \right.$$

$$\left. - \frac{1}{3} \int_{\psi} \frac{\cos^2\psi - \sin^2\psi \sin^2\Phi}{\sqrt{\cos^2\psi + \sin^2\psi \sin^2\psi}}\ d\psi \right]_1$$

$$+ \frac{1}{3} \sin\theta \left[\int_{\psi} \frac{\sin\Phi \sin 2\psi}{\sqrt{\cos^2\psi + \sin^2\psi \sin^2\Phi}}\ d\psi \right]_2 \qquad (39)$$

and

$$E_{yo} = \sin\theta \left[\ \right]_1 - \frac{1}{3} \cos\theta \left[\ \right]_2 , \qquad (40)$$

where for convenience constant amplitude factors independent of ψ have been dropped. The bracket subscripts indicate identical quantities within the brackets. With ψ distributed uniformly, $0 \leq \psi \leq 2\pi$, it can be shown that

$$\int_{\psi} \sqrt{\cos^2\psi + \sin^2\psi \sin^2\Phi}\ d\psi = \text{constant} > 0, \qquad (41)$$

$$\int_{\psi} \frac{\cos^2\psi - \sin^2\psi \sin^2\Phi}{\sqrt{\cos^2\psi + \sin^2\psi \sin^2\Phi}}\ d\psi = \text{constant}, \qquad (42)$$

and

$$\int_{\psi} \frac{\sin\Phi \sin 2\psi}{\sqrt{\cos^2\psi + \sin^2\psi \sin^2\Phi}} = 0. \qquad (43)$$

Therefore, the estimate becomes

$$\theta = \tan^{-1} \frac{E_{yo}}{E_{xo}} = \tan^{-1} \left[\frac{\sin\theta}{\cos\theta} \right] = \theta\ . \qquad (44)$$

This result indicates that provided that the polarization is uniformly distributed, correlation will produce an accurate result. In the more general case, polarization will produce no net error if ψ is summetrically distributed about the point $\psi = 0$. Otherwise, polarization errors will occur as indicated above.

Again for the spaced dipole array E_s and E_D display similar dependence so that for brevity consider only the single channel receiver model. Using equation (37) and with reference to Figure 1, the correlator outputs are found to be

$$E_{xo} = \cos\theta \cdot \int_{\psi} |\cos\psi| \, d\psi \,, \tag{45}$$

and

$$E_{yo} = \sin\theta \cdot \int_{\psi} |\cos\psi| \, d\psi \,, \tag{46}$$

where constant amplitude factors independent of ψ have been dropped. Obviously the bearing estimate based on the arctangent of the ratio of (46) and (45) does not depend on ψ.

V. SNR Improvement and Variance Reduction

To fully describe the performance of the orthogonal correlator, the output SNR and output angle variance as a function of the input SNR and variance must be determined. For all receiver models, the signal at the input to the correlator can be represented by

$$E_i(t) = A \sin[\omega_s t - \theta + \epsilon(t)] + n(t) \,, \tag{47}$$

where A is the amplitude of the input signal, $\epsilon(t)$ is the input phase error due to all causes, and $n(t)$ is the input noise. The noise component $n(t)$ can be represented by

$$n(t) = n_x(t) \cos(\omega_s t - \theta) - n_y(t) \sin(\omega_s t - \theta) \,, \tag{48}$$

where $n_x(t)$ and $n_y(t)$ are quadrature noise components. Thus,

$$E_i(t) = [A \sin\epsilon(t) + n_x(t)] \cos(\omega_s t - \theta] + [A \cos\epsilon(t) - n_y(t)] \sin(\omega_s t - \theta) \,. \tag{49}$$

After multiplication by orthogonal replicas of the scan signal and lowpass filtering and integration, the correlator outputs become

$$E_{xo}(t) = \cos\theta \left[A \int_t \cos\epsilon(t)dt - \int_t n_y(t)\,dt\right] + \sin\theta \left[A \int_t \sin\epsilon(t)dt + \int_t n_x(t)\,dt\right] \quad (50)$$

and

$$E_{yo}(t) = \sin\theta \left[A \int_t \cos\epsilon(t) - \int_t n_y(t)\,dt\right] - \cos\theta \left[A \int_t \sin\epsilon(t)\,dt + \int_t n_x(t)\,dt\right] . \quad (51)$$

The outputs $E_{xo}(t)$, $E_{yo}(t)$ can be visualized as representing the vector sum of four vectors: a "signal" vector at angle θ,
a "noise" vector at angle θ,
a "noise" vector at angle $\theta \pm \pi/2$, and
an "error" vector at angle $\theta \pm \pi/2$.

The signal vector magnitude is defined to be

$$S_v = \sqrt{\cos^2\theta \left[A \int_t \cos\epsilon(t)dt\right]^2 + \sin^2\theta \left[A \int_t \cos\epsilon(t)\,dt\right]^2} \quad (52)$$

$$= A \int_t \cos\epsilon(t)\,dt . \quad (53)$$

Noting that $n_y(t)$ does not produce output error, the noise vector magnitude is defined to be

$$n_v = A \int_t \sin\epsilon(t) + \int_t n_x(t)\,dt . \quad (54)$$

The output vector angle is seen to be

$$\theta_v = \theta - \tan^{-1}\left[\frac{A \int_t \sin\epsilon(t) + \int_t n_x(t)\,dt}{A \int_t \cos\epsilon(t)\,dt}\right] . \quad (55)$$

The following assumptions simplify the final results:

$$\epsilon(t) \text{ small with } \overline{\epsilon(t)} = 0, \ |\epsilon(t)|_{max} < \pi/2 \ , \tag{56}$$

$\epsilon(t)$ approximately gaussian

$$\sin \epsilon(t) \approx \epsilon(t), \tag{57}$$

$$\cos \epsilon(t) \approx 1, \text{ and} \tag{58}$$

$$n(t) \text{ gaussian with } \overline{n(t)} = 0. \tag{59}$$

Based on these assumptions, and assuming integration from 0 to T, it is apparent that

$$A \int_0^T \cos \epsilon(t) \, dt = AT \tag{60}$$

and

$$A \int_0^T \sin \epsilon(t) \, dt = A \int_0^T \epsilon(t) \, dt \ . \tag{61}$$

The output SNR can now be defined as the ratio of the expected mean square value of the signal vector to the expected mean square value of the noise vector, i.e.,

$$(SNR)_o = \frac{A^2 \, T^2}{E \left\{ A \int_0^T \epsilon(t) + \int_0^T n_x(t) \, dt \right\}^2} \ . \tag{62}$$

Now using the fact that $\epsilon(t)$ and $n_x(t)$ are independent and the fairly common approximation,[1]

$$VAR \left[\frac{1}{T} \int_0^T x(t) \, dt \right] \approx \frac{\sigma_x^2}{2B_x T} \ , \tag{63}$$

it is found that

$$(SNR)_o = \frac{A^2}{A^2 \frac{\sigma_\epsilon^2}{2B_\epsilon T} + \frac{\sigma_n^2}{2B_n T}} , \tag{64}$$

where σ_ϵ^2 is the variance of the input vector phase, B_ϵ is a measure of the bandwidth of $\epsilon(t)$, σ_n^2 is the variance of the input noise, B_n is a measure of the input noise bandwidth, and T is the integration time. Using a similar definition for input SNR, we find

$$(SNR)_i = \frac{\frac{A^2}{2}}{A^2 \sigma_\epsilon^2 + \sigma_n^2} . \tag{65}$$

A measure of the correlator SNR improvement can be obtained from

$$\frac{(SNR)_o}{(SNR)_i} = 2T \cdot \frac{A^2 \sigma_\epsilon^2 + \sigma_n^2}{\frac{A^2 \sigma_\epsilon^2}{2B_\epsilon} + \frac{\sigma_n^2}{2B_n}} . \tag{66}$$

For the case of no error variance, $\sigma_\epsilon^2 = 0$,

$$\left.\frac{(SNR)_o}{(SNR)_i}\right|_{\sigma_\epsilon^2 = 0} = 4B_n T , \tag{67}$$

and for no noise, $\sigma_n^2 = 0$,

$$\left.\frac{(SNR)_o}{(SNR)_i}\right|_{\sigma_n^2 = 0} = 4B_\epsilon T . \tag{68}$$

From equations (66), (67) and (68) it is apparent that $(SNR)_o$ increases with integration time. In principle, correlation will extract any signal regardless of the input SNR if unlimited integration time is allowed. Note from equations (67) and (68) that $(SNR)_o$ varies inversely with noise or error bandwidth. This dependence demonstrates that correlation is more useful for highly erratic (large error bandwidth) signals than for relatively stable (low error bandwidth) signals.

From (55) the correlator output bearing error is

$$\theta_{\epsilon o} = \tan^{-1}\left[\frac{A\int_t \epsilon(t)dt + \int_t n_x(t)\,dt}{AT}\right], \tag{69}$$

where the approximations (56)-(59) have been used. Assuming that the arctangent argument becomes small with integration, (69) reduces to

$$\theta_{\epsilon o} = \frac{1}{T}\int_o^T \epsilon(t)\,dt + \frac{1}{AT}\int_o^T n_x(t)\,dt\ , \tag{70}$$

and

$$VAR\left[\theta\right]_o = \frac{\sigma_\epsilon^2}{2B_\epsilon T} + \frac{\sigma_n^2}{A^2\,2B_n T}\ . \tag{71}$$

The input phase variance is

$$VAR\left[\theta\right] = \sigma_\epsilon^2 + \frac{\sigma_n^2}{A^2}\ . \tag{72}$$

The ratio of output to input variance becomes

$$\frac{VAR[\theta]_o}{VAR\,[\theta]} = \frac{\frac{\sigma_\epsilon^2}{2B_\epsilon T} + \frac{\sigma_n^2}{A^2\,2B_n T}}{\sigma_\epsilon^2 + \frac{\sigma_n^2}{A^2}}\ . \tag{73}$$

With no error, $\sigma_\epsilon^2 = 0$, this ratio becomes

$$\left.\frac{\mathrm{VAR}[\theta]_o}{\mathrm{VAR}\ [\theta]}\right|_{\sigma_\epsilon^2 = 0} = \frac{1}{2B_nT} \quad , \tag{74}$$

and with no noise, $\sigma_n^2 = 0$

$$\left.\frac{\mathrm{VAR}[\theta]_o}{\mathrm{VAR}\ [\theta]}\right|_{\sigma_n^2 = 0} = \frac{1}{2B_\epsilon T} \ . \tag{75}$$

Note from equations (74) and (75) that the output variance decreases inversely with integration time. Again, this result indicates that correlation is useful for reducing the variance of the estimate for the bearing angle. In general, the greatest improvement in variance is evident for large error bandwidths.

VI. Multiple Component Waves

It is instructive to consider the response of the correlator to multiple component incident waves. An analysis of this case for the dual channel receiver model is straightforward. Since the final result for the spaced dipole array is identical, the analysis is presented only for the spaced loop array. For simplicity let $\psi = 0$. The spaced loop differential signal for N components becomes

$$E_\Delta = \sum_{n=1}^{N} a_n(t) \cos(\omega_s t - \theta_n) \sin(\omega_s t - \theta_n) \cos[\omega_c t + \zeta_n(t)], \tag{76}$$

and the corresponding sum signal becomes

$$E_{\Sigma} = \sum_{n=1}^{N} b_n(t) \cos(\omega_s t - \theta_n) \cos[\omega_c t + \zeta_n(t)], \tag{77}$$

where θ_n is the azimuth arrival angle of the n'th signal, $\theta_n(t)$ is the amplitude of the n'th signal, and $\zeta_n(t)$ is the RF phase of the n'th signal. After the product detector and lowpass filter (Figure 3) the output is expressed by

$$E_s = \sum_{n=1}^{N} \sum_{n=1}^{N} a_n(t)\, b_i(t) \cos(\theta_n - \theta_i)\cos[\zeta_n(t)-\zeta_i(t)]\cdot\sin(\omega_s t - \theta_n) \; . \tag{78}$$

Now at the correlator outputs,

$$E_{xo} = \int_t \left\{ \sum_{n=1}^{N} \sum_{n=1}^{N} a_n(t)\, b_i(t)\cos(\theta_n - \theta_i)\cos[\zeta_n(t)-\zeta_i(t)] \cos\theta_n \right\} dt \tag{79}$$

and

$$E_{yo} = \int_t \left\{ \sum_{n=1}^{N} \sum_{n=1}^{N} a_n(t) b_i(t)\cos(\theta_n - \theta_i)\cos[\zeta_n(t)-\zeta_i(t)] \sin\theta_n \right\} dt \; . \tag{80}$$

As a realistic model it can be assumed that $\zeta_n(t) - \zeta_i(t)$ is uniformly distributed 0 to 2π radians and that the amplitude is independent of the RF phase. With these assumptions and recognizing that $b_n(t) = C\, a_n(t)$,

$$E\left\{ \frac{1}{T} \int_o^T a_n(t)\, b_i(t) \cos[\zeta_n(t) - \zeta_i(t)]dt \right\} = 0 \tag{81}$$

for $i \neq n$, and

$$E\left\{ \frac{1}{T} \int_o^T a_n(t)\, b_i(t) \cos[\zeta_n(t) - \zeta_i(t)]\, dt \right\}$$

$$= E\left\{ \frac{1}{T} \int_o^T C\, a_n^{\,2}(t)\, dt \right\} \text{ for } i = n. \tag{82}$$

Therefore,

$$E_{xo} = \frac{C}{T} \sum_{i=1}^{N} P_n \cos \theta_n \ , \tag{83}$$

and

$$E_{yo} = \frac{C}{T} \sum_{i=1}^{N} P_n \sin \theta_n \ , \tag{84}$$

where

$$P_n = \frac{1}{T} \int_o^T a_n^2(t)\, dt \ . \tag{85}$$

Note that P_n can be associated with the power content of the n'th component. The resultant estimate of the azimuth angle will be

$$\theta = \tan^{-1} \frac{\sum_{i=1}^{N} P_n \sin \theta_n}{\sum_{i=1}^{N} P_n \cos \theta_n} \ . \tag{86}$$

Note that the correlator output angle is exactly the angle of the resultant input vector. Thus, when processing a multiple component signal with the dual channel receiver, the display angle is the power weighted vector resultant angle of all incident signals. A result exactly equivalent to (86) can be demonstrated for a spaced dipole array used with a dual channel receiver.

VII. Application of Correlation Detection

Orthogonal correlation has been implemented for several small aperture DF systems including simple loop, spaced loop, and spaced vertical dipole systems. Results have demonstrated a significant improvement in sensitivity along with variance reduction for some of the DF systems. Recently, an existing operational spaced loop DF system [AN/VRD-( )] was modified to include the orthogonal correlation technique.[2]

Operational considerations for the correlation technique include methods of practical implementation, signal acquisition time, and maximum correlation time. In general, analog implementation methods have been used with reliance on the current availability of high performance operational amplifiers, analog multipliers, and integrated circuits. The integrators for the correlator have been designed around operational amplifier integrators with provisions for hold and reset modes. Signal acquisition times have been optimized by incorporating a short term correlator for rapid acquisition with automatic switchover to long term correlation. Weighted as well as true integration modes have also been investigated. Analog correlators with maximum integration time of up to 5 minutes have been constructed and tested.

Test results under a variety of signal conditions substantiate the analytical results presented herein. It has been demonstrated that correlation significantly improves the capability for obtaining a bearing estimate on weak signals. With correlation times of about 60 seconds, SNR improvements of about 15 dB and 25 dB have been measured for a single channel receiver and dual channel receiver respectively. Results obtained from spaced loop DF systems validate polarization dependence and indicate that polarization errors will average out for symmetric distributions of the polarization vector.

Bearing data obtained with correlation detection and compared with bearing data obtained from conventional displays under the same conditions demonstrate that variance reduction is possible.[3] Signal propagation conditions for data collection ranged from low angle skywave to very high angle skywave combined with a weak groundwave component. Generally, the standard deviation for correlative bearing data obtained with a spaced dipole array is about one half of the standard deviation for conventional bearing data. No significant reduction (or increase) in variance has been obtained with spaced loop arrays; this result is probably due to polarization bias errors produced by asymmetric polarization distribution. Efforts are currently underway to alleviate the spaced loop polarization effects on correlation.

Orthogonal correlation has been found to be an effective means for removing signal modulation effects from a DF display. In many cases it has been observed that operator response time is improved with correlation, albeit time is required for developing an estimate. Erratic signal conditions are particularly well suited for correlation. The apparent randomness many times produces useful bearing estimates.

VIII. Conclusions

Orthogonal correlation is an effective method for improving the performance of DF systems. For time variable errors symmetrically distributed about the mean direction of arrival, correlation reduces the variance inversely proportional to the integration time. Unless special processing is used, correlation used with a coaxial spaced loop DF system is sensitive to polarization errors with the amount of error dependent on the distribution of the polarization vector. Bearing estimates obtained from spaced vertical dipole arrays do not exhibit polarization dependence. Correlation produces an improvement in SNR directly proportional to the correlation time. Test results indicate that 15 to 25 dB improvements are possible with correlation times of about 60 seconds.

With the use of orthogonal correlation, modulation tolerance is increased and display readability is enhanced.

Acknowledgements

The work summarized in this paper was performed under Contract DAAB07-70-C-261 with the U. S. Army Electronics Command. The author acknowledges the efforts of Mr. H. H. Jenkins for his critical review of the results.

References

1. Julius S. Bendat and Allan G. Piersol, Measurement and Analysis of Random Data, John Wiley & Sons, Inc., New York 1966, pp. 184-185.

2. H. H. Jenkins, R. W. Moss, and C. S. Wilson, "Improved Small Aperture DF Systems," Engineering Experiment Station, Georgia Institute of Technology, Special Report No. 1, Contract DAAB07-70-C0261, April 1971.

3. H. H. Jenkins and R. W. Moss, "Tiltable, Rotating Vertical Loop DF System," Engineering Experiment Station, Georgia Institute of Technology, Final Report, Contract DAAB07-68-C0072, June 1970.

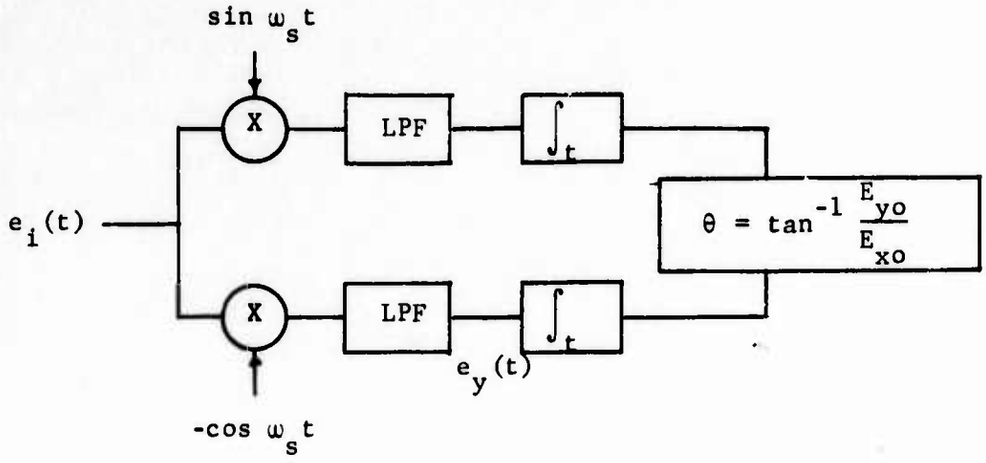

Figure 1. Basic Form of Orthogonal Correlator.

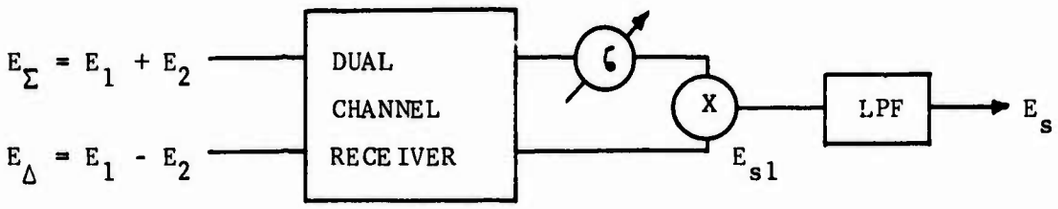

Figure 2. Dual Channel Receiver Model.

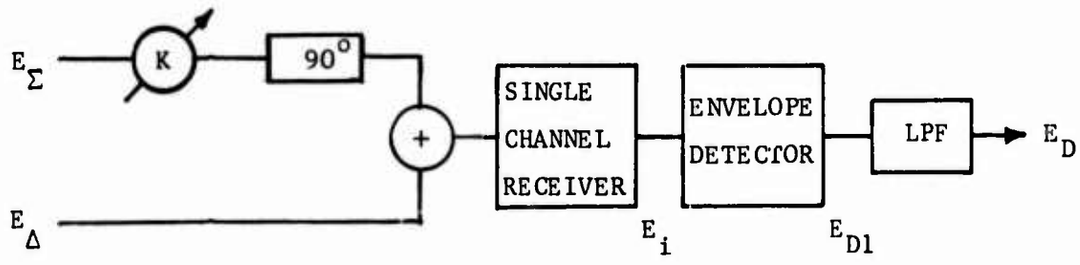

Figure 3. Single Channel Receiver Model.

R. B. MATHEWS, P. E. MARTIN

Southwest Research Institute, San Antonio, Texas

REAL-TIME COMPUTER PROGRAMMING TECHNIQUES FOR RADIOLOCATION PROBLEMS

ABSTRACT

The close interrelation of real time DF and SSL software with corresponding control hardware is reviewed. The development and processing of logic decision tables from system control functions is described.

I. INTRODUCTION

Automatic systems can perform many radiolocation tasks better than man. They can collect location generating data, perform statistical analysis, record and display results, and operate special equipment faster and with more accuracy than a man. It remembers better; it can tell when signals are too weak or too strong for its sensors; and it can handle a myriad of detail and be attentive for long periods.

The man is sophisticated in identifying targets of interest and controlling data acquisition, e.g., stop during periods of interference, "tag" co-channel signals, and to decide when enough data has been taken. In operating a well designed, automated system, the operator directs and the machine does; the man is not required to wait for the computer to request information but rather he enters commands as he requires. Put man and machine together in this system approach and the result is higher performance than either could produce alone.

II. OPERATING SYSTEMS

An "operating system" is the computer program that enables man and machine to work together. The man doesn't direct the "computer"; he directs an operating system program. (Figure 1). A directing type of operating system is dormant except while processing and responding to operator commands or system alarms.

The control program is that part of the operating system that responds to the commands and goes dormant as other programs execute tasks scheduled by the control program (Figure 2). The

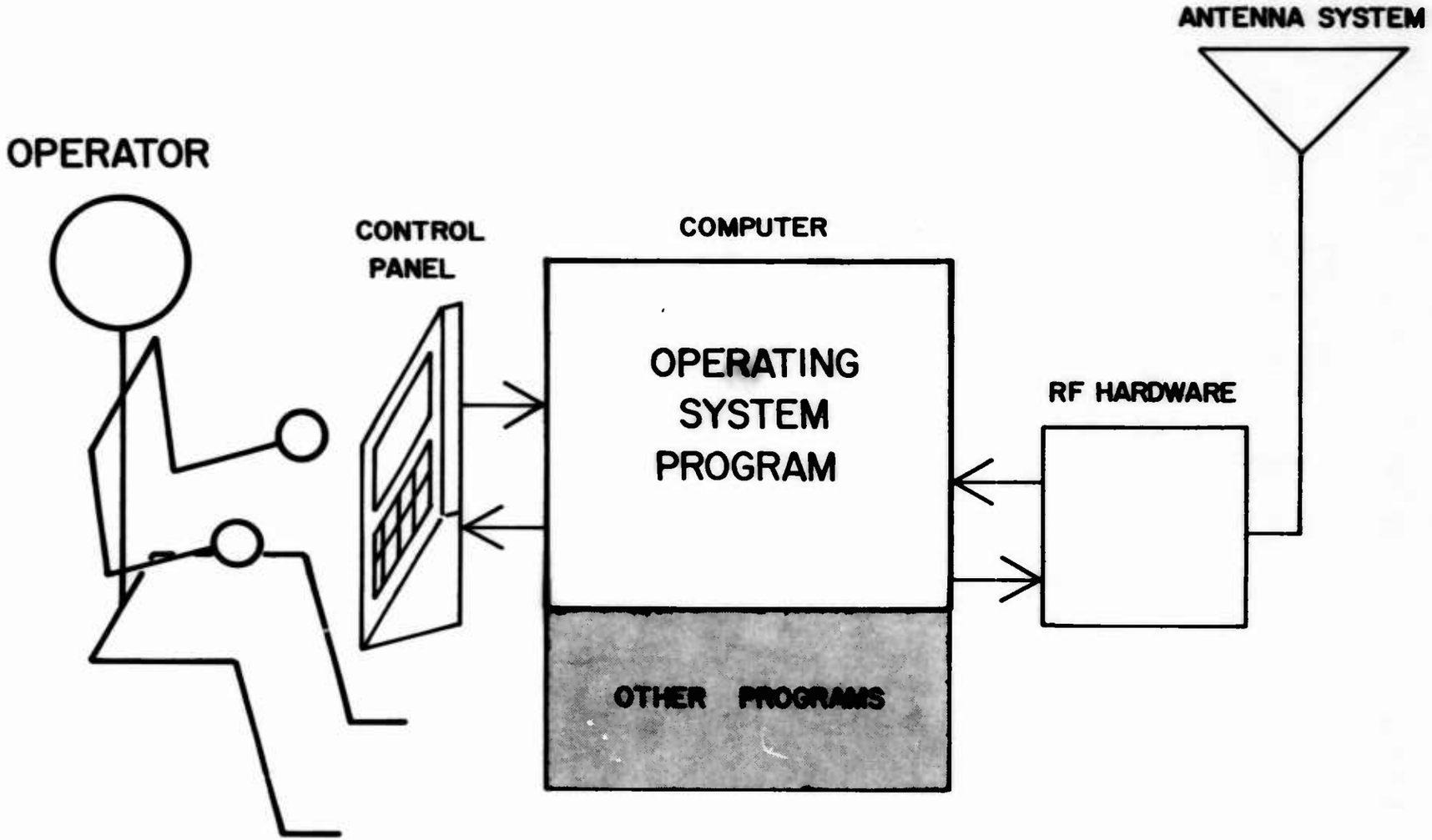

FIGURE 1. MAN AND OPERATING SYSTEM

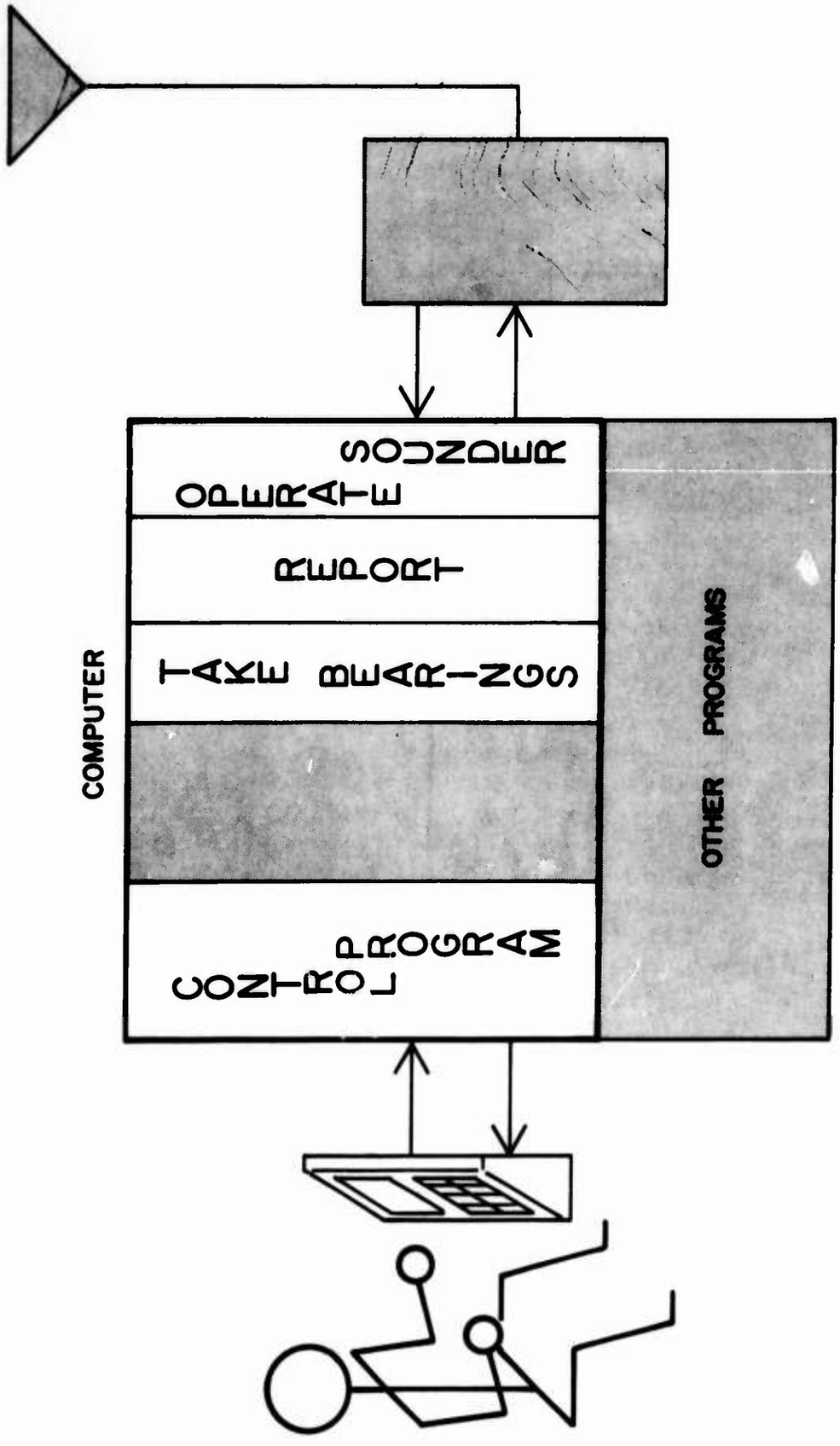

FIGURE 2. CONTROL PROGRAM

control program is dormant but alert. Its reactivation is not dependent on the system status or place in a program but only on the operator's command. This alertness is the key to having the man direct.

The real-time "executive" or executive program provides the alert factor for the control program and generally coordinates programs and input-output (Figure 3). It handles allocation of system resources to the programs it controls and in real-time programming it schedules programs to operate at specified times. The executive program is an environment which permits programs to operate concurrently without interference. The same kinds of interaction can be had without an executive program but the executive simplifies programming by providing a single method for all interprogram coordination. For example, the executive can coordinate concurrent input of new data, calculation on recent data and the output results of old data while all of yesterday's data is being dumped from secondary storage to magnetic tape. Good real-time executive software allows the system programmer to concentrate on the main task (in this case, radiolocation) rather than becoming involved with multiprogramming software development.

III. HARDWARE CONSIDERATIONS

Since the objective in a real-time radiolocation system is to have the computer program respond to external events, especially the control panel, an input-output interrupt system is essential. The main idea of an interrupt system is to allow events external to the computer to interrupt and suspend a running program, execute a program appropriate to the external event and resume the interrupted program at the point it was interrupted. The interrupt system allows the computer to compute where it would otherwise be waiting for input or output.

The interrupt system uses hardware in the interface between the input-output bus to cause the computer to "mark place and jump" to a routine that will service the interrupt. Figure 4 shows the SSL system hardware and three interfaces, each capable of generating an interrupt. All three can be active concurrently since the input and output bus of the computer is time shared by active devices. The control panel can interrupt with a command while the analog digital connector is inputting location data and the console is reading the system clock. Table 1 lists the devices controlled by the interface. The need to allow the operator to hold an index key down to acquire data gave some problems until it was decided to let the programs involved restrobe the control panel when a key might still be depressed.

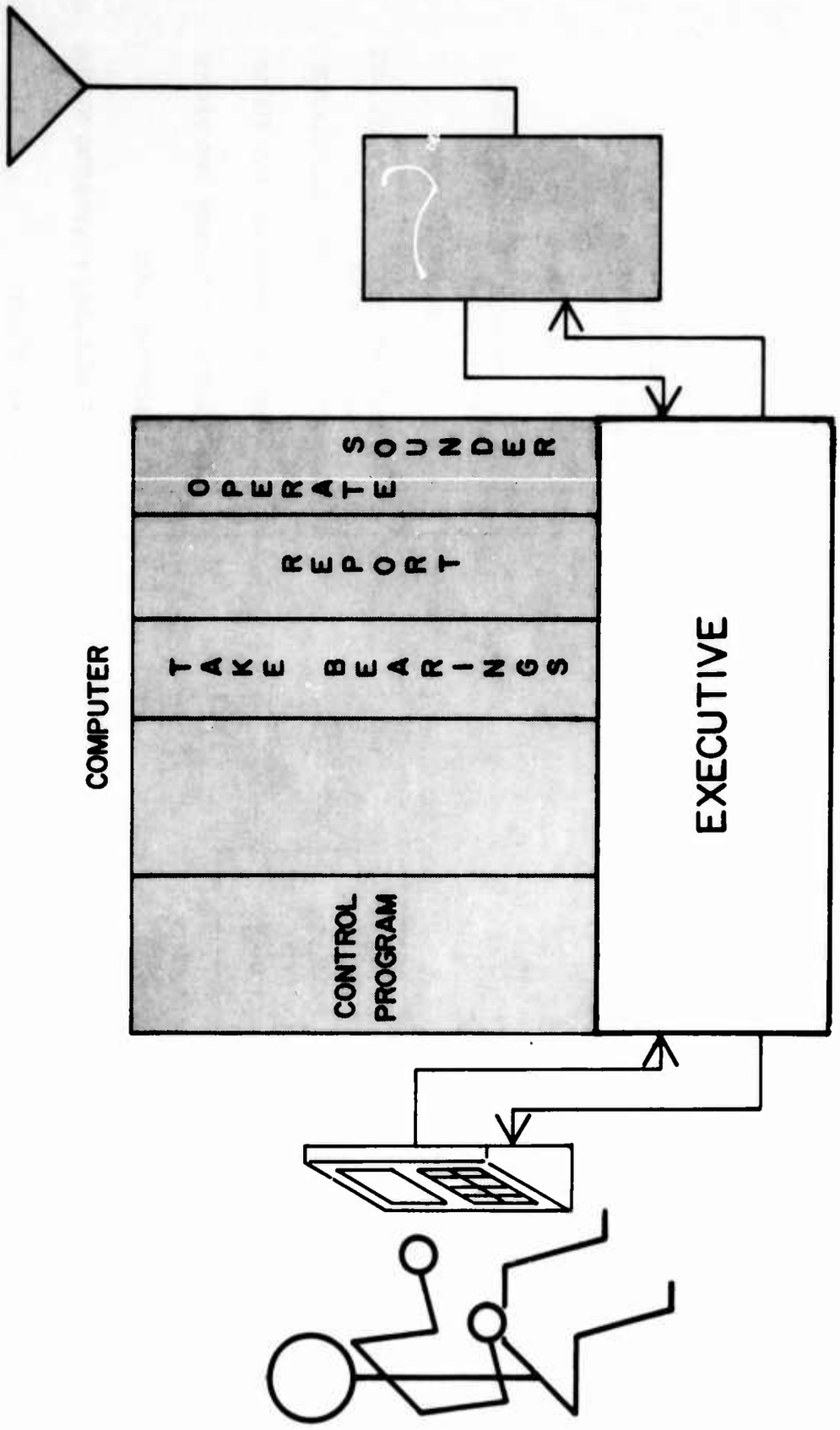

FIGURE 3. THE EXECUTIVE

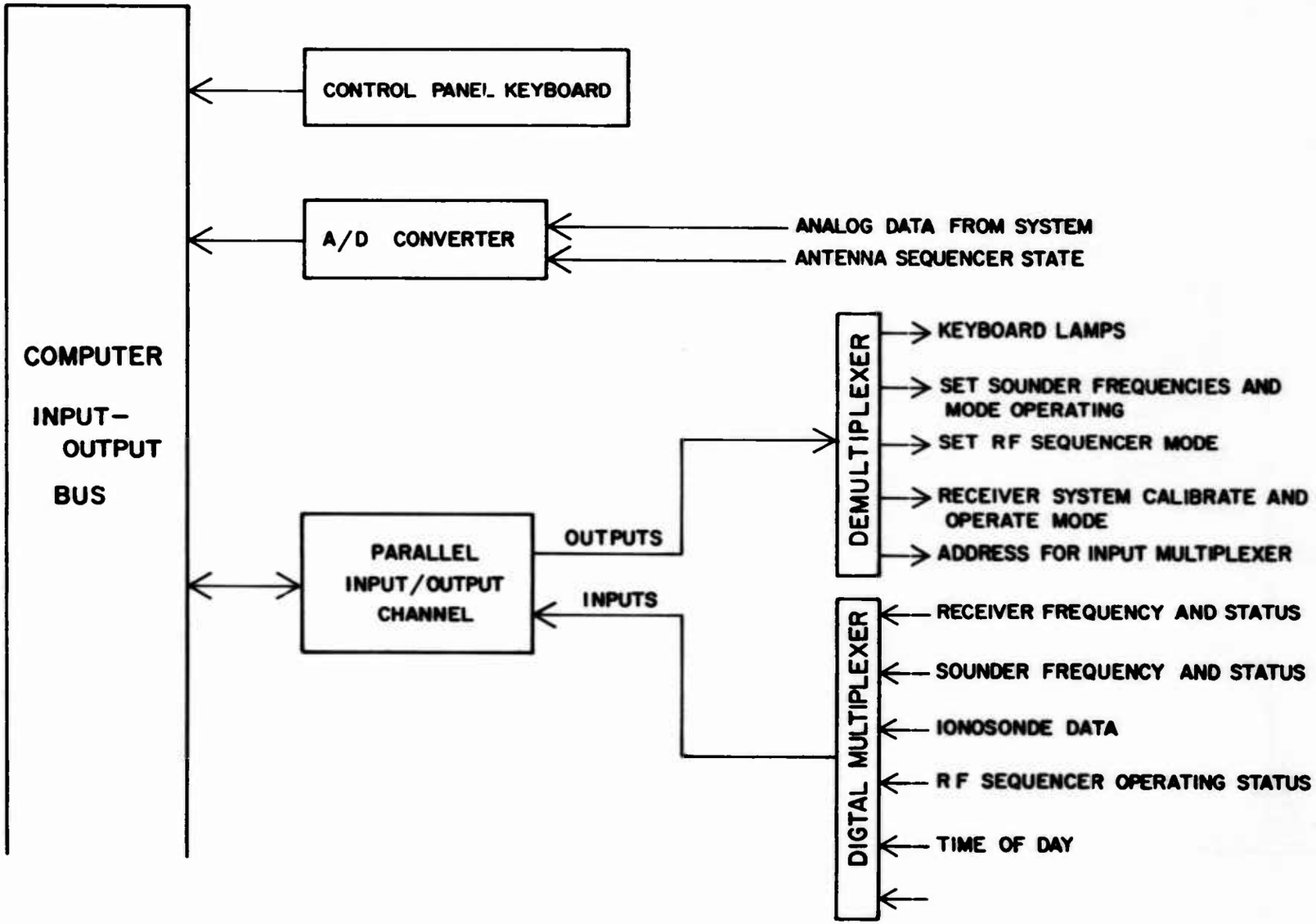

FIGURE 4. HARDWARE INTERFACE

TABLE 1

Devices under program control include:

(1) Control panel keyboard -- The initialization of all computer functions with respect to real-time on-line data acquisition

(2) Output instructions:

(a) Set the RF input sequencing mode

(b) Set ionospheric sounder high and low frequency sweep limits and sounder operating modes

(c) Set control panel status indicators (illuminated switches)

(d) Set receiver calibrate and operate modes (including automatic phase and gain balance, phasemeter balance, pilot signal inspection, etc.)

(e) Addresses for input multiplexer

(3) Inputs:

(a) Read receiver frequency and status

(b) Read sounder frequency and status

(c) Read RF sequencer operating mode

(d) Read time-of-day clock

(e) Read ionosonde data from spectrum analyzers (amplitude and phase)

(4) The analog-to-digital converter processes the phase angle and amplitude data from the interferometer system accompanied by identification data in a digital format that forms part of the digital word entered into the computer for each A/D conversion.

The restrobe simulates the man depressing the key a second time. As restrobes occur 50 to 100 ms after the initial event, the likelihood of a second key being depressed in the interim is remote. The worst effect would be a second occurence of the second key.

IV. CONTROL SYSTEM DESIGN

Recent efforts at Southwest Research Institute have included the design of a single-site radiolocation system to be operated by a man with the aid of an 8K word computer and a disc for secondary storage. After identification of a signal of interest, an ideal system would be one which provides location of the target with a minimum of action on the operator's part. For two important reasons the system final design provides 21 buttons for the various operator options: (1) more than one task is performed by the system and (2) the operator must have means to control data acquisition and to direct the disposition of data once acquired.

Major tasks are intercept, direction finding, location, and sounder operations. Some control functions are data collect, data end, and data mode selection (analog or digital). These tasks are integrated by a control program using a control panel for the operator.

The control system design procedure (Figure 5) takes into account the close interrelation of real time radiolocation software and corresponding control hardware. The procedure was executed in three steps: (1) control flow analysis, (2) decision table definition, and (3) sequential testing procedure. The output is a flow chart and detailed documentation describing the system ready for programming.

V. MAN-MACHINE INTERFACE

Interface design must carefully consider the flow of decision and make sense to a wide range of operators. Figure 6 shows the current SSL control panel. Each key represents a decision that the operator can make. At any time, this control panel "tells" the operator the current state of the system and what succeeding command options are available to him by using three levels of illumination for each key. Off means this key is not an option; dim, this key is an option; and bright, this key has been selected. Figure 7 shows a sample sequence to demonstrate the idea. Note also that the keys are placed in the order expected during operation and a "trail" of bright keys reminds the operator what he has set up.

CONTROL SYSTEM DESIGN PROCEDURE

STEP 1 CONTROL FLOW ANALYSIS

STEP 2 DECISION TABLE DEFINITION

STEP 3 SEQUENTIAL TESTING PROCEDURE

FIGURE 5. CONTROL SYSTEM DESIGN PROCEDURE

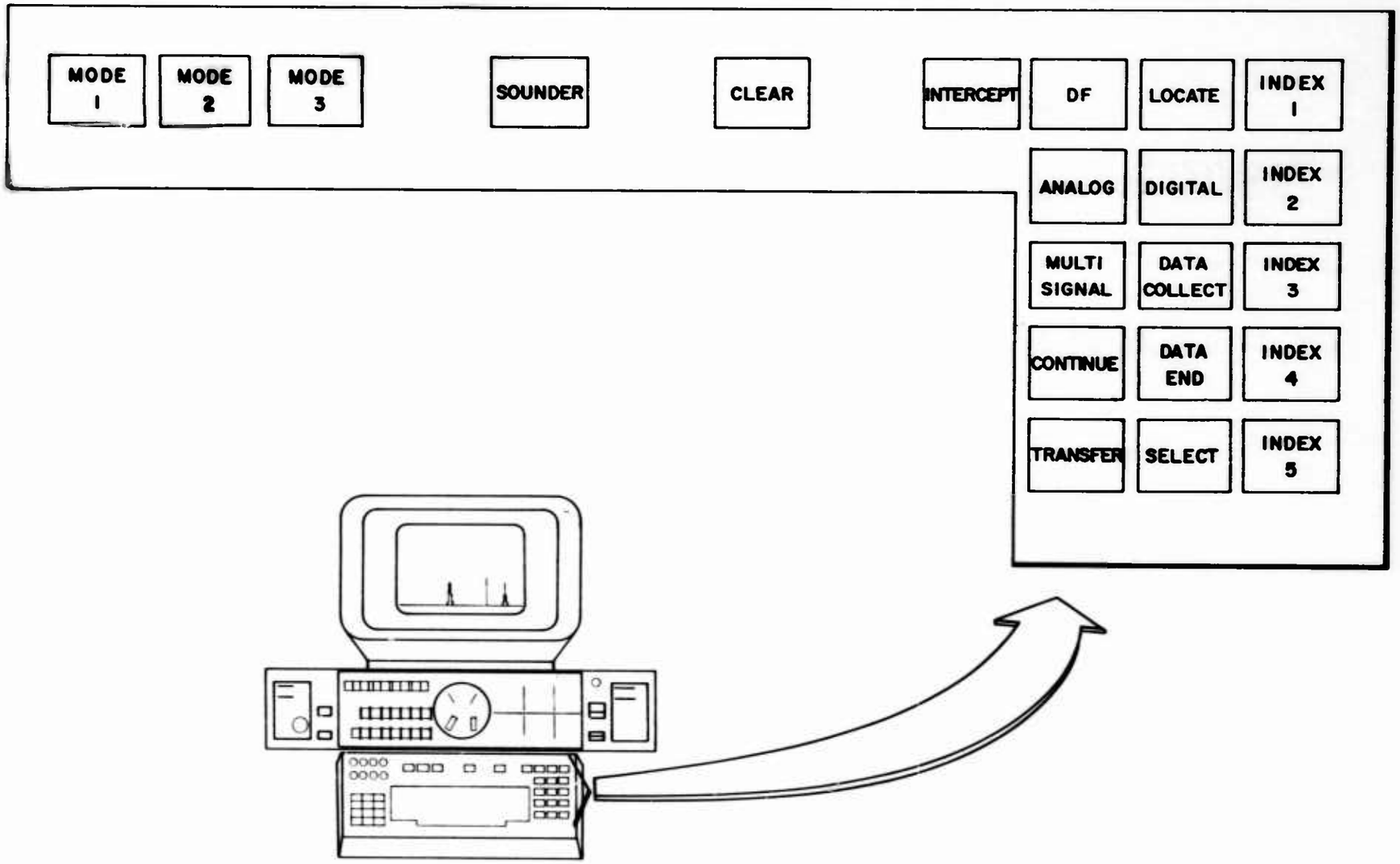

FIGURE 6. CONTROL PANEL

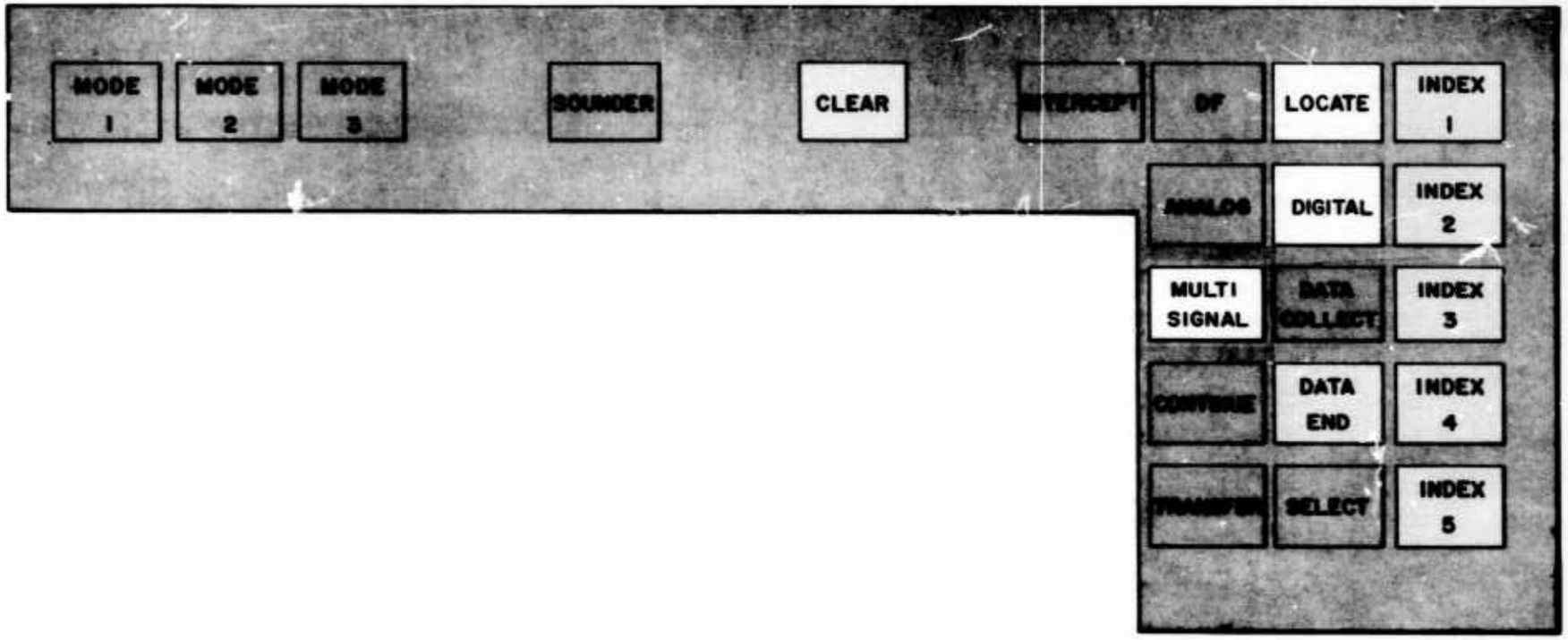

FIGURE 7. EXAMPLE OF CONTROL PANEL USE

VI. CONTROL FLOW

Figure 8 shows the normal control flow of the system which is very similar to the control panel except that it shows normal sequences of control. Note the duplication of names. If the DATA COLLECT key is depressed, the action required depends on which line is being followed on the control flow diagram. Similarly, the operations to be scheduled after a DATA END vary depending on whether the mode is ANALOG or DIGITAL and whether the task is direction finding (DF) or location (LOCATE). We can, however, define each meaningful move and detail tasks to fulfill the move. Many moves on the control flow diagram allow the operator to recover when he makes false starts or wishes to CONTINUE. These are necessary both for normal operation as when a signal goes off and to make it easy for the novice operator who makes an error.

The control flow diagram (Figure 8) also indicates five levels of command flow. If the current level is known and we know what keys are active in the current and previous levels, we can deduce the next move when a key is depressed. This relieves us of testing at specific points in a program and permits "setting switches" to redirect program flow. The actual method used is a function of the executive and will not be discussed further. To be considered is how to interpret the commands in a way that allows additions and changes with minimum reporgramming.

VII. DECISION TABLES

Decision tables provide a method of organizing decision and resultant actions. Figure 9 is an example of a decision table for taking a bearing. Figure 10 shows a portion of a decision table that describes a single site location system. The conditions are "keys and flags" and the actions show the responses to the rules. What the tables do not show is how to test the conditions efficiently with a computer. In the present system, there are 34 conditions involved in defining 36 rules. A straight forward approach is to inspect the conditions rule-by-rule. Assuming a uniform distribution, 17 conditions of 18 rules are tested for each decision for a total of 306 tests. This is a highly redundant and time consuming testing procedure for a real time system. Another method is to establish "masks" that conform to the yes, no, and don't care conditions in the table. This makes setting flags take a little longer in addition to the redundant operations which are required to test the masks.

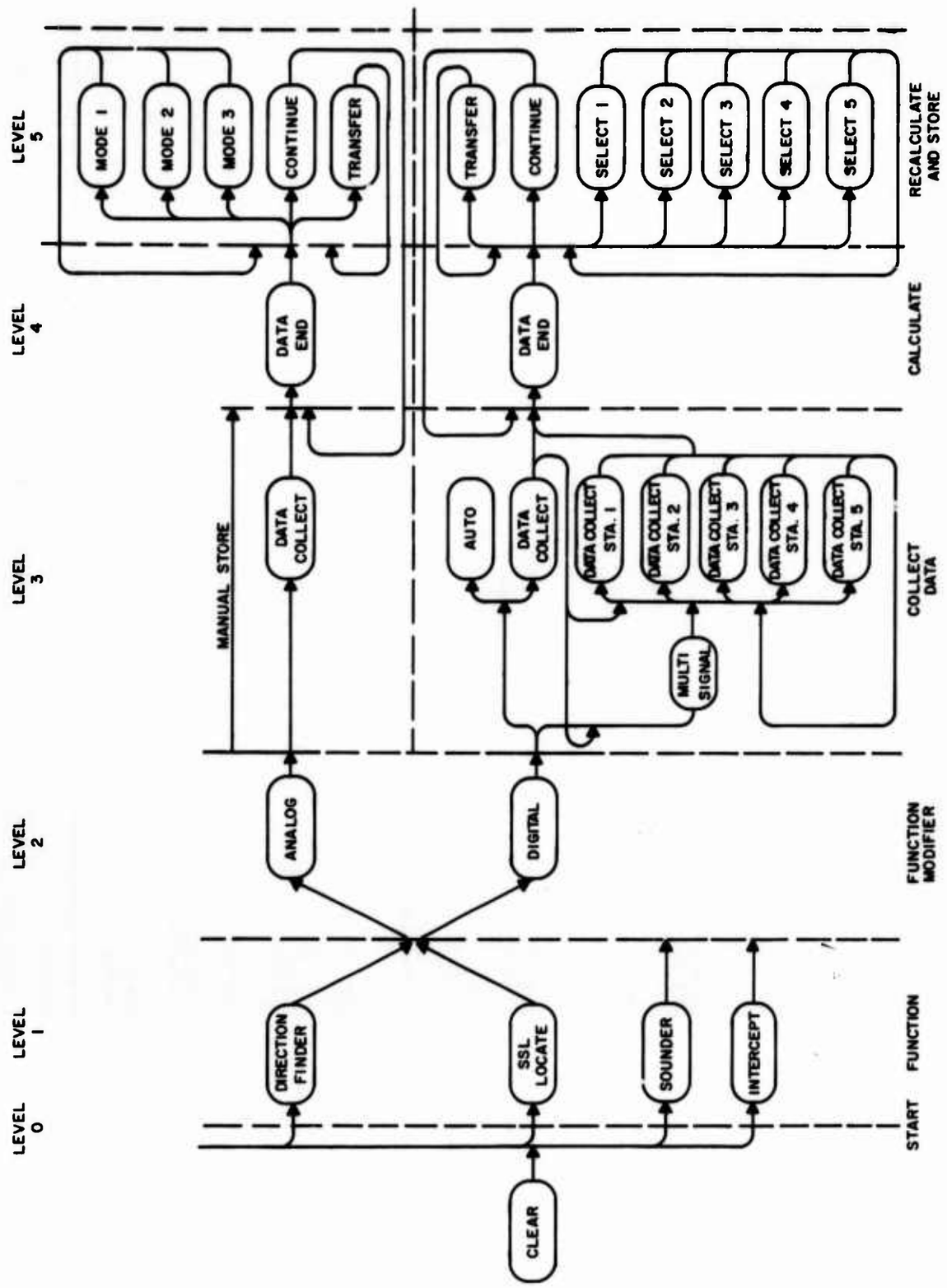

FIGURE 8. CONTROL FLOW DIAGRAM

		RULE 1	RULE 2	RULE 3	RULE 4	RULE 5
CONDITIONS	SIGNAL IDENTIFIED	YES	YES	YES	NO	NO
	ON TARGET LIST	YES	NO	NO	–	–
	SUPERVISOR APPROVAL	–	YES	NO	YES	NO
ACTIONS	TAKE BEARING	X	X		X	
	CONTINUE SEARCH			X		X

FIGURE 9. A DECISION TABLE

	RULE	01	06	07
CONDITIONS	CLEAR KEY	1	0	0
	INTERCEPT KEY	0	1	1
	SOUNDER ACTIVE			0
	LEVEL 1 ACTIVE		0	1
	LEVEL 2 ACTIVE			
	LEVEL 3 ACTIVE			0
	LEVEL 4 ACTIVE			

0- NOT ACTIVE

1 ACTIVE

Ø- DON'T CARE (Ø= blank)

ACTIONS

RULE 06

SET INTERCEPT ACTIVE

SET LEVEL 1 ACTIVE

RESET INTERCEPT KEY FLAG

INTERCEPT KEYLAMP BRIGHT

REQUEST INTERCEPT PROGRAM

RULE 07

RESET INTERCEPT KEY FLAG

CLEAR COMMAND BUFFER

ENTER CLEAR IN COMMAND BUFFER

ENTER INTERCEPT IN COMMAND BUFFER

FIGURE 10. EXTRACT OF SSL DECISION TABLE

VIII. SEQUENTIAL TESTING PROCEDURE

The method used for the SSL system is a sequential testing procedure, providing a method for converting decision tables into binary flow charts such that no test is made more than once while determining the rule (Figure 11). For 34 conditions, not more than 34 tests are needed to determine the rule. The procedure is detailed in references (1) and (2).

The procedure makes two smaller decision tables based on the 1, 0, and ϕ for one condition. An algorithm minimizes the number of smaller decision tables which must in turn be divided until only a single rule remains. The minimizing and dividing procedure was programmed on a time shared computer for interactive operation. Each operation of the program outputs two smaller decision tables ready as input for another "pass" at the program. When an output table contains only one rule, the remaining conditions are tested and the rule found. When an output table is empty either a rule has been found as for Rule 06 or the null rule (error in this case) is invoked.

Ambiguous and redundant rules end up with decision tables that output themselves and a null rule. A small program was prepared which analyzed the initial decision table for ambiguities. As suggested in Reference (2), ambiguities arise when it is known that certain conditions cannot exist simultaneously. The ambiguity is usually remedied by adding a condition (1 or 0) to the rule.

IX. SUMMARY

The three part procedure, control flow analysis, decision table definition, and sequential testing procedure, provides a detailed statement of the action required in response to a decision and a semiautomatic conversion to a program flow chart for rule determination. The action required of a rule is effected by "setting program switches" and interacting with the real-time executive which, in fact, controls program flow. The result is a flexible, responsive control system that lets the man direct and the computer do.

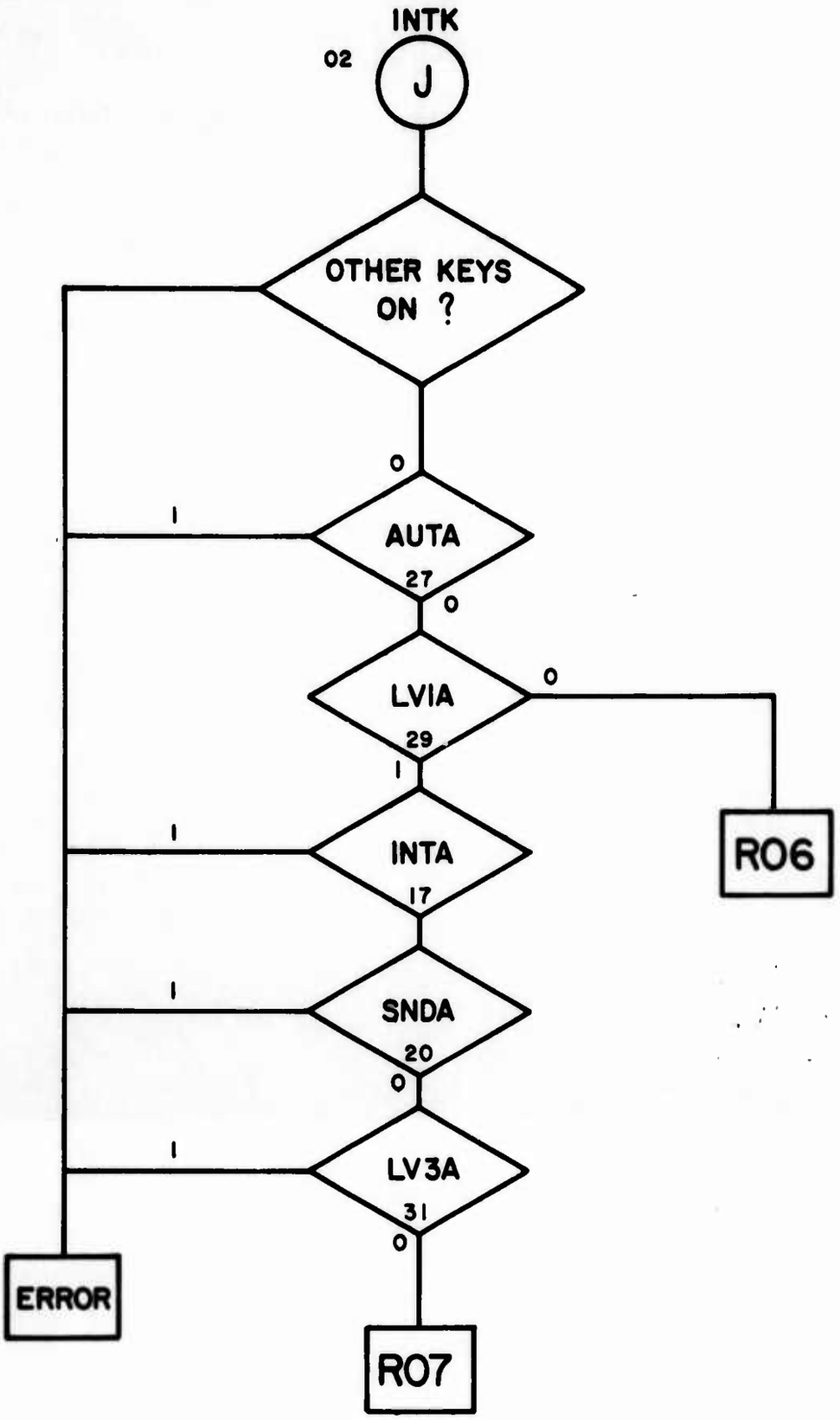

FIGURE 11. EXTRACT FLOW CHART

REFERENCES

1. Katzan, Harry, Jr., Advanced Programming, Van Nostrand, Reinhold, New York, 1970 (LBC 78-108648).

2. Press, L. I., "Conversion of Decision Tables to Computer Programs," Comm ACM, Vol. 8, No. 6, June 1965.

3. McDanile, Herman, Applications of Decision Tables - a Reader, Brandon/Systems Press, Inc., Princeton, 1970 (LBC 71-100988).

A CDAA RDF SYSTEM WITH AN ON-LINE COMPUTER

Leigh C. Cropper and Edward W. Ernst
Radiolocation Research Lab
Department of Electrical Engineering
University of Illinois
Urbana, Illinois 61801

I. Pre-Computer RDF System

The RDF system located at the Bondville Road Field Station processes signals received by a Wullenweber circularly directed antenna array (CDAA) and generates both an analog display and a digital record of signal patterns. This report is concerned primarily with the digital record.

The system elements are diagrammed in Figure 1. The signals from the receiver feed into the high speed data system (HSDS) where they are converted to digital form and subsequently stored on magnetic tape in a format suitable for decoding by a remote computer.[1] Timing and synchronization are controlled by the electronic strobe unit and the multiscan adapter (MSA).

The electronic strobe synchronizes to the 'north' pulse and the 0.1 degree pulse from the transducer mounted on the scanner and also monitors the sector center and sector width as set by the operator. The strobe unit generates gating signals which enable the HSDS to receive data over the specified azimuthal sector. The values of sector width and sector center are passed to the HSDS from the strobe unit in digital form.

The MSA selects particular scans for which data are actually recorded. The selection is determined on the basis of the time interval between the groups of scans and the number of scans in each group. The MSA gates the enabling signals (start, stop, sample) from the strobe unit to the HSDS upon receiving a pulse from the data repetition-rate unit. The repetition rate unit may be set by the operator.

The signals to the HSDS are shown and labeled in Figure 1. Start, stop, sample, sector width (WD), and sector center (CEN) are signals from the MSA and the strobe unit; TIME is furnished in digital format by a clock unit. The other input signals to the HSDS are output signals from the RDF receiver and directly related units. Except for FREQ, the signal frequency, these signals are all in analog format. Table 1 gives a brief description of all input signals to the HSDS.

The HSDS block diagram is given in Figure 2. The HSDS is a generalized data handling device which accepts fast analog signals on each of ten channels and either slow analog or digital signals on each of six other input channels. Control signals to the HSDS determine the timing and sequence for reading data from the channels. When one of the fast analog channels is selected to be read, a hold pulse is sent to the sample/hold amplifiers. The sampled signal of the selected channel is fed

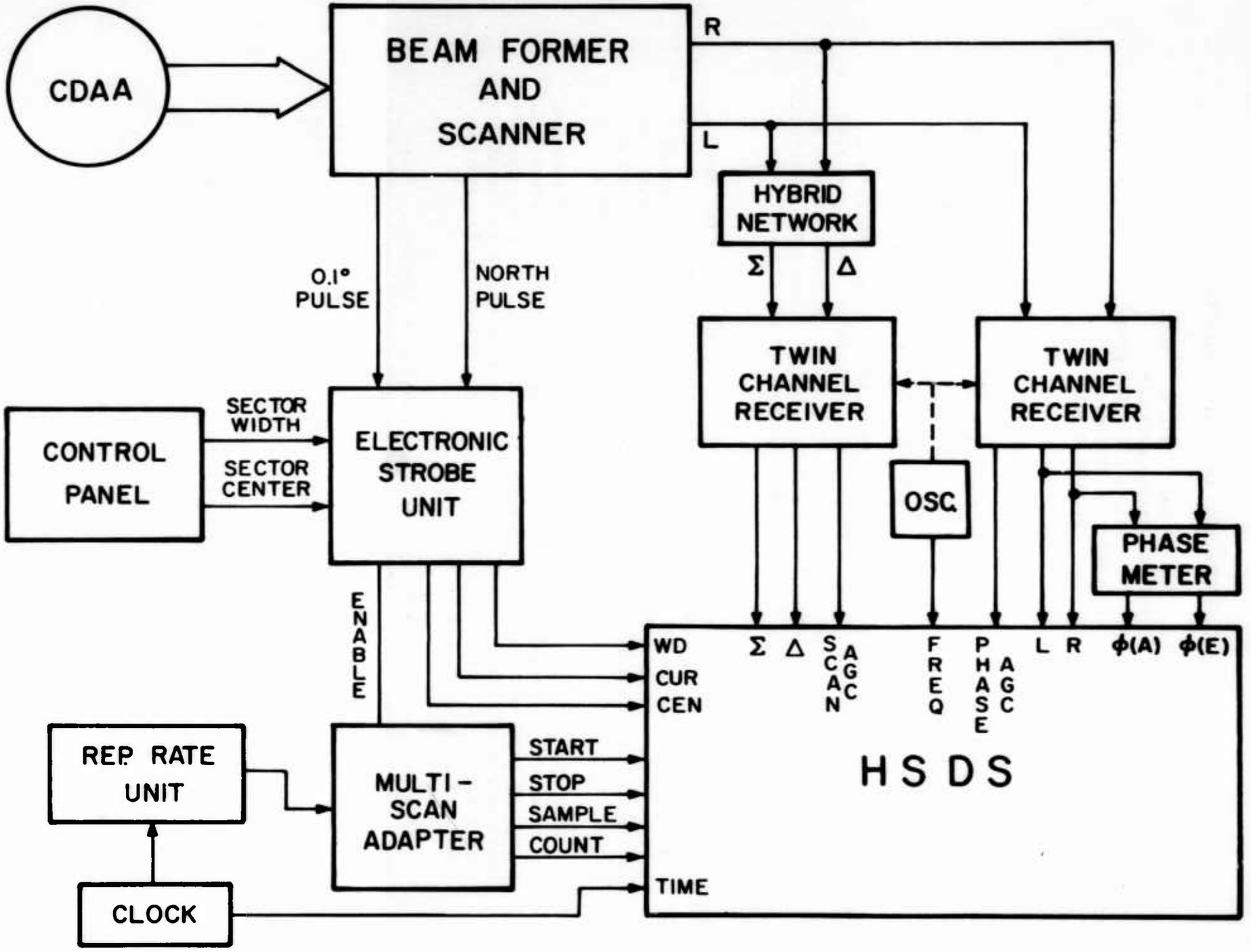

Figure 1. Pre-Computer RDF System Block Diagram

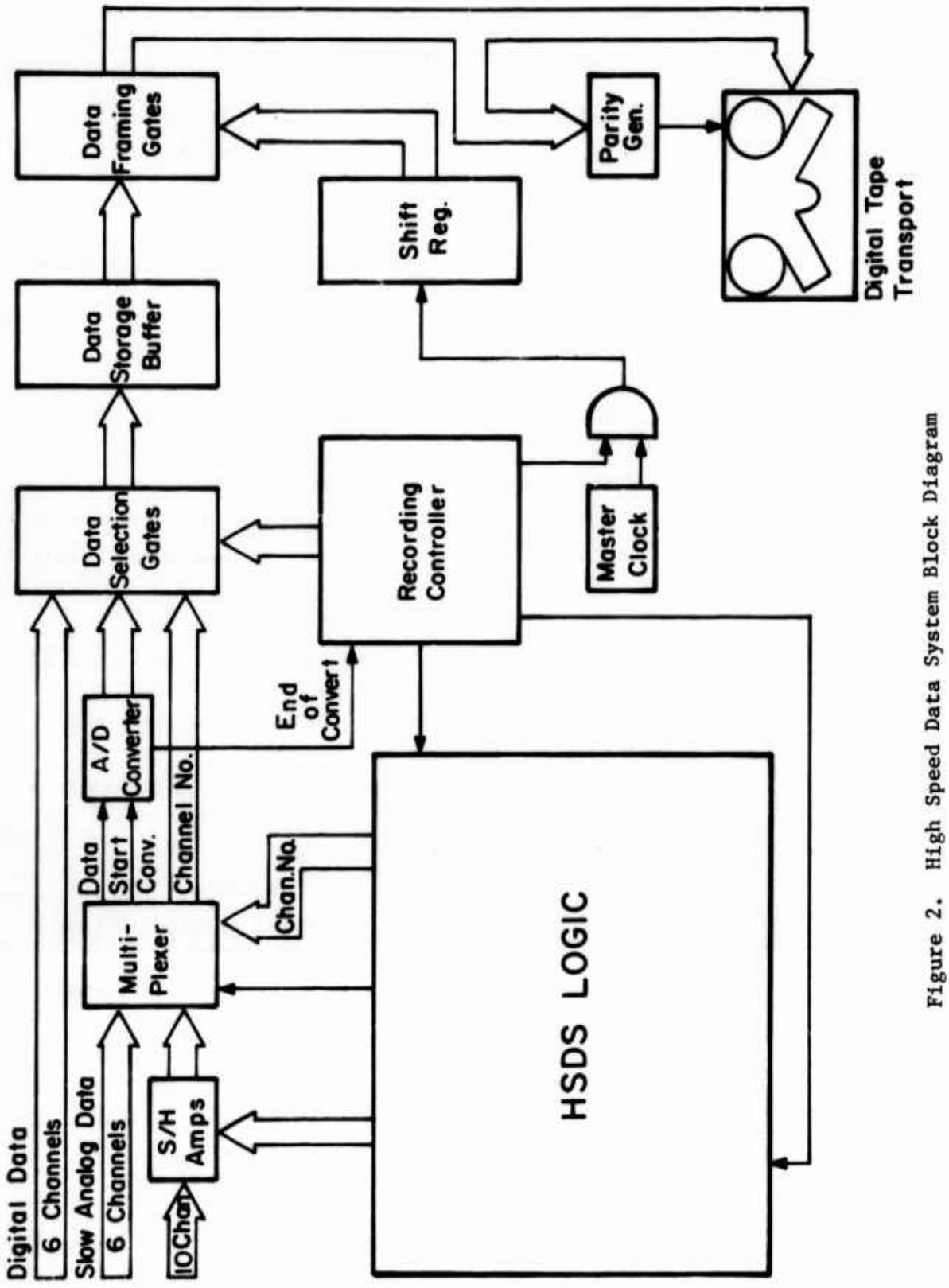

Figure 2. High Speed Data System Block Diagram

TABLE 1

HSDS INPUT SIGNALS

Channel	Label	Source	Format	Description
	Start	MSA	pulse	control signal
	Stop	MSA	pulse	control signal
	Sample	MSA	pulse	control signal
1	Σ	Receiver	analog	sum of signals from sector halves
2	Δ	Receiver	analog	difference between signals from sector halves
3	ϕ(A)	Phase meter	analog	left-right differential phase (azimuthal)
4	ϕ(E)	Phase meter	analog	differential phase (elevation)
5	ϕAGC	Receiver	analog	phase automatic gain control
6	Scan AGC	Receiver	analog	scan automatic gain control
7	L	Receiver	analog	signal from left half of sector
8	R	Receiver	analog	signal from right half of sector
10	Time	Clock	digital	real time in hours and minutes
11	CUR	Strobe	digital	angular position of electronic cursor
12	WD	Strobe	digital	sector width/2
13	CEN	Strobe	digital	sector center
14	Freq.	Frequency counter	digital	digital reading of receiver frequency
15	Count	MSA	digital	count of scans selected by MSA for recording (modulo 16)
15		Clock	digital	real time in seconds

Format Description:

Pulse - Control signals are short pulses having well defined leading and trailing edges.

Analog - The analog channels are single line inputs to the multiplexer.

Digital - The digital channels contain up to fourteen lines and carry parallel digital signals.

through the multiplexer to the A/D converter. The fourteen bit output of the A/D converter becomes a part of the input to the data selection gates. Channels carrying slow analog data are handled in the same way, except that the slow data is fed directly to the multiplexer without the "sample and hold" function. Digital data channels are selected by the digital input unit, from which the lines of the selected channel go directly to the data selection gates. The data selection gates also receive as input four bits of channel designation code which are gated through with the appropriate fourteen bits of data to the framing gates, where the combined eighteen bits are framed into three nine-bit words, which are stored on magnetic tape. (Extra bit positions are used for blocking marks and parity bits.)

Because of the nature of the HSDS, the inputs itemized in Table 1 can be assigned arbitrarily to the HSDS input channels as long as data format restrictions are observed. Which channels are read is controlled by the operator through the console switches.

II. Data Buffering by Computer

The system described in the foregoing section had several practical limitations which are being approached and eliminated in a systematic manner. The addition of a minicomputer (Figure 3) to the system is an initial step in this planned system evolution. The versatility of the computer suggests a large range of possible modifications. However, the initial modification adds only the following four capabilities: (1) data buffering by the computer to pack data from the HSDS before storage on magnetic tape; (2) on-line self-checking routines to detect system malfunctions; (3) on-line routines to allow simultaneous computation and data logging; and (4) off-line computation of azimuthal angle of arrival.

The previous system recorded data on 1/2 inch magnetic tape for later processing by the G-20 computer located on campus. The recording format utilized three magnetic tape characters for each data sample. Data samples were recorded at the variable rate at which they were acquired by the HSDS. Two undesirable consequences of the unstructured data recording were the resulting low density of data on the tape (about 20 per cent of the maximum possible) and the need for time-consuming reformatting by the remote computer before calculations could be performed. On-line data buffering can easily improve the recording density to better than 70 per cent of the maximum possible; and buffering creates a blocked data format which is easily handled by the remote computer.[2]

The design of the buffering system and software must take into account several different constraints imposed by the system elements. (1) In the mode of operation for which buffering is needed (the scanning mode), data samples arrive in bursts as the antenna array is scanned. A scan period of 200 ms with 101 data samples per scan is typical. (2) The arrival times of the data at the HSDS are not spaced evenly over the

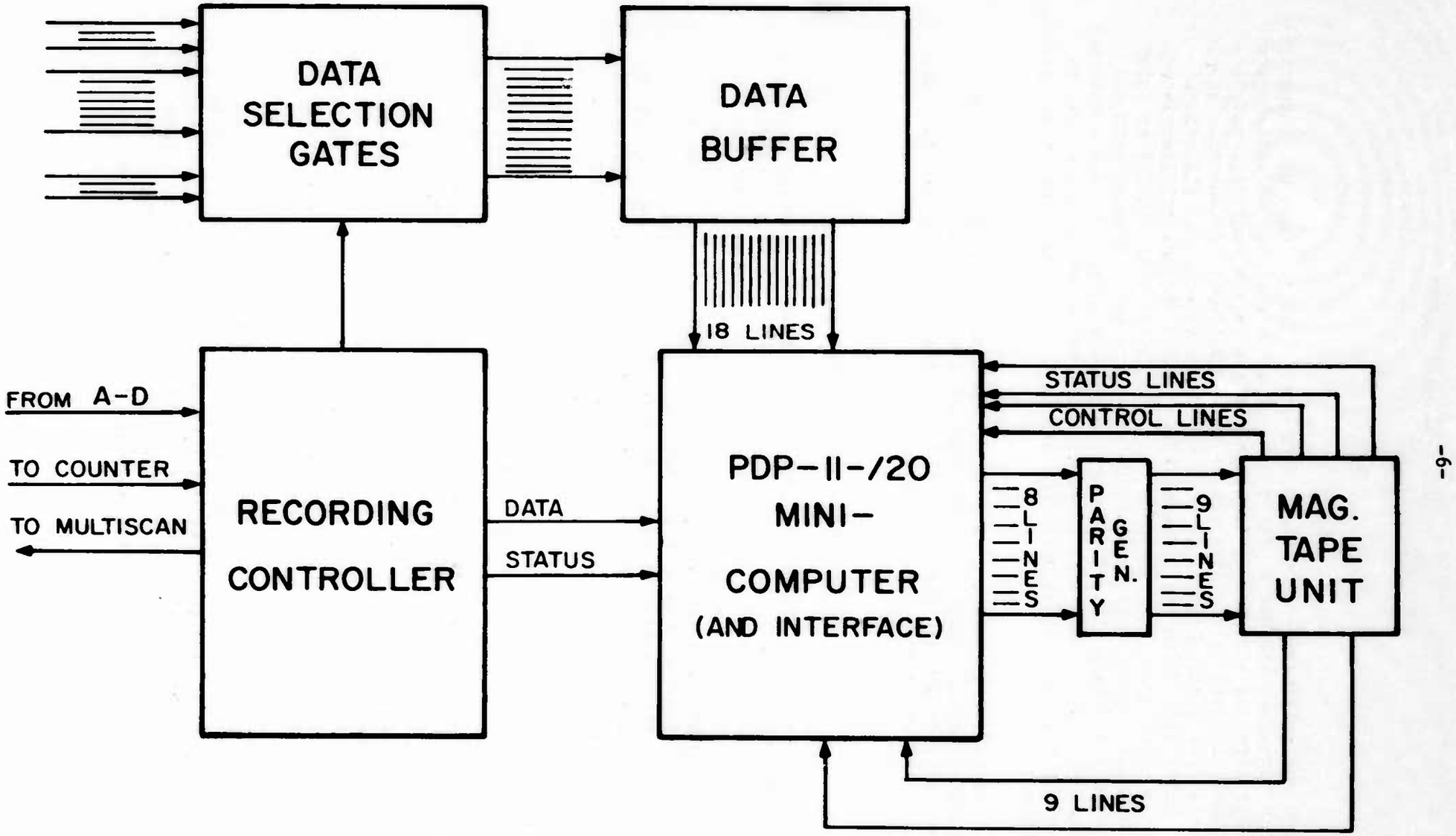

Figure 3. Minicomputer-System Interconnection Block Diagram

period of the scan. In fact, the minimum interval between data samples is 90 μs and may be decreased to as low as 45 μs by increasing the scan rate. (3) The magnetic tape unit specification for reaching proper speed is 10 ms. (4) The recording density of 800 bpi (per track) at 45 ips results in a recording frequency of 36,000 characters per sec. or one character every 27.8 μs. (That is, nine bits are read or written in parallel every 27.8 μs.) (5) The computer requires 39 μs to process an interrupt from the HSDS, read the four bit channel no. and the fourteen bit data value, and return to the interrupted sequence. (6) The computer requires 4.5 μs to transfer one sixteen-bit data word from core memory to the magnetic tape controller. (7) The amount of core memory available as a buffer region is not to exceed 2,048 words.

Taking into account the above constraints, the following questions may be resolved:

a. What character format should be used for recording an individual data sample?

b. What should be the sequence of data samples within a data record?

c. What sizes may be used for a data record and for pages within a data record?

In each case the goal is to maximize the data recording density on the magnetic tape.

The nine-track magnetic tape requires one parity bit, leaving eight bits per character for recorded data. Each data sample includes a fourteen bit data value and a four bit channel number code. To conserve tape, the channel number code is not written onto the tape as was done in the pre-computer system. Instead, the sequence of channels being read is typed into the computer before the start of the data run. Therefore, only fourteen bits must be recorded for each data sample. The following bit format is used:

TABLE 2

Track No.	Function	Char. 1	Char. 2
1	data	2^0	2^8
2	data	2^1	2^9
3	data	2^2	2^{10}
4	data	2^3	2^{11}
5	data	2^4	2^{12}
6	data	2^5	sign
7	data	2^6	*
8	data	2^7	*
9	parity	P_1	P_2

*--reserved for extended sign or for sixteen bit data words.

The parity bit is generated and checked by the tape controller.

As stated above, the sequence of channels being read is available to the computer before the beginning of a data run. (The operator must verify that the channel numbers typed in to the computer correspond to the settings on the control panel. The computer will detect a discrepancy, but it has no way of making the correction.) Using this information, the buffer routine generates a special heading record which contains a map of the data to follow on subsequent records. Data from the HSDS are stored as listed in Table 3. (Also, see Figure 4.)

TABLE 3

Word No.	Contents
0	Page designator*
1	Value for sample 1 of DC1
.	.
.	.
n	Value for sample n of DC1
n+1	Value for sample 1 of DC2
.	.
.	.
.	.
mn	Value for sample n of DCm
mn+1	Value at 1st channel
.	.
.	.
.	.
mn+k	Value at kth channel

n = no. of degrees per sector
m = no. of channels scanned n times
k = no. of channels to be sampled at end of scan
* - generated by the computer

The computer reformats the data as it arrives from the HSDS to facilitate faster computation. Such reformatting would be less efficient at computation time; but if computer time becomes too critical during the on-line recording, data will be stored in the format in which it arrives from the HSDS.

The upper limit on record size is 2,048 words or 4,096 magnetic tape characters. (That is, the entire contents of the buffer constitutes one data record.) However, a reduction in buffer size allows more room in the core memory for expanded programs. For that reason, the size of the

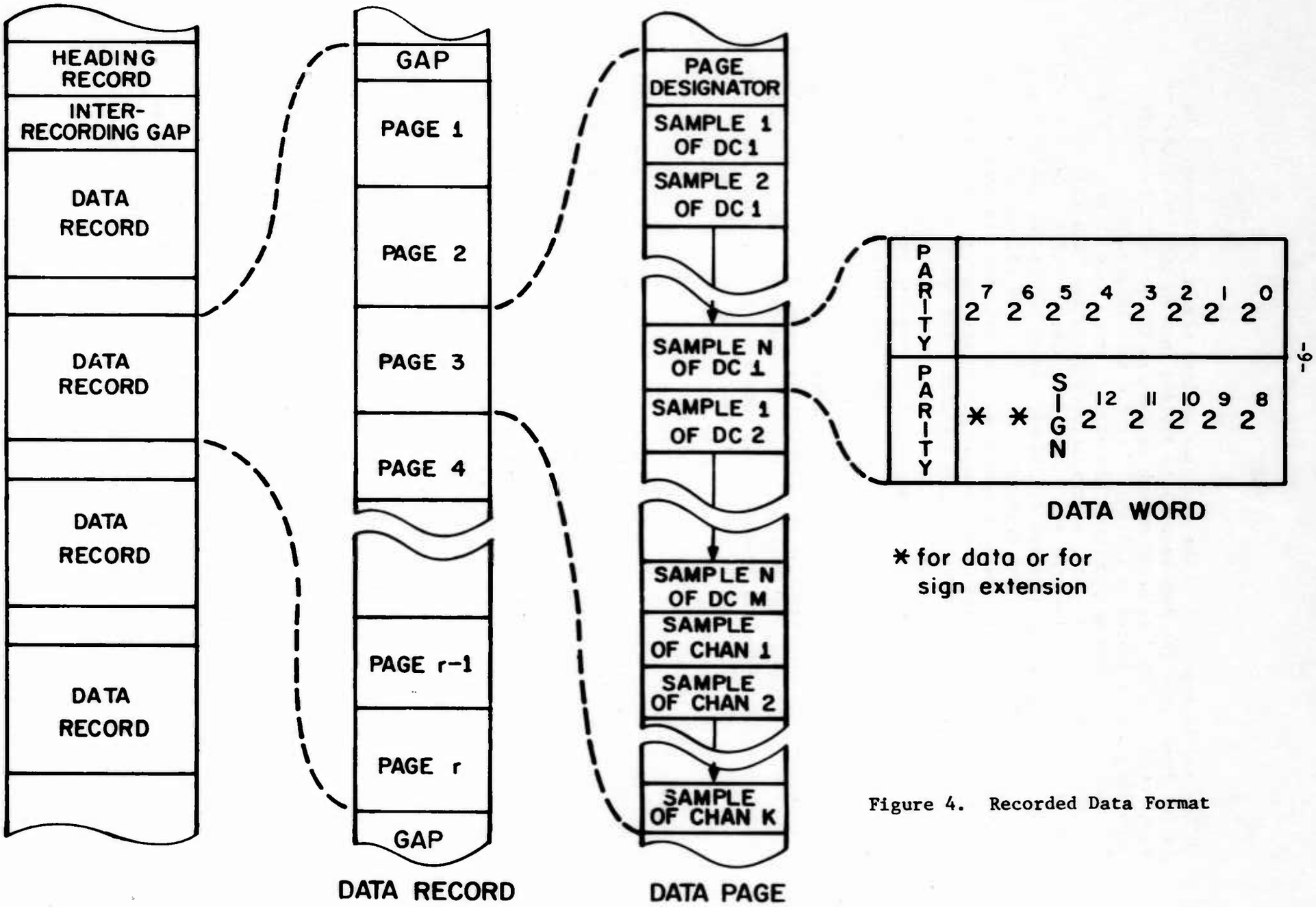

Figure 4. Recorded Data Format

buffer may be specified by the operator as less than 2,048 words. The buffer (and hence the data record) is divided into an integral number of equal pages. A page is large enough to contain the set of data values from one scan as listed in Table 3. Let P = page length, then $P \geq mn + k + 1$. The maximum possible values for m, n and k are 3, 90 and 16 respectively ($m + k \leq 16$), so the largest resulting page size of $P = 284$ is much smaller than the buffer size limit. The $P - (mn + k + 1)$ words remaining on the page are filled with zeros before the buffer contents are transferred to the magnetic tape. For this reason, an ill-chosen page size could result in nearly a fifty per cent decrease in storage density. The problem is avoided at the outset, during the initialization procedure to be followed by the operator. The operator supplies the buffering routine with values for B_1 = buffer size limit, k, and n. From these it computes $P = mn + k + 1$ and $r = B_1/P$ less the remainder, where r = number of pages in the buffer. Then the final buffer size, B, is $B = rP$.

To clarify the operation of the computer-controlled buffering system, a description of the handling of a typical sequence of data follows. The operator sets the control switches of the RDF and HSDS systems including those required to specify sector width, sector center, and channels to be scanned. Next, he loads the buffering routine into the computer. The routine is self-starting and immediately responds by typing a message on the teletype requesting in turn, values for B_1, n, channels to be scanned, and sector center. (See Appendix.) The operator responds by typing in the requested values. The routine calculates P and B and then generates a heading record (much shorter than B) which is immediately written onto the tape. Typically m = 3, n = 30, and k = 11 resulting in a page size of 102 words and a buffer size of 2,040 words. When this is completed, the routine signals the operator to start the data run.

When the first data sample arrives at the buffer gates of the HSDS, an interrupt pulse is sent to the computer. The computer then suspends execution of its current task and transfers control to the HSDS I/O routine. The routine first reads in the four bit channel code and compares it to the appropriate channel code in the predefined sequence. If the two do not agree, an error message is typed out and the operator is given a choice of further actions to be taken. Normally the two codes agree, so the routine continues by reading in and storing the fourteen bit data value. The I/O routine then returns control to the task which was interrupted. The total time occupied by the interrupt sequence is about 39 μs. Since data samples arrive at least 90 μs apart, the computer will not be interrupted again by the HSDS for at least 51 μs, during which time the computer is free to handle any other task requiring attention. The computer handles the subsequent data samples as it did the first, storing each one in the appropriate successive location in the buffer. The 101 data samples for the first scan arrive during the first 25 ms of the scan. The computer then inserts a page marker in the buffer and uses the remaining 175 ms for checking the system and performing on-line computation using the buffered data. As soon as the 101 data samples have been

received for the 20th scan, the buffer is full. The computer then signals the magnetic tape unit (MTU) to begin reading and storing bytes (a byte is eight bits or half of a full computer word) of data from the buffer. The MTU generates an additional parity bit which it stores in the ninth track on the tape. The MTU interrupts the computer on a cycle-stealing basis each 27.8 μs as it is ready for another byte of data. The interrupt is granted after a maximum delay of 3.5 μs and the actual transfer of data takes only 1.2 μs. As soon as the MTU has read the entire contents of the buffer, it stops the tape and waits until the buffer is full again. The time required to empty the buffer is less than 115 ms for the maximum size of 2,048 words. After adding the 10 ms to bring the tape up to speed and the 10 ms to stop the tape, the total of 135 ms is still well within the 175 ms between the last data sample for scan 20 and the beginning of scan 21. It should be observed that most of the 135 ms is still available to the computer for processing other routines because less than 4.9 ms of computer time is required for the actual transfer of data from buffer to MTU.

In the above example the storage density on the magnetic tape is very good. The inter-record gap caused by starting and stopping is .9 in. The 4,080 bytes of data are stored on 5.1 inches of tape. This results in a nominal figure of 85 per cent of maximum storage density. Taking into account the heading record and the page designators would reduce the percentage very slightly.

III. On-Line Data Monitoring

One of the chief drawbacks of the pre-computer system was the lack of any monitor for the data in digital format. The operator could observe the analog displays, but he had no way of being certain that the data were correctly digitized and stored on the magnetic tape. Verification was possible only by taking the tape to the remote G-20 computer and having the data analyzed. Ideally, the system should detect its own malfunctions and signal the operator. It should also allow examination of the digital data to verify that the data are indeed meaningful. The computer provides partial fulfillment of both aims.

The previous section outlined the time demands on the computer during the process of data buffering. By operating in an interrupt mode the computer processes the buffering routine during only a small fraction of the 200 ms scan period. The time is less than 4 ms for the example described at the end of Section II. Even during the 20th scan period when the buffer was emptied the total processor time required is less than 9 ms. During the remaining time, the computer can merely wait, or it can perform other tasks.

Methods for detection of system malfunctions by the computer are limited by the simple interface between the computer and the rest of the system. The computer connects to the HSDS but to none of the other system

elements. The interface that does exist is one directional. (That is, signals and data flow from the HSDS to the computer, but not in the other direction.) System faults must therefore be detected by examining the data from the HSDS.

Section II described briefly one of the techniques to be used during the operation of the HSDS interrupt handling routine. The computer is given the sequence of channels to be sampled during a scan in the set-up procedure followed by the operator. As each data sample arrives from the HSDS, its associated channel code is compared with the expected channel number in the core memory. If the values are unequal the computer transfers control to an error routine. The error routine will follow one of several courses depending on the instructions it received from the operator during the set-up procedure. It may:

a. Accept the data as though the error had not occurred.

b. Reject the sampled data value and flag the buffer location to indicate the channel error.

c. Reject the data for the entire scan and flag the page designator to so indicate.

d. Reject the entire record of data and reinitialize the buffer pointers to begin storing incoming data in a new record.

In each of the above cases the computer would continue recording data, but it would signal the operator by typing out an appropriate error message on the teletype. Another option would allow the operator to try to determine the cause of the channel error. The computer would:

e. Stop collecting data and wait for the operator to respond to the error message. The operator would then initiate a transfer to an error analysis routine, which would allow inspection of the channel sequence and incoming data in response to typed commands.

The error analysis routine would also be a very useful hardware debugging tool whenever changes are made in system circuits (assuming that the change could affect the data and channel code seen by the computer).

Verification of incoming data poses a more difficult problem than checking the channel number. However, it is potentially a powerful system check as well as a helpful tool when the system is operating properly. Several types of malfunctions can be envisioned which would leave the channel sequencing unaffected but would cause erroneous data to be recorded. If the computer had an internal standard for data as it does in the case of channel numbers, error detection would be a simple comparing process. At the present stage of system evolution, comparison must be left to the operator. The role of the computer is to display the incoming data in such a way that the operator can quickly make comparisons and judgements of his own with regard to the validity of the data.

The system provides an instantaneous analog display of the scanned sum and difference amplitudes on a ten-inch diameter CRT. The sector center

and sector bounds are also displayed so that the operator can determine the basic pattern of the incoming signal at a glance. Thus, comparison is possible for input patterns which remain relatively constant over a period of several seconds. For example, the computer would average the samples of the sum amplitude at 3 degree intervals taken during 10 scans and print the average values on the teletype. The delay is 2 seconds to record the data from the 10 scans plus about 7 seconds to type the values. The slow speed of the teletype is the chief limiting factor. A modest improvement could be achieved by adding an X-Y plotter or a CRT as a peripheral device, but the operator's response time would rapidly become a limiting factor. Until the time when the computer assumes a role in controlling the system operation, dynamic checks on rapidly varying signals are not feasible. However, if correspondence between the analog and digital forms can be demonstrated for slowly varying signals, the system may be assumed to be operating correctly.

IV. Direction of Arrival Computation

A simple form of on-line computation was introduced in Section III as a means of checking system performance. Averages of signal levels were computed at discrete intervals across the sector being scanned. They provided the operator with a very rough estimate of the azimuthal angle of arrival of the incoming signal. It is desirable for the computer to determine accurately, in real time, the angle of arrival. That is, the on-line computer should ideally be able to make the same calculations made by the remote computer. These include average center of gravity angle of arrival, deviation of a group, angle of arrival calculated from phase values, and angle of arrival calculations for non-scanning modes of system operation.[3,4]

The on-line computer has severe time and storage limits imposed on it during the buffering operation. It is estimated that the data buffering routine will occupy about half of core storage. (This includes the 2,048 words used for the buffer.) That leaves about 4,000 words of memory to be shared by resident system software (loaders, I/O handlers, and floating point routines), the system self-checking routines, and the bearing computation routines. The computation routines will therefore be limited to about 2,000 words of memory for both program and auxiliary data storage. The magnetic tape unit is, of course, unavailable for retrieval of data during the buffering operation. Any data examination by the computation routine must be done before the buffer is emptied onto the tape. The percentage of central processor time required by buffering and system checking is on the order of ten per cent. By averaging over many scans, several seconds can be made available for bearing calculation. Although timing checks have not yet been made on the present routines used in the remote G-20, it appears likely that the minicomputer will not find time to be a serious limitation. The storage is another matter. One of the present Fortran programs used for determining the center of gravity bearing includes approximately 500 Fortran statements.[3] The same program in PAL-11 (the PDP-11 assembly language) would probably require at least 1500

instructions. Since most PAL-11 instructions require more than one word of storage, such a program would occupy well over 2,000 words of memory. This does not take into account the extra data storage necessary during the execution of the program. Such a program can probably be simplified to fit into a smaller space, and the available storage may be increased by cutting down the buffer size. But it is obvious that some of the calculation must be done off-line when the entire storage capabilities of the machine are available. If part of the magnetic tape is reserved as an auxiliary memory, the minicomputer could duplicate any of the calculations now performed by the G-20. Although the time might be greater for the minicomputer, it will still be much faster than going through the batch processing system used with the G-20. The lack of peripheral display devices for the minicomputer will still require the use of the G-20 for obtaining plots and large printouts of data.

V. Conclusion

The addition of a minicomputer to the RDF system accomplishes four distinct improvements. (1) Data buffering improves the storage density of data on magnetic tape from 20 per cent to about 85 per cent of the maximum possible density. (2) Most system malfunctions are detected immediately by examination of incoming data. (3) Azimuthal direction of arrival can be calculated during the process of data buffering. (4) More involved calculations can be performed at the field station by using the computer in an off-line mode and providing the magnetic tape unit as an auxiliary memory.

APPENDIX

Initializing Dialog

In order to initialize the data gathering program at the beginning of a data run, the operator is required to enter several parameters and specify certain options. This is accomplished by a computer-operator dialog on the teletype.

The operator begins by loading the program into the computer or if the program is already loaded, he starts the computer at the beginning address of the program. The program signals that it is correctly loaded by typing:

*N	The program aeks for the value of N, number of degrees of sector width.
45	The operator types a value followed by a carriage return (hereafter designated by CR). If the operator types CR only, the default value is N = 30.
*DC	The program asks for the channels to be sampled n times each scan. (1, 2, 3 are selected as the default case.)
1,2CR	The operator types the channel numbers in ascending order.
*C	The program asks for the sequence of channels to be sampled at the end of the scan.
4,5,7,9,14CR	The operator types the channel numbers in ascending order.
*BL	The program asks for a limit on buffer size. (Default value is 2,048 words.)
CR	The operator accepts the default value.
* P = 142 B = 1988 R = 14	The program computes values for the page size, buffer length, and number of pages in the buffer.
*CE	The program asks the operator to specify the channel error option to be followed if a channel number error is detected. Possible responses are: I - ignore, W - flag data word and continue, P - flag page and continue, R - delete record and continue, D - discontinue processing and wait for operator response.
ICR	The operator specifies to ignore errors. (The error message will be typed out at the time an error occurs regardless of whether the data is flagged or not.)
*SC	The program asks for the sector center.
270CR	The operator types the angular position of sector center.

*START RUN — The program signals that it is ready for the operator to start the system.

The program examines each of the operator's responses and rejects any which it is unable to interpret. It signals the rejection by typing a '?' and then repeats the request. For example:

*N	Request for sector width.
150CR	The operator types a value larger than the system can realize (maximum is 90).
?	A question mark signals the rejection.
*N	The program repeats the request.

The program will not detect some typographical errors during the initialization dialog; eg., if the operator types 136 when he meant 126 as the sector center, the computer will accept the value because it lies between 0 and 360. However, the operator may be able to take advantage of the rejection feature of the program if he notices his mistake in time. By typing an illegal character before terminating his reply with a CR,he can cause the program to reject the reply and repeat the request. Using the above case:

*SC	The program asks for the sector center.
136ZCR	The operator sees that he typed 3 instead of 2 and adds the letter Z which is not a legal response.
?	The program rejects the entry.
*SC	The program repeats the request.
126CR	The operator types the correct value.

If the operator detects his mistake after he has typed the CR, he has no choice but to restart the program. (This can be done at any time by depressing the control key and typing a P.)

REFERENCES

(1) McClurg, W. C., "HSDS-A High Speed Data Acquisition System," RRL Publication No. 339, University of Illinois, Urbana, Illinois, 1968, ONR N00014-67-A-0305-0002.

(2) Barry, L. W. and Ernst, E. W., "A Buffer Memory for a Digital Data Acquisition System," RRL Publication No. 365, University of Illinois, Urbana, Illinois, 1970, ONR N00014-67-A-0305-0002.

(3) Ledbetter, R. J. and Ernst, E. W., "The Acquisition of Data for Digital Bearing Computation," RRL Publication No. 321, University of Illinois, Urbana, Illinois, 1967, ONR N00014-66-C0010A02

(4) Ernst, E. W. and Cox, E. W., "Procedures for Analyzing Direction of Arrival Data," RRL Publication No. 346, University of Illinois, Urbana, Illinois, 1968, ONR N00014-67-A-0305-0002.

AN INTERFEROMETER RDF SYSTEM WITH AN ON-LINE COMPUTER

Keith D. Stenzel and Edward W. Ernst
Department of Electrical Engineering
University of Illinois
Urbana, Illinois 61801

I. Introduction

The computer is becoming more and more important as an integral part of many instrumentation systems. This paper will describe the use of a computer as an on-line control and processing element for an interferometer radio direction finding system.

At the University of Illinois Radiolocation Research Laboratory, there is presently operating an RDF system using an interferometer antenna array. From the interferometer system it is possible to derive the information necessary to determine the direction of arrival of incoming radio signals.(1) The present RDF system shown in Figure 1A consists of the antenna arrays and associated switching equipment, two-and three-channel receivers, phase and amplitude meters, an A-D converter, and a data acquisition system. The data acquisition system controls the collection of data by the RDF system and outputs the data to the high speed paper tape punch. The paper tape containing the phase and amplitude data, time, frequency and other data is then taken to a large off-line computer for analysis to determine angles of arrival and other characteristics of the received signals. The system also contains analog equipment which can be used to display RDF information in real time to the operator; however, this equipment requires considerable skill and experience to operate and there is only a limited amount of time for the operator to interpret the display of the received signals. For this reason the major portion of the analysis of data is now done by processing the data on paper tape by a computer.(2)

II. Advantages of On-Line Computer System

Since the computer is already being used to analyze the RDF data, it is natural to think of fully integrating a computer into the RDF system and using the computer to analyze data on-line and also to control the operation of the system. Figure 1B shows the RDF system with the computer added. The computer will interface to the RDF system through the present data acquisition system and will output data to the paper tape punch and the teletype. Another way of looking at the computer system is shown in Figure 2. In this configuration the computer is seen as the central element with all the other devices as peripherals to the computer. The present RDF system is thus treated as a peripheral device to the computer in much the same sense that the teletype is a peripheral. Some possible additions to the system are also shown in Figure 2.

The on-line computer in the RDF system offers many advantages in the operation of the system and in the collection of data. One of the major

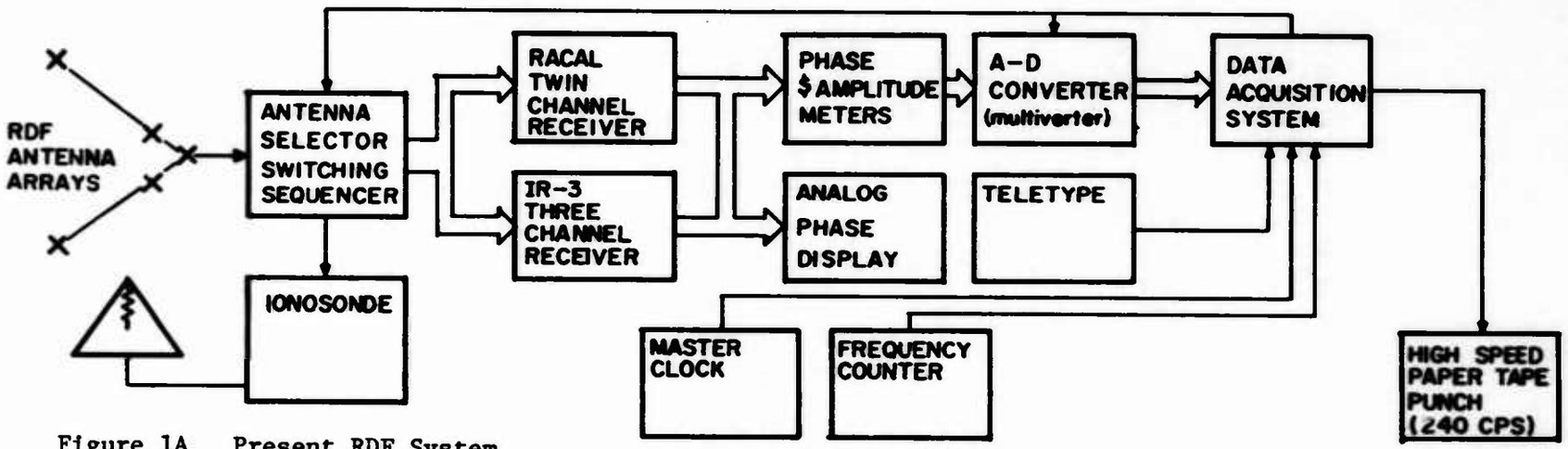

Figure 1A. Present RDF System

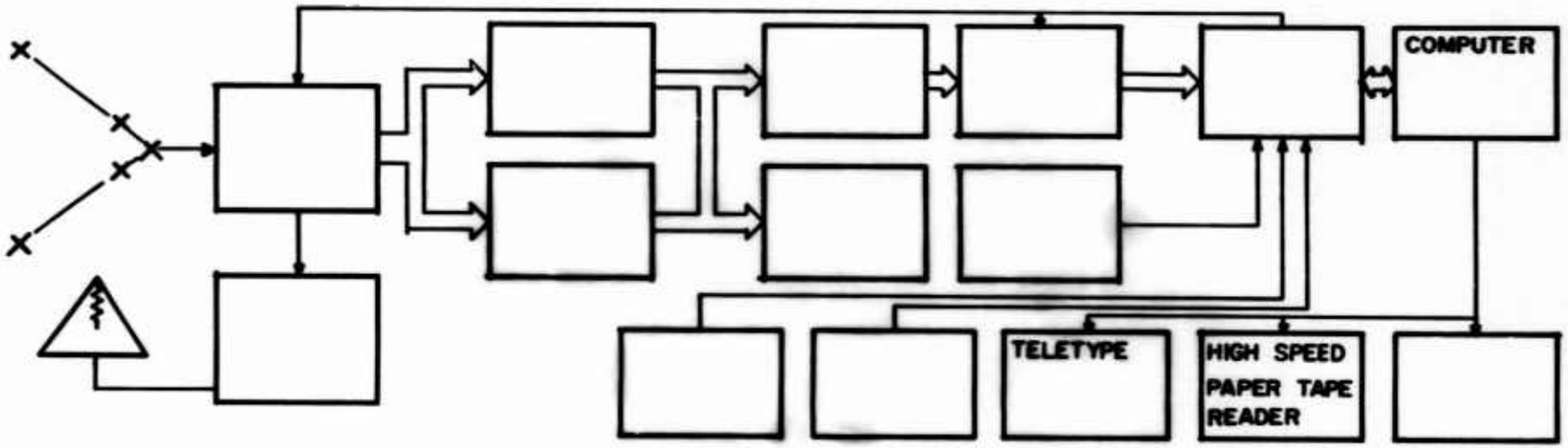

Figure 1B. RDF System with Computer

Figure 1A and 1B. RDF System

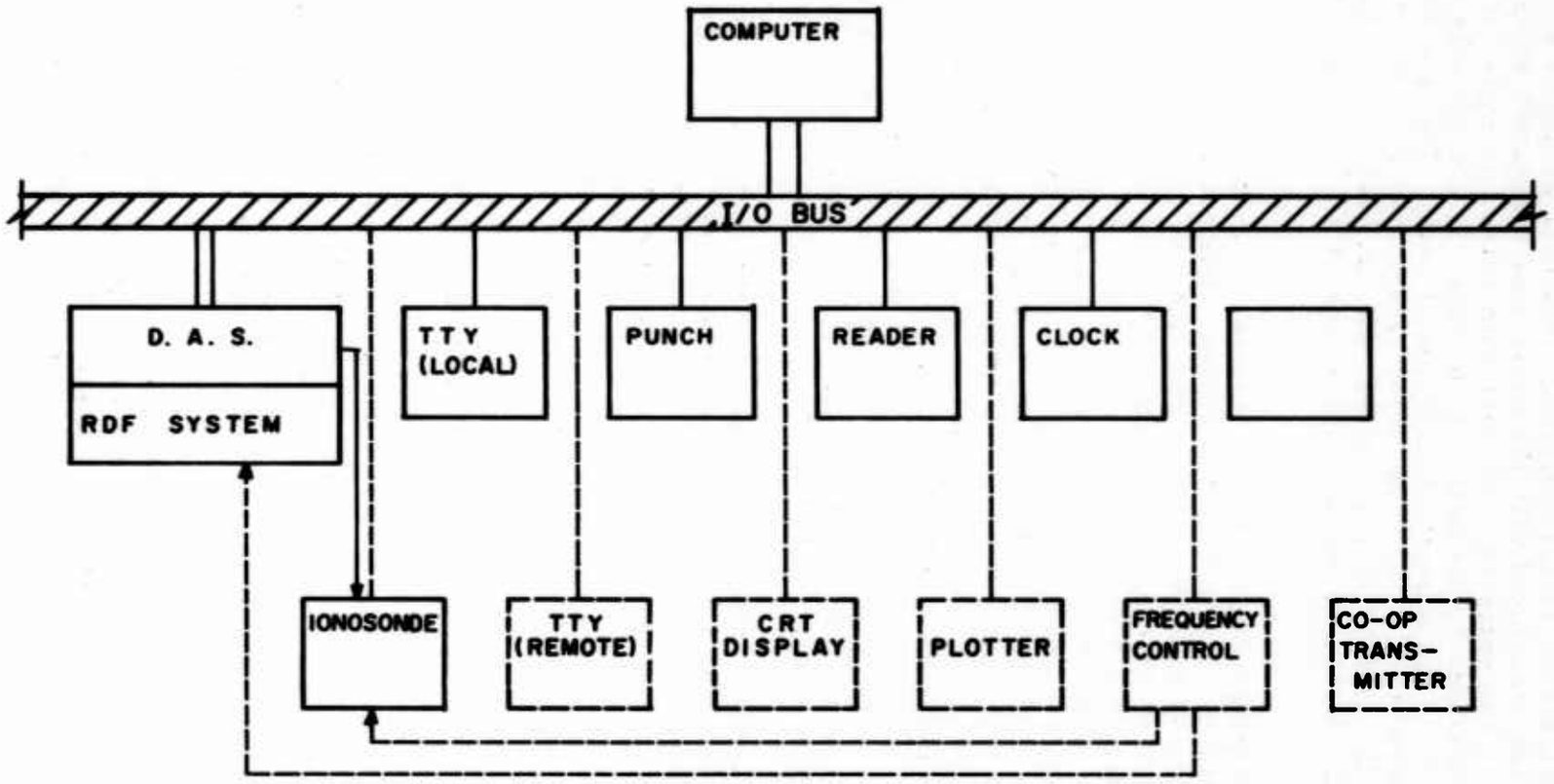

Figure 2. RDF System with Computer

SOLID LINE — INITIAL SYSTEM
BROKEN LINE — POSSIBLE ADDITION

advantages is the ability to compute angles of arrival in a real time mode and display these angles to the operator. This will eliminate the delays and other problems associated with the paper tape system and provide immediate feedback to the operator. The real time output of angles of arrival will allow the operator to evaluate the incoming signals and make any changes necessary to optimize the collection of data. The real time output will be limited by the teletype output rate in the initial system but the operator will still be able to control more actively the collection of data and will be able to evaluate system operation in a real time operating mode.

Another advantage of the on-line computer is that it will provide great flexibility for the user of the system. Changes in the operation of the system can be made by modifying the computer software instead of modifying the system hardware. By using the flexibility of computer programming, the system can be dedicated to a particular purpose by loading the appropriate programs into the computer. For example, if a particular phenomena such as periodicities in signals are being investigated, the system could be programmed to detect such periodicities and only process data associated with this phenomena. In this way more usable data can be collected and the processing of non-usable data will be reduced. Much of the statistical processing such as averaging, calculation of standard deviations, and correlations that is now done off-line could be done on-line. Another way the computer could be used to advantage would be to detect and isolate equipment malfunctions by using system maintainence programs. System calibration could also be checked by computer programs.

Since the computer will be the central element in the system, future additions will be relatively easy to make since they will be added on as peripheral devices. One of the future objectives of the RDF system is to integrate the vertical incidence ionosonde into the system to make measurements of the ionosphere. With this capability added to the RDF system and with the computer to process data in a real time mode, the goal of an automatic radio location system can be achieved.

III. System and Computer Requirements

The development of a system of this kind requires many factors to be evaluated and certain trade offs in the cost-performance area to be made to get the best system possible. In evaluating the requirements the RDF system imposed on the computer, it was found the most critical requirements were the speed with which the computer could perform the necessary arithmetic calculations and the speed and capability of the interrupt system of the computer.

One of the design objectives for the system is the ability to take data samples at a 25 sample per second rate with each sample consisting of a maximum of 16 data words. This means that in a time period of 40 milliseconds a data sample must be collected by the RDF system, input to

the computer, and the angles of arrival calculated. Since the calculations for the azimuthal and incidence angles of arrival require mathematical functions such as sine, arctangent and square root, it was determined that the most critical requirement for the computer was the ability to perform the calculations for the angles of arrival in the 40 millisecond-time period. To achieve the accuracy desired for the calculations and to allow for calculations on averages of data, the performance of the calculations in double precision arithmetic was taken to be the worst case condition. Since the mathematical functions required are usually developed from series expansion algorithms, it was determined that the computer capability for multiply and divide operations was an important requirement. By using approximations to the expansion of the mathematical functions required, the necessary speed of double-precision multiply-and-divide operations required was estimated to be 150 microseconds for each. This then became an approximate specification which the computers evaluated should meet. In evaluating these requirements it was found that computers with a memory cycle time of approximately 1 microsecond would be able to meet the necessary requirements for calculation speed. It was found that a hardware multiply and divide capability was also necessary since this typically had a 10-50 to 1 speed improvement over the software method of performing these operations.

The other basic requirement that was found to be necessary was a fast priority interrupt system. The speed requirement for the interrupt system is suggested by the requirements of the data system for the Bondville Road Field Station of the Radiolocation Research Laboratory. A computer system is to be used at that location also and it was desirable to use the same computer, if possible, for both applications. The Bondville Road system uses magnetic tape for data recording and has a high speed (~90μ sec/word) data system that requires very fast interrupt and input/output capabilities. The interrupt system in the RDF system is important because the computer must be operating several devices and performing the angle of arrival calculations at the same time. The interrupt system allows the computer to be running a program, be interrupted by a device such as the teletype, service the device and then return to the interrupted program and continue. The method and speed in which this interrupt process is done determine the basic input/output capability of the computer and its utility for use in a real time operating system. There are several different interrupt procedures. One conventional interrupt procedure is to poll each peripheral device after an interrupt is received to determine which device caused the interrupt. When the interrupting device is found, the program branches to a service routine for the device. This usually is a time-consuming procedure and when very fast devices are used, the risk of losing data while polling devices is present. Hardware vector interrupt is another method. In this method each device is assigned a vector address and the interrupt causes a program branch directly to an interrupt subroutine memory address determined by the vector address. This procedure is usually faster than the polling technique and also removes some of the programming requirements associated with handling the polling of devices. Since the system will have several peripherals with different priorities, a multilevel system of

interrupts and the capability for nesting of interrupts is a requirement. If an interrupt routine for a low speed device is in progress, the computer must be able to accept an interrupt from a high speed device, process this as a high priority interrupt, and then return to the low speed device interrupt routine.

Another requirement is that the interrupt structure must have a priority determining process. A priority interrupt system requires that all devices capable of interrupt be assigned a relative priority. In case of simultaneous interrupt requests, the device assigned a higher priority is then serviced first. With this system, a device requiring a fast response time, such as the Bondville Road high speed data system, would have a priority over a low response time device such as a teletype. The magnetic tape unit requires a direct memory access capability in order to utilize the recording rate of approximately 30 microseconds per word. The chief requirements for the interrupt are the speed to take care of the high speed devices of the Bondville Road system and priority and multi-level interrupt capability to process interrupts for both systems.

The other major requirement for the computer is the capability for expansion. The block diagram in Figure 2 shows the initial system configuration and some of the possible future additions. To provide for these additions, the computer must be capable of expansion to take care of both standard peripherals, such as a storage CRT, and special devices. The memory size of the computer should also be expandable to take care of increased program size as the system grows more complex.

Other requirements for the computer were more or less fixed by existing system equipment or were of a more intangible nature. The output of the analog-to-digital converter in the system contains 15 bits, so to utilize all 15 bits, a computer with a word size of 16 bits (a standard word size for many computers) was a requirement. To use the Basic or Fortran computer languages, it is generally necessary to have at least 8K words of memory. A real time clock for timing purposes in system operation was also a requirement. Peripheral equipment required was a teletype, high speed paper tape reader, and an interface to the existing high speed paper tape punch in the system. General purpose interfaces for interfacing special devices (such as the RDF system) to the computer were also a requirement. A power fail-restart capability was also needed for the system.

Some of the other factors evaluated that were more intangible or a matter of personal preference were related to the software available, the instruction set of the computer and the convenience of programming the computer. The basic software required is an assembler for the computer's machine language, a compiler for a higher level language such as Fortran, a package of mathematical programs such as floating point, sine, cosine, etc., and various utility programs such as debugging programs, text editor, and I/O programs.

The instruction set and programming of a computer is difficult to evaluate. Generally, a powerful and flexible instruction set is a requirement but the evaluation is really a subjective judgement in relation to previous experience in using other computers. Some computers are organized such that each instruction is executed very rapidly but several instructions are needed to accomplish the same operation another computer may be able to do in one instruction that is executed much slower. Various other factors such as relative core efficiency, I/O and interrupt handling, byte operations and subroutine calling and reentrancy are all difficult to evaluate. After evaluating several computers, the conclusion is inevitably reached that no computer (in the price-performance class evaluated) has every desirable feature and that some compromises or trade offs must be made. Thus, it was decided that any computer that could meet the basic requirements of calculation speed, interrupt and I/O handling, expansion capability and the fixed requirements such as 16 bit word and availability of basic software would be an acceptable computer for the system application.[1]

The configuration of the initial system, as shown in Figure 2, is presently in the process of being assembled. The operation of the various components will be described to show how each will function in the operation of the entire system.

The basic purpose of the system will be to collect the differential phases between signals at the antenna array elements, the amplitude of the signal at each element, the signal frequency and the time. The present RDF system will do this and store the collected data in memory registers in the data acquisition system. Modifications to the RDF system, primarily to the data acquisition system, are necessary in order for the computer to interface to the RDF system. The modifications to the data acquisition system will make its control and timing functions for collection of data and its data storage registers available to the computer. The capability of generating interrupts will also be added.

A general purpose interface unit designed to interface special devices to the computer is available with the computer and will be used for the interface between the data acquisition system and the computer. The general purpose interface provides a compatible interface to the I/O bus of the computer with the correct timing and logic levels for the bus signals. It includes a 16 bit storage register for output from the computer to the device, address decoding and selection circuits that give each interface

---

[1] The computer selected for the system is the Digital Equipment Corporation PDP 11/20. Much of the discussion in following sections refers specifically to certain features of the PDP 11/20. See Appendix A for a description of some of the features of the PDP 11/20.

a unique address location, and interrupt control circuits to provide priority interrupt capability. The interface also contains the bus drivers and receivers necessary to maintain the transmission line characteristics of the bus. The data acquisition system sees a simple interface of 16 input lines, 16 output lines, 2 interrupt request lines, and 2 control lines from the general purpose interface. Two of these general purpose interface units are necessary to provide the interface to the data acquisition system (DAS).

The DAS presently provides control of the RDF system through thumbwheel switches and pushbuttons. The switches provide for the selection of sixteen possible formats for data collection. Some of the formats used are two-channel or three-channel receiver operation with one antenna array, two- or three-channel operation with both of the antenna arrays, and a calibration format. Each format provides a fixed data collection sequence using the system and a sequence of data words for output to the high speed punch. Other switches are set for the number of data blocks to be taken for each format and the number of repetitions of a series of formats. Pushbuttons control the start, stop, and reset operations and the selection of continuous or single-cycle mode of operation of the system. The internal logic of the DAS provides control and timing signals for antenna switching, A-D conversion and gating of data for the internal scratch pad memory.(3)

Signals from the computer parallel the DAS control signals to provide the computer with control over the system. The DAS system control signals will be inhibited when the computer has control of the system. The storage registers in the two general purpose interfaces will serve as control registers with the bits in each register assigned a specific control function. For example, four bits in one register will select formats for data as the thumbwheel switches do for the DAS. Another eight bits are used to address the scratch pad memory of the DAS. Other bits are assigned to start data collection, stop data collection, select antennas, and to reset the system. To select a certain control function the program will instruct the computer to set a 1 in the correct bit of the control register and this bit will remain set until changed by the program. For example, to take a data block in a certain format, it is necessary for the computer to load the proper arrangement of format bits into the control register. The loading of the control register will initiate the collection of one data block in the format selected. To take more data blocks the computer must load the register with a format for each block. This mode of operation would essentially duplicate the present data collection process but with the difference that the computer will be receiving the data instead of punching the data on paper tape. In order to allow the necessary flexibility in the operation of the system, as many of the control functions as possible are provided to the computer. The use of the RDF system by manual control through the data acquisition system, as in the existing system, has also been retained as a possible mode of operation if the computer cannot be used.

The computer will operate in the system as a control and data processing element and will control the data acquisition system by means of command words output to the data system. When the data system has completed the collection of data it will issue an interrupt to the computer. The computer will then read the data out of the data system into the computer memory. With the phase, amplitude, frequency and time together with the geometrical constants of the antenna array, the computer can determine the angles of arrival. Processed data will then be output to the teletype and high speed punch.

The teletype and high speed punch will provide the output of data to the operator and permanent data recording. Since the teletype has a limited output rate (10 cps), samples of data or averages of data will be the real time output to the operator. The paper tape punch is also limited in output rate (240 cps) in relation to the speed at which the system will be able to operate, so only processed data will be punched on paper tape for data recording. If the recording of all raw data becomes desirable, a high speed output device could be added to the system. The teletype will also be used by the operator to specify to the computer the modes of operation of the system. The high speed paper tape reader will be used to load system operating programs into the computer. The high speed reader and high speed punch will also be very useful in the assembly of programs on the computer since they are much faster than the reader-punch combination of the teletype. The real time clock will provide timing pulses to the computer for use in generating timing data.

The operation of the system will be under the control of the computer, but the operator must tell the computer what is to be done. The operator will issue commands to the computer through the teletype to initialize the operation of the system and to start the data collection process. The operator will specify the data formats, number of data samples, the kind of processing, and the type of output. If special programs for processing of data are required, the operator will load the necessary programs using the tape reader. Once the proper commands have been issued to the computer, the operator will start the system by a command on the teletype and the computer will proceed to automatically collect, process and output data.

IV. Priority Interrupt System

The operation of all the peripheral devices in the system will be on a priority interrupt basis with the input and output of data to the computer handled by the interrupt system. The interrupt and I/O are an important part of the application of the computer to the RDF system. The block diagram in Figure 3 shows the different devices in the interrupt structure and the relative priority level of each. Each device is connected to the bidirectional I/O bus and is assigned a priority according to which device has to be serviced first by the computer. The priority levels are actually determined by jumper wires on the interface for each device and can be

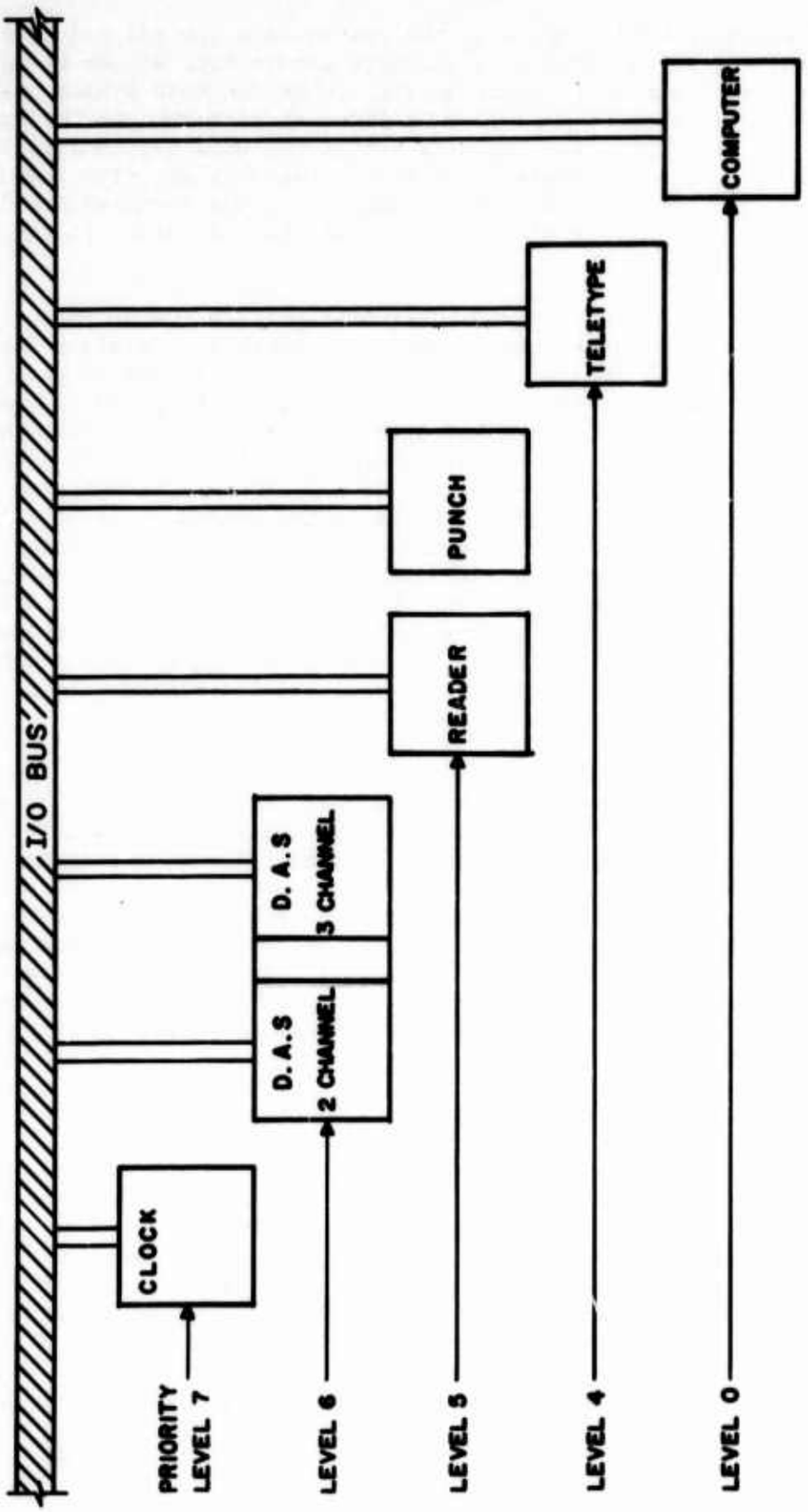

Figure 3. Priority Structure

changed if desired. When more than one device shares a priority such as the paper tape punch and reader, the highest priority is given to the device closest to the computer on a priority level.

The real time clock is assigned the highest priority because of the need to maintain time accurately. Much of the experimental data collected uses a clock to accurately start the data collection process at a particular time and to take data for a particular time interval. The real time clock will interrupt the computer with clock pulses and the computer will accumulate time for use in operating the system and also to be output as data.

The data acquisition system is assigned the next priority level. There are two interrupts possible from the data acquisition system because the RDF system will operate in two interrupt modes. The two modes are used because of the different operations that must be done when using two-or three-channel receivers in the system. The two-channel receiver can sample only two antenna signals at one time, so the receiver must be switched in sequence to each of the three antenna pairs of the three element antenna array. Because only two signals are sampled, only one differential phase and one amplitude are available to the computer. The antenna switching and resultant settling time of the instruments limits the speed of the data samples to approximately one phase and amplitude reading every 8-9 milliseconds. When the data for a sample have been converted and stored by the data acquisition system, an interrupt is generated and the computer reads in the data. This process is continued until the phases and amplitudes at each antenna pair have been received by the computer. The computer can then start the data collection process for another complete sequence of data samples, and process the data for the previous samples. This mode of operation will be limited in data sample rate by the equipment in the RDF system. The second mode of operation of the system is using the three-channel receiver and three phase and amplitude detectors to simultaneously make the phase and amplitude measurements at the three-antenna pairs. Since this operation does not involve switching antennas, the speed is basically limited by the response time of the phase meters and the conversion time of the A-D converter. With the three-channel receiver operating, the data acquisition system collects all the phase and amplitude data and then generates an interrupt to the computer. The computer then takes the data from the data system memory as fast as the I/O capability of the computer allows the data to be read. The signals generated by the I/O operation of the computer are used to clock the data into a register for access by the computer. The computer program keeps count of the data words that are input from the data system and at the end of the data block, the computer resets the system and starts a new data collection process. When the data are stored in memory using either mode, the computer will return to the program that was interrupted and continue processing the previous data to determine angles of arrival. The mode of operation using the three-channel system is much faster than the two-channel system; consequently, the three-channel interrupt on priority level 5 is of higher priority than the two-channel interrupt.

The high speed punch and reader are assigned to the next priority level. The main consideration in assigning the punch a high priority level is to maintain the maximum output word rate when punching tape. To keep the punch operating at its maximum rate (240 cps), a word must be supplied every 4 ms. The interrupt signal for the punch will indicate to the computer that the punching of a character is complete and that a new character may be transferred to the punch and punching initiated.

The paper tape reader will not be used when the system is operating but will be used to load program tapes into the computer. The interrupt is used to keep the reader operating at the maximum rate by requesting an interrupt when a new character has been read and is ready for the computer.

The teletype is assigned the lowest priority of the peripheral devices because it is the slowest device and can be serviced last in the priority list. The teletype printer will be used to output data to the operator. In order to keep the printer operating at its maximum rate (10 cps), a new character must be supplied by the computer every 100 ms. The interrupt will be used to indicate to the computer that the printer is ready to receive a new character. The keyboard of the teletype will also generate an interrupt when a key is struck on the keyboard. The keyboard must be read within 18 ms to ensure no loss of information, so the keyboard is assigned a higher priority than the printer on priority level 4.

The computer CPU in Figure 3 is shown with priority level 0, the lowest priority possible. This is normally the way the computer will operate since the main program the computer will be running will be considered the background program which can be interrupted by any of the peripheral devices. The computer used in the system has the capability to change the priority at which it is running any program and also all interrupts can be disabled by the computer if desired. For example, if an interrupt is received from the punch on level 5, the interrupt service routine for the punch can set the priority at which the service routine is being executed at level 6 and exclude all interrupts from level 6 or below until the service routine is completed and the computer returns to the interrupted program. The interrupt of each device can be enabled or disabled by the program by setting or clearing a bit in the control buffer for each device.

The typical operation of an interrupt starts with the computer enabling the interrupt in a device. When a device has data ready or can accept data, it issues an interrupt request on its priority level. The computer sees the interrupt request and sends a request grant signal in serial fashion to each device on the priority level. The device that requested an interrupt blocks the grant signal from other devices and puts its unique vector address on the data lines of the I/O bus. The computer reads the address and uses the address to locate the start of the device interrupt routine and also to locate a new priority status word. The computer has a facility for automatically maintaining a hardware stack in

memory that contains the location to which the program should return after completion of the interrupt and also the machine state at the time of the interrupt. In this way at the end of each interrupt service routine, the instruction to return from interrupt will automatically restore the machine state and will start executing the program at the proper location. The computer can maintain this memory stack to any level of interrupt, limited only by exceeding the memory size allotted to the stack. The device service routines can also use this stack to temporarily save the contents of the computer registers if they are used in the service routine and then restore the registers before returning to the interrupted program. The automatic interrupt and hardware stack is one of the outstanding features of the computer and eliminates the program software usually used to accomplish the same task.(4)

In summary, the operation of the computer peripherals will be on an interrupt basis. The computer will be running a background program using data collected from the RDF system to calculate angles of arrival and will be interrupted whenever a peripheral requests an interrupt. The peripherals will be interrupting either with data for the computer (RDF system, clock) or to signal the computer that it is ready to accept data (punch, teletype). The computer will automatically branch to the interrupt routine for the interrupting device, perform the requested service, and then return to the main program to continue the calculation of angles of arrival.

V. Angle of Arrival Calculation

After the data collection process for one data block has been completed, the computer will have stored in its memory the necessary differential phase data, frequency, and time that is necessary to calculate alpha (α) and theta (θ), the azimuthal and incidence angles of arrival of the signal. The differential phases are measured at each pair of antennas shown in Figure 4. The physical arrangement of the antennas in the nested arrays and the geometry for angle of arrival determination are shown in Figure 4.(5) The differential phases measured are the phase of the signal at antenna 2 with respect to 1 (B1), 3 with respect to 2 (B2), and 1 with respect to 3 (B3).

$$B1 = D\left(\frac{2\pi}{\lambda}\right) \cos \alpha \sin \theta$$

$$B2 = D\left(\frac{2\pi}{\lambda}\right) \cos(\alpha - 120°) \sin \theta$$

$$B3 = D\left(\frac{2\pi}{\lambda}\right) \cos(\alpha - 240°) \sin \theta$$

where the symbols shown are:

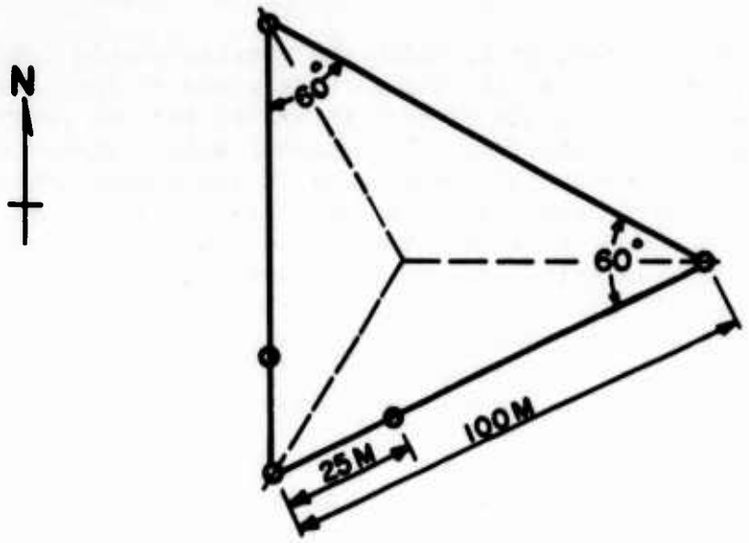

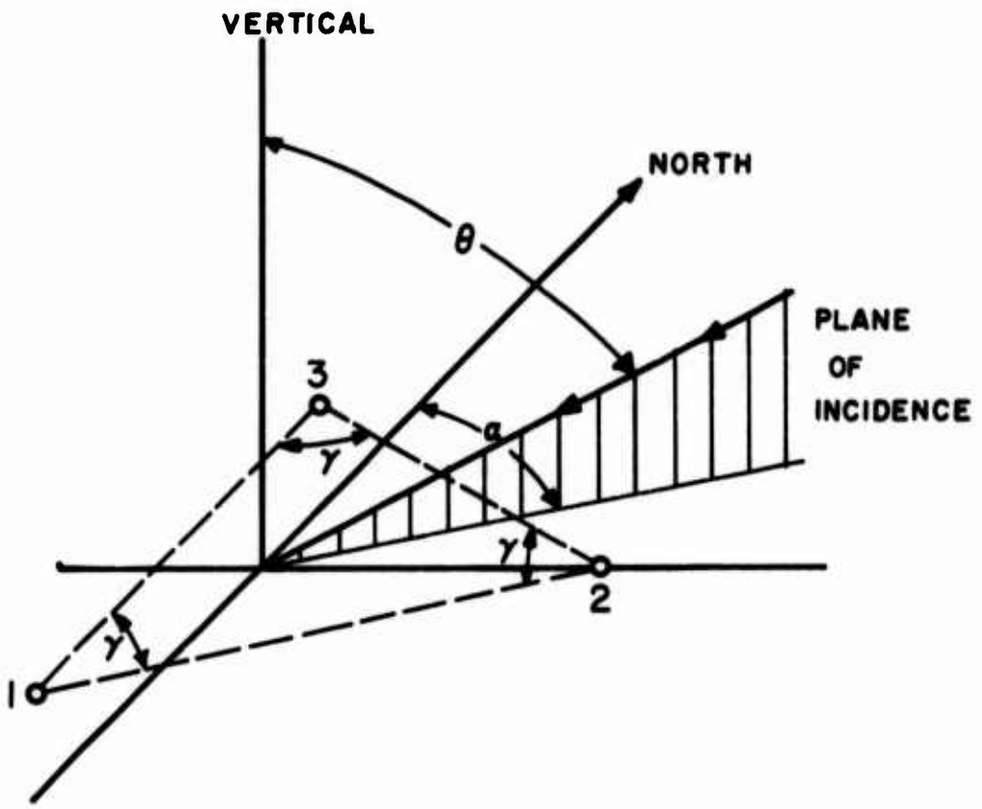

Figure 4. Angle of Arrival Geometry

α = azimuthal angle of arrival measured clockwise from north.

θ = incidence angle of arrival measured from vertical.

γ = angle between antennas (=60° for the U. of I. system).

D = antenna separation distance.

λ = wavelength of signal.

The equations are solved for the azimuth and incidence angles.

$$\theta = \arcsin \frac{\sqrt{B1^2 + B2^2 + B3^2}}{D\left(\frac{2\pi}{\lambda}\right)\sqrt{\frac{3}{2}}}$$

$$\alpha_{12} = \arctan \frac{2B2 + B1}{\sqrt{3}\ B1}$$

$$\alpha_{13} = \arctan \frac{-2B3 - B1}{\sqrt{3}\ \ B1}$$

$$\alpha_{23} = \arctan \frac{B2 - B3}{-\sqrt{3}\ (B2 + B3)}$$

Although only two of the three phase measurements are actually necessary to determine the angles (θ can be found from only 2 phases also), the redundant measurement is used in the calculations shown. The three values of alpha determined from the above equations are used to form a vector average angle in an effort to cancel random error in the measurements.

$$\text{Ave. X} = \cos(\alpha_{12}) + \cos(\alpha_{13}) + \cos(\alpha_{23})$$

$$\text{Ave. Y} = \sin(\alpha_{12}) + \sin(\alpha_{13}) + \sin(\alpha_{23})$$

$$\alpha = \arctan \frac{\text{Ave. X}}{\text{Ave. Y}}$$

These calculations for alpha and theta are to be performed by the computer in a real time mode. The objective is to perform these calculations for each data sample in the time period of 40 milliseconds. In order to achieve the necessary speed, the arctangent, arcsine, cosine, sine, and square root will have to be optimized for this application. Most programs for these functions that are available use floating-point arithmetic and provide answers with more precision than is necessary for these calculations. In general, the programs are also too slow to accomplish the calculations in the 40 millisecond time period. New subroutines for these functions will be written, where necessary, for accomplishing the calculations. The general flow diagram for the system is shown in Figure 5. This gives a rough idea of how the data proceeds through the program but much detail has been omitted.

VI. Summary

The computer can be of great use in instrumentation if properly used. This application of a computer to our existing system is an attempt to provide much better utilization of the system and of the data collected. Much of the advantage of an on-line computer is its flexibility through programming. Ideally, every function of the system should be available to the computer. There is a limit, however, to what can be accomplished without completely rebuilding the system so a compromise is made. The operation of the system,as described,is our attempt at an acceptable compromise that can accomplish the minimum requirements of our problem and perhaps have room for considerable expansion in capability.

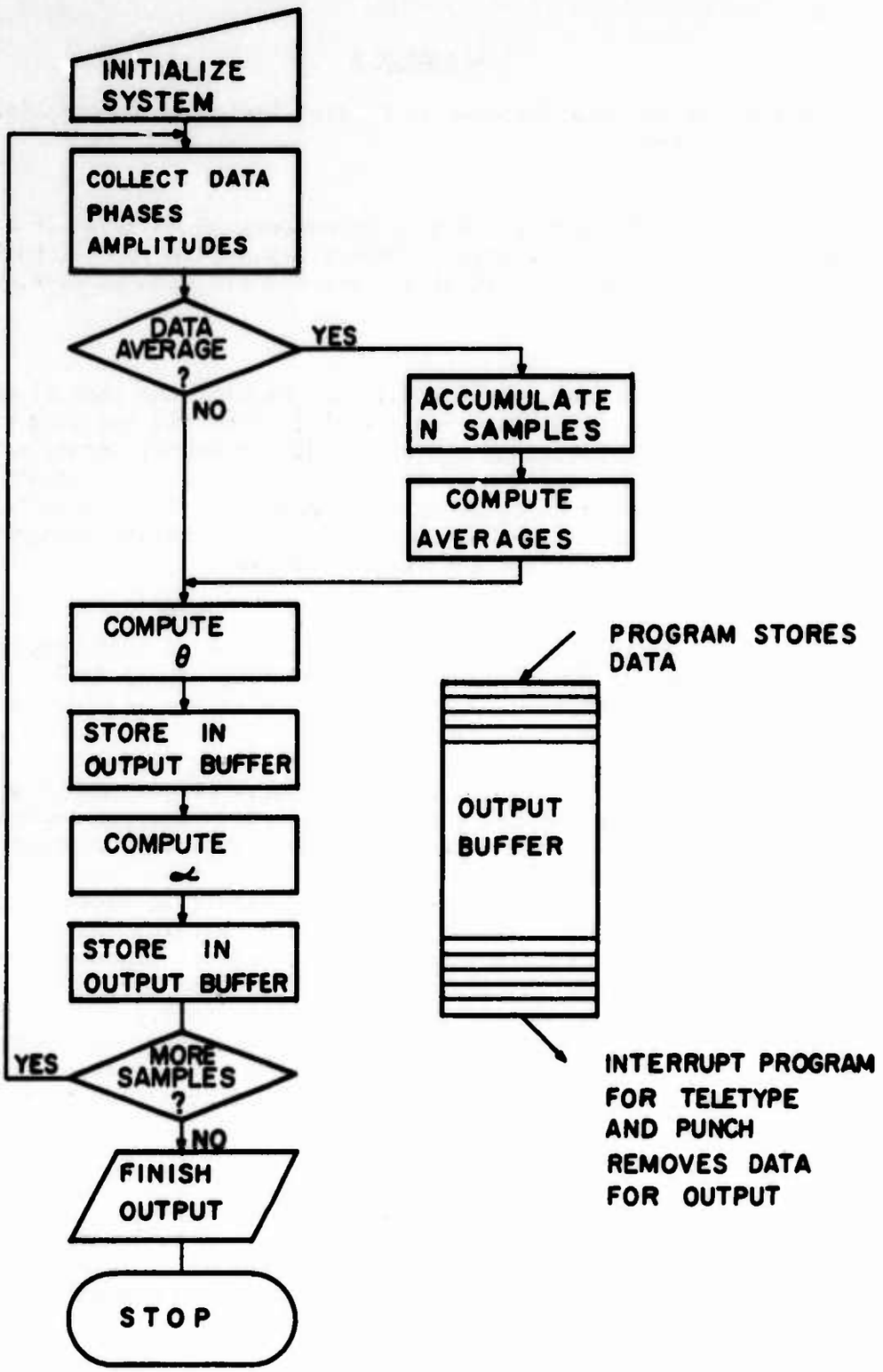

Figure 5. Operation Flow Chart

Appendix A

Description of some features of Digital Equipment Corporation PDP 11/20 Computer.

Systems

Basic system consists of central processor, 4K words of 16 bit read-write memory, and ASR 33 Teletype. Memory expandable to 32K, both read-write and read-only memory available. Peripherals such as disc, magnetic tape are available.

Unibus

Single bus structure in which all peripherals, the central processor and memory share the same bus. Peripheral devices are assigned memory locations and all instructions operate on device memory locations exactly as for regular memory locations. Devices can control the bus and transfer data directly to memory or to another peripheral device. Interlocked communication between devices on the bus makes communication independent of physical bus length and response time of devices.

Memory

Basic read-write core memory has a cycle time of 0.950 microseconds and an access time of 500 nanoseconds. Read-only memory in 256 word and 1024 word sizes available.

Central Processor

Eight general registers are program accessible and can be used as accumulators, index registers, etc. Six registers are general-purpose while the seventh is a stack pointer and the eighth is the program counter. A four-level automatic priority system uses a hardware vector address for each device to allow the interrupt servicing hardware to automatically select and begin executing the device service routine. A hardware stack is automatically maintained for interrupt processing which contains the return address for the interrupted routine and the processor status. Device service routine priority is independent of interrupt priority and can be changed by program. Data transfers can be made directly between any peripheral devices without participation by the central processor (NPR transfers). Transfer rate from memory is at memory speed of 0.950 microseconds per word.

Instruction Set

Both single and double operand instructions are used. Double operand instructions allow memory-to-memory operations. A full complement of byte instructions is provided. Addressing modes include full 16 bit, byte, deferred and indexed modes, autoincrement, and autodecrement addressing modes.

LIST OF REFERENCES

(1) Bailey, A. D., and W. C. McClurg, "A Sum-and-Difference Interferometer System for HF Radio Direction Finding," IEEE Transactions on Aerospace and Navigational Electronics, Volume ANE-10, March 1963.

(2) Young, Charles J., "Digital Methods for Resolving Angles of Arrival under HF Multipath Conditions," Thesis submitted in partial fulfillment of the requirements for the degree of Master of Science in Electrical Engineering, University of Illinois, Urbana, Illinois 1968.

(3) Mueller, Thomas O., "A Digital Data Collection System for a Three Channel RDF Interferometer." Thesis submitted in partial fulfillment of the requirements for the degree of Master of Science in Electrical Engineering, University of Illinois, Urbana, Illinois 1969.

(4) PDP 11 Handbook, Digital Equipment Corporation, Maynard, Massachusetts, 1969.

(5) Bailey, A. D., J. D. Dyson, and E. W. Ernst, Technical Report ECOM - 013333(E), "Studies and Investigations Leading to the Design of a Radio Direction Finder System for the MF-HF-VHF Range," Radiolocation Research Laboratory, University of Illinois, Third Quarterly Report, April 1966.

A COMPARISON OF METHODS FOR DETERMINING ANGLE OF ARRIVAL WITH A CDAA

R. E. Hunninghaus and E. W. Ernst
Radiolocation Research Laboratory
University of Illinois
Urbana, Illinois 61801

I. Introduction

This study is a comparison of the direction of arrival calculations for the sum, difference and differential phase modes of a Circularly Disposed Antenna Array (CDAA) - Direction Finding System. The three methods of direction of arrival calculation employ a digital computer to perform the necessary computation.

The sum and differential phase mode calculators used in this study are similar to those calculators which have been previously developed and described elsewhere.[1,2] The difference mode calculator has been specifically developed for use in this comparison study.

The CDAA system data used in this study has been generated with the simulation program GCAAS.[3] Ideal single signal, two signal wave interference and single signal with noise conditions have been simulated.

II. The Sum Mode Calculator

The directional patterns are obtained, for the CDAA system under consideration, by first combining the individual outputs from the two groups of scanning elements to form two separate outputs. These two outputs (the right bank voltage and the left bank voltage) are then combined to form the directional patterns for the CDAA system. The different ways in which the two outputs can be combined lead to the three different modes considered here. The sum mode pattern is the magnitude of the phasor sum of the two

separate outputs, for each sample point taken during one complete scan of the system.

The general configuration of the sum pattern (Figure 1) is such that there is one primary lobe, with lesser secondary lobes on either side. The sample points which comprise the primary lobe are those sample points for which the boresight setting is in the general vicinity of the direction of arrival of the incoming signal.

The sum direction of arrival is calculated as the centroid of sum data values for the sample points in the primary lobe. The primary lobe, for this calculation, is defined as the lobe containing the sample point with the maximum sum data value in the sum pattern (sample point P_m). The limits of the primary lobe are defined as the sample points (P_ℓ on the left and P_r on the right) for which the next sample point (away from P_m) will have a data value less than 10% of the maximum data value in the scan or for which the data value is less than the data values of the next two sample points (away from P_m). If the primary lobe is not centered in the sampling window, a situation may arise for which it is necessary to define P_ℓ or P_r as the side sample point in the window, i.e., if either of the two previously mentioned tests fail to find the limits of the lobe before running out of sample points. The sum direction (D_s) is then taken as the centroid of the sum data values ($Y_{s,i}$) for the sample points (i) whose boresight settings (X_i) lie within the primary lobe of the sum pattern.

$$D_s = \frac{\sum_{i=P_\ell}^{P_r} X_i Y_{s,i}}{\sum_{i=P_\ell}^{P_r} Y_{s,i}}$$

SUM PATTERN

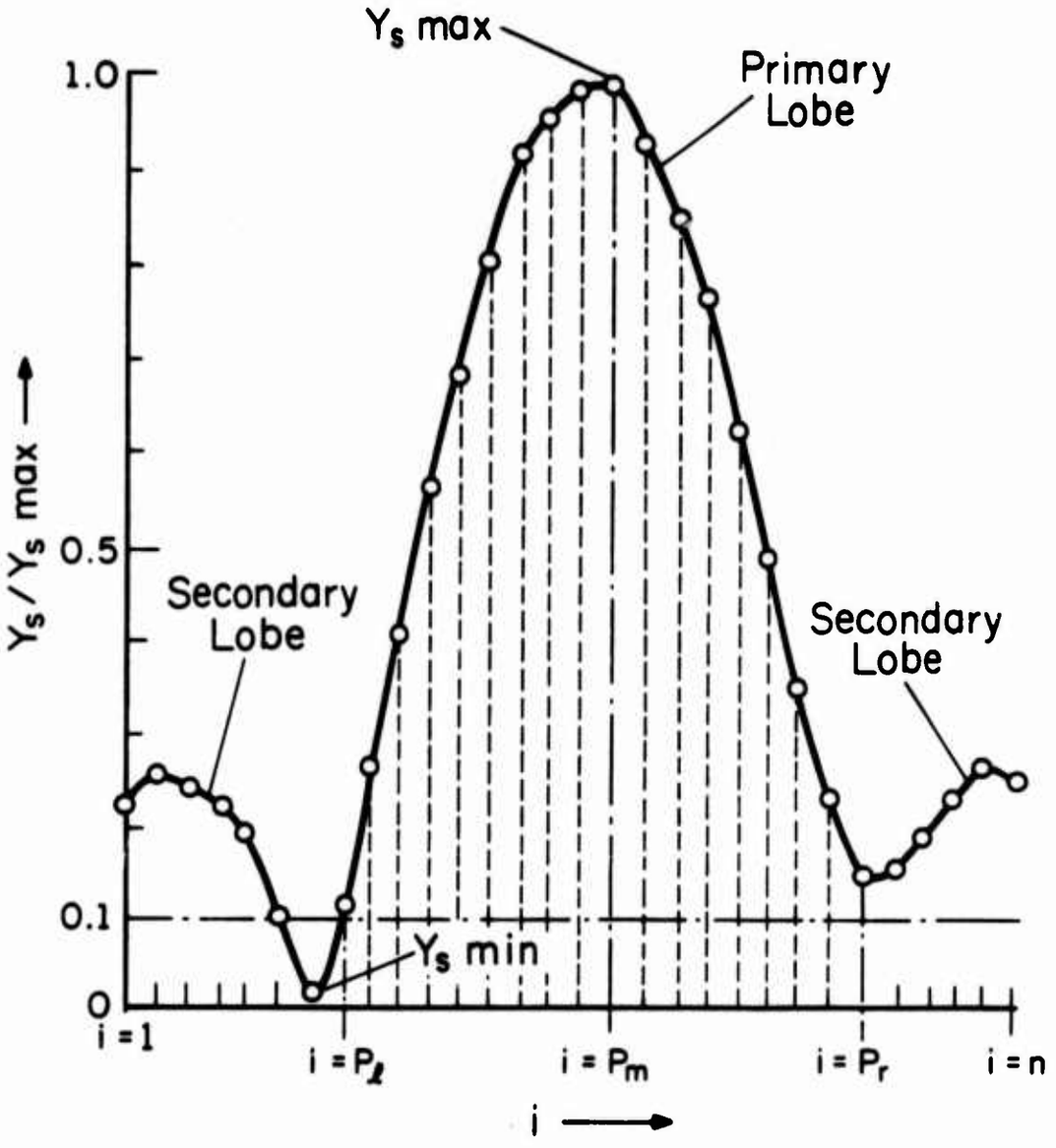

Figure 1. Sum Pattern.

Two arbitrary criteria have been established to determine whether or not the sum direction should be accepted as a valid direction of arrival. The first criterion, which must be met, is that the difference between the maximum and minimum sum data values ($Y_s max - Y_s min$) must be greater than or equal to the average sum data value for the n sample points in the sum pattern, i.e.,

$$\frac{Y_s max - Y_s min}{(\sum_{i=1}^{n} Y_{s,i})/n} \geq 1.0$$

The second criterion is that the number of sample points which comprise the primary lobe is greater than or equal to seven, i.e.,

$$(P_r - P_\ell + 1) - 7 \geq 0$$

(NOTE: The left refers to the counter-clockwise direction and the right refers to the clockwise direction. Since the scanner rotates in the clockwise direction, the first sample point, identified as i = 1, is on the left side of the sector and the last sample point taken in the scan, identified as i = n, is on the right side of the sector.) If both of these criteria cannot be met, the sum direction of arrival is rejected and it is considered that a direction of arrival for the incoming signal condition cannot be determined from the sum data in the scan.

A slight change was made in the routine for computing the direction of arrival from the sum pattern. The change affects the limit (P_ℓ or P_r) of the primary lobe when that limit is close to the edge of the sector. Specifically, the necessity of the change arises when the sample point next to an end sample point is being considered (i.e., i = 2 or n - 1).

When sample point i = 2 or i = n - 1 is under consideration as a limit of the primary lobe, the "next two points greater" test would use points i = 0 or i = n + 1 respectively, but these points are not valid sample points in the scan. The previous sum calculators did not detect this and supplied extraneous information as sum data values to carry out the test. This could lead to including one or two extra sample points in the primary lobe. This is rectified by changing the routine so that when sample points i = 2 and i = (n-1) are being considered as lobe limits, the sum value less than the next two sample points test is modified to test only the next sample point (i = 1 or i = n).

It should be noted that the other routines would include extra points in the primary lobe only when the direction of arrival of the incoming signal is not in the vicinity of the sector center. Since this is not usually the case the problem arises only infrequently.

III. The Differential Phase Mode Calculator

The differential phase mode pattern is the phase difference between the two separate outputs (right and left bank voltages), for the sample points taken during one complete scan of the system.

The general configuration of the differential phase vs. boresight azimuth pattern (Figure 2) is, in the ideal situation, a continuous smooth curve with a negative slope and a value of zero when the boresight azimuth corresponds to the direction of arrival. The physical limitations of the equipment cause the values of the phase data to be confined to within $\pm$ 180.00 degrees. Thus the differential phase pattern is a discontinuous curve (the discontinuties being at $\pm$ 180 degrees) with a negative slope at every point along the curve, other than the points of discontinuity.

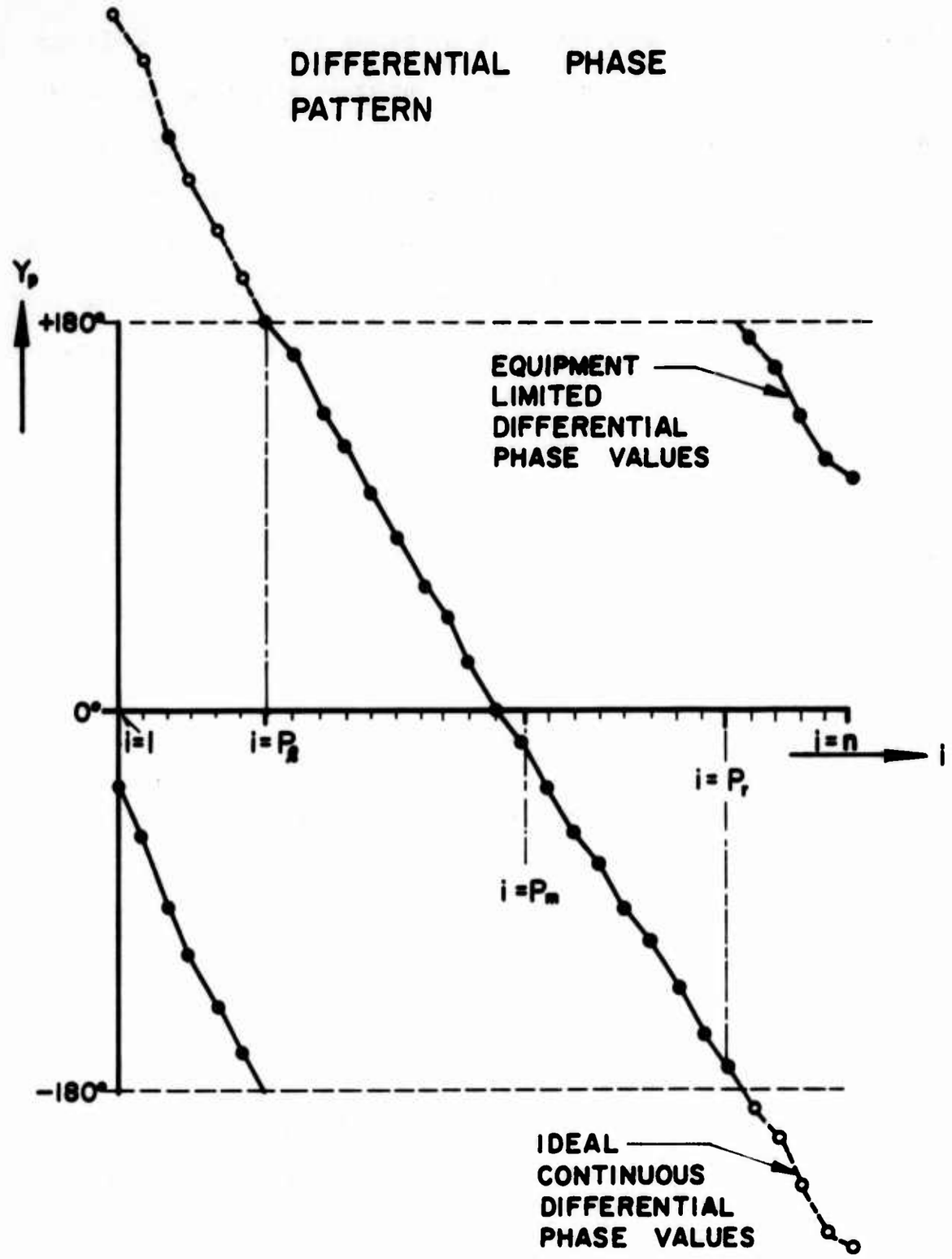

Figure 2. Differential Phase Pattern.

The differential phase direction of arrival is calculated as the intersection of a straight line which is fitted to the continuous portion of the pattern which corresponds to the primary lobe of the sum pattern and the zero degree differential phase axis. The desired portion of the differential phase pattern is located by first locating the sample point with the greatest sum data value (sample point P_m). The limits of the desired portion of the differential phase pattern are defined as the sample point (P_ℓ), to the left of P_m, whose differential phase value is greater than that of the next two sample points away from P_m and the sample point (P_r), to the right of P_m, whose differential phase value is less than that of the next two sample points away from P_m. If the direction of arrival is not in the vicinity of the sector center, a situation may arise for which it is necessary to define P_ℓ or P_r as the side sample points in the window if the limits of the portion of the curve are not found before running out of sample points. A straight line is then fitted to the differential phase data ($Y_{p,i}$) whose boresight settings (X_i) lie within the desired portion of the differential phase pattern by the method of least squares. The slope of the line is determined as

$$M = \frac{(P_r-P_\ell+1)\sum_{i=P_\ell}^{P_r} X_i Y_{p,i} - \sum_{i=P_\ell}^{P_r} X_i \sum_{i=P_\ell}^{P_r} Y_{p,i}}{(P_r-P_\ell+1)\sum_{i=P_\ell}^{P_r} X_i^2 - \left(\sum_{i=P_\ell}^{P_r} X_i\right)^2}$$

and the Y_p axis intercept is determined as

$$b = \frac{\sum_{i=P_\ell}^{P_r} X_i^2 \sum_{i=P_\ell}^{P_r} Y_{p,i} - \sum_{i=P_\ell}^{P_r} X_i Y_{p,i} \sum_{i=P_\ell}^{P_r} X_i}{(P_r-P_\ell+1)\sum_{i=P_\ell}^{P_r} X_i^2 - \left(\sum_{i=P_\ell}^{P_r} X_i\right)^2}$$

The differential phase direction (D_p) is then taken as the point where the Y_p differential phase value is zero.

$$D_p = -b/M$$

Three arbitrary criteria have been established to determine whether or not the differential phase direction should be accepted as a valid direction of arrival. The first criterion, which must be met, is that the difference between the maximum and minimum sum data values ($Y_s max - Y_s min$) must be greater than or equal to the average sum data value for the n sample points in the scan, i.e.,

$$\frac{Y_s max - Y_s min}{(\sum_{i=1}^{n} Y_{s,i})/n} \geq 1.0$$

The second criterion is that the number of sample points which comprise the desired portion of the curve is greater than or equal to seven, i.e.,

$$(P_r - P_\ell + 1) - 7 \geq 0$$

The third criterion is that the slope of the fitted line must be less than or equal to one and a half times the value of slope for an ideal single signal arriving with a 30 degree elevation angle and greater than or equal to one half the value of the slope for an ideal single signal arriving with a 0 degree elevation angle, i.e.,

$$.5M_{30°} \leq M \leq 1.5M_{0°}$$

If these three criteria cannot be met, the differential phase direction of arrival is rejected and it is considered that a direction of arrival for the incoming signal conditions cannot be determined from the differential phase data in the scan.

A change was also made in the differential phase mode routine which is similar to that of the change made in the sum mode routine. When the

sample point $i = 2$ or $i = n - 1$ is being considered as the limit of the desired portion of the curve, the differential phase value is only compared to the next point rather than the next two points.

A second change was also made in the differential phase mode routine to improve its operation when noise is added to the incoming signal and the continuous curve (i.e., not affected by the limitations of the equipment) can no longer be considered as smooth. For this case, consider the possibility of a sample point ($i = a$) to the left of P_m for which the following conditions hold,

$$Y_{p(a)} > 0°$$

$$Y_{p(a-1)} < 0°$$

$$Y_{p(a-2)} > 0°$$

$$Y_{p(a-1)} + 360° > Y_{p(a)}$$

and

$$Y_{p(a-2)} > Y_{p(a)}$$

(see Figure 3). For this case it is desired that $P_\ell = a$ since the sample point $i = a - 1$ is not considered as being part of the desired portion of the differential phase curve, but the previous routines would detect that $Y_{p(a-2)} > Y_{p(a)}$ and $Y_{p(a-2)} > Y_{p(a-1)}$, thus $i = a$ would not be detected as the limit and $Y_{p(a-1)}$ will be included in the least squares fit. This can be rectified by modifying the routine such that the left limit (P_ℓ) is defined as the next sample point closer to P_m than a sample point having a negative value which is to the left of three consecutive sample points with values greater than or equal to zero and the right limit (P_r) is defined as the next sample point closer to P_m than a sample point having a positive value which is to the right of three consecutive sample points with values less than or equal to zero. This test is made in addition to the previously used test for the limits P_ℓ and P_r.

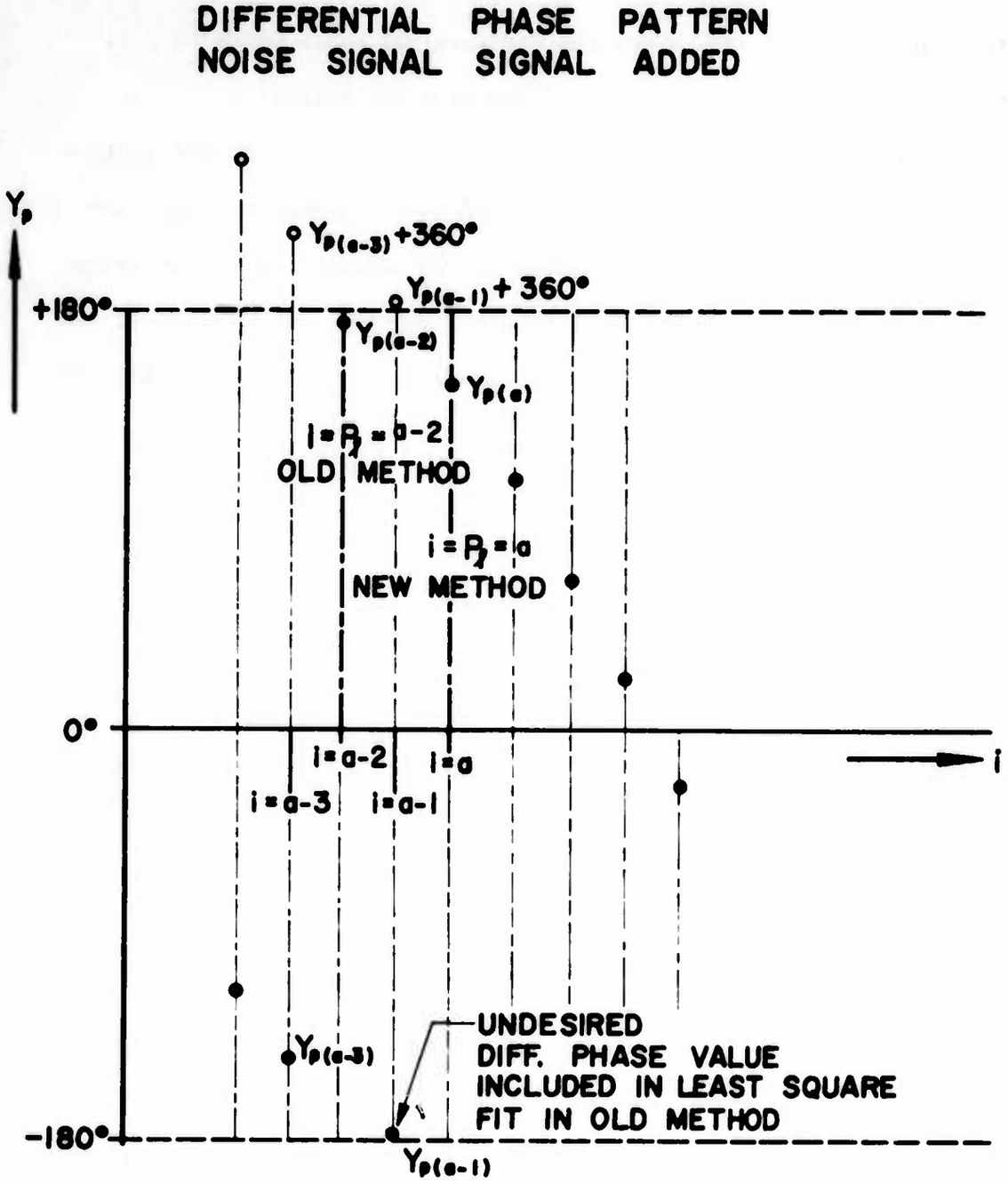

Figure 3. Differential Phase Pattern, Noise Signal Added.

It should be noted that this additional test was added to handle conditions where the noise level is approximately the same as that of the incoming signal, since this is not the case in the previously recorded data for the University of Illinois system, it should cause little effect on the results of previous calculations.

IV. The Difference Mode Calculator

The difference mode pattern is the magnitude of the phasor difference of the two separate outputs (right and left bank voltages), for the sample points taken during one complete scan of the system.

The difference mode direction of arrival calculation is based on the principle that when the boresight azimuth corresponds to the direction of arrival, for the incoming signal conditions, the magnitude of the difference between the right and left bank voltages will be at a relative minimum (see Figure 4) and when the boresight azimuth differs slightly from the direction of arrival, in either direction, the system will record the greatest values of the magnitude of the difference between the bank voltages. These two relative maximum values of difference data are referred to as the greater and lesser peaks of the primary lobes (depending upon which is greater than the other) in the difference data values (v s. boresight azimuth) scan pattern. The difference mode direction of arrival is then calculated by using those sample points between the peaks of the two primary lobes whose difference value is less than that of the difference value of the lesser primary lobe peak and the direction of arrival is then taken as the centroid of the difference between the lesser peak value and the values of these sample points at their corresponding boresight settings.

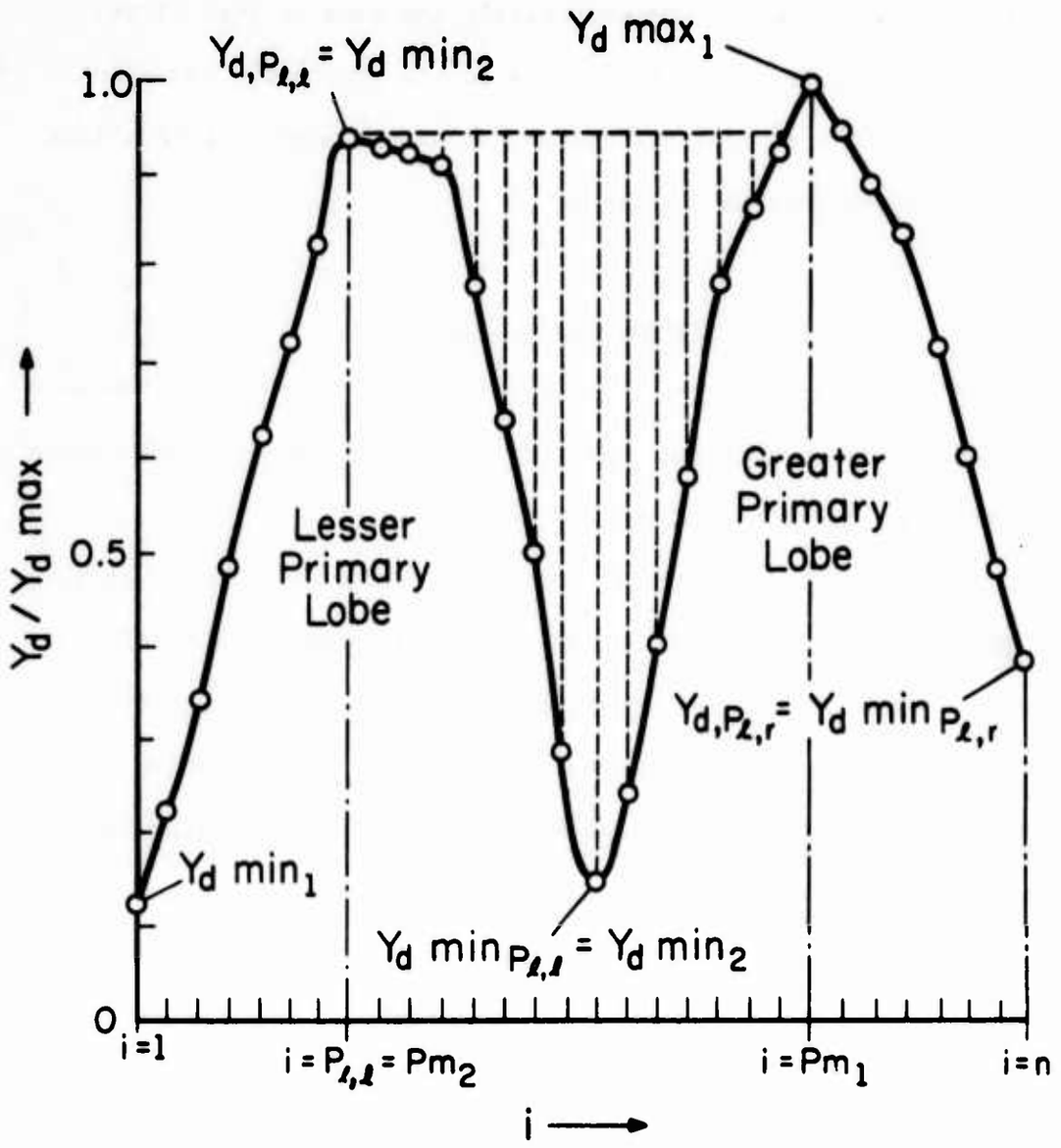

Figure 4. Difference Pattern.

For this digital computation of the direction of arrival no assumption is made about the direction of arrival in order to locate the relative minimum in the difference pattern, where the boresight azimuth corresponds to direction of arrival, as is made in the differential phase mode calculator. Thus, the difference mode direction of arrival is to be calculated by only considering the difference data for the scan.

Since there will be several relative minima within the scan pattern, which may have difference values less than that of the relative minimum of interest, it will not be possible to locate the relative minimum where the boresight azimuth corresponds to the direction of arrival upon an evaluation of the minimum values of the scan pattern. As an alternative solution, the relative minimum of interest will be located as the relative minimum between the peaks of the two primary lobes of the pattern.

The peak of the greater primary lobe can be easily located as the sample point having the greatest difference value in the pattern, but the location of the peak of the lesser primary lobe is a greater problem. After the consideration of several possible alternatives, it has been decided that the most effective method of locating the lesser peak is to define the lesser peak as the sample point which has the greatest difference between its difference value and lowest difference value found for a sample point between that sample point and the sample point defined as the greatest peak in the scan. This method of locating the lesser lobe peak tends to eliminate the possibility that a relative maximum which may still be considered as a part of the greater primary lobe will be detected as the peak of the lesser primary lobe. Once the peaks of the two primary lobes are located, the calculation for the direction of arrival may be developed in a straight-forward manner.

The first step in the routine for calculating the difference mode direction of arrival is to locate the sample point (P_{m_1}) which has the greatest difference value ($Y_d max_1$) in the scan. Considering first the sample points to the left of P_{m_1}, it is necessary to locate the lowest difference value ($Y_d min_{\ell,i}$) between P_{m_1} and the sample point of interest (i). The peak of the next greatest lobe to the left of P_{m_1} is then defined as the sample point ($P_{\ell,\ell}$) having the greatest difference between its difference value ($Y_{dP_{\ell,\ell}}$) and the lowest value ($Y_d min_{P_{\ell,\ell}}$) between $P_{\ell,\ell}$ and P_{m_1} for the sample points i = 1,2,...,P_{m_1}. If a minimum sample point cannot be found between i = 1 and P_{m_1}, then $P_{\ell,\ell}$ is defined as $P_{\ell,\ell} = 1$. Similar considerations are then carried out for the sample points to the right of P_{m_1} to locate the peak of the next greatest lobe to the right of P_{m_1} as the sample point ($P_{\ell,r}$) having the greatest difference between its difference value ($Y_{d\ P_{\ell,r}}$) and the lowest value ($Y_d min_{P_{\ell,r}}$) between $P_{\ell,r}$ and P_{m_1} for the sample points i = P_{m_1}, P_{m_1} + 1, P_{m_1} + 2,...,n. Again if a minimum sample point cannot be found between i = P_{m_1} and n, then $P_{\ell,r}$ is defined as $P_{\ell,r} = n$. Once the peaks of the lobes on each side of P_{m_1} have been defined, the peak of lesser primary lobe (P_{m_2}) is then defined as the adjacent lobe which has the greater difference between its value and the minimum value found between it and P_{m_1}, i.e., if

$$(Y_{dP_{\ell,r}} - Y_d min_{P_{\ell,r}}) \geq (Y_{dP_{\ell,\ell}} - Y_d min_{P_{\ell,\ell}})$$

then

$$P_{m_2} = P_{\ell,r}$$

$$Y_d max_2 = Y_{dP_{\ell,r}}$$

$$Y_d min_2 = Y_d min_{P_{\ell,r}}$$

and if $(Y_{dP_{\ell,r}} - Y_d min_{P_{\ell,r}}) < (Y_{dP_{\ell,\ell}} - Y_d min_{P_{\ell,\ell}})$,

then
$$P_{m_2} = P_{\ell,\ell}$$
$$Y_d max_2 = Y_{dP_{\ell,\ell}}$$
$$Y_d min_2 = Y_d min_{P_{\ell,\ell}}$$

The difference mode direction of arrival (D_d) is then calculated as the centroid of the area in the difference data (v s. boresight settings) scan pattern between the two primary lobes, as:

$$D_d = \frac{\sum_{i=P_{m_1}}^{P_{m_2}} X_i Y'_{d,i}}{\sum_{i=P_{m_1}}^{P_{m_2}} Y'_{d,i}}$$

where $Y'_{d,i} = Y_d max_2 - Y_{d,i}$ if $Y_d max_2 > Y_{d,i}$

and $Y'_{d,i} = 0$ if $Y_d max_2 \leq Y_{d,i}$

Three arbitrary criteria have been established to determine whether or not the difference direction should be accepted as a valid direction of arrival. The first criterion, which must be met, is that the difference between the maximum and minimum difference data values ($Y_d max_1 - Y_d min$) must be greater than or equal to 0.7 of the average difference data values for the n sample points in the scan, i.e.,

$$\frac{Y_d max_1 - Y_d min}{(\sum_{i=1}^{n} Y_{d,i})/n} \geq 0.7$$

The second criterion is that the number of sample points which were used in the calculation of D_d (i.e., the sample points between P_{m_1} and P_{m_2} for

which $Y_{d,i} < Y_d max_2$ is greater than or equal to four. The third criterion is that the difference between the difference value of the lesser peak and the lowest difference value found between the greater and lesser peak ($Y_d max_2 - Y_d min_2$) should be greater than or equal to 0.3 of the difference between the maximum and minimum difference values ($Y_d max_1 - Y_d min_1$), for the scan, i.e.,

$$\frac{(Y_d max_2 - Y_d min_2)}{(Y_d max_1 - Y_d min_1)} \geq 0.3$$

If these three criteria cannot be met, the difference direction of arrival is rejected and it is considered that a direction of arrival for the incoming signal conditions cannot be determined from the difference data in the scan.

V. Simulated Signal Conditions

The simulated signal conditions used in this comparison of the three modes of direction of arrival calculations were produced by the simulation program GCAAS,[3] using the system parameters of the University of Illinois CDAA-RDF system. These parameters are:

Number of antenna elements	= 120	
Reflecting cylinder radius	= 145.5 meters	
Reflecting cylinder to antenna element distance	= 6.0 meters	
Number of sample points per scan	= 30	
Spacing between successive sample points	= 1.0 degrees	
	Low Band	High Band
Number of scanning elements	= 48	24
Cophasal angle	= 20.0 degrees	10.0 degrees

It was desired to compare the three modes of direction of arrival calculations under single signal, two signal wave interference and single signal with noise conditions. The simulated signal data was produced by first arbitrarily establishing a standard signal condition, for each of the three classes of signal conditions, and then varying one of the signal conditions parameters about the standard conditions. The standard conditions for the three classes of signal conditions are given in Table 1 and the signal condition for which data was produced is listed in Table 2. It should be noted that the signal condition data was produced for both the low and high band system.

VI. Methods of Comparing the Three Calculators

The comparison of the performance of the modes of calculation will be carried out by an evaluation of the average, standard deviation and range (max - min) of the calculated directions of arrival and the number of rejections for each of the calculations, for those signal conditions containing more than one scan. For the single scan signal conditions (Class I), the directions of arrival for the scan and their acceptance or rejection will be the only method of evaluating the performance of the calculators.

Since the aximuthal angles of the primary and secondary signals and sector center are all arbitrary and the primary signal and sector center azimuth are usually the same, the direction of arrival and average direction of arrival will be given as the direction of arrival minus the sector center.

TABLE 1

		Class I Single Signal	Class II Two Signal Interference	Class III Single Signal With Noise
Frequency	Low Band High Band	FREQC = 7.0 MHz 12.0	7.0 12.0	7.0 12.0
Cophasel	Low Band High Band	CPHI = 20.0 deg 10.0 deg	20.0 10.0	20.0 10.0
Sector Center		SECT = 90.0 deg	90.0 deg	90.0 deg
Number of Scans		ISCAN = 1	10	50
Time per Scan		SCANT = 2.0 sec	2.0 sec	2.0 sec
PRIMARY SIGNAL				
Relative Amplitude		$WAMP_1$ = 1.0	1.0	1.0
Azimuthal Angle		AZM_1 = 90.0 deg	90.0 deg	90.0 deg
Elevation Angle		$ELEV_1$ = CPHI	CPHI	CPHI
Phase Shift/Scan		PST_1 = 0.0 deg/scan	0.0 deg/scan	0.0 deg/scan
SECONDARY SIGNAL				
Relative Amplitude		$WAMP_2$ = 0.0	0.8	0.0
Azimuthal Angle		AZM_2 = ——	92.0 deg	——
Elevation Angle		$ELEV_2$ = ——	CPHI + 10 deg	——
Phase Shift/Scan		PST_2 = ——	36.0 deg/scan	——
NOISE SIGNAL				
Relative Amplitude		ANOIS = 0.0	0.0	0.0

TABLE 2

Signal Condition	Class	Parameter Being Varied	Variation of Parameter
1	I	Frequency	FREQC = 4.0,7.0,12.0,16.0 & 21.0 MHz
2	I	Elevation Angle	$ELEV_1$ = 0.0 ⟶ 30.0, Δ 10.0 deg
3	I	Azimuthal Angle	AZM_1 = 105.0⟶ 7.50, Δ = 2.5 deg
4	II	Standard	
5	II	Secondary Azimuthal Angle	AZM_2 = 90.0 ⟶ 100.0, Δ 1.0 deg
6	II	Secondary Elevation Angle	$ELEV_2$ = 0.0 ⟶ 30.0, Δ 10.0 deg
7	II	Secondary Signal Amplitude	AZM_2 = 0.10 ⟶ 0.90, Δ = 0.1 & = 0.91 ⟶ 1.00, Δ = 0.01
8	II	Relative Phase Between Primary and Secondary	(ISCAN,PST_2) = (100, 3.6 deg/scan) = (10, 36.0 deg/scan) = (1, 360.0 deg/scan)
9	II	Relative Phase Between Primary and Secondary	ISCAN = 10 PST_2 = 324.0
10	III	Relative Noise Amplitude, Signal Centered	AZM_1 = 90.0 deg ANOIS = 0.1 ⟶ 1.0, Δ = 0.1
11	III	Relative Noise Amplitude, Signal off Center	AZM_1 = 95.0 deg ANOIS = 0.2 ⟶ 1.0, Δ = 0.2
12	III	Relative Noise Amplitude, Signal off Center	AZM_1 = 100.0 deg ANOIS = 0.2 ⟶ 1.0, Δ 0.2

It should be noted at this point that it was never expected that the criterion, imposed on the direction of arrival calculators, would reject all the calculated directions of arrival which were not within a reasonable displacement of the known direction of arrival. Rather, the selection criterion, as considered in this study, is used to determine whether the given scan pattern configuration conforms to the general scan patter which the direction of arrival calculators were developed to handle.

VII. The Calculated Directions of Arrival

SIGNAL GROUP I

Single Signal - Varying Frequency

FREQZ (MHz)	Low Band Sum	Low Band Diff.	Low Band Dif. P.	High Band Sum	High Band Diff.	High Band Dif. P.
	Direction of Arrival					
4.0	0.000	0.000	0.000	———	0.000	———
7.0	0.000	0.000	0.000	0.000	0.000	0.000
12.0	0.000	0.000	0.000	0.000	0.000	0.000
16.0	0.000	———	0.000	0.000	0.000	0.000
21.0	0.000	———	———	0.000	0.000	0.000
	Number of Rejections					
4.0	0	0	0	1	0	1
7.0	0	0	0	0	0	0
12.0	0	0	0	0	0	0
16.0	0	1	0	0	0	0
21.0	0	1	1	0	0	0

NOTE: The phase delays for the delay lines were calculated for the given frequencies.

The purpose of these signal conditions were basically to "check out" the three calculators and determine whether any of the selection criteria are overly severe.

The two difference mode rejections and one differential phase mode rejection in the low band were brought on when the number of sample points used in the direction of arrival calculations were less than the arbitrarily set minimum. These rejections are due to the narrower beam which is formed at higher frequencies; if the azimuthal angle between successive sample points was decreased, the direction of arrival could then be determined at these higher frequencies. The sum and differential phase mode rejection in the high band was a result of the fact that the maximum minus minimum sum value was less than the average sum value for the scan. This rejection was due to the broader beam which is formed at this lower frequency; if the sampling window was widened (i.e., more sample points of the same interval between points were taken in the scan) the direction of arrival could then be determined at this lower frequency. Since 16.0 and 21.0 MHz are not low band frequencies and 4.0 MHz is not a high band frequency, the rejections that occurred can be attributed to "over driving" the system.

Since the directions of arrival, which were not rejected, were all properly calculated (i.e., 00.0, AZM_1 - SECT = 0.0) and the rejections which occurred were to be expected from the design of the system, this indicates that the direction of arrival calculators are functioning properly.

SIGNAL GROUP 2

Single Signal - Varying Elevation

ELEV	Low Band			High Band		
	Sum	Diff.	Dif. P.	Sum	Diff.	Dif. P.
	Direction of Arrival					
0.0	0.000	0.000	0.000	0.000	0.000	0.000
10.0	0.000	0.000	0.000	0.000	0.000	0.000
20.0	0.000	0.000	0.000	0.000	0.000	0.000
30.0	0.000	0.000	0.000	0.000	0.000	0.000
	Number of Rejections					
0.0	0	0	0	0	0	0
10.0	0	0	0	0	0	0
20.0	0	0	0	0	0	0
30.0	0	0	0	0	0	0

Again the purpose of this group of signal conditions was to "check out" the three calculators and to determine whether any of the selection criterion were too severe over the range of elevation angles investigated. Since all the directions of arrival were properly calculated and no rejections occurred, this indicates that the three calculators are functioning properly.

SIGNAL GROUP 3

Single Signal - Varying Azimuth

AZM_1 - SECT	Low Band			High Band		
	Sum	Diff.	Dif. P.	Sum	Diff.	Dif. P.
	Direction of Arrival					
-15.0	-11.748	——	-15.035	-12.106	——	-15.022
-12.5	-10.642	——	-12.506	-10.976	——	-12.500
-10.0	-9.171	-10.000	-9.992	-9.450	-10.000	-9.992
- 7.5	-7.368	-7.500	-7.495	-7.500	-7.500	-7.499
- 5.0	-5.000	-5.000	-5.000	-5.000	-5.000	-5.000
- 2.5	-2.500	-2.500	-2.500	-2.500	-2.500	-2.500
0.0	0.000	0.000	0.000	0.000	0.000	0.000
2.5	2.500	2.500	2.500	2.500	2.500	2.500
5.0	5.000	5.000	5.000	5.000	5.000	5.000
7.5	7.368	7.500	7.495	7.500	7.500	7.499
10.0	9.171	10.000	9.992	9.450	10.000	9.992
12.5	10.642	——	12.506	10.976	——	12.500
15.0	11.748	——	15.035	12.106	——	15.022

	Number of Rejections					
-15.0	0	1	0	0	1	0
-12.5	0	1	0	0	1	0
-10.0	0	0	0	0	0	0
- 7.5	0	0	0	0	0	0
- 5.0	0	0	0	0	0	0
- 2.5	0	0	0	0	0	0
0.0	0	0	0	0	0	0
2.5	0	0	0	0	0	0
5.0	0	0	0	0	0	0
7.5	0	0	0	0	0	0
10.0	0	0	0	0	0	0
12.5	0	1	0	0	1	0
15.0	0	1	0	0	1	0

From the results from this group of signal conditions it can be seen that both the sum and differential phase modes will begin to show errors in the calculated direction of arrival when the incoming signal is offset more than five degrees from the sector center, while the difference mode accurately calculates the direction of arrival for a signal up to ten degrees off the sector center.

The errors in the sum mode calculations can be readily accounted for by the fact that a portion of the primary lobe is beyond the side of the window and the centroid of the remaining portion of the lobe is taken as the direction of arrival.

The difference mode rejections which occurred for the signal 12.5 degrees off the sector center were brought on when the number of sample points available for use in the direction of arrival calculation was found to be less than the required minimum number of points. The rejections at 15.0 degrees off the sector center occurred because the depth of the valley between the two "apparent" primary lobes was less than three tenths of the difference between the maximum and minimum

difference values in the scan. Upon consideration the reason for these rejections became quite apparent as one of the two primary lobes is lost, first diminshing the number of sample points in the valley between the primary lobes and then disappearing completely from the scan patterns causing a secondary lobe to be considered as a primary lobe.

The errors in the differential phase mode calculations are brought on by the nature of the least squares calculation when the sample points do not include a substantial portion of one side of the scan of interest decreasing the symmetry about the zero degree phase point. It should also be noted that these errors in calculation are small, 0.035 degree or less.

Even though the difference mode calculator has the greatest range of direction of arrival calculation without errors, it should be noted that the differential phase mode calculation has such small errors that it displays the best performance for off centered incoming signals over the entire range of sampling window. It should also be noted that the sum mode calculation gives the worst results for off centered signals.

SIGNAL GROUP 4

Two Signal Interference - Standard

	Low Band			High Band		
	Sum	Diff.	Dif. P.	Sum	Diff.	Dif. P.
	Average					
	-0.218	0.011	0.129	0.676	-0.025	0.112
	Standard Deviation					
	1.400	1.145	1.081	1.039	1.467	1.261
	Range					
	4.576	3.449	3.492	3.922	3.942	3.309
	Number of Rejections					
	0	0	0	0	0	0

From these first results for the two signal interference condition, it is interesting to note, that even though the amplitude of the secondary signal is eight tenths of the primary, how the calculated directions of arrival tend to favor the azimuth of the primary signal. It will be considered in the rest of this report that the primary signal azimuth is the desired answer to the direction of arrival calculations for two signal wave interference conditions.

SIGNAL GROUP 5

Two Signal Interference - Varying Secondary Azimuth

AZM_2 - SECT	Low Band			High Band		
	Sum	Diff.	Dif. P.	Sum	Diff.	Dif. P.
	Average					
0.0 deg	0.007	-0.004	0.001	0.071	0.002	-0.000
1.0	-0.009	-0.008	0.031	0.246	0.033	0.057
2.0	0.218	0.011	0.129	0.676	-0.025	0.112
3.0	0.515	0.015	0.130	0.678	0.049	0.191
4.0	0.572	-0.021	0.213	0.931	0.186	0.303
5.0	0.740	-0.030	0.371	0.978	0.069	0.497
6.0	1.024	0.074	0.436	0.955	-0.084	0.474
7.0	1.303	0.177	0.489	1.183	0.057	0.611
8.0	0.996	0.249	0.591	1.229	0.197	0.675
9.0	1.097	0.001	0.608	1.141	0.080	0.644
10.0	1.241	0.015	0.700	0.981	-0.014	0.783
	Standard Deviation					
0.0	0.033	0.041	0.011	0.187	0.041	0.006
1.0	1.096	0.640	0.647	0.593	0.726	0.663
2.0	1.400	1.145	1.081	1.039	1.467	1.261
3.0	1.460	1.561	1.467	1.674	1.941	1.672
4.0	1.853	1.882	1.773	1.825	2.105	1.897
5.0	2.043	2.102	2.014	2.024	2.503	2.099
6.0	2.173	2.378	2.153	2.140	2.573	2.264
7.0	2.267	2.443	2.277	2.393	2.579	2.372
8.0	2.248	2.449	2.410	2.289	2.528	2.323
9.0	2.319	2.410	2.396	2.288	2.447	2.388
10.0	2.303	2.469	2.407	2.020	2.359	2.406

AZM_2 - SECT	Low Band			High Band		
	Sum	Diff.	Dif. P.	Sum	Diff.	Dif. P.
	Range					
0.0	0.122	0.138	0.039	0.614	0.145	0.024
1.0	3.620	2.030	2.105	2.107	1.953	1.956
2.0	4.576	3.449	3.492	3.922	3.942	3.309
3.0	4.861	4.355	4.282	4.738	4.979	4.256
4.0	5.701	4.863	4.735	4.866	5.344	4.840
5.0	5.491	5.170	5.023	4.841	5.529	5.311
6.0	5.574	5.445	5.222	5.091	5.728	5.430
7.0	5.588	5.716	5.375	5.473	5.866	5.733
8.0	5.515	5.837	5.453	5.436	5.946	5.667
9.0	5.301	5.906	5.496	5.569	6.032	5.881
10.0	5.184	5.882	5.553	5.177	6.183	6.155
	Number of Rejections					
0.0	0	0	0	0	0	0
1.0	0	0	0	0	0	0
2.0	0	0	0	0	0	0
3.0	0	0	0	0	1	0
4.0	0	0	0	0	1	0
5.0	0	0	0	0	3	0
6.0	0	1	0	0	1	0
7.0	0	1	0	0	1	0
8.0	0	1	0	0	1	0
9.0	0	0	0	0	0	0
10.0	0	1	0	0	1	0

From this group of signal conditions it can be seen that the magnitude of the displacement of the calculated direction of arrival from the primary azimuth is for the most part directly related to the displacement between the incoming primary and secondary signals. It is again interesting to note, as in the standard two signal condition, how closely the direction of arrival favors the primary signal.

At first glance it might appear that the calculations are not functioning properly because the average, standard deviation and range are not zero at AZM_2 - SECT = 0.0 degrees. Consideration of the

operation of the simulation program in the multi-signal mode suggests that this is to be expected. Note that the zero simulated time is obtained for the first sample point in the first scan rather than when the boresight would correspond to the sector center. Thus, the scan patterns for the first scan in the group will not be symmetric about the boresight for AZM_2 = SECT.

After evaluating the average, standard deviation and range, the difference mode gives the least average error in the direction of arrival of the primary signal although the standard deviation and range are greater than those obtained for the sum and differential phase modes. Again the sum mode offers the least favorable results in calculating the direction of arrival of the primary signal.

A preliminary evaluation of the simulated scan patterns suggests no reason for the drop in the magnitude of the difference between the calculated direction of arrival and the azimuth of the primary signal in the difference mode at AZM_2 - SECT = 9.0 and 10.0 degrees.

SIGNAL GROUP 6

Two Signal Interference - Varying Secondary Elevation

$ELEV_2$	Low Band			High Band		
	Sum	Diff.	Dif. P.	Sum	Diff.	Dif. P.
	Average					
0.0	0.207	0.174	0.110	0.411	0.270	0.129
10.0	0.304	0.219	0.111	0.510	0.200	0.134
20.0	0.403	0.011	0.122	0.676	-0.025	0.112
30.0	0.218	0.011	0.129	0.390	0.007	0.102

$ELEV_2$	Low Band			High Band		
	Sum	Diff.	Dif. P.	Sum	Diff.	Dif. P.
	Standard Deviation					
0.0	1.556	2.131	1.764	1.421	1.456	1.392
10.0	1.410	1.851	1.635	1.363	1.497	1.380
20.0	1.463	1.611	1.482	1.039	1.467	1.261
30.0	1.400	1.145	1.081	1.036	1.146	1.026
	Range					
0.0	5.254	6.482	5.637	4.811	4.539	4.362
10.0	4.770	5.654	5.208	4.712	4.612	4.412
20.0	4.801	5.104	4.788	3.922	3.942	3.309
30.0	4.576	3.449	3.492	3.125	3.056	2.882
	Number of Rejections					
0.0	0	1	0	0	1	0
10.0	0	1	0	0	1	0
20.0	0	0	0	0	0	0
30.0	0	0	0	0	0	0

After considering the results for this group of signal calculations it is quite apparent that this is an insufficient amount of information for drawing any general conclusions. It will be noted though that the differential phase mode offers superior performance as far as standard deviation and range are concerned, but the difference mode has a somewhat better performance in terms of average angle of arrival at the higher elevation angle.

All the rejections except the low band rejection at $ELEV_2$ = 0.0 deg were due to the depth of the valley being less than three tenths of the difference between the maximum and minimum difference values in the scan. The exception was rejected because its average value was less than seven tenths of the difference between the maximum and minimum value in the scan. Note that this rejection occurred when the relative phase shift between the two signals was approximately 180.0 degrees.

SIGNAL GROUP 7

Two Signal Interference - Varying Secondary Amplitude

$WAMP_2$	Low Band			High Band		
	Sum	Diff.	Dif. P.	Sum	Diff.	Dif. P.
	Average					
0.10	-0.014	-0.001	0.001	0.005	-0.002	0.000
0.20	0.009	-0.004	0.003	0.021	-0.005	0.004
0.30	0.045	-0.009	0.006	0.067	0.004	0.010
0.40	0.066	-0.015	0.011	0.150	0.008	0.017
0.50	0.094	-0.011	0.020	0.185	0.008	0.029
0.60	0.250	-0.006	0.030	0.296	0.009	0.043
0.70	0.271	0.001	0.050	0.350	-0.004	0.070
0.80	0.218	0.011	0.129	0.676	-0.025	0.112
0.90	0.249	0.017	0.181	0.696	0.355	0.173
0.91	0.251	0.017	0.186	0.705	0.360	0.177
0.92	0.253	0.017	0.190	0.701	0.365	0.182
0.93	0.263	0.018	0.194	0.709	1.727	0.185
0.94	0.256	0.142	0.199	0.718	1.729	0.213
0.95	0.250	0.142	0.204	0.727	1.731	0.217
0.96	0.252	0.142	0.204	0.205	1.734	0.164
0.97	0.254	0.142	0.208	1.246	1.737	0.162
0.98	0.264	0.142	0.212	1.249	1.746	0.235
0.99	0.265	0.141	0.220	0.707	1.749	0.246
1.00	0.267	0.141	0.225	0.714	1.753	0.404
	Standard Deviation					
0.10	0.128	0.119	0.119	0.174	0.161	0.139
0.20	0.254	0.244	0.238	0.286	0.323	0.275
0.30	0.338	0.376	0.361	0.386	0.473	0.411
0.40	0.528	0.519	0.489	0.503	0.625	0.557
0.50	0.660	0.652	0.620	0.687	0.792	0.711
0.60	0.843	0.798	0.765	0.861	0.976	0.884
0.70	0.988	0.960	0.921	0.933	1.197	1.066
0.80	1.400	1.145	1.081	1.039	1.467	1.261
0.90	1.646	1.380	1.329	1.222	1.290	1.437
0.91	1.669	1.409	1.359	1.230	1.309	1.459
0.92	1.693	1.438	1.390	1.274	1.328	1.478
0.93	1.692	1.468	1.421	1.281	2.760	1.500
0.94	1.744	1.536	1.453	1.287	2.727	1.479
0.95	1.790	1.566	1.485	1.293	2.696	1.500
0.96	1.813	1.596	1.530	1.697	2.666	1.621
0.97	1.836	1.626	1.564	2.575	2.637	1.643
0.98	1.863	1.658	1.599	2.573	2.592	1.537
0.99	1.888	1.689	1.614	1.416	2.553	1.546
1.00	1.913	1.722	1.649	1.423	2.516	1.381

$WAMP_2$	Low Band			High Band		
	Sum	Diff.	Dif. P.	Sum	Diff.	Dif. P.
	Range					
0.10	0.359	0.319	0.321	0.453	0.426	0.363
0.20	0.707	0.651	0.644	0.745	0.855	0.720
0.30	0.990	1.014	0.988	1.054	1.251	1.080
0.40	1.582	1.430	1.362	1.447	1.665	1.478
0.50	1.960	1.806	1.763	1.904	2.136	1.893
0.60	2.636	2.269	2.244	2.528	2.638	2.366
0.70	3.151	2.814	2.801	2.698	3.244	2.843
0.80	4.576	3.449	3.492	3.922	3.942	3.309
0.90	5.550	4.285	4.331	4.587	4.036	3.785
0.91	5.564	4.386	4.427	4.628	4.091	3.841
0.92	5.701	4.490	4.524	4.788	4.149	3.898
0.93	5.695	4.595	4.623	4.824	8.761	3.955
0.94	5.860	4.703	4.723	4.859	8.658	4.013
0.95	6.008	4.797	4.824	4.891	8.560	4.072
0.96	6.078	4.889	4.964	4.374	8.466	4.063
0.97	6.150	4.982	5.070	10.722	8.374	4.150
0.98	6.225	5.077	5.177	10.719	8.248	4.237
0.99	6.301	5.175	5.218	5.256	8.128	4.325
1.00	6.379	5.274	5.327	5.294	8.015	4.413
	Number of Rejection					
0.10	0	0	0	0	0	0
0.20	0	0	0	0	0	0
0.30	0	0	0	0	0	0
0.40	0	0	0	0	0	0
0.50	0	0	0	0	0	0
0.60	0	0	0	0	0	0
0.70	0	0	0	0	0	0
0.80	0	0	0	0	0	0
0.90	0	0	0	0	1	0
0.91	0	0	0	0	1	0
0.92	0	0	0	0	1	0
0.93	0	0	0	0	1	0
0.94	0	1	0	0	1	0
0.95	0	1	0	0	1	0
0.96	0	1	0	0	1	0
0.97	0	1	0	0	1	0
0.98	0	1	0	0	1	0
0.99	0	1	0	0	1	0
1.00	0	1	0	0	1	0

The general appearence of the results for this group of signal conditions is exactly what would be expected. The sum and differential phase

mode averages are directly related to the secondary amplitude and the difference mode average is, at first, surprisingly close to the primary azimuth. Both the standard deviation and the range are directly related to the secondary amplitude, with the differential phase mode showing a slightly better performance.

A closer look at the results of these signal conditions shows that there are three situations which must be more closely investigated. The first two situations are the sudden jump, at $WAMP_2$ = .94 in the low band and $WAMP_2$ = .93 in the high band, of the difference mode direction of arrival from favoring the primary azimuth to favoring the secondary azimuth. The third situation is the two average sum directions of arrival, at $WAMP_2$ = .97 and .98 in the high band, favoring the secondary rather than the primary azimuth.

Consider first the sum mode; the sudden corresponding jumps in the range suggest that one of the directions of arrival calculated in the group of scans for $WAMP_2$ = .97 and .98 is way out of line. After an examination of the scan information obtained from the simulation program, it was found that this was the case. In the ninth scan of each of the two groups (at a relative phase shift of approximately 288°) directions of arrival of approximately 97.5 degrees were calculated. This ninth scan was also one of the two scans in the group of ten scans having the lowest maximum sum value for the scan; a value of 8.37 as compared to 42.78 in the third scan (relative phase shift of 72.0 degrees).

The sudden jumps of the difference mode calculator from favoring the primary to favoring the secondary azimuth are brought about by the same type of detrimental form of the difference pattern. In the high band it is

the eighth scan which cause the problem, the other scan having the lowest maximum sum and difference values in the scan. Here, there are two distinct valleys between which the calculator has to choose and it is apparent that the wrong one is being chosen causing a direction of arrival of 98.7 degrees to be calculated.

It should also be mentioned that all of the high band difference mode rejections occurred in the ninth scan and were a result of the valley depth being less than three tenths of the difference between the maximum and minimum difference value in the scan.

The jump in the low band average was caused by the same sort of problem. The low band rejections all occurred when the average difference value was less than seven tenth of the difference between maximum and minimum difference value in the scan.

As far as the best mode of performance under these signal conditions, the difference mode appears to give slightly better results for a secondary amplitude of less than nine tenths of the primary signal. Above nine tenths the differential phase mode is the only reliable method of calculation.

SIGNAL GROUP 8

Two Signal Interference -
Varying Rate of Phase Shift and Number of Scans.

PST_2 = 360.0 deg/ISCAN Scans.

ISCAN	Low Band			High Band		
	Sum	Diff.	Dif. P.	Sum	Diff.	Dif. P.
	Average					
100	0.224	0.003	0.081	0.547	0.081	0.116
10	0.218	0.011	0.129	0.676	-0.025	0.112
1	1.041	0.642	0.781	0.996	0.546	0.810

ISCAN	Low Band			High Band		
	Sum	Diff.	Dif. P.	Sum	Diff.	Dif. P.
	Standard Deviation					
100	1.242	1.092	1.043	1.160	1.323	1.212
10	1.400	1.145	1.081	1.039	1.467	1.261
1						
	Range					
100	4.740	3.438	3.499	4.994	4.295	3.996
10	4.576	3.449	3.492	3.922	3.942	3.309
1						
	Number of Rejections					
100	0	0	0	0	4	0
10	0	0	0	0	0	0
1	0	0	0	0	0	0

It can be seen from this group of signal conditions that the results obtained in all three modes of operations are dependent upon the sampling interval and rate of relative phase shift between the two incoming signals. In general the average direction of arrival shows less errors at the lower rate of relative phase shift than at the higher rates of relative phase shift.

It should be noted that the four rejections, in the high band operation for the lower rate of relative phase shift, occurred for four successive scans. It then becomes quite apparent that the results obtained for the three modes of operation are also a function of the initial phase shift for the first scan in the group, since a rejection would also be observed for the two higher rates of relative phase shift if the initial phase was set so that one scan in the group would have a phase shift which fell into the rejection range observed for the lower rate of relative phase shift.

SIGNAL GROUP 9

Two Signal Interference - Varying Rate of Phase Shift

ISCAN = 10
PST_2 = (360.0 * 9)10 = 324.0 degrees

ISCAN	Low Band			High Band		
	Sum	Diff.	Dif. P.	Sum	Diff.	Dif. P.
	Average					
10	0.157	0.026	0.065	0.632	0.228	0.129
	Standard Deviation					
10	1.328	1.160	1.161	1.370	1.248	1.226
	Range					
10	3.950	3.423	3.160	5.170	3.932	3.803
	Number of Rejections					
10	0	0	0	0	1	0

When the results obtained from this group of signal conditions is compared to the results for the last group of signal conditions, it is again observed that the results are a function of the initial phase shift for the scan and rate of relative phase shift.

SIGNAL GROUP 10

Single Signal With Noise - Varying Noise Amplitude,
at AZM_1 - SECT = 0.00 deg.

ANOIS	Low Band Sum	Low Band Diff.	Low Band Dif. P.	High Band Sum	High Band Diff.	High Band Dif. P.
	Average					
0.10	-0.062	0.015	0.006	-0.281	0.003	0.004
0.20	-0.074	0.025	0.010	-0.274	0.014	0.007
0.30	0.127	0.043	0.021	-0.370	0.014	0.015
0.40	-0.151	0.031	0.039	-0.352	0.032	0.018
0.50	0.067	0.021	0.057	-0.282	0.027	0.016
0.60	0.024	0.100	0.075	-0.290	0.029	0.016
0.70	0.192	0.092	0.063	-0.111	0.049	0.008
0.80	0.076	0.077	0.060	-0.057	0.052	0.000
0.90	0.111	0.081	0.064	0.148	0.019	0.037
1.00	0.457	0.303	0.082	0.168	-0.030	0.019
	Standard Deviation					
0.10	1.390	0.066	0.026	1.338	0.076	0.027
0.20	1.462	0.125	0.052	1.345	0.140	0.053
0.30	1.535	0.189	0.077	1.404	0.190	0.080
0.40	1.843	0.276	0.132	1.513	0.240	0.109
0.50	1.992	0.348	0.170	1.614	0.291	0.135
0.60	2.105	0.474	0.228	1.625	0.405	0.157
0.70	2.250	0.555	0.333	1.660	0.486	0.197
0.80	2.344	0.645	0.385	1.796	0.553	0.228
0.90	2.304	0.746	0.439	2.011	0.608	0.254
1.00	2.384	1.561	0.470	2.017	0.671	0.308
	Range					
0.10	6.579	0.359	0.143	5.849	0.376	0.119
0.20	6.658	0.657	0.286	5.913	0.625	0.230
0.30	7.279	0.968	0.433	5.980	0.835	0.356
0.40	7.413	1.595	0.889	6.131	1.047	0.431
0.50	7.966	2.004	1.078	6.119	1.242	0.534
0.60	8.212	2.700	1.257	6.192	1.881	0.636
0.70	7.898	3.143	1.811	6.267	2.238	0.973
0.80	8.371	3.559	1.988	6.878	2.539	1.096
0.90	8.490	3.806	2.154	6.939	2.797	1.208
1.00	8.607	9.214	2.135	7.002	3.162	1.417

ANOIS	Low Band			High Band		
	Sum	Diff.	Dif. P.	Sum	Diff.	Dif. P.
	Number of Rejections					
0.10	0	0	0	0	0	0
0.20	0	0	0	0	0	0
0.30	0	0	0	0	0	0
0.40	1	0	0	0	0	0
0.50	2	0	0	0	0	0
0.60	3	0	1	1	0	0
0.70	6	0	1	4	0	0
0.80	7	0	4	7	0	0
0.90	12	0	4	7	0	1
1.00	16	1	6	10	0	2

From a consideration of the standard deviation and the range it can be seen that the differential phase mode of calculation displays the best performance.

As would be expected both the standard deviation and the range are directly related to the amplitude of the noise signal. What is unexpected is the large range values for the sum mode at ANOIS = 0.1. This leads to the conclusion that the sum mode calculator is susceptible to errors in determining the limits of the primary lobe.

All of the rejections which occurred were because the number of sample points available for direction of arrival calculations were less than the required minimum.

SIGNAL GROUP 11

Single Signal With Noise - Varying Noise Amplitude
at AZM_1 - SECT = 5.00 deg.

ANOIS	Low Band Sum	Low Band Diff.	Low Band Dif. P.	High Band Sum	High Band Diff.	High Band Dif. P.
	Average					
0.20	4.861	5.043	5.004	4.996	4.983	5.004
0.40	5.452	5.096	5.045	4.980	5.022	5.013
0.60	5.432	5.106	5.079	4.915	5.044	5.031
0.80	5.225	5.039	5.081	4.839	5.096	5.029
1.00	5.277	5.030	5.138	4.887	5.123	5.016
	Standard Deviation					
0.20	0.807	0.145	0.059	0.090	0.103	0.050
0.40	1.739	0.294	0.158	1.001	0.204	0.100
0.60	2.073	0.455	0.271	1.503	0.310	0.155
0.80	2.238	0.564	0.378	1.871	0.422	0.204
1.00	2.398	0.708	0.520	2.050	0.530	0.319
	Range					
0.20	5.827	0.780	0.282	0.325	0.602	0.230
0.40	7.161	1.597	1.109	5.538	1.075	0.457
0.60	7.459	2.627	1.889	6.787	1.544	0.693
0.80	7.979	3.137	2.368	8.586	2.125	0.923
1.00	9.503	3.513	3.052	8.758	2.566	1.444
	Number of Rejections					
0.20	0	0	0	0	0	0
0.40	1	0	0	0	0	0
0.60	4	0	0	0	0	0
0.80	11	0	2	3	0	0
1.00	13	1	7	8	0	3

Again, on the basis of the standard deviation and the range for this group, it is apparent that the differential phase mode exhibits the best performance. It can also be seen that the performance of the differential phase mode at AZM_1 - SECT = 5.0 deg. is approximately equivalent to its performance at AZM_1 - SECT = 0.00 degrees. An unresolved question is the

reason for the decrease in the range and standard deviation in the sum and difference modes for AZM_1 - SECT = 5.00 degrees (Signal Group 11) over AZM_1 - SECT = 0.00 degrees (Signal Group 10).

Again all the rejections were a result of the small number of points.

SIGNAL GROUP 12

Single Signal With Noise - Varying Noise Amplitude, at AZM_3 - SECT = 10.00 deg.

ANOIS	Low Band Sum	Low Band Diff.	Low Band Dif. P.	High Band Sum	High Band Diff.	High Band Dif. P.
	Average					
0.20	9.186	9.940	10.004	9.450	9.948	9.998
0.40	8.684	9.861	9.994	9.305	9.901	9.991
0.60	8.443	9.750	9.945	9.037	9.837	9.983
0.80	8.764	9.277	9.887	8.931	9.764	9.980
1.00	8.955	7.895	9.825	8.815	9.273	9.958
	Standard Deviation					
0.20	0.111	0.113	0.073	0.062	0.096	0.054
0.40	1.139	0.238	0.150	0.559	0.194	0.108
0.60	1.339	0.364	0.241	1.002	0.298	0.167
0.80	1.627	2.108	0.389	1.020	0.432	0.218
1.00	1.601	4.421	0.483	1.256	2.265	0.273
	Range					
0.20	0.692	0.495	0.330	0.269	0.483	0.207
0.40	5.304	1.051	0.665	3.140	0.790	0.416
0.60	5.546	1.488	1.167	4.803	1.212	0.701
0.80	5.607	15.500	2.278	4.511	2.104	0.922
1.00	5.717	18.306	2.699	4.893	14.855	1.059
	Number of Rejections					
0.20	3	0	0	1	0	0
0.40	7	0	0	5	0	0
0.60	12	0	1	7	0	0
0.80	19	1	1	8	0	0
1.00	21	3	7	8	0	2

The differential phase mode again displays the best performance, but it now also shows signs of improved performance (decrease of range and standard deviation) at ANOIS = 1.00. The only other significant results is the drastic jump in the range for the difference mode. This was to be expected since the difference mode calculator was not designed to distinguish between the peak of a lobe and the peak of a spike.

VIII. Conclusion

This study is a preliminary presentation and evaluation of the results from the three modes for calculating direction of arrival which are presently employed for the set of simulated incoming signal conditions. At this time the following tentative conclusions can be drawn:

(1) From the relatively large variations in the range, it is obvious that the average of the results obtained over a group of scans gives a better determination of the direction of arrival than the results obtained from the individual scans.

(2) The sum mode calculation displays a greater amount of error in determining the direction of arrival than the difference or differential phase modes of calculation.

(3) There is a slight advantage in choosing the results obtained from the differential phase mode calculator rather than the difference mode calculator in the determination of the direction of arrival.

It should be stated that further evaluation of the results obtained from the three modes of calculation and the simulated scan information is planned in order to determine more effective selection criterion and methods of determining the limiting sample points used in the direction of arrival calculations.

REFERENCES

(1) Antolick, D. R. and Ernst, E. W., "Data Selection Criteria for Direction of Arrival Computation," RRL Publication No. 380, University of Illinois, Urbana, Illinois, 1970, ONR N00014-67-A-0305-0002.

(2) Jones, Jr., E. C., "A Digital Simulation of the Wullenweber Direction Finding System," RRL Publication No. 296, University of Illinois, Urbana, Illinois, 1965, ONR NOBSR 89229.

(3) Ernst, E. W. and Hunninghaus, R. E., "Generalized Digital Simulation of a CDAA Direction Finding System," RRL Publication No. 382, University of Illinois, Urbana, Illinois, 1970, ONR N00014-67-A-0305-0002.

THE V-SCAN DIRECTION FINDING TECHNIQUES

Prepared by:

J. H. Priedigkeit
Stanford Research Institute

To be presented at:

HF/DF Conference
Radio Locations Research Laboratory
University of Illinois
Urbana, Illinois

Research sponsored by:

U. S. Army Electronics Command
Fort Monmouth, New Jersey 07703
Contract No. 36-039-AMC-03393(E)

THE V-SCAN DIRECTION FINDING TECHNIQUE*

ABSTRACT

The development of a V-Scan technique that permits a physically fixed, two-element Adcock antenna array to electronically scan a $\pm 90^{o}$ azimuthal sector is described. Some of the considerations in the design of voltage-variable time delay lines used for the implementation of the V-Scan are discussed.

*Research sponsored by: U.S. Army Electronics Command, Fort Monmouth, New Jersey 07703, Contract No. 36-039-AMC-03393(E).

TABLE OF CONTENTS

I	INTRODUCTION
II	ANTENNA PATTERNS
III	DESCRIPTION OF THE V-SCAN SYSTEM
IV	THE V-SCAN PRESENTATION
V	THE V-SCAN BANDWIDTH
VI	THE TRI-SCAN SYSTEM
VII	DESIGN OF THE VOLTAGE-VARIABLE DELAY LINES
VIII	CONCLUSIONS

I INTRODUCTION

The use of the vertically polarized two-element H-Adcock antenna array with a figure-eight antenna pattern in the horizontal plane has been an accepted radio direction-finding technique since its invention by F. Adcock in 1919.

Although, depending upon the signal-to-noise ratio and the signal polarization, the two-element Adcock array is capable of resolving the direction of signal arrival to the order of one degree, the usual Adcock configuration has several disadvantages. Some of them are:

(1) The Adcock array must be physically rotated so as to null the signal.

(2) The Adcock has a 180° ambiguity that cannot be easily resolved.

(3) The signal-to-noise ratio is the most unfavorable where the best angular accuracy is desired (i.e., in the null).

(4) When the signal is nulled out, there is no assurance that a signal is being received.

The purpose of this paper is to describe a technique for electronically scanning the Adcock array that permits the measurement of signal bearings without physically moving the antenna array, provides a visual display that can result in effecting a better signal-to-noise ratio, and allows the signal presence to be monitored at all times.

Since the V-Scan requires no mechanically moving parts, it is capable of rapid scan rates and could be a useful tool for investigating multipath radio propagation phenomena.

II ANTENNA PATTERNS

Figure 1-A shows the familiar horizontal plane figure-eight pattern obtained from an Adcock antenna array in which the output signal is the difference between two vertical dipole antennas where electrical spacing is less than one-half wavelength. For equal-length cables between the dipole antenna elements and the array output, the resulting antenna pattern has a null plane perpendicular to the base line joining the antennas. Since this null is in a vertical plane, there is no error due to the vertical angle of arrival. This null may be referred to as the boresight axis of the antenna array.

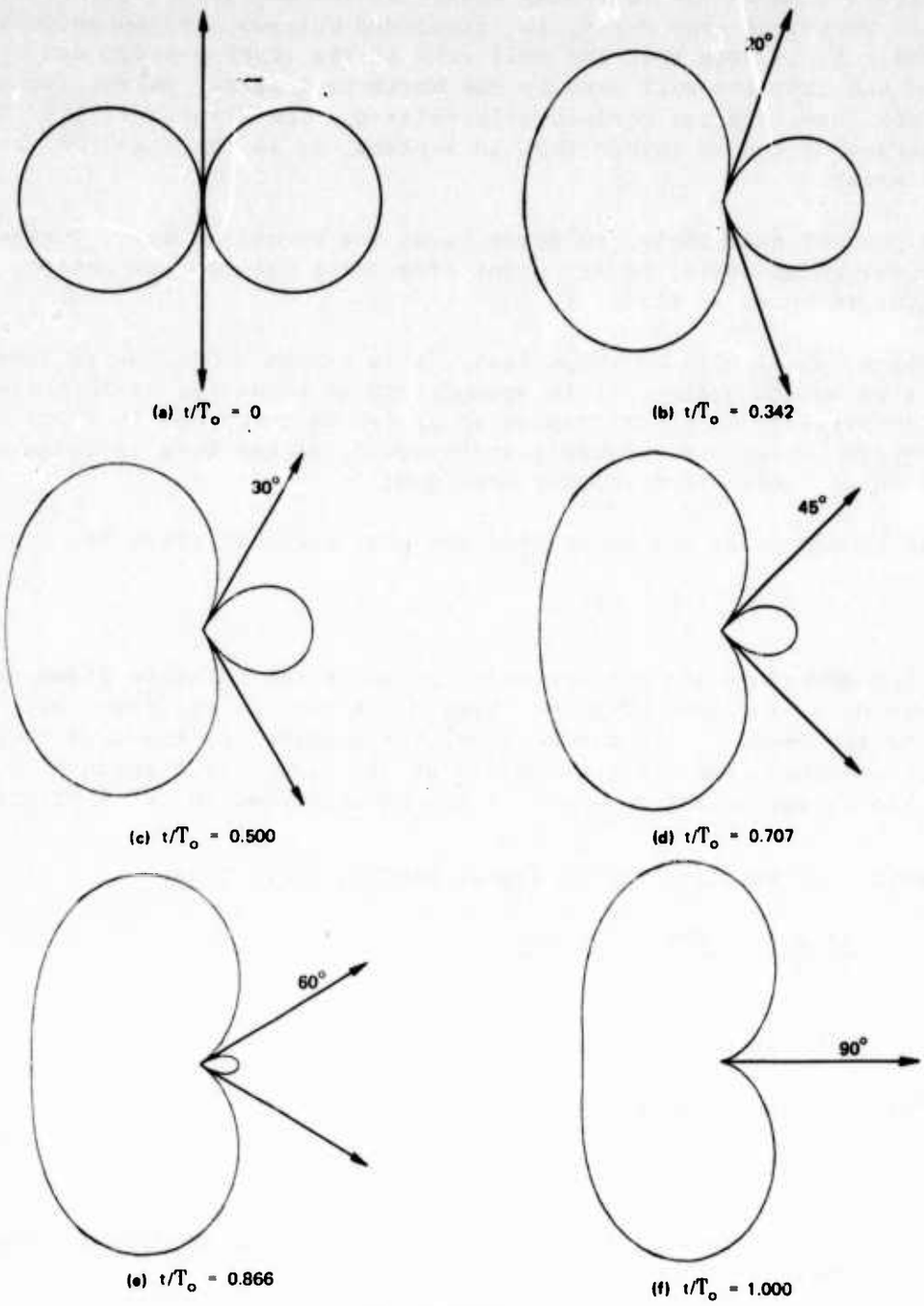

$$R = \sqrt{2}\sqrt{1 - \cos\psi}$$

where $\psi = 2\pi d/\lambda \sin\theta + \beta$

null angle occurs when $\theta = \sin^{-1} -\beta/2\pi\ \lambda/d = \sin^{-1} t/T_o$

TA-656531-1

FIGURE 1 ANTENNA PATTERNS FOR A TWO-ELEMENT ARRAY

Figure 1 shows the resulting change in the antenna patterns as a relative phase, or time delay, is introduced between the two antenna elements. It is seen that the null axis of the array pattern can be shifted and that the null axes in the horizontal plane, except for the boresight case, are not reciprocally related. The array null lies on the surface of a cone rather than in a plane, as is the case for the Adcock array.

A plot of null angle, referred to as the boresight axis, versus electrical phase angle, or different time delay between the antenna elements, is shown as Figure 2.

Since, as it will be shown later, this V-Scan technique is inherently a broadband system, it is appropriate to emphasize at this time that the performance of the V-Scan array can be described in terms of time delays, which are frequency-independent, rather than in terms of the RF phase, which is frequency-dependent.

On Figure 2, it was shown that the null angle is given by

$$\theta = \sin^{-1} \left(\frac{-\beta}{2\pi} \lambda/d\right)$$

where λ/d describes the antenna aperture and β the relative phase delay in terms of 2π radians. The aperture, d, in feet is approximately equal to the time, τ_o, in nanoseconds* for a signal to traverse the antenna aperture, and the time period at the signal wavelength λ is λ/c. Thus, λ/d is equivalent to $\frac{\lambda/c}{\tau_o}$. β can be expressed in terms of the time delay, t, relative to the signal period, λ/c. Thus,

$$\frac{-\beta}{2\pi} \frac{\lambda}{d} = - \frac{2\pi t}{2\pi \lambda/c} \cdot \frac{\lambda/c}{\tau_o} = - \frac{t}{\tau_o}$$

where c is the velocity of light.

The null angle becomes:

$$\theta = \sin^{-1} - \frac{t}{\tau_o}$$

where t is the differential time delay in the V-Scan RF circuit relative to the antenna aperture in nanoseconds.

The three-dimensional surface of constant differential time delay is a cone whose apex angle is 2θ.

---

* Actually 0.9836 foot per nanosecond.

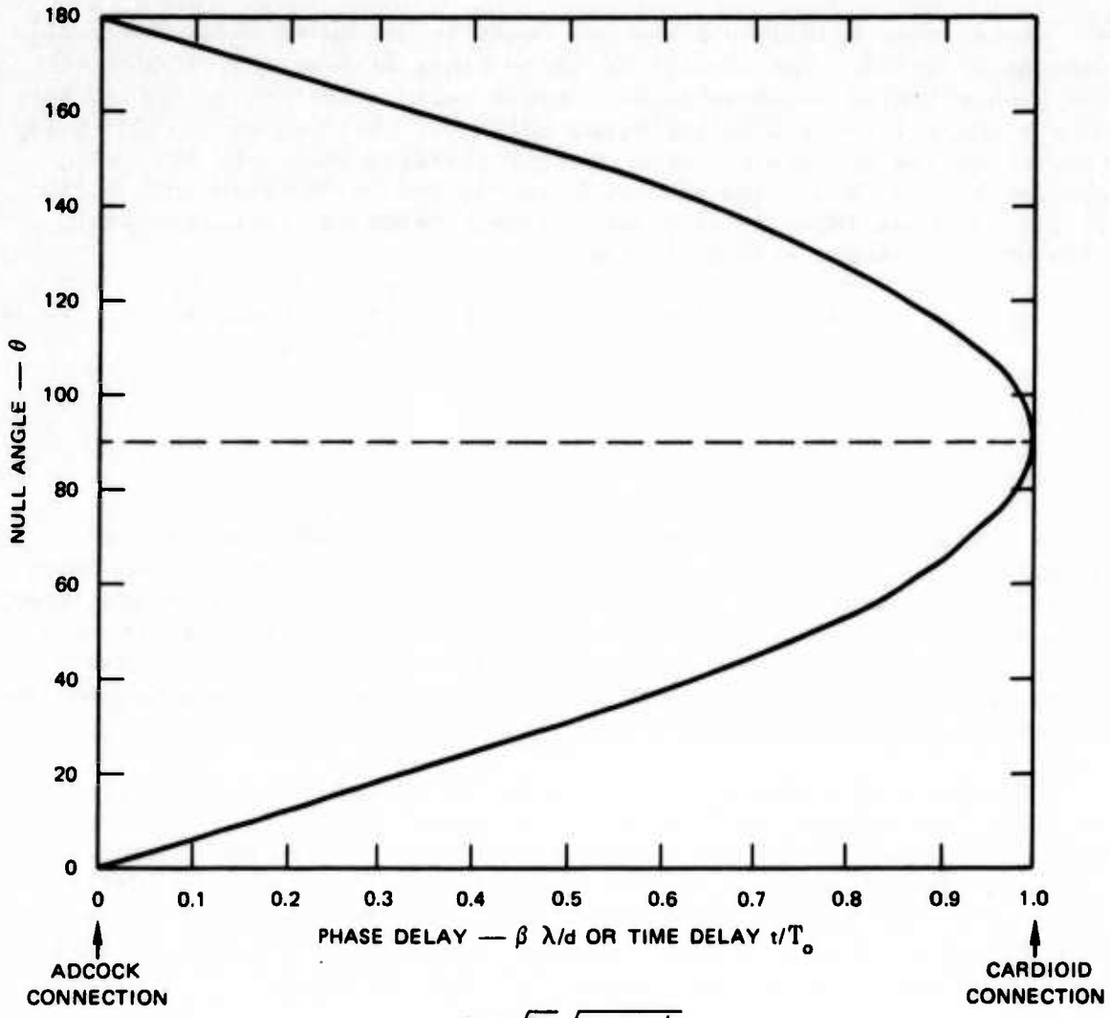

$$R = \sqrt{2}\sqrt{1 - \cos\psi}$$

where $\psi = 2\pi\ d/\lambda\ \sin\theta + \beta$

null will occur when $\psi = 0$

or

$$\theta = \sin^{-1} -\beta/2\pi\ \lambda/d = \sin^{-1}\ t/T_o$$

TA-656531-2

FIGURE 2 NULL ANGLE VERSUS PHASE OR TIME DELAY

III DESCRIPTION OF THE V-SCAN SYSTEM

Figure 3 shows a block diagram of a V-Scan system with an Adcock array aperture of τ_o. It is evident that the difference in the time of signal arrival at the two elements of the Adcock array is: $\Delta\tau = \tau_o \sin\theta$, where θ is the relative bearing of the signal with respect to the boresight axis of the antenna array.

Also shown in Figure 3 are two boxes to designate voltage-variable time delay lines. The details of these lines will be described later. The properties of these voltage-variable delay lines are such that they have a comparatively high insertion delay, τ, that can be changed a few percent by the application of a control voltage, v(t). If v(t) is applied to one delay line and -v(t) is applied to the other delay line, it can be shown that the time difference between the left and right side of the antenna system at time t is:

$$\Delta\tau = \left[t_o - \frac{\tau_o}{2} \sin\theta + \tau_i + \frac{\tau_o}{2} f(t)\right] - \left[t_o + \frac{\tau_o}{2} \sin\theta + \tau - \frac{\tau_o}{2} f(t)\right]$$

or

$$\Delta\tau = -\tau_o \sin\theta + \tau_o f(t).$$

Since the output of the Adcock array is the difference between two signals of equal amplitude, from each dipole, the result will be zero, or a null, when $\Delta\tau = 0$. Thus, if the output of the array, as amplified by a suitable RF radio receiver, is displayed on an oscilloscope as a function of the voltage used to control the voltage-variable delay lines, a null will occur on the oscilloscope sweep corresponding to the direction of signal arrival.

Figure 4 is a photograph of a complete V-Scan system constructed by SRI. The voltage-variable delay lines and sweep circuitry were built as a plug-in unit for a standard Hewlett-Packard Model 140 Oscilloscope. This V-Scan has an electronic cursor that can be manually adjusted to the notch in the V-Scan display by the bearing knob on the plug-in unit. A digital shaft encoder mechanically attached to this knob provides a digital data output for data recording.

A scan rate of 100 Hz was used as a matter of convenience. Higher scan rates may be used, provided that the receiver bandwidth is greater than approximately three times the scan frequency. This V-Scan system has operated with all types of signal modulation -- including SSB. However, it must be admitted that it is difficult to tune the receiver to an SSB signal.

The block on Figure 3 marked "Image Align" is a phase shift circuit for the 100-Hz sweep voltage to compensate for the time delay of the radio receiver. If the time delay through the 100-Hz sweep circuit is not equal to the time delay through the receiver, the forward and retrace images on the CRT will not be in alignment.

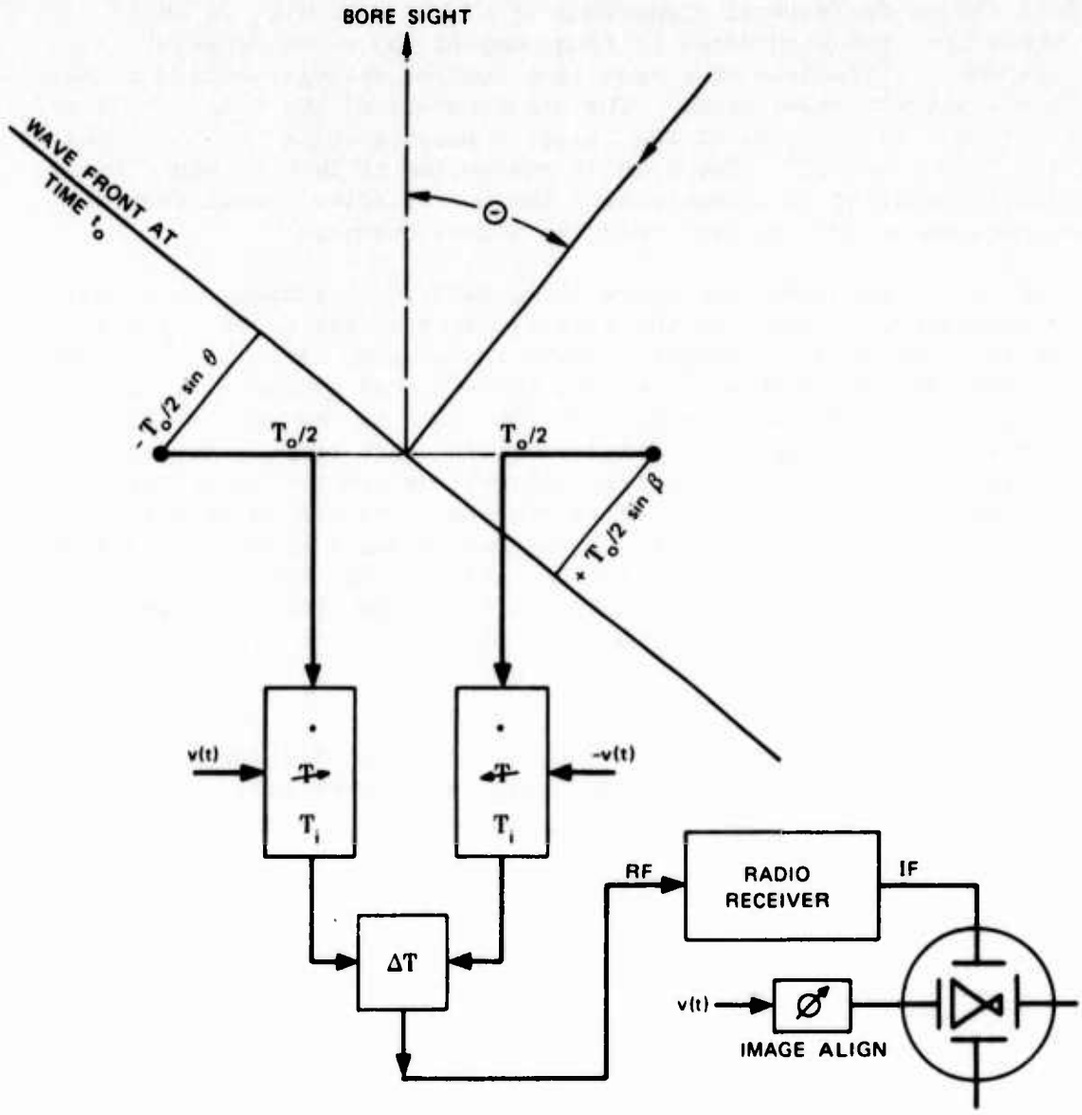

$$\Delta T = \left[t_o - \frac{T_o}{2} \sin\theta + T_i + \frac{T_o}{2} f(t) \right] - \left[t_o + \frac{T_o}{2} \sin\theta + T_i - \frac{T_o}{2} f(t) \right]$$

$$\Delta T = -T_o \sin\theta + T_o f(t)$$

NULL OCCURS WHEN $\Delta T = 0$ or $f(t) = \sin\theta$

*Voltage variable time delay line.

TA-656531-3

FIGURE 3 BLOCK DIAGRAM OF THE V-SCAN SYSTEM

IV THE V-SCAN PRESENTATION

Figure 5 shows oscilloscope presentations of the SRI-developed V-Scan system for several directions of signal arrival. In this presentation, the undetected IF frequency of the radio receiver is displayed as a function of a sine wave control voltage applied to the voltage-variable delay lines. The displacement of the V-Scan null is proportional to the sine of the relative bearing angle and is approximately linear to $\pm 45^{\circ}$. The angular resolution of this V-Scan display is nearly constant to approximately $\pm 60^{\circ}$ of relative signal bearing and degrades to zero at $\pm 90^{\circ}$ relative signal bearing.

It is to be noted that there is no left/right ambiguity in this V-Scan display. Signals to the left or right of the boresight axis are always correctly displayed. There is, however, a fore/aft ambiguity, since the time difference of arrival for a signal source at a particular bearing relative to the forward boresight axis is the same as that for a signal source at the same relative bearing with respect to the aft boresight axis. Since the bearing ambiguities are not reciprocal, but have a symmetry about $\pm 90^{\circ}$ relative bearing, they can be resolved. For example, by physically rotating the antenna a small amount, a forward relative bearing will move toward the center of the V-Scan display as the antenna array is rotated toward the indicated relative signal bearing. An aft relative bearing will move away from the center of the V-Scan display under the same conditions.

Since the V-Scan Indicator displays the time difference of signal arrival, the indicated bearing, θ_i, will be in error by:

$$\theta_i - \sin^{-1} \frac{\sin \theta_i}{\cos \psi}$$ where ψ is the vertical angle of signal arrival.

V THE V-SCAN BANDWIDTH

Assuming that the V-Scan is designed for a specific antenna spacing, or aperture size, the upper frequency limit can be described as the maximum signal frequency for which only one null will appear in the V-Scan display pattern.

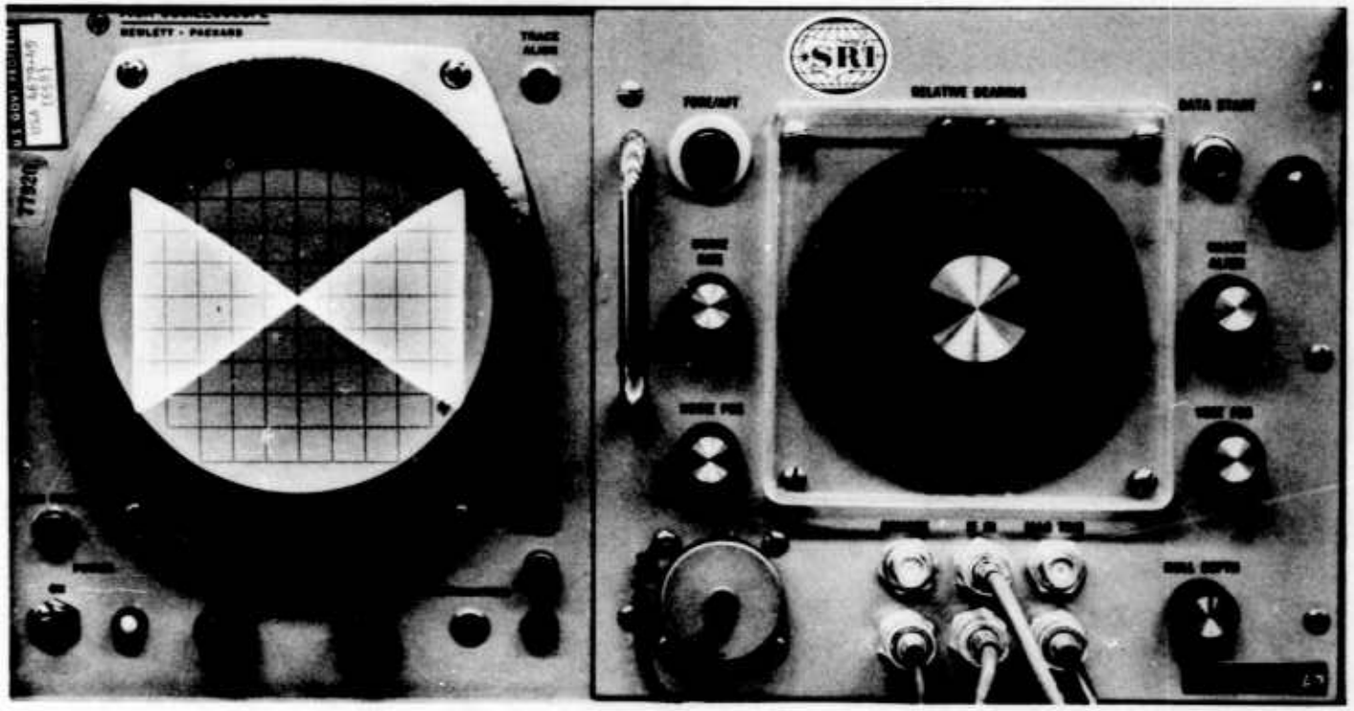

TA-656531-4

FIGURE 4 HP 140A OSCILLOSCOPE WITH SRI V-SCAN PLUG-IN UNIT

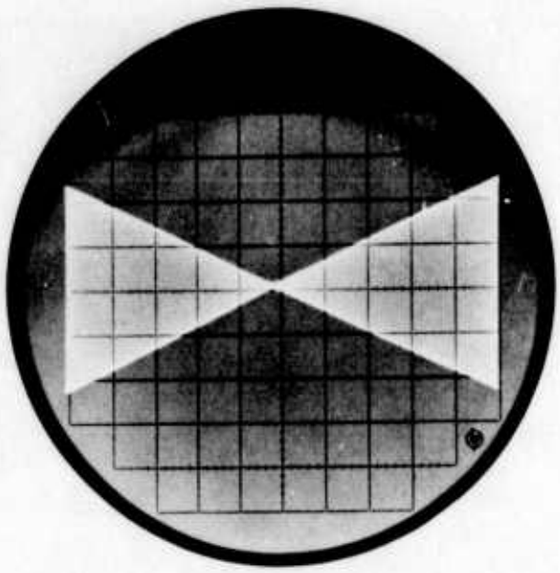

(a) BEARING APPROXIMATELY ON BORESIGHT

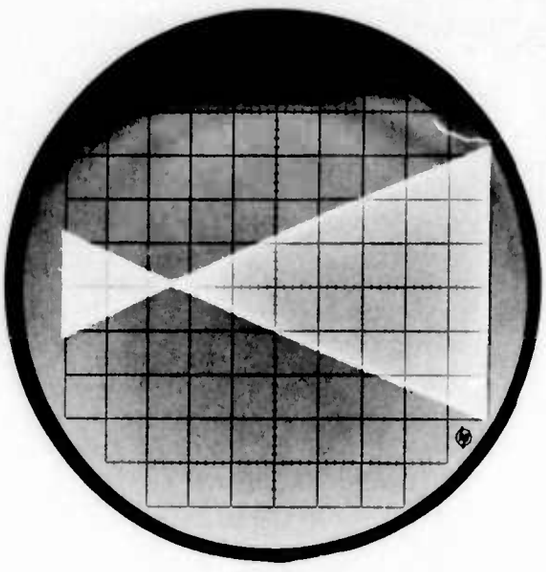

(b) BEARING APPROXIMATELY 30° LEFT

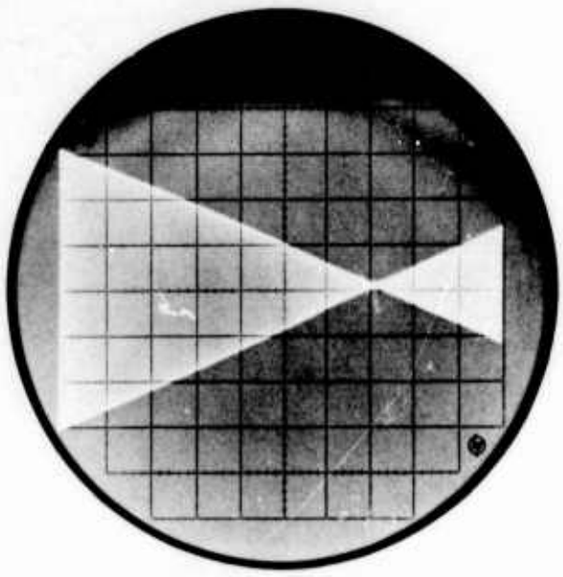

(c) BEARING APPROXIMATELY 30° RIGHT

TA-656531-5

FIGURE 5 TYPICAL V-SCAN PRESENTATIONS

This frequency corresponds to an aperture of $\lambda/2$ and may be calculated as:

$$f_h = \frac{492}{d} \text{ MHz, where d is in feet.}$$

A useful lower frequency limit for the V-Scan array is that for which the aperture is $\lambda/6$. At this point, the array gain is equal to the gain of one dipole. Below this frequency, the array gain decreases at a rate of 6 dB per octave of frequency. This lower frequency limit may be calculated as:

$$f_\ell = \frac{164}{d} \text{ MHz, where d is in feet.}$$

It is to be noted that these frequency limits give exactly a 3-to-1 bandwidth for the V-Scan. However, the V-Scan may be operated below f_ℓ with reduced signal sensitivity. It may also be operated above the upper frequency limit, f_h, if multiple nulls in the V-Scan display are accepted.

Since the voltage-variable delay lines are designed as a low-pass filter, it should be clear that these lines do not limit the low-frequency performance. It is the loss in sensitivity of the Adcock array that determines the lower limit. Exceptions to this statement are the problems of matching the antennas to the transmission lines and of using RF transformers to match the characteristic impedance of the delay lines.

SRI has constructed a series of V-Scan systems to operate over a frequency range of more than 50 to 1.

VI THE TRI-SCAN SYSTEM

The V-Scan direction finder described has a 360° azimuthal coverage. However, unlike direction finders such as the spinning goniometer with crossed Adcocks and the various circularly disposed antenna arrays, the angular resolution of the V-Scan is not uniform with azimuth angle. The V-Scan has excellent angular resolution to $\pm 60^\circ$, but the angular resolution degrades in the region of $\pm 60^\circ$ to $\pm 90^\circ$ relative signal bearing.

By the use of three antenna elements arranged on an equilateral triangle, it is possible to select one pair of these Adcock arrays such that a signal arriving from any azimuthal direction will not exceed a 60° relative bearing from the Adcock pair selected for that particular signal. Furthermore, by sequentially sampling the three Adcock pairs,

it is possible to resolve all ambiguities, without any need to rotate the antenna system.

The geometry for the Tri-Scan is shown in Figure 6. Again, since there are no mechanically moving parts in the V-Scan, or Tri-Scan, system, the scanning and antenna switching rates are limited only by the allowable bandwidth of the receiving system.

VII DESIGN OF THE VOLTAGE-VARIABLE DELAY LINES

The voltage-variable delay lines were initially designed as a constant-k low-pass filter using varicap diodes as the shunt capacitive elements. The characteristics of the back-biased varicap are such that they are nonconducting and that the diode junction capacity is a function of the bias voltage. Phase shift, or time delay, through this filter is a function of the ratio of the signal frequency to the cutoff frequency of the low-pass filter. The varicap bias determines the shunt capacity, which, in turn, determines both the cutoff frequency and the characteristic impedance of the filter.

For the varicap diode $C = k(v/4)^{\frac{1}{2}}$, where k is the value of the diode capacitance in picofarads for a back bias, v, of 4 volts. For small changes in bias voltage:

$$\frac{\Delta c}{c_0} \approx \tfrac{1}{2} \frac{\Delta v}{v_0}$$

For the constant-k low-pass filter:

$$D = \sqrt{LC}, \qquad Z_0 = \sqrt{L/C}, \quad \text{and} \quad f_c = \frac{1}{\pi D}$$

It is evident that changing c will change the delay, the characteristic impedance of the line, and the cutoff frequency.

The incremental time delay with respect to the change in capacity is:

$$\frac{\Delta D}{D} = \sqrt{1 + \frac{\Delta C}{C}} - 1 \approx \frac{\Delta C}{2C} \approx 1/4 \frac{\Delta v}{v_0}$$

Similarly, the incremental impedance variation with respect to the change in capacity is.

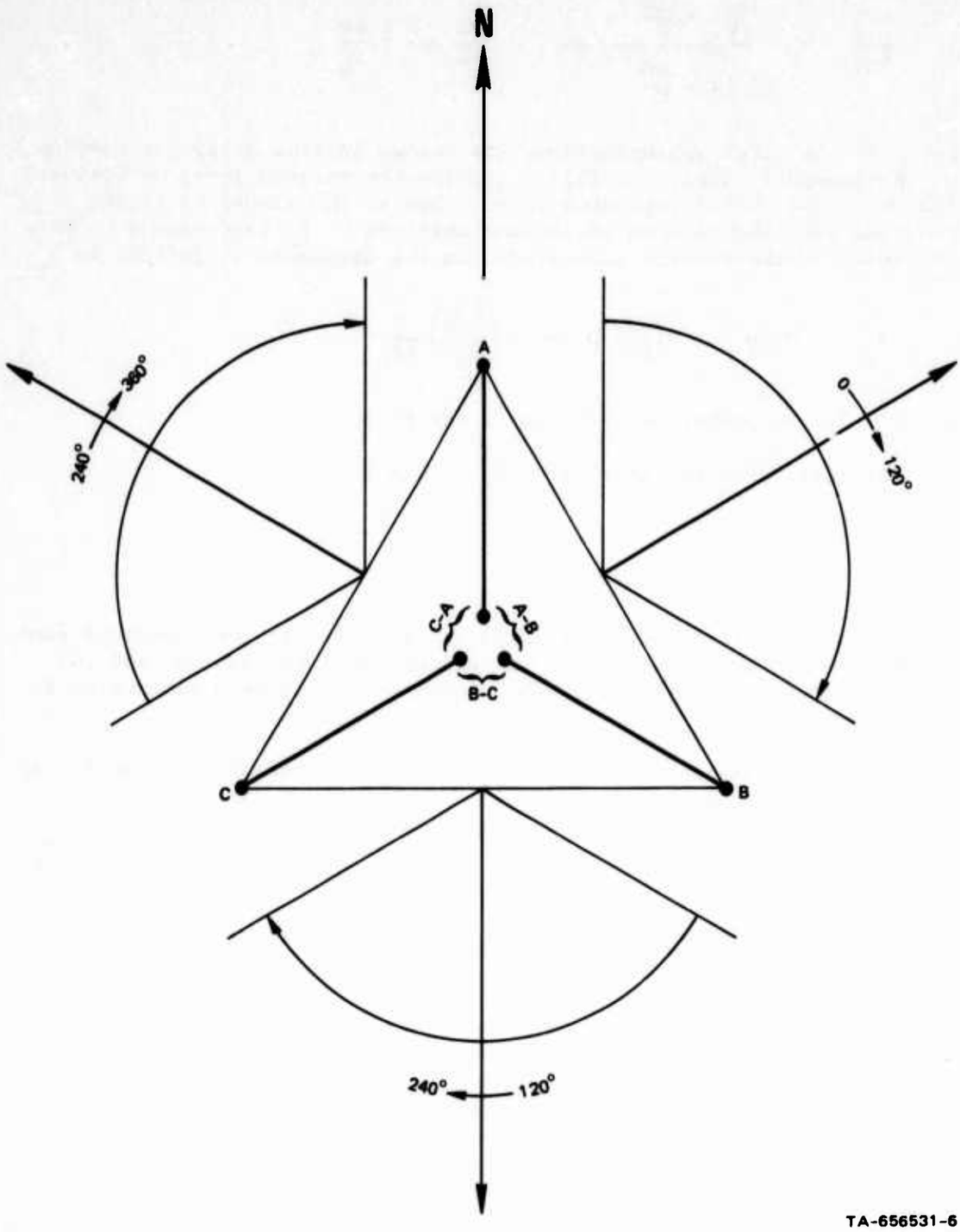

FIGURE 6 THE TRI-SCAN CONFIGURATION

$$\frac{\Delta Z_0}{Z_0} = \frac{\sqrt{1 + \frac{\Delta C}{C}} - 1}{\sqrt{1 + \frac{\Delta C}{C}}} = \frac{\Delta C}{2C} \approx \frac{1}{4} \frac{\Delta v}{v_0}$$

Thus, to the first approximation, the change in time delay per section of the low-pass constant-k filter is directly related to the allowable change in the filter impedance level. Hence, the number of filter sections required to scan an antenna aperture of T_0 nanoseconds is proportional to the restrictions placed on the allowable variations in Z_0.

$$T_0 = n \Delta D = n\left(\frac{\Delta D}{D}\right) D = n\left(\frac{\Delta Z_0}{Z_0}\right) \frac{1}{\pi f_c}$$

where n is the number of sections in the filter.

As will be shown later, $f_c = \frac{1}{\tau_o}$, thus:

$$n = \pi \frac{Z_0}{\Delta Z_0}$$

For example, 4π filter sections would be required if the impedance were allowed to change by 25 percent as the aperture was scanned, and 10π sections would be required if the impedance changes were restricted to 10 percent.

Although this simple, voltage-variable, constant-k low-pass filter network did serve to demonstrate the V-Scan concept, the oscilloscope calibration for relative signal bearing was found to be dependent upon the signal frequency. The reason for this is that the group delay,[1] D_g, for the constant-k filter is:

$$D_g = \frac{D}{(1 - (f/f_c)^2)^{\frac{1}{2}}}$$

Figure 7 is a plot illustrating the group time delay as a function of the signal frequency. Three curves are shown in this figure to indicate the time delays relative to the boresight condition. At some particular instant in time other than boresight, there will be a difference in delay, Δt, between the two delay lines, corresponding to the

---

[1] M. H. Hebb, C. W. Horton, and F. B. Jones, "On the Design of Networks for Constant Time Delay," J. Applied Physics, Vol. 20, p. 616 (June 1949).

sine of the null angle, θ. It is seen from Figure 7-A that this time difference, Δt, for the same instantaneous varicap bias is dependent upon the signal frequency. Thus, with the constant-k low-pass filter, the relative signal bearing calibration of the oscilloscope display will be dependent upon the signal frequency.

A digital computer program written for the CDC 6400 computer explored the frequency dependence of both a lattice and an m-derived filter. From the results of the computer calculations, it was decided that the m-derived low-pass filter with m = 1.27 and with terminating half sections of M = 0.6 should have a nearly constant differential time delay to approximately half the cutoff frequency. This is illustrated in Figure 7-B.

Careful construction of the m-derived delay lines has shown that an essentially constant calibration can be achieved over a 3-to-1 frequency range. The following expressions are useful to estimate the delay line parameters. Starting with the constant-k section:

$$L_k = \frac{Z_0}{\pi f_c} \quad \text{and} \quad C_k = \frac{1}{\pi f_c Z_0}$$

where f_c is the delay line cutoff frequency and Z_0 is the impedance level of the delay line. Since $f_c = 2f_h$, and f_h, the frequency for which the antenna aperture is one-half wavelength, is approximately

$$f_h \approx \frac{1}{2d} \quad \text{or} \quad f_c = \frac{1}{d} \ ,$$

where d is the antenna aperture in nanoseconds ($\approx$ feet),

$$L_k = \frac{Z_0 d}{\pi} \quad \text{and} \quad C_k = \frac{1}{\pi} \frac{d}{Z_0} \ . \quad \text{Thus,}$$

$L_k = 0.323\ dZ_0$ nanohenry and

$C_k = 323 \frac{d}{Z_0}$ picofarad, where Z_0 is in ohms and d is in feet.

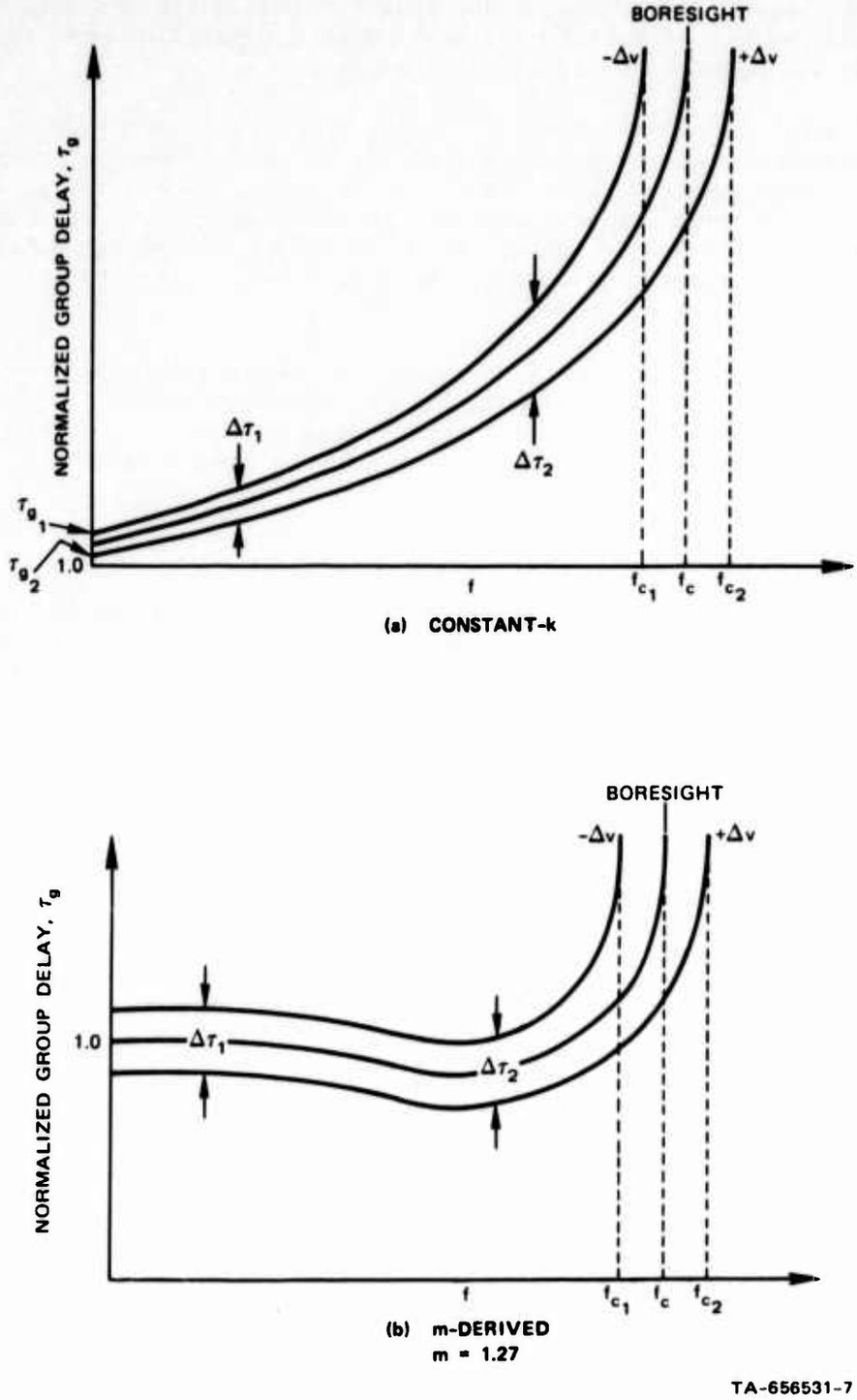

FIGURE 7 GROUP DELAY VERSUS SIGNAL FREQUENCY

For each of the m = 1.27 midsections:

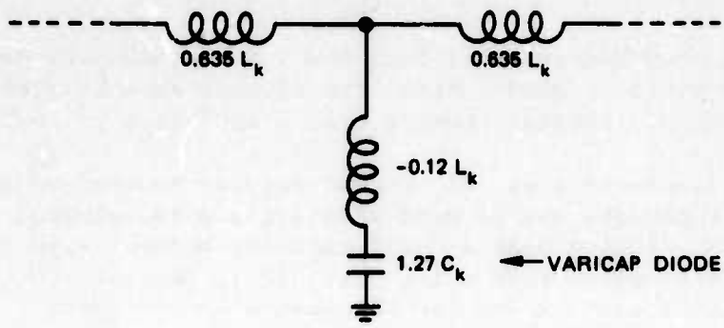

For the m = 0.6 half sections used at both ends of the delay line:

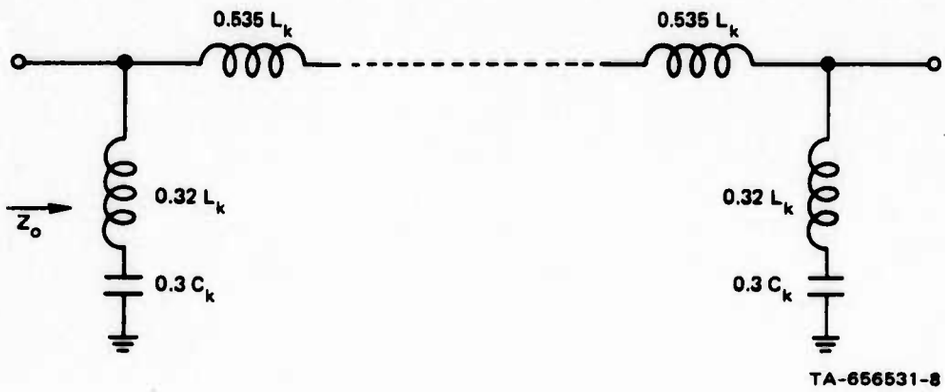

Note the varicap diodes are not used in the end sections.

Depending upon the cutoff frequency and the available varicap diode capacity, it is often necessary to design the varicap delay lines for a higher characteri tic impedance than the 50-ohm level usually used for coaxial line and to use broadband RF transformers at the input and output of the delay lines.

VIII CONCLUSIONS

It has been demonstrated that the V-Scan technique developed at SRI makes it possible to used a fixed two-element Adcock antenna array for rapid precision direction finding over a 120^{o} (i.e., $\pm 60^{o}$) sector.

It is concluded that, if reduced angular resolution is acceptable, the V-Scan technique may be used with a fixed two-element Adcock array for direction finding over a $\pm 90^{o}$ azimuth sector. With the addition of a third element to form a Tri-Scan, it is possible to cover 360^{o} azimuth without reduced angular resolution or ambiguity.

It is also concluded that, as a result of the high angular scan rates possible with the SRI V-Scan technique, the V-Scan may have application to the investigation of multipath radio propagation.

RELATIVE PERFORMANCE OF SMALL-APERTURE HF/DF SYSTEMS

L. Scott
Supporting Developments Technical Area
Electronic Warfare Laboratory
United States Army Electronics Command
Fort Monmouth, New Jersey

May 1971

ABSTRACT

The relative performance of several current rotating small-aperture high frequency direction finding systems are compared. The aperture size of these systems is much less than one tenth of a wavelength. Systems discussed are the simple loop, tiltable rotating vertical loop, coaxial spaced loop, and the short-baseline vertical dipole interferometer. The frequency range of interest is 2-20 MHz with major emphasis given to the 4-10 MHz range. Relative performance characteristics of interest are: (1) aperture size and compactness; (2) sensitivity; (3) method of bearing determination; (4) bearing sensing; (5) elevation angle determination; (6) environmental susceptibility; (7) modulation tolerance; (8) bearing accuracy and dispersion. Comparison is based on the use of the latest techniques in antenna design and signal processing. Relative performance test data from these small-aperture DF systems for ground-wave, sky-wave, and combination ground and sky-wave signals is discussed.

RELATIVE PERFORMANCE OF SMALL-APERTURE HF/DF SYSTEMS

I. BACKGROUND AND INTRODUCTION

Radio direction finding has a long history of development and the technological problems associated with the various schemes that have been employed are well known and, in many cases, remain unsatisfactorily resolved.

A problem of major concern is the sensitivity of a vertical loop antenna or antenna array operating in the 2-20 MHz frequency range to downcoming waves which have a significant amount of horizontal polarization together with the consequent bearing errors which result therefrom. In fact, a 90° error in the indicated angle of arrival can result when such a downcoming wave dominates.

Wave interference or multipath errors have their sources entirely external to a loop antenna and are a source of bearing errors for all DF systems. The loop antenna is much more susceptible to wave interference errors because it is a small aperture device. Multimode signals which are incident to the loop are not only of comparable amplitude, but also arrive at different bearing angles. In addition, the relative phases between these modes are time-variable. The resultant of all these variations is a corrugated phase front whose pattern is changing as a function of time. Small-aperture DF systems, particularly the loop, follow every corrugation and shift of the equi-phase surface since the aperture size is too small for significant averaging across corrugations. It is even possible that large (±90°) bearing

errors can occur due to multipath effects even though no horizontal components exist in the incident field.

During unstable propagating conditions the relative strength of the ground and sky-wave may vary greatly. The ground-wave and sky-wave combine to produce a time-variable elliptically polarized field with the major axis which is also a time-variable, neither vertically nor horizontally polarized. These variations cause a noise-like time variation of the indicated angle of arrival of a signal. The signal at the bearing indicator is further contaminated due to a stochastic rotation of the polarization of the sky-wave originating with variations in the ionospheric plasma. Typically, this "indicator noise" degrades system performance considerably in terms of both psychological harassment of the operator and actual bearing error.

The virtues of small-aperture antenna systems, particularly the loop, for mobile or portable HF/DF systems seem to warrant one's "learning to live with its idiosyncrasies." However, in recent years several universities and research institutes, i.e., Southwest Research Institute and Georgia Institute of Technology, have contributed much toward the advancement of the state-of-the-art of small-aperture HF/DF systems. Georgia Institute of Technology, in particular, has been actively engaged in the development of new and improved HF/DF systems through work sponsored by the United States Army Electronics Command under Contract Nos. DA 28-043 AMC-01207(E), DAAB07-68-C0072, and DAAB07-70-C0261.

This paper discusses and presents the relative performance of several current rotating small-aperture HF/DF systems either developed by Georgia Institute of Technology or used by them as GFE for the

purpose of improving DF performance through the implementation of signal processing techniques.

II. SYSTEMS DISCUSSED

The systems which are discussed herein include the simple loop[1], tiltable rotating vertical loop[2,3,4], coaxial spaced loop[5,6], and the vertical dipole interferometer[7]. Tables I, II, and III list the operational features of those HF/DF systems developed by Georgia Institute of Technology, i.e., the simple loop, tiltable rotating vertical loop, and the vertical dipole interferometer, respectively.

TABLE I

Operational Features of Simple Loop Dual-Channel HF/DF System

ANTENNAS: 1. Vertical, One-Turn, Untuned Loop - 1 ft^2 area.
2. Whip - 5 ft, Vertical.

RECEIVERS: Tracked HQ-145s.

SIGNAL PROCESSING:

Null Display. Each null is displayed separately, i.e., for one loop scan, each null paints only one-half of the propeller pattern. (Most conventional DF displays generate a complete propeller pattern for each null).

Fade Crest Detection. Bearing error reduction by unblanking display when conditions are favorable for minimum bearing error. Three types of fade crest detection can be selected based on signal and fade conditions.

Swing Rate Discrimination (SRD). Error-reducing technique for time-varying polarization errors. Unblanks display at minimum time-rate-of-change of bearing swing.

BEARING INDICATOR DISPLAY: Variable-persistence, storage scope.

COMMENTS: Feasibility model only. SRD work lead to tilted loop concept.

TABLE II

Operational Features of
Tiltable Rotating Vertical Loop Dual-Channel HF/DF System

ANTENNA: 1. Tiltable, Rotating Vertical Loop (2.25 ft^2 area).
2. Vertical Probe (9 inches).

RECEIVER: Dual-Channel RACAL 6253B

SIGNAL PROCESSING:

Fade Crest Detection.

Clutter Reduction.
Clutter reduction to eliminate carrier on-off transitions on signals such as ICW and SSB which clutter scope.

Synchronous Detection.
Used to increase sensitivity and improve display characteristics such as propeller sharpness and dynamic range.

"Instantaneous", On-Line Sensing.
Synchronous detection provides for instantaneous direct, on-line, sensing.

Tilted Loop.
Delineates accurate from inaccurate bearings by creating asymmetry in erroneous bearings.

Elevation Angle Determination.
Tilted loop allows for measure of elevation angle based on change in display characteristics with loop tilted to or near the elevation angle.

DISPLAY: Variable-persistence, storage scope with display shaping and selectable modes for bearing shaping.

COMMENTS: Advanced feasibility model. Poor performance on combination groundwave/skywave conditions lead to consideration of the short-baseline vertical dipole interferometer for operation in the presence of these signal conditions.

TABLE III

Operational Features of
Short-Baseline Dual-Channel Vertical Dipole Interferometer HF/DF System

ANTENNA: Short-baseline ($d < 0.1\lambda$) spaced-vertical electrically-short dipoles. Ferrite-loading is used to reduce susceptibility to horizontal polarization and environment.

RECEIVER: Dual-Channel RACAL 6253B.

SIGNAL PROCESSING:

Σ and Δ Hybrid.
Interferometer output feeds RF hybrid to obtain Σ and Δ signals to operate signal processing features such as fade crest detection, clutter reduction, synchronous detection, etc.

Others.
This system uses some post-IF signal processing. Correlative real-time averaging has also been evaluated with this system.

DISPLAY: Averaging display feature added. Tilted loop features included.

The coaxial spaced loop systems whose performance characteristics are discussed herein are the AN/VRD-( ) and the High Speed Spinning Spaced Loop, both developed by Southwest Research Institute.

The AN/VRD-( ) consists of the following:

(1) Antenna: Short-baseline ($d < 0.1\lambda$) coaxial spaced loops. Loop elements are tunable and are 29 inches square. Rotation rate is 150 rpm.

(2) Receiver: R-1218

(3) Control Unit: Modified TRQ-23 Control Unit

(4) Azimuth Indicator: IP-926( )/VRQ

The High Speed Spinning Spaced Loop DF System consists of the following:

(1) Antenna: Short-baseline ($d < 0.1\lambda$) coaxial spaced loops. Rotation rate is 300RPM. It uses a radome.

(2) Receiver: R-390/URR

(3) Main System Control Unit

(4) Remote System Control Unit

(5) Azimuth Indicator.

The AN/PRD-5 direction finder listed in Table IV is man-portable and can be operated in either an aural or visual mode. The diameter of the loop antenna is 25 inches. Maximum antenna rotation rate is is 60 RPM. It consists of a loop antenna, vertical monopole sense antenna, control unit, receiver, and azimuth indicator.

III. RELATIVE PERFORMANCE CHARACTERISTICS OF INTEREST

The relative performance characteristics of interest are:

(1) Aperture size and compactness.

(2) Sensitivity.

(3) Bearing sensing.

(4) Method of bearing determination.

(5) Elevation angle determination.

(6) Environmental susceptibility.

(7) Modulation tolerance.

(8) Bearing accuracy and dispersion.

The frequency range of interest is 2-20 MHz with major emphasis on the 4-10 MHz range. Comparison is based on the use of the latest techniques in antenna design and signal processing. Comparisons for the vertical loop systems assume that either post-IF signal processing or the tilted loop technique is used for bearing error reduction. Without these techniques, simple loop performance is virtually useless

in the presence of sky-wave propagated signals.

System performance using synchronous and correlation detection is cited in many many instances.

Aperture Size and Compactness

The simple loop is the smallest and most compact, followed by the coaxial spaced loop and spaced dipole. Table IV compares the longest linear dimensions of the DF antenna systems being discussed.

TABLE IV

Comparison of Longest Linear Dimensions

HF/DF System	Longest Linear Dimension
AN/PRD-5	25 inches
Simple Loop	1 foot
Tiltable Loop	1 foot
AN/VRD-( ) Spaced Loop	5 feet
High Speed Spinning Spaced Loop	6 feet
Vertical Dipole Interferometer	6 feet

Since simple loop systems are more compact they are therefore rotatable at higher scan rates. Simple and spaced loop systems have been rotated as fast as 300 RPM. The High Speed Spinning Spaced Loop antenna system was designed to rotate at 400 RPM and is enclosed in a radome. The rotation rate of vertical dipole interferometer systems

is limited by cantilevering and rigidity of the vertical elements.

The aperture size of simple loops is limited by the requirement that the circumference not exceed a fraction of a wavelength at the highest operating frequency so as to prevent pattern break-up.

The aperture size of spaced elements can be larger - up to approximately $\frac{\lambda}{4}$ at the higher operating frequencies - and is basically limited by mechanical or physical size and rotation consideration.

Loop systems are also more amenable to further compactness by use of ferrite loading whereby the μ is increased, resulting in increased pickup and smaller aperture size.

Research and development relative to improvement in performance of electrically-short dipoles may, however, lead to spaced vertical dipole antenna systems that are physically smaller and more competitive aperture-wise.

Sensitivity

In general, systems using an interferometer mode have a lower sensitivity relative to a simple loop. This reduction in sensitivity is approximately $\frac{\pi d}{\lambda}$ where d is the baseline. However, this difference can be compensated for by increasing the effective height of the interferometer elements.

Relative sensitivity can be related to basic sensitivity for an elementary dipole and loop. The ratio of dipole pickup to loop pickup is $\frac{l}{2\pi N \frac{A}{\lambda}}$.

At a frequency or 10 MHz, for a 6 foot dipole and a single turn loop with an area of 1 square foot, the dipole pickup is approximately 20 dB higher than the loop pickup. This agrees fairly well with measured relative sensitivity.

In comparing the relative sensitivity of a spaced loop with a simple loop it is interesting to note that increasing the number of turns on a spaced loop is not very effective in increasing its sensitivity due to the fact that increasing the number of turns increases the mutual coupling between turns, thereby decreasing its Q and efficiency.

Spaced loops and spaced dipoles must be electrically matched on each side of the interferometer phase center for optimum response and balanced operation.

Signal processing (synchronous and correlation detection) increases sensitivity - synchronous detection by 8-10 dB; correlation detection by 25-30 dB.

Bearing Sensing

Simple loop systems require a separate sense antenna. This is no problem if dual-channel signal processing is being used because the sense antenna is the auxiliary antenna and sensing is instantaneous through the use of synchronous or correlation detection.

For spaced loop systems, two forms of ambiguity must be resolved, i.e., (1) the four-way pattern due to the presence of combination simple and spaced loop nulls; (2) the normal two-way ambiguity on the interferometer (spaced loop) nulls. In the former case, four-way

ambiguity resolution is accomplished by changing polarization characteristics. This is fine if the polarization is changing; otherwise, polarization hang-up may prevent resolution for a relatively long period of time.

For spaced dipole systems, sensing presents no problem if sum and difference RF signals can be obtained from the antenna array.

Through the use of synchronous and correlation detection, instantaneous sense is provided with all systems that are so implemented.

Method of Bearing Determination

For the simple loop, the bearing is related to the null in the loop antenna response pattern. The null response varies as a function of the polarization of the incident signal.

For the spaced loop or spaced dipole system, the bearing is related to the null in the array or interferometer response pattern. This null is relatively invariant as a function of signal polarization.

Elevation Angle Determination

The tiltable rotating vertical loop HF/DF system is the only one which can provide an estimate of the elevation angle. Exact performance has not yet been fully and quantitatively evaluated, however, its accuracy has been estimated to be $\pm 10^{\circ}$ over an elevation angle range of from $20\text{-}70^{\circ}$. This implies that an estimate of the angle of elevation can best be obtained at distances in the neighborhood of several hundred kilometers. Best performance has been obtained on one-hop transmissions which are dominated by polarization rotation. Performance is limited on greater than 70° elevation angle signals with low

signal to noise ratios because the sensitivity drops off as the cosine of the tilt angle.

Environmental Susceptibility

HF/DF systems using loop elements are less susceptible to near-field coupling due to the electrostatic shielding of the elements and can thus operate in more cluttered environs.

The susceptibility to near-field coupling with dipole interferometer systems has been significantly reduced through the use of ferrite loading on transmission lines to break up current coupling loops.

Modulation Tolerance

All mechanically rotated antenna systems are effected by interrupted carrier type transmissions such as OOK, SSB, FSK (wide band), etc. Antenna systems with both higher scan rate capability and improved bearing display stability (inherent in interferometer systems) are less effected.

The simple loop can possibly be scanned faster, but the bearing display will indicate increased fluctuation (wide dispersion).

One problem with spaced loop systems is the resolution of the four-way sense ambiguity. Interrupted carrier type transmissions make this ambiguity resolution more difficult.

Correlation detection is inherently modulation tolerant and is virtually unaffected by interrupted carrier type modulations.

Bearing Accuracy and Dispersion

Ground-Wave Only.

On vertically polarized ground-wave transmissions, all systems have essentially the same accuracy and are limited solely by local site effects.

Theoretically, on horizontally polarized ground-wave transmissions, none of the systems should have a response.

Practically, however, relatively large errors occur with simple loops while interferometer systems have small errors. Table V shows examples of bearing errors on vertically and horizontally polarized ground-wave transmissions.

TABLE V

Examples of Bearing Errors on Ground-wave Transmissions

HF/DF System	Bearing Error for Horizontal Polarization	Bearing Error for Vertical Polarization
Simple Loop	43°	±1°
Spaced Loops and Dipoles	±1°	±1°

Ground-Wave/Weak Sky-Wave.

Table VI shows typical data over 8-10 kilometer paths for vertically polarized ground-wave/weak sky-wave transmissions.

TABLE VI

Bearing Accuracy and Dispersion Over 8-10 Kilometer Paths for Vertically Polarized Ground-wave/Weak Sky-wave Transmissions

HF/DF SYSTEM	Bearing Accuracy	Bearing Dispersion
Simple Loop	±6°	7°
Vertical Dipole Interferometer (Instantaneous display)	±1°	3°
Vertical Dipole Interferometer (Correlation display)	±1°	1°

Table VI also indicates a 3:1 reduction in bearing dispersion through use of correlation detection.

Comparable Ground-Wave/Sky-Wave.

This combination together with the presence of severe multipath effects presents a worse case condition for HF/DF systems.

Interferometer systems are most often used under these conditions because their antenna response is such that the high elevation angle sky-wave component is rejected. Attempts are then made to DF on the weak vertical ground-wave component. The simple loop has only a uniform elevation angle rejection capability. Sky-wave rejection for the spaced loop, spaced dipole, and the spaced dipole using synchronous and correlation detection is a function of cos ϕ, $\cos^2 \phi$,

and $\cos^3 \delta$, respectively, where δ is the elevation angle.

It is, therefore, apparent that performance is best obtained with the Vertical Dipole Interferometer used with synchronous and correlation detection. Table VII shows typical data over a 22 kilometer path for vertically polarized combination ground and sky-wave components of comparable levels.

TABLE VII

Bearing Accuracy and Dispersion Over a 22 Kilometer Path for Vertically Polarized Comparable Level Combination Ground and Sky-wave Components

HF/DF System	Bearing Accuracy	Bearing Dispersion
Simple Loop (Instantaneous display)	Generally Unusable	
Simple Loop (Correlation display)	±4° (about 10% of the time)	±40° (at any given time)
Spaced Loop	4°	7°
Vertical Dipole Interferometer (Instantaneous display)	1°	8°
Vertical Dipole Interferometer (Correlation display)	1°	4°

High Angle Sky-Wave Only.

Due to the inherent interferometer mode rejection of high elevation angle sky-waves, the simple loop may show a slight advantage under these conditions.

With a good signal to noise ratio, and over a 126 kilometer path the Tiltable Rotating Vertical Loop DF System had a mean bearing error and standard deviation of approximately 1^{o} and 9^{o}, respectively.

With a poor signal to noise ratio, use of fade crest detection with the tiltable loop resulted in a mean bearing error and standard deviation of about 10^{o} and 14^{o}, respectively.

The vertical dipole interferometer has not yet been completely evaluated on its performance over several hundred kilometer paths.

Although, as has been previously stated, the simple loop may have an advantage over the interferometer in that it does not reject the sky-wave component, it suffers from polarization hang-up effects. As the polarization rotates due to the Faraday effect, its direction of rotation may reverse. Prior to its reversal, the polarization rotation may become stationary at some non-vertical orientation, thereby resulting in constant bearing error off-set which is not reducable by present antenna and signal processing techniques. This situation may exist for minutes. Usually the length of time of polarization hang-up is inversely proportional to the prevailing fade rate, i.e., the lower the fade rate, the longer the polarization hang-up.

Nothing is said about spaced loop system performance over this path as little performance data has been obtained.

Low Angle Sky-Wave Only.

At ranges exceeding several hundred miles, interferometer systems appear to have lower dispersion of bearing information than the simple loop. The accuracy, however, is about the same. Transmissions over

these ranges are usually dominated by multipath effects. The larger aperture of spaced element arrays may enable a slightly higher degree of aperture averaging. Table VIII shows the mean error and standard deviation of bearings over paths exceeding several hundred miles.

TABLE VIII

Mean Bearing Error and Standard Deviation Over Paths Exceeding Several Hundred Miles for Low-Angle Sky-Wave Transmissions

HF/DF System	No. Bearings	Mean Error	Standard Deviation
Simple Loop (Used with fade crest detection)	208	0.5°	5.6°
High Speed Spinning Spaced Loop	393	0.7°	3.2°
Vertical Dipole Interferometer (Correlation display)	257	0°	4°

Additional performance data for the High Speed Spinning Spaced Loop over paths exceeding several hundred miles is shown in Table IX.

On transmissions over these long paths, propagation path moding effects, i.e., steady off-path deviations, are a problem of serious concern with all small-aperture HF/DF systems. Perhaps, the reduced inaccuracy and increased dispersion at the lower elevation angles as noted in Table IX was due to the presence of larger moding effects.

TABLE IX

Mean Bearing Error and Standard Deviation for the High Speed Loop Over Paths Exceeding Several Hundred Miles

Distance	Sample Size	Mean Error	Standard Deviation
300-1000 miles	145	0.6°	2.8°
Greater than 1000 miles	232	0.9°	3.4°

IV. SUMMARY

It has been felt worthwhile to convey the general relative performance that has been observed on several current rotating small-aperture high frequency direction finding systems. All comparisons were based on the use of the latest techniques in antenna design and signal processing. The tiltable rotating vertical loop and the short-baseline vertical dipole interferometer were designed to enable better DF performance on ionospherically propagated signals. The signal techniques used, particularly synchronous and correlation detection, greatly improved small-aperture HF/DF performance.

The tiltable loop, spaced loop, and vertical dipole interferometer systems are rated relative to their performance under each of the performance characteristics of interest as shown in Table X.

The numbers relate to performance as follows: 1 - excellent; 2 - good; 3 - fair; 4 - poor; 5 - unusable.

TABLE X

Relative Rating of the Performance of the Tiltable Loop, Spaced Loop, and the Vertical Dipole Interferometer

Performance Characteristics	System		
	Tiltable Loop*	Spaced Loop	Vertical Dipole Interferometer*
Compactness	1	2	3
Rotation Rate	1	1	2
Sensitivity	1	2-3	1
Bearing Sensing	1	3	1
Method of Bearing Determination	2	1	1
Elevation Angle Determination	1	5	5
Environmental Susceptibility	1	1	3
Modulation Tolerance	1	3	1
Bearing Accuracy and Dispersion for:			
Ground-wave (Vertically Polarized)	1	1	1
Ground-wave (Horizontally Polarized)	4	1	1
Combination Ground and Sky-wave	4	2	1
High Angle Sky-wave	1	#	#
Low Angle Sky-wave	2	1	1

* Signal processing is used
\# More data required to assess performance

REFERENCES

(1) Jenkins, H. H., R. W. Moss, and L. Scott, "Error Reduction in HF Loop DF Systems," IEEE Transactions on Aerospace and Electronic Systems, Vol. AES-5, No. 3, May 1969, pp 468-498.

(2) Jenkins, H. H., R. W. Moss, and L. Scott, "The Tilted Loop - An Error Reduction Technique for Loop Direction Finders," IEEE Transactions on Aerospace and Electronic Systems, Vol. AES-5, No. 6, November 1969, pp 1005-1006.

(3) Jenkins, H. H. and R. W. Moss, "Tiltable Rotating Vertical Loop DF System," Georgia Institute of Technology, Atlanta, Georgia, Contract DAAB07-68-C0072, Annual Report, ECOM-0072-5, October 1969.

(4) Jenkins, H. H. and R. W. Moss, "Tiltable Rotating Vertical Loop DF System," Georgia Institute of Technology, Atlanta, Georgia, Contract DAAB07-68-C0072, Final Report, ECOM-0072-F, June 1970.

(5) Castles, M. P. and J. D. Moore, "Direction Finder Set AN/VRD-( )," Southwest Research Institute, San Antonio, Texas, Contract DAAB07-69-C0114, Report, ECOM-0114-IM-1, April 1970.

(6) Castles, M. P. and J. D. Moore, "High Speed Spinning Spaced Loop Direction Finder," Southwest Research Institute, San Antonio, Texas, Contract DAAB07-67-C0420, Final Report, ECOM-0420-F, September 1969.

(7) Jenkins, H. H., R. W. Moss, and C. S. Wilson, "Improved Small Aperture DF Systems," Georgia Institute of Technology, Atlanta, Georgia, Contract DAAB07-70-C0261, Report, ECOM-0261-1, October 1970.

THE CHANGING SCOPE OF RDF IN THE NAVY

Prepared by: Edward J. Kolb

Naval Security Group Command

Washington, D. C.

The Naval Security Group has been a mission oriented function of the U. S. Navy for over 30 years. A significant task associated with that mission has involved the art of Radio Direction Finding. Perhaps one would prefer to call DF a science but I am sure that many would argue that it is indeed also an art. The Navy today almost exclusively uses Radio Direction Finding as a step in the progress of deriving the (approximate) location of a target of interest (sometimes very approximate).

The birth of Radio Direction Finding in the U. S. Navy occurred around the 1920s. The domain of interest in this era was restricted to what we now know as the Medium Frequency Band. Though the 1930s the Navy expanded this effort into the High Frequency Band. Individual stations began experimenting with combining efforts to form nets. The geographic coverage was limited to the Atlantic Ocean area. During the early 1940s the Navy essentially abandoned the use of the Medium Frequency Band.

At the onset of World War II the Atlantic HF Net was ready to operate. A total of about 50 high frequency radio stations involving the United States, Canada and Britain were operating and many of these were tied together as nets. The Navy began Direction Finding Operations in the Pacific in the early part of the 1940s. The first known attempt of operational shipboard high frequency Direction Finding application was on a small aircraft carrier during World War II. The flash report was copied directly by HF radio to get the frequency of the desired signal. The ship took bearings with manually rotated loops. In less than one hour the ship received the fix generated by the shore system and fitted his bearing to that fix.

Time and frequency schedules were followed to track targets of interest on given hours of given days.

Experience during the war years enabled the development of a strong central net control which directed the efforts of the entire net. This net control did not necessarily participate in deriving a bearing. Smaller subnets were used to provide bearing information for fix computation. A crossed loop hand rotated antenna came into use and the Navy introduced the use of a Spinning Goniometer, a Collins DAB (2 matched receivers) was used with the crossed loop. Three rotating loop equipments with a 24 foot diameter were built and placed in operation: one each at Mare Island, Calif., Cheltenham, Maryland and at Wahiawa, Hawaii. These were mounted on gun turrets and weighted 20 tons. They were desigated CXK. They were of limited use in that they could not cope with signals of duration shorter than about 30 seconds. Antennas designated DT and DY were simi-portable tripod mounted Direction Finders also in use. The operator rotated the loops by hand.

Direction Finding and Position Fixing during World War II was essentially accomplished from fixed shore sites, except for the limited shipboard participation previously mentioned. Standard

shore equipment during this time was designated DAJ. The HF range was covered in four bands

L 1.5 to 3
M 3 to 7.5
N 7.5 to 15
O 15 to 32

Each band had its own receiver, Goniometer, RF distribution and 4 element fixed Adcock Antenna.

In the 1950s the DAJ was replaced with the GRD-6a: 2 band 8 element array, 2 to 8 MHZ and 8 to 32 MHZ. This became the standard in the HF modernization program of the early 50s. In the mid 50s Directed-Tuning was introduced wherein the net control broadcast digitally tuned the remote receiver. In 1959 plans were formulated to develop a highly automated world wide network of HFDF arrays known as the Navys BULLSEYE System.

The University of Illinois Electrical Engineering Department became the custodian of the United States first full scale circularly disposed antenna array commonly known as the "WULLENWEBER". This array is still offically the property of the U. S. Navy however historically the University has had complete authority to use this array and modify it or its terminal equipment as they desire.

Thus studies and tasks involving the use of this array may in fact be sponsored or financially supported by the other services, or organization - government or non-government.

As a consequency of this dedicated research effort of the University of Illinois and the Naval Research Laboratory, the Navy now has a highly automated world wide network of WULLENWEBER arrays capable of on-line HF monitoring and target position fixing. This system is virtually free of instrumental error and site error has been defined using satellite calibration. The only remaining error is caused by ionospheric misbehavior and that problem is the principal objective or our currently sponsored research.

Lets us consider now the significant aspects of technology that bear upon us in such a way that they are changing the scope of RDF in the U. S. Navy.

1. The compression of signals in the time domain is becoming a significant threat to the technology of acquiring, integrating and processing signals energy.

2. Techniques are being used which result in suppressed signals energy available at the intercept receiver due to low power used by the uncooperative transmitter. Thus propagations conditions are being used to optimum advantage to deny unintentional intercept.

3. The past 10 years has seen an "Explosive" population of signals in the HF band which is continually growing and compounding the problem of sorting signals of interest from the signal population.

4. Complex instrumentation is assuming a significant role in HF Direction Finding and Position Fixing. This enables one to transmit and receive over long distances and inhibit or avoid detection. Such techniques include modulation schemes which vary frequency, amplitude, band width, time associated with these variables or a combination of these.

5. The matured computer industry is making a significant contribution to the scope or RDF. Factors such as, large scale integration, molecular electronics etc., enable bulk reduction and increased memory size. The development of the dedicated computer and the mini computer is enabling terminal on-site computation. Computer to computer conversation mode, optical character recognition and computer language translation will have a definite bearing on our business in the coming decade.

6. Automatic techniques for energy detection and differentiation will assume a prime role in store, process and forwarding of critical information.

7. Techniques of sensing signals which has been merged with electromagnetic energy will be developed which will make total use of the as-received signal. Thus, frequency, phase, amplitude, time and variations of these variables will be included in the data bank of the 1975-80 RDF process.

When you couple these technological changes with the geopolitical changes you get a fair picture of what the ballgame is going to be in the 70s and possibly the 80s.

The geopolitcal problems confronting us include:

1. Continual pressure to return overseas base real estate to the host country to enable them free use of their land.

2. Continual pressure to abandon overseas bases to reduce overseas presence and thus reduce the U. S. military image.

3. Continual pressure to reduce operational expenses to enable the mission functions to be fulfilled with reduced financial support brought about by the international balance of payments.

Perhaps one should consider including the problem of adequate intercept of non NATO, CEATO, CENTO, OAS and alliance for progress nations as of prime concern however, intercept of many nations not belonging to these leagues can only effectively be accomplished by monitoring the ground wave. The growing evidence of limited wars increases the problem of space diversity for position fix triangulation from Navy shore sites. The need for intercept and position fix capability is a function of range and geopolitical climate. It is therefore incumbent that the Navy achieve a flexible mobile capability which can be dispatched and assigned to a geographic area of interest. There may be several systems available and the crisis situation involved would dictate which system should be deployed.

During most of the 30 years just discussed the requirements for Radio Direction Finding and Position fixing were clearly dictated by factors which were existant in this era. These factors include population, economics, politics and their inter-relationships. It should be clear that uniquely it is not these factors but rather the threat resulting from them that concerns the Navy. Today the threat resulting from these factors continues to be at the core of our requirements, however, the impact of the factors has much more significance.

The post war expansion in population has changed the geopolitical situation and this coupled with phenominal advances in technology has resulted in considerable change in the threat. Technological advances responsible for this change include such things as:

1. Energy Conversion which affects propulsion systems design and thus mobility.

2. Time Standards which affects synchronization.

3. Microminiaturization which affects packaging.

4. Computerization which affects information access.

We are now in an era which is characterized by these and many other technological advances. We must therefore build our competance around this 1970-1980-and-beyond technology.

The Navy's BULLSEYE System prides itself with the success of fixing targets at a range of 2 or 3 thousand miles with dependable accuracy. This was and continues to be the prime asset of the Navy Security Group. We can, however, no longer think of the range of concern of the Navy as limited to the span of the oceans. The Navy is becoming increasingly involved in surveillance problems associated with limited wars or restricted geography thus presenting short range and tactical direction finding problems to the vessels afloat and suggest a need for fixed portable operation.

I would like to challenge the research community to consider the comments I have made regarding the changing scope of RDF and the geopolitical trends and to project their role in the climate of these facts. Come forward and show us the way to meet technology of the future head on!

The statements expressed in this paper are those of the author and do not necessarily reflect official U. S. Navy Policy.

THE RADIOLOCATION RESEARCH AND THE PATRON

by

Edward J. Kolb
Naval Security Group Command
Washington, D. C.

The implied/stated objective of this conference is to bring together those principal United States researchers or representatives of those researchers who are dedicated to performing basic and/or applied research in High Frequency Ionospheric Radio Propagation as it affects the direction finding process. This is the forth such conference hosted by the University of Illinois, the first in 1959, the second in 1964, and the third in 1969. Attendees at these conferences have included representatives from:

Government

Industry

Universities

You will note that this conference is attended by representatives from:

Government

Industries

Universities

Non Profit Research Institutes

Attendees for the first conference numbered about 30. For the second, about 40, and the third 50. This conference numbers approximately 60. The point I wish to make is that through the decade one can see that those people instrumental in pushing the forefront of this technology number of the order of less than 100 and they represent about 15 organizations. (If one were to counter that the conference is by invitation only and we only invited 60 people, I would hasten to add that we carefully polled the "community" to assure that those invited were indeed a representative sample of the HFDF research population.)

The people in this room thus represent this country's expertise in HF radio propagation as applied to the direction finding problem.

This may not be exceptionally profound bit of information, but my intent is to lay a foundation for my following remarks.

I doubt that anyone here is completely immune to the pressure of austerity in his organization. We are all confronted with the problem of the threat of reduced financial support in the face of increasing expenses and growing

requirements. Managers of defense sponsored research must relate the research to a mission fulfillment. We refer to the work at hand as mission oriented basic research and now it must be mission oriented to qualify for Department of Defense sponsorship. If we look at the 50 or so attendees of this conference and consider the work they represent, it is likely that the Department of Defense would be found responsible for 90% or more of this sponsorship. This means that when the going gets rough and the sponsor has to tighten his purse strings every one of us are going to have to justify and rejustify the necessity to continue the work which has been discussed at this conference. Now we all know that our work is of the utmost importance. We are always convinced of that, but unfortunitely there are many people in the decision making heirarchy who are convinced of absolutely nothing. A simple stroke of their pen can mean disaster to our existance. It is, therefore, extremely important that steps are taken to assure, and reassure the research sponsors that the work is meaningful, is essential, has an overtone of mission utility, is progressing and can be structured in a systematic way. We may feel that these aspects are being fulfilled, but it is becomming increasingly necessary to assure that documentation formally supports what is frequently only in the minds of those associated with a program.

I recognize that this is not the basic obligation of most attendees of this conference. This is the job of the manager or the sponsor of the work being discussed. I would, however, urge that serious consideration be given to these remarks in the spirit in which they are offered. It will take the best efforts of all of us to enable us to ride through the trough of the "magnitude of support" cycle. I may be optimistic to call it a cycle. I can say with certainty, however, that Secretary of Defense, Melvin Laird, and Director of Defense Research and Development, Dr. John Foster, are vigorously working to expose the undesirable effects of reduced support for defense research in the face of the rapidly growing strength of our opposition.

My intent, therefore, is to foster an enhanced understanding between the sponsor and the researcher. I would hope that this will enable us to express in a logical way a necessity to continue our work and perhaps chart a course for the future. We all know that basic research, even mission oriented basic research, thrives best and yields greatest return under a program of unfettered endeavor. We are also well aware of the necessity to carry a dialog between the researcher and the sponsor just as the necessity to interface from researcher to researcher. It may be forever frustrating to have to discuss the details of our work with some people who don't understand all of these details or more important who don't fully appreciate the potential significance of the accomplishments. It is, however, the harsh facts of life, that those programs which are best documented, best organized and best justified are the ones that get approved. I guess the current appropriate buzz

phrase is, "the relevance of the work is an indication of the likelihood of sponsorship approval."

It should be noted that there is a rather high threshold associated with the support of this research. Program maintenance costs are so high that a large percentage of research support costs are consumed before we can begin to push the forefront of technology. This is the point I refer to as a threshold. There is also a critical "point" associated with this threshold. If we approach this critical point by reducing dollar support then we must begin to consider turning off the effort and going home. This critical point may be reached even though support runs into six fugures.

It is, therefore, essential that a concerted effort be made to stress the significance of continuity of support. It is further imperative that when a research endeavor is being proposed for initiation or proposed for continuation the long term (several fiscal years) aspects of the work be made as clear as can be envisioned by the principal investigation. As representatives of the research community we know very well of the "building block" aspects of unfolding technology. We experience the step wise progress ourselves. Most of the people in the management chain who sponsor our work are, however, far more mobile than research people. We are constantly "re-educating" the people that determine our future. For this reason it is most important that we have a champion of our cause who clearly sees where we are, where we are going, and possibly how we are going to get there. Unfortunately, it is not always possible to have such a champion, and therefore, we must do our best to serve in that capacity ourselves.

I have been thinking about just such matters and having spent over ten years as a researcher, before moving over into the area of managing researchers, has given me some unique insight into the work bench and slide rule side of the story.

I therefore want to pass along some of the philosophy which I have formulated with the hope that it may be applicable to bolster your justification for future research support.

I recently visited the FCC offices in Washington to pursue the question of what U. S. organizations uses the HF band. You may be interested to know that there are 28 official categories of organizations who are allotted segments of the HF spectrum. These 28 include Government, Industrial, Commercial Maritime, Civilian and Experimental.

Admittedly the allocations of frequencies implies that we are referring to transmitting frequencies when in fact our area of concern is more associated

with receiving. I must, however, use the U. S. High Frequency allocation to develop my logic.

Now that we have a pretty clear picture of who uses the HF spectrum, lets take a look at which of these users are concerned with direction finding. You may take exception to my breakout, but I would say the bulk of these users are:

> Government, including the services, National Security, and possibly Central Intelligence Agencies.

Of these users which ones need precision? Which need accuracy? Which are concerned with long range propagation? Which people are concerned with getting as much information as they can from intercepted electromagentic energy?

I don't think anyone in this room would argue with me that it is the DOD that needs this information. To be sure there are many ramifications of HF ionospheric propagation research that involve others, but by and large, those users are second order users. They use the principals of HFDF as a tool to achieve another primary objective. For this reason they cannot be expected to involve in sponsoring the research to push the state of the art in HFDF.

It is therefore my thesis that those DOD sponsors whose research has been discussed at this conference are the organizations who have the greatest need for the results of this research and therefore are most responsible to continue the financial support.

The facts should be evident then that if we are to expect research sponsorship to continue we must repeatedly express the relationship of this research to the mission of the sponsor.

I have carefully considered the relationship of the HFDF propagation research and the sponsorship of the Navy. My interpretation of this relationship is illustrated in the accompanying diagram. This is intended to depict the interplay of organizations, the subgoals and goals of the program, and the cyclic or feedback aspect of this structure.

The Navy derives requirements from Documents of the Joint Chiefs of Staff, Defense Intelligence Agency, Navy Operations Intelligence Reports, National Requirements, and Navy Fleet Commanders.

These requirements can take the form of "reacting" to a threat or of "acting" to thwart an envisioned threat.

RADIOLOCATION RESEARCH INTERRELATIONSHIPS

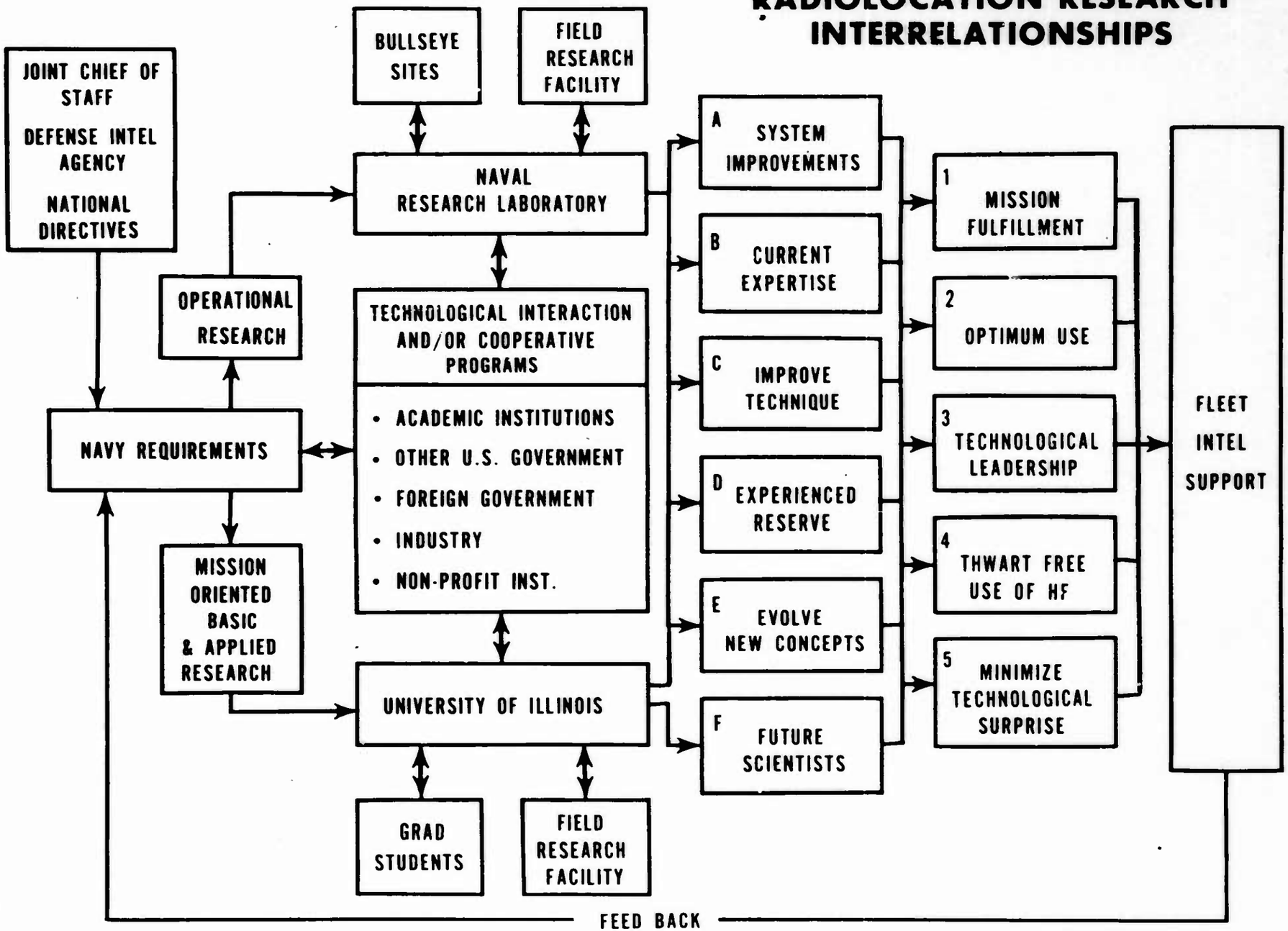

The requirements are reviewed for approval by the R&D office for the Chief of Naval Operations. He forwards approved requirements to the Chief of Naval Material who then assigns the requirement to the appropriate command responsible for the area of concern. This could be Naval Electronics Command, Naval Ship Systems Command, Naval Air Systems Command, etc.. The Command then proceeds to fulfill the requirement by issuing contracts or work requests to the Navy Laboratories or outside contractors. In the case of the ionospheric propagation work some support is channeled to the Naval Research Laboratory and some is channeled to the University of Illinois. We think of NRL as a resource for operationally oriented research and of the University as a resource for Mission Oriented Basic and Applied Research.

The Naval Research Laboratory has access to the Navy field sites throughout the world and can draw upon their operational data as well as task them to perform specific research exercises. The NRL also has their own field research site which is close to NRL and fully equipped for research on such problems.

The University of Illinois has preformed mission oriented basic and applied research for the Navy for over 20 years. This work is possible through the flow of graduate students guided by an excellent academic, research and administration staff and through the access to a unique field facility, terminal equipment and automatic data processing capability.

There is a high level of coupling between the University of Illinois and the Naval Research Laboratory and research people in both of these organizations, also interact with the people in other academic institutions, other U. S. Government organizations, Foreign Goverments, Industry, and nonprofit institutions. This interaction is accomplished by informal and formal meetings, cooperative synoptic data efforts and interpersonal relationships.

Some of the benefits of the research efforts of the University and the Naval Research Laboratory can be characterized by what one may consider as sub-goals. These are system improvement, current expertise, improved techniques, experience reserve, and new concepts. A further subgoal which must be credited to the University is the preparation of future scientists sensitive to the problems of radio location.

These subgoals, however, lead to the prime goals of:

> Mission fulfillment, achieve optimum use of a multimillion dollar investment, achieve and retain technological leadership to thwart the free use of HF and to minimize technological surprise.

These prime goals combine to provide the fleet with tactical and strategic intelligence support. One must then consider the essential aspect of feed-back which bridges the gap between the fleet operational use of the product of this research and identification of the Navy requirements.

I hope that this brief picture of the Navy-University relationship and this perspective of sponsorship justification can provide an insight into your needs in research management.

Thank you.

Thoughts expressed in this paper are those of the author and do not necessarily reflect official Navy endorsement.

References

Education and the Federal Laboratories; An assessment of Federal Laboratory Educational Activities and Their Present and Potential Relationships with Universities. Federal Council for Science and Technology Committee on Federal Laboratories, March 1968

Proceedings of a Sumposium on Education and Federal Laboratory, University Relationship, Federal Council for Science & Technology. American Council on Edication, October 29/31, 1968, U. S. Government Printing Office, $2.00

The Administration of Government Supported Research at Universities, Bureau of the Budget, Executive Office of the President, March 1966

Federal Support of Basic Research in Institutions of Higher Learning, National Academy of Science, 1964

Science Policy and the University, Edited by Harold Orlans, The Brookings Institution, 1968, $2.95

Fundamental Research and the Universities by Joseph Ben-David, Organization for Economic Cooperation and Development, Paris 1968, $1.50

Graduate Education - Parameters for Public Policy, National Science Board, U. S. Government Printing Office 1969, $1.25

The Physical Sciences, Chapter III, Section A, The Universities, National Science Board, 1970

Basic Research and National Goals, National Academy of Sciences, March 1965, $1.25

Government Contracting and Technological Change, Clarence H. Danhof, The Brookings Institution, 1968, $8.75

The Implications of President Johnson's Memo of September 13 and 14, 1965, for the Funding of Academic Research by Federal Agencies by James D. Carroll, Syracuse University, 1967

Defense Research and the University, Dr. William J. Price, Defense Industry Bulletin, July 1970

G. A. SMITH, W. M. SHERRILL, W. G. GUION

Southwest Research Institute, San Antonio, Texas

MODE ANGULAR WIDTH MEASUREMENTS

ABSTRACT

Estimates of propagation mode angular widths are given based on interferometric visibility function measurements. Baselines of 5, 50, 150, and 300 meters are used oriented perpendicular to the plane of incidence. A sum-and-difference phasemeter with CRT was instrumented to read out phase difference plus the antenna sum-and-difference amplitudes for each baseline. Sum-and-difference intensity ratios are interpreted by the visibility function for mode angular width. Measured phase variation with time provides a concurrent measure of apparent direction scintillation. Angular widths measured at frequencies less than 25 MHz show a variation from approximately 3° to $\ll 1°$ (unresolved at 20 λ, 300 m).

I. INTRODUCTION

In recent years the interferometer technique has been used to measure azimuth and elevation direction finding for single and multiple mode signals (1). However, HF interferometry may also be employed to estimate source angular width when the angle of arrival is assumed or known.

Eckersley's early interferometer measurements with a spaced loop interferometer and 20-meter spacing provided not only azimuth direction finding but also angular width measurements for F, E, and sporadic E observations (2) (3). More recently, Whale (4) and Hughes and Morris (5) have derived source angular width from coherence ratio measurements involving phase difference statistics for a single propagation mode.

A more direct approach to angular width measurement is described in this paper based on visibility function measurement from a sequence of four successively longer baselines with the assumption of a Gaussian source distribution. A concurrent oblique ionogram was used in all the measurements to provide independent verification of single mode propagation conditions at the observing frequency.

II. THEORETICAL BASIS

The source angular width parameter (ρ) conventionally represents the apparent angular radius of the source as seen by the receiver. The quantity (ρ) for a uniform circular source distribution is related to the fringe visibility (V) by (6)

$$V = \frac{I_{max} - I_{min}}{I_{max} + I_{min}} = \frac{J_1(2\pi\rho u)}{\pi\rho u}$$

where $u = d/\lambda \cos\phi \cos\psi$

d = interferometer spacing

J_1 = 1st order Bessel function of the first kind

ϕ = off boresite azimuth

ψ = elevation angle

I_{max} and I_{min} are the maximum and minimum intensities of the interference fringes respectively, obtained at the summed output (Σ) of two antennas. I_{max} occurs where $\phi = 0$, i.e., the waves are incident perpendicular to the baseline and the signals are in phase. I_{min} occurs when $2\pi u = \pi$, i.e., the two antenna outputs are 180° out of phase. For a fixed baseline array and constant angle of arrival ($\phi = 0$), $I_{max} = I_\Sigma$, the sum of the two antennas and $I_{min} = I_\Delta$ is the difference of the two signals. The fringe visibility becomes

$$V = \frac{I_\Sigma - I_\Delta}{I_\Sigma + I_\Delta}$$

For a fixed λ, ψ, and ρ, the visibility is only a function of the antenna spearation, d, while for the case $\rho = 0$ (point source), $V = 1$ is independent of d for all antenna separations. For $\rho \neq 0$, the visibility function behaves as shown in Figure 1 for various values of d/λ.

Using the sum-and-difference signal intensity, the visibility can be measured for various antenna separations. (In this experiment four different baseline lengths were used). When the visibility is plotted against d/λ for an estimated ψ, ρ is determined at the first zero of $J_1(X) = 3.8\ldots$ by fitting $J_1(2\pi\rho u)/\pi$ to the measured data.

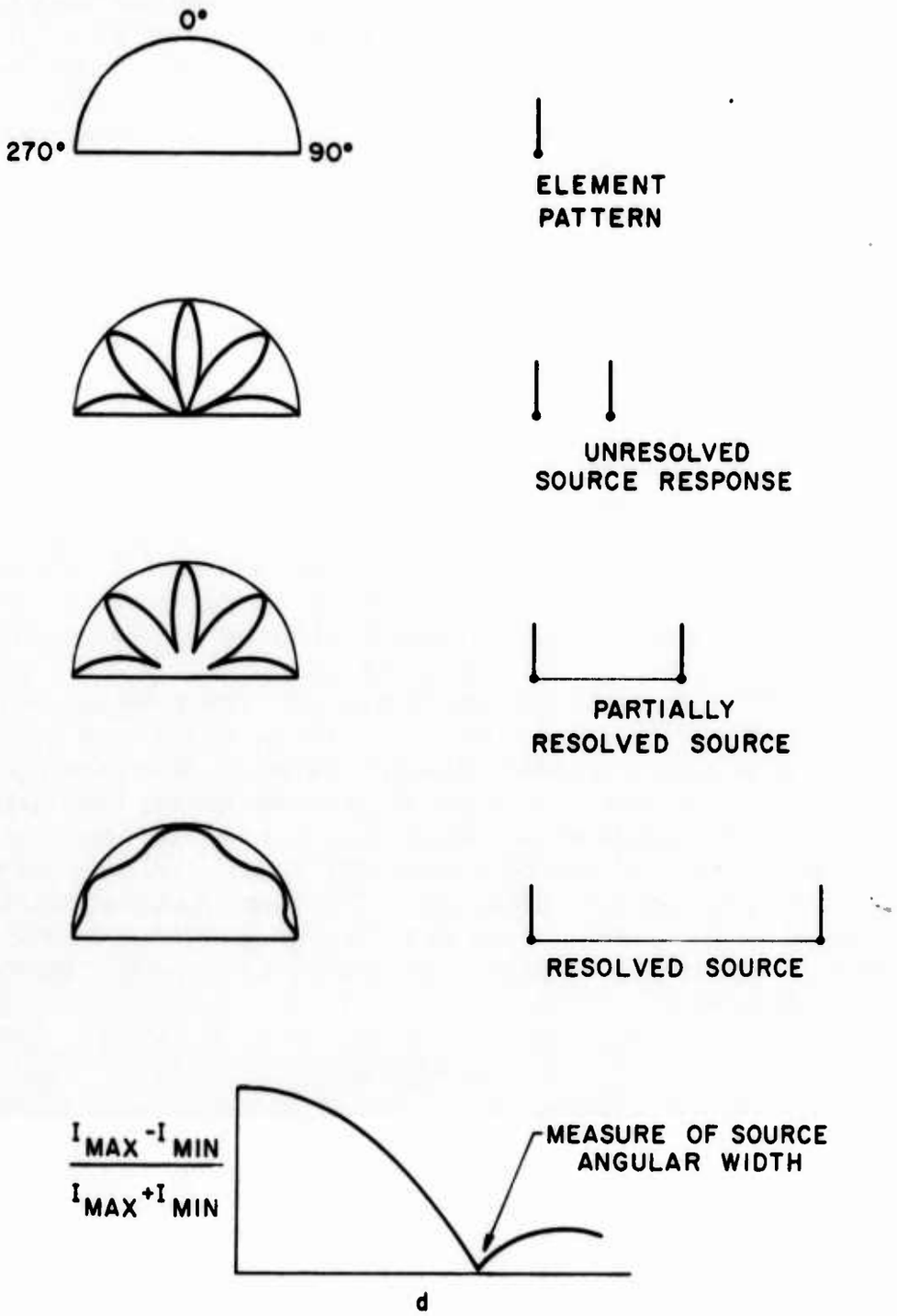

FIGURE 1. VISIBILITY FUNCTION

Since the above analysis is valid only for a single incident mode an oblique ionogran was taken concurrent with the angular width measurement. Observing frequencies were selected for single mode 1 hop or 2 hop paths. An ionogram obtained over a 2000 km path is shown in Figure 2. The regions of interest in this ionogram are the 1F region 12-20 MHz (low ray) and the 2F region 6-9 MHz where valid width measurements can be made.

III. INSTRUMENTATION

Figure 3 shows the array geometry. The colinear 5, 50, 100, and 300 meter baselines were oriented perpendicular to the plane of incidence for the propagation path of interest. The elements were vertical monopoles with one element used as reference. The quadrature fed crossed loop was placed in the array to provide a method of distinguishing polarization from wave interference fades utilizing the elliptical loop antenna axial ratio.

The system block diagram is shown in Figure 4. The five vertical antennas are fed to multicouplers where one output from each is fed through a R-390 receiver and the detected IF recorded on an oscillograph. The crossed loop is fed directly to a R-390 channel with a similar detected and record channel. The reference antenna and each of the four other antennas are fed in sequence to the IR-3 phase and gain matched triple channel receiver. The receiver sum-and-difference outputs are displayed on a cathode ray oscilloscope while the sum-and-difference amplitudes are also detected and recorded. The sum-and-difference CRT display indicates the phase difference between the antenna pair. The phase balance control on the receiver was instrumented with a DC potentiometer so that the operator adjusted for in-phase condition as a measure of the direction scintillation.

IV. RESULTS

Figure 5 shows a recording for a transmitter located in Greenville, North Carolina at 15.41 MHz. The ionogram (transmitter in Burlington, North Carolina) corresponding to this data was shown in Figure 2. At 15.4 MHz single mode, single hop propagation is observed. The increasing difference signal amplitude with increasing baseline shows a partially resolved source. The visibility function corresponding to the baseline sequence is shown in Figure 6 with the $J_1(2X)/X$ curve fitted corresponding to 0.86° radial width.

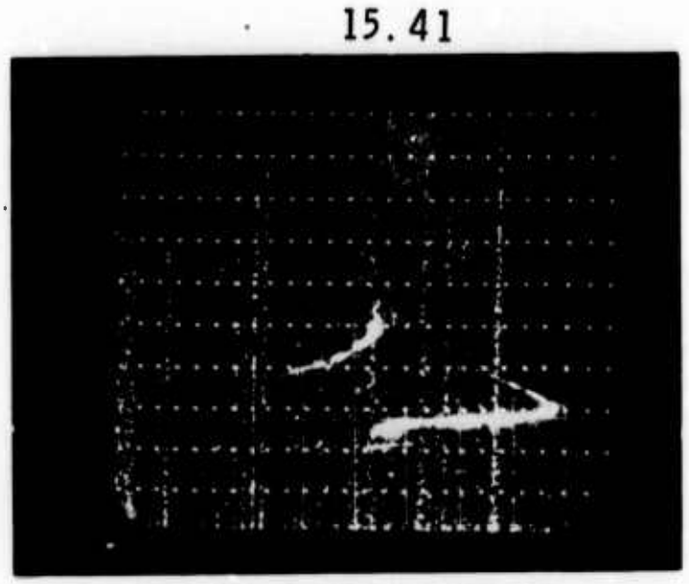

FIGURE 2. OBLIQUE IONOGRAM

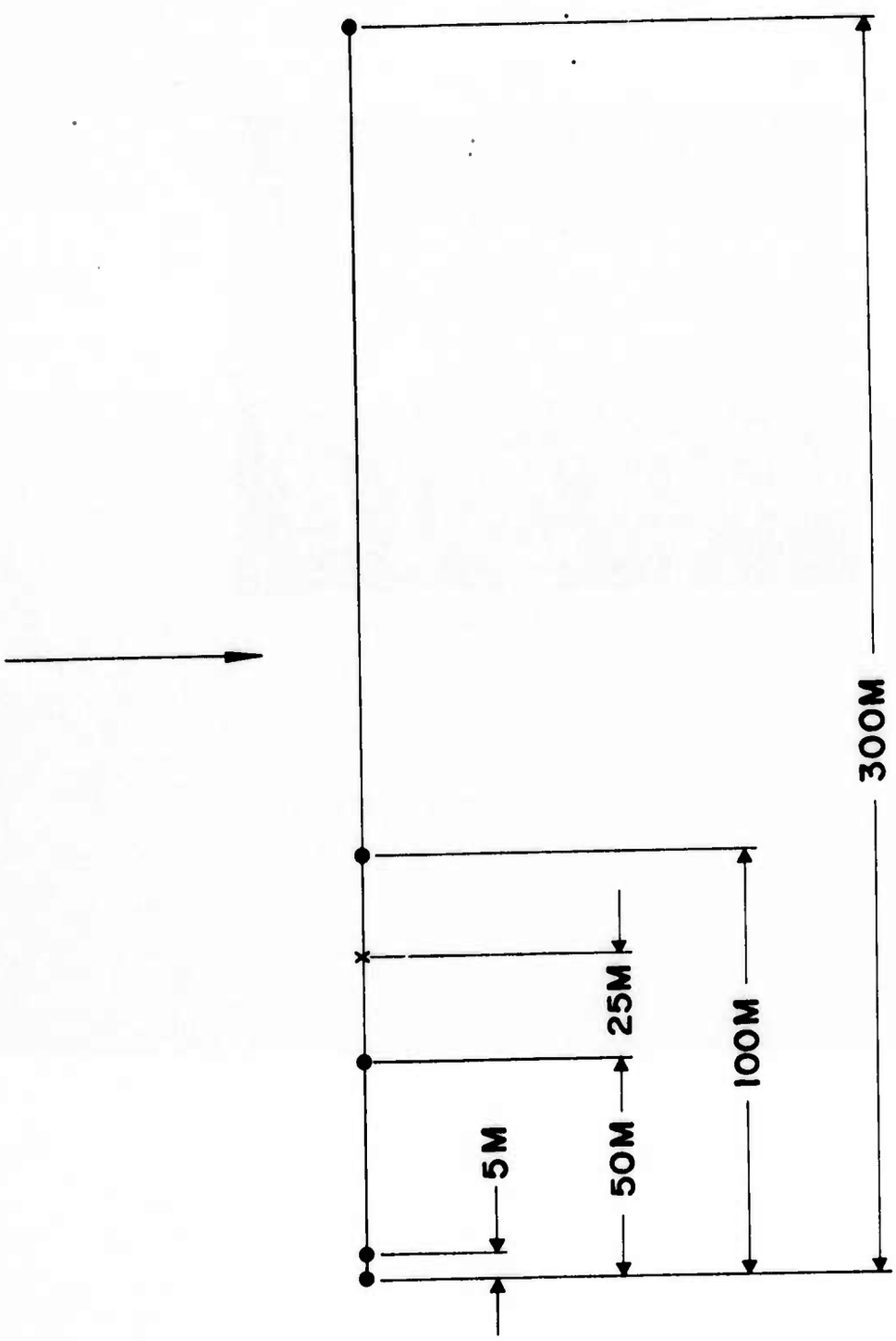

FIGURE 3. ANTENNA ARRAY SPACING

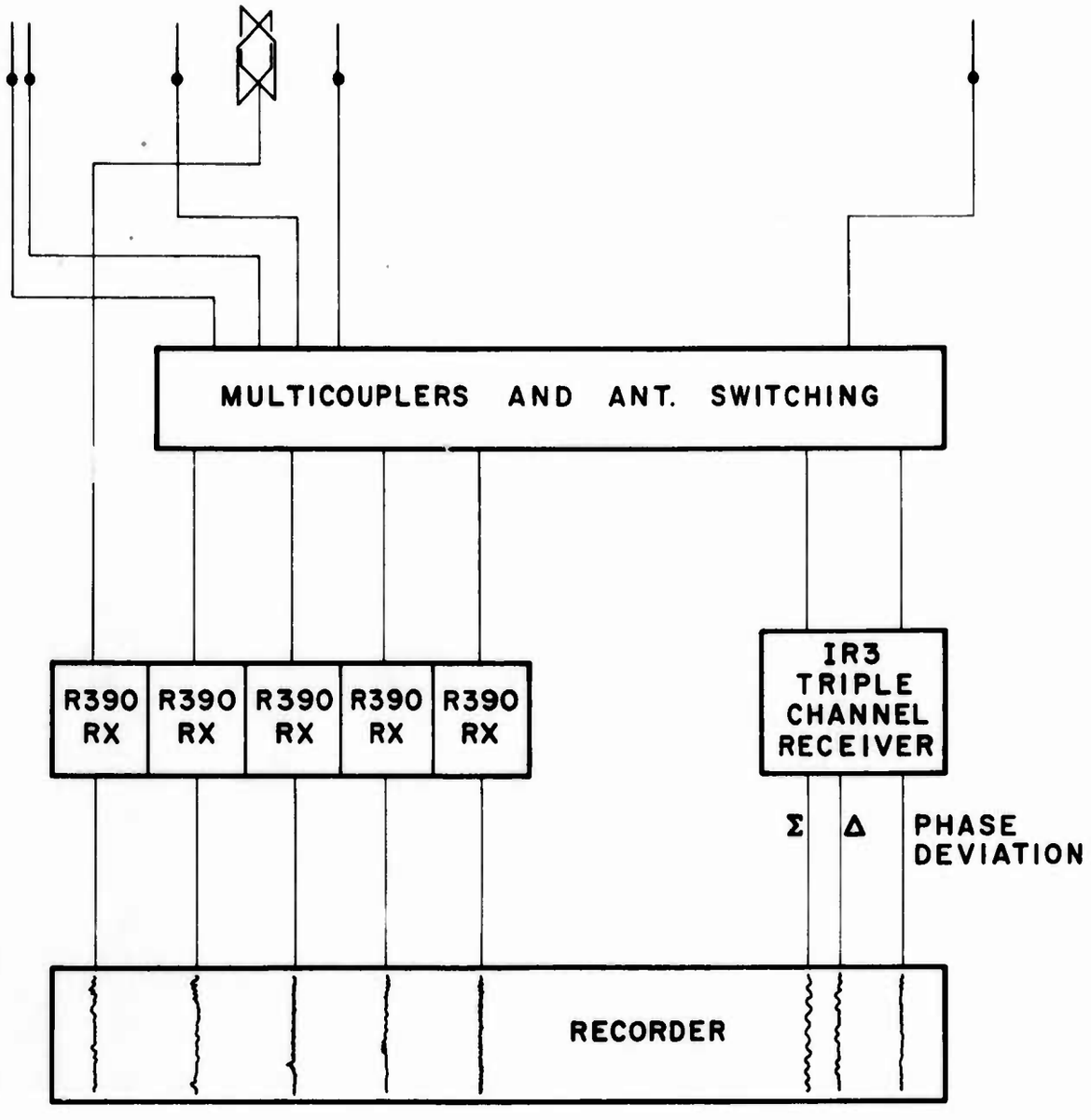

FIGURE 4. SYSTEM BLOCK DIAGRAM

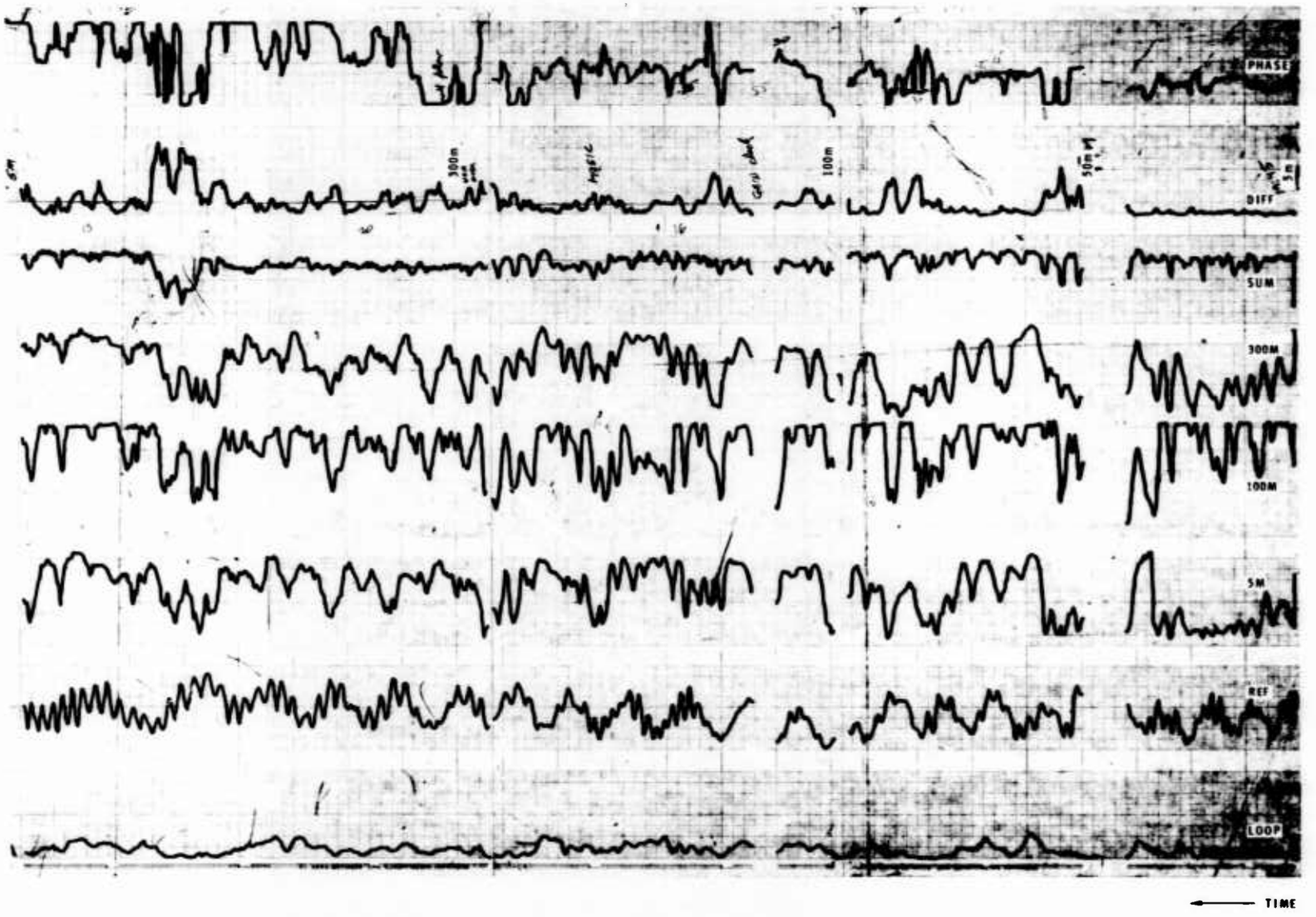

FIGURE 5. VOICE OF AMERICA--15.41 MHz

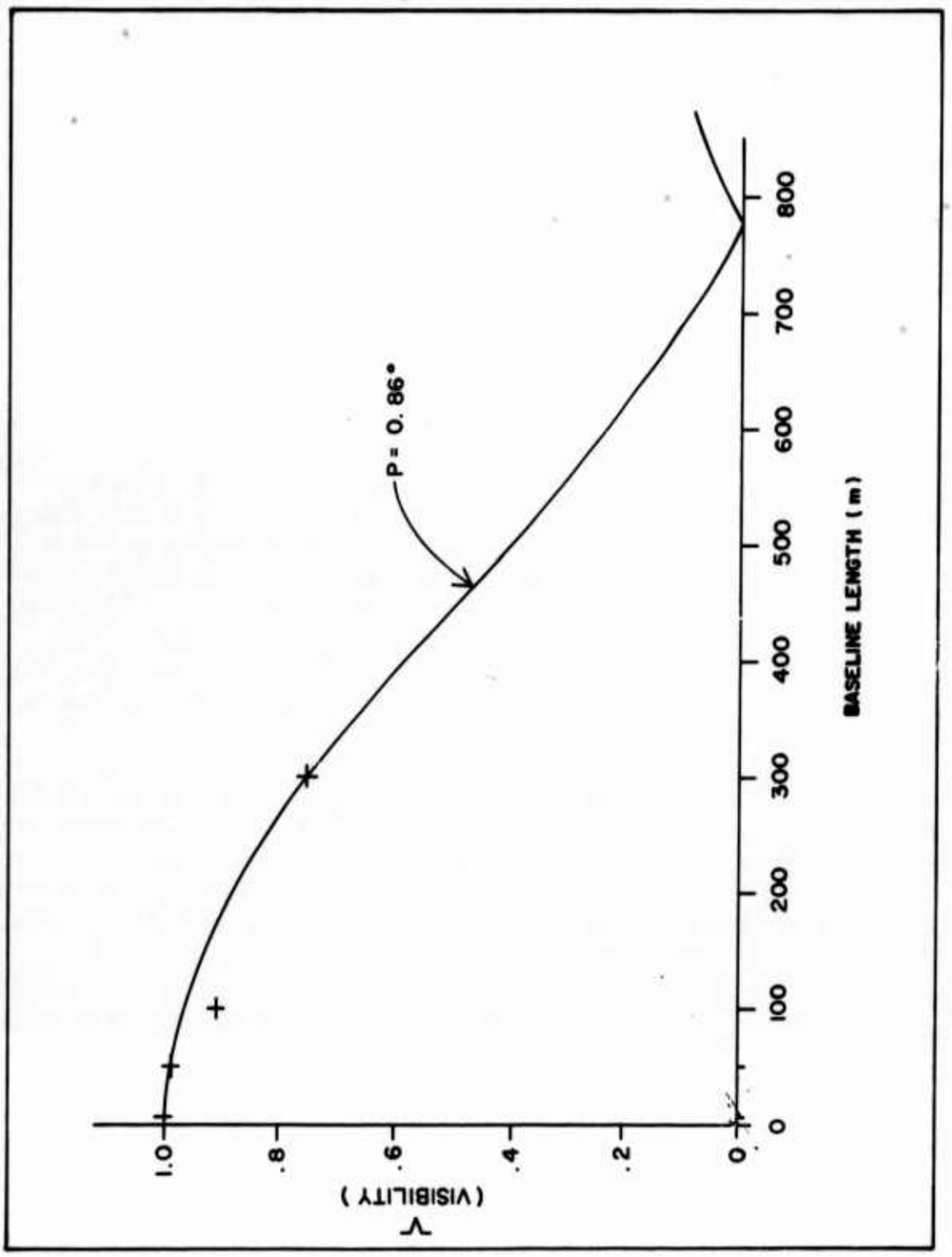

FIGURE 6. 1 Hop F VISIBILITY FUNCTION (15.41 MHz)

Figure 7 summarizes other transmission paths studied. The majority of the data reported herein was obtained on the Houston path. The Biloxi data for the hours observed showed negligible direction scintillations and unresolved angular width.

Figure 8 shows a family of oblique ionograms over the Houston path concurrent with angular width measurement. Single mode, single hop propagation paths were obtained from approximately 6 to 12.MHz. Figure 9 shows the width record taken at 12. 34 MHz corresponding to Figure 8d. The measurement was made near the X mode critical frequency and shows a very stable virtually single ray mode with no azimuth scintillation and unresolved angular width.

Figure 10 shows 8 MHz data indicating a very stable nonscintillating signal but a partially resolved angular width of the order of 2°. This large width parameter is partially affected by lack of precision in the 300 meter baseline for the 60° incident elevation angle.

Figure 8e shows an oblique ionogram indicating single hop, single mode propagation at 6. 25 MHz. Figure 11a shows the corresponding width data indicating an unresolved nonscintillating source. Approximately 5 minutes later the character of the fading changes (Figure 11b) and angular width plus scintillation occurs. The slow fade is attributed to polarization fading by comparing the vertical reference antenna amplitude to the crossed loop antenna. The fast fading, which is the same for both crossed loop and referenced antenna, is attributed to an interference fading.

Figures 8a through 8c show a sequence of ionograms taken from 9:35 a.m. to 10:30 a.m. with O and X mode critical frequency increasing with time. At the 9. 356 MHz observing frequency at 10:04 a.m. a single X mode is present, which changes to O plus X mode (1 hop F) as time increases. X mode and O mode critical frequencies are plotted vs time in Figure 12.

Figure 13a shows the width data with only X mode present. The angular width for this data is about . 5°. Notice also there are no scintillations. In Figure 13b a short time later, a cyclic oscillation in fading is seen and a resolved angular width of approximately 1° is obtained. At this time both O and X modes were present at the observing frequency.

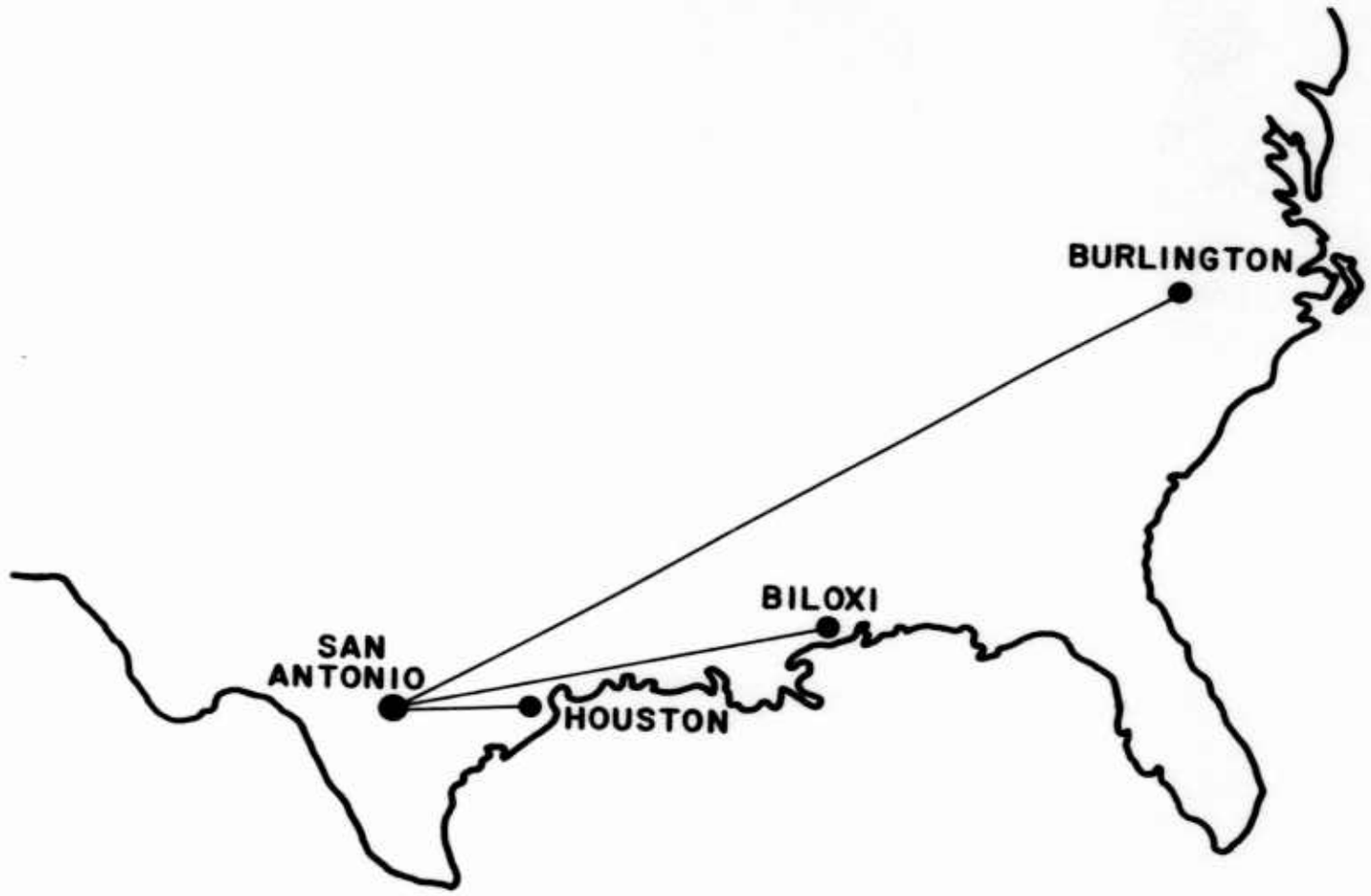

FIGURE 7. DATA TRANSMISSION MAP

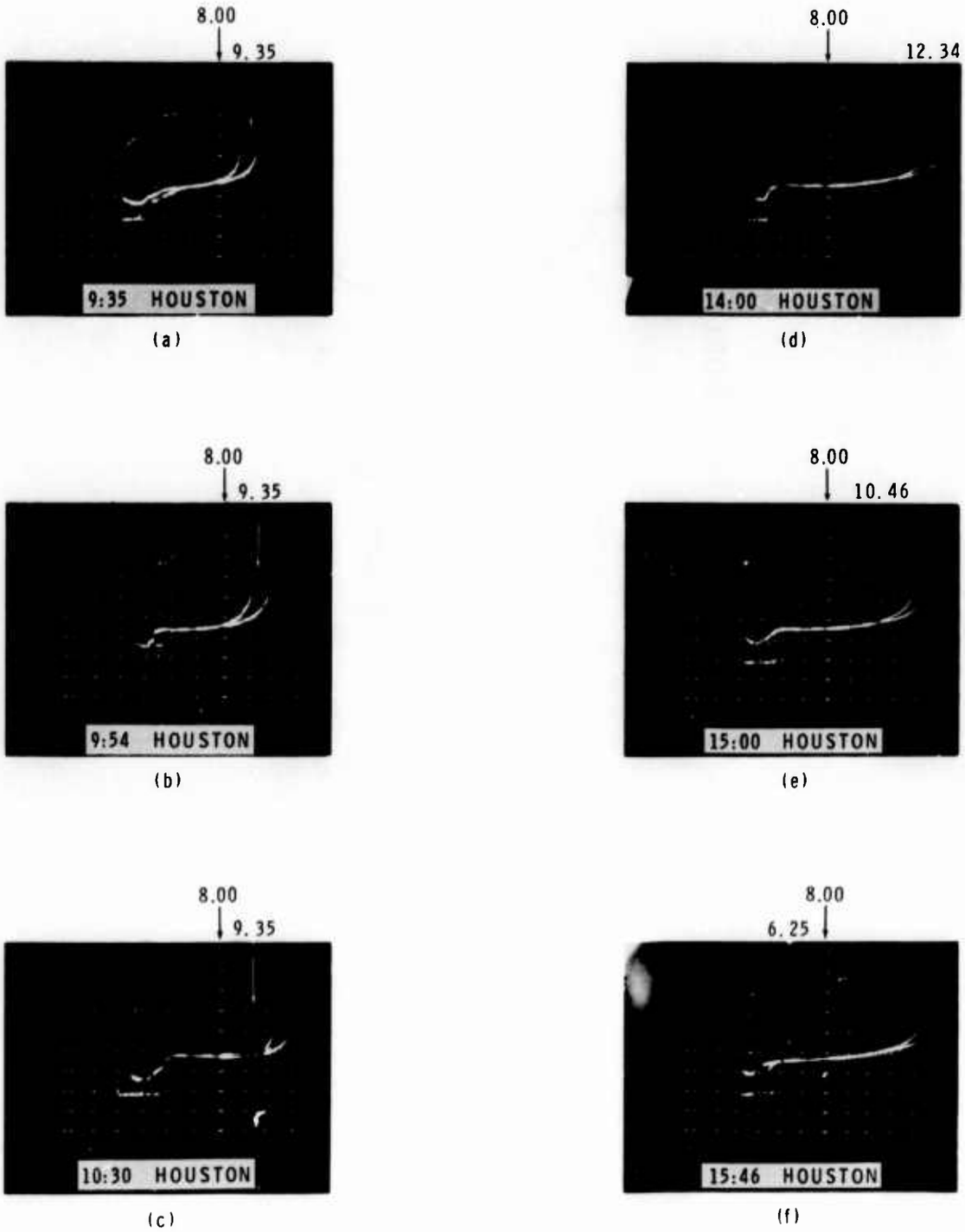

FIGURE 8. OBLIQUE IONOGRAMS

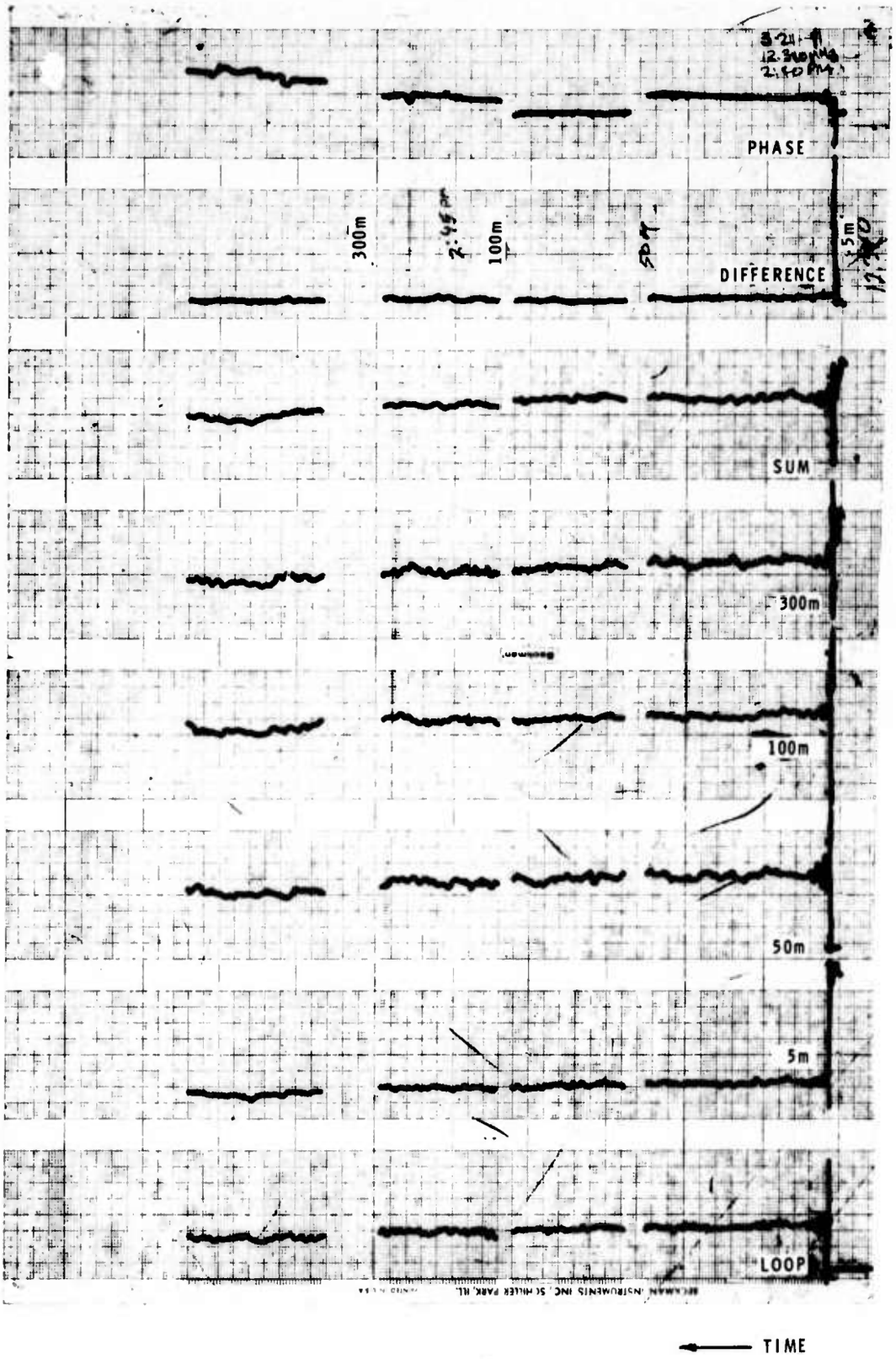

FIGURE 9. HOUSTON--12.340 MHz

FIGURE 10. HOUSTON--8.000 MHz

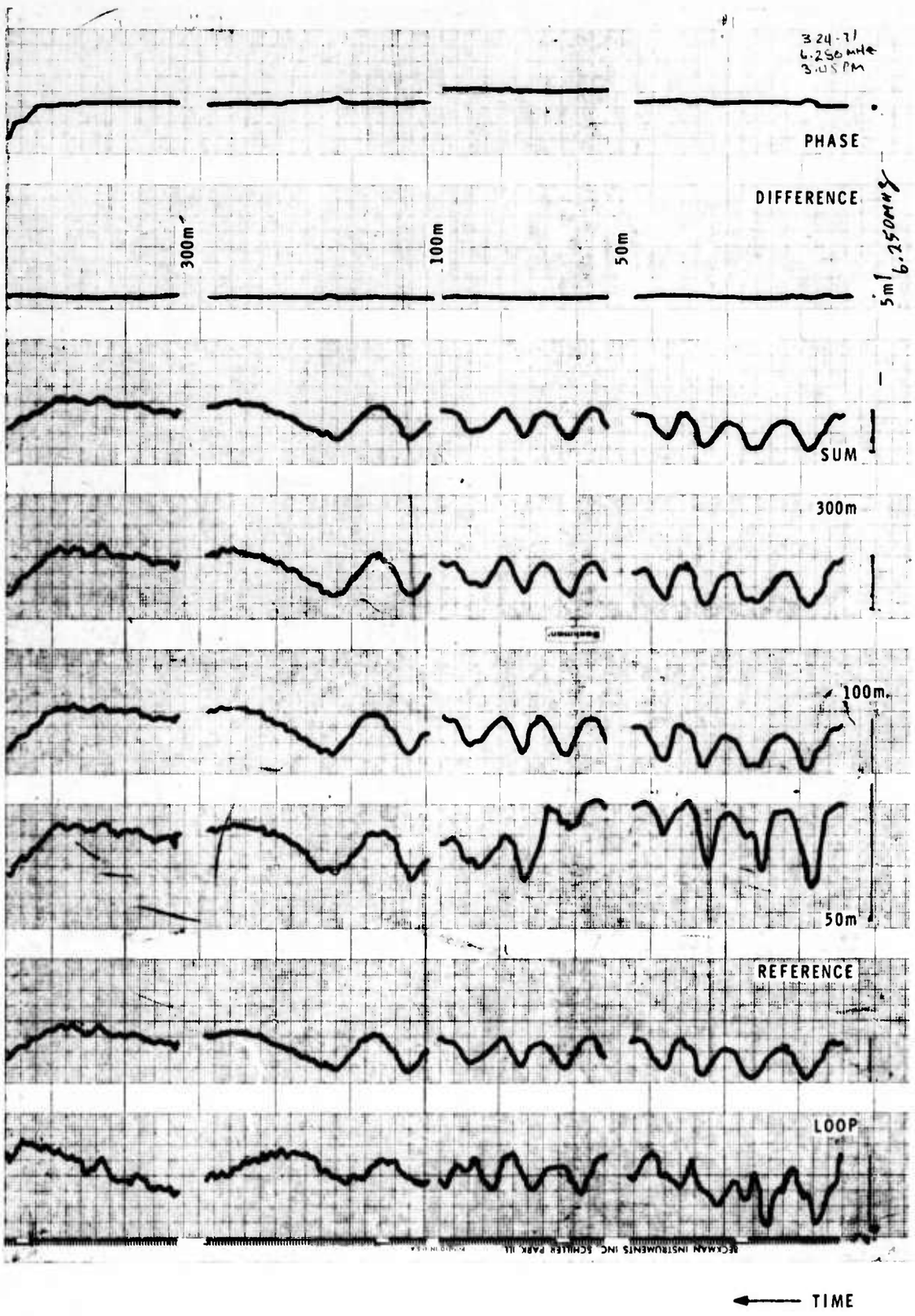

FIGURE 11a. HOUSTON--6.250 MHz

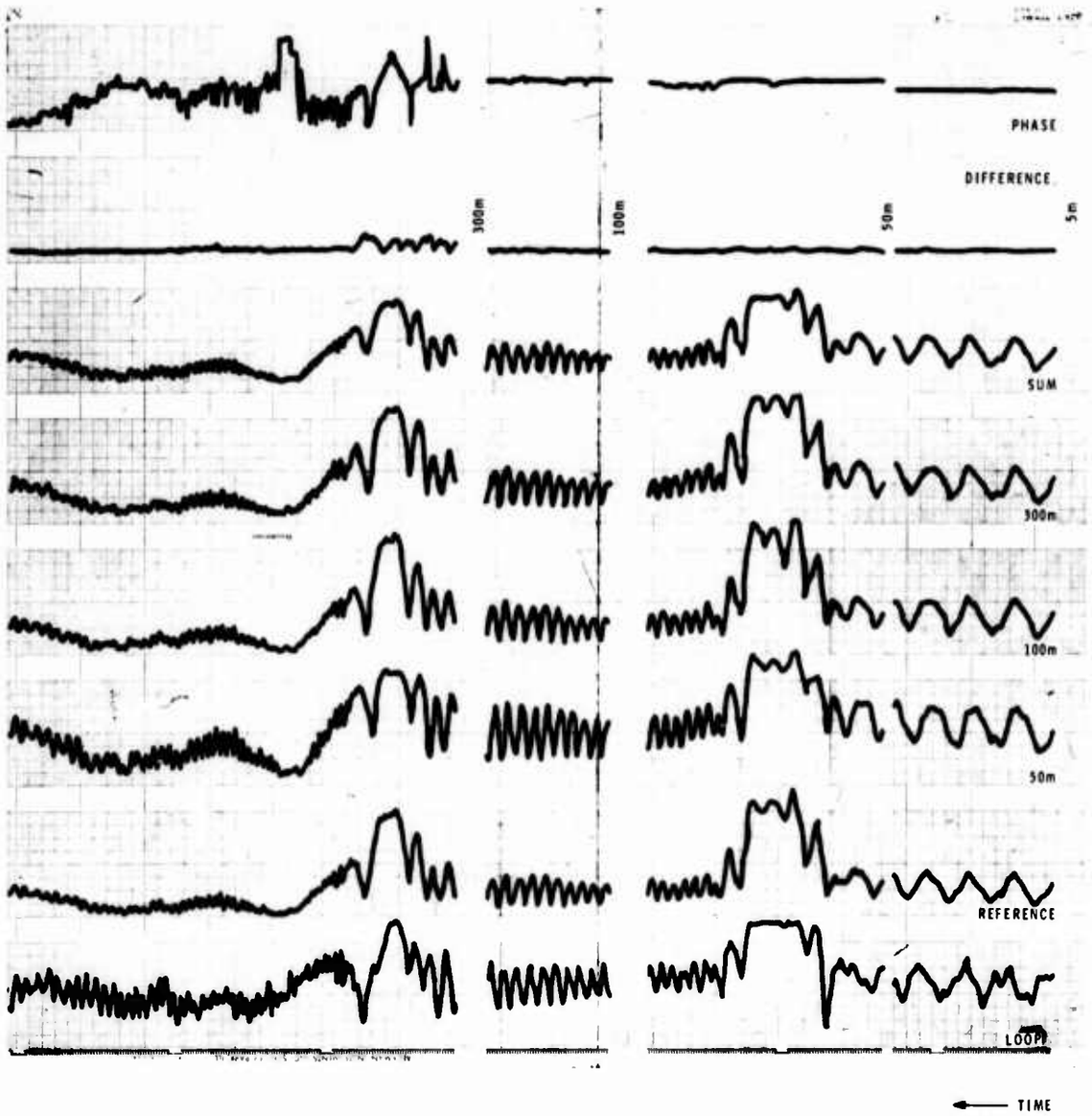

FIGURE 11b. HOUSTON--6.250 MHz

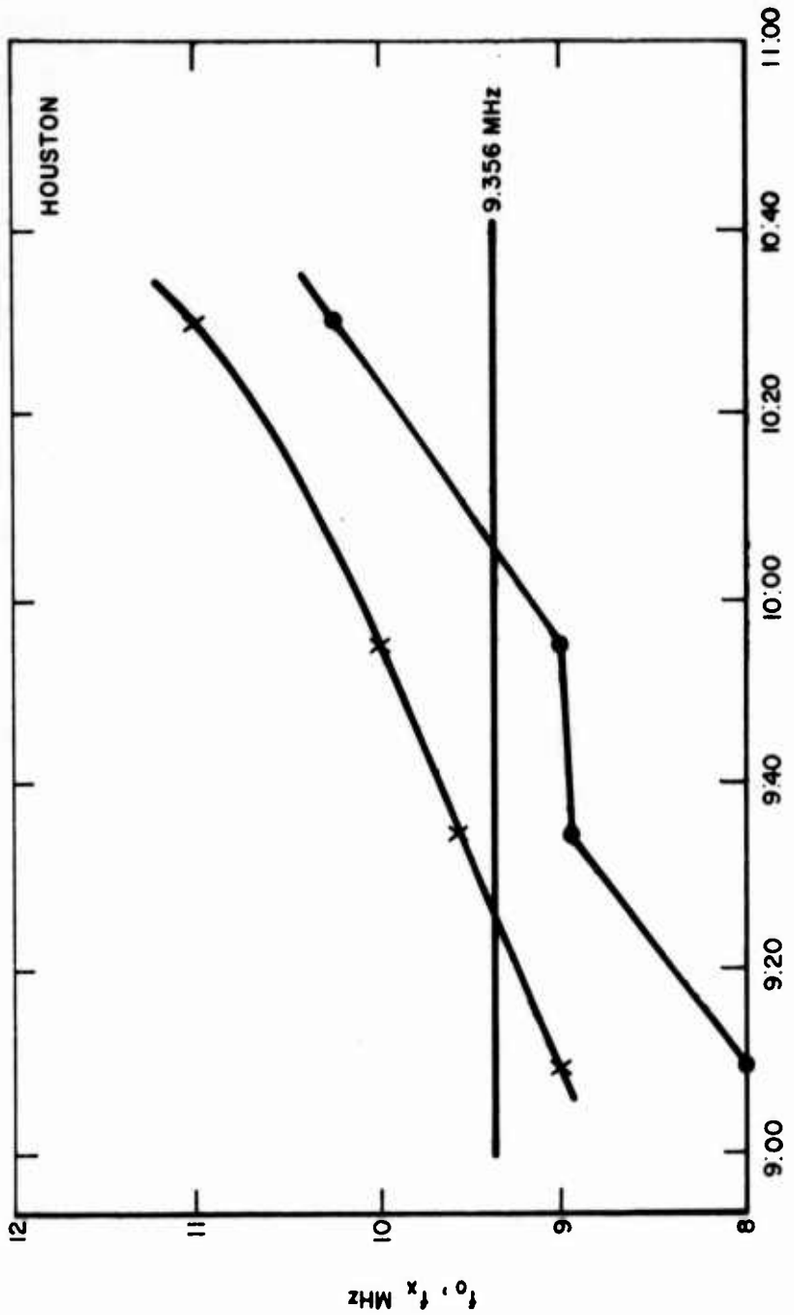

FIGURE 12. IONOGRAM OF f_o AND f_x WITH TIME

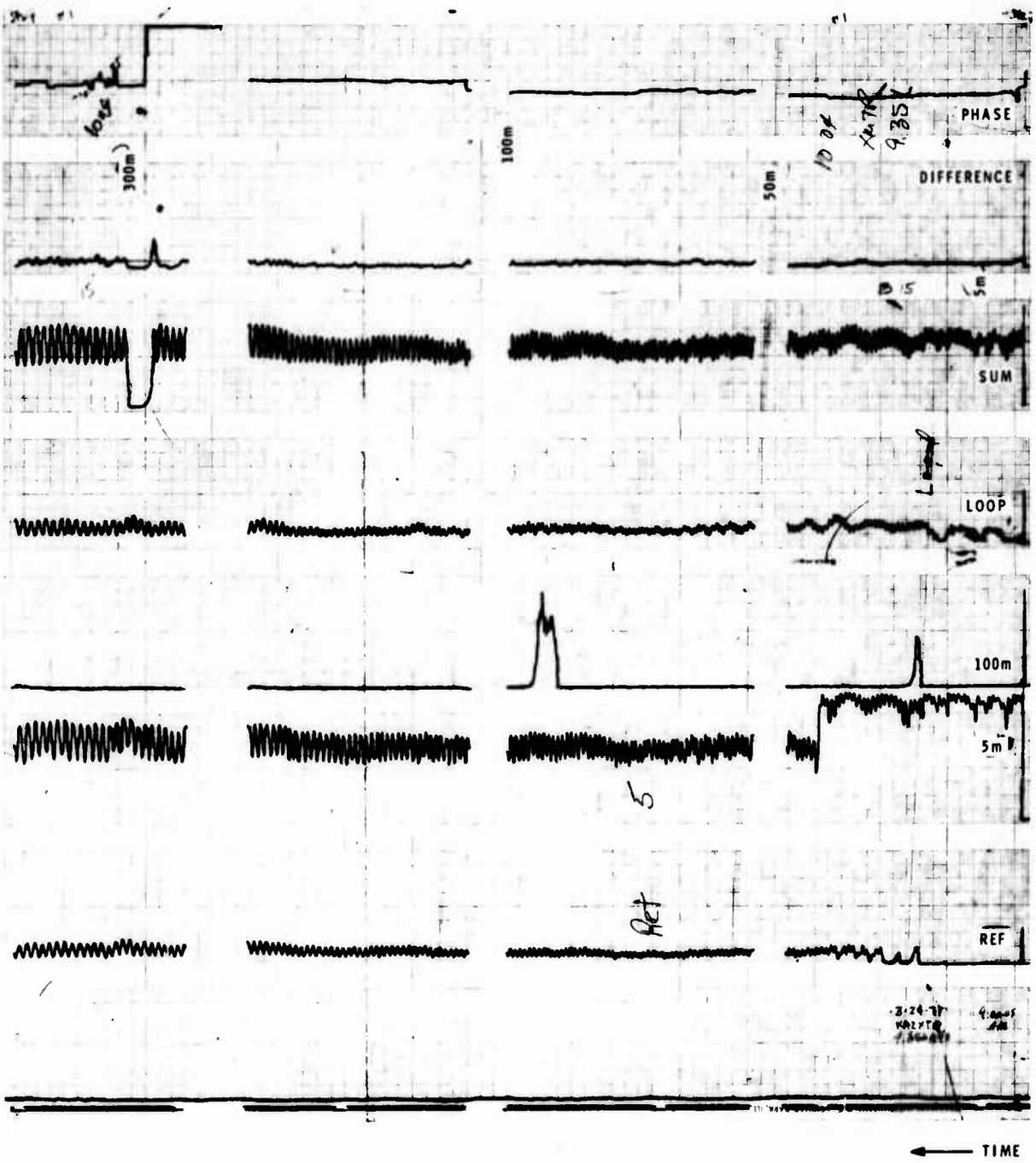

FIGURE 13a. HOUSTON--9.356 MHz

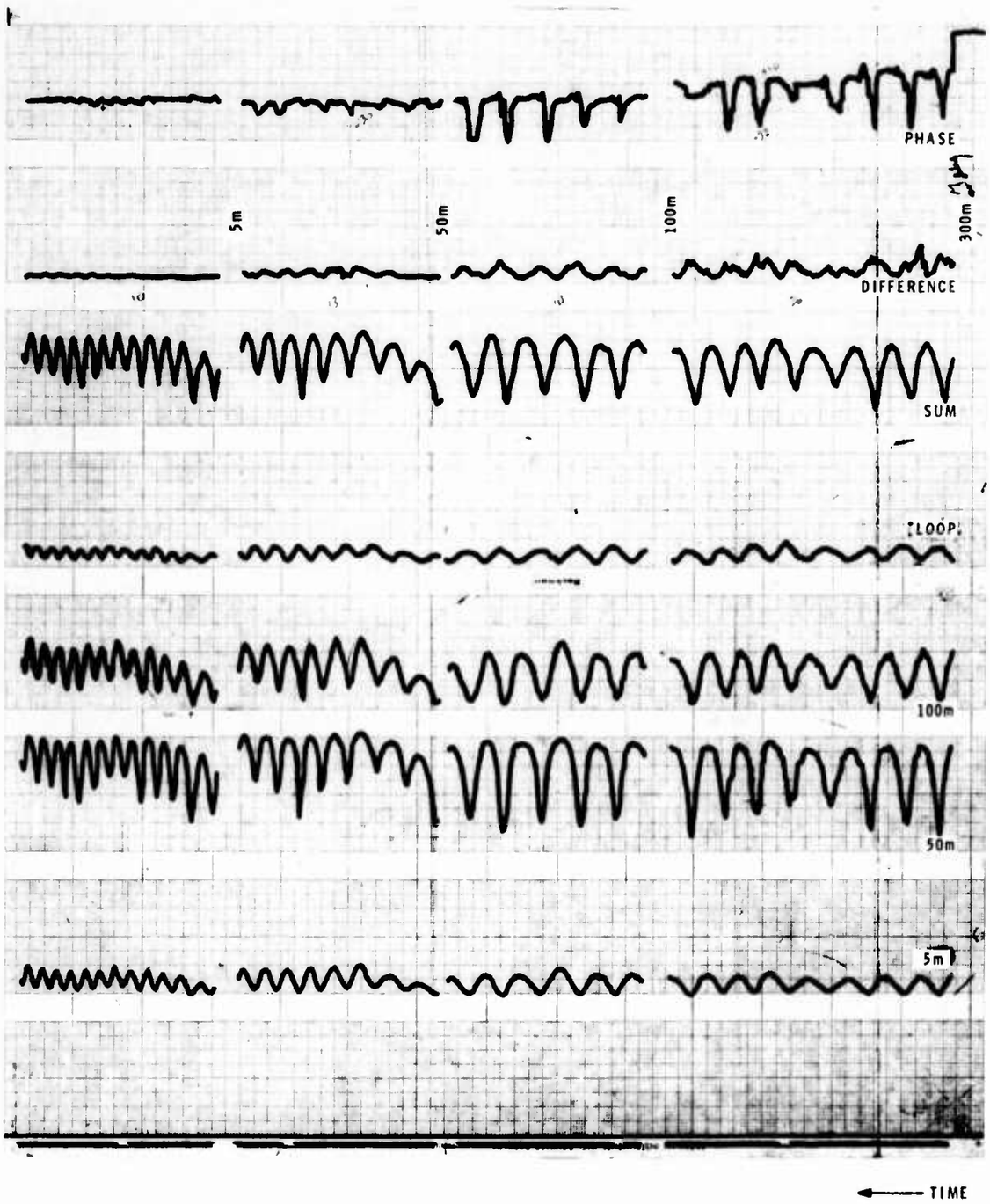

FIGURE 13b. HOUSTON--9356 MHz

V. CONCLUSION

The angular width measurements described herein illustrate the dynamic character of the mode structure for single propagation mode conditions. The conventional single ray picture of the propagation mode, conventional in direction finding engineering, is appropriate only for a single magneto-ionic mode. These measurements show that a single propagation mode may be unresolved in angular width (less than .1°) but show angle of arrival scintillation of the order of 1/2 to 1-1/2°. Under other conditions a single propagation mode may give no evidence of direction scintillation but provide a resolved angular width of the order of .7 to 1.5°. Finally, both resolved angular width and direction scintillation may occur simultaneously.

Local ionospheric conditions will cause changes in the angular width characteristics of the modes on a time scale of the order of minutes. These data show examples of significant changes in angular width and direction scintillation occuring within a 5-minute interval.

A systematic program of angular width measurement is now being planned at Southwest Research Institute to provide statistically valid width data for a variety of frequency and propagation conditions over the next 12 months. It is anticipated that the systematic angular width characteristics for two hop and single hop modes, E and F mode reflections will be better defined at the end of this program.

REFERENCES

1. Sherrill, W.M., "Interferometry for HF Propagation Research," Radio Science, May 1971 (In Press).

2. Eckersley, T.L., "A Wireless Interferometer," Nature, 141, 369, 1938.

3. Eckersley, T.L., "Scattering, Polarization Errors, and the Accuracy of Short Wave Direction Finding," The Marconi Review, 20, 53, 1935.

4. Whale, H.A., "The Angular Spread of Radio Waves in Long-Distance Ionospheric Propagation," Radio Science, 1, 743, 1966.

5. Hughes, C. J. and D. W. Morris, "Phase Characteristics of HF Radio Waves Received After Propagation by the Ionosphere," Proc. IEEE, 110, 1720, 1963.

6. Swenson, G. W. and N. C. Mathur, "The Interferometer in Radio Astronomy," Proc. IEEE, 56, 2114, 1968.

UNCLASSIFIED

MEASUREMENT OF THE VERTICAL ANGLES OF ARRIVAL OF A SKYWAVE SIGNAL IN THE PRESENCE OF MULTIPLE MODES

John M. Kelso
ITT Electro-Physics Laboratories, Inc.
Columbia, Maryland 20810

UNCLASSIFIED

ABSTRACT

The measurement of the vertical angle of arrival of HF skywave, multi-mode signals generally requires either highly complicated mathematical manipulations or observing techniques which necessitate a waiting period until the relative phases among the modes either reach a desired condition or pass through a desired range of variations. This paper utilizes an extension of a very old method (the Prony method, c. 1795), for approximating sums of exponential functions. The technique uses relatively simple calculations based on an instantaneous (or nearly so) set of samples from a uniformly-spaced, vertically-disposed array of antenna elements. Unlike many other methods, the technique discussed here does not require time variations of phase, does not require a perfectly-reflecting ground plane, and is valid for arbitrary polarization of the (similar) antenna elements and any general wave polarization.

It is noted that the mathematical basis for this work may also have useful information to the resolution of targets in the Doppler domain.

Experimental results from some field tests of the process for vertical angle estimation are presented.

1. INTRODUCTION

The problem of measuring the vertical angle of arrival of HF skywave signals is of interest in a number of research and system applications. As is well known, such measurements suffer from the difficulty of providing an adequate antenna aperture because of the cost of high vertical structures or extremely large apertures disposed horizontally. The difficulties are greatly enhanced when the signal format does not permit mode-separation in the time domain, and requires the resolution of multiple modes arriving simultaneously with different vertical angles.

This paper presents a technique for the computation of the vertical angle of arrival in the multiple-mode case, using the sampled outputs of a vertically-disposed array of antenna elements. The required computations reduce to the solution of a set of linear, simultaneous, algebraic equations, and the determination of the roots of a polynomial. The computation is thus shorter and less complicated than other methods proposed for solving this problem [Gething, 1969]. In addition, the method proposed here is applicable to much more general conditions of ground constants and element polarization than seems to be the case for most other methods. Further, this method can be applied to an instantaneous set of samples (or a set obtained by rapid sequencing); many other methods involve waiting until time-variations of inter-mode phase difference produce a specific condition or sequence of conditions.

Although this method appears to be an efficient way to take advantage of the available antenna aperture, it does not offer any "magic" way to avoid the necessity of a tall vertical structure.

The technique uses a generalization of a very old method for approximating a function which is the sum of terms of exponential form. The original work is due to deProny (1795). A more recent discussion is given by Hildebrand (1956) and other works on numerical techniques. As employed here, however, the solution uses a level of generality not considered in any of the references which have thus far come to the author's attention.

After the author began the study of this technique, it was brought to his attention that the Prony method had been considered by Sylvania (1967) for application to mode separation in the azimuthal direction using a horizontally-disposed array. However, in that application, the method fails to offer some of the advantages which it provides in the vertical case, and yields poor results in the broadside direction. Thus, Sylvania dropped this method from consideration. It would be noted that, translated to the vertical case, the broadside direction corresponds to an angle of elevation of zero degrees, in which direction any method of solution may be expected to experience difficulties. For these reasons, it is felt that many of Sylvania's reasons for losing interest in the Prony method do not apply to the vertical angle case, and that it can provide a valuable tool in vertical-angle measurement.

2. METHOD OF COMPUTATION

For the moment, let us consider the simplest applications of this technique to vertical angle measurements with multiple modes, and indicate the computations that are required.

Consider a vertically-disposed array of horizontally-polarized elements having a uniform inter-element separation d and consider the ground to be perfectly conducting. The lower element is located at some arbitrary height, h_o. The phase-detected output of the i^{th} element at a particular sampling instant is designated f_i, where i = 0, 1, 2, ..., m-1, for an m-element array.

For two simultaneous modes, three computational steps are required. First the quantities α_1 and α_2 are obtained by solving the following pair of linear, simultaneous algebraic equations

$$\begin{aligned} \alpha_1 (f_1 + f_3) + \alpha_2 f_2 &= f_0 + f_4 \\ \alpha_1 (f_2 + f_4) + \alpha_2 f_3 &= f_1 + f_5 \end{aligned} \tag{1}$$

Second, two values for the quantity cos Ω are obtained as the roots of the quadratic equation

$$\cos^2 \Omega - \frac{\alpha_1}{2} \cos \Omega - \frac{(\alpha_2 + 2)}{4} = 0 \tag{2}$$

Finally, the vertical angles Δ corresponding to each of the two values of cos Ω are obtained as follows

$$\Delta_i = \sin^{-1} \left[\frac{\lambda}{2\pi d} \Omega_i \right], \quad i = 1, 2 \tag{3}$$

where λ is the wavelength.

This is the complete computing algorithm required for a two-mode solution, for a single set of recorded outputs from each of the elements of the array. As can be seen, the array must have six elements. However, if the lower element is taken to be at ground level, its output is known to be zero for horizontal polarization and a perfect ground. In such a case only five actual elements are necessary.

The corresponding expressions for the three-mode case are the solution for α_1, α_2, and α_3 in the simultaneous equations

$$\begin{aligned} \alpha_1 (f_1 + f_5) + \alpha_2 (f_2 + f_4) + \alpha_3 f_3 &= f_0 + f_6 \\ \alpha_1 (f_2 + f_6) + \alpha_2 (f_3 + f_5) + \alpha_3 f_4 &= f_1 + f_7 \\ \alpha_1 (f_3 + f_7) + \alpha_2 (f_4 + f_6) + \alpha_3 f_5 &= f_2 + f_8 \end{aligned} \tag{4}$$

and the evaluation of the three roots of the cubic equation

$$\cos^3 \Omega - \frac{\alpha_1}{2} \cos^2 \Omega - \left(\frac{\alpha_1 + 3}{4}\right) \cos \Omega + \left(\frac{2\alpha_1 - \alpha_3}{8}\right) = 0 \tag{5}$$

The three roots of $\cos \Omega$ lead to three values of vertical angle Δ by applying Equation (3) to the individual roots.

These relations indicate the basic simplicity of the method. The following sections describe the nature of the wave field that is being sampled, provide a derivation of the mathematical technique, and show the generalization of the above simplified results.

3. NATURE OF THE WAVE FIELD INCIDENT ON THE ARRAY

Figure 1 shows a diagram of the direct and reflected waves, corresponding to a single mode, arriving from an elevation angle Δ at an element at height h above a horizontal ground. As indicated, the conditions are referenced to the wave as it reaches the ground directly below the element. The complex nature of the electric-field vectors is denoted by use of the symbol (~), and their vector nature is shown by use of the arrows. Waves polarized in the direction perpendicular to the vertical plane containing the wave normal and the element (horizontally polarized waves) are denoted $\tilde{\vec{E}}_{\perp}$; while the components polarized in that plane are denoted $\tilde{\vec{E}}_{\parallel}$ (sometimes called, loosely, "vertically polarized"). Phase changes at reflection are not depicted, since such changes are incorporated through use of a complex ground-reflection coefficient.

Although the results can be generalized to include arbitrary polarization of the incident wave and antenna element, only horizontally and vertically polarized elements are treated here, and are considered as two separate situations. For convenience, let it be noted that the incident and reflected components of $\tilde{\vec{E}}_{\perp}$ must be resolved along the vertical direction. With this in mind, the cases of horizontal and "vertical" polarization can be treated identically, so that no further distinction is made in most of the following.

The field E_o at the base of the antenna can be written as

$$\tilde{\vec{E}}_o = \tilde{\vec{E}}_o e^{j(\omega t + \varphi)} \qquad (6)$$

Figure 1

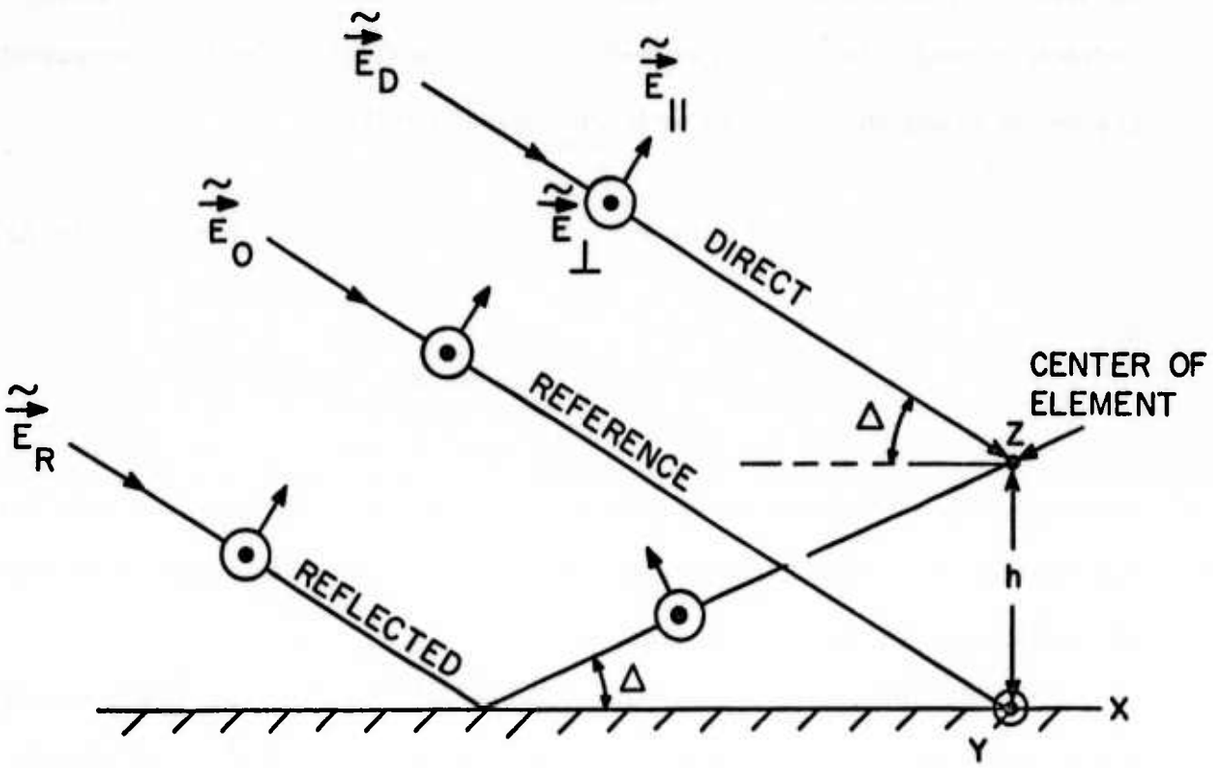
$\tilde{E}_D$
$\tilde{E}_{\parallel}$
$\tilde{E}_{\perp}$
$\tilde{E}_O$
$\tilde{E}_R$
DIRECT
REFERENCE
REFLECTED
CENTER OF ELEMENT
Δ
Δ
Z
h
X
Y

The direct wave is advanced in phase with respect to the reference wave because of the path difference $s = h \sin \Delta$, as illustrated in Figure 2. Similarly, the reflected wave is retarded by a like amount. In either case, the phase difference from the reference wave is given by $ks = kh \sin \Delta$, where $k = 2\pi/\lambda$ is the propagation constant.

Noting that the reflected wave undergoes a change in phase and amplitude by an amount specified by $\tilde{K}$, where $\tilde{K}$ is the complex ground reflection coefficient, the net field at height h is given by the component (resolved along the vertical or horizontal direction)

$$\tilde{E} = E_o \left[e^{j(\omega t + \phi + k h \sin \Delta)} + \tilde{K} e^{+j(\omega t + \phi - k h \sin \Delta)} \right]$$

or (7)

$$\tilde{E} = E_o e^{j(\omega t + \phi)} \left[e^{j(k h \sin \Delta)} + \tilde{K} e^{-j(k h \sin \Delta)} \right]$$

Although this is not the most general form to which the present solution is applicable, it is adequate for use with either horizontally polarized elements or vertically polarized elements.

In what follows, the time factor $e^{j\omega t}$ is removed (as it would be by heterodyning), and the complex response to the wave for an element at height h is written in the abbreviated form,

$$\tilde{f}(h) = \tilde{A}_1 e^{jkh \sin \Delta} + \tilde{A}_2 e^{-jkh \sin \Delta} \quad (8)$$

where the complex "constants" $\tilde{A}_1$ and $\tilde{A}_2$ involve the phase ϕ and the ground reflection coefficient $\tilde{K}$ (and in more general cases, the element and wave polarization).

However, we note that for horizontal polarization and a perfect

Figure 2

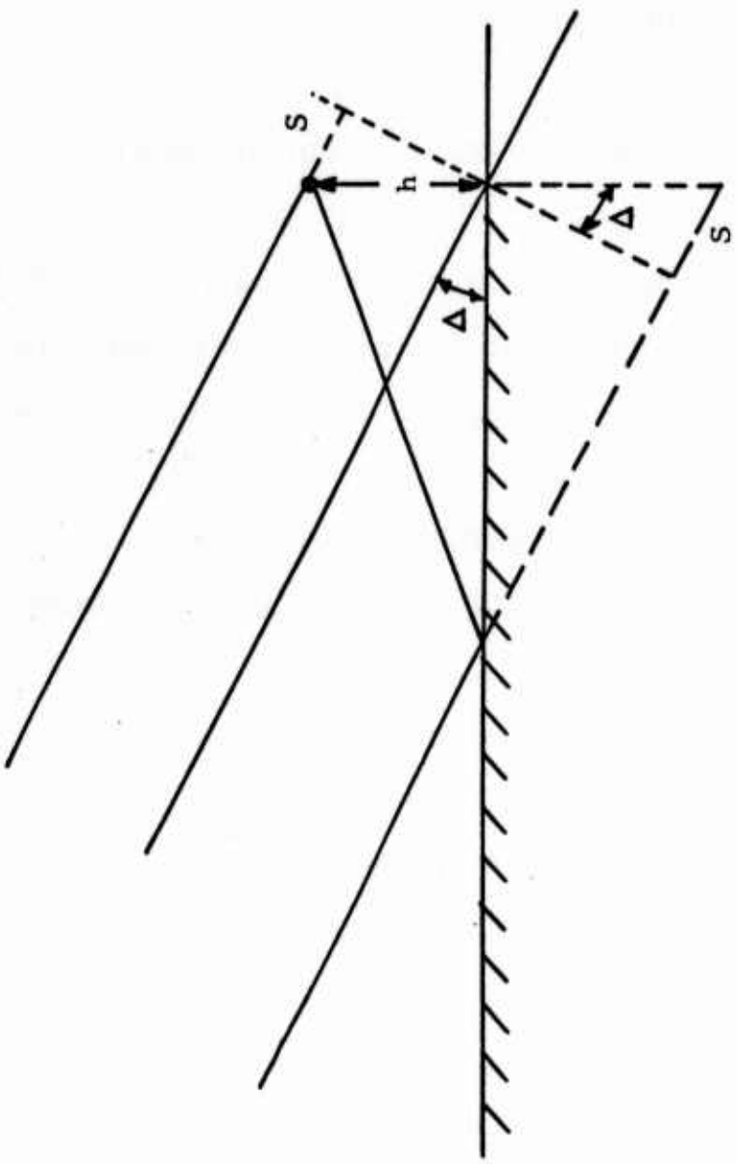

ground, we have $\tilde{K} = -1$, so that Equation (8) reduces to

$$\tilde{f}(h) = 2jE_o e^{j\phi} \sin (kh \sin \Delta) \tag{9}$$

The real part of $\tilde{f}(h)$ then becomes

$$Re(\tilde{f}) = -2E_o \sin \phi \sin (kh \sin \Delta) \tag{10}$$

This is the quantity utilized in most vertical angle solutions, which apply only for horizontal polarization and a perfect ground. The present method is not restricted in this fashion, and is valid for more general modes as expressed by Equation (8).

In the multiple mode case, each mode can be expressed in the form of Equation (8), and the net output from the element is the complex sum of the individual mode contribution. The individual modes can differ not only in vertical angle Δ and complex amplitude $\tilde{A}$, but also may differ in propagation constant k (i.e., in frequency) and in ground reflection coefficient $\tilde{K}$. For present purposes, differences other than in Δ are considered to be included in the respective quantity $\tilde{A}_1$.

Before leaving the mode-structure discussion, we note that a comparison of Equations 7 and 8 shows that if the quantities Δ and $\tilde{A}_1$ and $\tilde{A}_2$ can be determined, it is then possible to calculate the ground reflection coefficient appropriate to the mode that is of interest.

4. DERIVATION OF SOLUTION

The following derivation is generally similar to that given by Hildebrand (1956), but is generalized to include the complex outputs (in-phase and quadrature components) of the separate elements; Hildebrand's derivation used only real samples and real coefficients.

For convenience of notation, the following derivation is for the two-mode case. The general solution is stated but not derived; the general derivation is readily developed by simple extension of the results presented here.

The complex output $\tilde{f}(h)$ for two modes, each of the form of Equation (8) may be written as

$$\tilde{f}(h) = \tilde{A}_1 e^{j\,k\,h\,\sin\,\Delta_1} + \tilde{A}_2 e^{-j\,k\,h\,\sin\,\Delta_1} + \tilde{A}_3 e^{j\,k\,h\,\sin\,\Delta_2} + \tilde{A}_4 e^{-j\,k\,h\,\sin\,\Delta_2} \tag{11}$$

Let us write

$$h = h_o + xd \tag{12}$$

where h_o is the height of the lowest element of the array, and x expresses the height variation in units of the inter-element distance d. Then each term of Equation (11) can be written in the form

$$\tilde{A} e^{j\,k\,h\,\sin\,\Delta} = \tilde{C} e^{j\,k\,x\,d\,\sin\,\Delta} \tag{13}$$

where the complex quantity $\tilde{C}$ is independent of the height of the individual elements, but includes the factor exp ($jkh_o \sin \Delta$).

We also define an angle Ω_i as

$$\Omega_i = kd \sin \Delta_i, \quad i = 1, 2 \tag{14}$$

Then the quantity $\tilde{f}(h)$ in Equation (11) can be expressed as a function of the height parameter x in the form

$$\tilde{f}(x) = \tilde{C}_1 e^{j\Omega_1 x} + \tilde{C}_2 e^{-j\Omega_1 x} + \tilde{C}_3 e^{j\Omega_2 x} + \tilde{C}_4 e^{-j\Omega_2 x} \tag{15}$$

We further simplify this expression by writing

$$\mu_1 = e^{j\Omega_1}, \quad \mu_2 = e^{-j\Omega_1}, \text{ etc.}, \tag{16}$$

to obtain

$$\tilde{f}(x) = \tilde{C}_1 \mu_1^x + \tilde{C}_2 \mu_2^x + \tilde{C}_3 \mu_3^x + \tilde{C}_4 \mu_4^x \tag{17}$$

Now we note that the elements correspond to integral values of x = 0, 1, 2, ..., N-1, for N elements so that we have the following set of equations to solve,

$$\begin{aligned}
\tilde{f}(0) &= \tilde{C}_1 + \tilde{C}_2 + \tilde{C}_3 + \tilde{C}_4 = \tilde{f}_0 \\
\tilde{f}(1) &= \tilde{C}_1\mu_1 + \tilde{C}_2\mu_2 + \tilde{C}_3\mu_3 + \tilde{C}_4\mu_4 = \tilde{f}_1 \\
\tilde{f}(2) &= \tilde{C}_1\mu_1^2 + \tilde{C}_2\mu_2^2 + \tilde{C}_3\mu_3^2 + \tilde{C}_4\mu_4^2 = \tilde{f}_2 \\
&\cdots\cdots\cdots\cdots\cdots\cdots\cdots \\
\tilde{f}(N) &= \tilde{C}_1\mu_1^{N-1} + \tilde{C}_2\mu_2^{N-1} + \tilde{C}_3\mu_3^{N-1} + \tilde{C}_4\mu_4^{N-1} = \tilde{f}_{N-1}
\end{aligned} \tag{18}$$

This set of transcendental equations may be reduced to a set of linear (complex) equations and one non-linear equation by introducing a variable μ expressed as a non-linear equation whose roots are μ_1, μ_2, μ_3, and μ_4. Thus, we write

$$(\mu-\mu_1)(\mu-\mu_2)(\mu-\mu_3)(\mu-\mu_4) = 0 \tag{19}$$

This may be expanded in coefficients α_1, α_2, α_3, α_4 as

$$\mu^4 - \alpha_1\mu^3 - \alpha_2\mu^2 - \alpha_3\mu - \alpha_4 = 0 \tag{20}$$

Since by Equation (16) we have $\mu_2 = 1/\mu_1$, $\mu_4 = 1/\mu_3$, Equation (20) must be equally valid if we replace μ by $1/\mu$. This leads to the condition that $\alpha_3 = \alpha_1$ and $\alpha_4 = -1$, so that Equation (20) reduces to

$$\mu^4 - \alpha_1\mu^3 - \alpha_2\mu^2 - \alpha_1\mu + 1 = 0 \tag{21}$$

Introducing the values of μ from Equation (16) into Equation (21), it is easy to show that both α_1 and α_2 are real quantities.

If we put $\mu = e^{j\Omega}$ into Equation (21), factor out the term $e^{j2\Omega}$,

and write cos 2Ω in terms of $\cos^2 \Omega$, Equation (21) reduces to

$$\cos^2 \Omega - \frac{\alpha_1}{2} \cos \Omega - \left(\frac{\alpha_2 + 2}{4}\right) = 0 \tag{23}$$

which was given earlier as Equation (2). The remaining step is to derive the simultaneous equations to be solved for α_1 and α_2.

Multiply the first equation of Equation (18) by the last term (= 1) in Equation (21), the second Equation (18) by the coefficient $(-\alpha_1)$ of μ in Equation (21), the third by the coefficient $(-\alpha_2)$ of μ^2, etc., and add the resulting equations. The left hand side then will consist of four terms, each of the form of

$$\tilde{C}_i (\mu_i^4 - \alpha_1 \mu_i^3 - \alpha_2 \mu_i^2 - \alpha_1 \mu_i + 1), \quad i = 1, 2, 3, 4$$

But, since μ_i is a root of Equation (21), each of these terms vanishes. Thus, the sum of these equations reduces to

$$\tilde{f}_0 - \alpha_1 \tilde{f}_1 - \alpha_2 \tilde{f}_2 - \alpha_1 \tilde{f}_3 + \tilde{f}_4 = 0$$

or, re-arranging

$$\alpha_1 (\tilde{f}_1 + \tilde{f}_3) + \alpha_2 \tilde{f}_2 = \tilde{f}_0 + \tilde{f}_4 \tag{24}$$

Except for the complex nature of the $\tilde{f}_i$, this is in the form of the first of Equation (1). In the complex case, the two equations necessary to solve for α_1 and α_2 may be obtained by taking the real and imaginary parts of Equation (24) to yield

$$\alpha_1 \text{ Re } (\tilde{f}_1 + \tilde{f}_3) + \alpha_2 \text{ Re } (\tilde{f}_2) = \text{Re } (\tilde{f}_0 + \tilde{f}_4)$$

$$\alpha_1 \text{ Im } (\tilde{f}_1 + \tilde{f}_3) + \alpha_2 \text{ Im } (\tilde{f}_2) = \text{Im } (\tilde{f}_0 + \tilde{f}_4) \qquad (25)$$

These two equations would then be used in place of Equation (1). If the f_i are real, the second equation of Equation (1), is obtained by the above process, but starting with the second equation in Equation (18).

The general solution for m modes, using N complex samples, may be expressed by generating a set of simultaneous equations in α_1, α_2, ..., α_m, in a manner similar to that used in the two-mode case. The first complex equation of the set is,

$$\alpha_1 (\tilde{f}_1 + \tilde{f}_{2m-1}) + \alpha_2 (\tilde{f}_2 + \tilde{f}_{2m-2}) + \ldots + \alpha_{m-1} (\tilde{f}_{m-1} + \tilde{f}_{m+1}) + \alpha_m \tilde{f}_m = \tilde{f}_0 + \tilde{f}_{2m} \qquad (26)$$

A second complex equation is obtained by increasing all of the subscripts on the f_i by one, to get

$$\alpha_1 (\tilde{f}_2 + \tilde{f}_{2m}) + \alpha_2 (\tilde{f}_3 + \tilde{f}_{2m-1}) + \ldots + \alpha_{m-1} (\tilde{f}_m + \tilde{f}_{m+2}) + \alpha_m \tilde{f}_{m+1} = \tilde{f}_1 + \tilde{f}_{2m+1} \qquad (27)$$

This process of increasing the subscripts is continued until one obtains m real equations to solve for the m values of α. Since each complex equation yields two real equations, it is necessary to obtain m/2 complex equations if m is an even number and (m+1)/2 if m is an odd number. It is seen that each successive complex equation requires the addition of one more element to the set being employed. If one supposes that the 2m elements 0 through 2m-1

were required before the process was started, then it is seen that the total number N of elements must be given by $N = 5m/2$ if m is even and by $N = (5m+1)/2$ if m is odd. Table 1 shows the number of elements required for various numbers of modes.

If the available number of elements exceeds the required value as given in Table 1, then additional equations can be developed. This redundant set of equations can be reduced to the necessary m equations by obtaining normal equations in the usual least-squares manner. In effect, this use of redundant elements increases the antenna aperture and improves the quality of solution that can be obtained for a given input signal-to-noise ratio.

When the values of Δ have been found for each mode, the quantities μ_1 can be evaluated and substituted into Equation (18). These equations then are a redundant set of linear, simultaneous equations in the complex coefficients $\tilde{C}_{\mu}$. Thus, these coefficients can be evaluated by solution of four (complex) normal equations obtained by least-squares reduction of the redundant set.

Table 1. Required Number of Elements for Various Numbers of Modes

N = Number of Elements	m = Number of Modes
3	1
5	2
8	3
10	4
13	5
.	.
.	.
.	.
5k	2k
5k+3	2k+1

5. APPLICATION TO DOPPLER RESOLUTION

The extension of the Prony method that was employed in Section 4 is also applicable to other problems involving the summation of nonharmonically-related sinusoids sampled at equally spaced intervals. One such problem is the determination of the doppler frequencies of multiple targets, either for pulsed signals, or for CW signals that are sampled periodically. In such a case, an application of the Prony method could offer an alternative to the more usual technique of spectrum analysis. For a modest number of targets, the Prony method, using a highly redundant (or over determined) set of equations, might offer some attractive advantages to a system in which the processing is handled rather completely in digital form. One such advantage is that output would be given only for the targets that are seen, and does not require thresholding or other means to ascertain the interesting Doppler frequencies.

6. EXPERIMENTAL RESULTS OF VERTICAL-ANGLE MEASUREMENT

The theory presented above has been applied to field data obtained at the ONR/ARPA field site at Whitehouse, Virginia, using CW transmissions originating at the ONR field site at Lincoln, Nebraska.

The receiving antenna at the Whitehouse field site is a specially-constructed, vertical array. The array consists of eight, horizontally-polarized, log-periodic elements spaced at thirty-foot intervals on a 260-foot, vertical tower. All guys are non metallic. A photograph of the antenna is shown in Figure 3.

The array output is measured by switching the elements sequentially to the receiver input and using quadrature detection to record the in-phase and quadrature components of the receiver output in digital form on computer-compatible magnetic tape. The time and the frequency to which the receiver is tuned are also recorded. The data to be discussed here were taken at a switching rate of 100 per second, so that the full array was scanned in a period of 0.08 seconds.

At the time of interest (1634 U.T. on 11 December 1970) the Lincoln site transmitted a CW signal at a level of about one kilowatt into a vertically polarized antenna having a gain of about 10 dbi. The transmitting frequency was 21.610 MHz.

Round-trip oblique pulse soundings between Whitehouse and Lincoln, using a bandwidth of 100 KHz and an active repeater at Lincoln, showed the presence of a mode with a round-trip time delay of 12.1 ms. Since the ground distance between Lincoln and Whitehouse is 1725 km, a mirror reflection from the ionosphere would imply a vertical angle of 10.9 degrees, to produce the observed delay.

Figure 3

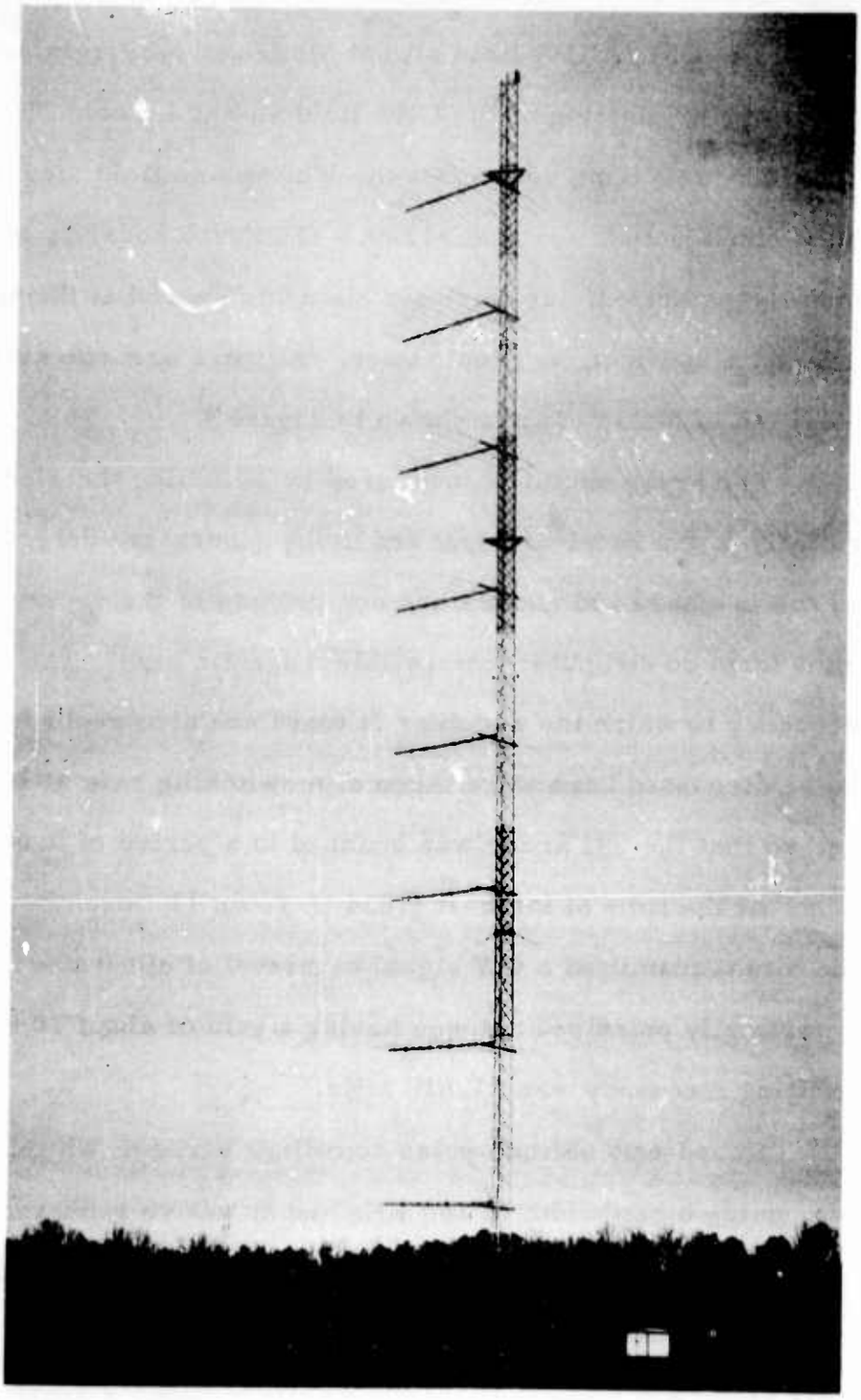

The resulting data were processed in accordance with the preceding theory, using a complex solution and least-squares reduction to normal equations. The results of a single-mode solution were erratic, leading to a trial of a two-mode solution. The angles obtained from the two-mode solution are plotted as functions of time in Figure 4, which encompasses about a 12-second period (each individual reading, yielding two angles, corresponds to a single scan period of 0.08 seconds). It is seen that the expected mode with a vertical angle from 10.5 to 11 degrees was obtained, but also a mode at an angle of approximately 25 degrres was found. The fact that this latter mode, identified as a high-ray component by ray-tracing methods, did not appear on the oblique soundings is not surprising, since the oblique sounding records have a somewhat limited dynamic range.

Since the oblique soundings were made about twenty minutes after the vertical measurements were taken, the observed angles from 10.5 to 11.0 degrees compare very favorably with the value of 10.9 derived from the oblique soundings.

This early result has been most encouraging, and strongly suggests that the approach described here should be a powerful tool in the investigation of vertical angles of arrival of HF, skywave signals. The coherence of the results for the mode near a vertical angle of 11 degrees, especially in the form of well-defined oscillations, is particularly noteworthy, since it gives considerable hope that the technique may offer a new way for measuring fine-scale ionospheric effects having periods of seconds or less.

Figure 4

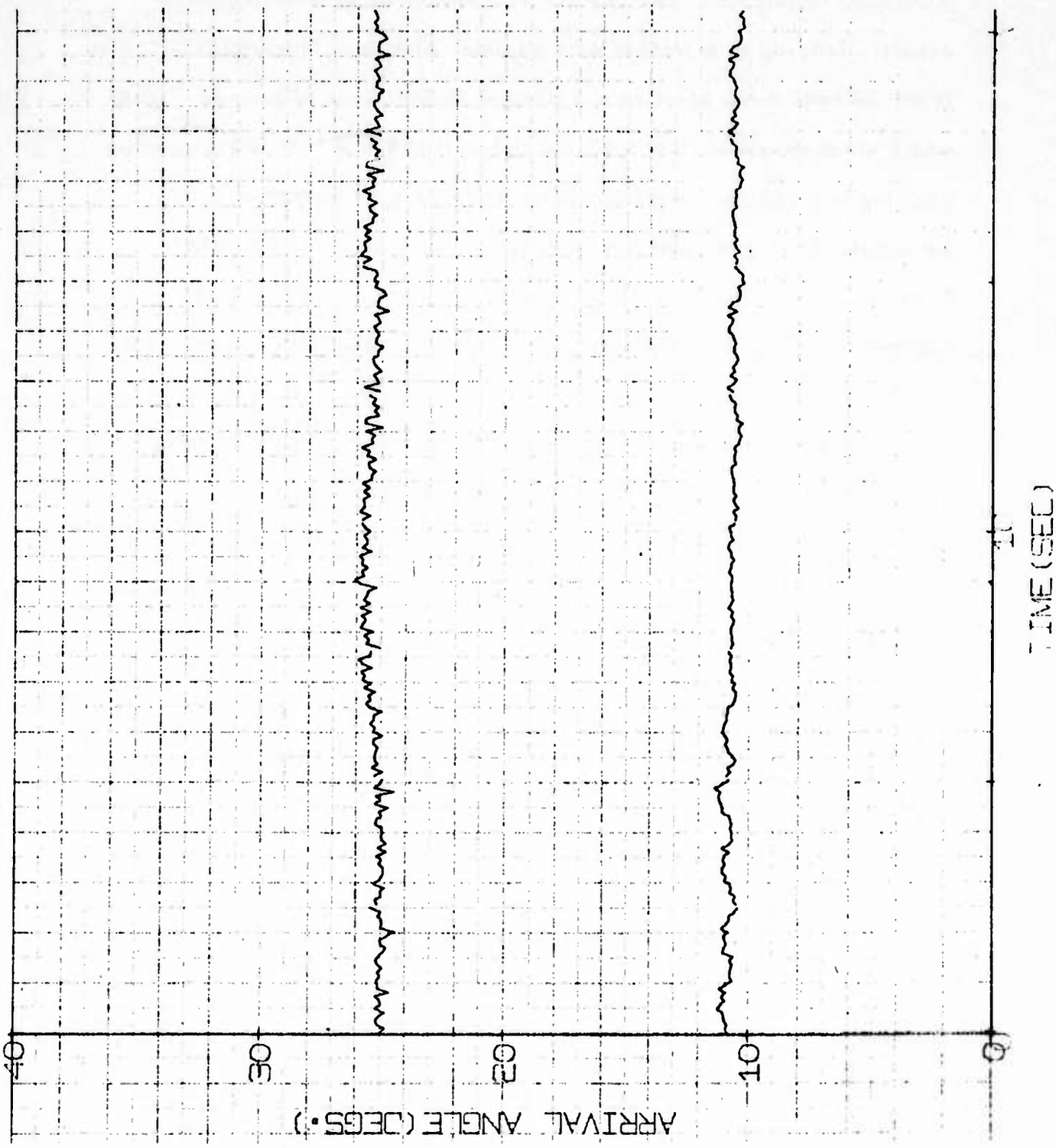

ACKNOWLEDGMENTS

This work was supported by the Office of Naval Research under Contract Number N00014-70-C-0208.

References

Gething, P.J.D., J.D. Morris, E.G. Shepperd and D.V. Tibble "Measurement of Elevation Angles of H.F. Waves", Proc. IEE Vol. 116, No. 2, Feb. 1969, pp 185-193.

deProny, R., "Essai experimentale et analytiqne", J. Ecole Polytech. (Paris), 1 (2) 24-76 (1795).

Hildebrand, F. B., "Introduction to Numerical Analysis" McGraw Hill Book Co. Inc., 1956. pp. 378 - 386.

Applied Research Laboratory, Sylvania Electronic Systems, "Ionospheric Propagation Studies", Quarterly Report No. 5, Contract DA-18-119-AMC-02522 (x). 20 Feb. 1967. pp 5.17-5.53.

List of Figures

Figure

1. Diagram of the direct and reflected waves arriving at an antenna element at height h, together with the reference wave incident at the ground directly below the element. The vertical arrival angle is Δ. Each wave has a complex vector component $\tilde{E}_{\parallel}$ in the plane of the paper and another complex vector component $\tilde{E}_{\perp}$ perpendicular to this plane.

2. Diagram illustrating the path differences between the reference wave and the direct and reflected waves.

3. Vertical array of log-periodic elements.

4. Experimental observations of the vertical angles of arrival of a multi-mode CW signal at 21.610 MHz, over a 1725 Km path.

RANGE ESTIMATION BASED ON BACKSCATTER MEASUREMENTS

L. H. Tveten
U.S. Department of Commerce
Office of Telecommunications
Institute for Telecommunication Sciences
Boulder, Colorado 80302

A technique has been developed by which range to the location of a transmitter can be estimated using measurements of the incoming elevation angles and of simultaneous backscatter delay versus elevation angles as input data. The backscatter measurements are used to determine the parameters of a parabolic layer model of the F region, and range estimates are made by a solution of the incoming mode angles with the ionospheric parameters for the given time. These parameters include the E region whose characteristics are determined from long-term predictions. With the exception of the initial data scaling process the entire range estimation procedure has been programmed for the CDC 3800 digital computer.

A quite extensive test of the procedure has been performed with data gathered during the Institute for Telecommunication Sciences/University of Illinois coordinated propagation experiment of 1966-68. Approximately 1700 range estimates have been made using elevation angle measurements of incoming propagation modes from Meridian, Mississippi, and Orlando, Florida. Range estimates with these data were compared with the actual known ranges, and median errors usually considerably less than 10 percent were obtained. Variations and trial improvements of the technique are discussed.

1. INTRODUCTION

In the radio-location community the idea of estimating range to an unknown transmitter by using measured incoming mode elevation angles and a model of the pertinent ionosphere is not new.

However, some added impetus developed at the Institute for Telecommunication Sciences to try the idea again as a result of the development of some new ideas for deriving a realistic model of the ionosphere appropriate to the given region and time. These ideas centered around the use of the backscatter signal received on a high resolution elevation angle scanning antenna. Briefly stated, the technique consists of fitting the parameters of a parabolic model ionosphere to backscatter versus elevation angle data from the appropriate ionospheric area, and then, with this ionosphere, computing the ranges appropriate to the measured mode elevation angles associated with the signal in question. When one considers the multiple-hop modes and various combination modes, he discovers that quite a number of ranges are possible. Thus the other important part of the problem is to sort out the most likely mode combination to provide the range estimate. These problems will be discussed at considerably greater length in what follows.

2. MODEL IONOSPHERE PARAMETERS

Figure 1 is an example of an elevation-scan backscatter record showing elevation angle versus backscatter delay time. The longer delay returns are associated with the lower elevation angles. This particular record shows the single-hop F-layer returns. The situation becomes much more complicated when multiple hop and E-layer returns are included. Most of the time, however, it is a rather simple matter to sort the various backscatter modes on such a record. This sort of record is really an ionospheric sounding which can be transformed with an appropriate layer model to a partial vertical sounder record. Some assumptions concerning uniformity of the ionospheric electron densities in the horizontal plane are required since this type of sounding looks at the ionosphere at different ranges. However, relatively small variations, which nevertheless have a considerable effect for range estimation purposes, are allowed.

The problem resolves itself into that of fitting the parabolic layer parameters of semi-thickness, height of the layer bottom, and critical frequency to the input backscatter data. It has also been discovered that the longitudinal component of ionospheric tilt can be determined with the other parameters in the fitting process.

Figure 2 shows the geometry to be used in the parameter calculations. The virtual ray paths are illustrated for an ionospheric tilt angle, δ, takeoff Δ_2 and reception Δ_1 angles; slant range legs from the ground end points to the ionospheric virtual reflection point are

d_1 and d_2 and have corresponding ground ranges of D_1 and D_2. The angles φ_1 and φ_2 are at the ionosphere between the extending earth radius and the slant range legs d_1 and d_2 at their point of intersection. The equivalent angle φ for use in the parabolic layer calculations is defined by the equation:

$$\varphi = \varphi_1 + \delta = \varphi_2 - \delta$$

$$\varphi_2 = \varphi_1 + 2\delta.$$

The basic equations, derived for oblique transmission from the parabolic layer vertical incidence equations (Mitra, 1952), used in determining the ionospheric parameters are the following:

$$d_1 \sin\left(\Delta_1 + \frac{D_1}{R}\right) - R\left[1 - \cos\left(\frac{D_1}{R}\right)\right] = h_o + f(D_1 - D_{1o}) + \frac{y_m}{2} X_1 \sec\delta \log\left(\frac{1 + X_1}{1 - X_1}\right)$$

$$d_2 \sin\left(\Delta_2 + \frac{D_2}{R}\right) - R\left[1 - \cos\left(\frac{D_2}{R}\right)\right] = h_o + f(D_1 - D_{1o}) + \frac{y_m}{2} X_2 \sec\delta \log\left(\frac{1 + X_2}{1 - X_2}\right)$$

$$X_1 = \frac{f_{op}}{kf_c} \sin\left(\Delta_1 + \frac{D_1}{R} - \delta\right) = \frac{f_{op}}{kf_c} \sin\left(\Delta_2 + \frac{D_2}{R} + \delta\right) = X_2$$

f_c = layer critical frequency,

f_{op} = operating frequency, and

y_m = layer semi-thickness.

Since a tilt implies a change in the height of the layer bottom with range, the factor $h_o + f(D_1 - D_{1o})$ is included to take this into account. The factor h_o is the height at some range D_{1o}, and $f(D_1 - D_{1o})$ gives the functional dependence with range. The slope is essentially the value of δ at D_1.

The curved ionosphere factor k (Wieder, 1955) is a function of range, assuming the nontilt case, appropriate to the angle φ. Hence to a first approximation

$$k(D) = k\left(2\left[D_1 + h'\delta - D_1\delta^2\right]\right),$$

where h' is the virtual height of reflection above the surface of the earth.

In a similar way the basic equations for calculating ground range for a given tilt and standard parabolic layer parameters are:

$$R\left[\sin\frac{D_1}{R}\tan\left(\Delta_1 + \frac{D_1}{R}\right) + \cos\left(\frac{D_1}{R}\right) - 1\right] =$$

$$h_o + f(D_1 - D_{1o}) + \frac{y_m}{2} X_1 \sec\delta \log\left(\frac{1 + X_1}{1 - X_1}\right),$$

$$R\left[\sin\frac{D_2}{R}\tan\left(\Delta_2 + \frac{D_2}{R}\right) + \cos\left(\frac{D_2}{R}\right) - 1\right] =$$

$$h_o + f(D_1 - D_{1o}) + \frac{y_m}{2} X_2 \sec\delta \log\left(\frac{1 + X_2}{1 - X_2}\right).$$

X_1 and X_2 were defined previously and $D_1 + D_2 = D$, the quantity to be determined, and Δ_1, h_o, y_m, f_c, δ and $f(D_1 - D_{1o})$ are given.

To provide some insight into the way in which some of these quantities vary we show figures 3 and 4, which illustrate the variation of backscatter delay and ground range respectively with elevation angle as a function of operating frequency to critical frequency ratios for the parabolic parameters shown. Zero tilt is assumed in the calculations for these two figures. Figures 5 and 6 show similar figures for the cases of various tilt angles. It can be seen that there is quite a dependence on the value of tilt.

The fitting of the parabolic parameters to the backscatter data is done on the 3800 CDC digital computer using least squares techniques. In general one can derive an ionospheric model which fits the data points very well when backscatter data is simulated using the model. Ordinarily, the backscatter data do not provide the entire elevation angle versus delay curve including both the data at very low angles or the data for the high angle response. The latter exclusion is caused by rather rapid defocusing of the high ray. However, the high ray information is very important for the precise determination of all of the parameters. When the high ray information is missing, the fit to the actual input points is very good, but there are some tradeoffs between the parameters - particularly the semithickness, critical frequency, and tilt - which can, in some cases, affect the range estimation procedure for high or low angles.

There are several variations of the fitting procedure which can be used. One can begin with one or two parameters fixed and thus reduce the dimensions of the space in which the fitting must take place. Figure 7 shows an example of three different fits to the same set of input data points indicated by the small x's. Curve 1 was calculated presuming that the tilt angle was zero and the other three parameters were allowed to vary with the restriction that $5 \leq y_m \leq 200$ km. Curve 2 shows the case in which the semithickness was fixed at 80 km and the remaining parameters allowed to vary. For curve 3 the tilt was restricted to the range $\pm$ 0.5 degrees and y_m was allowed to vary between 5 and 200 km. The other parameters have no restrictions. It can be seen that the experimental points are fitted quite well in all three cases. There are some deviations at the extremes of the curves, however. In addition, there is some variety in the listed parameters shown for each case.

Figure 8 shows a similar set of curves for ground range versus elevation angle for the three cases. Here we see that there is considerable deviation in the ranges associated with the larger tilt angle. Experience has shown that the fitting technique identifies tilt angle quite

accurately for simulated cases, but that with real data the variance of the calculated tilt angles may be larger than that of the real tilts themselves. Therefore, tilts have to be treated with considerable care.

We conclude that this sort of backscatter sounding with this present interpretation may well be quite useful for range calculations, but may be in considerable error when it comes to identifying the actual critical frequency and semithickness.

3. FURTHER RANGE ESTIMATION PROCEDURES

With a given ionosphere model one can obtain a large number of ranges for the different E-layer and F-layer hops which can be associated with the several incoming mode angles. The problem is to develop tests, procedures, and auxiliary data which can be used to effectively choose the correct mode combination for the most accurate range determination. The two principal considerations are the probability of a given mode's existing and its probability of being detected with the given observation system. In addition there is the related criterion of reasonableness and the requirement that for two or more modes the different ranges must coincide to a degree which can be prescribed by the selection process.

The calculation of the probability of a given mode's existing can best be described by illustration. Thus, the probability of an E-hop is determined by whether the E-layer critical frequency is sufficiently high to reflect the ray at the given angle of incidence. For E_s some of the energy may pass through the layer and some may be reflected and this situation affects the probability of an F-layer mode existing. In addition, for the F-mode the F-layer critical frequency must be high enough to support propagation at the given angle. The last control point for the F-hop is located at the point where the ray passes through or is reflected from the top of the E-layer. For multihop modes there are a large number of control points to be calculated. The program as presently constituted uses the techniques of long-term predictions to determine the probability of the critical frequency of the E-layer exceeding the operating frequency divided by secant φ, the minimum E-layer critical frequency required to support propagation. The ordinary E-layer critical frequencies are first calculated and if they are sufficiently high to cause reflection at the given angle, no further calculations for that particular control point are necessary. If no reflection from ordinary E takes place, the coefficients for both blanketing and non-blanketing E_s are examined

for probabilities of either complete or partial reflection. While it is likely that the probabilities at the different control points for a given mode angle are not completely independent, we are forced to assume that they are, since we have little information as to their relationship. Thus the total probability for a given mode consists of the product of the probabilities at the individual control points.

The question of whether a given mode will be detected by the system is principally determined by the signal strength of the mode and the antenna patterns of the receiver and transmitter. For the range estimation program path loss information is derived from a program similar to the long term predictions program described in ITS-78 (Barghausen, et al. 1969) but tailored to the specific geometry of a given mode.

Perhaps the range estimation procedure can best be illustrated by showing an example of a computer printout for a specific case. Figure 9 shows a set of calculations made for a transmission from a transponder location at Orlando, Florida, for February 14, 1967. At the top of the page is the date, universal time, location of the transmitter source (which would not ordinarily be known in actual application), the ionospheric parameters derived from the backscatter data, and the operating frequency. The received mode angles head columns which list calculated ranges, mode probabilities, and path loss figures appropriate to the modes tabulated in the column at the far left of the figure. From this listing the correct combination of modes must be chosen to obtain the range estimate. This combination must include a range from each of the mode angle columns but cannot include more than one contribution from each row. This simply says that in the final estimate average there can be only one range for each mode angle and only one angle for each mode.

Figure 10 is another computer printout which can be used to illustrate the remaining range estimation procedure. By the choice procedure which will be described, the first five range estimate rankings are printed. At the left are the mode listings along with the probability and path loss data. In succeeding columns are the mean range, range standard deviation, mode combination probability average, field strength average and maximum deviation (between the extreme values of the individuals in the mode combination), a special category called weighted modes and the final rank number. The column heading labeled field strength average is really a path loss figure so smaller numbers correspond to stronger signals. The figures in the parentheses are the rankings for the mode combinations considering only the parameter appropriate to the column. Some of the information in the columns

do not enter into the ranking procedure so the parentheses are left unfilled. A column of true deviations is included only for the testing procedure where the range to the transmitter is known and can be compared with the range estimate and used in various tabulations of error statistics.

The final rankings are performed on the basis of the range standard deviation, the probability average, field strength average, and the weighted combination weights. The final rank is determined by summing the individual column rankings weighted in the above order by multiplying by 1, 3, 1, 1 respectively and ordering from low numbers to high ones. In the case of ties we again look to the individual column rankings in the order, 1) combination weights, 2) probability average, 3) field strength average, and 4) range standard deviation, until the tie is broken.

The development of the combination weights was done using the above procedure with many different mode weight combinations and determining which combination provided the best answers. The rank weightings were determined in much the same way. With weightings determined in this way, however, there is a question as to how much changing the location of the transponders would have changed the value of the weightings. Therefore, to be completely general one should probably leave out the arbitrary mode weightings from the selection procedure. However, the weighting values can be developed and tailored for particular areas.

4. TESTS OF THE RANGE ESTIMATION COMPUTER PROGRAM

During the coordinated propagation experiment of 1966-1968 mode angles for transponder transmissions from Meridian, Mississippi, and Orlando, Florida,were measured. Elevation angle versus delay time backscatter records were also made. To test the range estimation program these data were used as input to the program. At the time of the experiment only two mode angles from each transponder location were measured with some effort to achieve precision. Sometimes there were more than two mode angles present. To work most effectively the range estimation program must input all of the authentic mode angles received. To that end we scaled the filmed reductions of the backscatter magnetic tapes whose signal gains were optimized for the backscatter rather than the mode angle responses. Nevertheless, we were able to obtain at least one reasonable set of mode angles for each hour of operation. There seemed to be little point in scaling

mode angles at a greater frequency than once each hour since independent data points were desired for the test. This approach allowed between 1700 and 1800 range estimates to be made with about half associated with each transponder location.

For one run of the data any range between 0 and 4000 km was allowed. For the other run it was assumed that it was known whether the "unknown" location fell in the range 0-2000 or 2000-4000 km. The first situation mentioned has been designated as Case I and the second as Case II. In determining the ionospheric parameters from backscatter no tilts were allowed and the semi-thickness was allowed values between 5 and 200 km. Figures 11-14 show the statistics of the errors for Case I for both the Meridian and the Orlando data considering both the first choice estimates and the best of the first two choices in terms of the least error from the known range. It can be seen that the Meridian results are in general quite good although the Orlando results are poor especially for the first choices. Figures 15-18 show the results in a similar way for the Case II. The results are much improved, particularly for Orlando. This set of results illustrates one of the principal problems with the range estimation program -- that it often estimates one-half or double the correct range. Most of the large errors are estimates at one-half range. These errors result from the association of incorrect propagation modes with the observed mode angles. There is some dispersion caused by errors in the measurement of the mode angles themselves, estimation of the ionospheric parameters, and in the failure of the long-term prediction program to correctly predict characteristics of E_s at a given time.

The program was also used with an allowed tilt which was determined from the backscatter data. The statistics were not as good as for the non-tilt case. Apparently the backscatter delay versus elevation angle data can be fitted very well with the tilt allowed. However, the variance in the calculated tilt angles can result in some fairly large errors in range. Thus there are smaller errors if no tilt is allowed. It is possible with a very careful scaling of the backscatter data that the tilt model would provide better answers.

A number of attempts were made to improve the results. Among them were:

1) including antenna pattern effects in the signal strength calculation,
2) ignoring the path loss in the selection process,
3) limiting the number of possible modes considered, and
4) ignoring E_s effects in the selection process.

The latter approach improved some of the statistics considerably but resulted in no estimate being made in 30 percent of the cases, which is probably above the tolerable level. Various other trials were made but resulted in no improvement. Thus the initial approach appears to have been the best one.

A fairly detailed study of a sample of the larger errors was made and compared with a sample of small errors. The conclusion was that about 10 - 15 percent of the bad estimates were caused by gross scaling errors of the mode angle data. Perhaps 5 - 10 percent of the bad estimates were caused by scaling errors of the backscatter data. Most of the remaining large errors were caused by improper mode combination choices. Many of these bad choices can be traced to an improper assessment of the sporadic E behavior at a given time by the predictions program. In the case of the Orlando results some of the improper choices could be traced to the influence of the path loss computations.

5. DISCUSSION AND CONCLUSIONS

It appears that with the backscatter interpretation given here it is better to ignore tilts and use non-tilt geometry for range estimation unless scaling of the data can be performed with greater precision than used here. The range estimation program as presently constituted will do quite well with very carefully taken and scaled data as would be the case under circumstances in which range estimation was the main objective. Very great improvement of the error statistics could also be achieved with real time information concerning the sporadic E conditions. Some of this information could be derived from the backscatter records. How well the program works will not be known until a full scale test under these conditions is performed.

6. REFERENCES

1. Barghausen, Alfred F., James W. Finney, L. Lee Proctor, and Larry D. Schultz, Predicting long-term operational parameters of high-frequency sky-wave telecommunications systems, ESSA Technical Report 110-ITS 78, Boulder Laboratories (1969).

2. Mitra, S. K., The upper atmosphere, second edition, The Asiatic Society, 1 Park Street, Calcutta, India,252-253 (1952).

3. Wieder, B., Some results of a sweep-frequency propagation experiment over a 1100 km east-west path, J. Geophys. Res. 60, 395, (1955).

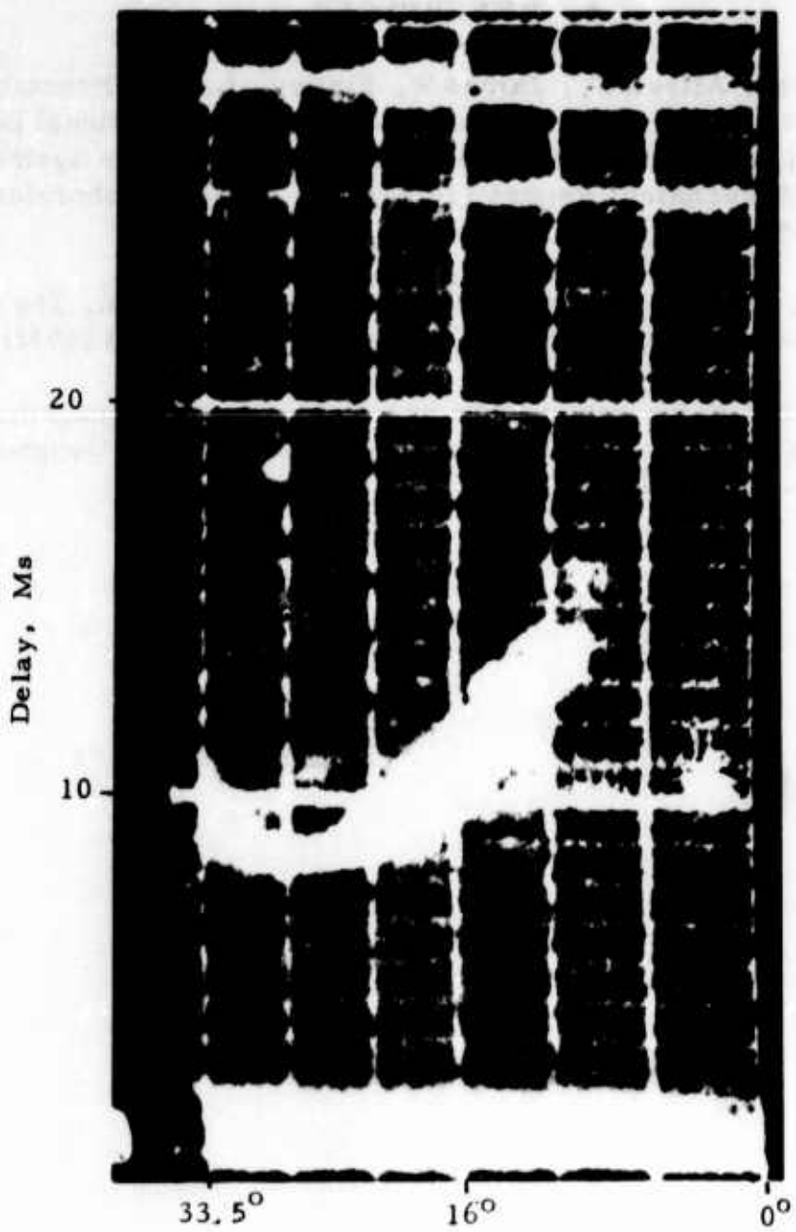

Figure 1. Elevation scan display of backscatter at about 15.5 MHz taken during a November day in 1966 at 1435 MST.

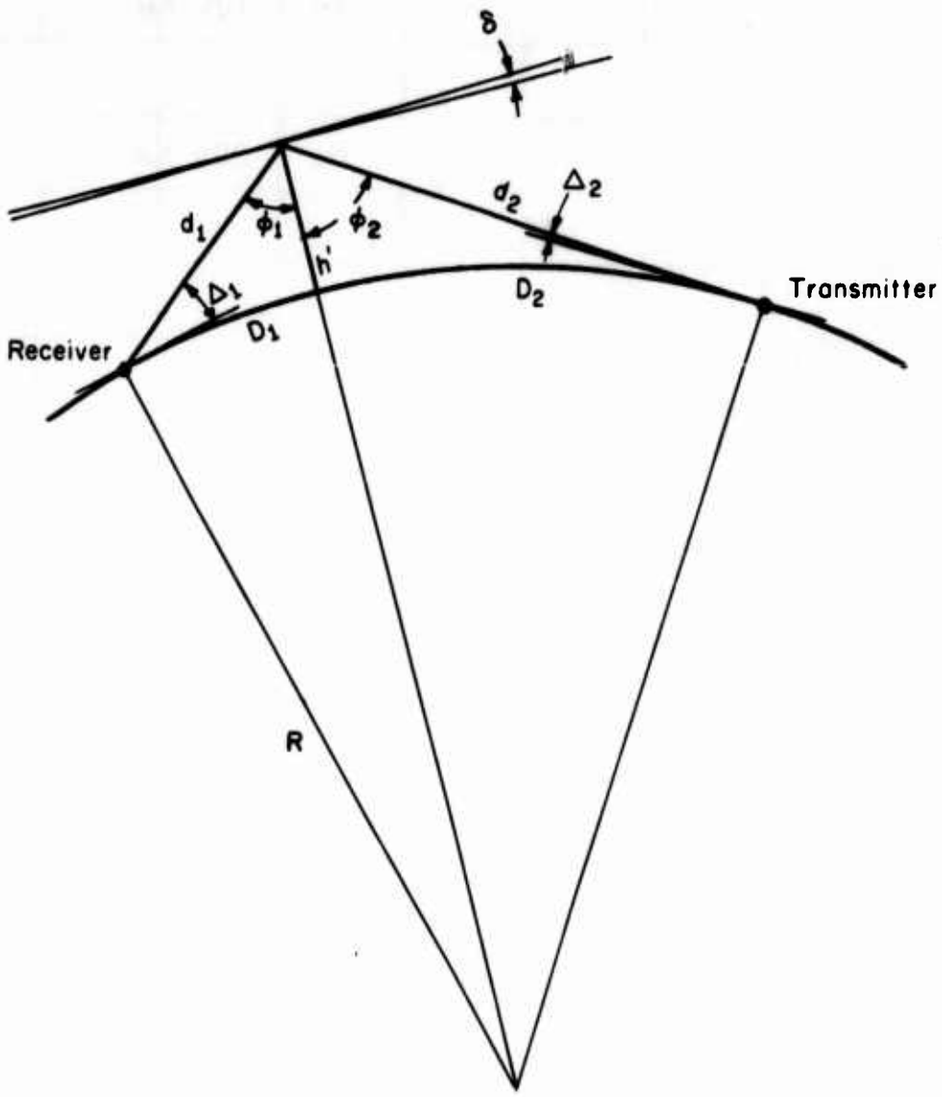

Figure 2. TILT VIRTUAL PATH GEOMETRY

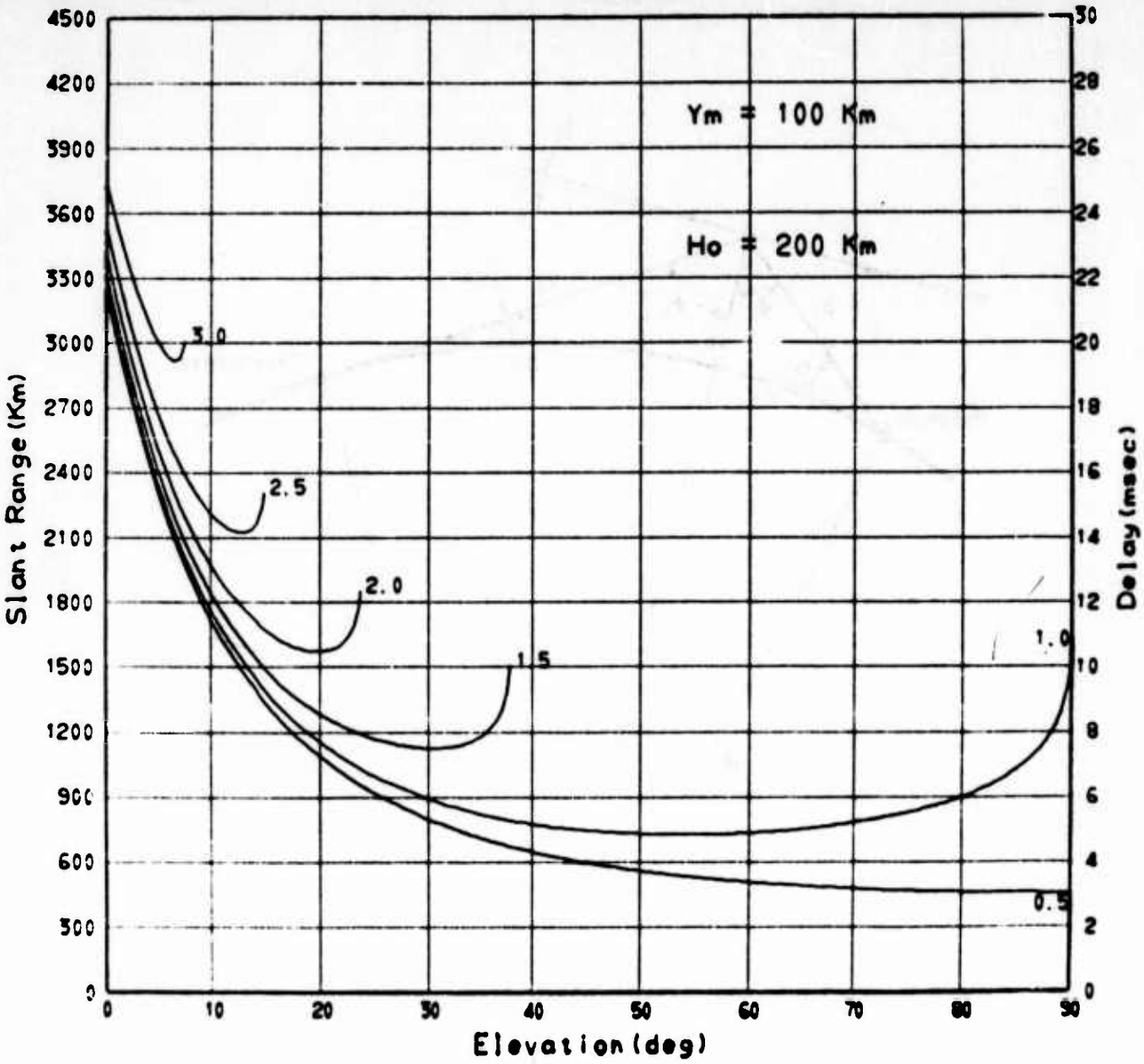

Figure 3. Curves of slant range or backscatter delay versus elevation angle parametric in ratios of operating frequency to critical frequency for parabolic layer parameters indicated.

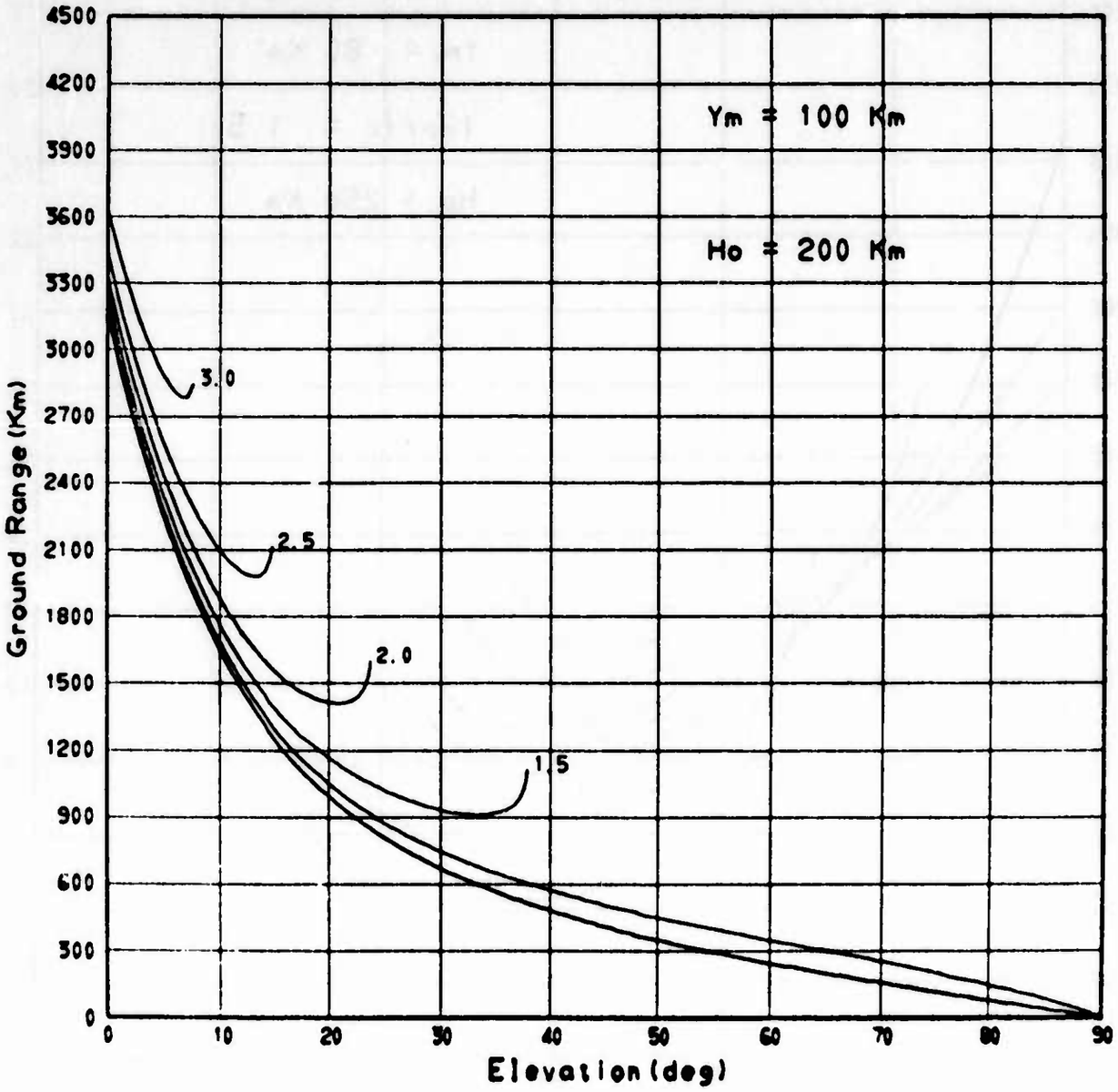

Figure 4. Curves of ground range versus elevation angle parametric in ratios of operating frequency to critical frequency for parabolic layer parameters indicated.

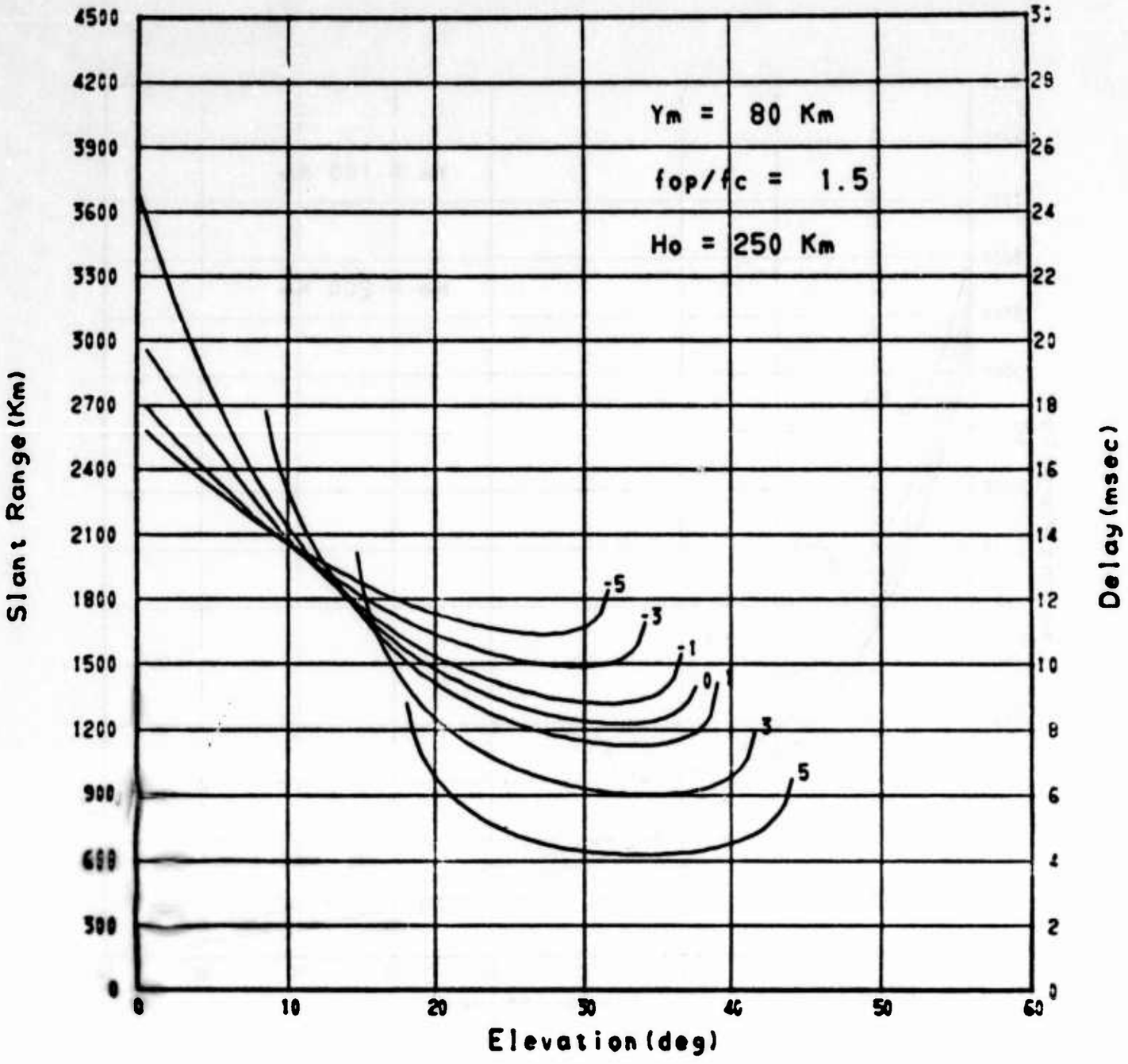

Figure 5. Slant range versus elevation angle (Δ_1) for various ionospheric tilt angles between -5^o and $+5^o$ for the parameters shown. H_o is the height at 2000 km range.

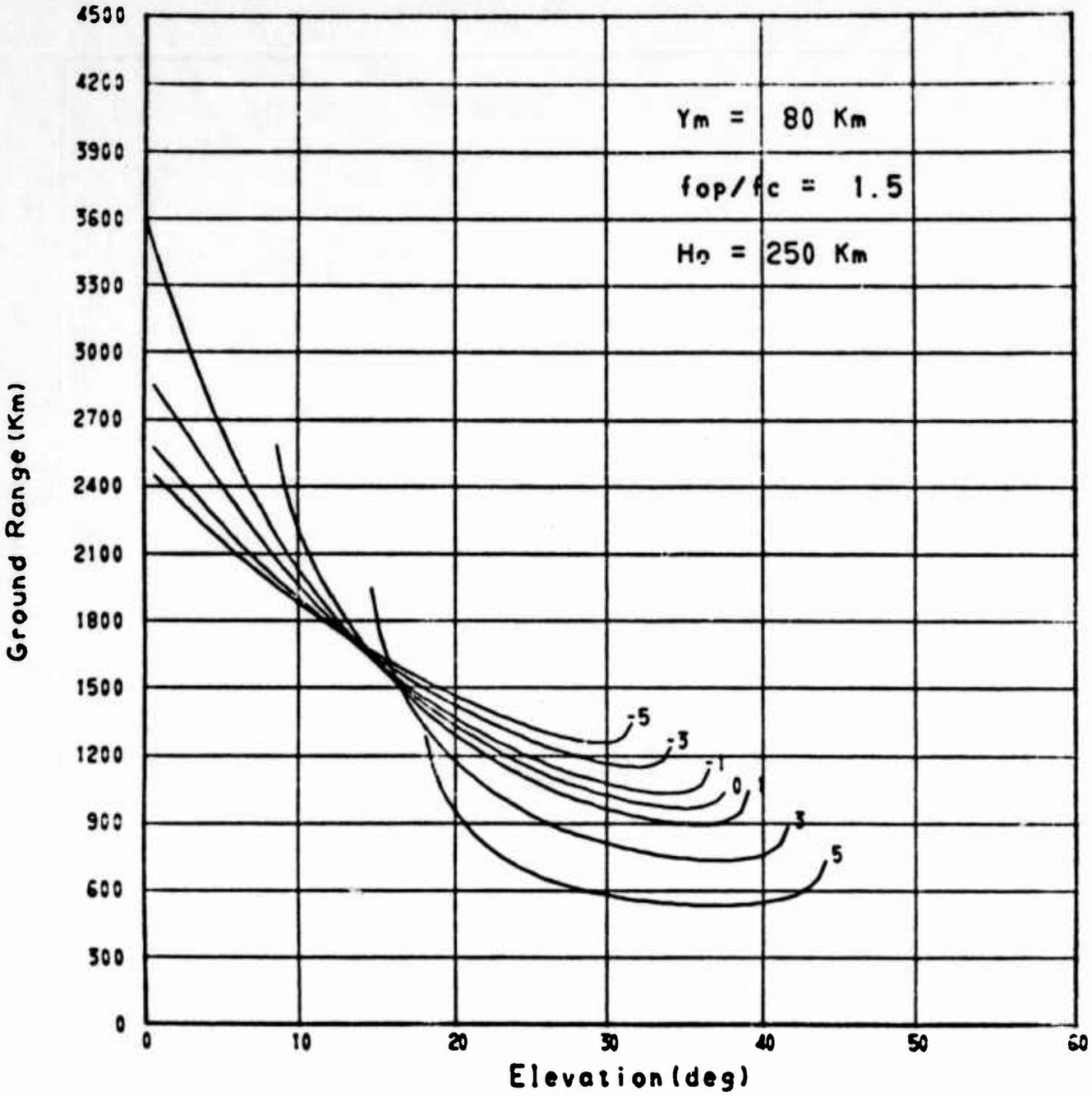

Figure 6. Ground range versus elevation angle (Δ_1) for various ionospheric tilt angles.

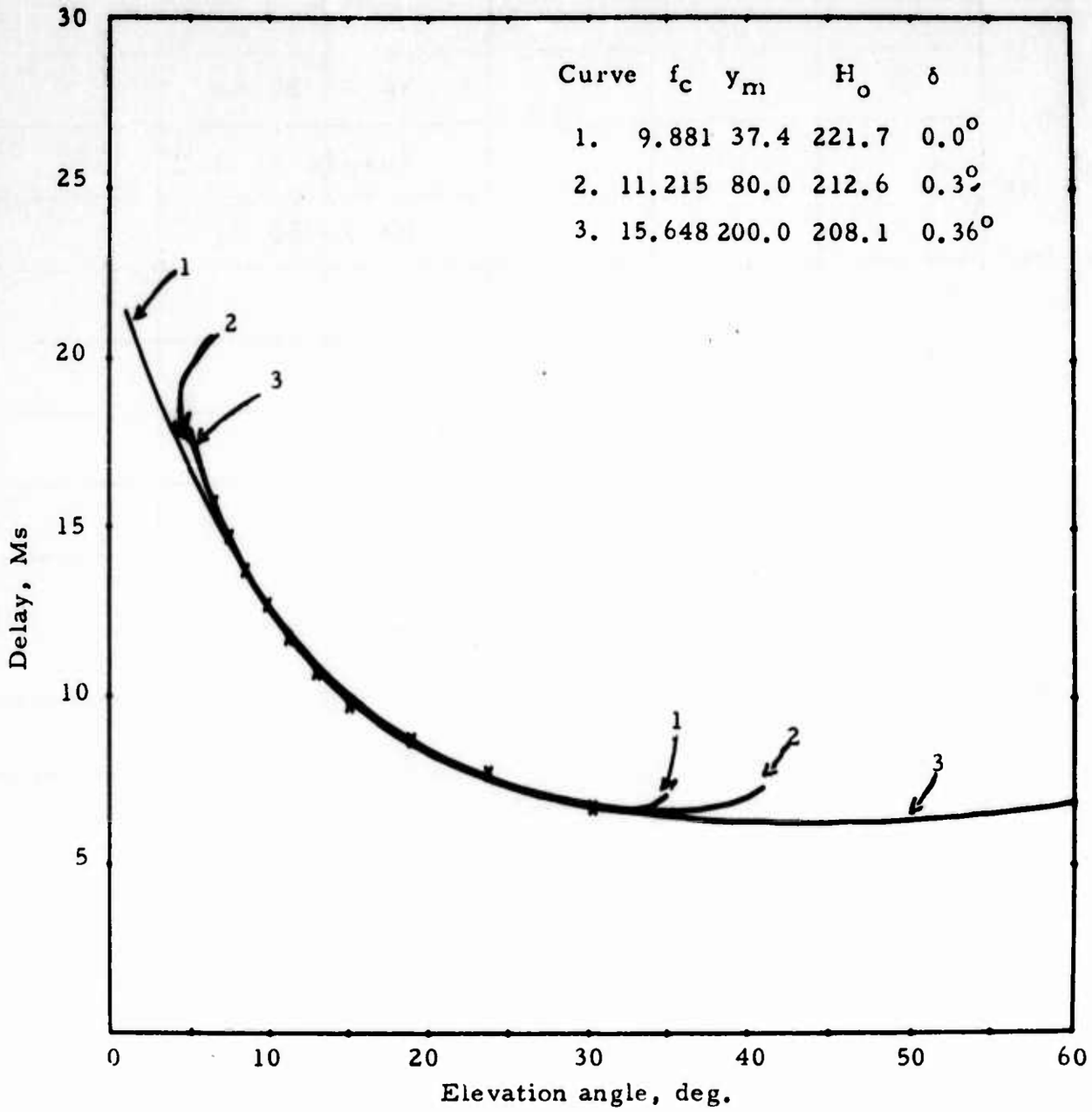

Figure 7. Examples of elevation angle versus backscatter delay curves for three sets of ionospheric parameters derived from the same set of input points indicated by the small x's.

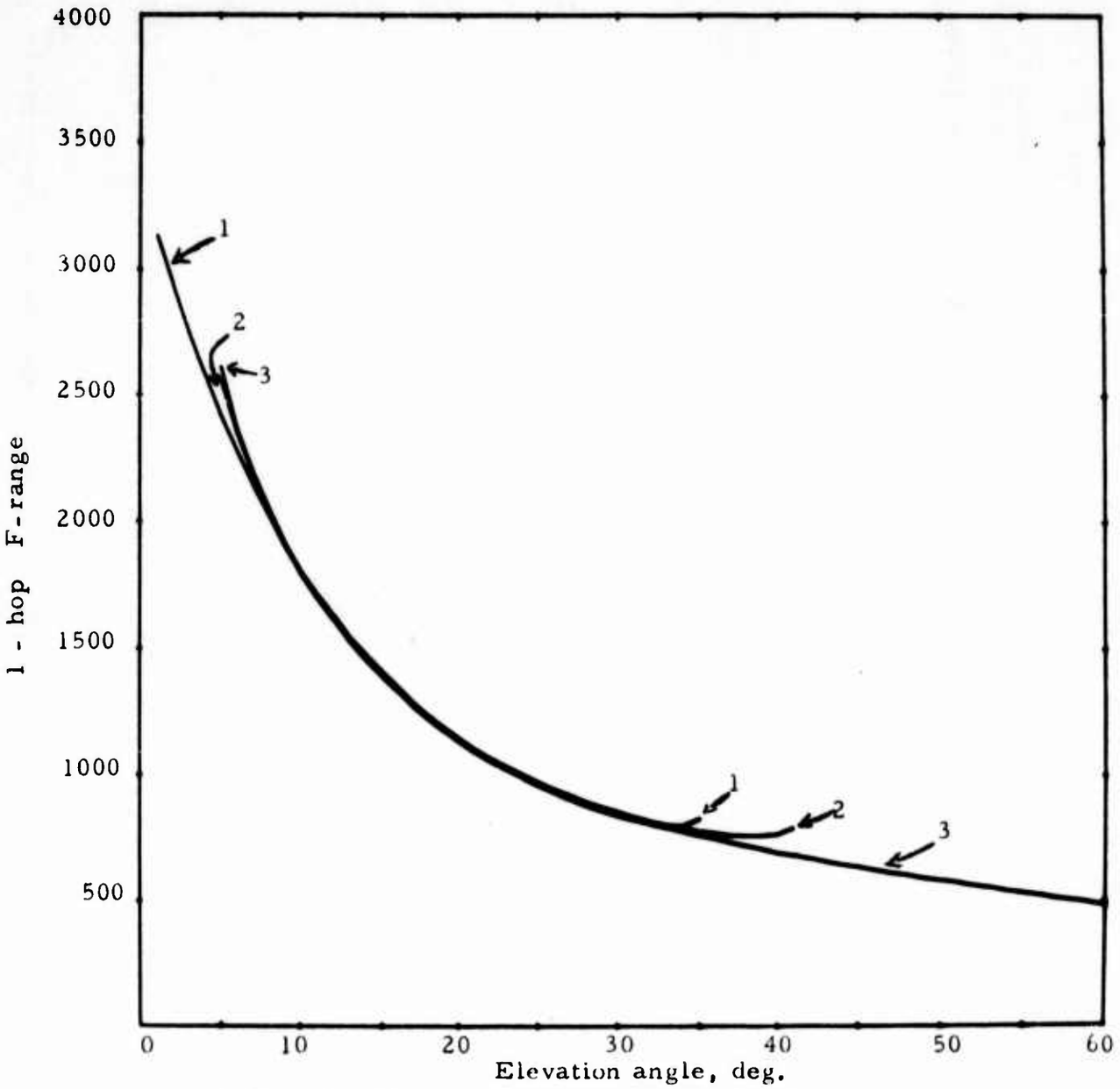

Figure 8. One-hop F ground ranges for the same three sets of ionospheric parameters shown in figure 7.

FB DATE: 67/ 45 TIME: 1420 OP. FREQ. = 11.530 MHZ COMPUTED 01/23/70

CRIT. FREQ. = 7.242 MHZ H_0 = 179.62 KM Y_M = 56.61 KM LEAST SQ RMS = 4.875+000

FED DATE: 67/ 45 TIME: 1420 OP. FREQ. = 11.430 MHZ E LAYER HEIGHT = 110.00 KM

MODE NO	MODE COMB	MODE ANGLE IN DEGREES 7.53	14.23	24.19
1	1E	1206,1.000, 115	763,0.020, 112	463,0.000, 108
2	2E	2412,1.000, 128	1526,0.001, 124	926,0.000, 120
3	3E	3618,1.000, 144	2290,0.000, 134	1389,0.000, 129
4	1F	1614,1.000, 119	1261,1.000, 116	874,1.000, 114
5	2F	3627,1.000, 136	2522,0.995, 129	1748,1.000, 126
6	3F	5441,1.000, 150	3783,0.886, 143	2623,1.000, 136
7	1F+1E	3019,1.000, 132	2024,0.100, 127	1337,0.003, 123
8	1F+2E	4225,1.000, 148	2787,0.016, 137	1800,0.000, 132
9	2F-1E	2421,0.000, 122	1759,0.000, 119	1286,0.000, 117
10	2F+1E	4833,1.000, 149	3285,0.186, 140	2211,0.023, 134
11	2F+2E	6039,1.000, 160	4048,0.210, 154	2674,0.038, 143
12	3F-2E	3029,0.000, 125	2256,0.000, 122	1697,0.000, 119
13	3F-1E	4235,0.000, 139	3019,0.005, 132	2160,0.000, 128
14	3F+1E	6547,1.000, 161	4546,0.215, 155	3086,0.053, 146
15	3F+2E	7853,1.000, 172	5309,0.211, 165	3548,0.067, 156
16	4F-3E	3637,0.000, 127	2754,0.000, 124	2108,0.000, 121
17	4F-2E	4843,0.000, 140	3517,0.000, 134	2571,0.000, 130
18	4F-1E	6049,0.000, 151	4280,0.061, 146	3034,0.000, 139
19	4F+1E	8460,1.000, 172	5807,0.669, 166	3960,0.076, 157
20	4F+2E	9666,1.000, 183	6570,0.669, 175	4423,0.007, 169

(02)

Figure 9. Example of computer print-out of basic computations for range estimation.

FFO DATE = 67/ 45 TIME = 1420 OP. FREQ. = 11.430 MHZ E LAYER HEIGHT = 110.00 KM (15)

(MODE, ANGLE, RANGE, PROB, FIELD)	RANGE TRUE DEV	RANGE AVERAGE	RANGE STD DEV	PROBABILITY AVERAGE	FIELD STRENGTH AVERAGE	FIELD STRENGTH MAX DEV	WEIGHTED MODES	WEIGHTED COMB PAR	FINAL RANK
(2E , 7.53, 2412,1.0000, 128)	9( )	2519( )	86(3)	1(2)	131(16)	8( )	4(1)	42( )	1
(2F , 14.23, 2522,0.9951, 129)									
(3F , 24.19, 2623,1.0000, 136)									
(2E , 7.53, 2412,1.0000, 128)	146( )	2382( )	128(10)	1(7)	131(15)	6( )	4(1)	62( )	2
(2F , 14.23, 2522,0.9951, 129)									
(2F+2E, 24.19, 2211,0.0226, 134)									
(2F , 7.53, 2412,1.0000, 128)	8( )	2536( )	108(5)	1(6)	133(21)	15( )	4(1)	66( )	3
(2F , 14.23, 2522,0.9951, 129)									
(2F+2E, 24.19, 2674,0.0385, 143)									
(1F+1F, 7.53, 2019,1.0000, 132)	193( )	2721( )	215(24)	1(2)	133(19)	7( )	1(3)	71( )	4
(2F , 14.23, 2522,0.9951, 129)									
(3F , 24.19, 2623,1.0000, 136)									
(2E , 7.53, 2412,1.0000, 128)	175( )	2353( )	248(31)	1(4)	130(14)	10( )	3(2)	72( )	5
(1F+1E, 14.23, 2024,0.9997, 127)									
(3F , 24.19, 2623,1.0000, 136)									

(21)

Figure 10. Example of computer print out of range estimate choice ranking procedure.

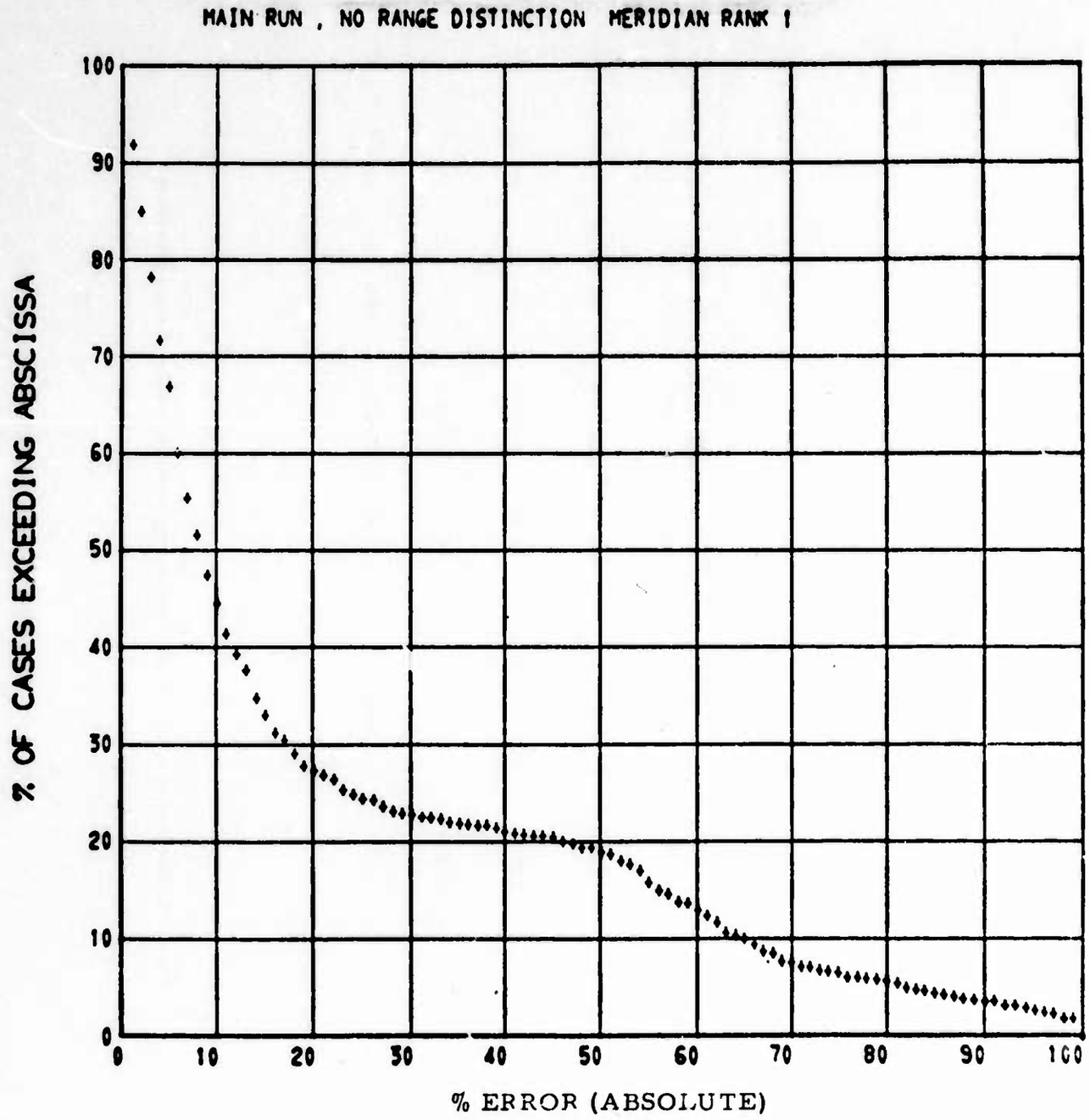

Figure 11. Absolute error distribution of first choice Case I range estimates for all Meridian data.

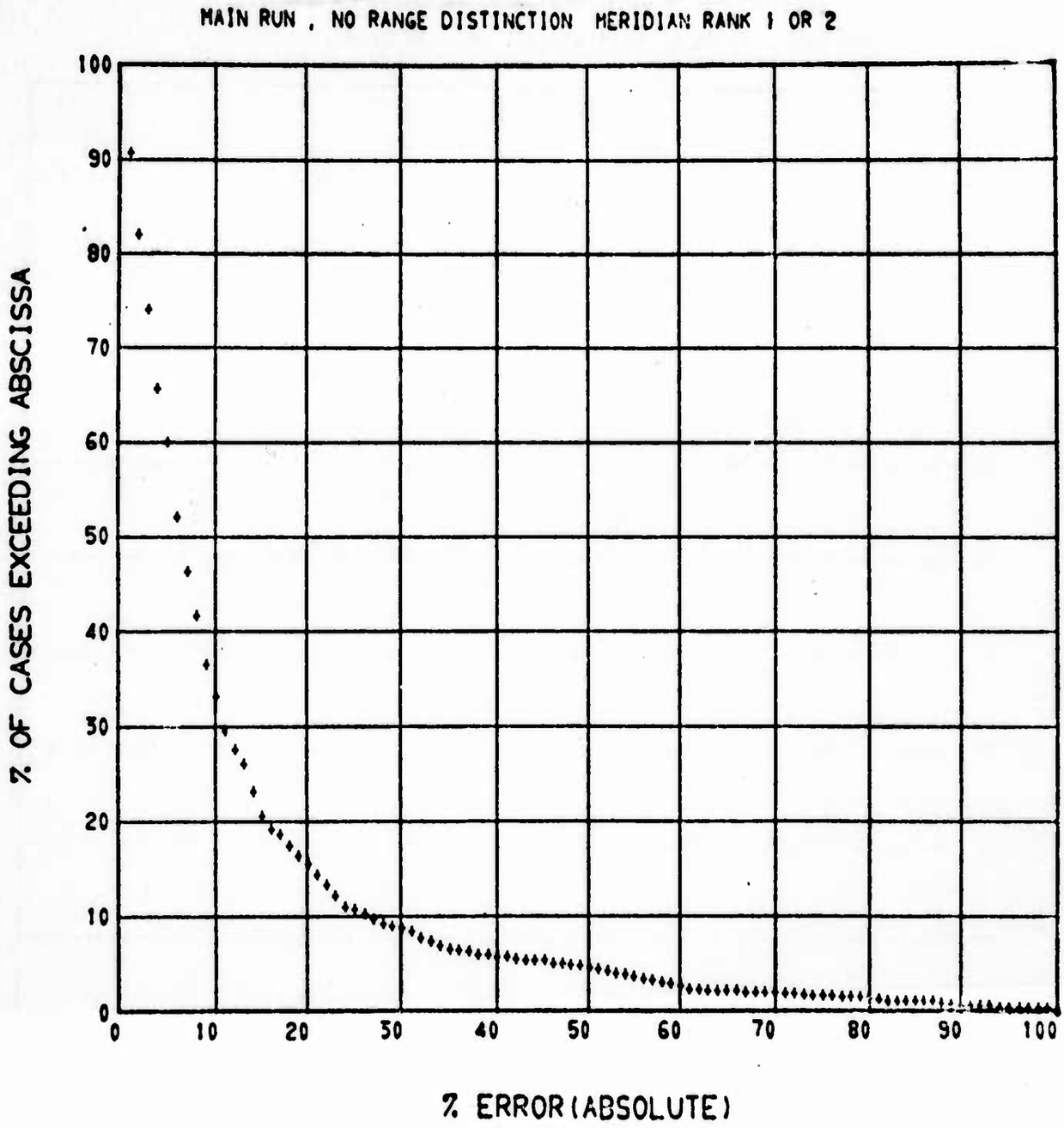

Figure 12. Absolute error distribution of the best of the first and second choice Case I range estimates for all Meridian data.

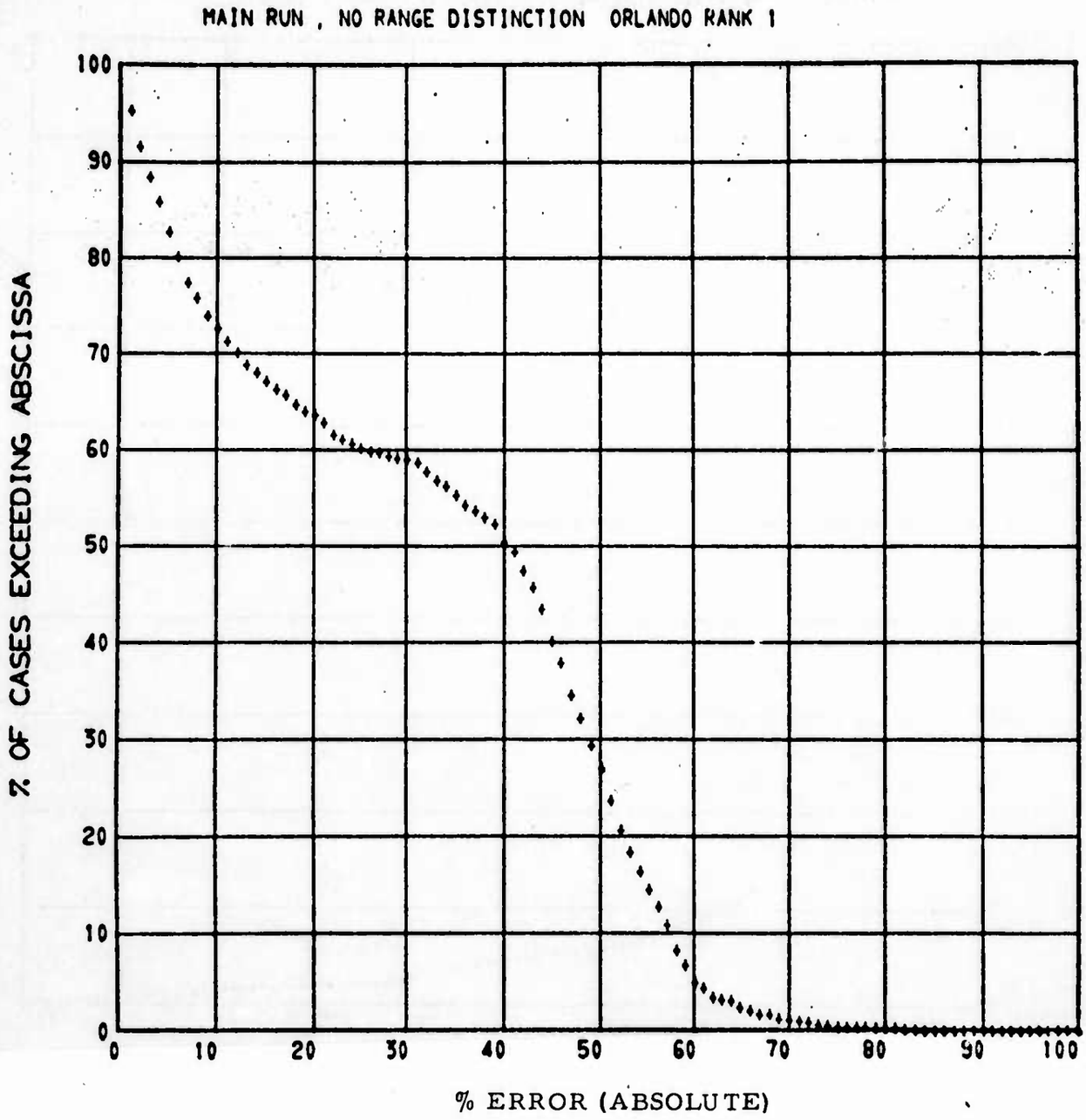

Figure 13. Absolute error distribution of first choice Case I estimates for all Orlando data.

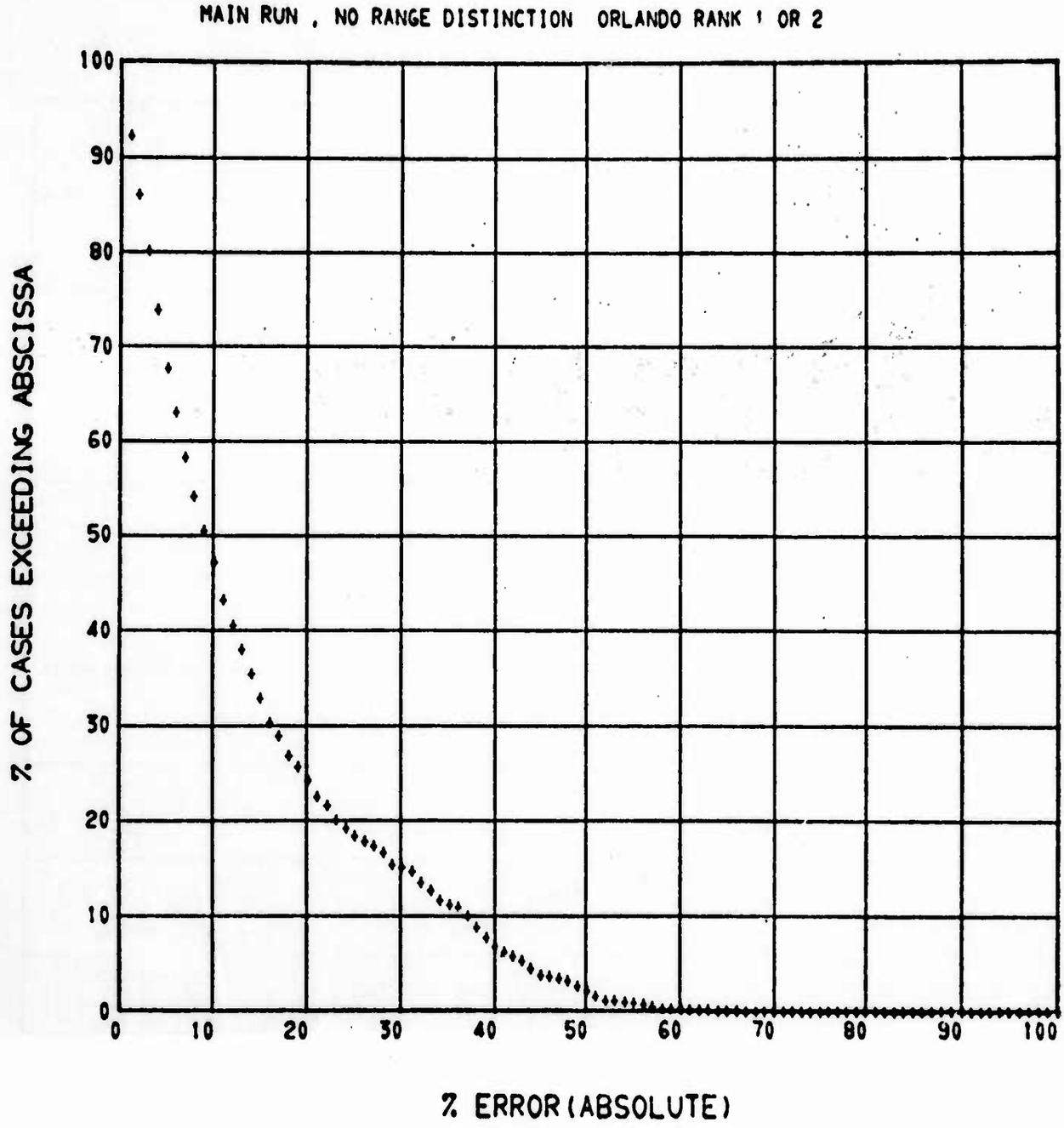

Figure 14. Absolute error distribution of the best of the first and second choice Case I range estimates for all Orlando data.

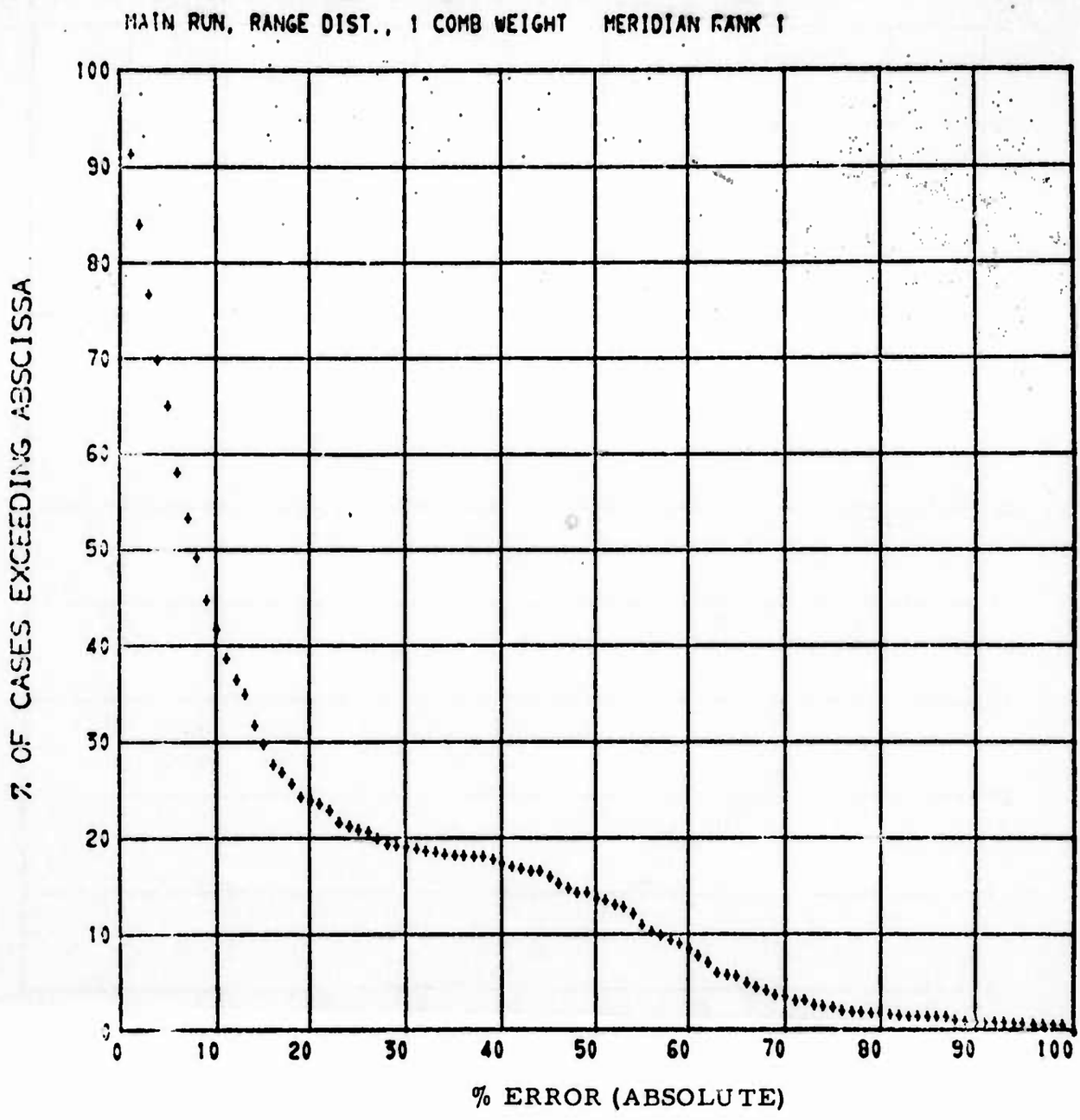

Figure 15. Absolute error distribution of first choice Case II range estimates for all Meridian data.

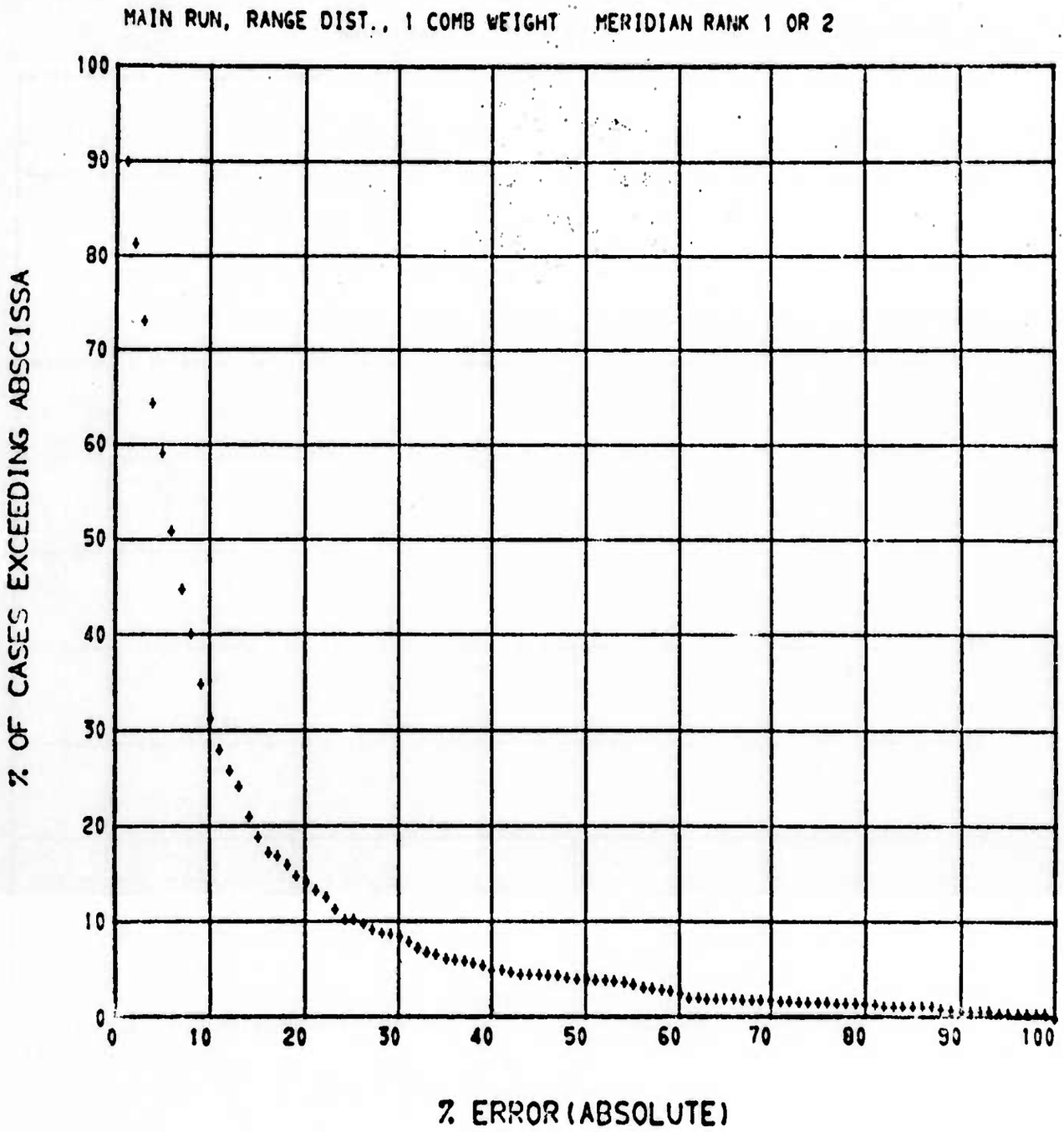

Figure 16. Absolute error distribution of the best of the first and second choice Case II range estimates for all Meridian data.

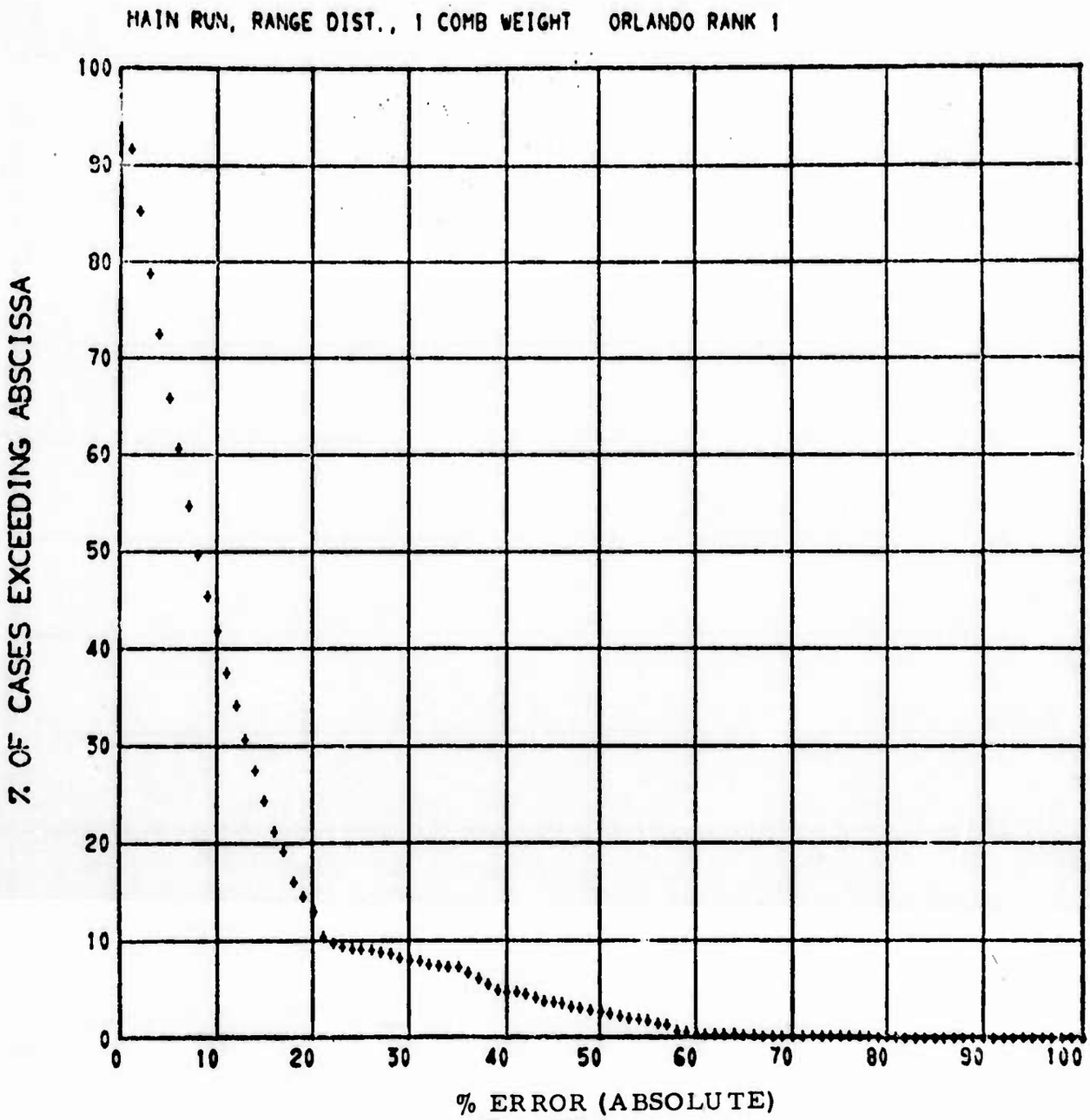

Figure 17. Absolute error distribution of first choice Case II estimates for all Orlando data.

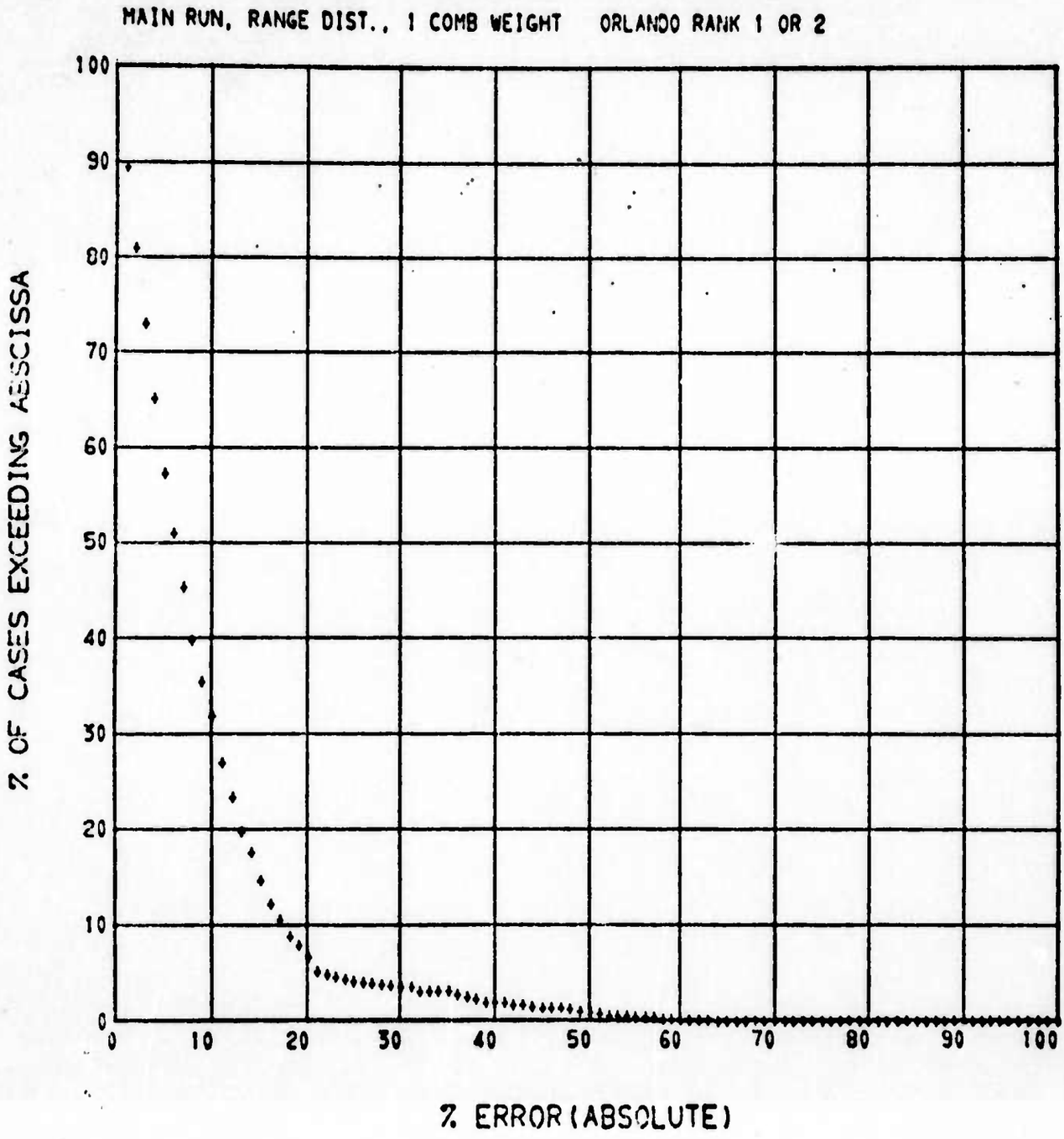

Figure 18. Absolute error distribution of the best of the first and second choice Case II range estimates for all Orlando data.

USCOMM - ERL

THE EFFECTIVENESS OF SPECTRUM AND AZIMUTH SPREAD MEASUREMENTS IN DETECTING SIDESCATTER

J. C. Blair
U.S. Department of Commerce
Office of Telecommunications
Institute for Telecommunication Sciences
Boulder, Colorado 80302

Radio DF measurements made from HF signals of unknown origin can be considerably in error due to offpath reception from ground sidescatter. Sidescatter signals are received with greater spectrum and azimuth spread than those propagated via great circle.

An experiment was conducted over two paths (1300 and 2300 km) to determine the effectiveness of spectrum and azimuth spread measurements in determining if a received signal is propagated via sidescatter or great circle.

The fading component of the complex spectrum was found to provide most of the detection capability. From fading spread measurements, about 75 percent of sidescatter could be detected with an estimated 95 percent probability of success over the shorter path. From azimuth spread measurements (1300 km path), about 85 percent of sidescatter could be detected with an estimated 95 percent probability of success. The spread measurements over the long path proved to be less effective in sidescatter detection. The overall results of the experiment indicate that an effective detection system can be designed for unknown paths.

1. INTRODUCTION

Sidescatter is the mode of propagation that includes two or more ionospheric hops with an intermediate encounter with the ground at a location that is not along the great-circle path. The existence of this mode has been known for many years (Feldman[1]; Edwards and Jansky[2]; Dieminger[3]). Sidescatter signals are usually received in scattered

attenuated form via deviated paths, sometimes with widely fluctuating azimuths of arrival. Off-path signals can, of course, be caused by other effects such as ionospheric irregularities (Whale[4]) and scattering from sporadic E and spread F (Hayden[5]). However, in the author's opinion, most multihop transmissions propagating via paths not on the great circle appear to be due to sidescatter.

Radio DF measurements made from HF signals of unknown origin can be considerably in error due to off-path reception from ground sidescatter. The purpose of the experiment reported in this paper was to determine the effectiveness of spectrum and azimuth spread measurements in determining if unknown signals are sidescatter or great circle propagated.

2. EXPERIMENTAL ARRANGEMENT

Transmissions were received at Boulder, Colorado. During the first part of the experiment, 300-μs and 6-ms pulse signals were received from Long Branch, Illinois (1300 km path length). During the last part, 300-μs and 6-ms pulsed transmissions were received from Washington, D.C. (2350 km path). For convenience the 1300 km path will be referred to as the short path and the 2350 km one will be called the long path. Dates and times when data were taken are given in table 1 for the short path and in table 2 for the long one.

About 40 kW of power was radiated at both transmitting locations. Azimuthal spread was measured from records obtained from the ITS high resolution scan array with a beam width of about 2°. The way in which the scan sector of this array (about 60° wide at 17 MHz) is illuminated by the two transmitters is shown in figure 1. The Havana antenna is directed at 215° E of N and the Washington antenna has a bearing of 190°. The two transmissions illuminate the scan sector at different areas for sidescatter, but the beams are wide enough to allow great-circle propagation. Sidescatter signals were separated from those propagated via the great circle on the basis of time-of-arrival differences. The 300-μs pulses were transmitted 10 minutes out of each hour and were used only for operators to keep track of closely spaced modes. All azimuth and spectrum spread measurements were made from the 6-ms pulses which were transmitted 50 minutes of each hour. A new set of azimuth and spectrum records was made every 10 minutes.

Fading and Doppler spread measurements were made from sidescatter received on both 2° and 70° beam width antennas. Great circle spectrum measurements were made from signals received on 70° beam width antennas only.

Table 1. Schedule of data runs for the Long Branch-Boulder path.

Date	Time, UT	Type of Data
Feb. 27, 1969	2005 to 2115	Spectrum and azimuth
April 3	1622 to 2300	Spectrum and azimuth
April 5	0000 to 0220	Spectrum and azimuth
April 5	0225 to 0615	Spectrum and azimuth
April 8	0825 to 1215	Spectrum and azimuth
April 8	1224 to 1445	Spectrum and azimuth
June 3	0820 to 1020	Spectrum and azimuth
	1026 to 1220	Spectrum and azimuth
	1225 to 1235	Spectrum and azimuth
June 4	1400 to 1620	Spectrum and azimuth
	1620 to 2200	Spectrum and azimuth
June 5	2230 to 0000	Spectrum and azimuth
June 6	0000 to 0600	Spectrum and azimuth
	0320 to 0330	Spectrum and azimuth
July 7	1440 to 1835	Spectrum and azimuth
	1840 to 2200	Spectrum and azimuth
July 8	1430 to 1700	Spectrum and azimuth
	1710 to 1845	Spectrum and azimuth
	1850 to 2000	Spectrum and azimuth
	2000 to 2200	Spectrum and azimuth
July 9	1430 to 2035	Spectrum and azimuth
	2040 to 2200	Spectrum and azimuth
July 15	0644 to 0822	Azimuth only
	0824 to 1400	Azimuth only
July 16	1436 to 1917	Azimuth only
	1920 to 2200	Azimuth only
July 17	2200 to 2315	Azimuth only
	2320 to 0000	Azimuth only
July 18	0000 to 0530	Azimuth only
Aug. 12	0625 to 1110	Spectrum and azimuth
	1120 to 1400	Spectrum and azimuth
Aug. 13	1350 to 2200	Spectrum and azimuth
Aug. 15	0039 to 0310	Spectrum and azimuth
Aug. 15	0320 to 0510	Spectrum and azimuth
Aug. 26	0630 to 0950	Spectrum and azimuth
	1005 to 1400	Spectrum and azimuth
Aug. 27	1415 to 1610	Spectrum and azimuth
	1630 to 2200	Spectrum and azimuth
Aug. 28	2220 to 0000	Spectrum and azimuth
Agu. 29	0315 to 0545	Spectrum and azimuth

Table 1. Schedule of data runs for the Long Branch-Boulder path (cont.)

Date	Time, UT	Type of Data
Oct. 7	0705 to 1300	Azimuth only
	1305 to 1350	Azimuth only
Oct. 8	1420 to 2200	Azimuth only
Oct. 9	2240 to 0000	Azimuth only
Oct. 10	0000 to 0251	Azimuth only
Oct. 21	0545 to 0620	Spectrum and azimuth
	0623 to 1120	Spectrum and azimuth
	1121 to 1218	Spectrum and azimuth
Oct. 22	1440 to 2140	Spectrum and azimuth
Oct. 23	2210 to 0000	Spectrum and azimuth
Oct. 24	0000 to 0222	Spectrum and azimuth
	0222 to 0317	Spectrum and azimuth
	0317 to 0440	Spectrum and azimuth

Table 2. Schedule of data runs for the Washington-Boulder path

Date	Time, UT	Type of Data
June 16, 1970	2217 to 0000	Spectrum only
June 17	0000 to 0522	Spectrum only
	0522 to 0727	Spectrum only
	0727 to 1315	Spectrum only
	1315 to 1330	Spectrum only
	1330 to 2137	Spectrum only
	2137 to 0000	Spectrum only
June 18	0000 to 0401	Spectrum only
	0401 to 0710	Spectrum only
	0710 to 1730	Spectrum only
	0730 to 1231	Spectrum only
August 25	1228 to 1330	Spectrum and azimuth
	1330 to 1515	Spectrum and azimuth
	1515 to 1740	Spectrum and azimuth
	1740 to 0000	Spectrum and azimuth
August 26	0000 to 0037	Spectrum and azimuth
	0037 to 0137	Spectrum and azimuth
	0137 to 0318	Spectrum and azimuth
	0318 to 0605	Spectrum and azimuth
	0605 to 1212	Spectrum and azimuth

Azimuth records were made from sidescatter signals sampled at four ranges (times of arrival) and the range with greatest azimuth spread was selected for the detection data. A running average technique was used that required a range to have more average azimuth spread for one hour before it was selected over the one previously chosen. This procedure prevented the inclusion of data influenced by ionospheric changes.

All fading, Doppler and azimuth records were carefully edited to eliminate those made during weak signal, high noise or interference conditions. Doppler and fading spectrums were obtained by taking Fourier transforms of receiver coherent and envelope detector outputs respectively. Doppler spread was not measured on the Boulder-Washington path because it proved to be less effective than fading spread on the Long Branch-Boulder path.

3. EXAMPLES OF RECORDS

Fading and Doppler waveforms, from receiver envelope and coherent detectors, were transformed into amplitude spectrums and normalized with a maximum value of unity. A 2-Hz offset was used to obtain a two-sided Doppler spectrum. Figure 2 shows examples of both types of spectrums for great circle and sidescatter. Examples of azimuth records (also with a maximum of unity) are presented in the form of the amplitude vs azimuth profiles of figure 3. These are shown for both paths and for great circle and sidescatter. At the frequency at which these records were made (about 16 MHz), the azimuth sector is scanned from 84 to 144°.

4. MEASUREMENT PARAMETERS

Spectrum and azimuth spread were defined in several ways to determine which was the most effective in sidescatter detection. Each definition was denoted by a parameter name. The two most effective parameters for spectrum spread are defined as follows:

(a) If a line is drawn parallel to the horizontal axis of the spectrum plot (see fig. 2) at the 0.3 amplitude level, some parts of the spectrum will extend above certain segments of this line. The sum of these horizontal segment lengths in Hz is defined as ϵ_3.

(b) The parameter θ_1 is defined as the width of a rectangle having the same area and height as the spectrum above the 0.1 amplitude level.

The two most effective parameters for azimuth measurement are defined as follows:

(a) If a line is drawn parallel to the horizontal axis of the azimuth record (see fig. 3) at the 0.3 amplitude level, some parts of the record will extend above certain segments of this line. The sum of these horizontal segment lengths in degrees is defined as α_3.

(b) The parameter γ is defined as the width of a rectangle having the same area and height as the azimuth profile above the 0.3 level.

Measurements below the 0.3 level were not made from azimuth records because antenna sidelobes which were normally about 15 dB down from the main lobe amplitude could cause spurious results when reinforced by interference from two or more modes.

5. COMPARISON OF SPECTRUM SPREAD FOR LONG AND SHORT PATHS

Figure 4 shows cumulative distributions of fading spread θ_1 for sidescatter and great circle for the long and short paths. Doppler spread is not shown because it was not measured over the long path. Great circle fading spread on the long path (curve 2) was about twice that measured on the short path (curve 1). The long-path sidescatter measured on the 2^o beam width antenna (curve 5) has a value of θ_1 at the median level about 50 percent greater than that shown by curve 3 for the short path. Comparison of curves 4 and 6 shows that the fading spread is somewhat greater on the long path when sidescatter is received on wide beam antennas. All great circle signals were received on 70^o beam widths during the experiment.

6. COMPARISON OF AZIMUTH SPREAD DATA FROM LONG AND SHORT PATHS

Figure 5 shows cumulative distributions of azimuth spread of sidescatter and great circle for the long and short paths. Great circle azimuth spread for both paths is about one fourth that for sidescatter at the median level. Great circle and sidescatter azimuth spread for the long path appear to be slightly less than for the short path. This result is statistically doubtful because only 62 samples of great circle and 56 samples of sidescatter had noise levels low enough to be accepted by the editing process. Moreover, all of these azimuth data for the long path were taken in one 24-hour period.

7. EFFECTIVENESS OF FADING AND AZIMUTH SPREAD MEASUREMENTS IN SIDESCATTER DETECTION

7.1 EFFECTIVENESS FOR KNOWN PATH LENGTHS

Figure 6 shows the distribution of all data samples as a function of fading bandwidth and estimated great circle probability. The upper numbers on each graph give the percent of all great circle signals received with spread corresponding to each 0.05 Hz segment of fading spectrum bandwidth; the lower numbers give the percent of all sidescatter in each spread range. Great circle data taken at times when the operating frequency was above the MUF were omitted from the plots because these are forward scatter from the ionosphere.

The assumption is made that only two kinds of signals will be received; these are great circle and sidescatter. The left-hand scale on the graphs gives the probability an unknown signal is great circle; the right-hand scale gives the probability it is sidescatter. As an example, of how the graphs are obtained, figure 6 (a) shows probability a signal is great circle or sidescatter for different values of fading spread measured by the parameter θ_1. The estimated great circle probability corresponding to a given range of spread is computed as the percentage of all signals received in this spread range that are great circle. For example, in figure 6 (a), the estimated probability a signal is great circle when θ_1 is between 0.15 and 0.20 Hz is

$$\frac{20.3 \times 100}{20.3 + 1.0} = 95.3\%$$

and the estimated probability a signal with this spread is sidescatter is

$$1 - 95.3 = 4.7\%$$

The estimated probability should be read from the dashed curve, which is smoothed to average out irregularities due to the limited number of data samples. If the value of θ_1 (figure 6(a)) of a received signal is between 0 and 0.2, the probability the signal is great circle is 95 percent or more and the probability of sidescatter is 5 percent or less. Adding the top numbers on the graph out to 0.2 Hz gives

$$3.2 + 22.3 + 19.8 + 20.3 = 65.6\% .$$

This means that about 66 percent of all great circle signals received over this path would be expected to have fading spread values between 0 and 0.2 Hz and that signals in this spread range have a 5 percent or less probability of being sidescatter. The plots in figure 7 for azimuth spread are similar to those for fading in figure 6.

At this point, it will simplify the presentation of data if the expressions "detection probability" and "detection effectiveness" are defined. If one is using a sidescatter detection technique to increase the accuracy of direction finding, he is really interested in determining if his signals have a high probability of being great circle propagated. It is therefore useful to define the detection probability associated with a range of spread as the probability that signals with such parameter values are great circle.

Knowing spread ranges with high detection probability is not enough, however. If one knew, for example, that signals with a fading bandwidth of 0 to 0.001 Hz were always great circle, the information would be of little value if only one great circle signal in ten thousand had spread in this range. Detection effectiveness corresponding to a given range of spread and given detection probability is defined as the percent of all great circle signals received that would be expected to have such a range of parameter values. The detection effectiveness is determined from graphs like those in figures 6 and 7 by adding the top numbers over the range in question as was done for figure 6 (a). Here we obtained a detection effectiveness of 65.6 percent for the spread range of 0 to 0.2 Hz. Over this spread range the detection probability is 95 percent or better.

Plots of the type shown in figures 6 and 7 are useful for smoothing the data and obtaining detection probability and effectiveness values for summary tables. A tabulation of effectiveness values for the long and short paths for spectrum bandwidths corresponding to 95 percent detection probability is given in table 3. Parameter ϵ_3 and θ_1 are tabulated along with receiving antenna beam widths for sidescatter. The highest effectiveness value for the short path is 76.0 for ϵ_3. The highest effectiveness for the long path is 68.5 for ϵ_3 on the narrow antenna. It is interesting that the wide antenna beam was more effective than the 2° one on the short path and less effective on the long path. Detection effectiveness was generally better on the short path.

The azimuth spread data in table 4 shows the highest value of effectiveness, 85.3 percent for the short path, but the value of 79 percent for α_3 for the long path is almost as good. However, the long-path data in table 4 is based on a small amount of data (62 samples of great circle and 56 samples of sidescatter) and confidence in the results given is not high.

Table 3. Detection effectiveness of spectrum spread measurements for 95% or better probability of successful detection.

Parameter	Type of spectrum	Antenna beam width for sidescatter	Spectrum band, Hz, for 95% detection probability		Percent Effectiveness	
			1300 km PATH	2350 km PATH	1300 km PATH	2350 km PATH
ϵ_3	fading	2^o	0.05-0.15	0 -0.3	60.6	68.5
ϵ_3	fading	70^o	0-0.15	0 - 0.15	76.0	23.8
ϵ_3	Doppler	2^o	0.05-0.10	---	19.8	---
ϵ_3	Doppler	70^o	0-0.10	---	20.8	---
θ_1	fading	2^o	0-0.10	0- 0.20	72.2	65.6
θ_1	fading	70^o	0-0.10	0 -0.15	72.2	45.5
θ_1	Doppler	2^o	0-0.10	---	37.6	---
θ_1	Doppler	70^o	0-0.10	---	37.6	---

Table 4. Detection effectiveness of azimuth spread measurements for 95% or better probability of successful detection.

Parameter	Azimuth spread, degrees, for 95% detection probability		Percent Effectiveness	
	1300 km Path	2350 km Path	1300 km Path	2350 km Path
α_3	$0 - 8^o$	$2 - 12^o$	78.5	79.0
γ	$0 - 4^o$	$0 - 2^o$	85.3	48.4

7.2 EFFECTIVENESS OF SIMULTANEOUS MEASUREMENTS FOR KNOWN PATHS

A statistical analysis similar to the one just described but for azimuth and fading spread considered jointly was done to determine the effectiveness of simultaneous measurement of the azimuth and fading spread. The analysis was done only for the short path because of the small amount of azimuth data on the long one. Results showed 97 percent effectiveness with a 95 percent or better detection probability when α_3 for azimuth spread was paired with ϵ_3 for fading spread. These values were obtained using the wide beam antenna for fading spread.

7.3 DETECTION EFFECTIVENESS ESTIMATES FOR PATH OF UNKNOWN LENGTH

From plots of the type shown in figures 6 and 7, one can estimate worst-case effectiveness values for a path of unknown length, but not less than 1300 and not greater than 2350 km. This is done for 95 percent detection probability by finding spread ranges corresponding to this probability that overlap for the long and short paths. The effectiveness values are taken from the path with the lowest sum in this overlapping spread range. For example, figure 7 (a) shows an effectiveness of 48.4 for azimuth spread, γ, for 0 to 2° and a 95 percent detection probability. Figure 7 (b) (dashed line) shows a detection probability of 95 percent or better for values of γ between 0 and 4.0 degrees. The range of spread for 95 percent or better detection probability for the unknown path would be 0 to 2 degrees and the detection effectiveness corresponding to this would be 29.8. Estimated effectiveness values for azimuth and fading spread for an unknown path are given in table 5. The highest value is 71 percent for α_3, the other values are between 20 and 30 percent.

8.0 CONCLUSIONS

The unknown path estimates given here based on the fading spread measurements should be reliable for midlatitude paths of lengths 1300 to 2350 km if seasonal effects, sporadic E and disturbed conditions do not change the picture too much. Azimuth spread measurements listed for the short path should be equally reliable. Not enough azimuth data were taken over the long path for the effectiveness values of the azimuth spread estimates of the unknown path to be conclusive.

It is concluded, however, on the basis of all data taken that an effective sidescatter detection system that measures either fading or azimuth spread or both can be designed. More measurements need to be made on different path lengths to estimate the expected performance of such a system.

Table 5. Fading and Azimuth Spread effectiveness estimated for a path of unknown length.

Fading Spread Measurements			Azimuth Spread Measurements		
Parameter	95% probability of successful detection		Parameter	95% probability of successful detection	
	Fading band, Hz	Percent effectiveness		Azimuth Spread range, degrees	Percent Effectiveness
ϵ_3	0-0.15	23.8	α_θ	2 - 8°	71.0
θ_1	0-0.10	20.0	γ	0 - 2°	29.8
Based on 213 samples of sidescatter and 106 samples of great circle from the short path; 175 samples of sidescatter and 130 samples of great circle from the long path. Sidescatter was received on the 70° beam width antenna.			Based on 142 samples of great circle and 319 samples of sidescatter from the short path; 62 samples of great circle and 56 samples of sidescatter from the long path.		

9. REFERENCES

1. Felden, C. B., Deviations of short waves from the London-New York great-circle path, Proc. IRE 27, No. 10, 635-645, 1939.

2. Edwards, C. F., and K. G. Jansky, Measurement of the delay and direction of arrival of echoes from nearby shortwave transmitters, Proc. IRE 29, No. 6, 322-329, 1941.

3. Dieminger, W., The scattering of radio waves, Proc. Phys. Soc. B, 64, 374B, 142-159, February, 1951.

4. Whale, H. A., Ionospheric irregularities and long-distance radio propagation, J. Research NBS 66D (Radio Prop.) No. 3, 265-272, 1962.

5. Hayden, E. C., Propagation studies using direction-finding techniques, J. Research NBS 65D (Radio Prop.) No. 3 197-211, 1961.

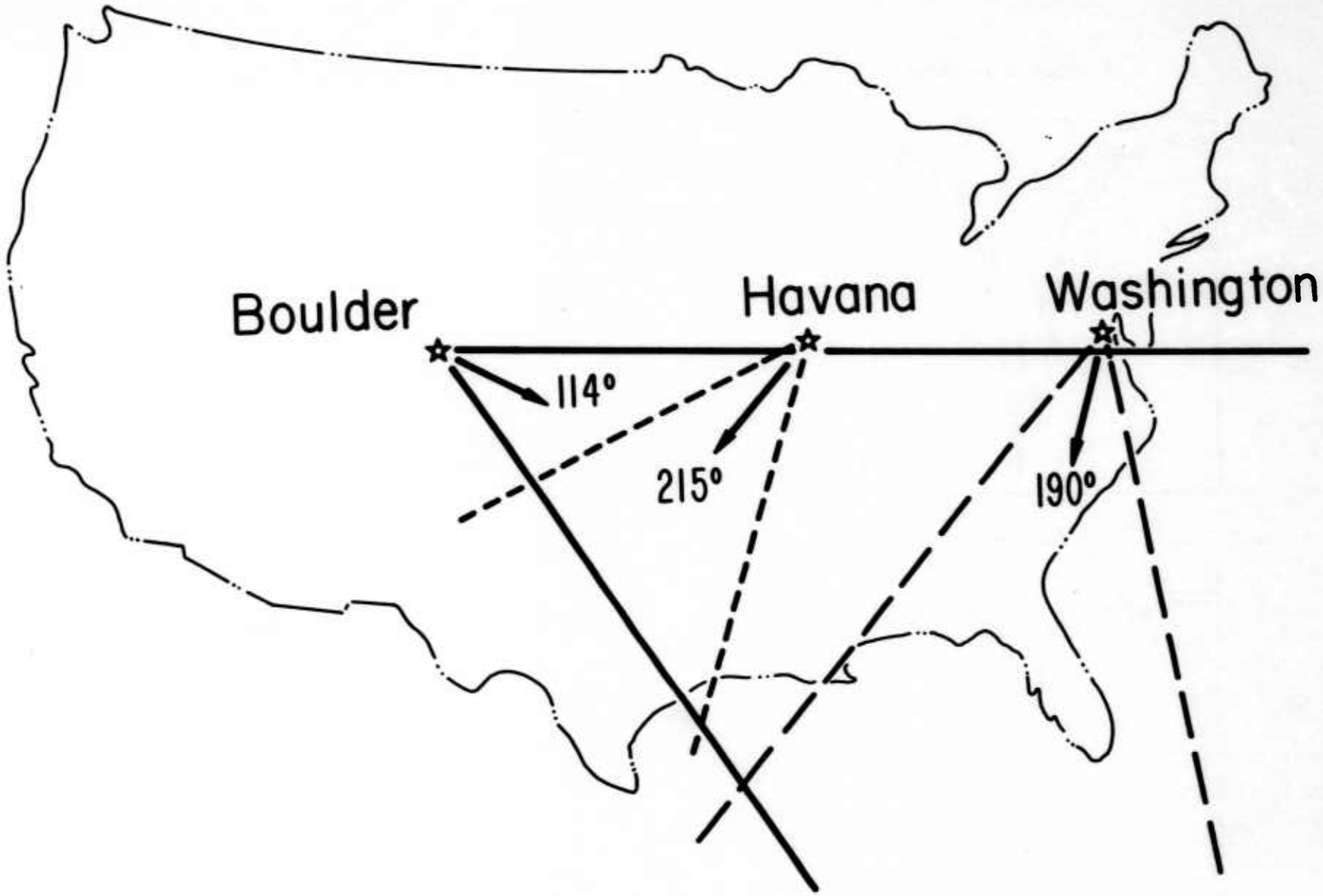

Figure 1. Geometry of propagation paths.

83924

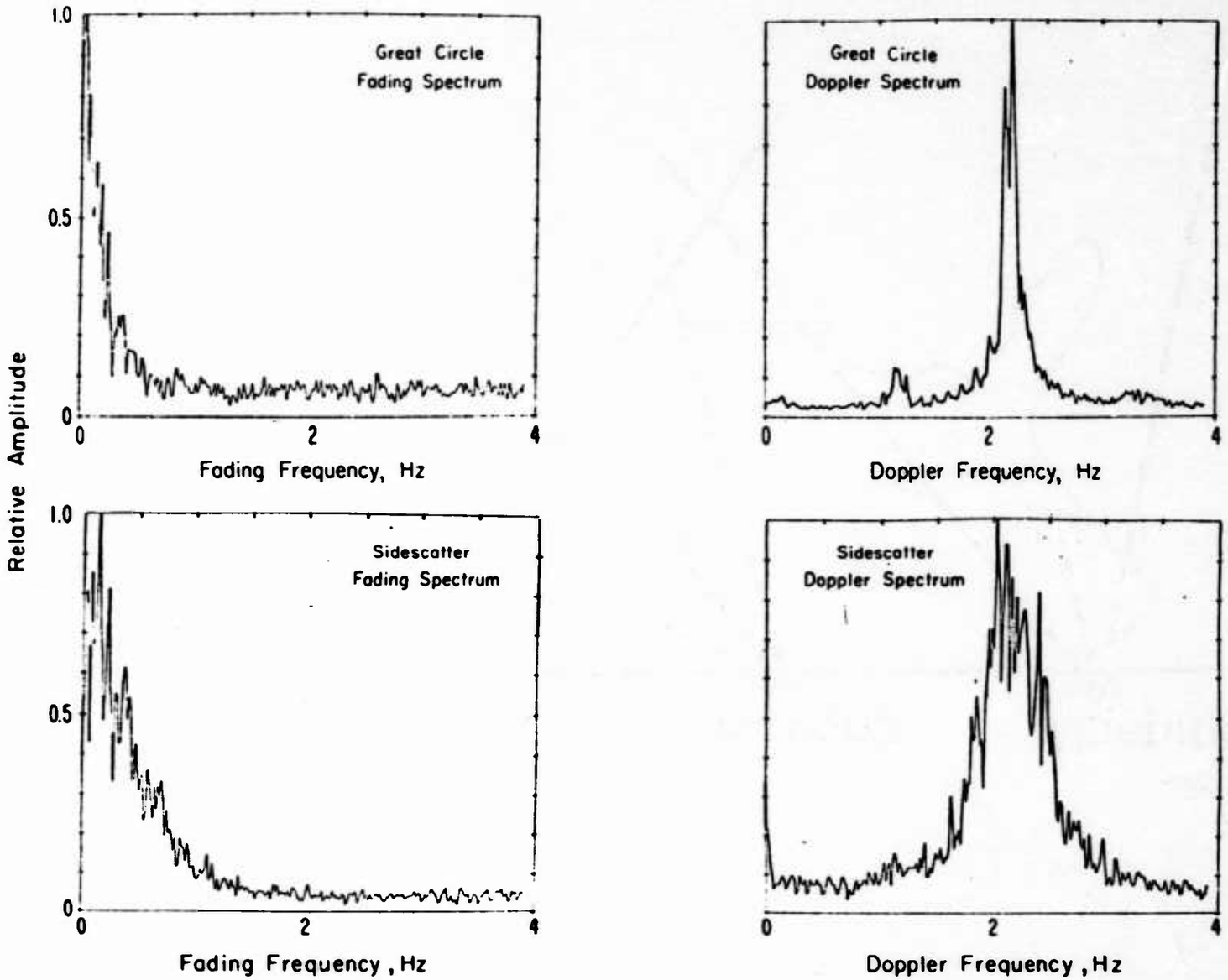

Figure 2. Examples of fading and Doppler spectrums.

93029

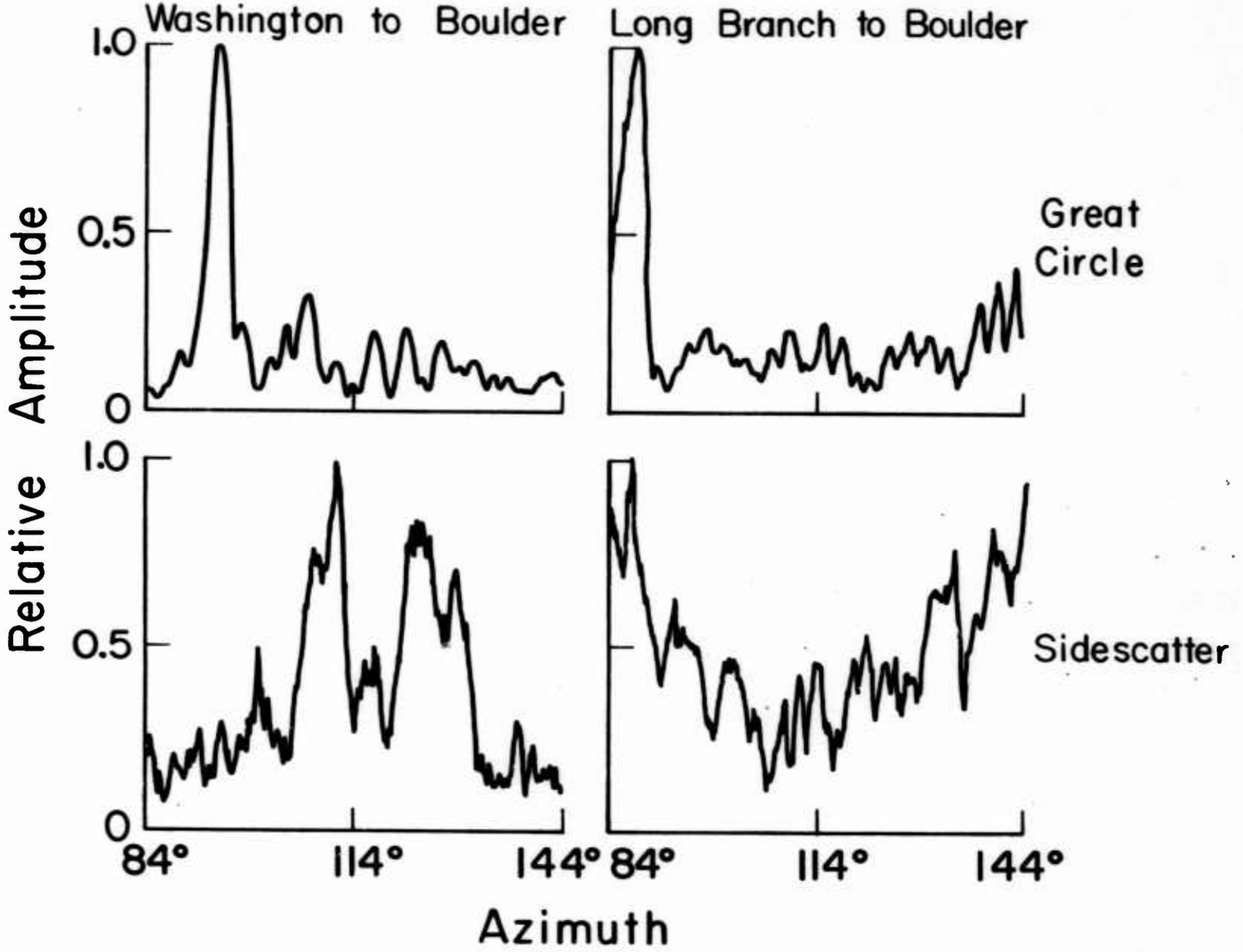

Figure 3. Examples of azimuth records.

B-82721

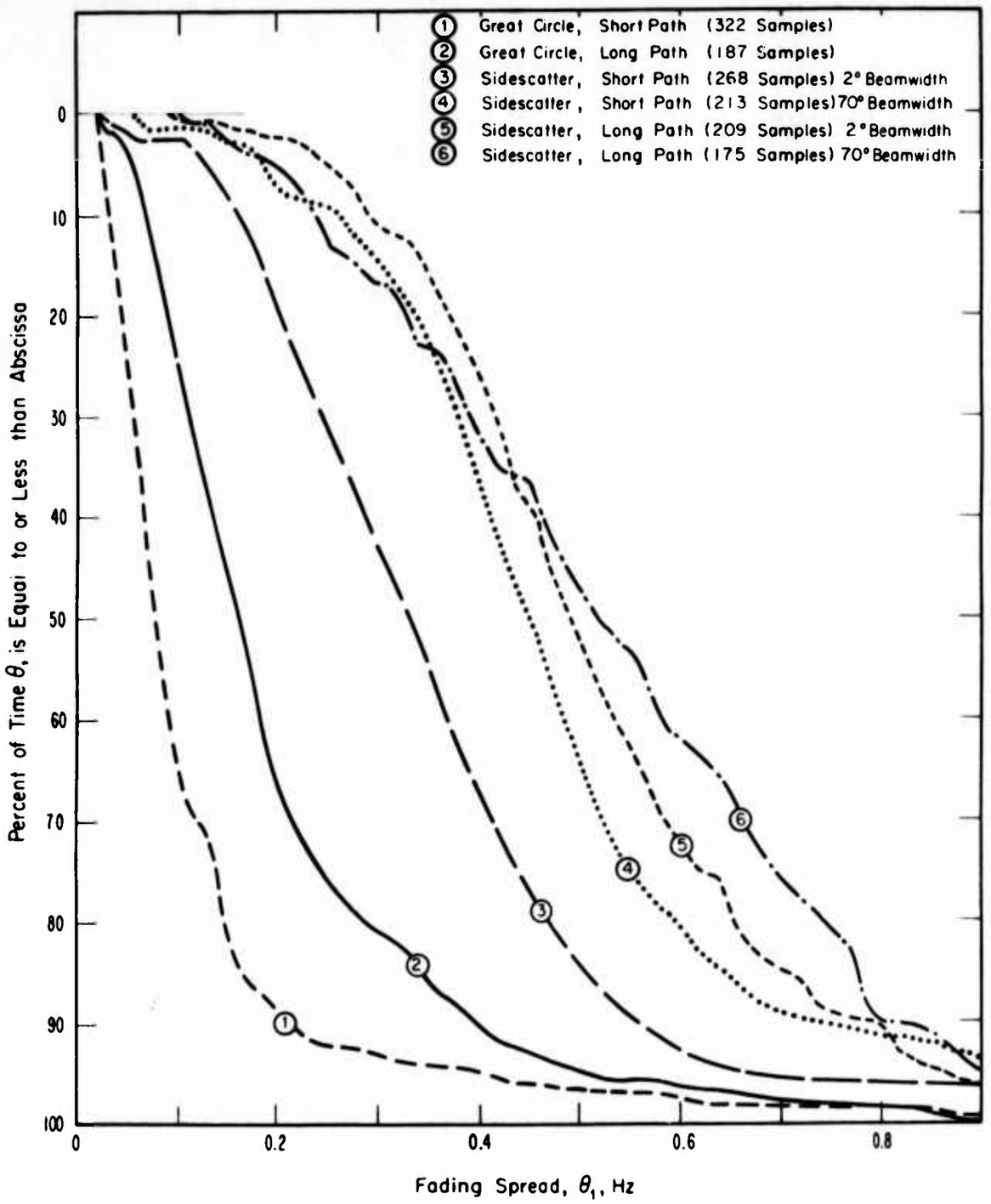

Figure 4. Cumulative distributions of fading spread for sidescatter and great circle for long (Washington-Boulder) and short (Long Branch-Boulder) paths.

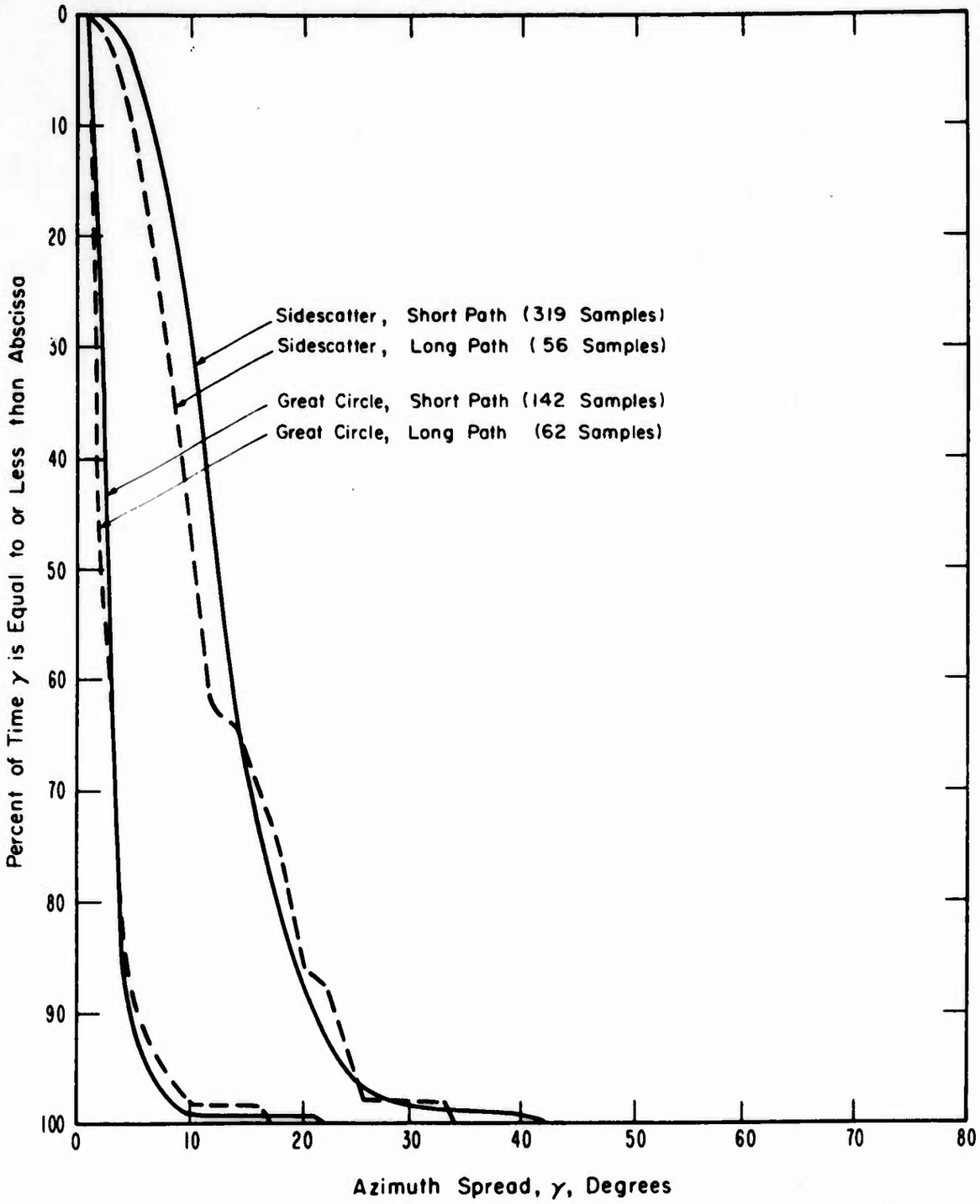

Figure 5. Cumulative distributions of azimuth spread for sidescatter and great circle for long (Washington-Boulder) and short Long Branch-Boulder) paths.

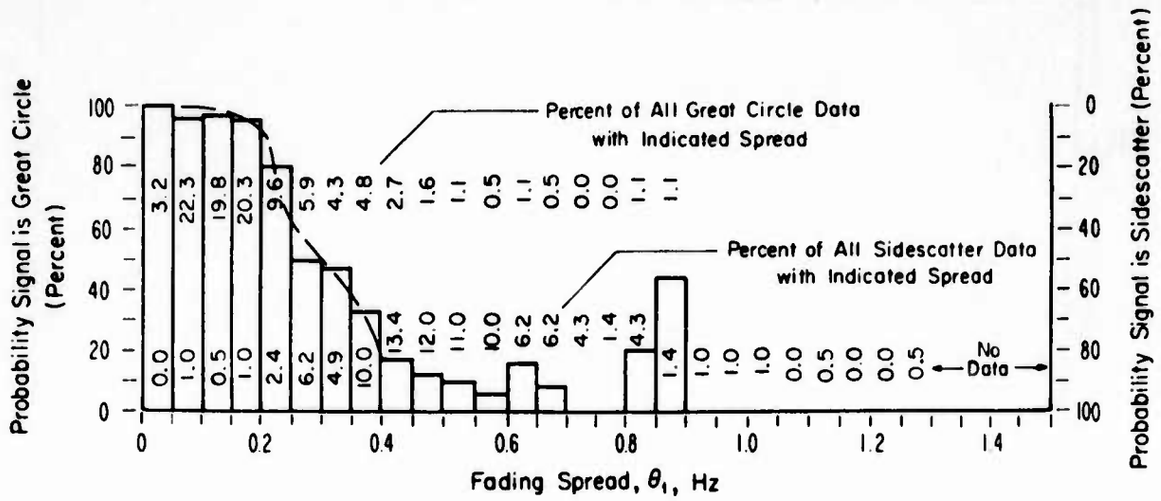

(a) Great circle was received on a 70° Beamwidth antenna; sidescatter was received on a 2° beamwith antenna.

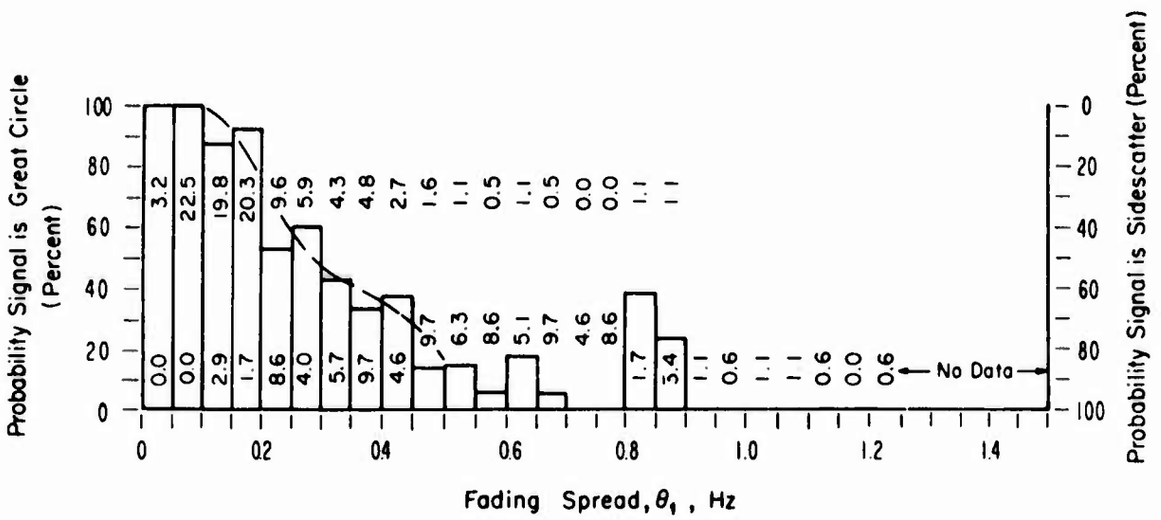

(b) Great circle and sidescatter were received on 70° beamwidth antenna.

Figure 6. Distribution of data samples as a function of fading bandwidth and estimated great circle probability. The estimated probability is shown as a dashed curve.

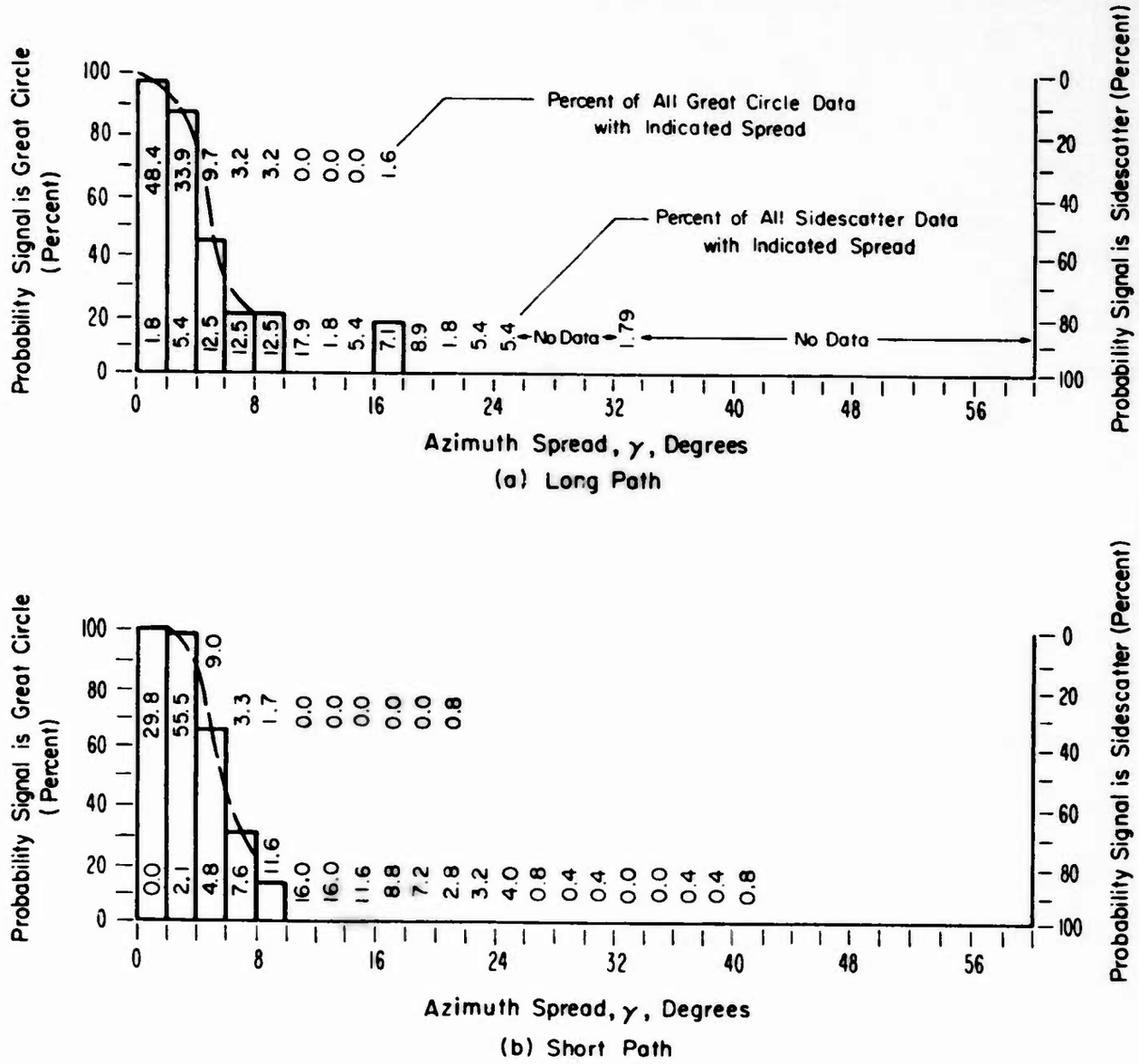

Figure 7. Distribution of data samples as a function of azimuth spread and estimated great circle probability. The estimated probability is shown as a dashed curve.

Presented at the 1971 DF Conference, 2-4 June 1971,
University of Illinois, Urbana, Illinois

FADE RATE CORRELATION*

by

Mark Epstein
Page Communications Engineers, Inc.
3300 Whitehaven Street, N. W.
Washington, D. C. 20007

I. INTRODUCTION

The purpose of this paper is to describe measurements of the limits of both frequency separation and physical separation within which two transmitted HF signals exhibit similar received fade rate characteristics. The results of these measurements provide insight into ionospheric coherent communications bandwidths and into the ground area within which a coherent wavefront can be received after ionospheric propagation. The size of the coherent ground area has application in the design of wide baseline antenna arrays.

The experiment employed two mobile transmitters operating within several radio frequency bands between 4 and 23 MHz. N-S and E-W paths varying from 1000- to 5000-km were employed. At each transmitting location the two mobile transmitters were increasingly separated in range and subsequently in azimuth, with respect to the receiver site, until appreciable differences in the received signal strength fade rate characteristics were observed. Similar tests were performed by separating the transmitted radio frequencies. An additional experiment was performed with one transmitter operating at twice the range of the other transmitter

*This work is supported by Rome Air Development Center under Contract F30602-70-C-0237.

to determine if signals arriving at a receiver site at similar azimuthal angles of arrival could be separately identified on the basis of fade rate characteristics.

This present paper is a report of work in progress; the results described here are preliminary. Section II describes radio wave fading phenomena, Section III deals with experimental arrangements, and the results are described in Section IV.

II. RADIO WAVE FADING

A. GENERAL

This section describes amplitude variations of received skywave signals. Previous work is reviewed dealing with the decorrelation of signal strength variations received from transmitters which were separated in either space or frequency. A description is presented of the fundamental manner in which the present experiments differ from previous work.

Amplitude variations of skywave HF radio signals are produced by several different ionospheric phenomena. These phenomena include interference fading, both intramode and intermode, polarization fading due to the variation of the received polarization of radio wave signals as a function of both time and radio frequency, variations in ionospheric absorption, focusing of radio wave energy, and amplitude variations due to radio wave skipping, which are produced for a specific path when the radio frequency of transmission passes through the LOF or MOF.

The period of observed amplitude variations varies widely. Interference fading between modes, e.g., between one-hop and two-hop rays, can produce fading that varies from a fraction of a second to a few seconds. Amplitude variations due to polarization can vary from approximately fifteen seconds to five minutes. Absorption fading can produce amplitude variations on the order of an hour, and amplitude fluctuations due to MOF or LOF failure can vary from a few seconds to hundredths of seconds. In addition to the aforementioned types of amplitude variations, there is the normal very small scale amplitude variations produced by radio wave noise and small-scale changes in the ionospheric path.

For a review of general aspects of radio wave fading see K. Davies book,"Ionospheric Radio Propagation."[1] Davies describes each of the types of signal amplitude variations that may occur and illustrates these variations with signal strength and spectra records.

B. PREVIOUS WORK

1. Space Decorrelation. Pulsed high frequency transmissions short enough in duration (100 μs or less) to separate the different geometric modes have fade rate periods of approximately 15 seconds to three minutes. This fading can be either due to destructive interference between the two magnetoionically propagated components (a polarization effect), or the fades can be due to a random scattering process as described by Balser and Smith,[2] who found spatial correlation distances of about 40 wavelengths in the direction perpendicular to the raypath for single mode propagation. The Balser and Smith experiment, however, did not reveal the true signal decorrelation over a wide area, as discussed below.

CW signals for which the received signal voltage is the sum of voltages propagated by several modes usually fade with a period on the order of one or two seconds. The amplitude of fading CW signals generally follows a Rayleigh probability distribution except at special times, such as when the upper and lower rays are interfering near the MOF. Grisdale, Morris and Palmer[3] in 1957 discussed this effect and also reported that the spatial correlation of signal strength falls significantly at a distance of about 200 or 300 meters. Bixby[4] in 1953 gave a theoretical derivation for the fading at and near the MOF based on a nontilted ionosphere with a smooth parabolic electron density distribution.

Ames,[5] in 1964, employed an L-shaped antenna array to determine and measure the various types of fading interference patterns produced along the ground by waves propagated over an ionospheric path. He employed 12 dipole antennas arranged in an L, 300 m on a side. The outputs of the antennas were sequentially connected to a receiver whose output was recorded as intensity on moving film. An analysis of the recorded receiver output yielded the dimensions, orientation and motion of the signal fading patterns. Like most of the previous workers in the field,

Ames was primarily interested in the amount of amplitude decorrelation that occurred along the ground, so that it could be applied to the problem of correct siting of space diversity antennas. He found that the destructive interference between modes produces bands of amplitude fadelines along the ground which move rapidly. He found that the straight line fading null patterns are measurable 33% of the time on signals propagated over a 2000 km path, and about 10% of the time on signals propagated over a 5000 km path. The mean value of the null spacings are:

1F mode	1.4 kilometers
2F mode	0.75 kilometers
3F mode	0.4 kilometers

The mean velocity of the nulls along the ground varies from about 0.7 km/sec during layer formation and decay, to about 0.3 km/sec during midday.

The Ames results show that much of the observed amplitude fluctuations of received radio signals can be interpreted as a sampling of the amplitude variations induced by the moving lines of interference nulls along the ground. What Ames did not show is how far along the ground one needs to go before the rate of amplitude fluctuations induced by the moving diffraction pattern of fading null lines is decorrelated. In the light of Ames' work, all previous fading decorrelation measurements only measured decorrelation from the peak to the first trough of one strip of the signal interference pattern, and did not determine the full wide area decorrelation as performed in the present experiments.

2. Frequency Decorrelation. An experiment was performed by Epstein[6] in 1966 which corresponds to the situation of transmitting two signals of differing frequencies in order to observe the amplitude decorrelation between them. In the Epstein experiment, an FM-CW transmitter was employed to simulate the effect of two transmitters, one of which has a varying frequency. For a 2000 km path, Epstein found that the amplitude versus frequency characteristic across a 500 kHz band decorrelated to 1/e in approximately 70 kHz.

In addition, as part of Epstein's experiments, oblique ionograms were regularly made with an FM-CW sounder over a 1200 km and a 2000 km path. It was found on all ionograms made over these paths, that while the one-hop mode was typically spread to less than 50 microseconds in time delay, the two-hop mode was spread several times larger. This indicates that for the paths tested the amplitude fluctuations on two-hop modes have a much higher rate of amplitude variations with time than the one-hop signal.

C. DECORRELATION OF SIGNALS

It is expected that in comparing the amplitude versus time records, or frequency spectra records, of two different received signals that, as the sources of transmissions are moved in space or shifted in radio frequency with respect to each other, the fading rate of the two signals will slowly change. At a sufficiently large spatial or frequency separation, the fading of the two signals will be unrelated.

The primary reason for the decorrelation of the amplitude variations observed on two radio signals is that the specific paths over which the two radio waves travel change both as a function of the spatial separation of the two transmitted signals, and as a function of the radio frequency difference between the two signals. In general, for small changes in the radio frequency and for small changes in the spatial separation of the transmitting sites, the general characteristics of the modes of propagation will not be fundamentally different. If one source is being received simultaneously over a one-hop and two-hop path, then the other radio wave signal will be received over a very similar one-hop and two-hop path. Under these conditions, all that will happen will be perhaps a time shift between the patterns of the two received amplitude fluctuations. As the frequency and spatial separations are further increased, the differences in these amplitude fluctuations will also increase until, when the two radio wave paths pass through sufficiently different ionospheric regions, the amplitude variations of the received signals will no longer be similar.

The difference between two received multipath signals are primarily due to differences in the multipath interference pattern. Therefore, signal comparisons between single hop modes will show far slower changes in their cross-correlation as spatial and frequency differences are increased than that observed between two multihop modes because the rate of polarization variations doesn't depend on the interference between several widely separated modes, but between the two closely separated magnetoionic components.

PRECEDING PAGE BLANK - NOT FILMED

III. EXPERIMENTAL ARRANGEMENTS

Mobile transceivers mounted in two automobiles transmitted 75 watts CW power from vertical, loaded, bumper-mounted whip antennas. Transmissions were made from the vicinity of Tallahassee, Florida (21 January to 3 February 1971), Normal, Illinois (6-19 February and 5 April 1971), Grand Island, Nebraska (24 February - 4 March and 1 April 1971), and Williams, California (17-23 March 1971). The site locations are shown in Figure 1.

The signals were received employing a vertical 35-ft telescoping whip antenna with ground screen located on the roof of a 70-ft building in Washington, D.C. The path lengths from Washington, D.C. to Florida and from Washington, D.C. to Illinois are 1250 km. The path from Washington, D.C. to Nebraska is 2300 km, and the path from Washington, D.C. to California is 5000 km. Transceivers at all sites provided voice communications. The purpose of the widely separated site locations was to obtain fade rate data over a variety of paths and azimuthal orientations. For the E-W paths transmissions were repeated after a month's time to determine data reproducibility.

One automobile was designated the "fixed" site and the other the "mobile" site. At each transmitting location, the mobile site drove to increasingly large distances from the fixed site so as to provide several spacings between the two remote sites in both range and in azimuth with respect to the receiving site. The spacings were increased until the received signal amplitude variations decorrelated in terms of a fade rate count. In addition, as part of the experiment, when the vehicles were collocated, one transmitter maintained a fixed-frequency CW transmission, while the other transmitter stepped to increasingly large frequency separations until fade rate decorrelation was achieved. This situation is illustrated in Figure 2, which illustrates typical comparative signal strength

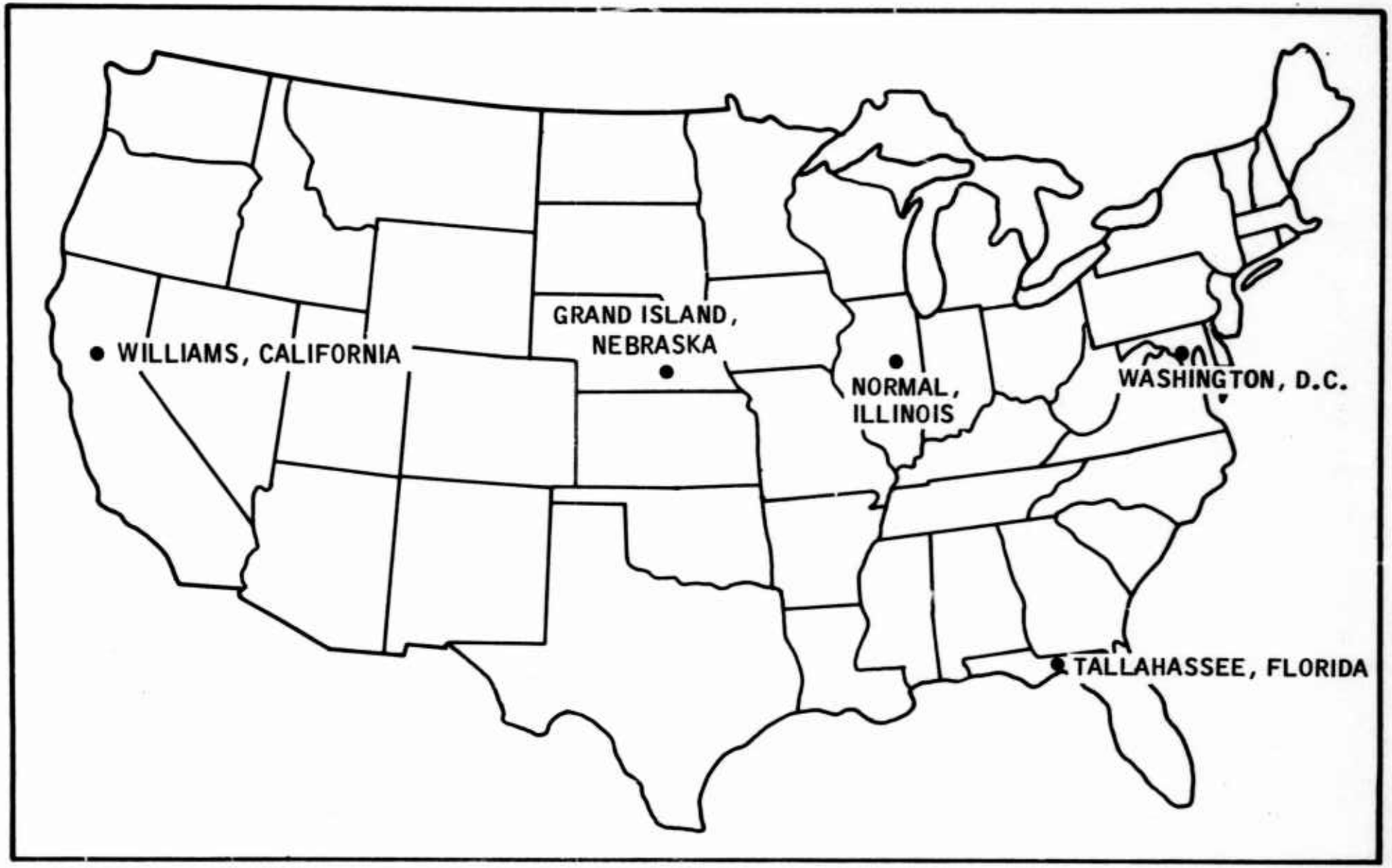

Figure 1. Site Locations

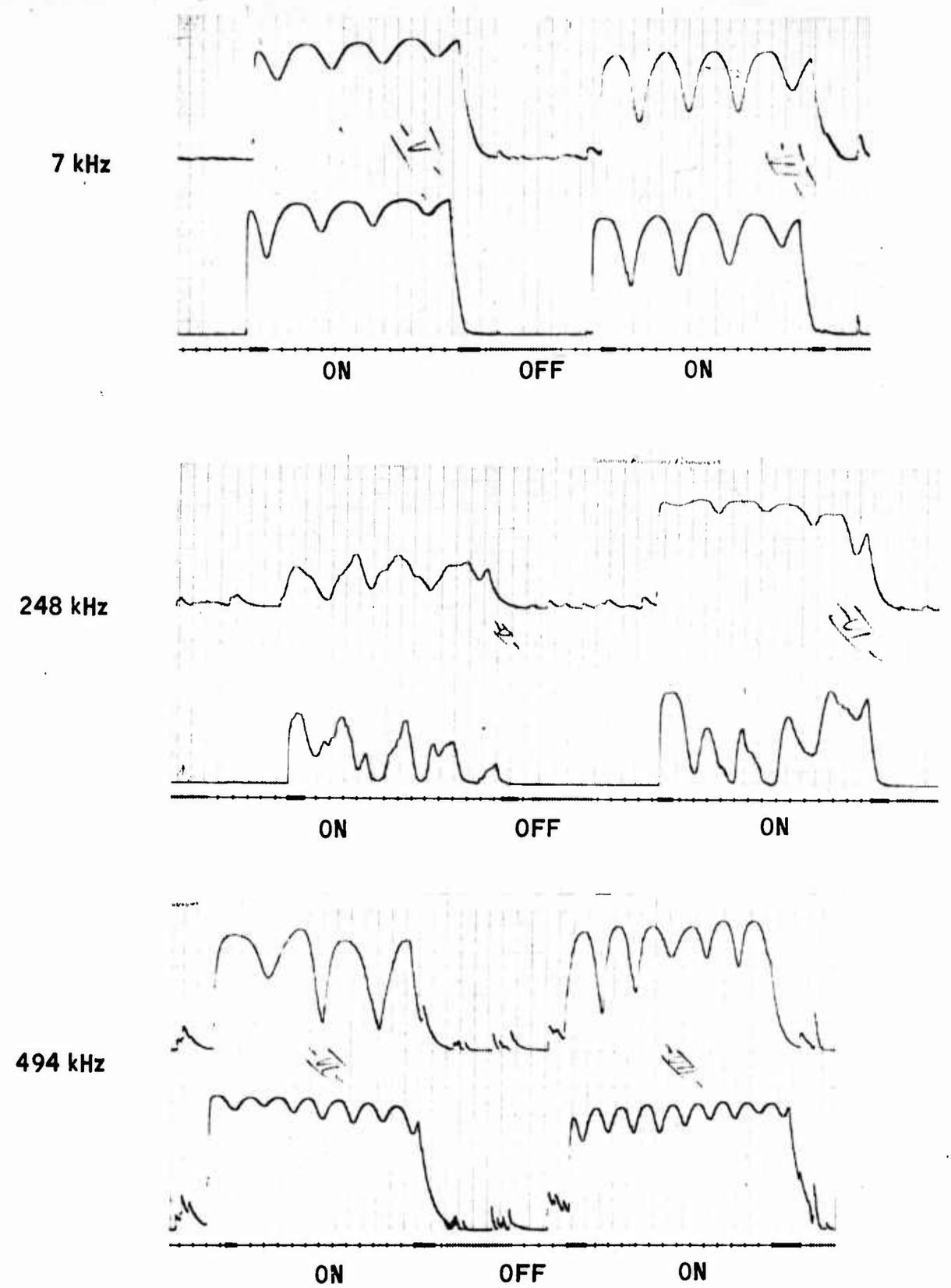

Figure 2. Typical Frequency Shift Data - Washington, D.C. to Nebraska Path, 15 MHz

changes obtained with increasing radio frequency spacing. The tic marks on the charts occur once a second. A duty cycle of 15 sec "ON" and 30 sec "OFF" was employed to protect final amplifier tubes.

IV. RESULTS

In this section several of the types of data collected are described and preliminary conclusions are presented. Figure 2 illustrates a typical dual channel strip chart recording of the detected signal strengths of two received skywave signals. In Figure 2a the received signal strength variations of both traces correspond to a fade rate of approximately 5 fades per 15 secs. Note that the two received signals exhibit relative time shifts between the received amplitude fading patterns. For the 248 MHz frequency separation shown in Figure 2b, the shapes of the individual amplitude variation patterns have changed, but the fade rate count is nearly the same. For the 494 kHz frequency separation shown in Figure 2c, the fading pattern is changed appreciably in structure and in fade rate count.

Employing the empirical criteria of requiring a change in the amplitude fading pattern shape and also a fade rate difference of at least 2 fades per 15 sec period, the data was analyzed over all the paths and over the 9, 15 and 23 MHz frequency bands. The results are presented in Chart I. These results indicate that the size of the area within which the signals will be received with similar fade rates increases with increasing range from the receiver and decreases with increasing frequency.

During the experiment several features of received signal characteristics were noted. Figure 3 illustrates a case when fade rate comparisons cannot be made because both signals are propagating over one-hop paths. Little amplitude fading is evident. One-hop propagation such as shown in Figure 3 can last several hours under certain conditions. During these tests, however, the typical duration of one-hop propagation was about one half hour. At the end of this period, the received signal strength vs time structure changes rapidly to multimode propagation as illustrated in Figure 4.

Path	Path Length (Miles)	Decorrelation Distance (Miles)						Decorrelation Frequency Difference (kHz)		
		Perpendicular			Parallel					
		9 MHz	15 MHz	23 MHz	9 MHz	15 MHz	23 MHz	9 MHz	15 MHz	23 MHz
Washington, D.C. Tallahassee, Fla.	780	10	60	*	N.A.	40	*	Greater than 1096	Greater than 385	*
Washington, D.C. Normal, Ill.	780	N.A.	N.A.	*	40	30	*	Greater than 1010	300	*
Washington, D.C. Grand Island, Neb.	810	N.A.	20	20	N.A.	N.A.	40	N.A.	Greater than 393	590
Washington, D.C. Williams, Cal.	3,100		60	80		80	N.A.		Greater than 345	597

* Above MOF

N.A. Not Available due to noise

Chart I. Preliminary Fade Rate Count

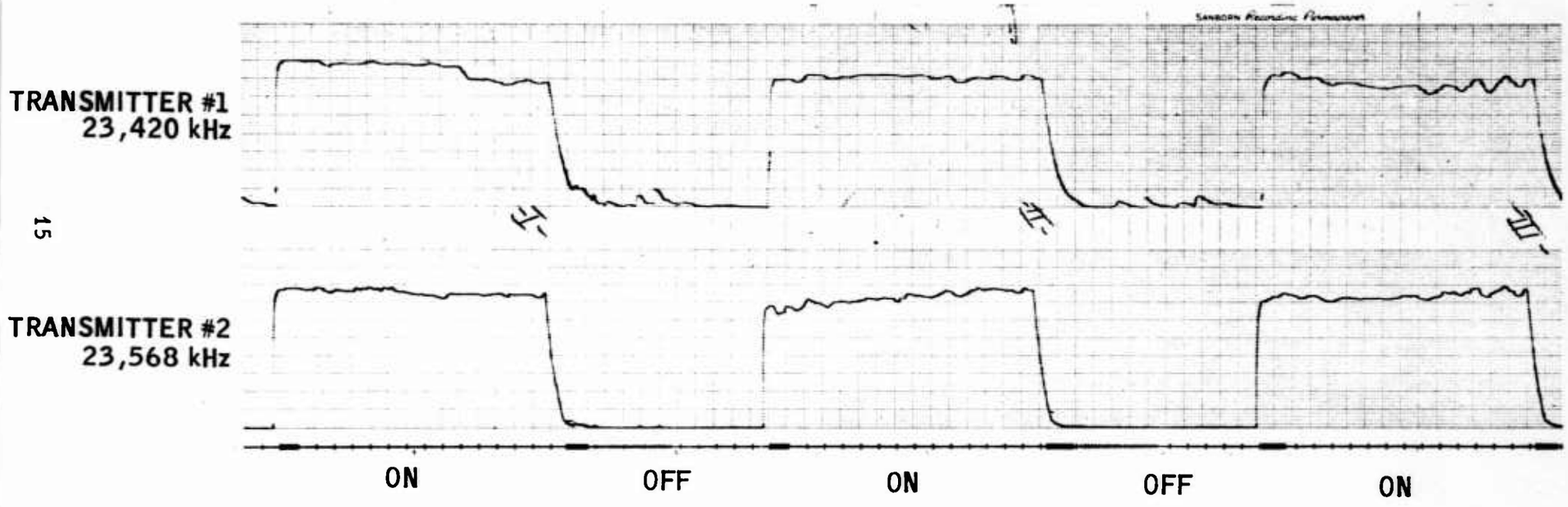

Figure 3. One-Hop Propagation

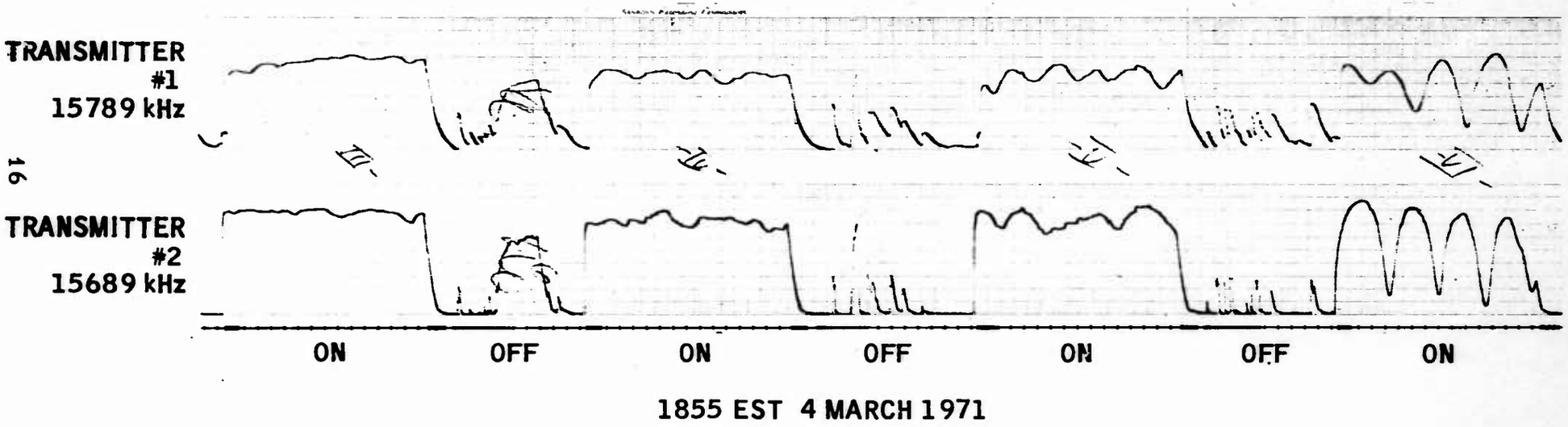

Figure 4. Change from One-Hop to Multimode Propagation

A test was performed in which one transmitter was located at a distance of 2500 km from Washington, D.C., while the other transmitter was located at a distance of 1250 km, in order to determine if it would be possible to readily identify the two signals. The receiving azimuth angle of arrival for the two signals were nearly the same, but as shown in Figure 5, the two signals are readily separable on the basis of their received signal strength fade rate differences.

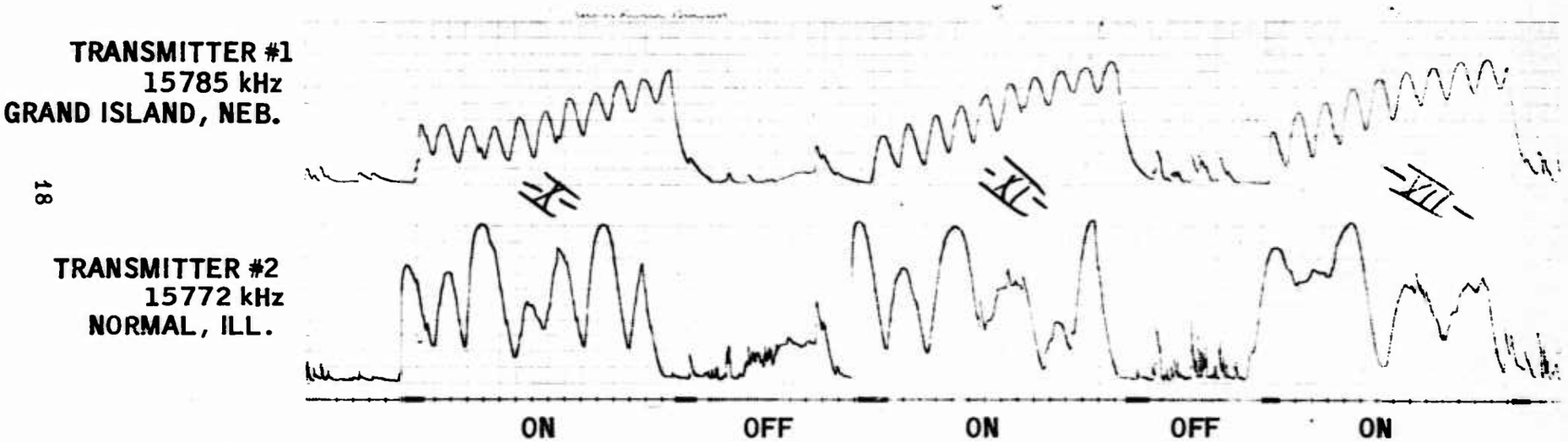

Figure 5. The Double-Range Experiment

V. REFERENCES

1. K. Davies, "Ionospheric Radio Propagation," NBS Monograph 80, U.S. Government Printing Office, Washington, D.C., 1965.

2. M. Balser and W.B. Smith, "Some Statistical Properties of Pulsed Oblique HF Ionospheric Transmission," J. NBS, 66D, 721-730, Nov-Dec 1967.

3. G.L. Grisdale, J.G. Morris, and D.S. Palmer, "Fading of Long Distance Radio Signals and a Comparison of Space and Polarization Diversity Reception in the 6-18 Mc/s Range," Proc IEEE, 104B, 39-51, 1967.

4. L.H. Bixby, "Calculation of High Frequency Radio Field Intensity Over a 4000 km Ionospheric Path," Radio Propagation Laboratory, Stanford, California, May 1953.

5. J. Ames, "Spatial Properties of the Amplitude Fading of Continuous HF Radio Waves," Radio Science, 68D, No. 12, 1964.

6. M.R. Epstein, "Polarization of Ionospherically Propagated HF Radio Waves with Applications to Radio Communication," Radio Science, 4, No. 1, 53-67, Jan. 1969.

7. F. Terman, Electronic and Radio Engineering, p. 809, McGraw Hill Book Co., N.Y., 1955.

STUDIES OF TRAVELLING IONOSPHERIC DISTURBANCES WITH A TRIPLE RADIO INTERFEROMETER SYSTEM

Eric K. Walton
Radiolocation Research Laboratory
University of Illinois
Urbana, Illinois 61801

In 1967 and 1968, an experiment was performed by Dr. John E. Jones of ESSA's research labs in Boulder* in which travelling ionospheric disturbances could be detected. The experimental technique employed three radio transmitters in a triangular configuration as shown in Figure.1. The three reflection points form the vertices of an equilateral triangle of 40 km on a side, Doppler measurements were made on the received signals, and correlation techniques were used to detect ionospheric periodicities and wave-like movements. The results, in terms of medium scale disturbances, are shown in Figure 2. In general, the waves detected by Jones had periods ranging from 15 to 70 minutes and a velocity of approximately 150 m/s in magnitude. The direction varied as shown in Figure 2 and also contained a downward component of 15 to 70 degrees below the horizontal. In general there is good agreement with the acoustic gravity theory of C. O. Hines. The most interesting finding in the data in relation to this study is the seasonal variation of the data. The wave-like effects move southward in the winter and northward in the summer, with a westward movement in the spring and fall. It is this seasonal effect which we will try to study here.

The first question to be answered is: "What effects can one see in a radio direction finding experiment due to waves of this type?" In order to answer this question, a corrugation model was proposed for the ionospheric waves. This model, described in Figure 3, is a sinusoidal wave-like reflection surface moving transversely through the ionosphere. Note that to allow the wave to move at any angle with respect to the transmitter-receiver path, the variable of interest is the variation of the reflection point rather than the incidence angle or the azimuthal angle of arrival of the signal. The result of applying this model to a particular geometry and finding the variation of the reflection point as a function of time, as well as the variation of the received signal amplitude, is shown in Figure 4. It is assumed that the wave is travelling at a constant velocity here, and to remove the necessity of assigning a particular velocity to the wave, the phase of the wave at the point over the receiver is used as the independent variable. The variations in the amplitude are assumed to be due entirely to focusing and defocusing effects as the curvature at the reflection point varies. Of particular interest in this curve is the sawtooth-like shape of the reflection point curve and the sharp peak in the amplitude as the reflection point passes through its point of maximum slope. This is a property of nearly all

---

*"Observations on Travelling Ionospheric Disturbances by the Doppler Technique with Spaced Transmitters," John E. Jones, ESSA Technical Report ERL 142-SDL 11, December 1969, Boulder, Colorado.

geometries studied in this project. The technique suggested by this property, then, is to search direction of arrival data for deviations which have this shape or "signature" and are periodic in time.

An experiment in which this may be done was performed by the Radiolocation Research Lab during 1962 through 1964. The geometry of this experiment is shown in Figure 5. Pulsed signals were transmitted from Columbus, Ohio, to an interferometer site near Champaign, Illinois. This is a distance of 450 km along an east-west path. There was a midpath ionosonde in Anderson, Illinois. The midpath ionosonde data were used for path reconstruction and for mode resolution. The reduced data from this experiment consisted of azimuthal and incidence angle of arrival of the signal as a function of time. Ionospheric waves would be expected to perturb these data as shown in Figure 6. Note that a northward and a southward moving wave produce distinctly different deviation patterns. The technique of studying these data, then, was to search the data for signatures of the type shown in Figure 6, identify them as to northward or southward-type patterns, and then to find the period, number of periods, the azimuthal deviation, and the ionospheric layer from which each signal was reflected. Several examples of the data are shown in Figure 7, 8, 9, 10. The result of this study is summarized below:

93 days of data throughout the 2 years were studied.
56 wave-like patterns were observed.
44 of the patterns had 15-to 25-minute periods.
29 examples had more than one period.
46 examples had enough clarity to determine all desired parameters.

These data were analyzed in such a way as to compare them with the Jones data. The Jones data are given in terms of velocity vector (speed and direction) vs. time of year. The data from the Columbus experiment, on the other hand, are given in terms of azimuthal deviation and northward or southward type vs. time of year.

It is possible to compare these data, however, if some assumptions are made and typical values from the Jones experiment are used. Assume F-layer data in the Jones experiment to apply at a height of 250 kilometers. Assume typical Jones ionospheric wave values to be the following:

amplitude	2.9 km
wavelength	204 km
speed	150 m/s

Jones' speed is nearly constant (only the direction varies).

Using these values from the Jones experiment, the Columbus experiment data can be predicted. The above plus the seasonal variation of the direction of arrival were used to calculate the comparison data shown in Figure 11. As can be seen, there is a great deal of correlation between the results of these two experiments. The seasonal effect is quite clear in both curves.

Several conclusions might be drawn from these data. First, it is clear from these data that the effective tilt described by Bramley and Ross is not a random parameter as has been proposed. Also, the usefulness of the sinusoidal model developed here is clearly justified by the success of this study. Finally, the seasonal effect in these data may point the way for discovery of one of the geophysical mechanisms for the generation of waves of this type.

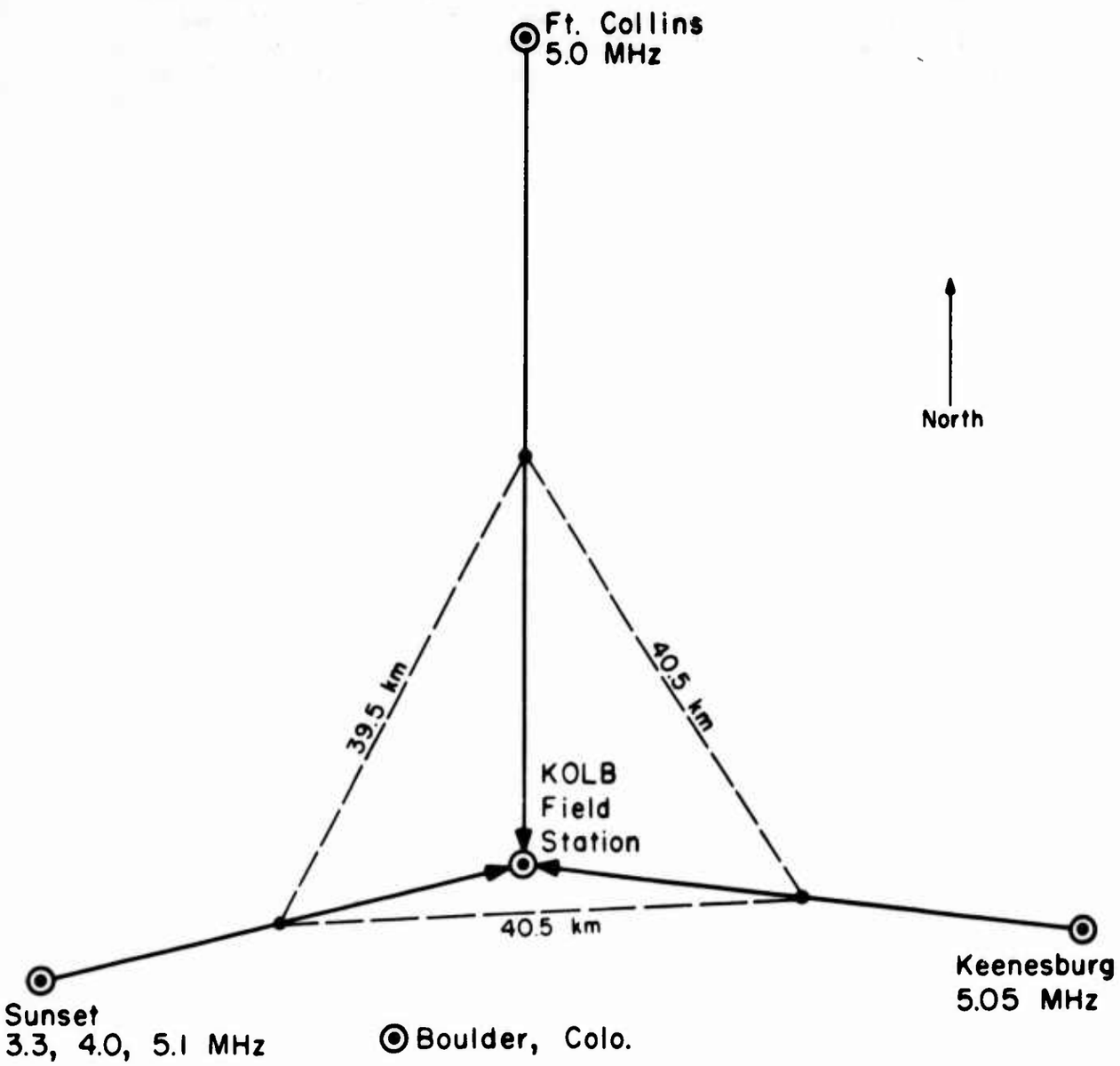

Figure 1

Configuration of John E. Jones Spaced Transmitter Experiment

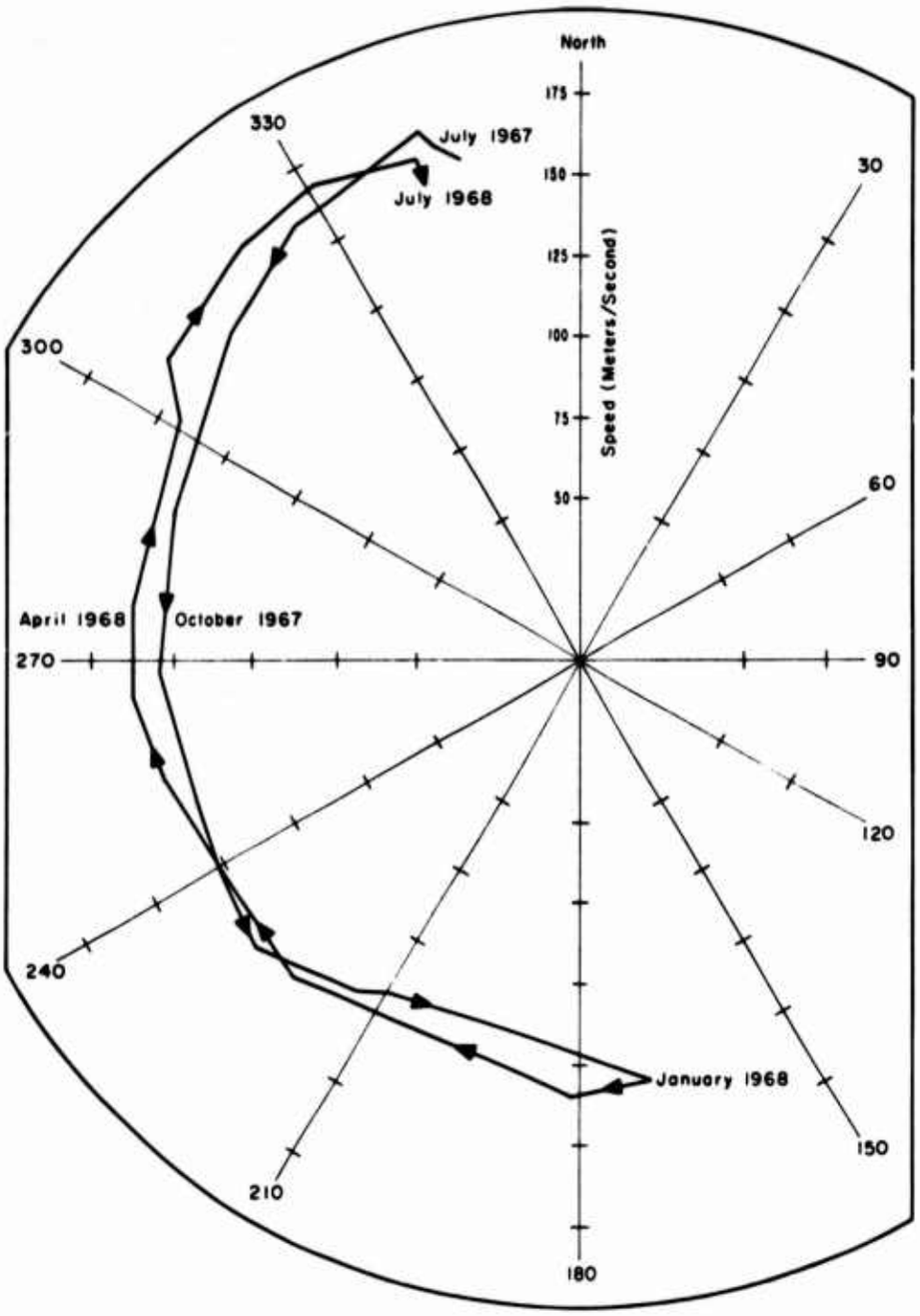

Figure 2

Seasonal Variation of T.I.D. Velocity

(After John E. Jones, ESSA Technical Report ERL 142-SDL 11.)

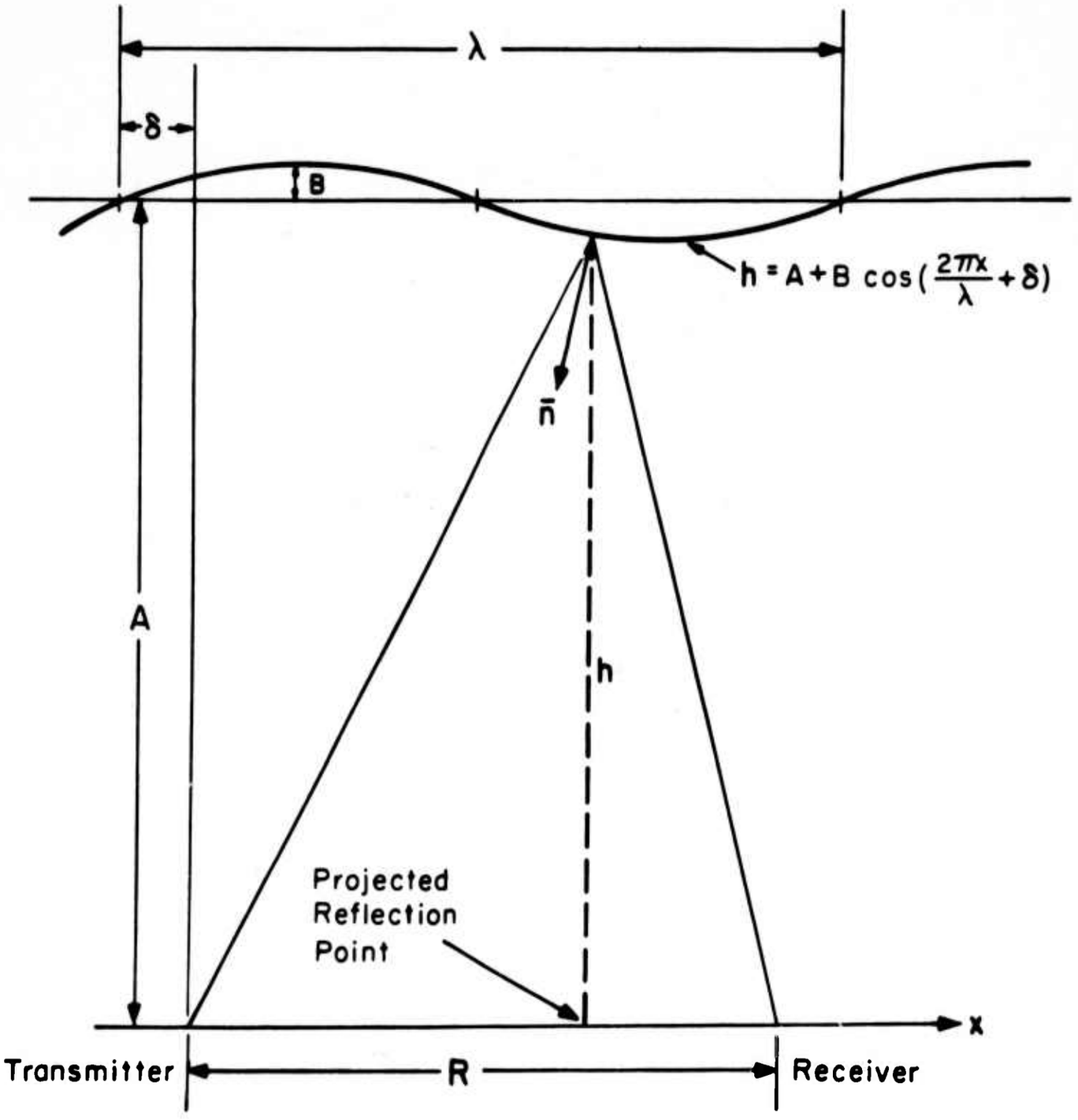

Figure 3

Corrugation Model for Ionospheric Waves

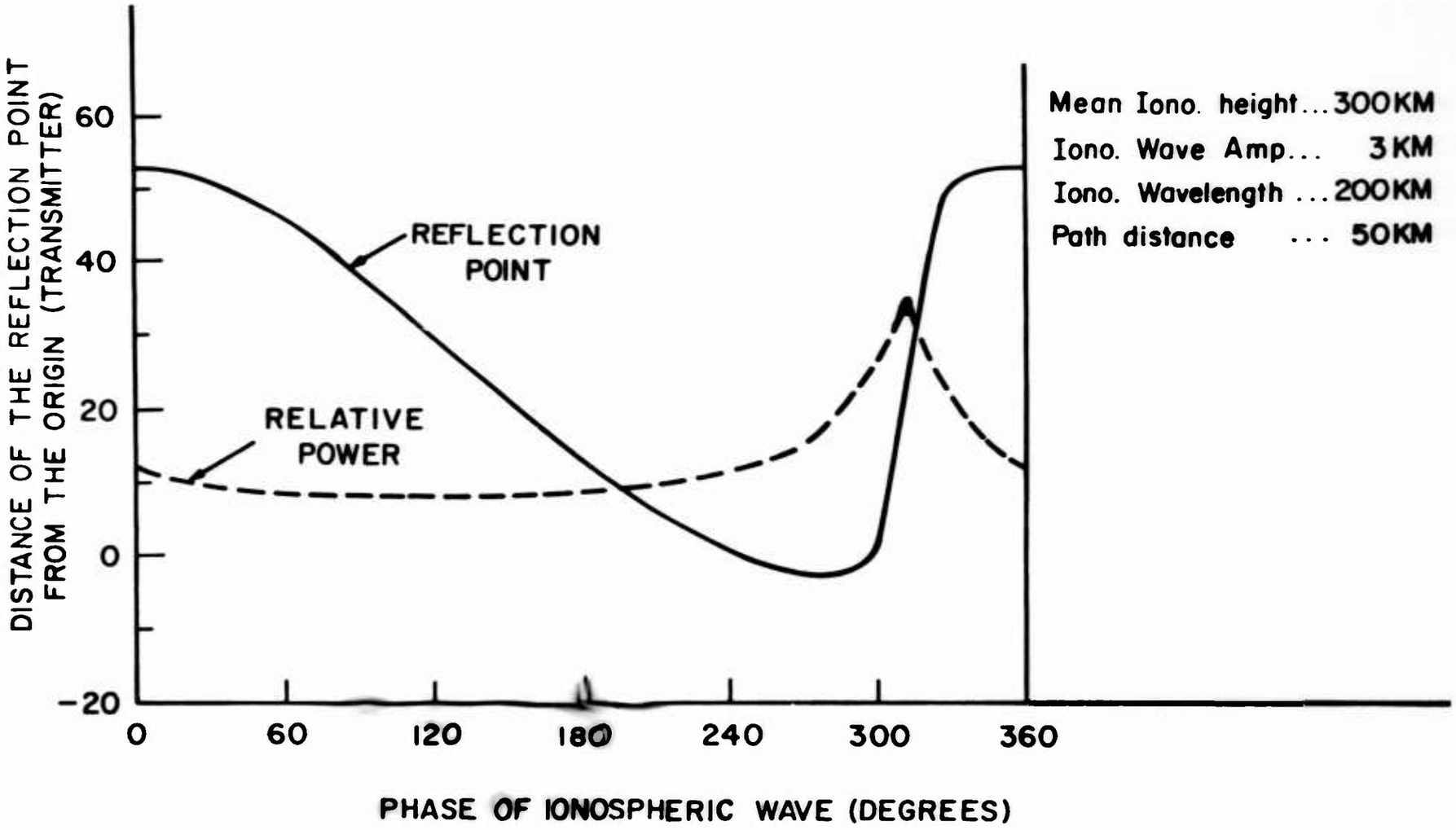

Figure 4

Example of Reflection Point Variation Predicted by Corrugation Model

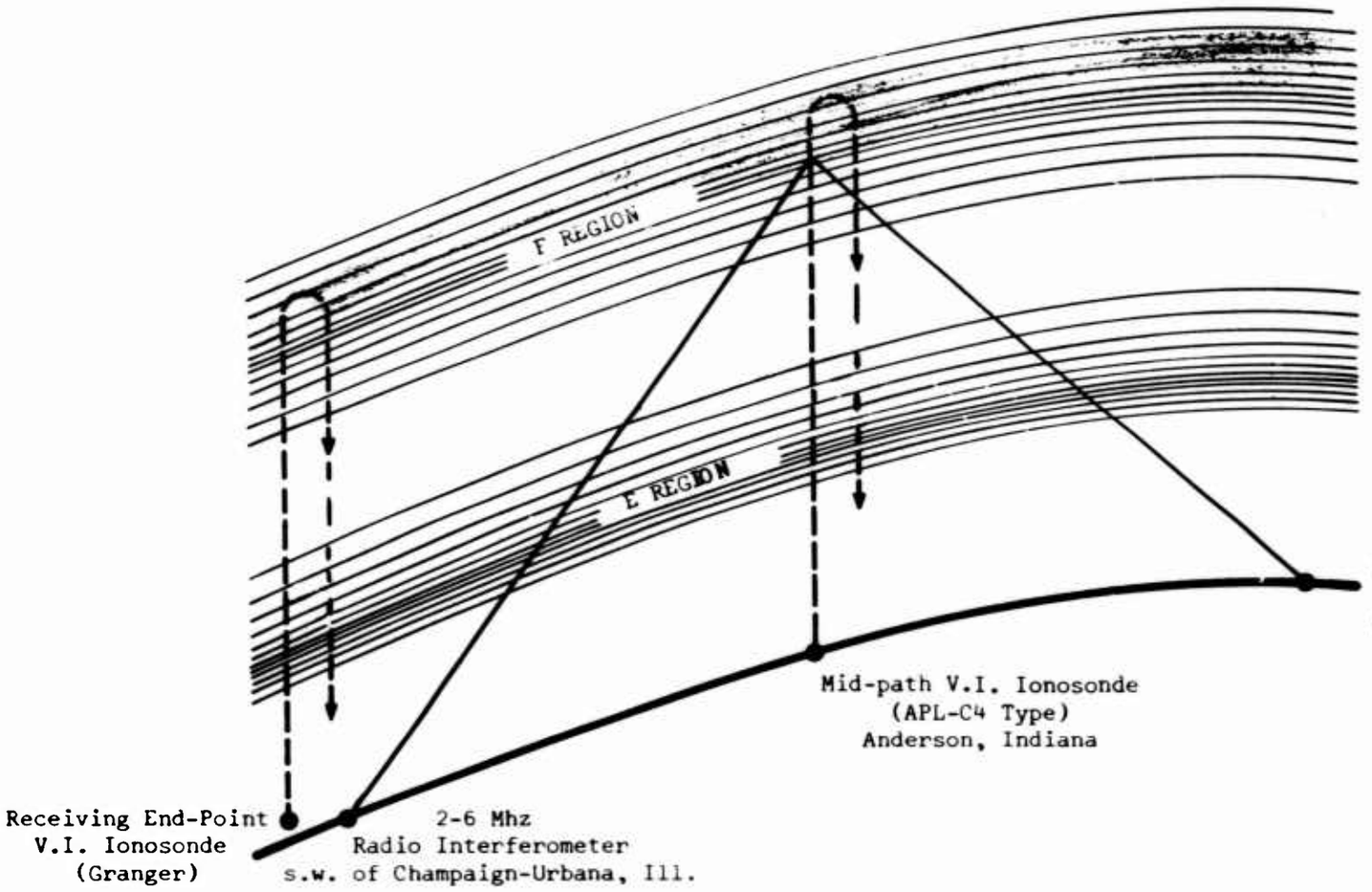

Figure 5

Geometry of Columbus Experiment

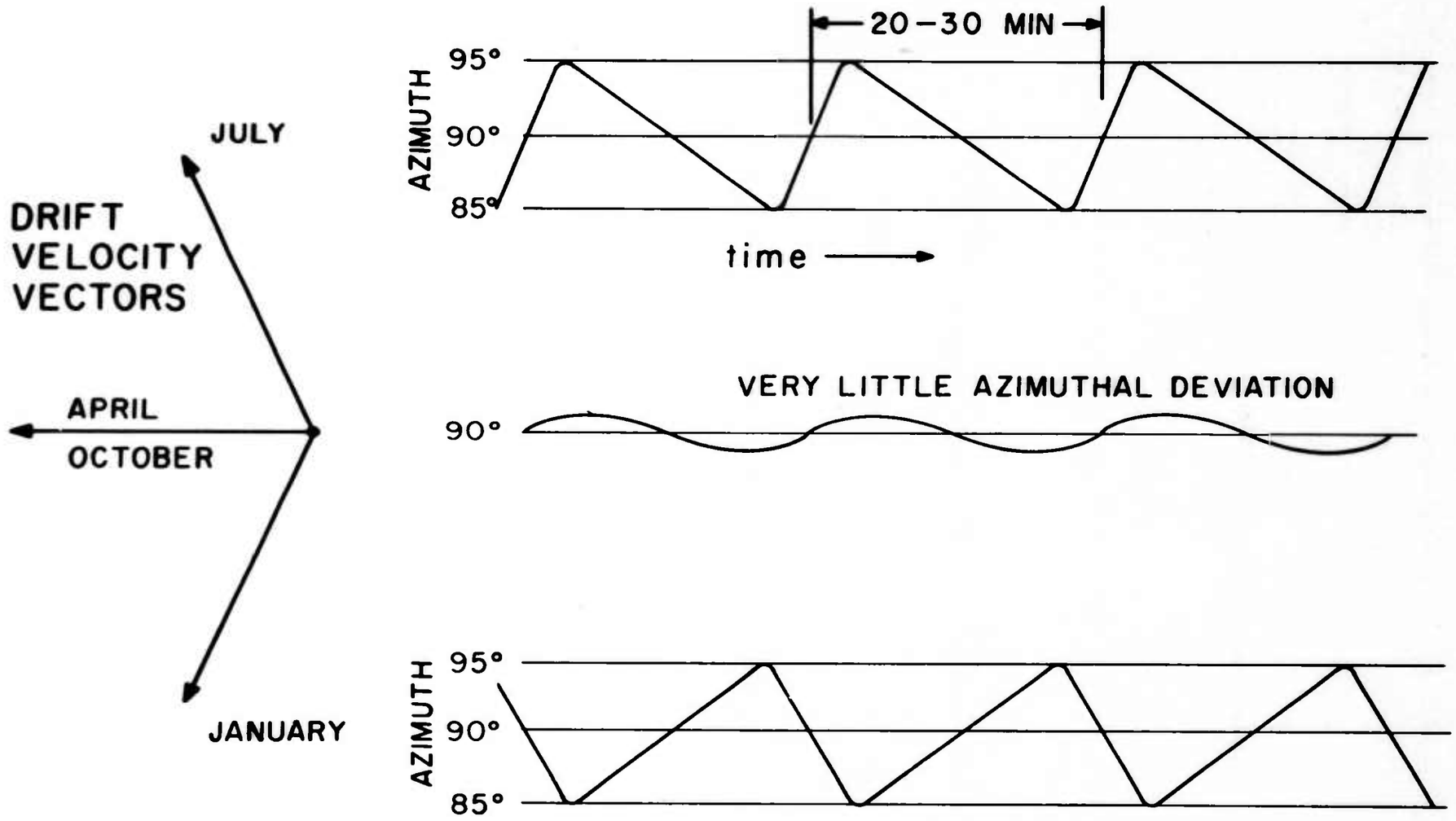

Figure 6

Pertinent to Explanation of Seasonal Lateral Deviations in the Azimuthal Angle of Arrival over an East to West Ionospheric Propagation Path

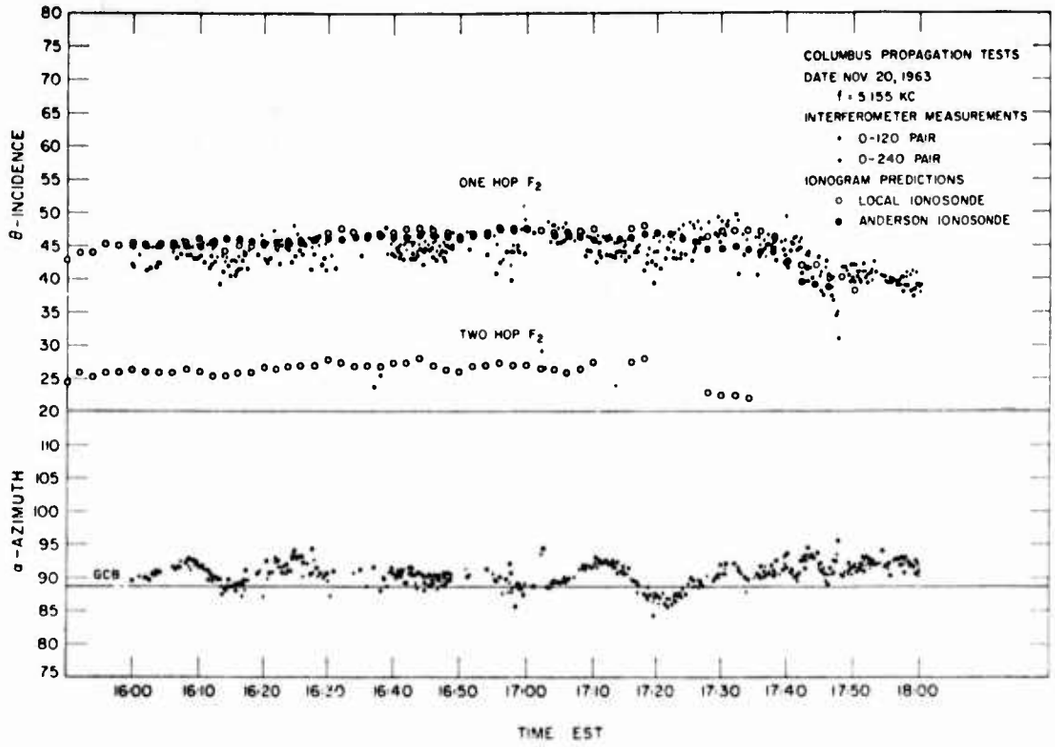

Figure 7

Example of Columbus Data for November 20, 1963

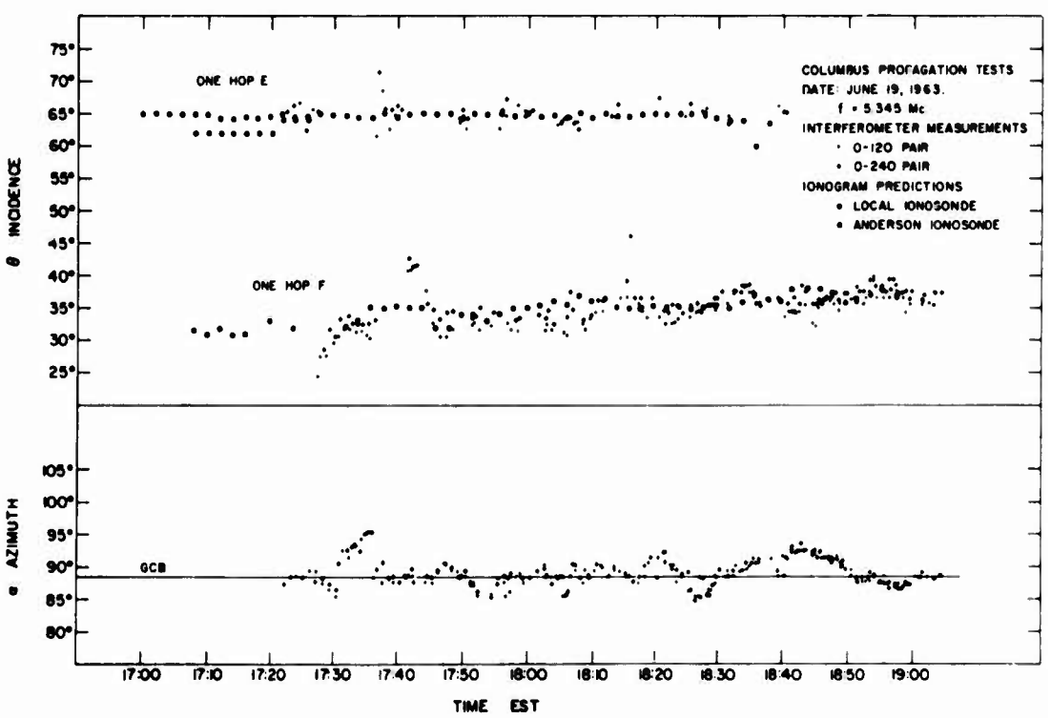

Figure 8

Example of Columbus Data for June 19, 1963

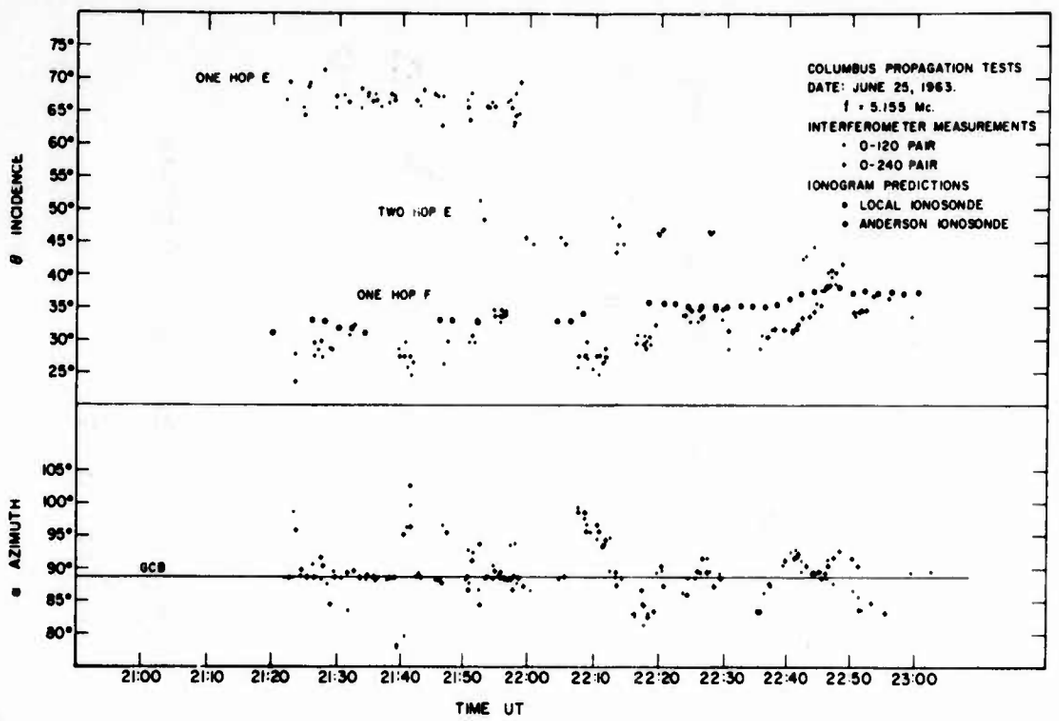

Figure 9

Example of Columbus Data for June 25, 1963

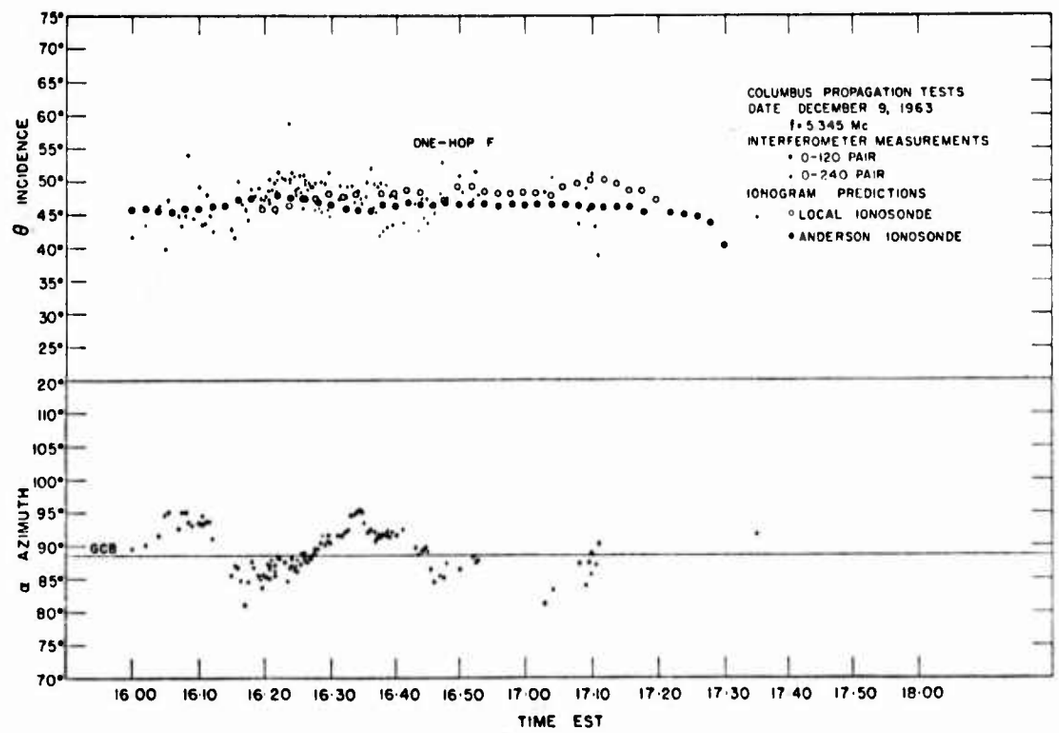

Figure 10

Example of Columbus Data for December 9, 1963

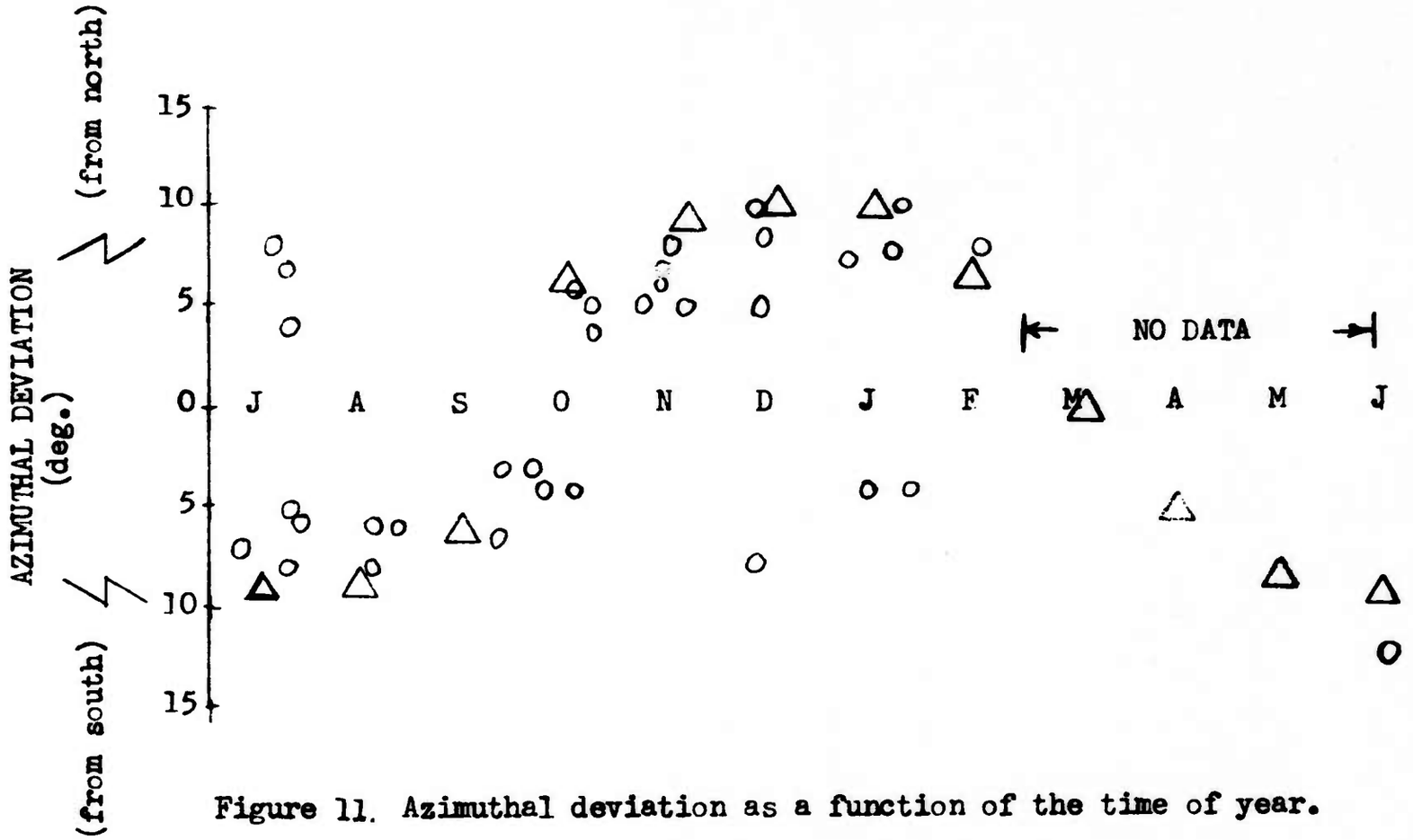

Figure 11. Azimuthal deviation as a function of the time of year.

F layer only; 15 - 25 min. periods only.

○ Columbus experiment data

△ Jones experiment data

THREE TRANSMITTER EXPERIMENTS IN RADIOLOCATION RESEARCH

A. D. Bailey and E. K. Walton
Radiolocation Research Laboratory
Department of Electrical Engineering
University of Illinois
Urbana, Illinois 61801

The strong implication made in the previous paper is to the effect that there are traveling-wave-like disturbances in the ionosphere which appreciably perturb the angle of arrival of short range high angle signals but which are also predictable in a quantitative way. If certain parameters which characterize these effects are measured in real time at a few points in the neighborhood of interest, extrapolations can then be made to other points in the region. These extrapolations may be moved forward and backward in time for intervals of 10 to 20 minutes and over spatial regions having diameters of 100 to 200 kilometers. These conclusions are based upon the experimental findings in our own researches as well as others', such as Munro in Australia and Davies and Jones at ESSA.

Our immediate problem is to measure effectively the velocity vector of the traveling-wave-like disturbance and its amplitude distribution as a function of time and lateral extent. Given this, we can solve another problem.

There are several methods for measuring tilts and drifts in the ionosphere that have been used by various investigators in different parts of the world. These were summarized in the IGY Annals for the Geophysical Year, Part III (1957). Listed below are several of these methods which have been found to be useful for one application or another.

1. Closely spaced receivers. (approximately one-wavelength separation)
2. Recordings of group height as a function of time for widely spaced receivers. (approximately 200 wavelengths)
3. Recordings of amplitude as a function of time for widely spaced transmitters. (approximately 200 wavelengths)
4. Simultaneous observations of changes of amplitude and phase path.
5. Method of large arrays of many elements, e.g., the Buckland Park array having 100-meter element-to-element separation in a square or circular grid array with a maximum dimension of approximately 1 kilometer.
6. Very widely spaced transmitters, e.g., spaced ionosondes with 200 to 400 kilometer separation or more.
7. Frequency modulated continuous wave techniques employing Doppler-effect principles.

The experiment at Illinois is directed toward finding an optimum solution for a specific application. Accordingly, we have instrumented

the experiment to have both the widely spaced transmitter capability and the closely spaced receiver capability. The complete experiment will permit one to make comparisons, draw inferences and, hopefully, reach a decision as to the best way to solve a particular problem.

These experiments are being made in the area surrounding the RDF-Ionosonde site at the Monticello Road Field Station. The triple-interferometer RDF and the compatible, collocated and complementary vertical incidence ionosonde constitute the closely spaced receiver/transmitter system. The geometry for the widely spaced transmitters is shown in Figure 1. The transmitter separation is approximately 30 kilometers; this makes the effective separation of the specular reflection point approximately 15 kilometers at the ionospheric height of reflection.

We do not have the capability to observe simultaneous transmissions from all stations. The practical compromise is to switch rapidly in sequence around the system of transmitters. Figure 2 shows the block diagram of the sequencer-timer unit which permits this operation from a common 60-hertz power supply utility. Figure 3 shows the complete circuit diagram for the sequencer-timer unit.

The transmitters are of a simple kit-type which were modified slightly and assembled in the laboratory. The transmitting antennas are elevated horizontal doublets or dipoles oriented so that reception of the ground wave is minimized.

Two kinds of data are recorded from each transmitter. The amplitude function of time is recorded as well as the differential phase information measured by the triplet of antenna pairs in the interferometer. Cross-correlations may be made between the amplitude data of different transmitters to determine the horizontal components of drift velocity or traveling-wave velocity. Angles of arrival in azimuth and elevation together with their temporal deviations may be determined from the differential phase data.

One example of reduced data is shown in Figure 4. Analysis of these data imply that there is a traveling-wave effect moving in a 287° azimuthal direction over the region with an effective velocity of 125 meters per second. The wavelength is approximately 98 kilometers.

REFERENCES

(1) Beynon, W. J. G., and G. M. Brown, "Annals of the International Geophysical Year," Part III (The Measurement of Ionospheric Drifts), Pergamon Press, London, 1957, pp. 233-287.

(2) Jones, John E., "Observation of Traveling Ionospheric Disturbances by the Doppler Technique with Spaced Transmitters," ESSA Technical Report ERL 142SDL 11, Boulder, Colorado, 1969.

(3) Munro, G. H., "Travelling Disturbances in the Ionosphere," Proc. Roy. Soc. of London, 1950, A202, pp. 208-223.

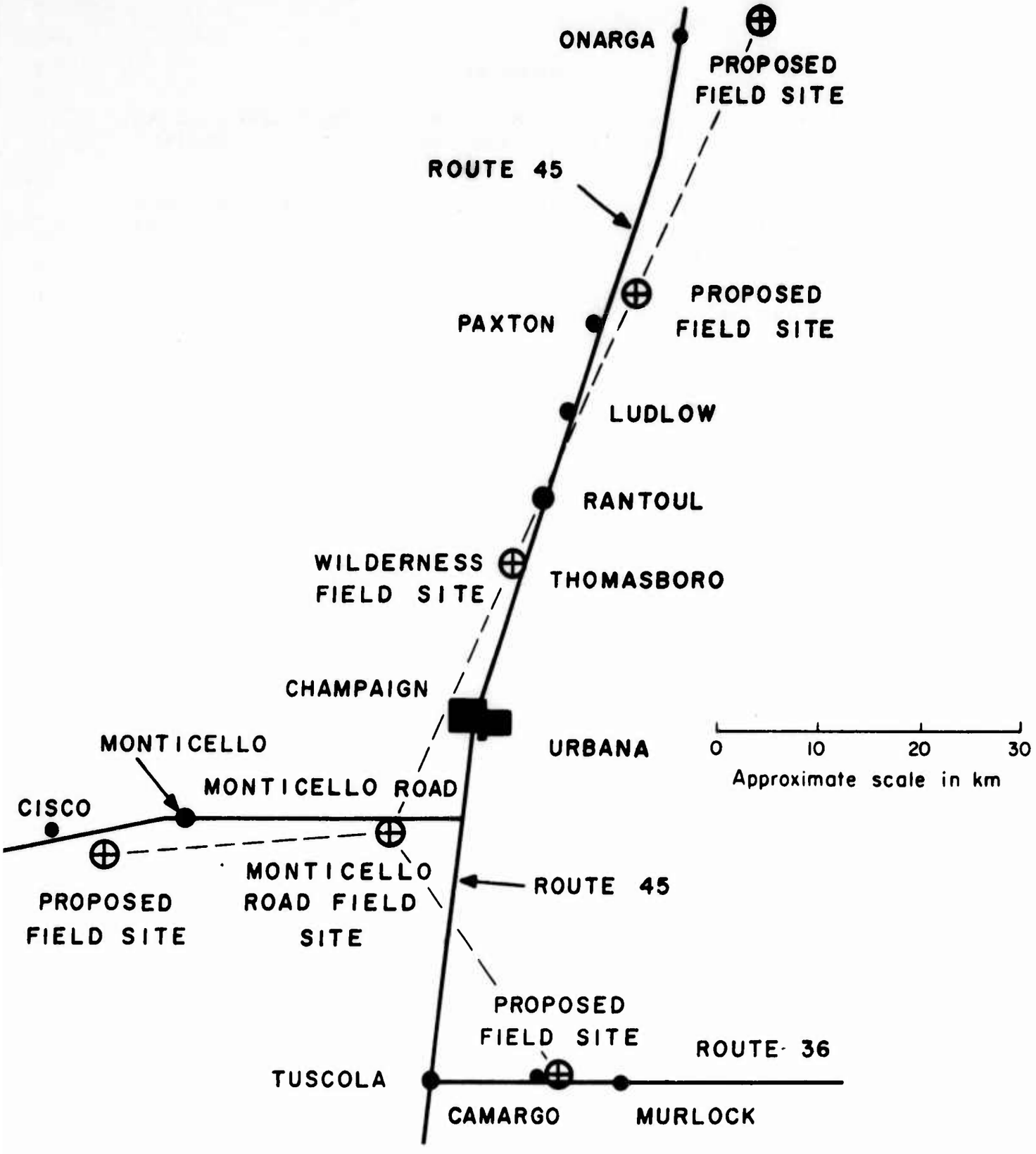

Figure 1. Map showing proposed locations of five cooperative HF transmitters for extended tilt measurements

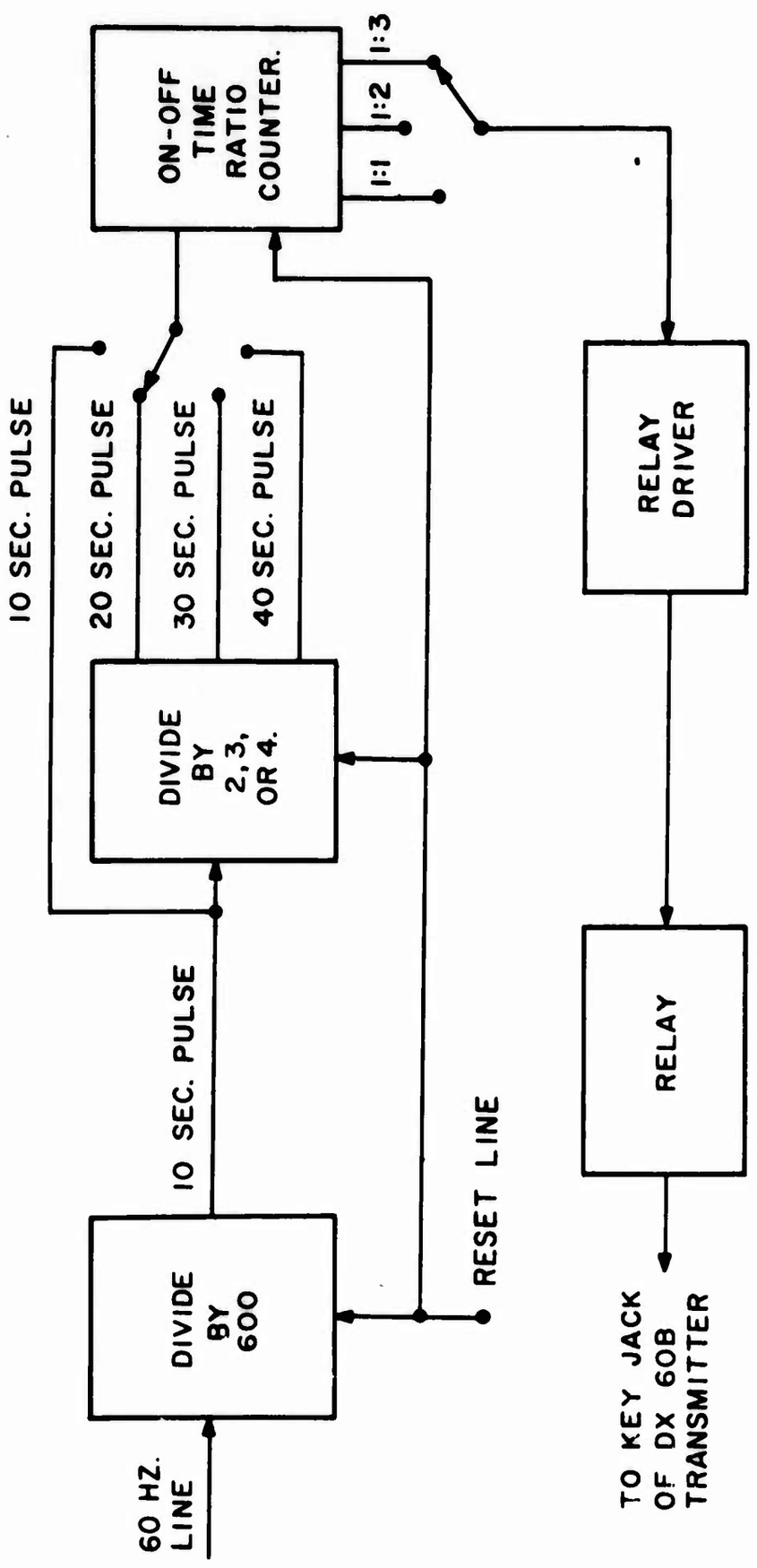

Figure 2. Block diagram of a sequencer-timer unit for the spaced, cooperative transmitters

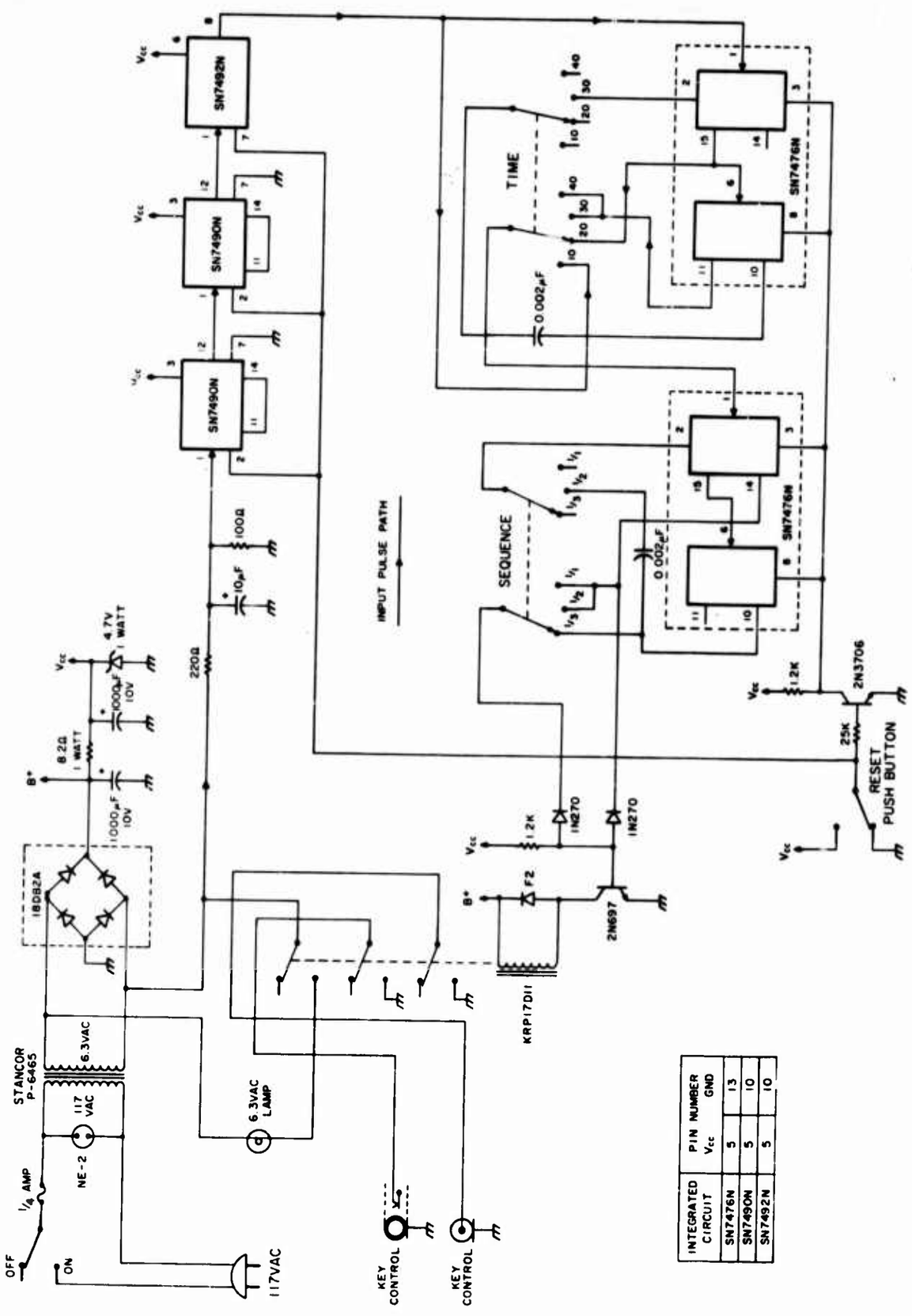

INTEGRATED CIRCUIT	PIN NUMBER Vcc	GND
SN7476N	5	13
SN7490N	5	10
SN7492N	5	10

Figure 3. Circuit diagram for three-transmitter sequencer and interval timer

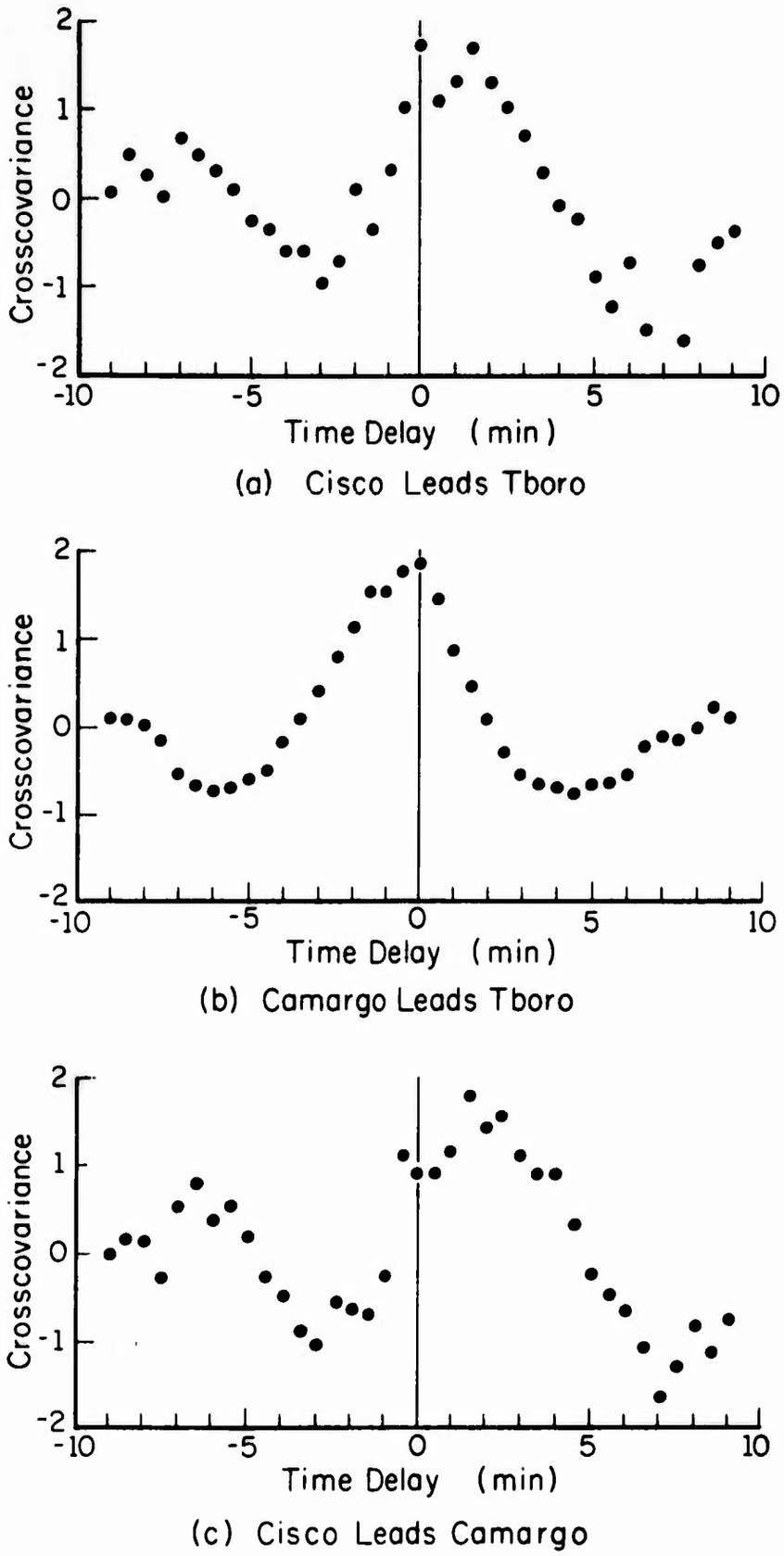

Figure 4. Crosscovariance of the amplitude data on paper tape 104 (time interval=2100-2150)

R. L. JOHNSON, P. E. MARTIN, T. C. GREEN

Southwest Research Institute, San Antonio, Texas

SHORT TIME SCALE IONOSPHERIC TILT MEASUREMENTS FOR LATERAL DEVIATION COMPENSATION

ABSTRACT

Tilt parameters were computed using a cooperative transmitter located 55 km from the DF interferometer at a GCB of 306°. These values were used to tilt correct DF measurements from a target transmitter located 64 km and GCB of 347°. A study was made of the autocorrelation and crosscorrelation of the tilt parameters to determine correlation time. The short correlation times indicated, demonstrate a need for rapid tilt measurements which are possible with a cross spectral analyzer and an FM/CW sounder.

The DF interferometer configuration used in this study is shown in Figure 1. The antenna array consists of five quadrature fed crossed loops set on 13 and 150 meter baselines. The antenna outputs are sampled by the switching network and fed through the twin channel receiver. Phase measurements are made from the receiver outputs. The switching rate is set to produce a frame of four phase measurements every 100 milliseconds. Each set of four phase measurements is used to calculate the azimuth and elevation of the incoming wave. These values are averaged over a 10 to 30 second period to compute a bearing cut. Additionally, the 2σ point (for an assumed normal) of the azimuth scatter is computed and labeled tolerance in the data to be reported.

The tilt geometry is illustrated in Figure 2. It is assumed that the lateral deviation of the received signal can be characterized by the triangle ROP. Hence, through knowledge of the ionospheric height, tilt incidence and azimuth of the tilt vector, the measured elevation and azimuth can be used to compute tilt angles (azimuth and incidence) suitable for compensating measured observed bearings for tilt effects.

In the data to be presented, the tilt parameters were computed from the bearing cuts and ionogram data using a cooperative transmitter with location known apriori. The first group of tilt experiments

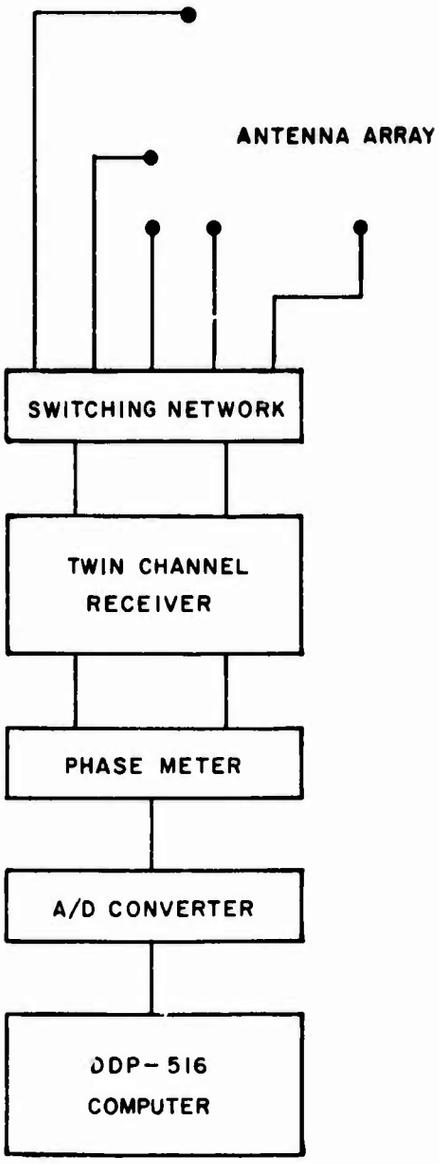

FIGURE 1

BLOCK DIAGRAM OF DF
INTERFEROMETER

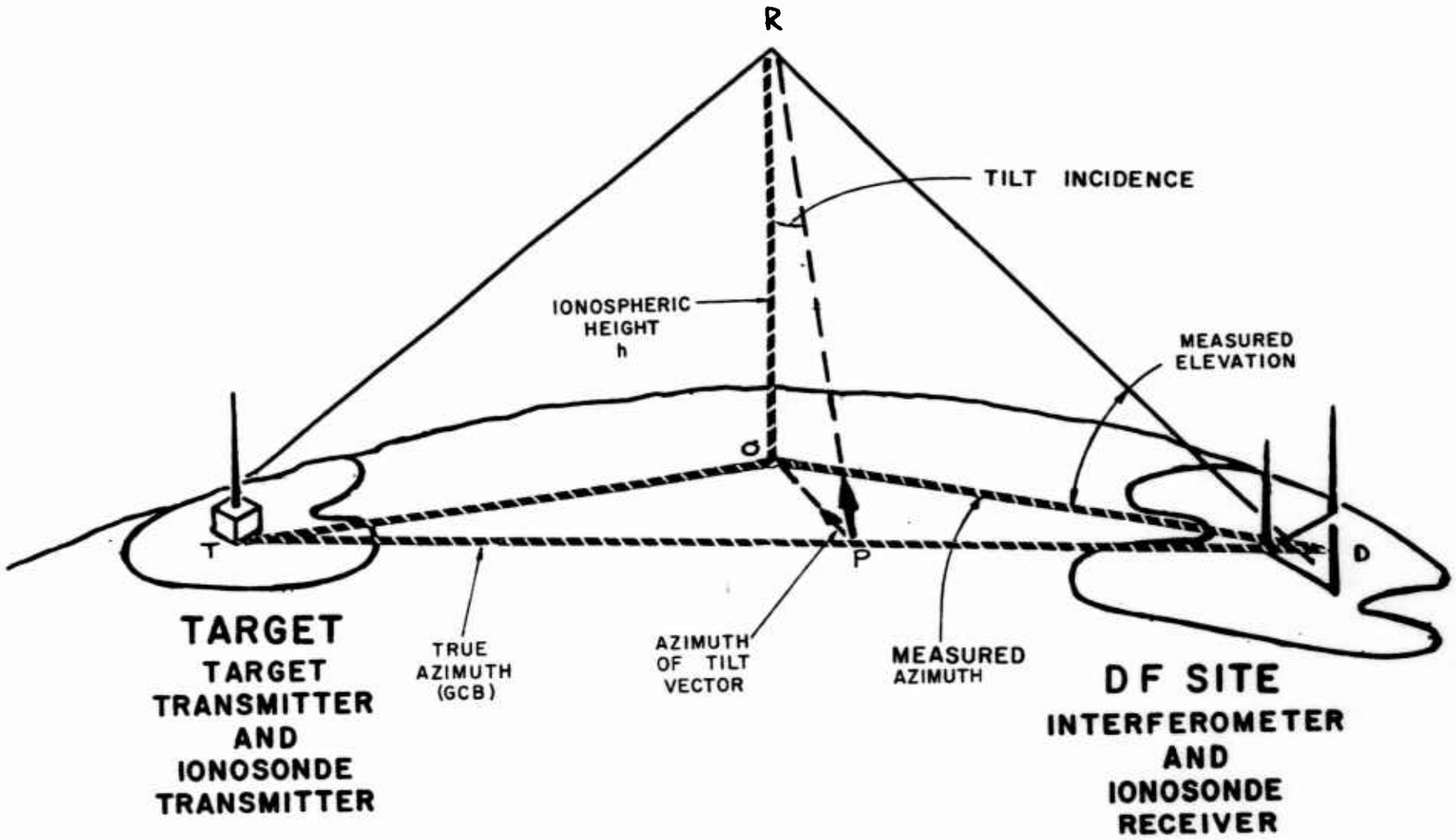

FIGURE 2

IONOSPHERE TILT EFFECT

used a known target at Bandera, Texas at a 55 km great circle path and a secondary target near Comfort, Texas 40° to the north of Bandera and 64 km distant (see Figure 3). An FM/CW ionosonde transmitter was also located at Bandera to provide path length data. During each minute a DF measurement was made on both targets with a sounding made every two minutes. Tilt parameters were calculated from target azimuth and elevation angle measurements and ionosonde path length.

Time series of tilt azimuth and incidence angle and the corrected azimuth are shown in Figures 4 and 5. A time series of the same data for no correction is also shown. The tilt angle compensation serves to improve the average azimuth with a residual scatter about the great circle bearing. The improvement is achieved in spite of the 40° difference in azimuth and 10 km difference in range between the corrected measurement (Comfort) and the correcting tilt measurement (Bandera).

In another experiment the tilt parameters were computed successively on the Bandera target every 20 seconds. Data were collected from a transmitter operating on 6.3 MHz and collocated with a sounder in Bandera, Texas (see Figure 3). Bearing cuts were taken over a period of approximately one and a half hours to generate a collection of 250 samples.

Figure 6 is a time series representation of the parameters mentioned previously. Note the tilt azimuth angle rotates through 360° with time at the end of the record. The relatively rapid apparent tilt angle variation may be attributed to residual wave interference error although the ionograms show single IF modes predominating at least 15 db above the second hop.

Figure 7 shows 10, 20, and 30 second time averaged data per sample. The smoothing obtained from 10 seconds to 20 seconds is probably due to wave interference error reduction. From 20 to 30 seconds little change is noted, thus suggesting an approximate mode coherence time of 20 seconds.

The cross correlation of azimuth tolerance and tilt azimuth, shown in Figure 8 implies that there exists negligible "long term" correlation between wave interference and tilt azimuth over the measurement period involved. The question then arises, how fast does the path direction change? Figure 9 shows the computed autocorrelation of the tilt azimuth. The data appears to be essentially uncorrelated after 20 seconds, partially caused by the circular nature

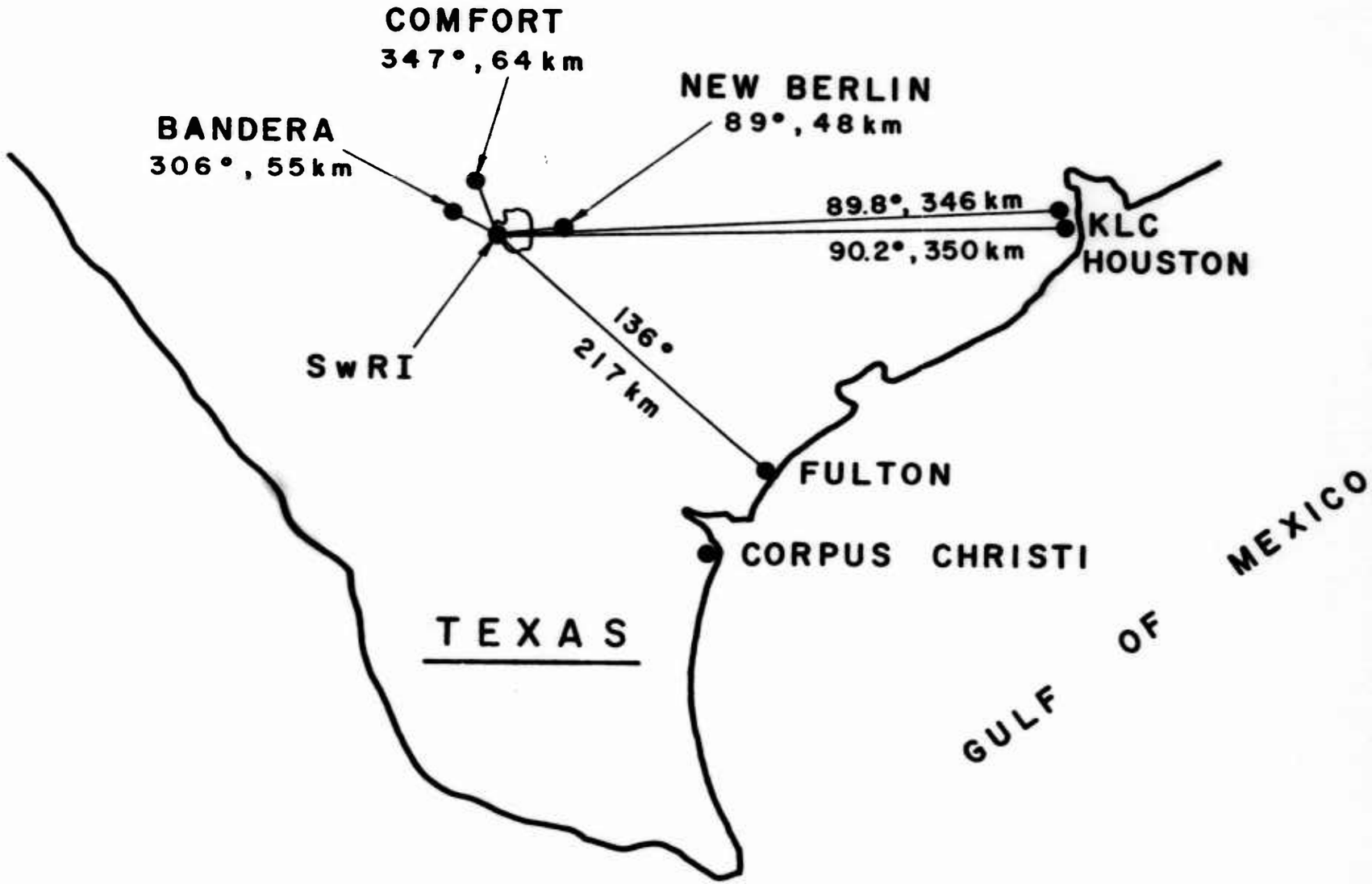

FIGURE 3

TARGET LOCATIONS FOR DF INTERFEROMETRY
PERFORMANCE TESTS

COMFORT, TEXAS - 6.3 MHz
64 KM RANGE

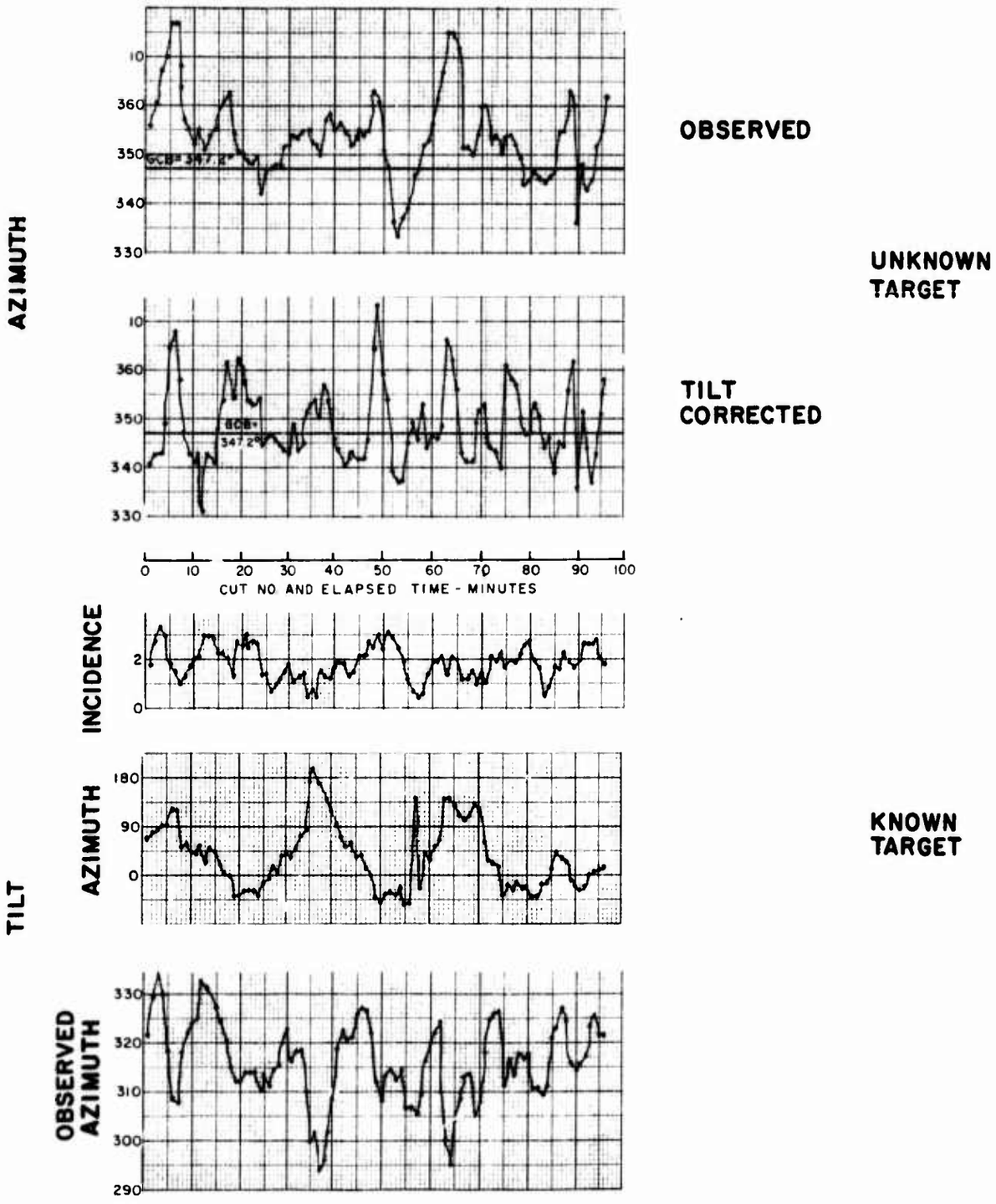

FIGURE 4

TIME SERIES--SSL CUTS--COMFORT, TEXAS TARGET

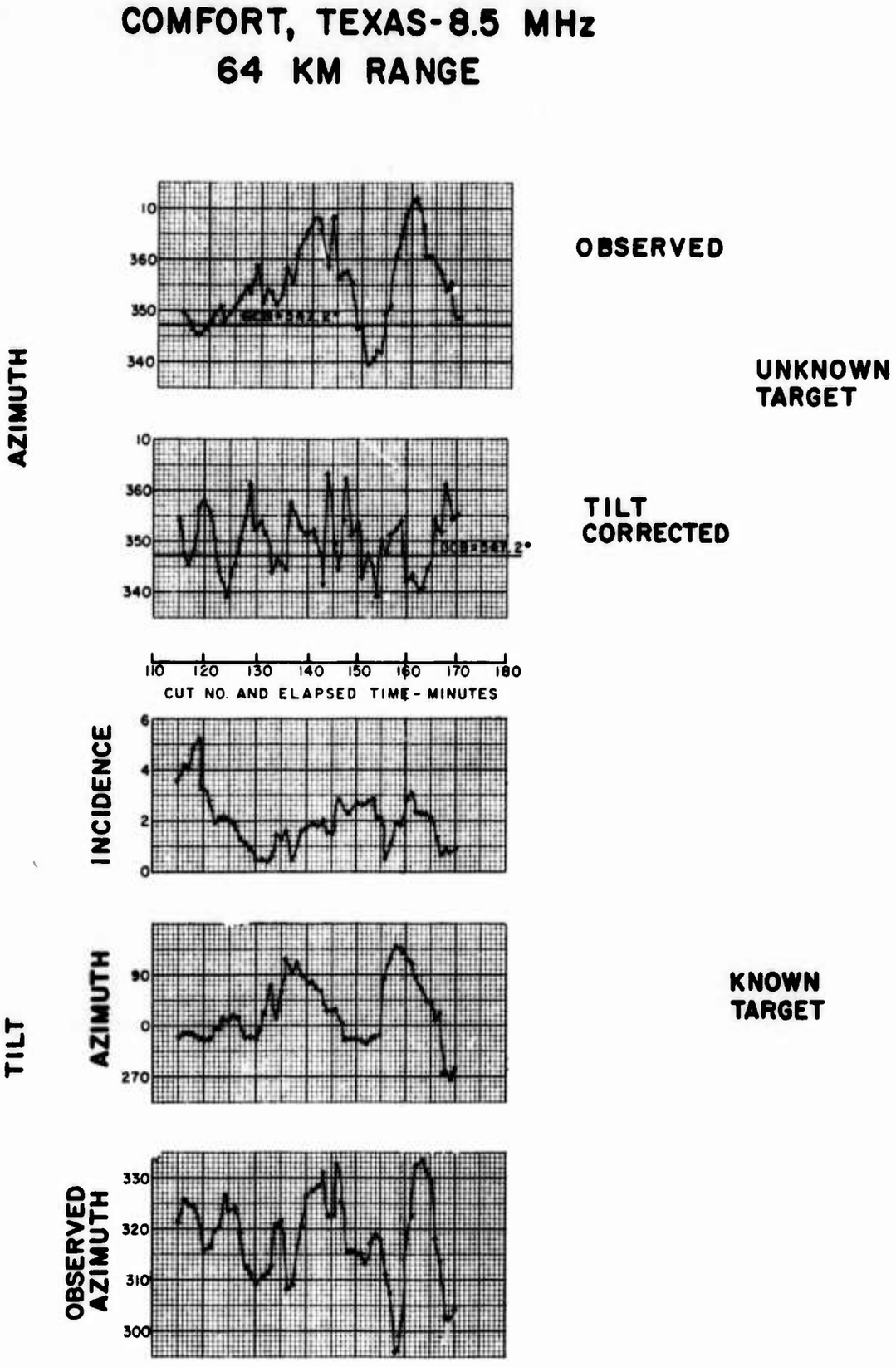

FIGURE 5

TIME SERIES--SSL CUTS--COMFORT, TEXAS TARGET--8.5 MHz

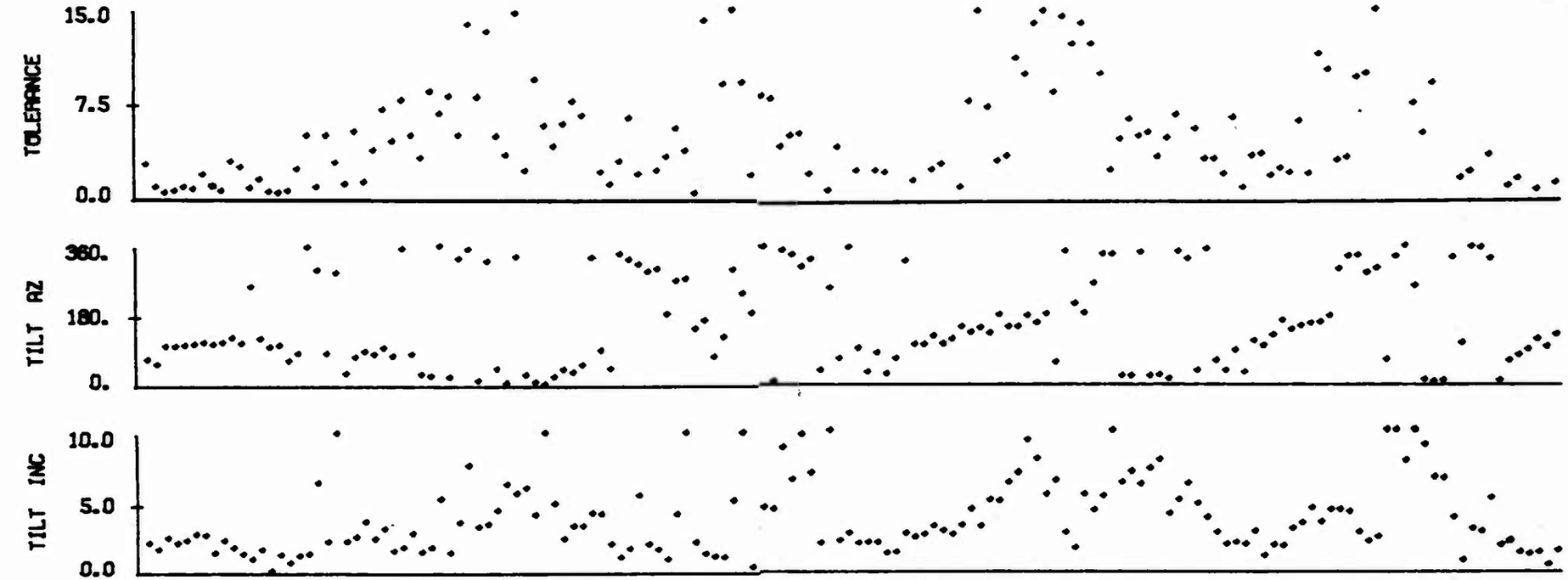

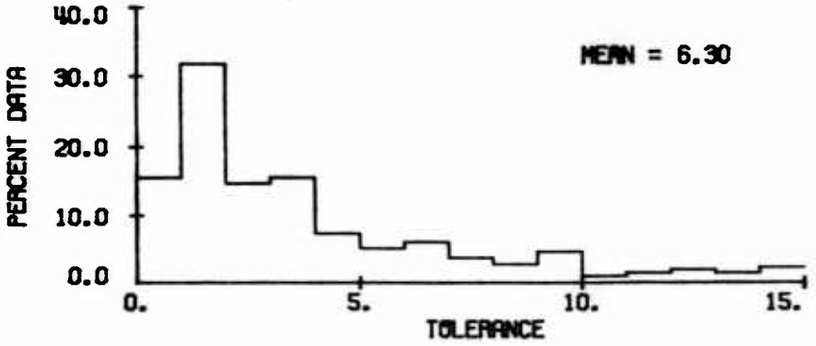

FIGURE 6

TIME SERIES OF TILT PARAMETERS

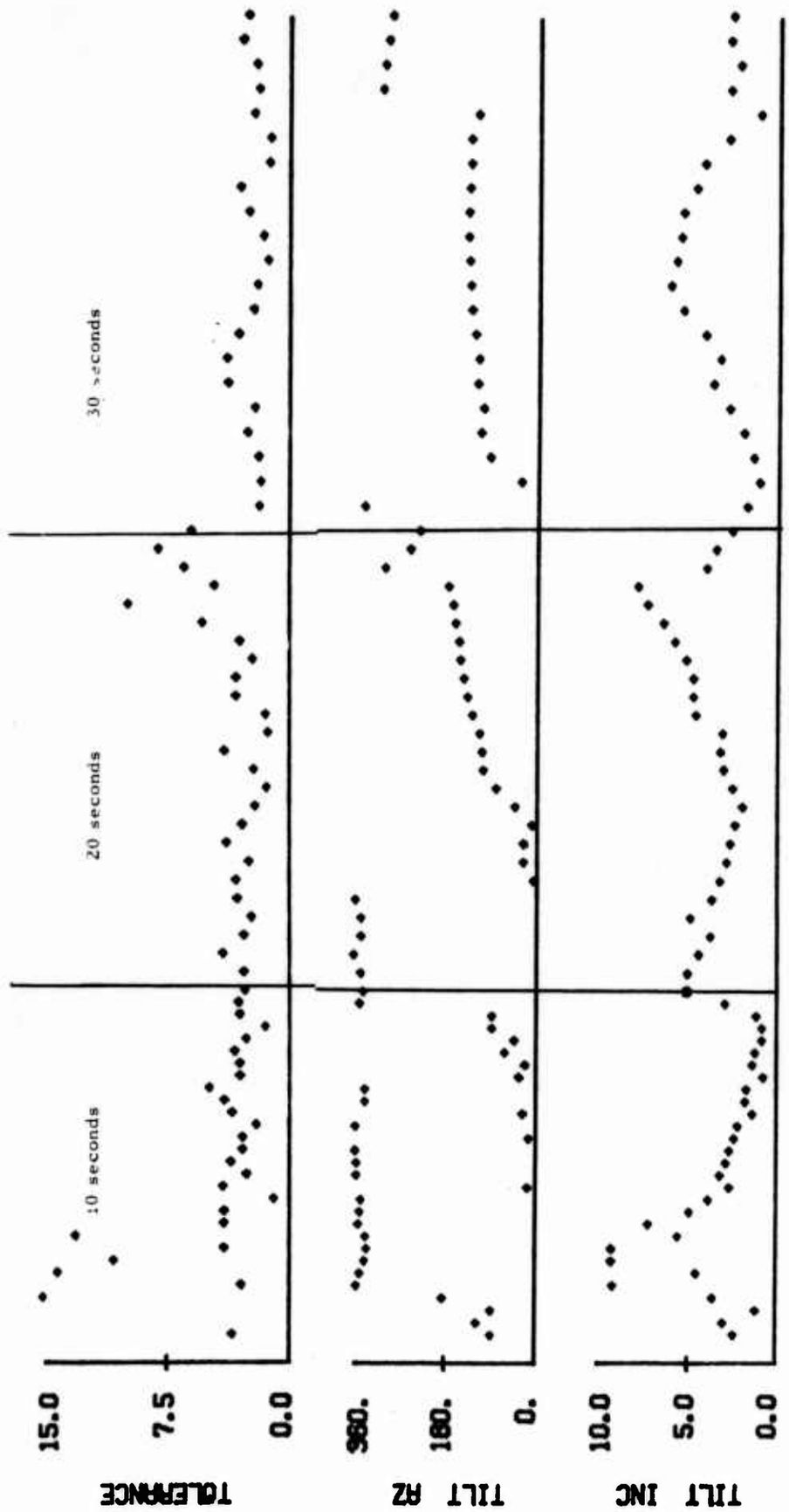

FIGURE 7

COMPARISON OF AVERAGING TIMES

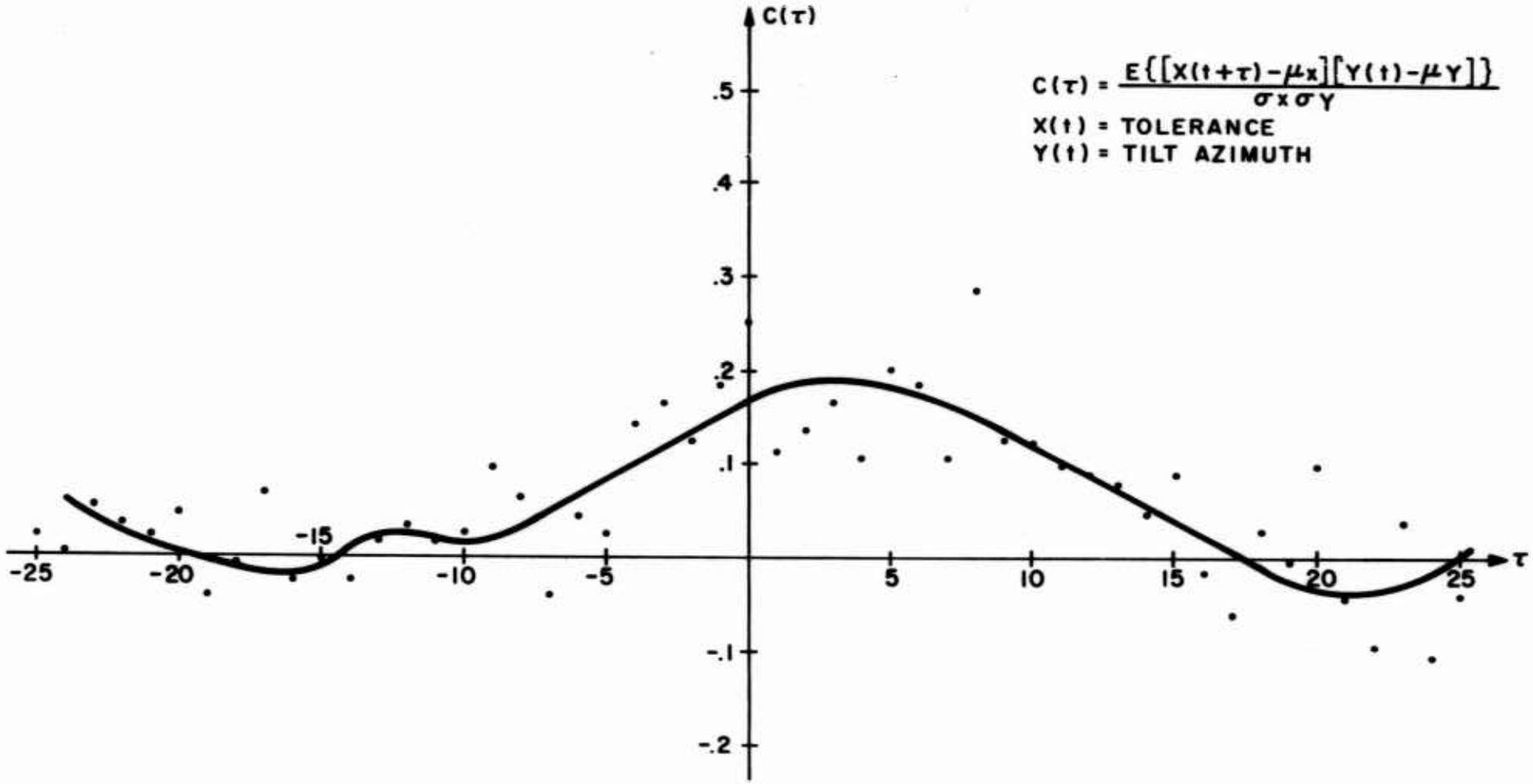

FIGURE 8

CROSSCORRELATION BETWEEN AZIMUTH TOLERANCE AND TILT AZIMUTH

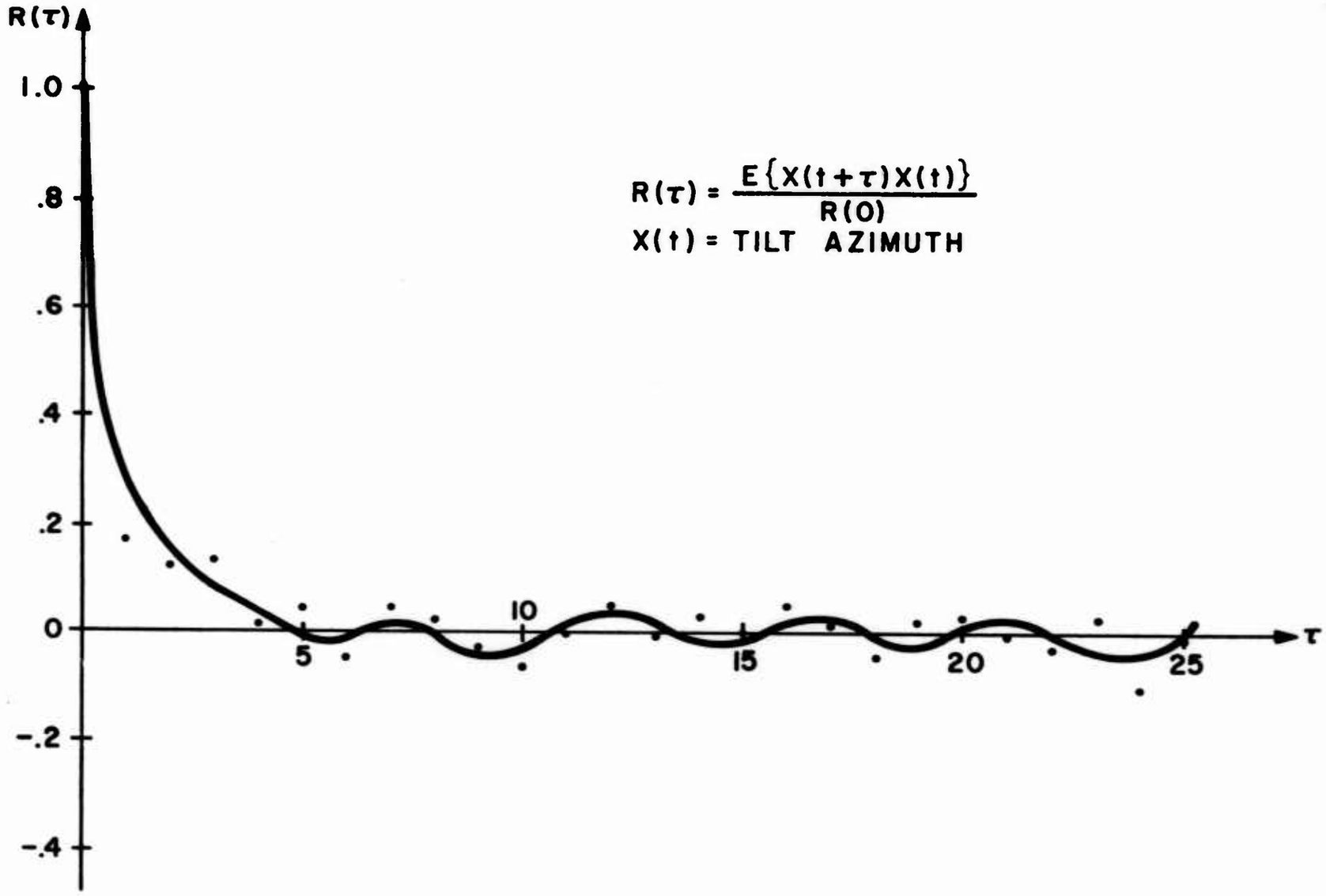

FIGURE 9

AUTOCORRELATION FUNCTION OF TILT AZIMUTH

of the azimuth function. The time series shows that 10 minute segments tend to be highly correlated on a 20 second time scale, whereas the azimuth rotation at the end of the record reduces the average correlation over 90 minutes.

Figure 10 shows the cross correlation between tilt incidence and azimuth tolerance. This function indicates a weak degree of correlation in wave interference effects with lateral deviation and depth of penetration. Again, investigating the rate of change, Figure 11 is a plot of the autocorrelation function of tilt incidence. This figure shows that the changes in lateral deviation and depth of penetration are somewhat slower than the changes in tilt azimuth alone, but are fast with respect to the 10 second averaging period.

These short correlation periods indicate the need for rapid tilt measurement with wave interference effects eliminated. DF measurement on each sounder return in real time provides this capability using a cross spectrum analyzer with a FM/CW sounder. We have performed initial experiments demonstrating interferometric direction finding on an HF linear FM/CW signal.

A three-element orthogonal baseline interferometer and a twin channel receiver modified for linear FM synthesis were used to obtain the phase measurements. Figure 12 shows the conventional orthogonal baseline arrangement.

The relative phases were measured between the apex antenna and the two orthogonal antennas, each baseline being 75 meters. Measured phase differences were used to compute incident azimuth and elevation. Phase ambiguities were resolved by prior knowledge of the sounder location.

A block diagram of the equipment is shown in Figure 12. A calibrate mode injects a pilot signal obtained from the coherent synthesizer into both channels as a measure of receiver mismatch.

Skywave data were obtained from the Naval Research Laboratory mobile FM/CW transmitter unit in Pueblo, Colorado and later from Boulder, Colorado. A sample ionogram for the propagation conditions between Pueblo and San Antonio is shown in Figure 13. Note that single mode propagation conditions existed in the 15-16 MHz range.

Sum-and-difference phase displays for the Pueblo-San Antonio path (1120 km ground distance) are shown in Figure 14 for the single

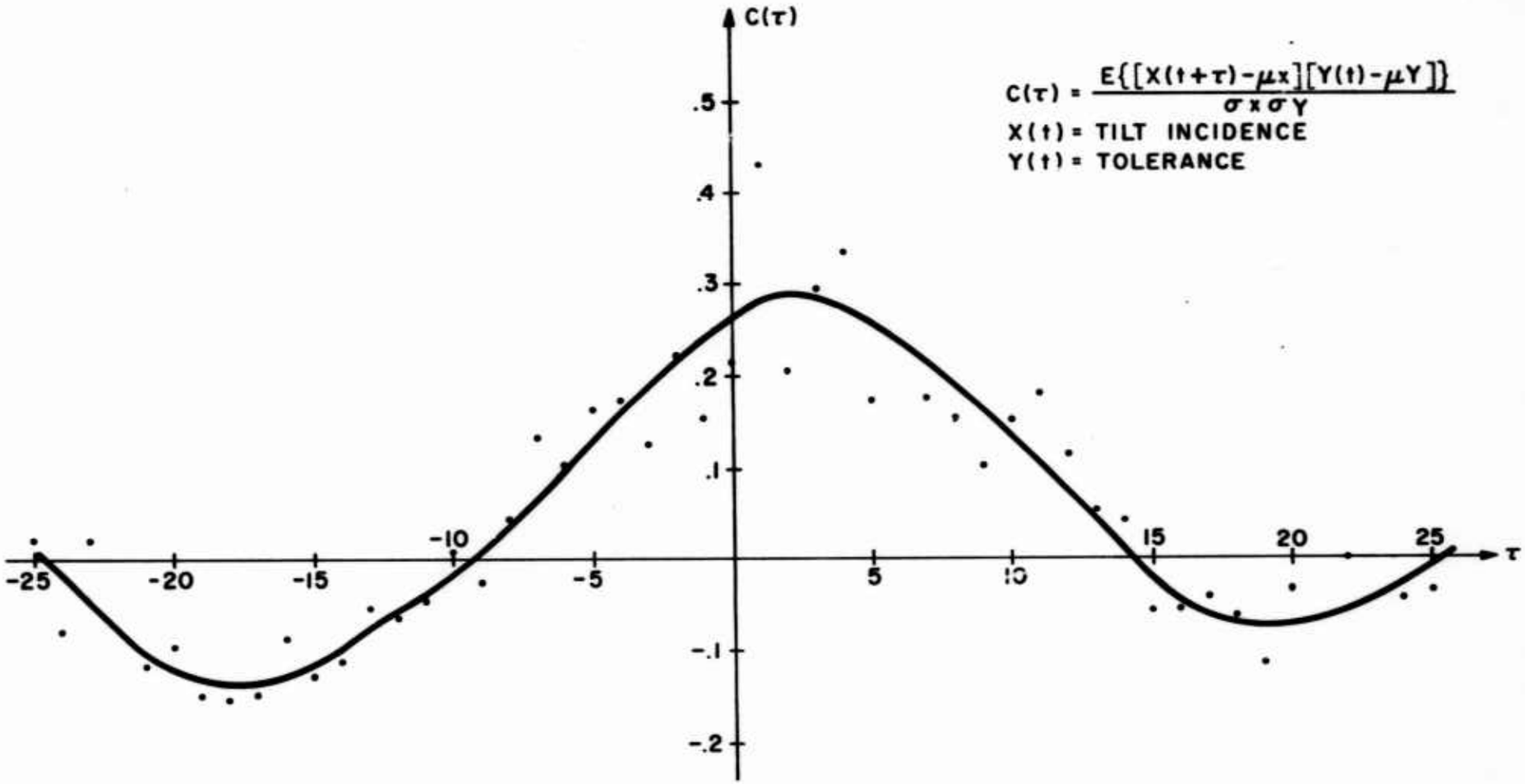

FIGURE 10

CROSSCORRELATION BETWEEN TILT INCIDENCE AND AZIMUTH TOLERANCE

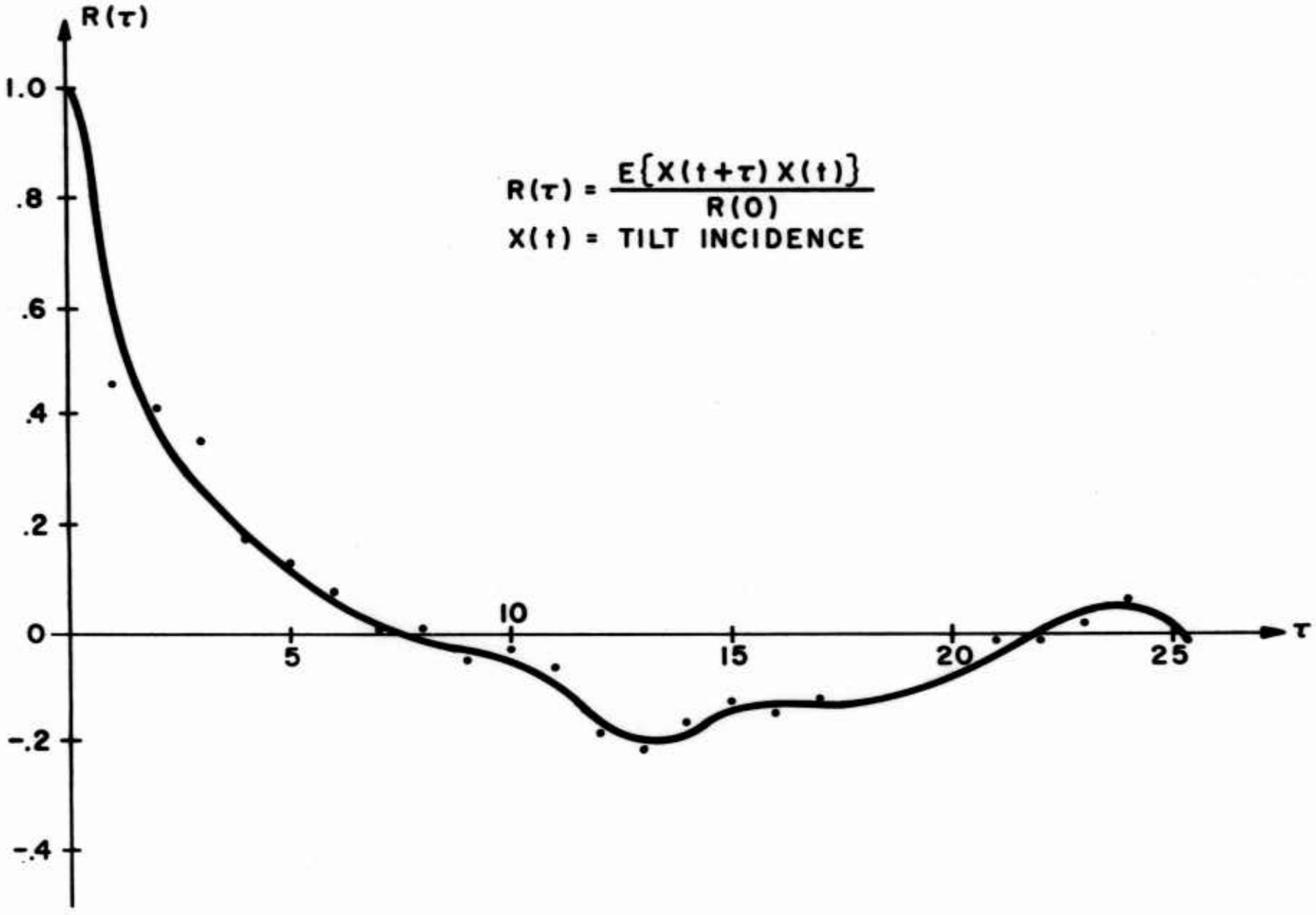

FIGURE 11

AUTOCORRELATION FUNCTION OF TILT INCIDENCE

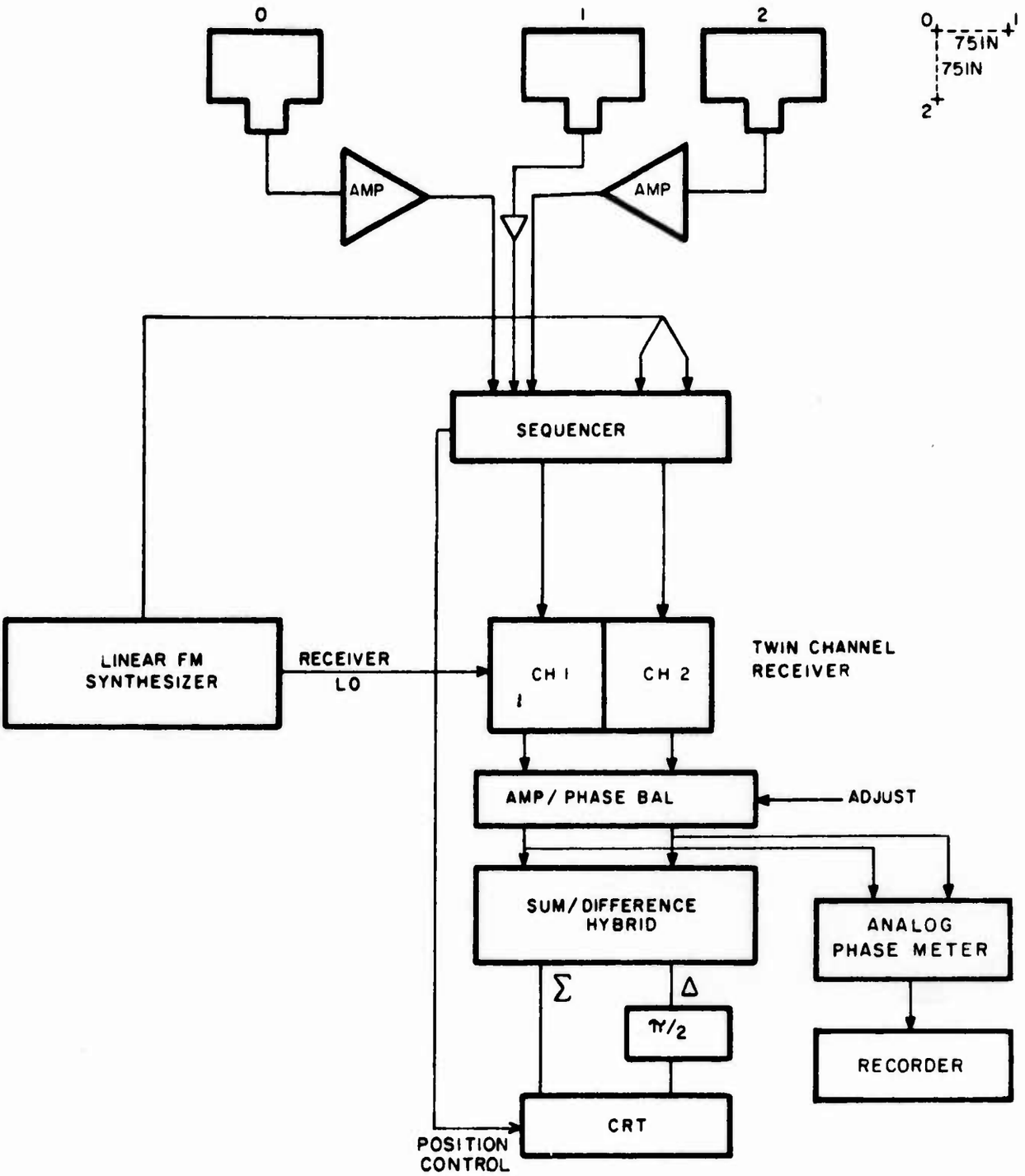

FIGURE 12

INSTRUMENTATION

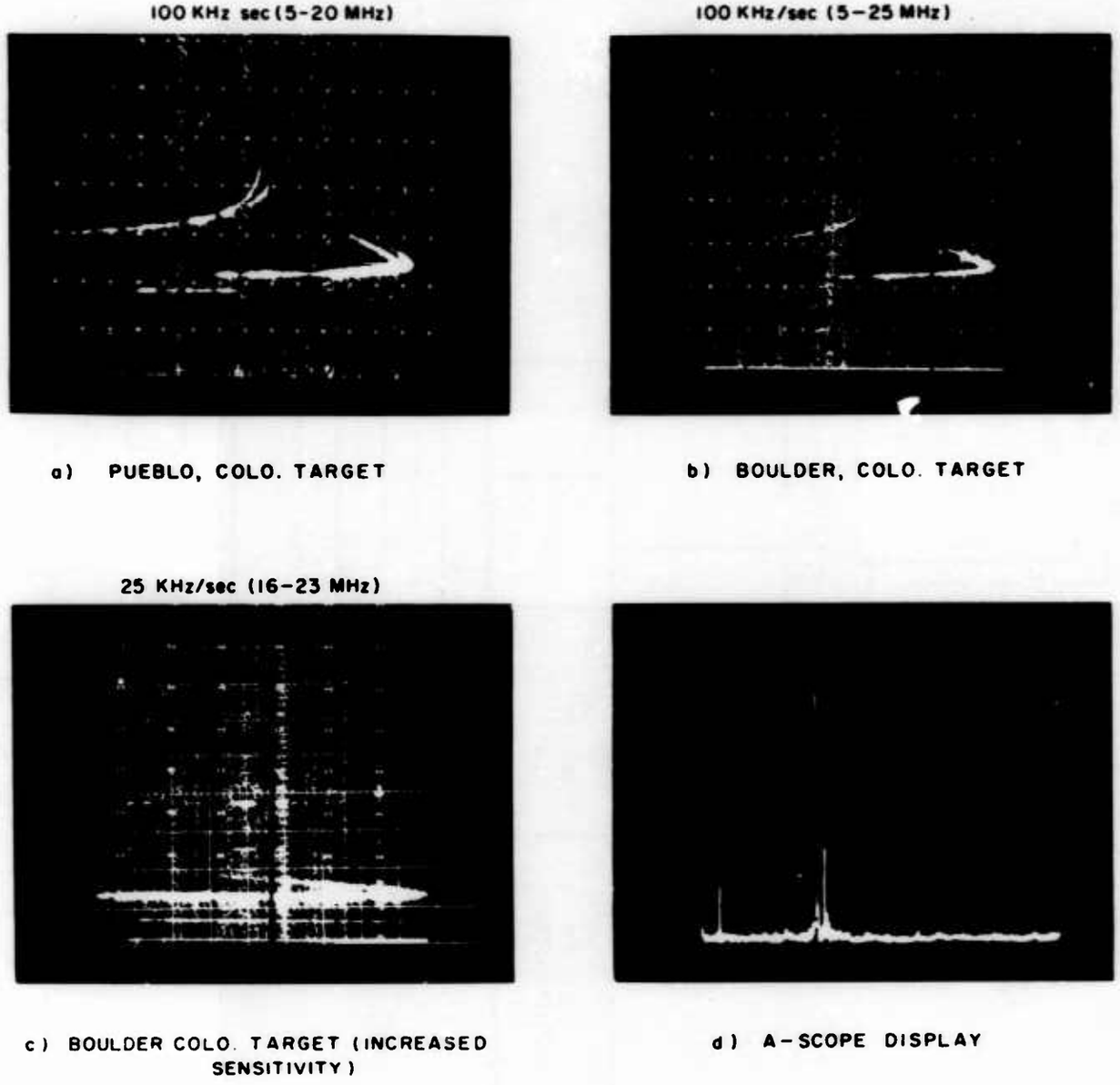

FIGURE 13

SAMPLE IONOGRAMS

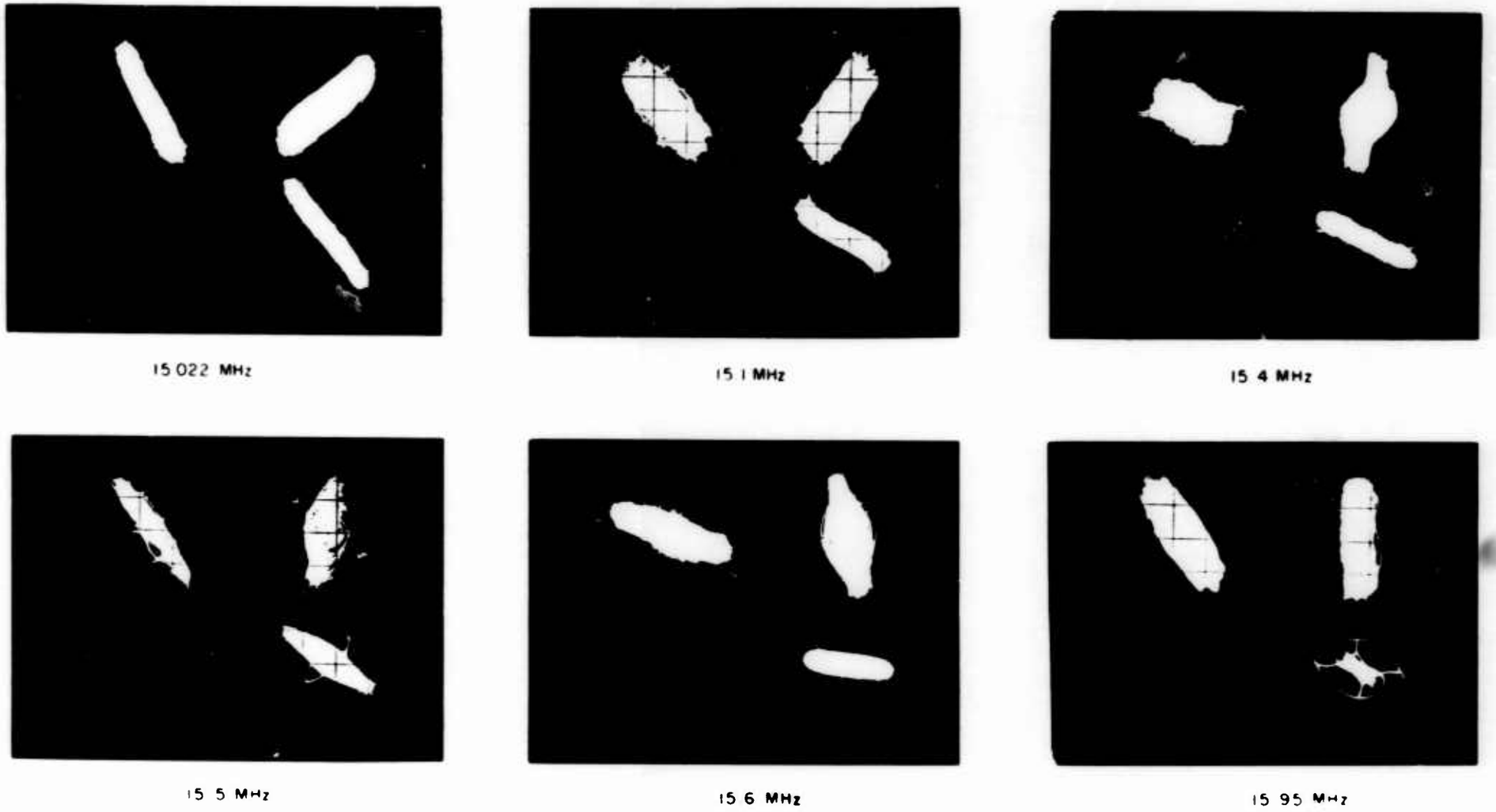

FIGURE 14

SUM-DIFFERENCE PHASEMETER DISPLAYS PUEBLO-SAN ANTONIO PATH

mode propagation region where a relatively high signal-to-noise ratio was obtained without the use of spectrum analysis.

The computed azimuth and elevation angles between 15 and 16 MHz are shown in Figure 15. Azimuth angles for the 1 MHz range agree very weli with the great circle bearing of 332. 7° varying no more than 1° or 2°. The elevation angle also is tightly grouped around a nominal 20° value with a slight increase as the function of frequency.

Another FM/CW direction finding experiment performed for a Boulder, Colorado to San Antonio path yielded essentially the same results. The frequency range was 19-21 MHz. The computed azimuth angles again agree well with the true great circle bearing of 334. 5° as shown in Figure 16. The slightly greater deviation for the Boulder path as compared to the Pueblo path is attributed to weak two-mode propagation conditions encountered. The elevation angle data is also approximately 20° although also showing more dispersion than was found for the Pueblo path.

These results demonstrate the capability to perform direction finding measurements on a linear FM/CW signal. With two channel spectral analysis providing phase difference measurements between each spectral component (part of the cross spectrum function), it is possible to measure angle of arrival data on each of the modes present in the sounder return without wave interference.

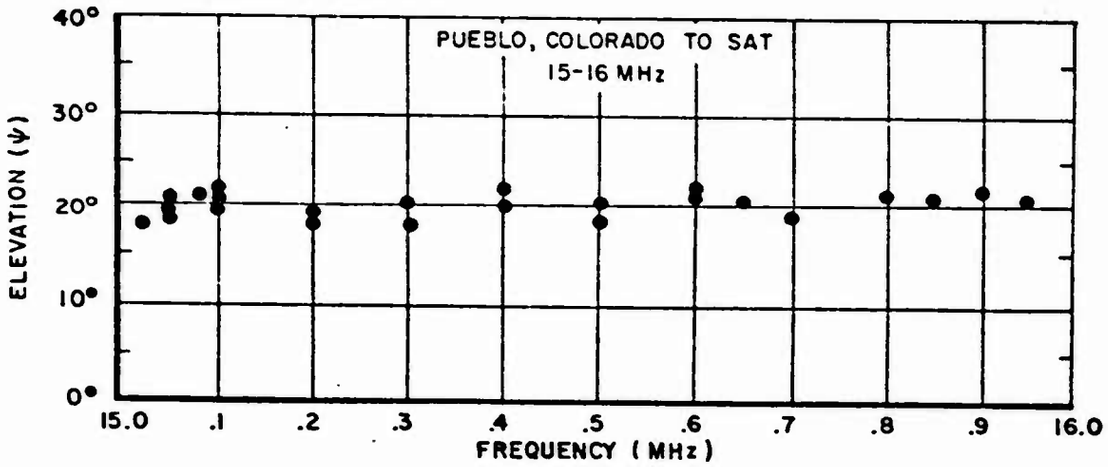

● – SUM AND DIFFERENCE

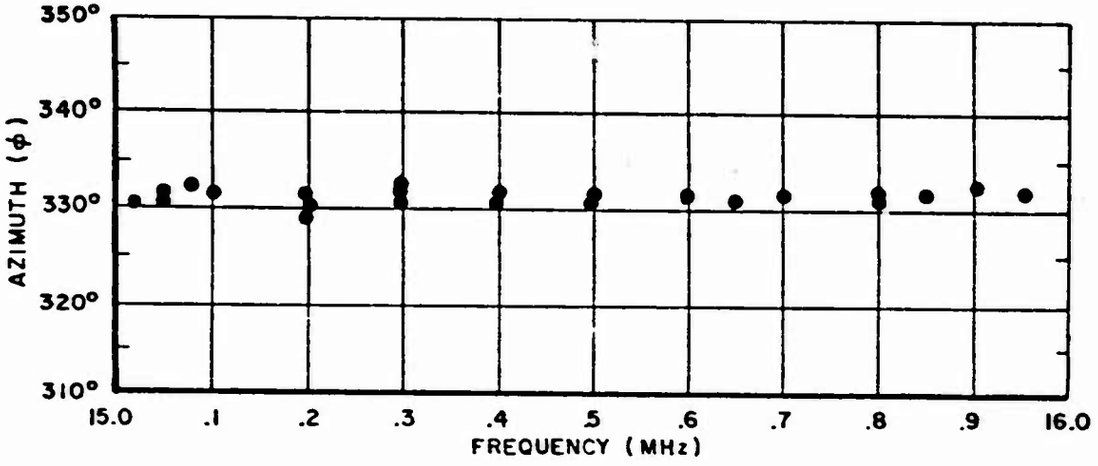

TRUE GCB: 332.7°

FIGURE 15

FM/DF RESULTS, 15-16 MHz, PUEBLO TARGET

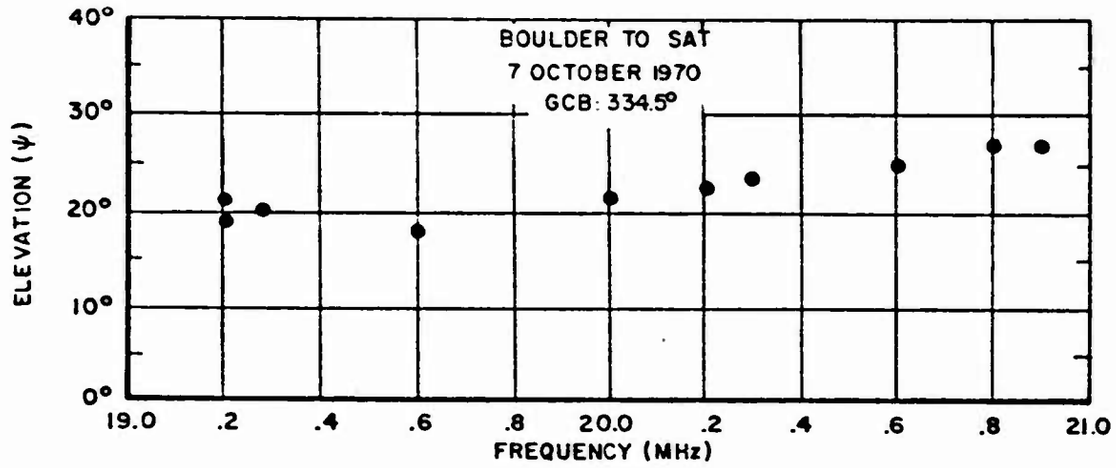

● – SUM AND DIFFERENCE
GCB – GREAT CIRCLE BEARING

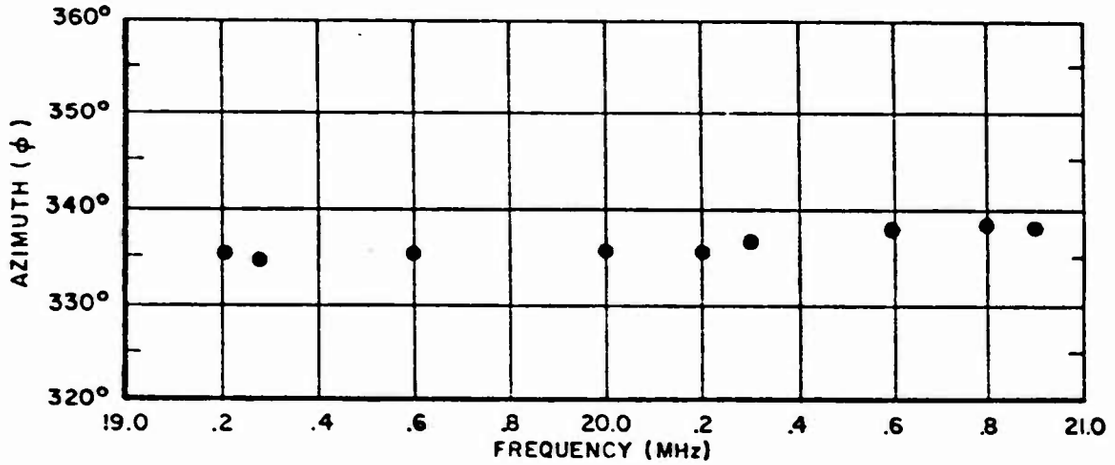

TRUE GCB: 334.5°

FIGURE 16

FM/DF RESULTS FROM BOULDER, COLORADO TARGET

THE PREDICTION OF DIURNAL DEVIATION EFFECTS

Roy I. Beckwith
Radiolocation Research Laboratory
University of Illinois
Urbana, Illinois 61801

1. Abstract

The problem of predicting expected mean angle-of-arrival deviations from a great circle path due to large scale diurnal ionospheric tilt effects is discussed. A technique for obtaining approximate values for these predicted deviations is presented. This technique involves the use of the ITS Ionospheric Predictions in conjunction with an approximate ray tracing procedure.

The main features and limitations of this prediction technique are illustrated, and preliminary results are presented and compared with experimental HF data collected during 1967 over a 1330 km path between Houston, Texas, and Urbana, Illinois.

2. Introduction

In recent attempts to predict the mean angle-of-arrival deviations from a great circle path due to large scale diurnal tilt effects in the quiet ionosphere, two somewhat different techniques have been devised and are presently under study.

One of these techniques is comparatively simple but has serious practical limitations. This technique involves the calculation of the effective ionospheric tilt using predictive information scaled from the ESSA/ITS ionospheric maps at the estimated midpoint of the path. The other technique, which will be discussed in more detail, is relatively complex, but is capable of more general application. Both techniques involve several realistic approximations and assumptions which have been made in the interest of speed and convenience in use.

3. Experimental Data

In order to test the success of the angle of arrival (AOA) prediction schema, the results obtained are being compared with experimental data collected during the "cooperative experiment."[1,2] During this experiment, which took place over the period March 1967 to March 1968, a large amount of AOA data was collected with the CDAA located near Bondville, Illinois, on a CW transmission originating near Houston, Texas (a 1330 km path). These data were collected continuously over a five-day period chosen to bracket the international geophysical days for each month. The frequency of the CW transmission was changed twice each day; 8.0 MHz being used during the local nighttime hours and 12.2235 MHz being used during the daytime hours.

In order to remove wave-interference and other short-duration effects, a two-hour "averaging window" was applied to the azimuthal AOA data collected. Since available predictive information describing the ionosphere is on a median basis, these running average data should provide an excellent basis for comparison.

An example of the resulting smoothed average data is shown in Figure 1. These data are for the month of March 1968. From these data, it is evident that although there is considerable day-to-day variation during the nighttime hours, there seems to be a very definite diurnal trend. During the daytime hours, for example, there is a fairly consistent positive error of between 0.5 and 1.0 degrees. Also, what has been identified as an MUF-related effect is noticeable during the early morning hours. Diurnal trends in angle of arrival have also been noted by other authors[3,4] and are also evident in data collected in this experiment during other months.

These diurnal effects, which are observed in the received AOA, have been attributed to deviations in the ray path (from great circle) due to large scale tilt effects in the quiet ionosphere.[3,5] These tilt effects, in turn, may be attributed to the regular height variation of electron density, the normal geographic variation of maximum electron density, and the effect of the Earth's steady magnetic field. Since the variation in height and maximum electron density of the quiet ionosphere may be predicted with considerable confidence, at least in a median sense, it is not unreasonable to expect that tilt effects, and consequently angle-of-arrival deviations, may similarly be predictable.

4. Preliminary Results

Figure 2 shows the results (for March 1968) of an early attempt made at the University of Illinois to predict the diurnal variation in AOA. This technique was based upon predictive information obtained graphically from ionospheric contour maps at the approximate midpoint of the Houston-Bondville path. Although this attempt was concerned only with the one-hop-F mode, the results show considerable promise. In agreement with the experimental data, a positive deviation in AOA was obtained after 1330 hours UT (7:30 CST) and large deviation effects near local sunrise were also found. A correction obtained on this basis and applied to the received angle of arrival could be expected to reduce the tilt-induced error for at least 14 hours of the 24.

The MUF and sunrise effects noticeable in Figure 2 are of considerable interest. The standard MUF for this path evidently dipped slightly below 8 MHz at some time prior to 2:00 A.M. CST and returned above 8 MHz (to permit propagation) at some time after 6:00 A.M. CST. However, the only time interval in which propagation did not occur was between 3:15 CST and 4:30 CST. During the intervals 2:00-3:15 A.M. and 4:30-6:00 A.M., propagation is possible only in conjunction with large path deviations (from great circle) and with consequent large AOA deviations.

While these early efforts indicated that it is possible to use ionospheric predictive information to predict AOA deviations with some degree

of success, they also indicated that more comprehensive techniques are necessary, especially during the nighttime hours. It was felt that the main limitations inherent in this initial prediction method were:

a) lack of consideration of the ionospheric E and/or Es layers,
b) lack of consideration of possible mixed-mode (EF, FE, etc.) and multihop propagation, and
c) limitation to one geographic location at which the tilt could be calculated.

5. A More Comprehensive Method

Recently, a more comprehensive method (a better mousetrap) has been devised for predicting AOA deviations--one which incorporates optional consideration of the abovementioned factors. In this method the major ionospheric parameters (i.e., peak height, maximum electron density, and semithickness of E and F2 layers) are predicted through direct use of sets of coefficients available from ESSA/ITS.[6] A modified "control point" procedure is utilized and an analytical approximation describing the orientation of the equivalent virtual reflection surface is obtained for each hop of each chosen path structure. A simple three-dimensional ray tracing procedure is then used in an iteration loop to obtain the geometrical properties of the equivalent path between the transmitter and the receiver.

This technique will, in theory, allow the calculation of approximate deviations in angles of arrival for any given time, month/year, frequency, geographical path location and common path geometry. The technique has been programmed on the University of Illinois IBM 360/75 and initial indications are that the necessary computations are performed very rapidly.

In order to provide a better understanding of the use of this technique, and to illustrate some of the more complex problems encountered, a step-by-step outline of the program operation may be useful. The order of the calculations performed is as follows:

1) Path data input (cards)--frequency, time (U.T.), month, year, receiver location, path geometry type or types, and an estimate of the source location.

2) Prediction data input (mag. tape)--predictions coefficients describing the regular variations in foF2, $M_{3000}F2$, foE, and foEs (optional). Coefficients describing foF2 and $M_{3000}F2$ may be either short-term (three months in advance) or long-term (over entire sunspot cycle). Coefficients describing the other parameters are available on a long-term basis only.

3) Estimate control point locations. As illustrated in Figure 3, the choice of control points is somewhat arbitrary. Some effort has been made, however, to choose these control points so that they are coincident with the probable reflection areas of the most common path types. In order that tilt effects may be described, each control point shown actually consists of a group of four points spaced quite closely together.

4) Calculate time-dependent polynomial coefficients for the ionospheric parameters at the chosen control points (i.e., remove the geographical variation).

5) Calculate foF2, hpF2, y_mF2, f_cE at control points for time specified.

6) Choose path type (i.e., E, F, EE, FF, FFF, etc.). Two-hop and three-hop mixed modes may be considered, but these modes rarely propagate.

7) Estimate hop reflection point locations, ionospheric parameters at hop reflection points (by linear interpolation between control points), and hop ranges for chosen path type.

8) Calculate equivalent vertical incidence frequency and the virtual height at each of four locations near the estimated reflection point on each hop. This involves an iterative technique which is in common usage.[7] Note that this virtual height is strongly dependent on both hop range and frequency. Tests for cutoff or penetration of the ray on each hop are also made at this time.

9) Find the best fit spherical approximation to the reflection surface for each hop. The radius of curvature R_c and the eccentricity vector D are found for a sphere which contains in its surface the four previously calculated oblique incidence virtual heights. This method has been used previously to describe the ionospheric tilt on the basis of the height of the bottom of a model layer.[8]

10) Trace a ray in three dimensions to the end of the path (all hops) using a simple Snell's Law ray tracing method. Calculate a new value of ground range for each hop and determine the location of the touchdown point at the end of the path. The geometry for one hop is shown in Figure 4.

11) Compare the location of the touchdown point with the estimated source location. If the comparison is unsatisfactory, return to step 8) and iterate. For a multiple hop path, adjust the location of the estimated reflection point on the first hop.

12) If the ray has reached the estimated source location, calculate the path loss (approximate) and elevation and azimuth angles of arrival at the receiver. Print results (two lines per hop).

13) If another path type is specified, return to step 7) and repeat.

14) If the calculation is to be made for another time, return to step 5) and repeat.

While the above outline of the steps involved in this latter technique can in no sense be considered a complete description, it will hopefully provide some insight into the problems involved.

6. Discussion

There are almost certainly other methods by which AOA deviations may be predicted. In fact, if one is willing to sacrifice calculation speed, the above described method could be modified to reduce the number of approximations made (for example, it would be nice to eliminate the control-point concept). The approximations and assumptions inherent in this technique were made with the goal of rapid, easy utilization without a serious sacrifice of reliability or accuracy. Early results obtained indicate that this goal has been attained. Studies are continuing with regard to the reliability of using the predicted AOA deviation results as corrections to be applied to received angles of arrival. Multimode propagation considerations are also being investigated.

References

1. Bailey, A. D., E. W. Ernst, L. J. Miller, and W. W. Wood, "An atlas of reduced data obtained in a co-operative HF directional propagation experiment over a 1330 km. path (March 1967-March 1968)," RRL Publication No. 344; September 1968.

2. Bailey, A. D., "Direction of arrival studies on a long path (summary)," Proceedings of a Conference on HF Radio Propagation, June 1969, ed. by E. W. Ernst, RRL Publication No. 375; August 1970.

3. Whale, H. A., Effects of Ionospheric Scattering on Very-Long-Distance Radio Communication, Plenum Press, New York; 1969.

4. Titheridge, J. E., "Variations in the direction of arrival of high-frequency radio waves, JATP, 13, 1968, pp. 17-25.

5. Hayden, E. C., "Correlation of DF errors with ionospheric radio propagation phenomena," University of Illinois, Urbana, Illinois, Report RADC-TDR-62-236, Contract AF30(602)-2413; March 1962.

6. Jones, William B., Ronald P. Graham, and Margo Leftin, "Advances in ionospheric mapping by numerical methods," NBS Technical Note No. 337; May 1966.

7. Barghausen, Alfred F., James W. Finney, L. Lee Proctor, and Larry D. Schultz, "Predicting long-term operational parameters of high-frequency sky-wave telecommunication systems," ESSA Technical Report ERL 110-ITS 78; May 1969.

8. Rao, N. N. "Bearing deviation in HF transionospheric propagation," Radio Science (New Series), Vol. 3, No. 12, pp. 1113-1123; December 1968.

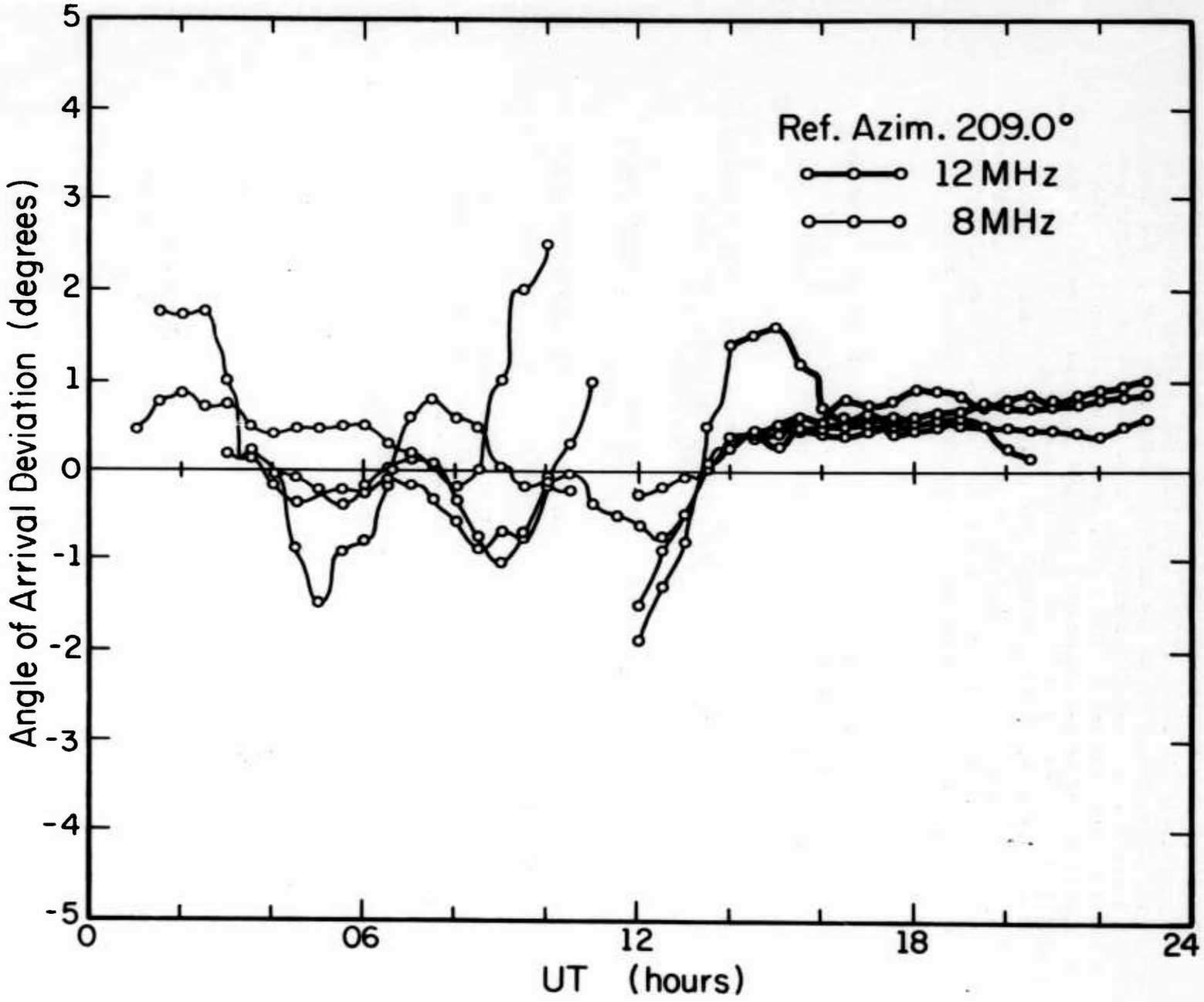

Figure 1. Average AOA data for March 1968.

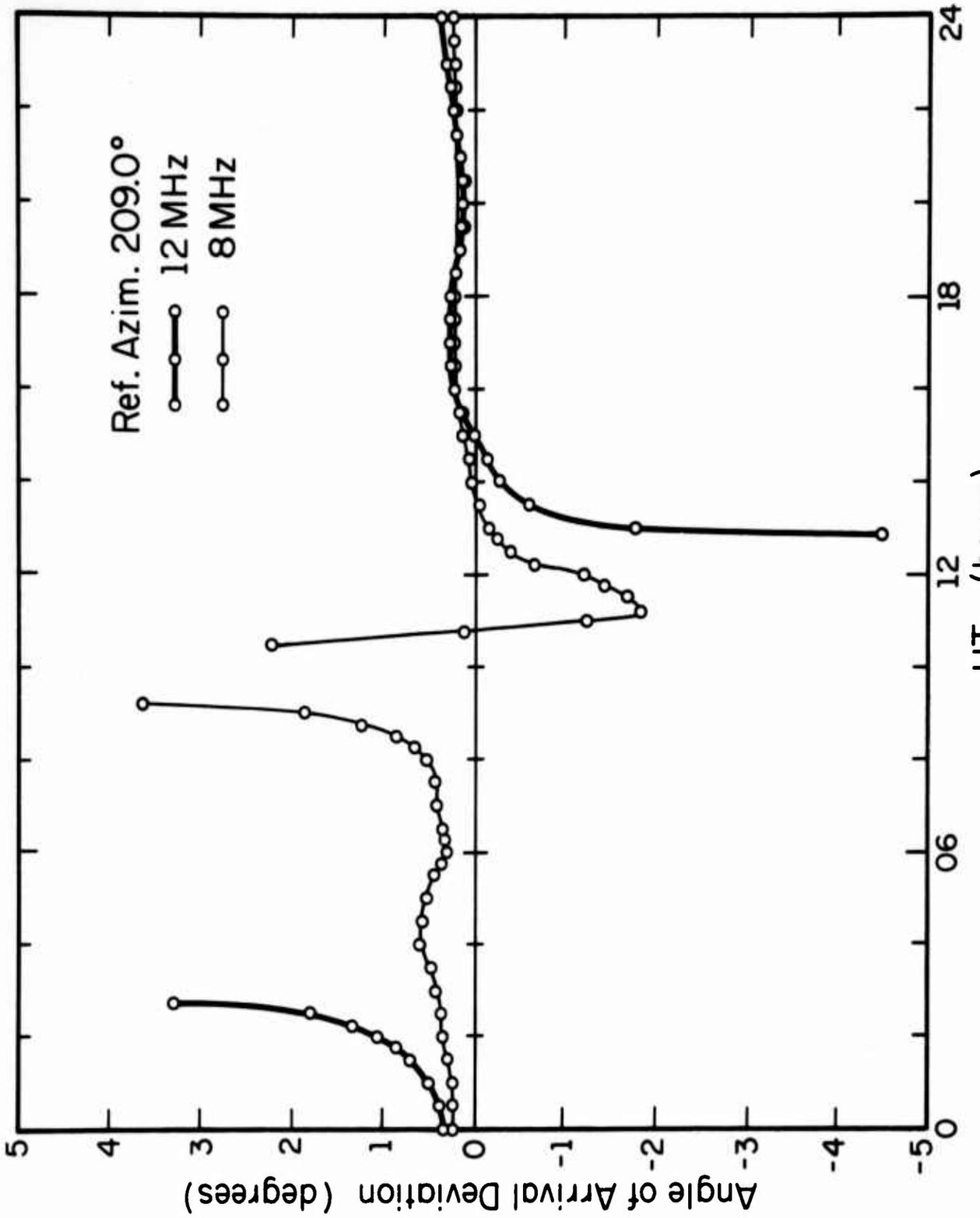

Figure 2. Predicted AOA for one-hop-F path for March 1968.

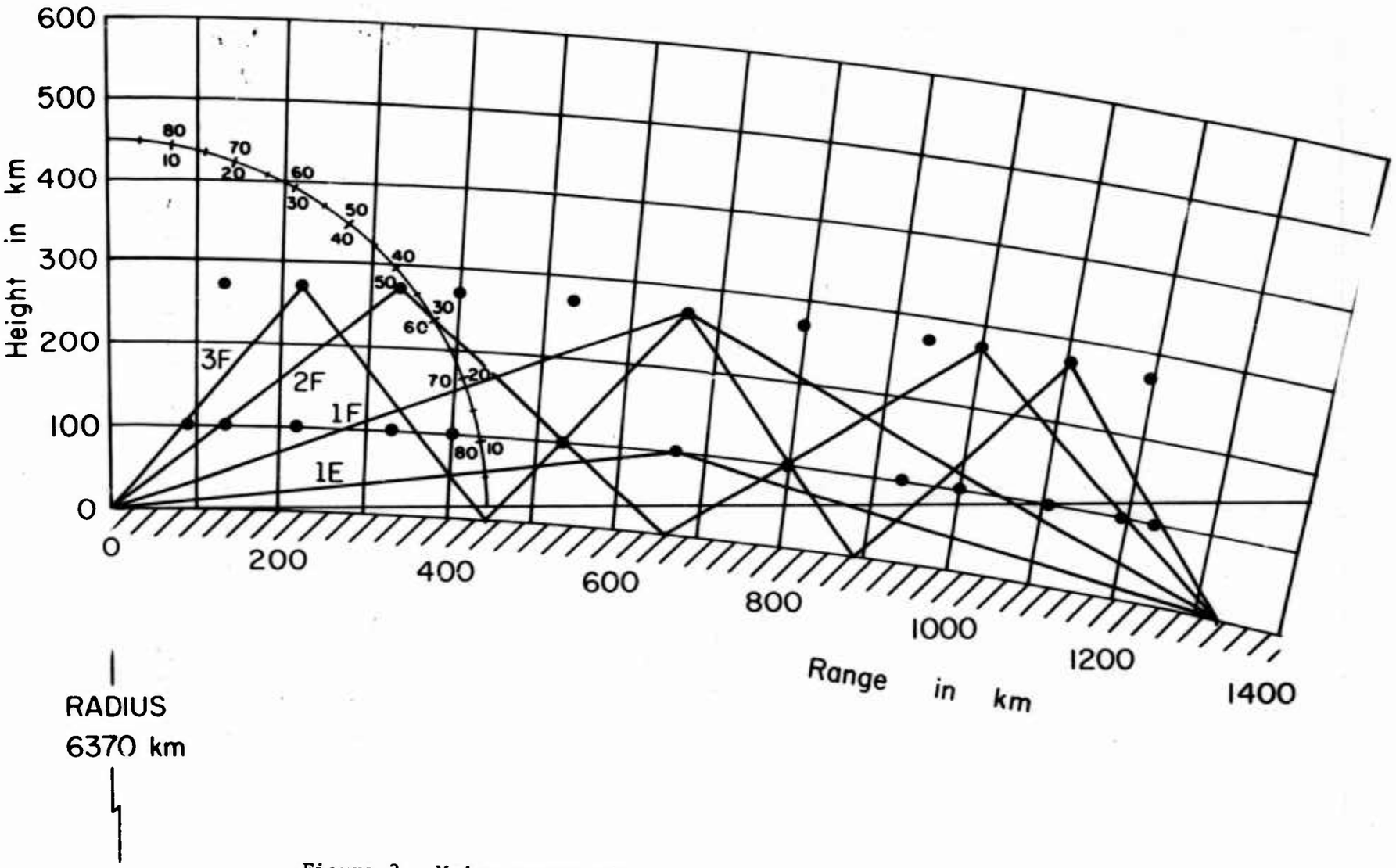

Figure 3. Major propagating path types and necessary control points.

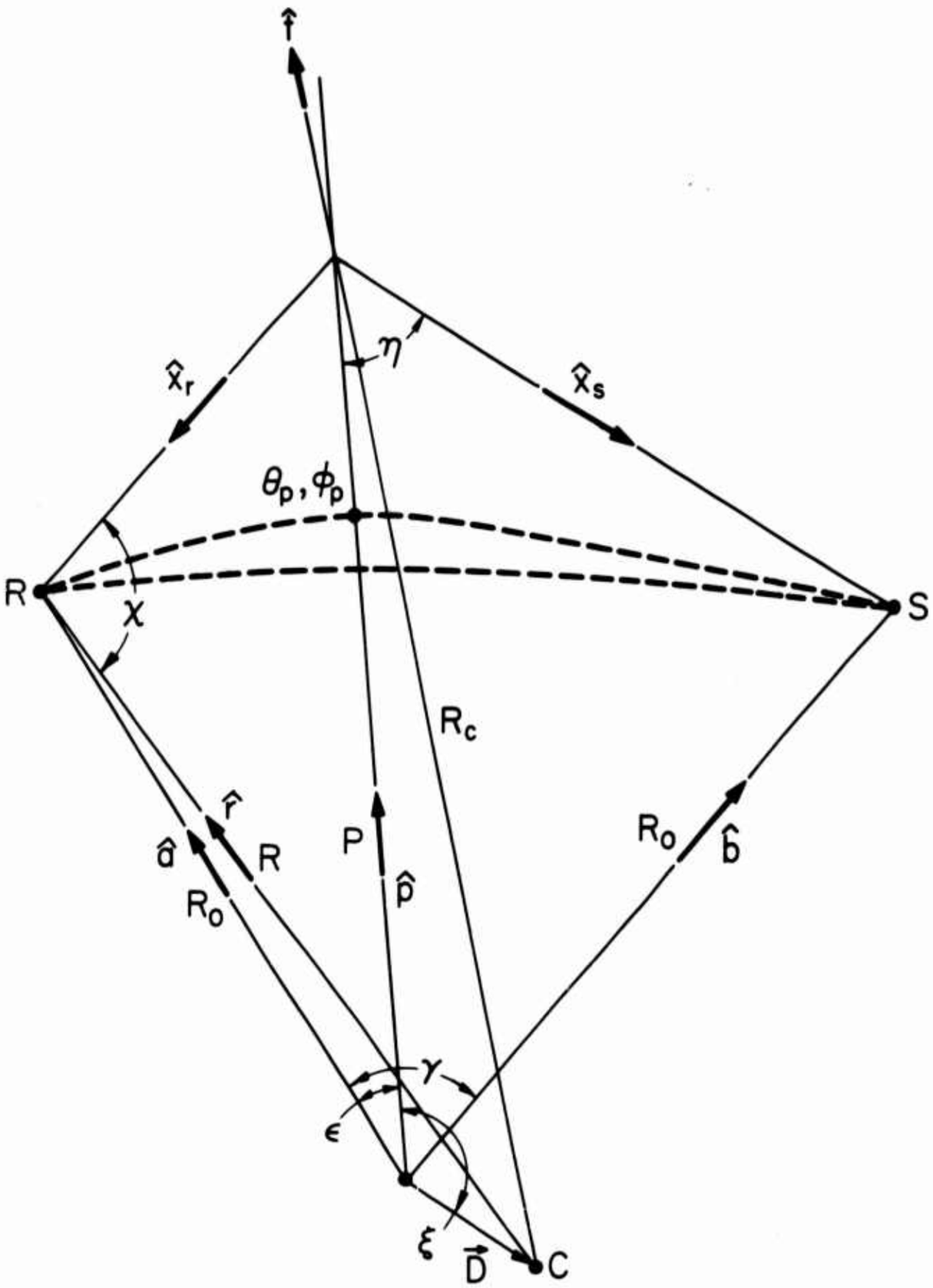

Figure 4. Geometry of the N^{th} hop.

SINGLE-ANTENNA, FM/CW VERTICAL INCIDENCE SOUNDING

S. M. Bennett
W. E. Woolhiser

AVCO CORPORATION
Lowell, Massachusetts

ABSTRACT

The low peak transmitted power and substantial immunity to interference inherent in the linear FM/CW waveform have suggested the design of a vertical incidence ionosonde. Due to the siting constraints, isolation between the transmitted and received signals cannot be conveniently accomplished, in many instances, by the use of separate antennas for transmission and reception. When a single antenna is employed, the transmitted signal must be commutated to permit reception. The implications of commutation with respect to the range visibility function are discussed. It is anticipated that a demonstration of a prototype sounder will be presented.

Presented at the Fourth Allerton House Conference on Radiolocation Research, Monticello, Illinois, June 1-4 1971

INTRODUCTION

Ionospheric sounding technology has traditionally (with the exception of Appleton) utilized swept or fixed frequency pulse transmissions to measure the group delay of HF returns. About six years ago, the linear FM/CW waveform was applied to ionospheric measurements by Prof. O. G. Villard, Jr. and his students at Stanford University; shortly thereafter, our laboratory also began investigation of the technique. The linear FM/CW waveform has proved successful in all types of HF sounding, viz. oblique incidence, backscatter, RTW, and most recently, vertical incidence sounding. In all but the latter application, the linear FM/CW waveform has the desirable property of unity duty factor coupled with an achievable range resolution limited only by the ionospheric dispersion; experimental evidence suggests that this may be considerably less than 1 μsec under ideal conditions. A corresponding disadvantage is the necessity for isolating the receiver from the transmitter to eliminate a substantial fraction of the direct (ground wave) coupled transmitter energy. The separation required depends on the transmitted power level and the relative amplitude between the ground wave (and associated phase noise spectrum) and the anticipated level of the desired return. In the case of low-power vertical-incidence sounding, antennas oriented orthogonally and spaced by 1000 feet are adequate, while in higher power backscatter systems, the separation must be tens of miles.

Most applications for vertical incidence sounding systems mitigate against the use of two antennas separated even by 1000 feet. The desire for portability, use of existing antennas, or airborne use precludes the implementation of a practical system if it utilizes two antennas. Consequently, another method of isolating the transmitter and receiver must be sought. The most obvious, and the one, in fact, selected is to pulse the linear FM/CW waveform in a manner which might, at first, appear similar to a conventional sounder, but is, in reality, quite a departure from a pulsed-cw system. The advantage gained is that the typical duty factor is approximately 0.7 and that the signal processing is similar to unity duty FM/CW.

CONCEPTUAL APPROACH

Figure 1a is the basis for understanding single antenna sounding. The discussion is given as if the transmitter output frequency and receiver l.o. were the same, resulting in homodyne detection, whereas the actual system offsets the receiver l.o. by the nominal first IF frequency. For illustrative purposes, we have assumed that the FM/CW generator is sweeping in the positive sense at a sweep rate df/dt and the transmitter and receiver are gated on alternately every 2 msec. During the entire

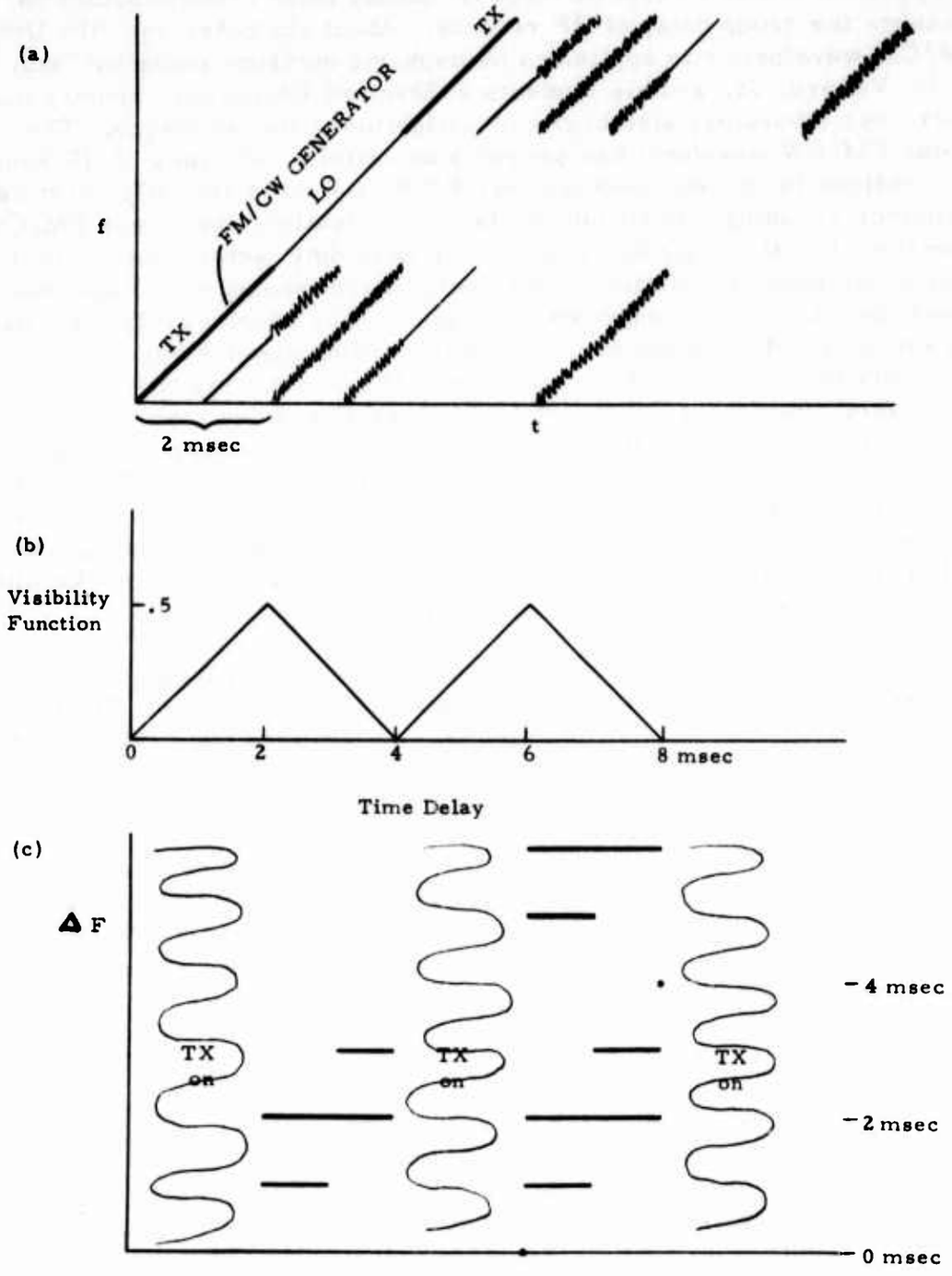
(a)
f
TX
FM/CW GENERATOR
LO
TX
2 msec
t
(b)
Visibility
Function
.5
0
2
4
6
8 msec
Time Delay
(c)
Δ F
TX
on
TX
on
TX
on
4 msec
2 msec
0 msec

FIGURE 1.

sequence, the FM/CW generator continues to sweep, with the generator output utilized alternately as the transmitted signal and receiver l. o. during the transmit and receive periods respectively; the antenna is transferred between the transmitter output and the receiver input in accordance with the mode.

Shown also are returns from reflections at 1, 2, and 3 msec range, which are delayed replicas of the transmitted pulse. Note that the return at the closer range begins to arrive prior to the commencement of the receive interval and a portion of the return is lost, while a return from 2 msec entirely fills the receiver on gate; at greater ranges, the trailing portion of the return is lost, until finally for a delay of 4 msec the return is contained entirely within the subsequent transmit interval and cannot be received. The portion of each return which can be observed by the receiver is indicated by the wavy line. The effect of commutating the FM/CW waveform is, therefore, to impose a range visibility function on the data, which is sketched in Figure 1b, revealing the presence of a zero response at 0, 4, 8... msec, which is obviously undesirable since desired data may lie in the vicinity of 4 msec. We shall discuss, in a moment, how this problem can be overcome. Before treating that topic, consider the effect of homodyne detecting the received signal by mixing it with the FM/CW generator. In the case of a unity duty factor waveform, the difference frequency would be given by

$$\Delta F = \frac{df}{dt}\tau \qquad (1)$$

where ΔF = difference frequency in Hz

$\frac{df}{dt}$ = sweep rate in kHz/sec

τ = time delay in msec

When the waveform is commutated as described above, the same difference frequency relation obtains, but the energy at each frequency occurs in bursts, related to the visibility function. This effect is shown schematically in Figure 1c, where the magnitude of the difference frequency is plotted as a function of time for several pulses. Since the spectrum analyzer employed to process the data has a typical frequency resolution of 0.5 Hz, 2 seconds of data is accumulated for analysis purposes, representing 500 pulses of the type shown. This results in recovery of the nominal frequency of each component plus the addition of sidebands related to the chopping rate. Provided that the chopping rate and sweep rate are suitably scaled, the sidebands will fall outside the data analysis bandwidth.

In order to proceed further, with the analysis of the system, some of the parameters of the real-time spectrum analyzer need to be specified. A typical analysis bandwidth would be 200 Hz with 400 frequency resolution cells (0.5 Hz bandwidth). Since the readout rate of the analyzer is of the order of 200 msec, the spectrum analysis is redundant by a factor of 10, and is utilized primarily to achieve a suitable display. Table 1 summarizes the range gate, τ_{max}, 3 db range resolution, τ_{3db}, and the time to sweep a 1 MHz frequency band. From this set of parameters one must optimize performance based on some set of criteria. For purposes of establishing such criteria, we chose to specify that the system should have a range resolution of 10 μsec since it is normally desired to scale critical frequencies to 100 kHz accuracy; this results in selecting 50 kHz/sec as the optimum sweep rate (N. B. if other than flat weighting is desired in the spectrum analysis process, a slightly higher sweep rate will be more effective). Faster sweep rates may be utilized if the spectrum analyzer bandwidth is set at 500 Hz and a higher chopping frequency selected.

TABLE 1

df/dt (kHz/sec)	τ_{max} (msec)*	τ_{3db} (μsec)**	T/MHz(sec)
20	10.0	25	50
30	6.66	16.66	33.3
40	5.0	12.5	25
50	4.0	10.0	20
60	3.33	8.3	16.6
70	2.85	7.1	14.3
80	2.5	6.25	12.5
90	2.22	5.5	11.1
100	2.0	5.0	10

Returning to the question of the visibility function again, we note that the zero visibility points are related to the sum of the duration of the transmit and receive periods; i.e., to the pulse repetition frequency. Consequently, the position of the zero may be adjusted by varying the prf. This is in fact what is done, and in a manner such that the visibility function is optimized over the range gate of interest. Let us look at a practical example shown in Figure 2. Traces 1 and 2 are the transmitter and receiver states for the high prf and traces 3 and 4 for the low prf, respectively. A guard band is provided between transmitter turn off and receiver on to permit the decay of any circulating pulses in the antenna

*200 Hz spectrum analysis bandwidth

**400 spectral resolution cells

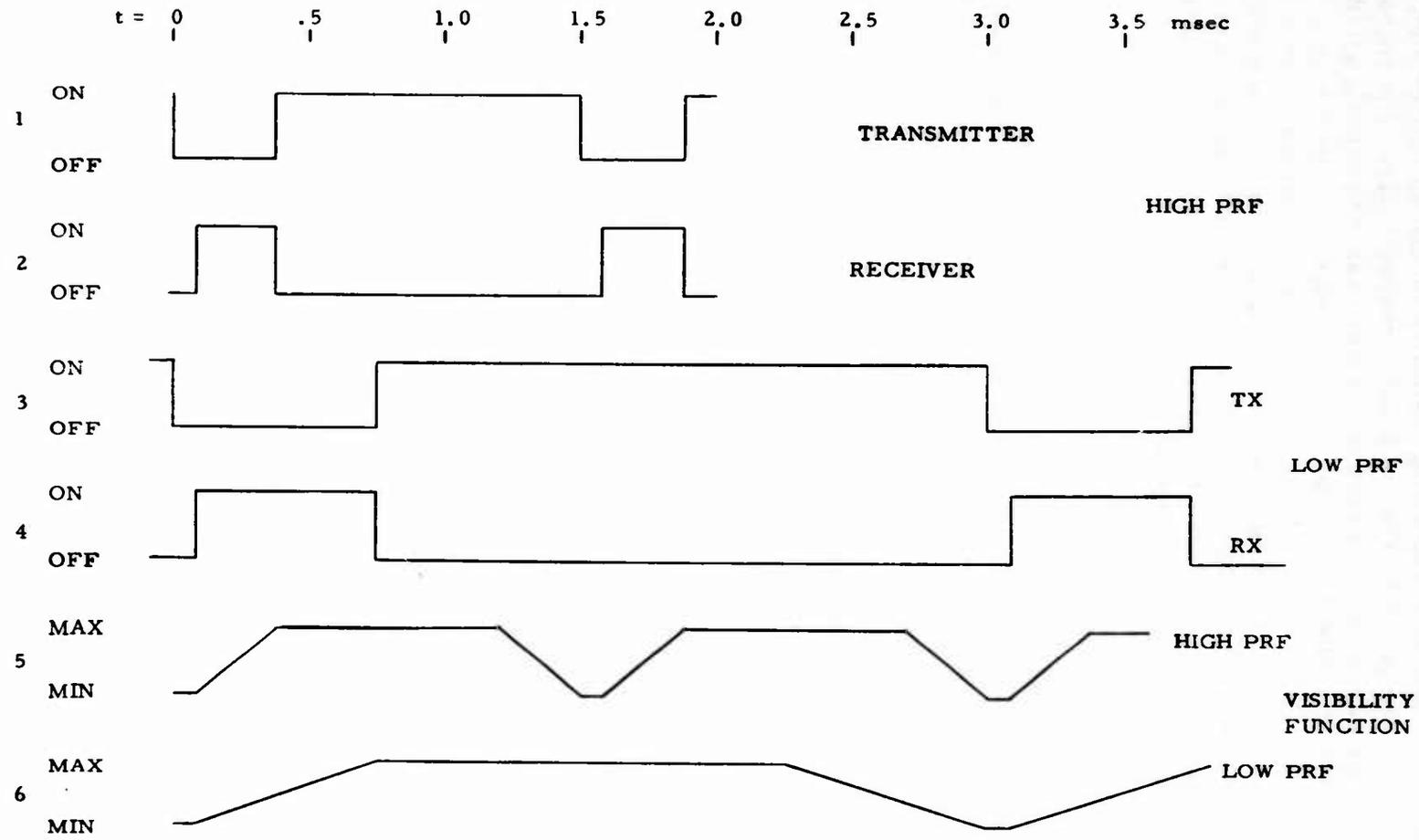

FIGURE 2.
RELATION BETWEEN PRF AND RANGE VISIBILITY FUNCTION

transmission line. The corresponding visibility functions for the high and low prf states are given by traces 5 and 6 respectively. The transmitter duty factor has been increased to greater than 50 percent, yielding a flat-top function at a slight increase in the effective receiver noise figure. In practice, there are a total of 10 distinct prf states, only the maximum and minimum prf being shown here. Once complete sequence of prf states is accomplished during the time necessary to sweep over a 100 kHz band resulting in a relatively uniform visibility function consistent with obtaining a range resolution of 10μ sec.

HARDWARE REALIZATION

The implementation of the concept is outlined in Figure 3. In practice, the receiver has a first IF which is substantially offset from zero (viz. 40 MHz). A FM/CW generator based on remote control of a DANA Laboratories 7010 Digiphase frequency synthesizer by an AVCO LFM-2 sweep control provides simultaneous outputs of 1-30 MHz and 41-70 MHz which are utilized as the transmitted signal source and receiver local oscillator respectively. They are alternately supplied to the transmitter, which is a ten watt broadband transistor amplifier and to the receiver first mixer. The prf control is synchronized with the sweep rate and sequences the low level rf switches and high power T/R switch to achieve a timing plan similar to that shown in Figure 2.

The receiver is a double conversion superheterodyne output translated to baseband in a coherent (undetected) manner, and with all conversion frequencies phase locked to the synthesizer frequency standard. Manual or AGC modes are provided. The last IF bandwidth is limited to 200 Hz by a crystal filter to permit the AGC to operate and to reduce fold over of interfering signals. Spectrum analysis is performed by a real-time audio spectrum analyzer and the resultant signal displayed as z-axis modulation on a facsimile recorder.

Typical equipment specifications are shown in Table 2.

TABLE 2

TYPICAL FM/CW OPERATING PARAMETERS
(Vertical Incidence)

Frequency Range:	1-30 MHz (100 kHz minimum bandwidth)
Power Output:	8 watts peak, 6 watts average
Sweep Rate:	50 kHz/sec
Range Gate:	0-4 msec (0-600 km)
Range Resolution:	10 sec
Sweep Time:	20 sec/MHz

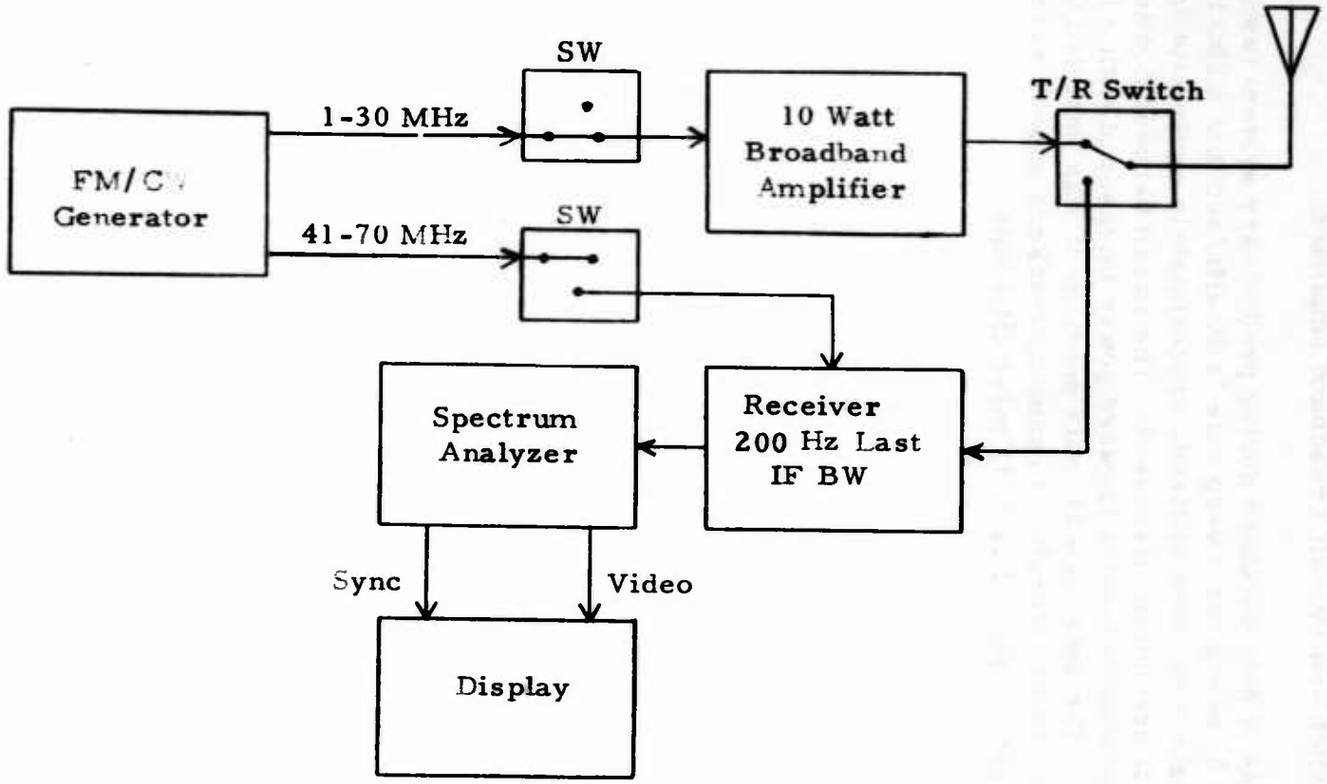

FIGURE 3.
FUNCTIONAL BLOCK DIAGRAM OF SINGLE-ANTENNA
VERTICAL-INCIDENCE FM/CW IONOSONDE

Figure 4 is a photograph, sans spectrum analyzer and display of a system similar to that described in the text. From top to bottom are the LFM-2 Sweep Control, DANA 7010 Synthesizer, receiver and prf control, T/R Switch and 10 watt broadband amplifier.

An example of data obtained during preliminary system testing is given in Figure 5, where the sweep rate is 30 kHz/sec and a 100 Hz bandwidth analysis range was utilized, approximately equivalent in range resolution to that previously discussed. The sweep bandwidth was 2-10 MHz with approximately 3 watts forward power (measured with a thruline wattmeter). The antenna was quite poor, as it was intended to simulate one aboard an aircraft. Frequency markers appear every MHz; the total range gate displayed is 3.33 msec (500 km).

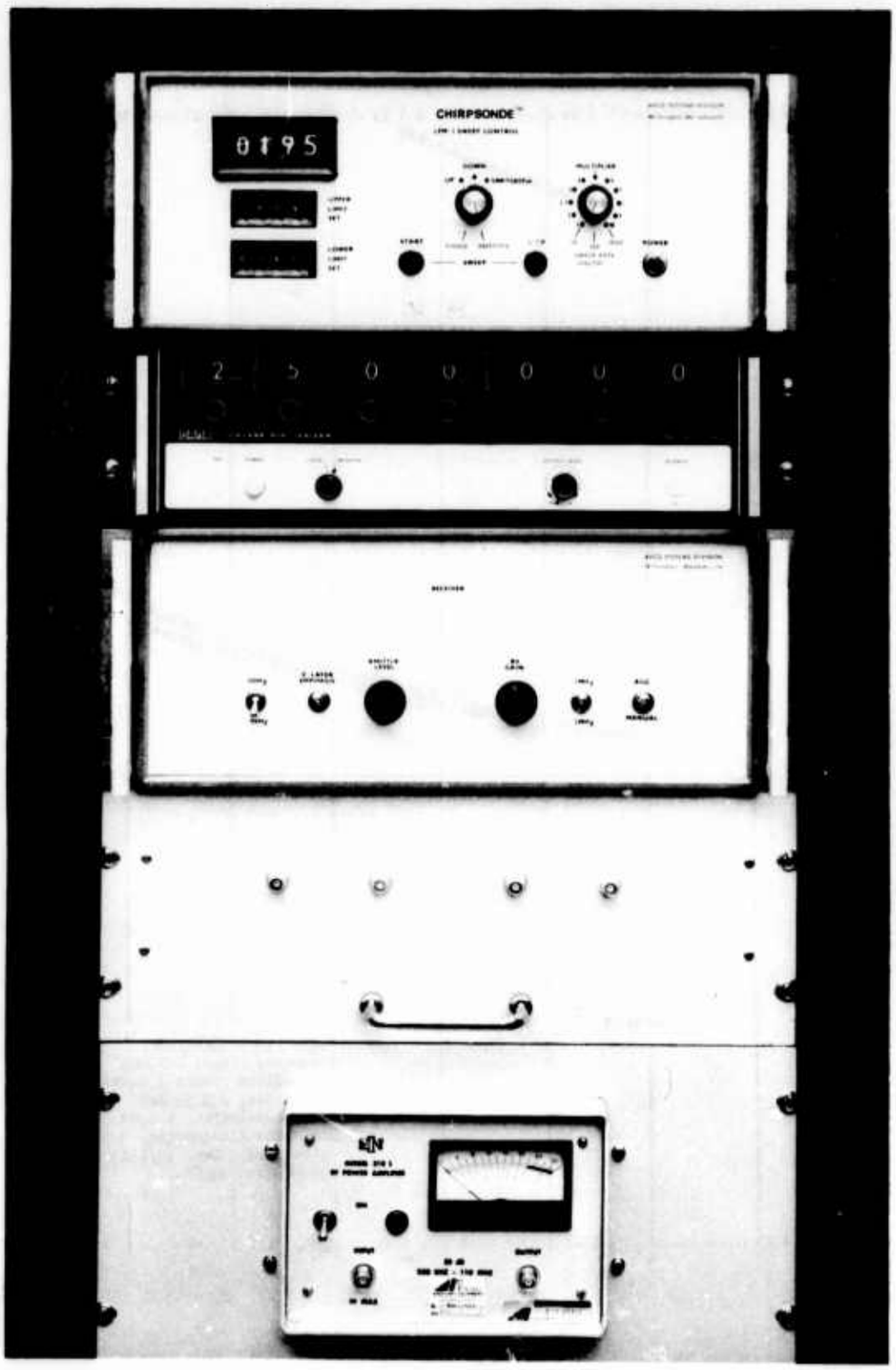

FIGURE 4.

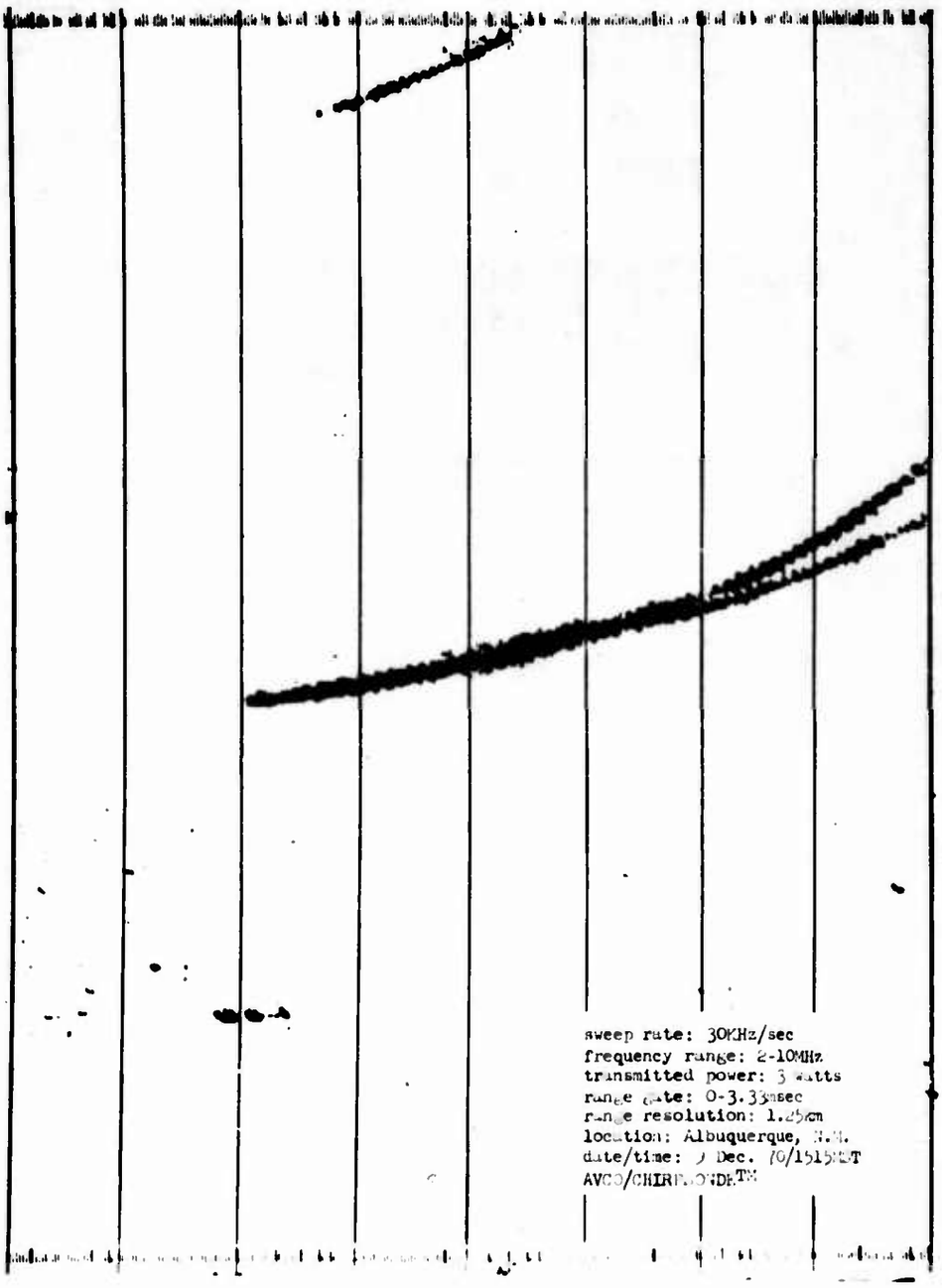
sweep rate: 30KHz/sec
frequency range: 2-10MHz
transmitted power: 3 watts
range gate: 0-3.33msec
range resolution: 1.25km
location: Albuquerque, N.M.
date/time: 7 Dec. 70/1515GMT
AVCO/CHIRP SONDE™

FIGURE 5.

AMPLITUDE STUDIES OF HF AURORAL BACKSCATTER

F. O. Fahlsing and N. Narayana Rao
Radiolocation Research Laboratory
University of Illinois
Urbana, Illinois 61801

This report describes the measurement of the amplitudes of short pulses propagated over a bistatic path involving auroral reflection. The geometry of the experiment is shown in Figure 1. The transmitter is a Granger stepped-frequency pulse sounder with 20 kW peak power located near Rome, New York. The transmitter drives a 6-60 MHz log-periodic antenna directed at an azimuth of 330°. The receiving antenna is the University of Illinois Wullenweber array located near Bondville, Illinois. The ionosonde receiver and a separate amplitude receiver were connected to the array through multicouplers. The amplitude receiver was tuned to 6.75 MHz (one of the Granger frequencies) and a gain curve was obtained for signal strengths from 10-1000 μV. The detected output of the amplitude receiver was displayed on a cathode ray oscilloscope (standard "A-scope" display) and photographed. The boresight of the receiving antenna was stepped from 345°-45° azimuth in 15° steps at the rate of 1 step/min. Oblique-incidence ionograms and signal amplitude photographs were recorded each minute between 2200 UT on March 10, 1971 and 1400 UT on March 11, 1971. The sounder was programmed as follows:

Pulse width = 200 microseconds
Pulse repetition rate = 50 pulses per second
Pulses/channel = 8
Frequency Range = 4-16 MHz

Auroral backscatter signatures were observed in the data between 0200 and 0345 UT on March 11, 1971. The greatest frequency of occurrence and the largest pulse amplitudes appeared at an azimuth of 15°. Therefore, it is assumed that the direction of arrival of the backscattered pulses is very near to 15° and only those data observed at this azimuth will be considered. The time delays and amplitudes of the observed pulses are shown in Figure 2. Symbols on the amplitude graph correspond with those symbols on the time delay graph. A reproduction of an experimental ionogram is shown in Figure 3. The direct 1F and 2F modes are clearly seen as well as 3 auroral backscatter modes.

A simplified model is used to synthesize auroral backscatter ionograms and to calculate theoretical values of received signal amplitude which are compared with the experimental data. This model consists of a quasi-parabolic F layer with a perfectly reflecting mirror aligned along the dipole field lines at a fixed geomagnetic latitude. The propagation modes simulated in this study are defined in Figure 4. The reflection at the mirror follows Snell's law. First, a ray that arrives at the receiver after satisfying all the requirements of the model is traced. This ray is defined as the "solution-ray." For each such "solution-ray," the group delay, received azimuth and received elevation angle are calculated. The amplitude is calculated by tracing 2 rays in addition to

the "solution-ray" as shown in Figure 5. The power transmitted into the triangular cone is

$$\Delta P = \Phi \Delta \Omega$$

where Φ is the power/unit solid angle transmitted in the ray direction and $\Delta\Omega$ is the solid angle of the cone. It should be pointed out that $\Delta\Omega$ is very small, e.g., of the order of 10^{-6} steradians. The received power density is

$$P_r = \frac{\Delta P}{A}$$

where A is the cross-sectional area of the triangular cone at the receiver. Figure 6 shows calculated time delay vs. frequency for several values of mirror latitude. Figure 7 shows calculated received amplitude at 6.75 MHz as a function of time delay before and after the receiving antenna gain is introduced.

It was expected that the propagating modes could be identified by comparing the experimental ionograms to the synthetic one. However, the results of this comparison are inconclusive. It can be stated that many of the observed modes are beyond the maximum range of a DF-DF mode and therefore must be more complex. The 1FDF-1FDF mode is one possibility. The range of observed amplitudes is nearly 16 times smaller than the range of calculated amplitudes. Although several effects were ignored in the simple model (e.g., pulse spreading and polarization) the most likely source of the large error is the assumption of unity reflection coefficient at the mirror.

In future studies of this type, the following improvements should be made:

1. Use a wide-beam antenna such as a log-periodic for amplitude measurement.

2. Improve model to include pulse spreading and polarization.

3. Use theoretical and experimental results to calculate an "effective reflection coefficient."

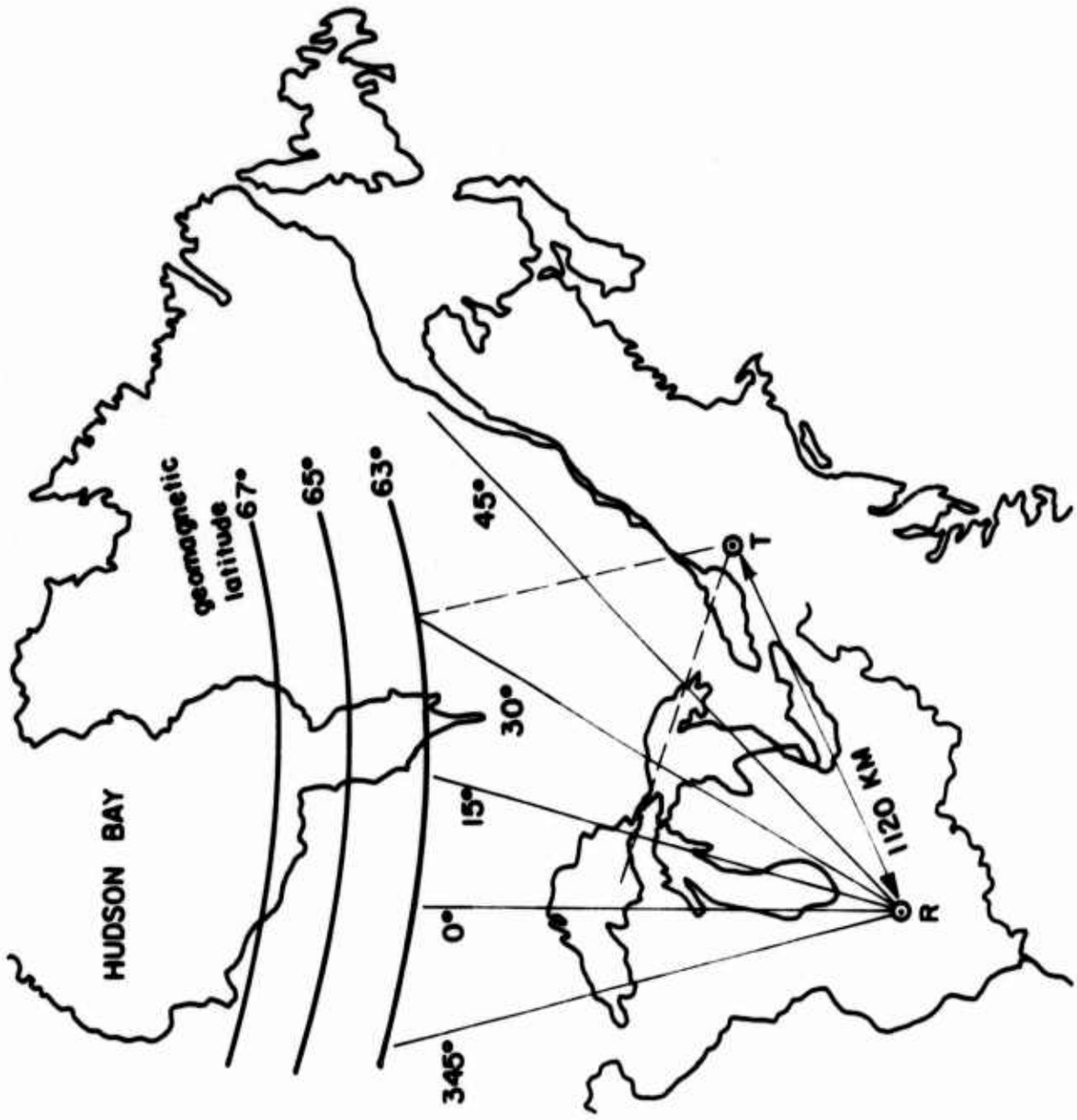

Figure 1. Geometry for the bistatic auroral backscatter experiment.

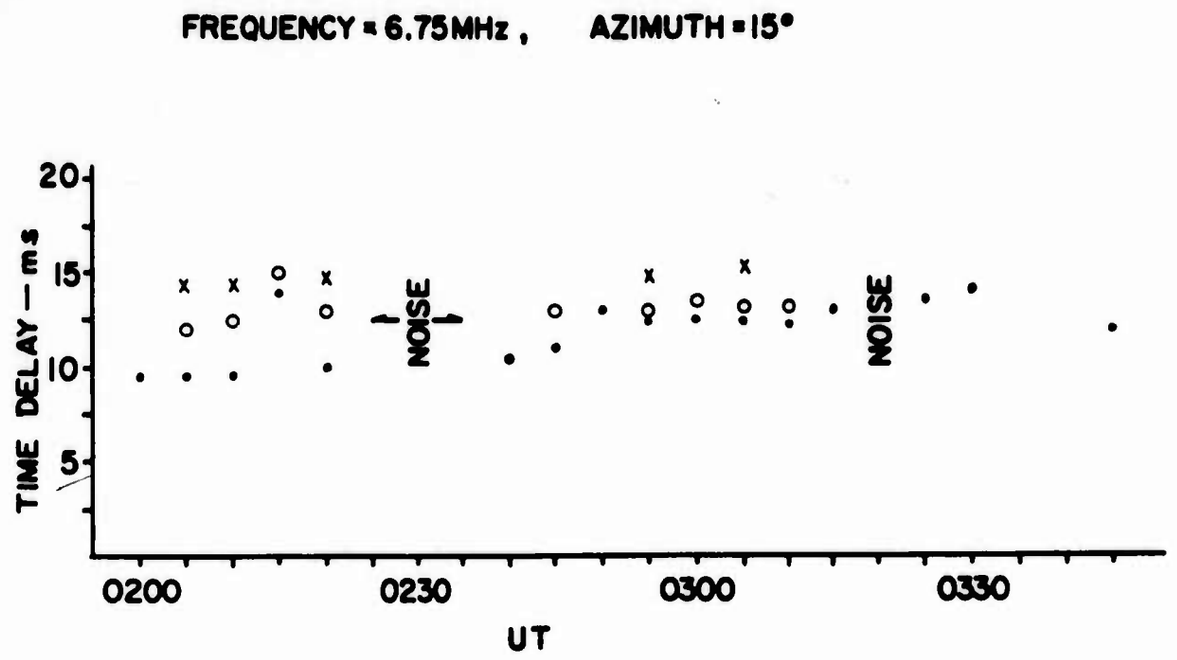

a) amplitude of voltage at the output of the antenna scanner vs. time

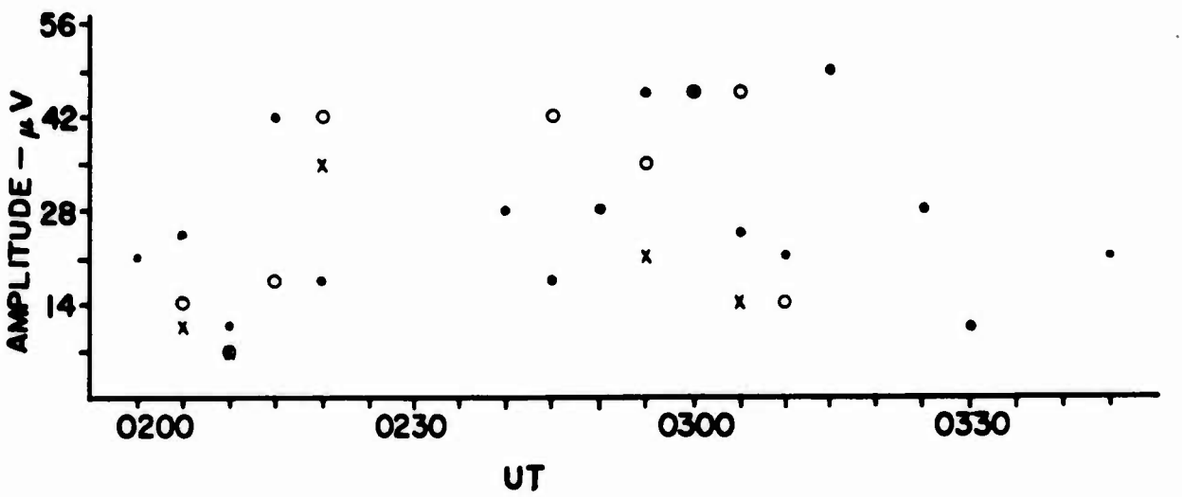

b) time delay in milliseconds vs. time

Figure 2. Summary of auroral backscatter data obtained on 6.75 MHz at 15° azimuth on 11 March 1971.

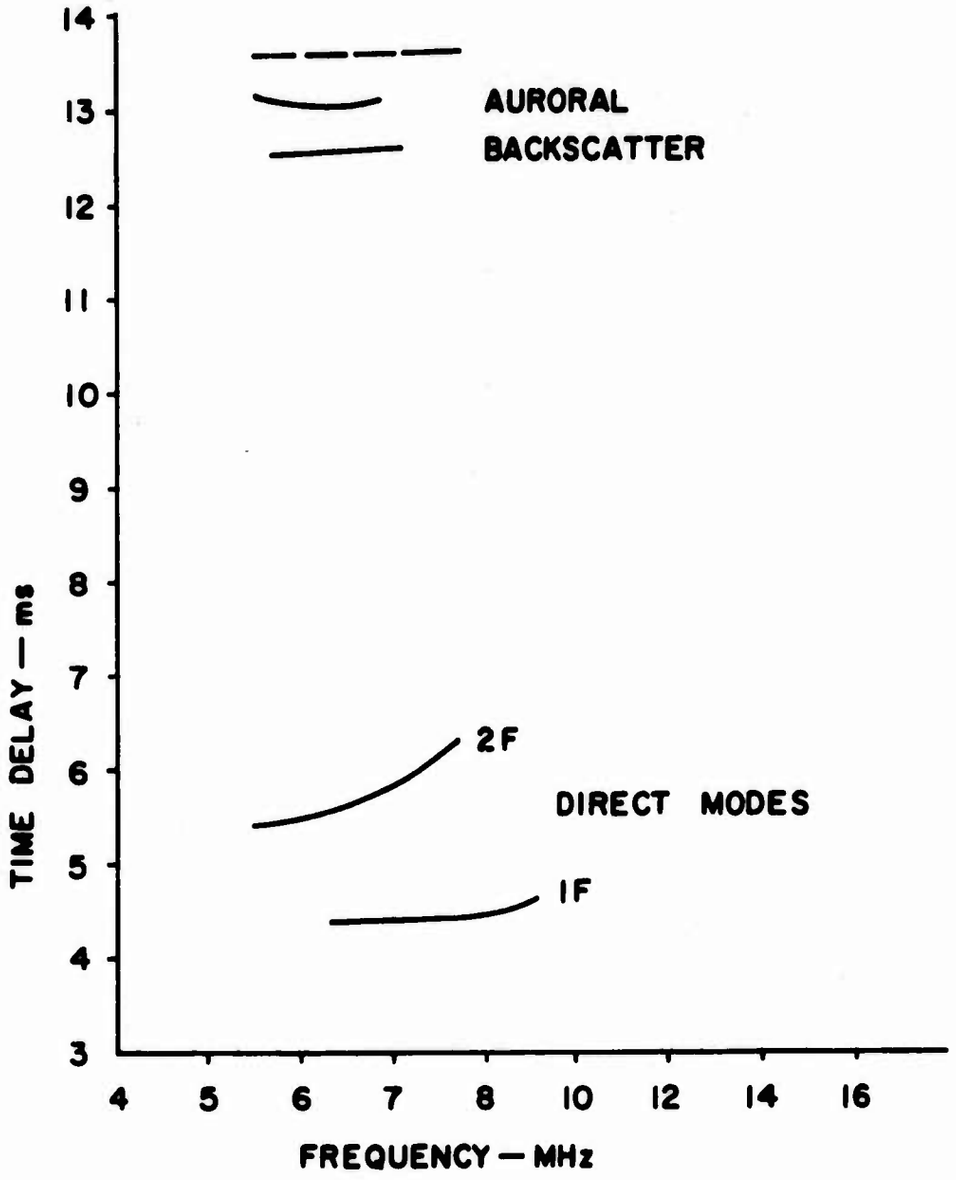

Figure 3. Reproduction of ionogram recorded at 0255 UT on 11 March 1971.

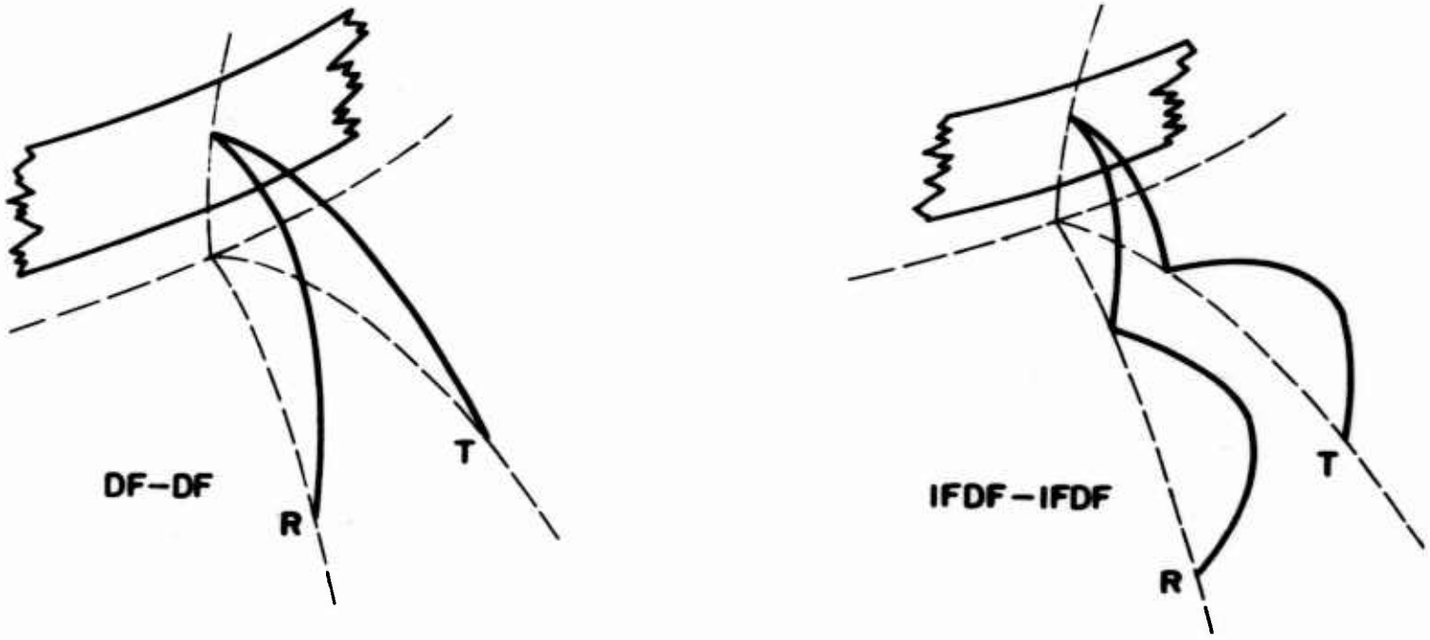

Figure 4. Propagation modes as synthesized.

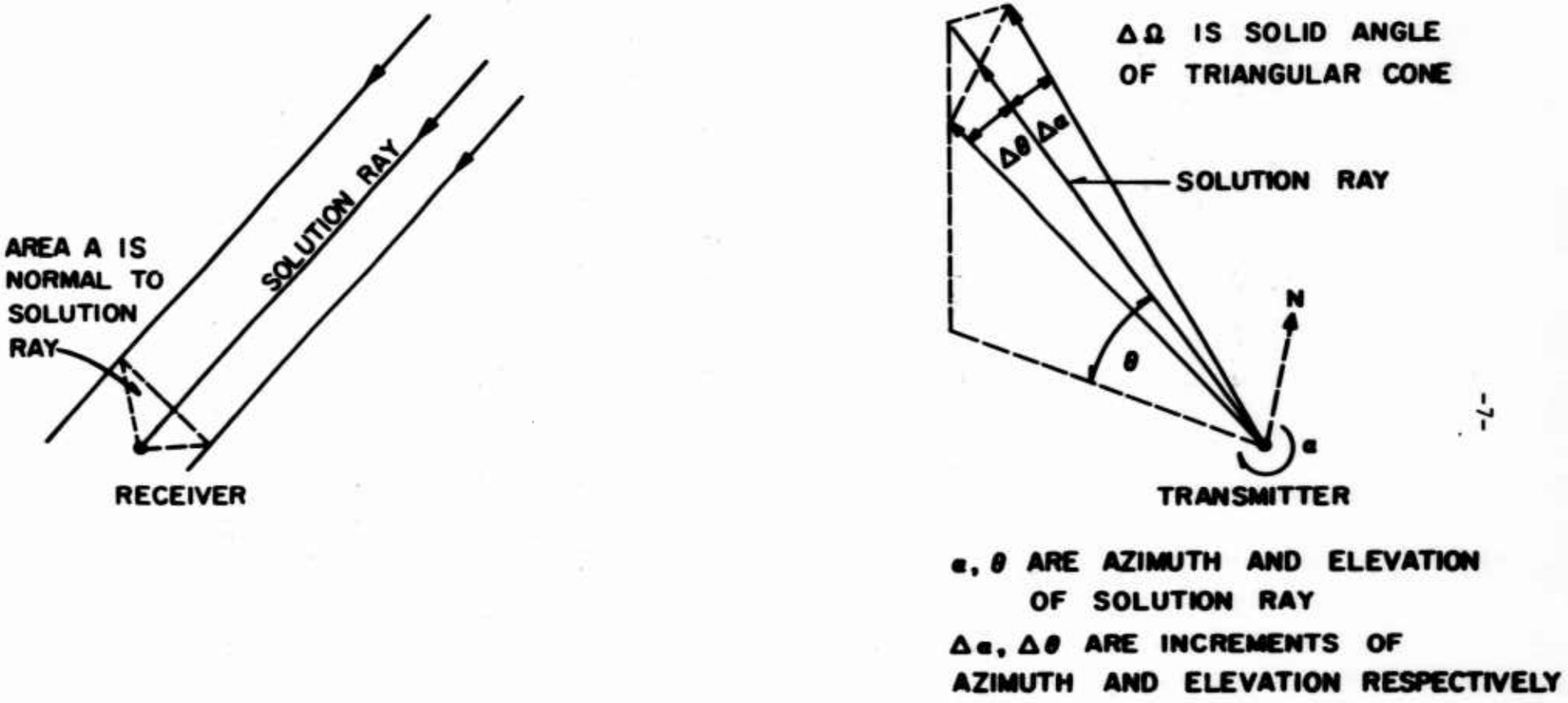

Figure 5. Geometry pertinent to amplitude calculations.

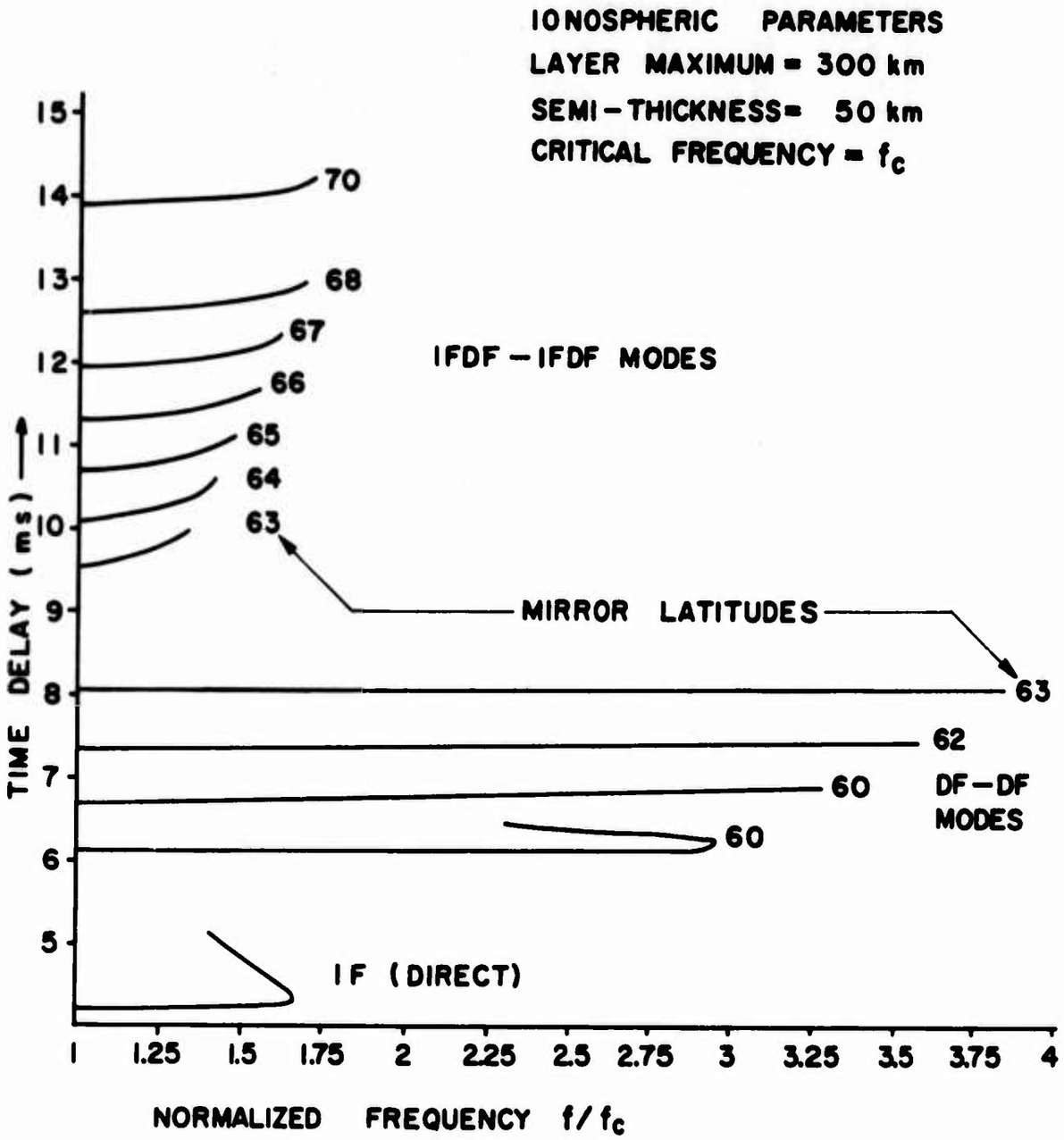

Figure 6. Synthetic ionogram.

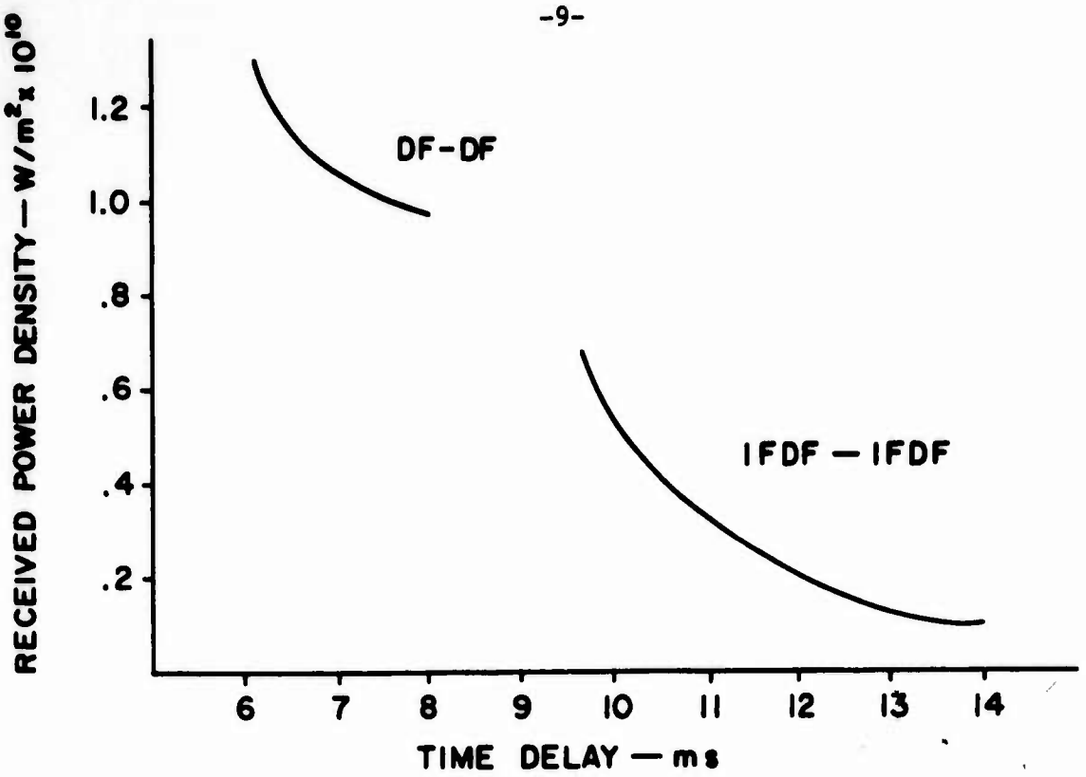

a) power density in incident wave

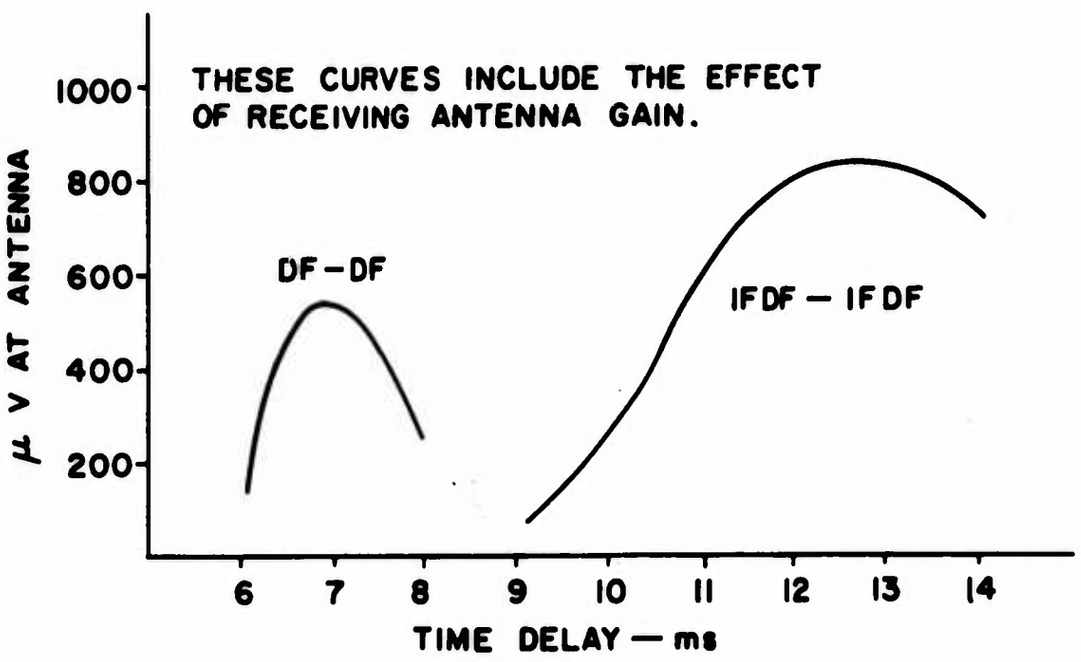

b) amplitude at antenna terminals

Figure 7. Calculated incident power density and antenna scanner output voltage.

PRECEDING PAGE BLANK - NOT FILMED

OBSERVATIONS OF DOPPLER COMPONENTS OF HF OBLIQUE PROPAGATION

A. H. Katz
A. S. Weeks

AVCO SYSTEMS DIVISION
Lowell, Massachusetts 01851

ABSTRACT

Transmissions from WWV (Fort Collins, Colorado) were recorded at the University of Illinois's highly directional Wullenweber array located in Champaign, Illinois. The signals were subsequently processed for Doppler deviations to an effective frequency resolution of 0.024 Hz. The Doppler spectra from these signals are compared with the expected and measured modal propagation between the transmitting and receiving sites. Comparison between FM/CW oblique ionograms from Boulder to the University of Illinois and Doppler spectra from WWV will be described. The data will include sunrise and MUF failure effects on the Doppler spectra. A statistical analysis of Doppler separation as a function of frequency separation for night, day, sunrise, and sunset conditions will be shown.

PRECEDING PAGE BLANK - NOT FILMED

1.0 DATA COLLECTION AND REDUCTION

All data used in this investigation were acquired at the University of Illinois Wullenweber receiving site. A block diagram of the collection scheme is presented in Figure 1. After selecting the transmitter to be observed during a data collection period, the antenna beam was formed with its bore sight along the great circle path and connected to the receiver. The receiver was tuned to the desired frequency and manual gain set so that the 90 Hz beat frequency coherent IF output was approximately 2 Vp-p. Final adjustment of the receiver tuning was achieved by comparing the 90 Hz IF output with a 90 Hz reference oscillator. The 90 Hz IF output of the receiver was recorded on an FM tape recorder along with a time code. After initial setup, the collection process proceeded unattended.

Doppler shifts in the received frequency of an ultra-stable, fixed-frequency transmitter occur due to variations in the index of refraction along the ionospheric transmission path. Conceptually, different modes of propagation should experience different Doppler shifts, and if the received signal arrives via multi-mode propagation, each mode will contribute to the total received energy and total Doppler spread. By spectral analysis of the received signal, the individual modes can be separated in Doppler space. The high resolution necessary (0.01 Hz) to separate the modes during undisturbed propagation periods was achieved using a "real time" spectrum analyzer and a tape speed-up technique

before analysis of the data by the analyzer. From the original recording speed of 1 7/8 ips, the tape was played back at 120 ips giving a 64 times speed-up factor. The data from the tape was then recorded on a second tape whose recording speed was 30 ips and this second or dubbed tape used as the source of data for the analyzer. By playing back the dubbed tape at 30, 60, or 120 ips, speed up factors of 64, 128, or 256 were obtained. The speed up factor of 128 proved sufficient for resolution of the modes and was the primary speed-up factor used during analysis of the data. Figure 2 is a block diagram of the analysis scheme, and Table 1 gives a summary of the relevant parameters for the three speed-up factors.

TABLE 1

speed-up factor	center frequency after speed-up	effective analysis bandwidth	effective bandwidth
64	5,760 Hz	20 Hz	.047 Hz
128	11,520 Hz	10 Hz	.0235 Hz
256	23,040 Hz	5 Hz	.0117 Hz

The spectrum analyzer employed for the analysis described herein has a 1260 Hz bandwidth and a dynamic range of 35 db. A facsimile recorder was used for visual observation.

2.0 DOPPLER SPECTRA FROM WWV - UNIVERSITY OF ILLINOIS

The data described in this section were taken over a 24-hour period at two frequencies, using WWV as a highly stable transmitter. Figures 3 and 4 illustrate the type of Doppler spectra that are commonly observed.

The nighttime data (0209-1500 UT, 3 November 1970) utilized 5 and 10 MHz while the daytime data (1703-0245 UT, 3-4 November 1970) was recorded at 10 and 15 MHz. The WWV programmed off periods from 45:15-49:15 after the hour are clearly observed, and provide a visual time reference in the data. The data was processed at 128 times speed-up at an effective resolution of 0.0235 Hz. Sunset occurred at 0010 UT at 97.5°W longitude for a 100 km height. Sunrise at 97.5°W longitude for 100 km height occurred at 1217 UT. (97.5°W longitude was chosen because it is the midpoint of the 1F mode between WWV-University of Illinois.)

Figure 3 shows the Doppler spectra for the 5 and 10 MHz signal for the nighttime period. Several modes are observed with separation to 0.2 Hz. The largest mode separation occurs at shortly after 1200 UT, which coincides with occurrence of sunrise. The 5 MHz signal fades out after 1300 UT, and by 1400 UT, the 5 MHz is very faint. This is attributed to the high absorption which occurs during the day at the lower frequencies.

The simultaneous 10 MHz signal shows a radically different behavior. The signal level shows a decrease at 0500 UT, and by 0740 UT no signal is observed. MUF failure for the 10 MHz transmissions is occurring but of a rather interesting type. At 0515 UT, we observed that the weakened signal has an off period of 5 minutes. This corresponds to the off period of WWVH. (WWVH is a time standard station located in

Hawaii, which has the same frequency allocations as WWV but with a different off period.) It is observed from the data that the 10 MHz MUF failure for WWV occurred shortly before 0500 UT. WWVH becomes visible shortly after and clearly shows an off period between 0515-0520 UT. The WWVH signal shows some signal fading until 0740 UT when it also undergoes MUF failure.

Since the distance between WWVH and University of Illinois is 6706.19 km, the data from 0500-0740 UT represent Doppler spectra for a long path. A question as to the extent to which WWVH interferes with the Doppler spectra of WWV during the time WWV is being received is of interest. Since the off times are different, a cursory look at the signal levels in the offtimes of WWV will give some clues as to the amount of WWVH contamination. Before 0400 UT, the off times for WWV do show some interference, but before 0300 UT the off time is relatively clear. The off times at 5 MHz are always clear of WWVH interference effects.

In Figure 3, the 10 MHz signal appears shortly after 1100 UT, before sunrise at 97.5°W, and then becomes much stronger after 1220 UT. The signal observed between 1100-1220 UT is from WWVH, as is confirmed from the off-period times. The longitude of WWVH is 156°W and sunrise occurs later than 1220 UT for this path. The WWV signals are clearly observed after 1220 UT, which is the time of sunrise control for the 1F modes between WWV-University of Illinois. The observations of WWVH

before this can only be attributed to a pre-sunrise increase in foF2 near the midpoint between WWVH and University of Illinois. This is only a hypothesis as no supporting ionospheric data is currently available. The sunrise influence on WWV is very large, and shifts of 1-2 Hz between modes can be observed.

Figure 4 shows 10 MHz and 15 MHz during the day to evening hours on the 3-4 November 1970 (1703-0245 UT). The signal strength is higher for the 10 MHz signal. The 15 MHz signals show larger Doppler shifts than the 10 MHz observations. There does not appear to be a one-to-one correlation between the modal separations seen on the two frequencies.

3.0 MUF FAILURE EFFECTS

From 2300-0200 UT on 9-10 October 1970, the spectral analyzed data for WWV is shown; a time mark every 5 minutes is indicated (Figure 5). The blank regions on the data at 2345 and 0045 UT are the off periods of WWV. The jumps (i. e., at 0010 UT) are due to synthesizer instabilities. From 0035 to 0140 UT, an interesting frequency event occurs. Two modes are observed which show a decreasing frequency separation with increasing time. At 0125 UT, the modes are not separated, and by 0140 UT, MUF failure at 15 MHz occurs. Chart of frequency shift between modes versus MUF at 5 minute intervals is listed in Table 2.

TABLE 2

Time, UT	0035	0040	0045	0050	0055	0100	0105
Freq. separation between modes, Hz	1.7	1.5	1.4	1.0	0.8	0.6	0.5
MUF, MHz	20	20	18.5	18	---	17	16.5

0110	0115	0120	0125	0130	0135	0140	After 0145
0.5	0.4	0.25	0	0	0	0	No Propagation
16.2	15.5	15.4	15.3	16.0	14	14	< 15 MHz

From the Doppler data and the ionograms, the mode splitting appears to be due to high and low ray oblique propagation. The two modes are only observed when both the high ray and low are visible at 15 MHz. As the 1F MUF drops below 15 MHz, the frequency splitting decreases until no separations are discernible after which MUF failure occurs (see Figure 6a and b). The fading rate of the amplitude data reflect this change with very high fading rates apparent at the larger frequency separation and showing decreases in the fading rate as the mode separation decreases to zero (Figure 7a and b).

Figure 6a and 6b shows the Boulder-University of Illinois FM/CW oblique ionograms.* One ionogram every five minutes from 0015 to 0140 UT. There were two transmitters in operation: one at Boulder, Colorado, the other at San Antonio, Texas. The 1F, 2F, 3F traces are from the Boulder sounder transmitter, and are the ones we are interested in. The returns in some areas that appear strange are from the second

*We would like to thank SWRI for informing us of their operational schedule.

transmitter. The FM/CW transmitter at Boulder was swept from 2-30 MHz at 100 kHz/sec, 2 Watts average power. The vertical lines on each ionogram at 15 MHz further point out where the MUF of the 1F mode is with respect to 15 MHz. Where only the lower vertical line is shown, the high ray cannot be seen but should be observable. Figure 7a and 7b shows the sum beam amplitude is from 0031 to 0150 UT. A relative amplitude scale is indicated. The fading rates show good correlation with frequency separation of the propagating signal.

4.0 STATISTICAL ANALYSIS

An analysis of the data to determine the dependence of Doppler shift on frequency and time-of-day was carried out. The transmissions used in the analysis were the WWV frequencies of 5, 10, and 15 MHz, with 10 and 15 MHz typically being observed during the day, and 5 and 10 MHz during the night. To analyze the data, the diurnal period was divided into four intervals of sunrise, day, sunset, and night. The ionospheric sunrise and sunset times* were determined for a 100 km height at the midpoint of the propagation path. Sunrise and sunset periods were assumed to begin 30 minutes prior to, and continue 2 hours after, the computed times.

Each hour of data was divided into six ten-minute sections, and the maximum frequency spread for each section determined. The frequency spread was scaled in increments of 0.1 Hz. Figures 8a, 8b, 9a, and 9b indicate the Doppler shift as a function of frequency, where the

*Obtained from NASA Technical Memorandum X-1233: "Computed Times of Sunrise and Sunset in the Ionosphere."

ordinate is the percent of the total number of 10-minute sections with corresponding Doppler deviation given on the abscissa. Doppler shift as a function of time of day is indicated in Figures 10a, 10b, and 11. Since 10 MHz was observed during all four of the periods, Figure 11 shows the statistics for a complete diurnal period. Figures 8a and 9a indicate that for frequencies nearer the path MUF, the Doppler shifts are greater. During sunrise periods, the Doppler shifts observed on the 5 and 10 MHz transmissions are similar, as shown in Figure 8b with somewhat larger shifts seen at the higher frequency due to the MUF increasing through 10 MHz after sunrise (Figure 3). Figure 9b indicates a similar Doppler shift in the 10 MHz and 15 MHz frequencies, again with greater deviations noted in the higher frequency, caused by the decreasing MUF after sunset. In the majority of the data taken, the 15 MHz underwent MOF failure during the sunset period. Doppler shifts observed during the day and sunset periods for 15 MHz are shown in Figure 10a, where the sunset period experiences larger shifts than the day periods. The Doppler deviation at 5 MHz is greater during sunrise than at night, as indicated in Figure 10b. Figure 11 presents Doppler statistics for a complete diurnal period at 10 MHz, indicating greatest Doppler shifts at sunrise followed by sunset, night, and day. The cumulative distribution for the 10 MHz diurnal period is given in Figure 12.

From analysis of the data, it is seen that maximum Doppler shifts occur during sunrise and sunset and that Doppler deviations during these times are greater for frequencies near the MUF.

LIST OF ILLUSTRATIONS

Figure 1. Data Collection Scheme

Figure 2. Data Analysis Scheme

Figure 3. Example of Doppler Spread from WWV at 5 and 10 MHz, 0200-1500 UT, 3 November 1970.

Figure 4. Example of Doppler Spread from WWV at 10 and 15 MHz from 1703-0245 UT, 3-4 November 1970.

Figure 5. Doppler Spectra from WWV on 15 MHz, from 2300-0300 UT, 9-10 October 1970.

Figure 6a. FM/CW Oblique Ionograms (2-25 MHz) from Boulder to University of Illinois from 0015-0055 UT, 9-10 October 1970 (one ionogram every five minutes).

Figure 6b. FM/CW Oblique Ionograms (2-25 MHz) from Boulder to University of Illinois from 0100-0140 UT, 10 October 1970 (one ionogram every five minutes).

Figure 7a. Amplitude (fading rate) of the WWV Signal at 15 MHz from 0031-0110 UT, 10 October 1970.

Figure 7b. Amplitude (fading rate) of the WWV Signal at 15 MHz from 0110-0150 UT, 10 October 1970.

Figure 8a. Percentage of occurrence of Doppler spread within 0.1 Hz intervals from 0-1.4 Hz for 5 and 10 MHz at night.

Figure 8b. Percentage of occurrence of Doppler spread within 0.1 Hz intervals from 0-1.4 Hz for 5 and 10 MHz during sunrise.

Figure 9a. Percentage of occurrence of Doppler spread within 0.1 Hz intervals from 0-1.4 Hz for 10 and 15 MHz during daytime.

Figure 9b. Percentage of occurrence of Doppler spread within 0.1 Hz intervals from 0-1.4 Hz for 10 and 15 MHz during sunset.

Figure 10a. Percentage of occurrence of Doppler spread within 0.1 Hz intervals from 0-1.4 Hz for 15 MHz for the daytime and sunset periods.

Figure 10b. Percentage of occurrence of Doppler spread within 0.1 Hz interval from 0-1.4 Hz for 5 MHz for the night and sunrise period.

Figure 11. Percentage of occurrence of Doppler spread within 0.1 Hz intervals from 0-1.4 Hz for 10 MHz for the daytime, sunset, night, and sunrise periods.

Figure 12. Cumulative distribution for the data described in Figure 11.

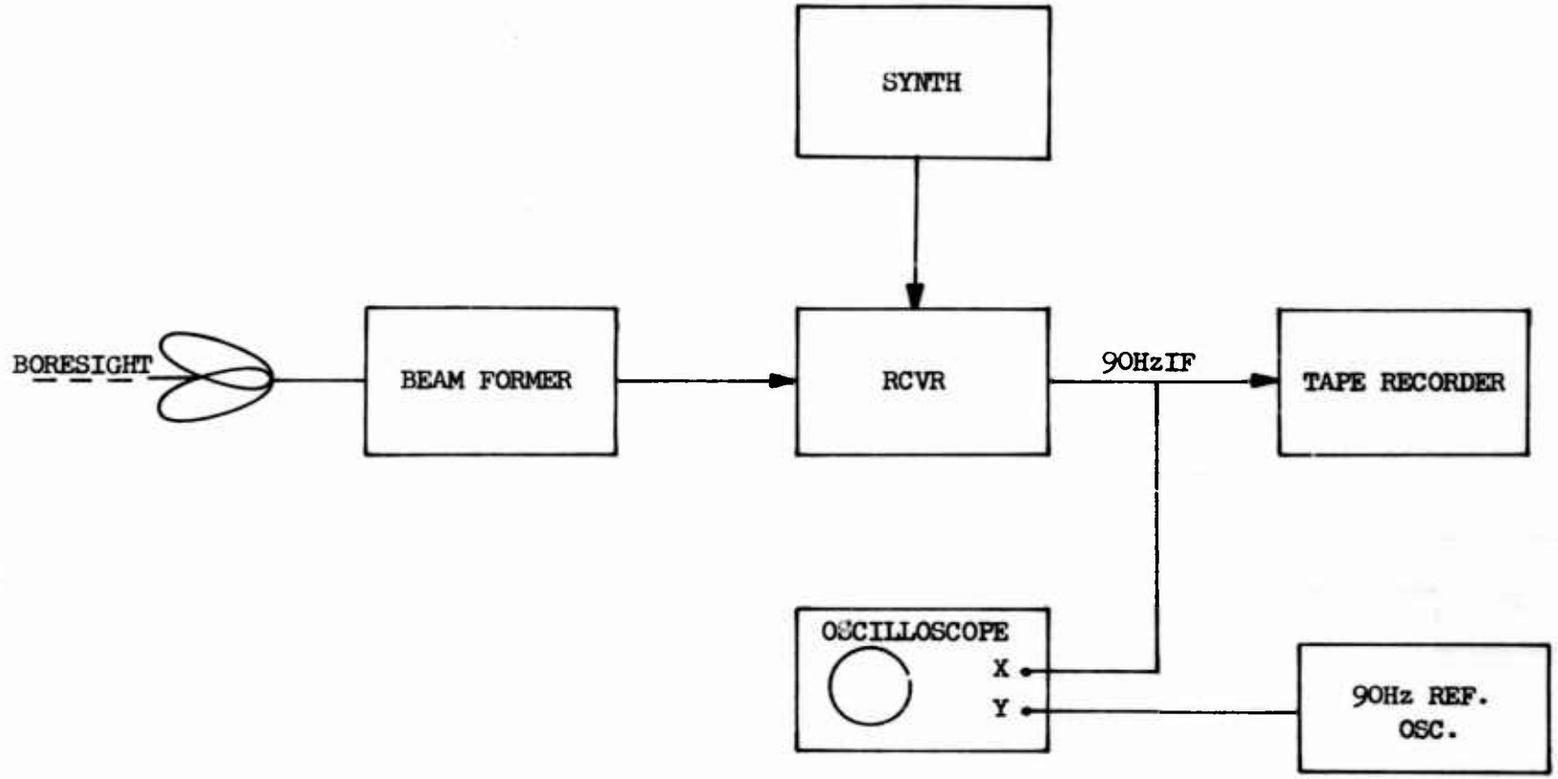
SYNTH
BORESIGHT
BEAM FORMER
RCVR
90Hz IF
TAPE RECORDER
OSCILLOSCOPE
X
Y
90Hz REF.
OSC.

FIGURE 1

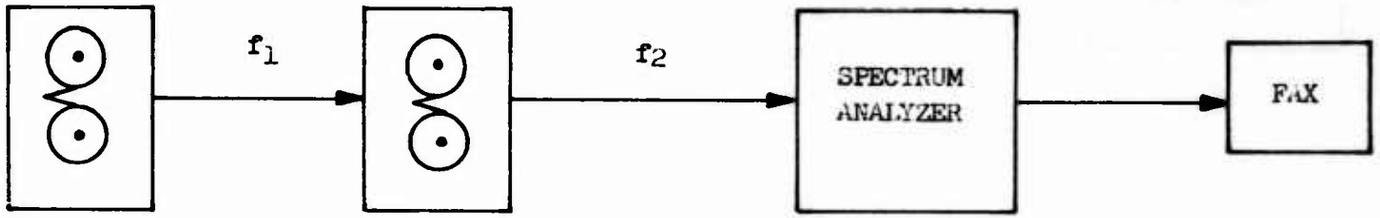

f_1 = 90Hz X (speedup of 64)

f_2 = 90Hz X (speedup factor) X 64

FIGURE 2

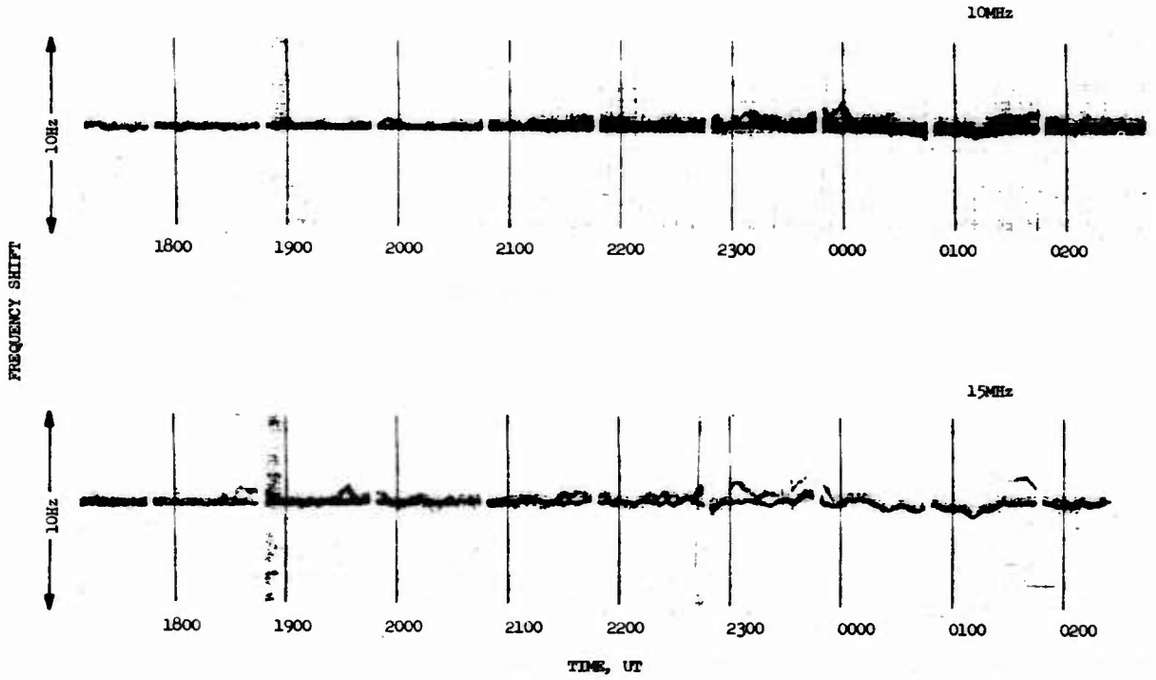
10MHz
10Hz
1800
1900
2000
2100
2200
2300
0000
0100
0200
15MHz
10Hz
1800
1900
2000
2100
2200
2300
0000
0100
0200
FREQUENCY SHIFT
TIME, UT

FIGURE 3

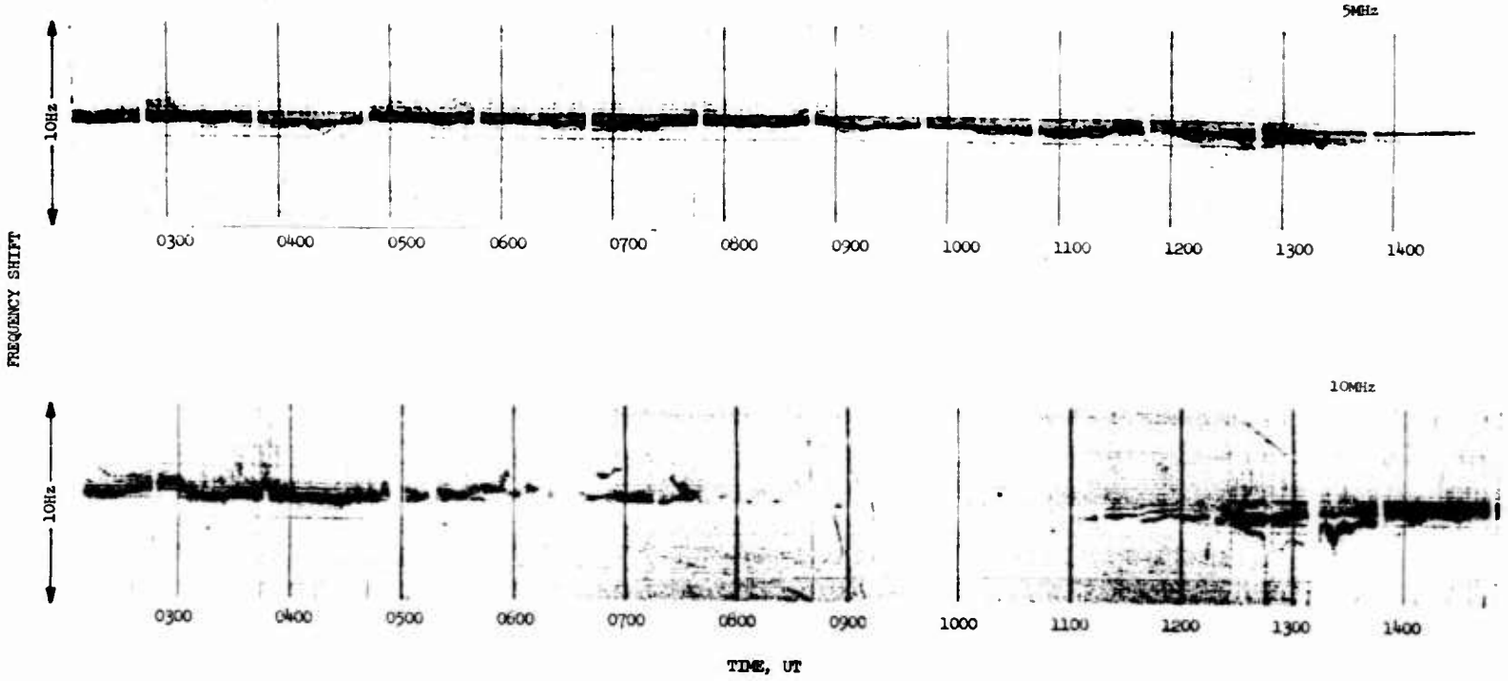
5MHz
10Hz
FREQUENCY SHIFT
0300
0400
0500
0600
0700
0800
0900
1000
1100
1200
1300
1400
10MHz
10Hz
0300
0400
0500
0600
0700
0800
0900
1000
1100
1200
1300
1400
TIME, UT

FIGURE 4

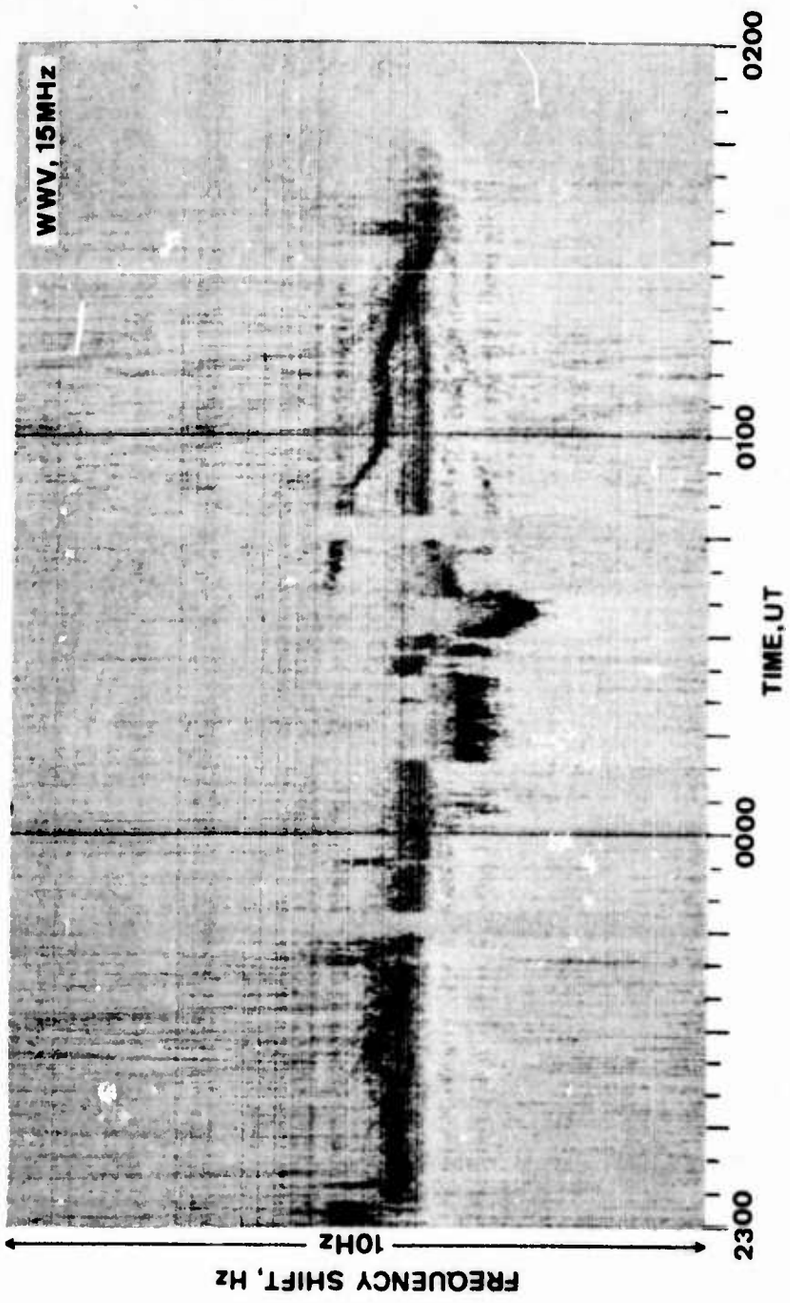
WWV, 15MHz
0200
0100
0000
2300
TIME, UT
10Hz
FREQUENCY SHIFT, Hz

FIGURE 5

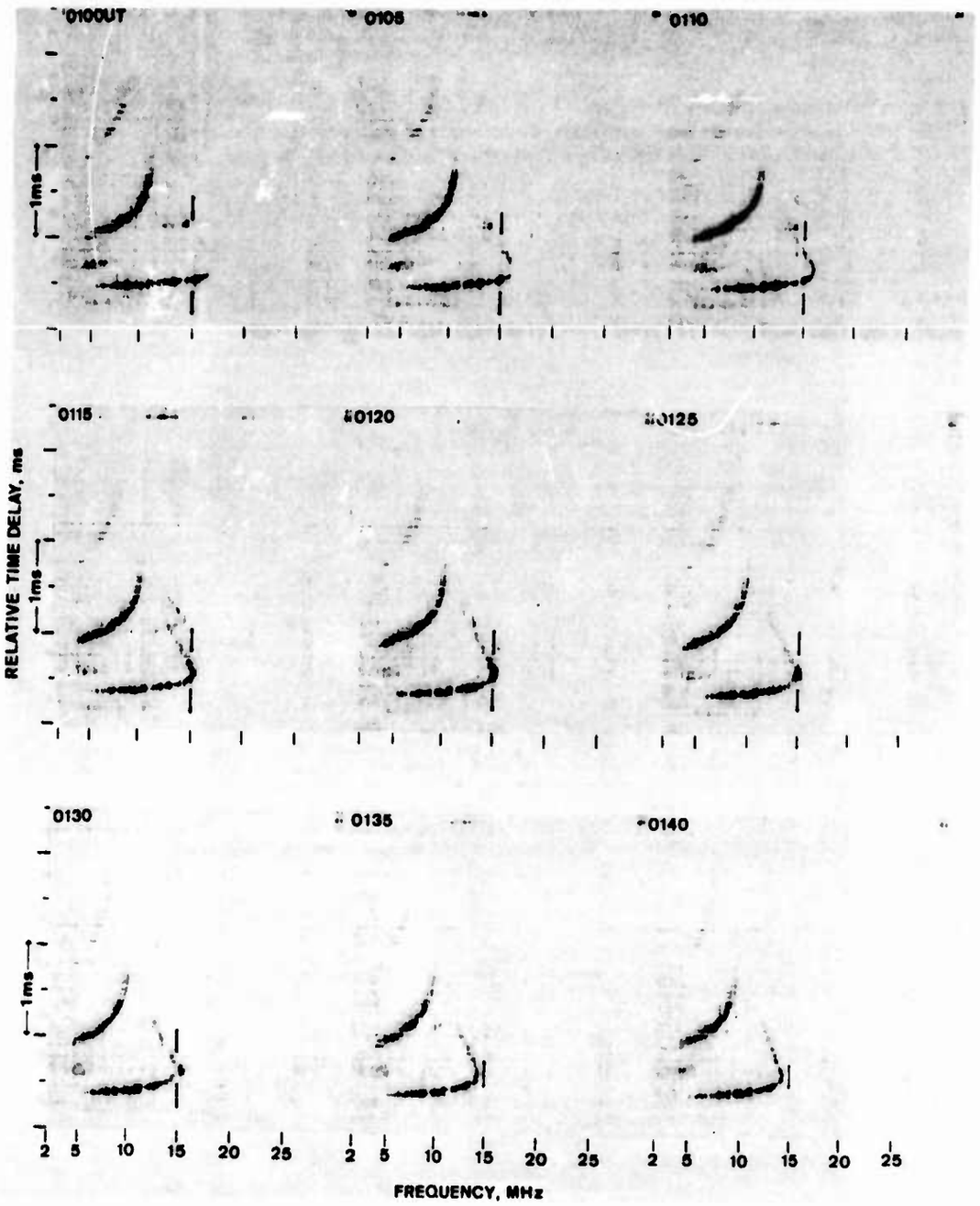
0100UT
0105
0110
0115
0120
0125
0130
0135
0140
1ms
RELATIVE TIME DELAY, ms
2 5 10 15 20 25
FREQUENCY, MHz

FIGURE 6b

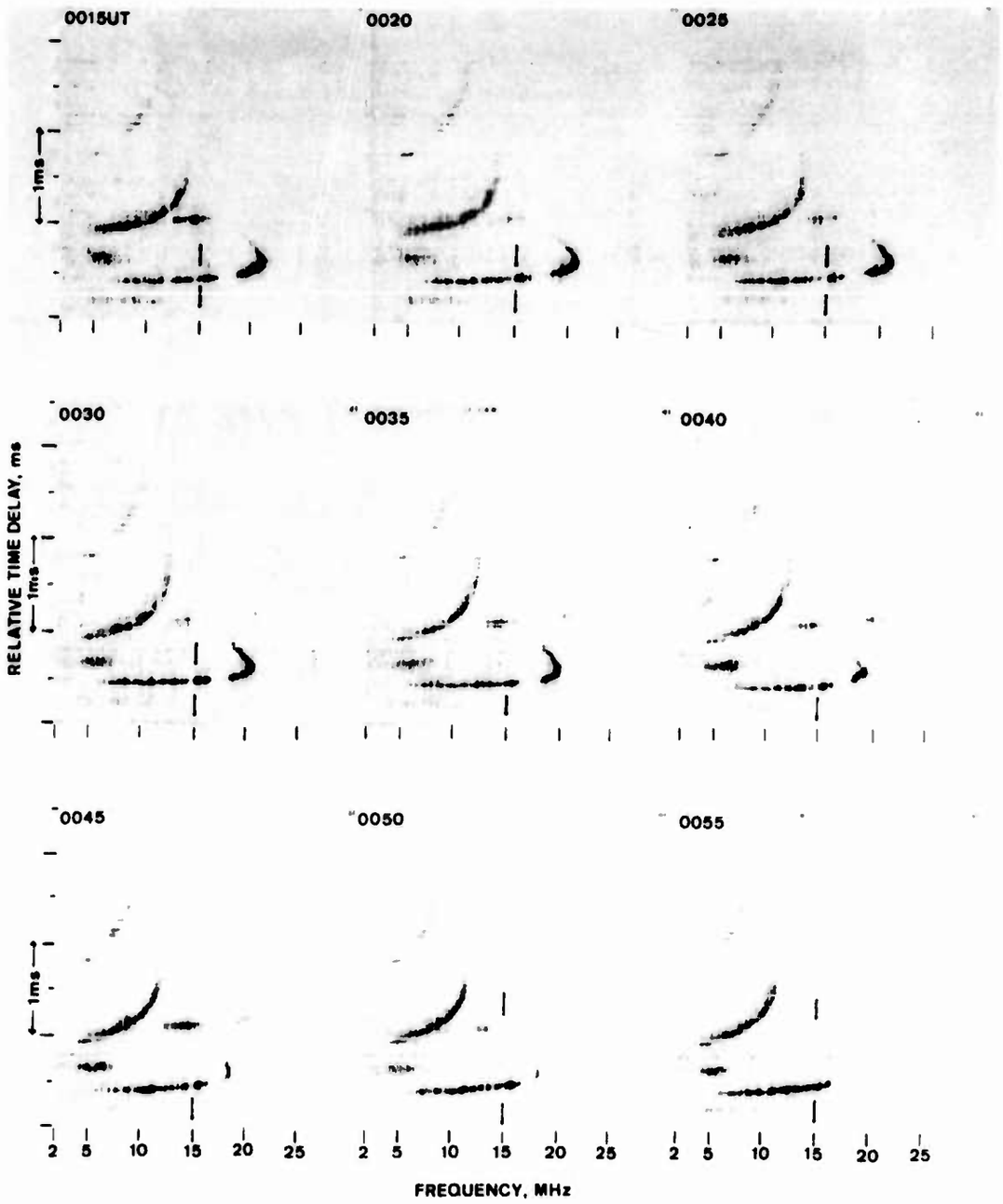
0015UT
0020
0025
0030
0035
0040
0045
0050
0055
1ms
RELATIVE TIME DELAY, ms
2 5 10 15 20 25
FREQUENCY, MHz

FIGURE 6a

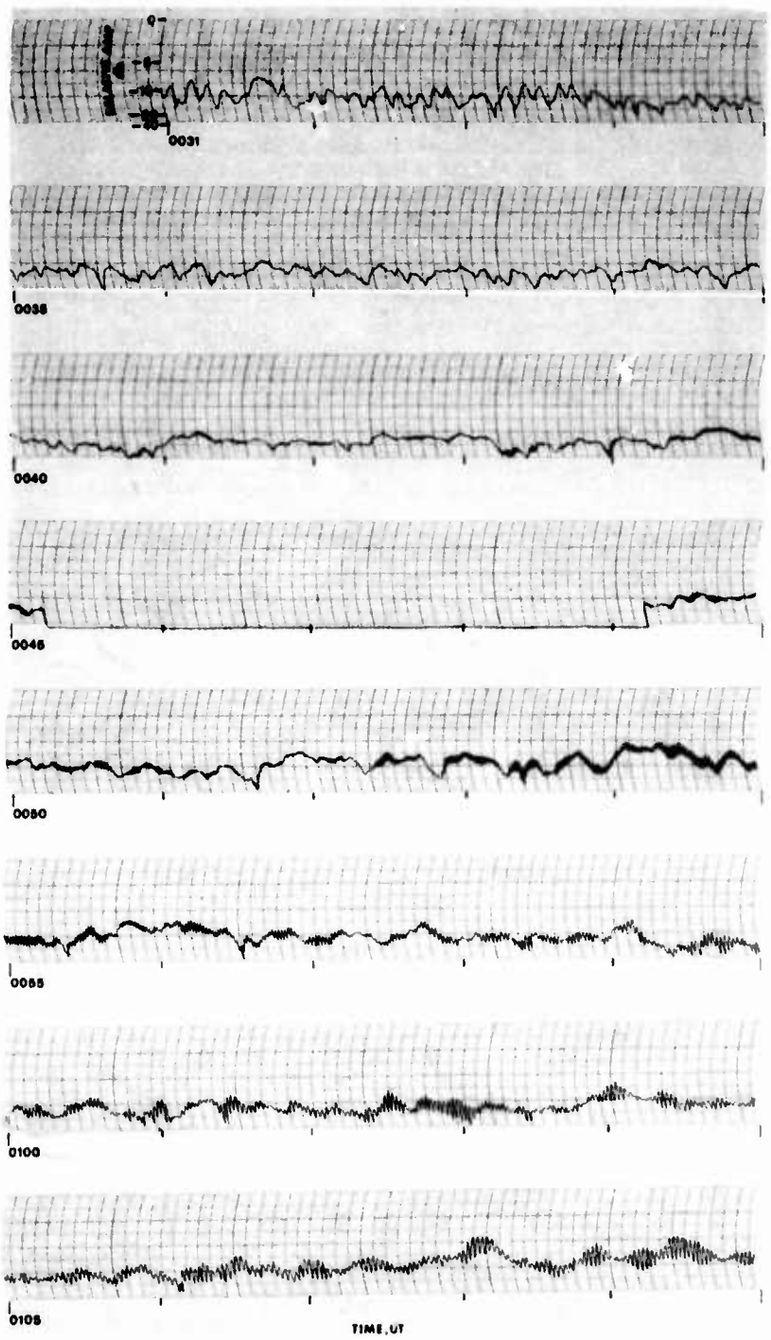

FIGURE 7a

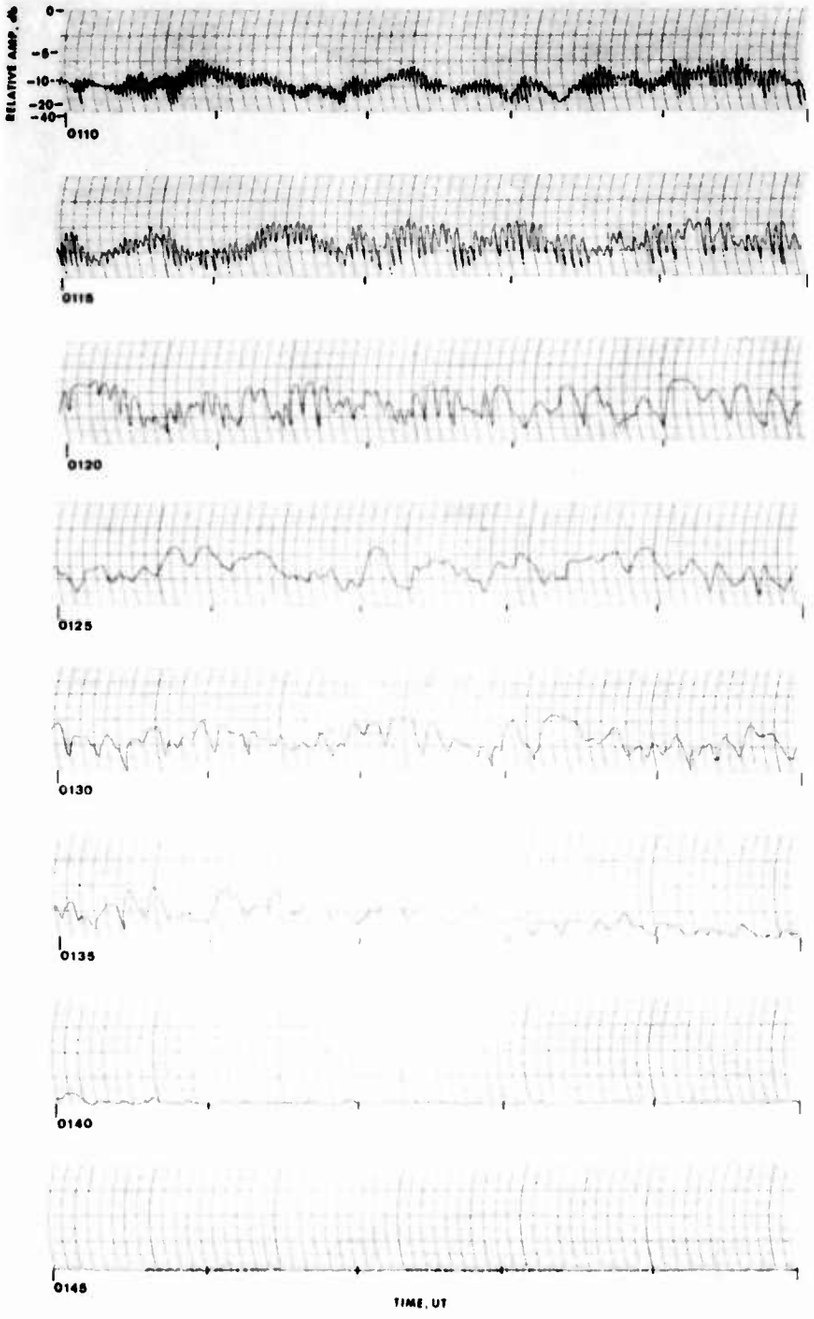
RELATIVE AMP., db
0
-6
-10
-20
-40
0110
0115
0120
0125
0130
0135
0140
0145
TIME, UT

FIGURE 7b

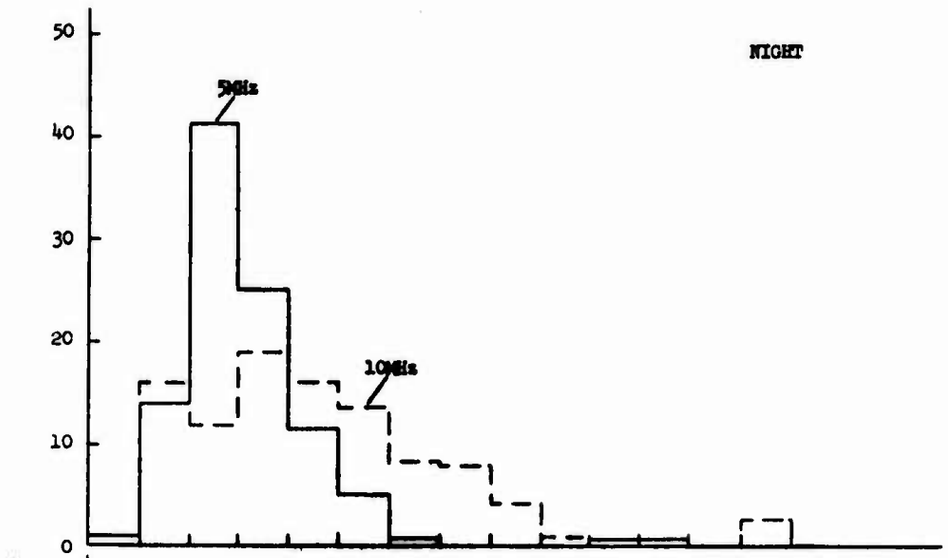

FIGURE 8a

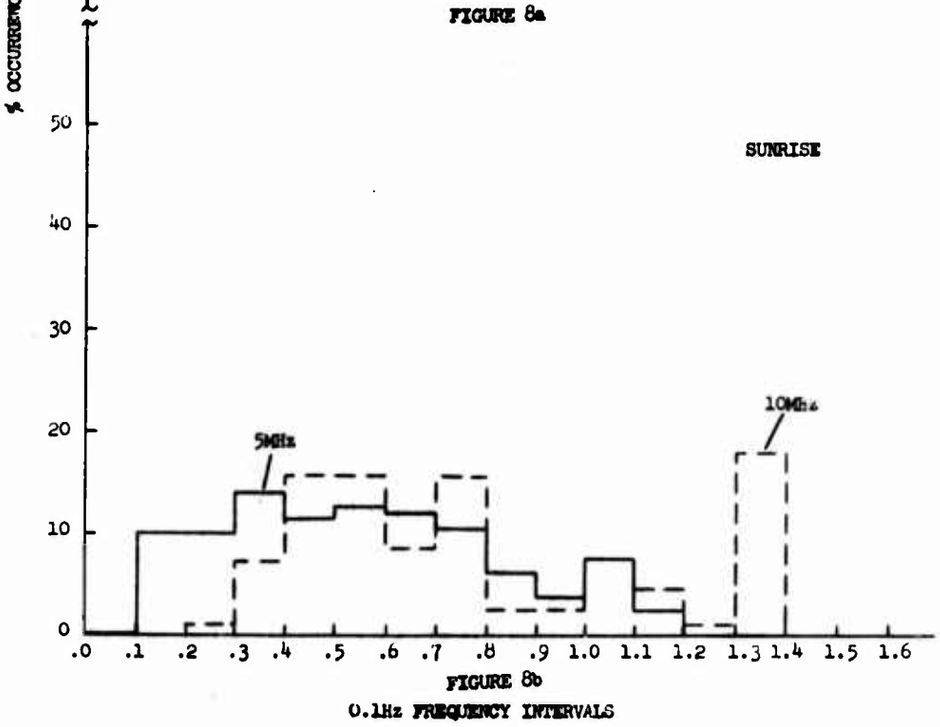

FIGURE 8b

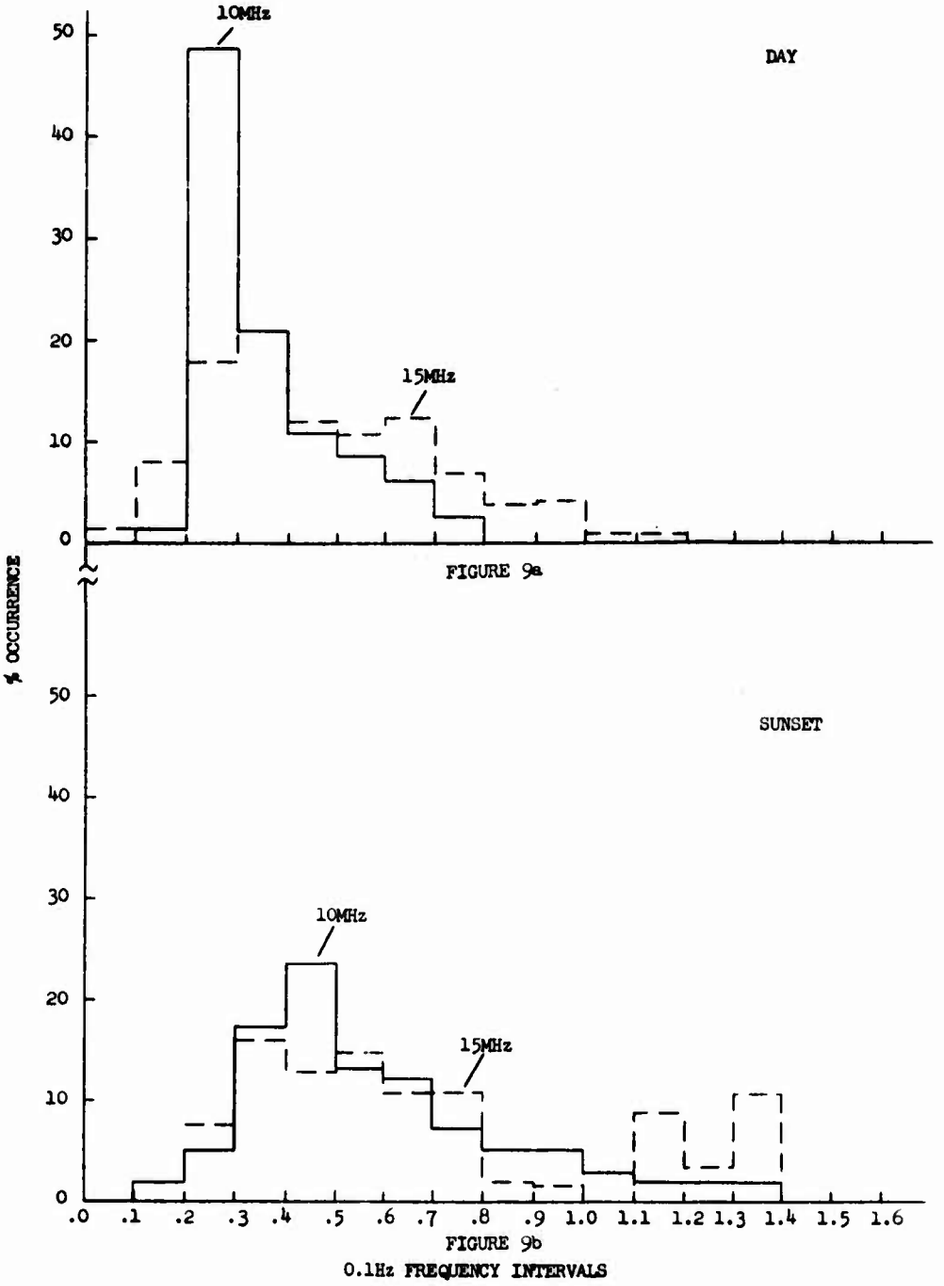

FIGURE 9a

FIGURE 9b

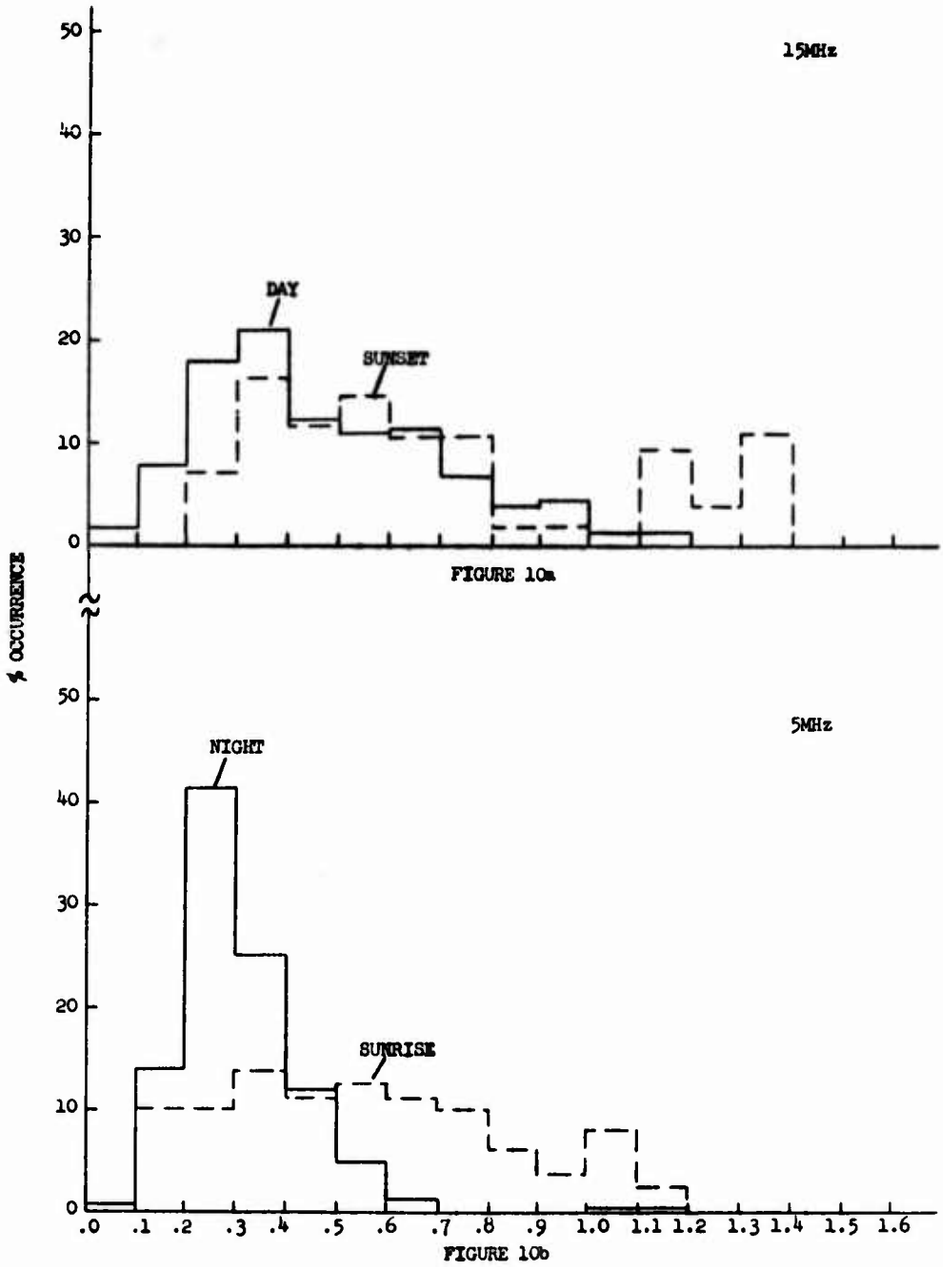

FIGURE 10a

FIGURE 10b

0.1Hz FREQUENCY INTERVALS

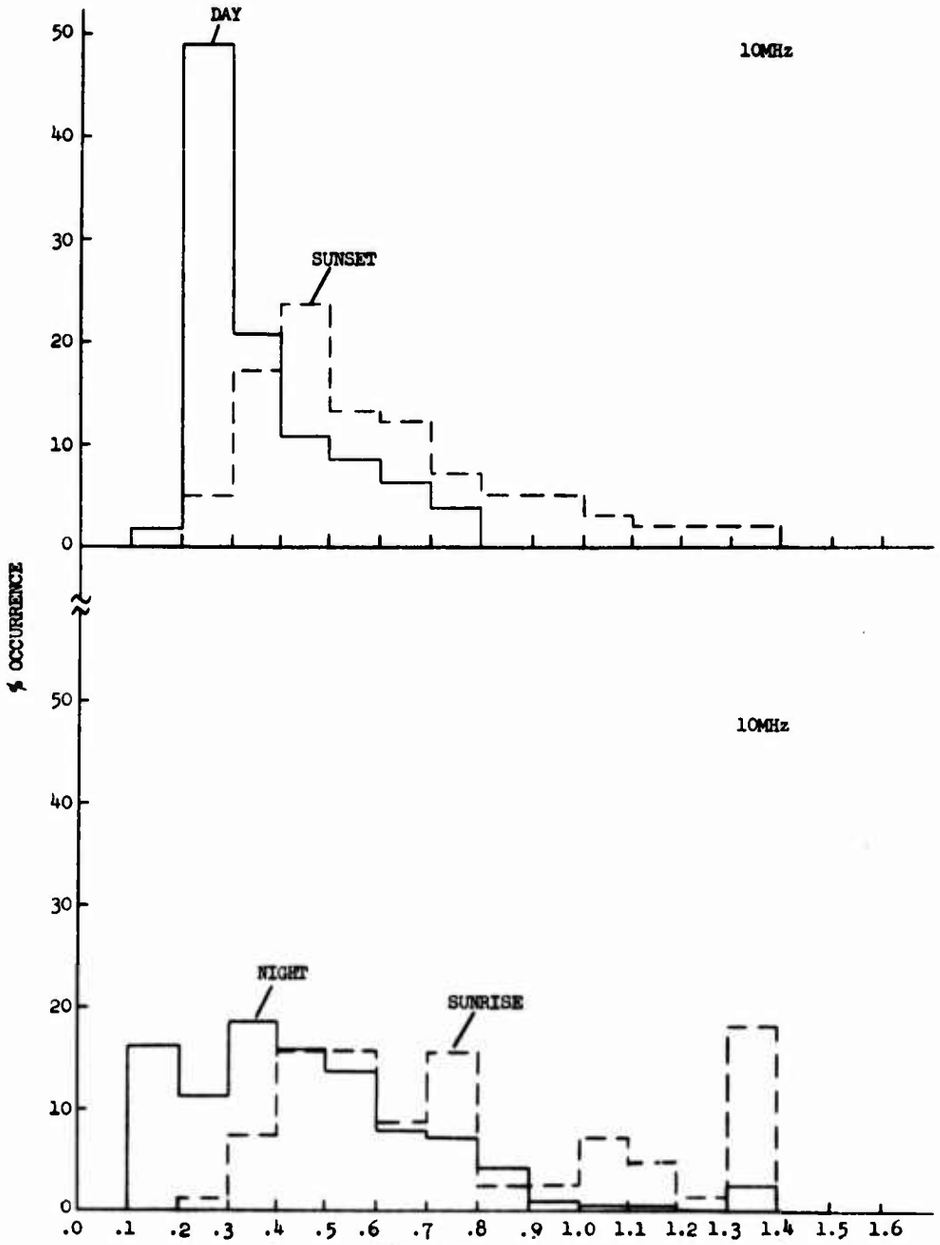

FIGURE 11
0.1Hz FREQUENCY INTERVALS

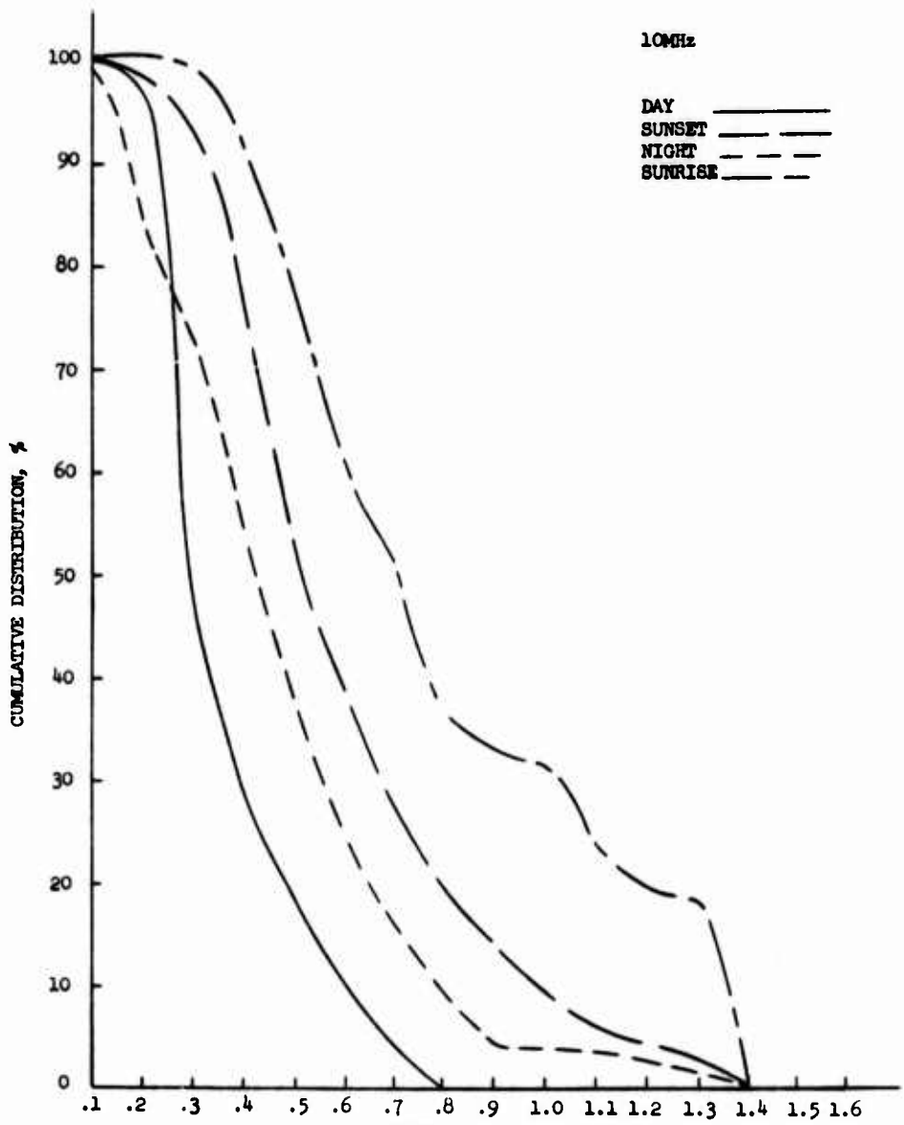

FIGURE 12
0.1Hz FREQUENCY INTERVALS

AZIMUTHAL VARIATION

of

MEASURED HF NOISE

L. M. Posa, D. J. Materazzi and N. C. Gerson

LIST OF ILLUSTRATIONS

FIGURE	CAPTION
1	Average thunderstorm probability over the planet: a. Winter 0800 UT b. Winter 2000 UT
2	Location of the receiver site showing the azimuthal sectors in which noise was measured.
3	Comparison between median and mean (determined over 20 seconds) noise values. The median is a much more representative central tendency when several extremely high values enter the data sample.
4	Measured diurnal and azimuthal variation of noise between 2-3 MHz (winter 1966-67).
5	Measured diurnal and azimuthal variation of noise between 4-5 MHz (winter 1966-67).
6	Measured diurnal and azimuthal variation of noise between 6-7 MHz (winter 1966-67).
7	Measured diurnal and azimuthal variations of noise between 8-9 MHz (winter 1966-67).
8	Calculated diurnal and azimuthal variation of noise between 2-3 MHz.
9	Calculated diurnal and azimuthal variation of noise between 4-5 MHz.
10	Calculated diurnal and azimuthal variation of noise between 6-7 MHz.
11	Calculated diurnal and azimuthal variation of noise between 8-9 MHz.
12	Population density over Europe.

AZIMUTHAL VARIATION OF MEASURED HF NOISE

L. M. Posa, D. J. Materazzi and N. C. Gerson

Department of Defense

HF noise (2-8 MHz) as a function of azimuth, frequency and time of day was measured in England during the winter of 1966-67. For a given frequency interval eight unequal azimuthal sectors (with 5 sectors between 45^{o}-180^{o}) were sampled each four hours in a standardized fashion. Power levels for the 10th, 50th and 90th percentiles were derived and plotted. The results provide the integrated total external noise (both local and propagated). In addition to the well known distinctive diurnal and frequency changes, a marked variation with azimuth is present. A separate examination of noise intensities measured simultaneously from several azimuths reveals marked differences with azimuth. The investigation indicates that noise levels as a function of azimuth are needed, and are the ones to be applied to practical HF systems.

I. INTRODUCTION

In all noise measurement techniques, the equipment characteristics (e.g., the time constant, bandwidth, and circuitry of the receiver-recorder) influence the recorded intensities. Similarly, the antenna pattern (e.g., vertical and azimuthal lobe structure) determines the extent of the total noise environment delivered into the receiver. In this connection a basic deficiency in past observations has been the employment of an omnidirectional antenna which superposed noise arriving from all azimuths. Since noise (either natural or man-made) is not uniformly or isotropically distributed in space, the latter procedure can provide data which is misleading for some practical systems. This paper is concerned only with the azimuthal variation of HF noise.

It is obvious that noise as a function of azimuth is a basic and useful parameter. Many HF systems employ highly directive antenna arrays beamed to particular orientations. If the noise density were uniformly distributed throughout the vertical hemisphere tangent to the ground at the antenna point, any decrease in antenna beamwidth would be compensated by an increase in gain, thus introducing the same noise power into the receiver. When discrete and distributed noise sources are present, the noise magnitude is no longer independent of antenna beamwidth or of antenna orientation. Indeed changing the beamwidth or the direction will exclude discrete noise sources.

On the earth, noise is mainly generated within given areas and propagates to the receiving site within particular sectors. Examples of large distributed sources are the three semi-permanent natural noise centers located along the equator at Brazil, central Africa and the East Indies (see Figure 1). Man-made

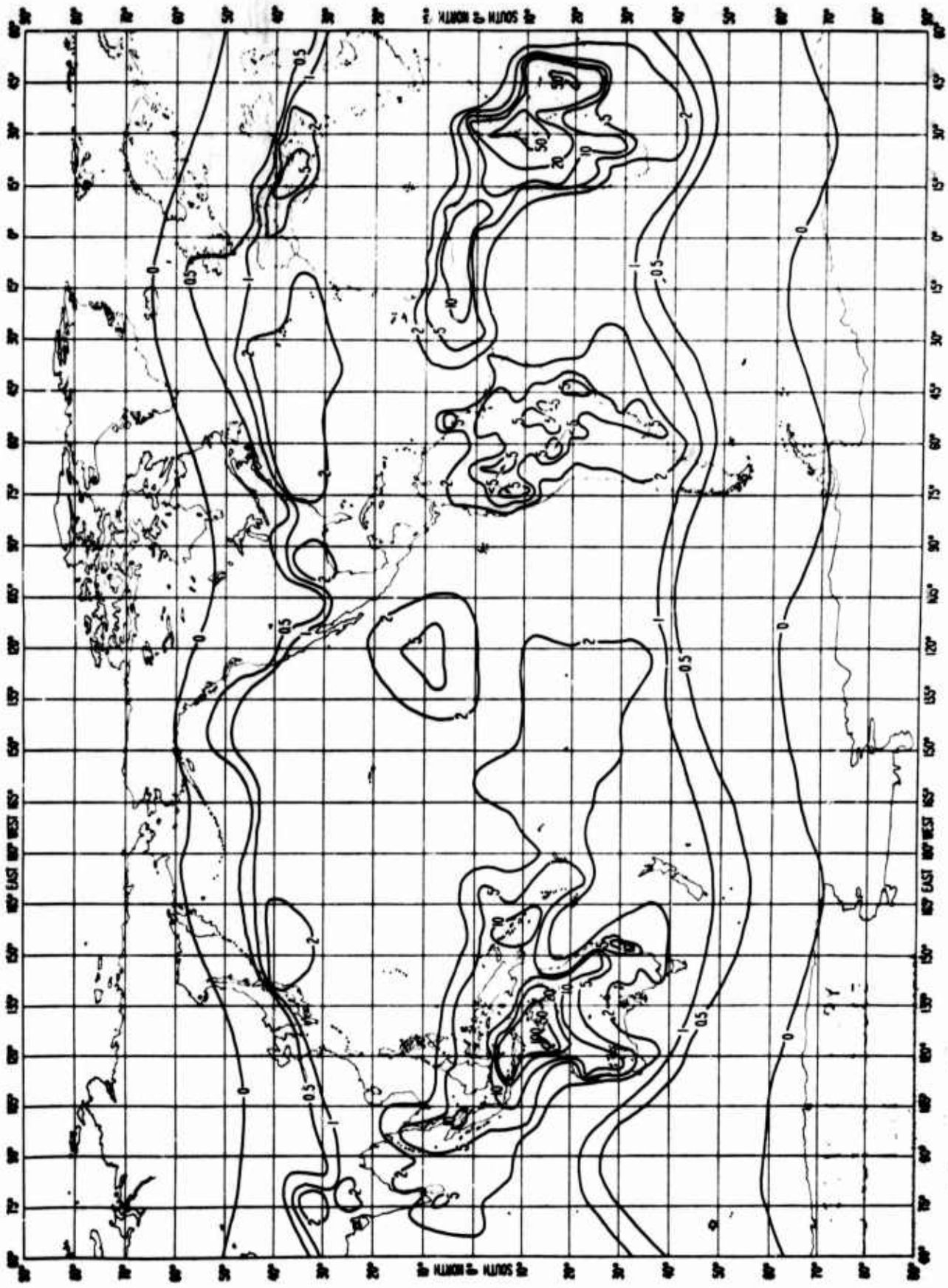

FIGURE 1A

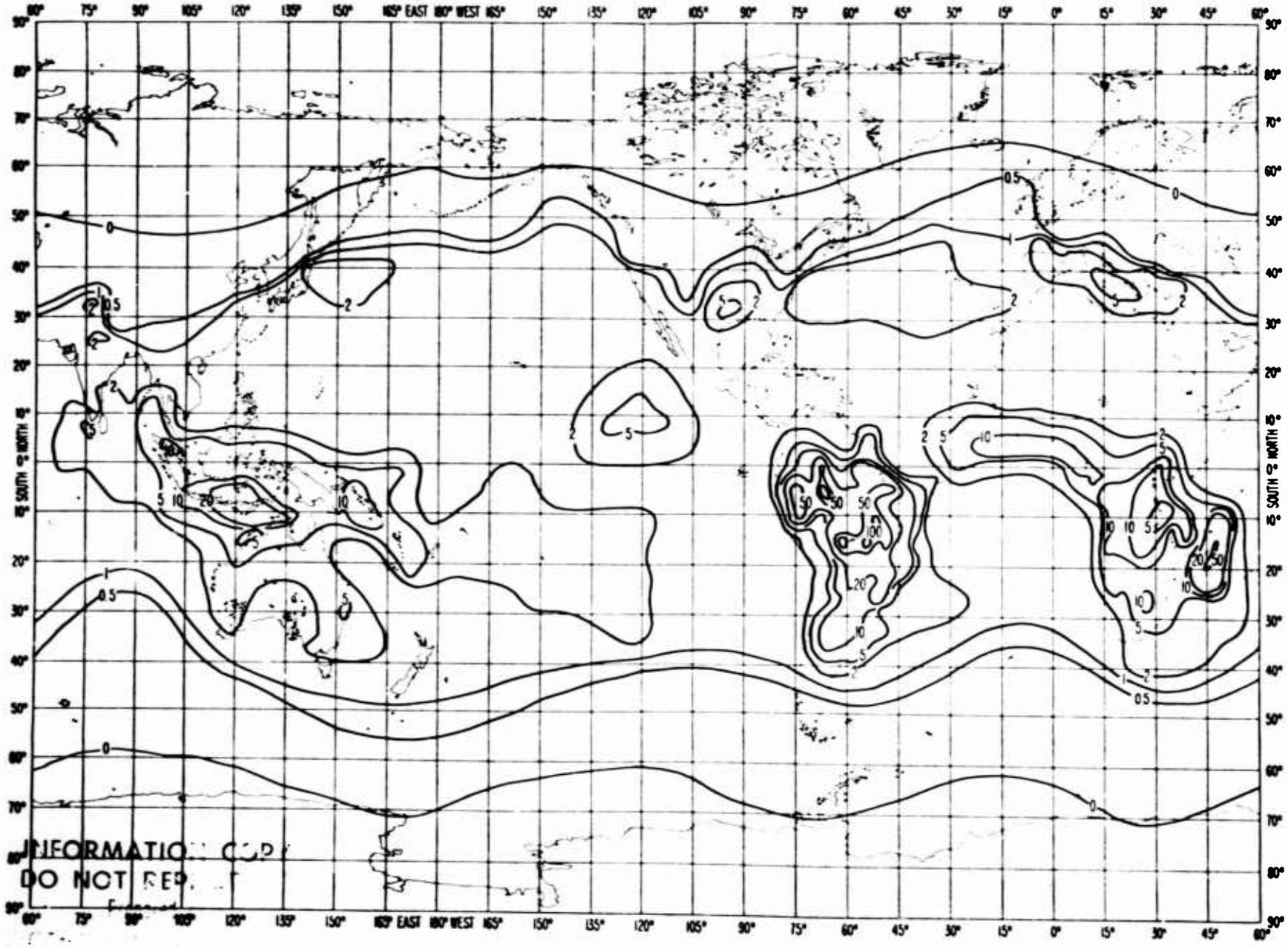

FIGURE 1B

noise arises from the trappings of an industrial civilization; it also is confined to specific geographic areas. The long term noise output from the terrestrial natural sources may be considered to be essentially constant with characteristic diurnal and annual variations (CCIR, 1963)

In addition to noise arising from the three semi-permanent sources a strong origin is found in the Northern Hemisphere. For example: Over North America thunderstorm activity moves northward from the Gulf Coast like a tide (to about 50°N) from spring to late summer. It then recedes to the Gulf of Mexico. Contributions from both sources cause natural noise (as measured in North America) to maximize during summer. The received noise also varies because of propagational factors (Gerson, 1964)

Man-made noise likewise displays its peculiar diurnal and azimuthal variations. The major sources are the industrial areas of the globe. Thus, a site in Ireland would measure more man-made noise to the east (toward Europe) then to the West (toward the Atlantic). The temporal characteristics of man-made noise are related to the human work day, work week and time zone of the source region.

The above illustrations clearly reveal that terrestrial noise originates in particular areas and that the output varies with time. A realistic noise measurement program must determine the noise anisotropy with respect to the operational site. Otherwise noise may not be related to practical HF systems. Most noise observations have been collected with vertical omnidirectional antennas. Contrarily, most existing HF systems employ directive antennas. To provide information useful in designing and operating these systems,

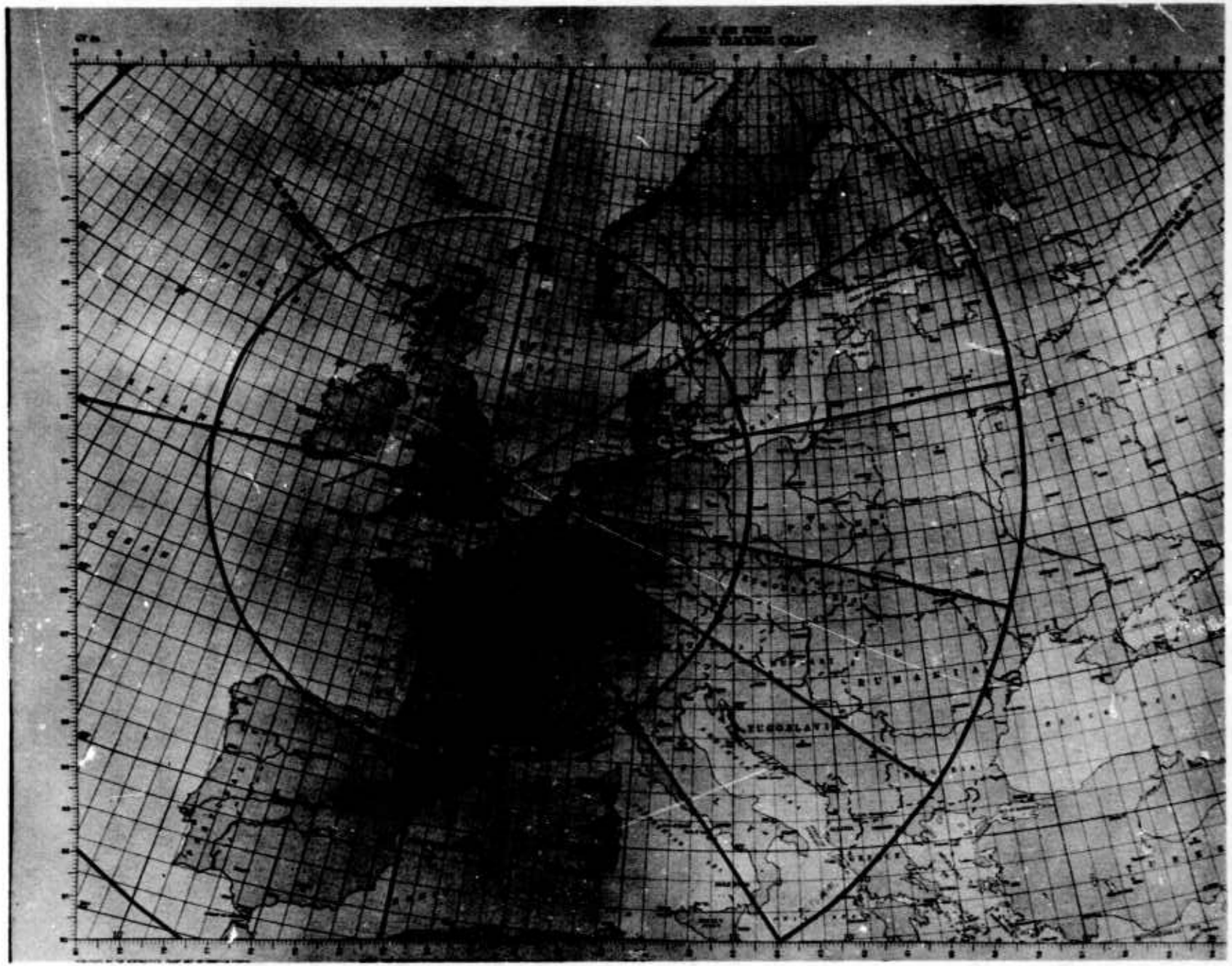

FIGURE 2

statistics on the spatial distribution of the incident noise energy is needed.

At operational or experimental stations, the introduction of unwanted man-made noise or interference through the side lobes may cause considerable system degradation; a factor sometimes forgotten.

This paper presents some measured results on the azimuthal variation of noise.

II. EXPERIMENTAL DETAILS

HF noise was recorded in Southern England between December 1966 - February 1967 (see Figure 2) employing a digitally tuned HF receiver with a bandwidth of 100 Hz. For a given azimuth and frequency the AGC output was sampled every 70 millisec during a 16.8 second period, thus providing a total of 240 samples. The frequency intervals sampled were one MHz in width; only four (i.e., 2-3 MHz, 4-5 MHz, 6-7 MHz and 8-9 MHz) are discussed here. Observations were not necessarily distributed uniformly within any given frequency band; rather they were recorded in a signal free region within the band. The frequency bands were sampled sequentially. During the observations the audio output was continuously monitored to insure that the measurements were being obtained in a noise free region of the band.

Equipment and experimental details are listed in Table I. Eight unequal azimuthal sectors were examined utilizing a sliding azimuthal sampling procedure; e.g., 0°-44° on the first day; 45°-67.4° on the second day; etc. Any instances of interference were noted and eliminated from the subsequent analysis. The data were digitized and stored on magnetic tape. Prior to initiating the measurements, each sampled AGC voltage was referenced to an

TABLE I

EQUIPMENT AND EXPERIMENTAL DETAILS

Receiver	Three digitally tuned HF receivers
Measurement Bandwidth	100 Hz
Frequency Intervals	2-3; 4-5; 6-7; 8-9 MHz
Observation Hours	0030, 0430, 0830, 1230, 1630, 2030 UT
Azimuthal Sectors	$0\text{-}44^{\circ}$, $45\text{-}67.4^{\circ}$, $67.5\text{-}89^{\circ}$, $90\text{-}112.4^{\circ}$, $112.5^{\circ}\text{-}134^{\circ}$, $135\text{-}180^{\circ}$, $180\text{-}269^{\circ}$, $270\text{-}359^{\circ}$.
Sampling Interval	16.8 secs with samples every 70 msec
Total Samples	240
Antenna Type	Circular Disposed Antenna Array

equivalent rms sinusoid at the receiver input.

The calibration process involved sixteen 10 db steps. All noise recordings were corrected by the calibrations using linear interpolations in frequency and voltage. In the statistical analysis, power levels for the 10th, 50th and 90th percentiles were derived and plotted. In a separate study simultaneous noise intensities at various azimuths (as obtained in a series of 20 millisec samples) were recorded.

The choice of a central tendency was carefully considered. Whenever a distribution contains a number of randomly distributed, extremely high values, the arithmetic mean, while mathematically proper, has severe limitations. It is greatly influenced by the extreme values of a distribution whereas the median is little affected. Although not as mathematically precise as the mean, the median can be much more representative. It is often employed in summarizing many types of geophysical observations, and in other instances when a few extreme values are injected into the data.

An example of the noise levels, in terms of both the median and mean, obtained from the same short term sample is depicted in Figure 3. For the data obtained during this period the median provided a more consistent and reproducible central tendency than did the arithmetic mean. In short, as with ionospheric and similar data, the median provides a more meaningful measure of central tendency. Median values will be employed in this paper.

III. SHORT TERM VARIATIONS

As is well known, the ambient noise power displays a high degree of variability especially over relatively short time periods. During this

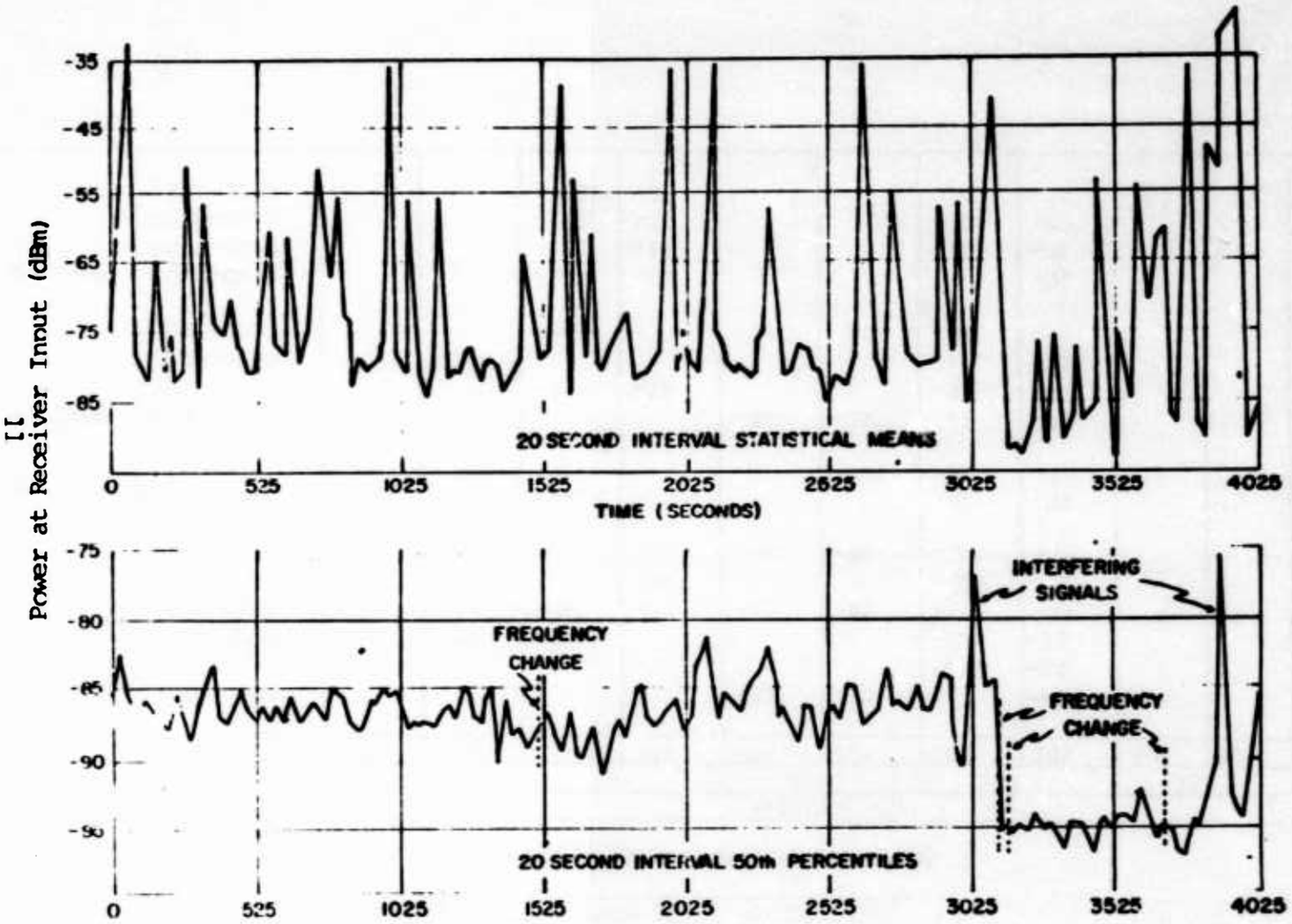
Power at Receiver Input (dBm)
-35
-45
-55
-65
-75
-85
20 SECOND INTERVAL STATISTICAL MEANS
0
525
1025
1525
2025
2525
3025
3525
4025
TIME (SECONDS)
-75
-80
-85
-90
-95
FREQUENCY CHANGE
INTERFERING SIGNALS
FREQUENCY CHANGE
20 SECOND INTERVAL 50th PERCENTILES
0
525
1025
1525
2025
2525
3025
3525
4025

FIGURE 3

TABLE II

SIMULTANEOUS SHORT TERM NOISE INTENSITIES

(3.5 MHz; MEDIAN POWER AT RECEIVER INPUT, dBm)

DATE	HOUR (UT)	AZIMUTH (°)											
		70		100		130		158		218		278	
		50%	90%	50%	90%	50%	90%	50%	90%	50%	90%	50%	90%
Mar 1, 1966	0000-0010					-89	-77	-101	-81				
	0010-0120			-92	-81			-103	-84				
	0020-0030	-89	-79					-104	-83				
	0030-0035			-89	-77	-90	-83	-103	-83				
	0035-0040	-97	-80	-90	-76			-103	-81				
	0040-0045	-97	-80			-85	-76	-100	-83				
Mar 3, 1966	0033-0040	-91	-83	-93	-79			-81	-79				
	0040-0045	-96	-87			-98	-79	-99	-81				
Mar 4, 1966	0000-0010					-84	-59	-91	-73				
	0010-0020			-91	-76			-99	-77				
	0020-0030	-89	-79					-101	-82				
	0030-0035			-88	-77	-98	-83	-99	-79				
Mar 6, 1966	0000-0010			-103	-83			-106	-89			-104	-93
	0010-0020			-105	-85			-106	-86	-92	-73		
	0020-0025			-103	-86			-106	-87			-104	-93
	0025-0030			-101	-81			-106	-87	-89	-73		

experiment simultaneous measurements revealed that instantaneous and median values differ along distinct azimuthal sectors. This sharp variability from one sector to another indicates a high lack of correlation among noise propagating over different azimuthal sectors.

A portion of the results is tabulated in Table II. Samples were obtained every 20 ms. Figure 3 indicates that although marked short term fluctuations are present, a useful central tendency is represented by the median.

IV. AZIMUTHAL VARIATIONS

Figures 4-7 represent the azimuthal and temporal variations of median noise intensities for the one MHz frequency intervals beginning at 2, 4, 6 and 8 MHz, respectively, during the winter of 1966-67. Large differences in intensity along particular azimuthal sectors are evident. Further, the time variation of noise within given sectors is not the same.

The data reveal that at the lower frequencies examined, highest intensities occur at night and lowest during daylight. The reverse condition is found for the higher frequencies.

V. TERRESTRIAL NATURAL NOISE MODEL

Since the major source of atmospheric noise arises from thunderstorms, a model may be developed based upon (a) the diurnal variation of thunderstorm activity over the globe and (b) the diurnal variation in radio wave propagation characteristics from the noise source to the receiver. This model was first presented by Materazzi (1968). The model considers only natural noise emitted within 4200 km of the antenna.

The temporal variations of noise may be clarified by considering the changes

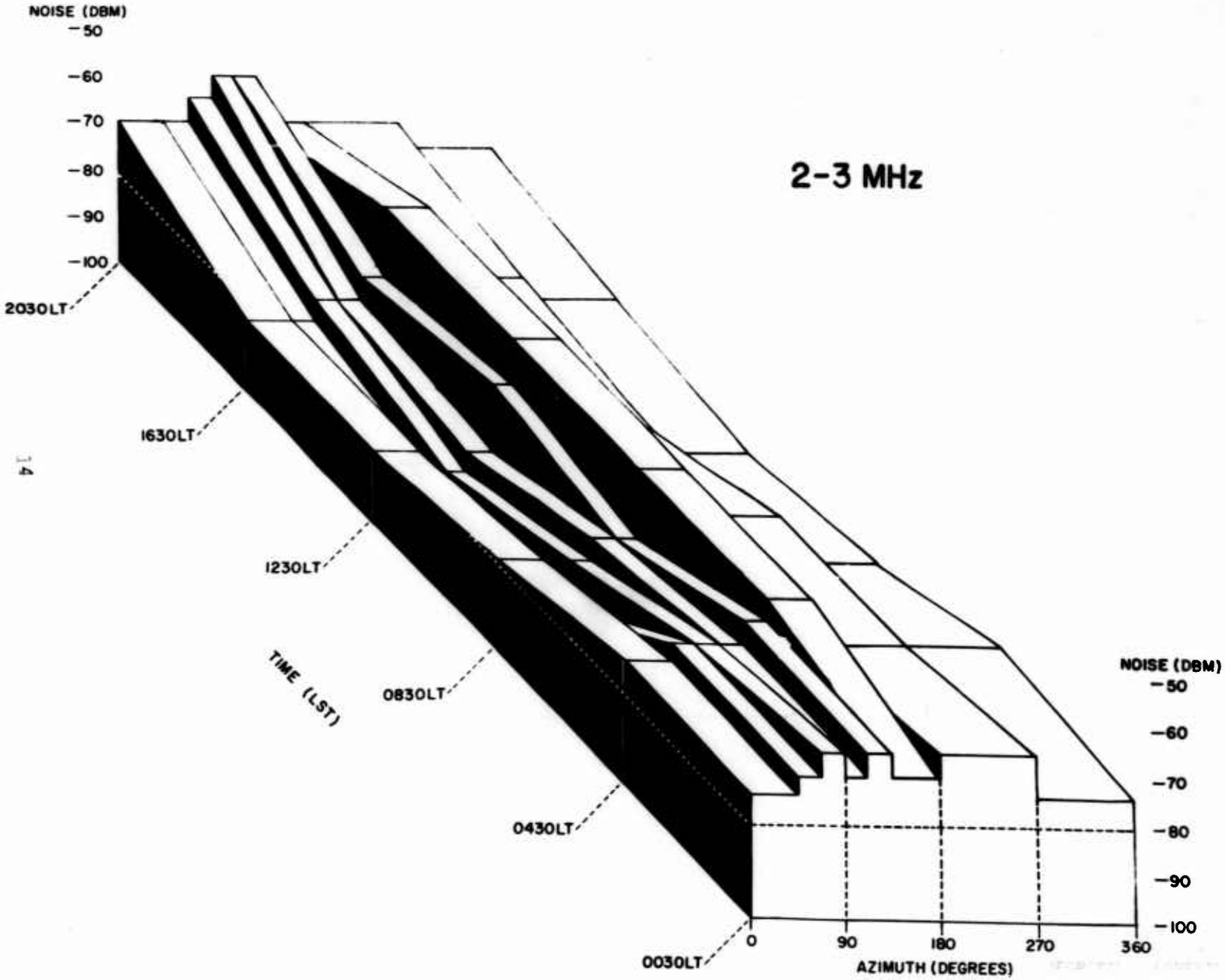
NOISE (DBM)
-50
-60
-70
-80
-90
-100
2-3 MHz
2030LT
1630LT
1230LT
0830LT
0430LT
0030LT
TIME (LST)
NOISE (DBM)
-50
-60
-70
-80
-90
-100
0
90
180
270
360
AZIMUTH (DEGREES)

FIGURE 4

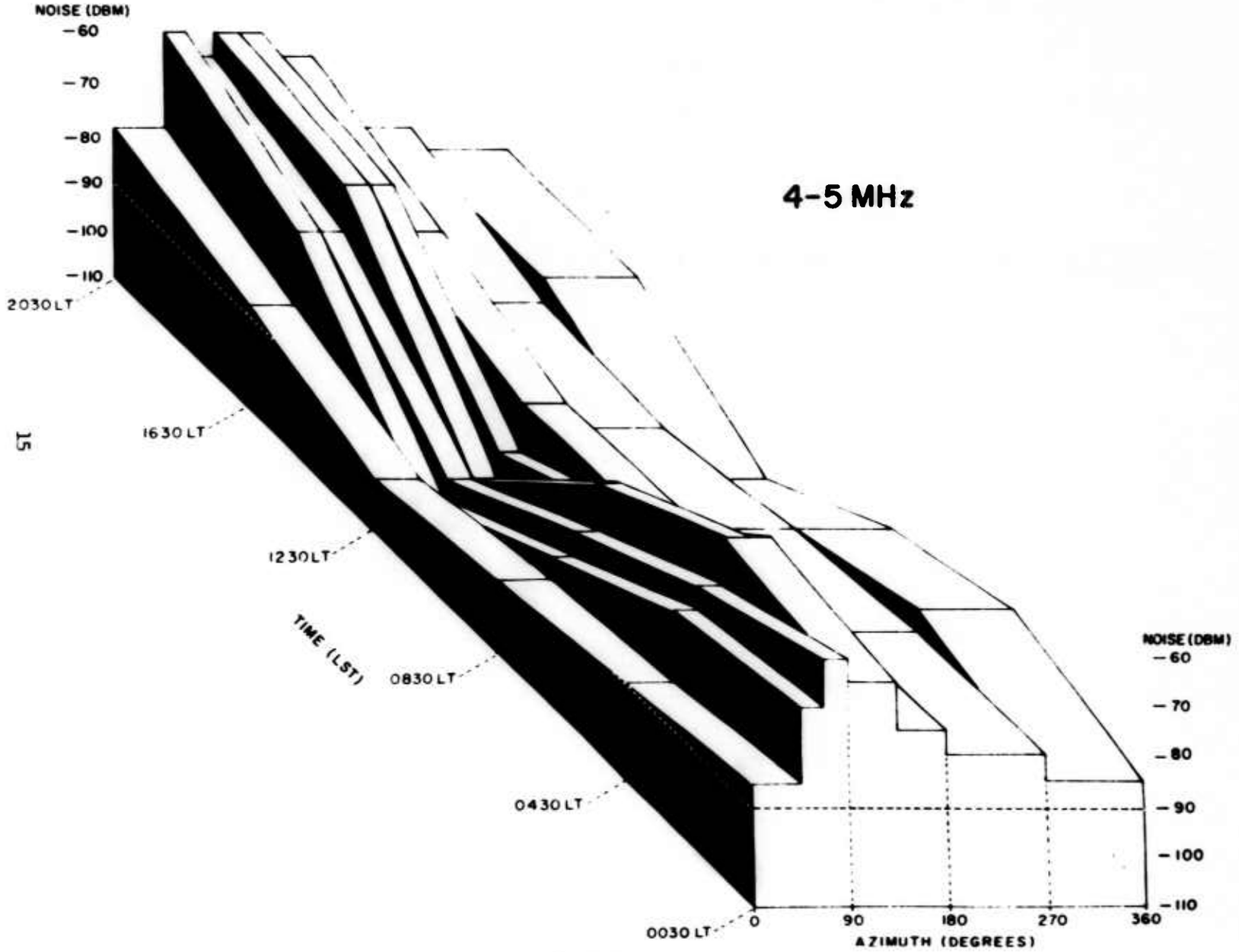
NOISE (DBM)
-60
-70
-80
-90
-100
-110
2030 LT
1630 LT
1230 LT
TIME (LST)
0830 LT
0430 LT
0030 LT
4-5 MHz
NOISE (DBM)
-60
-70
-80
-90
-100
-110
0
90
180
270
360
AZIMUTH (DEGREES)

FIGURE 5

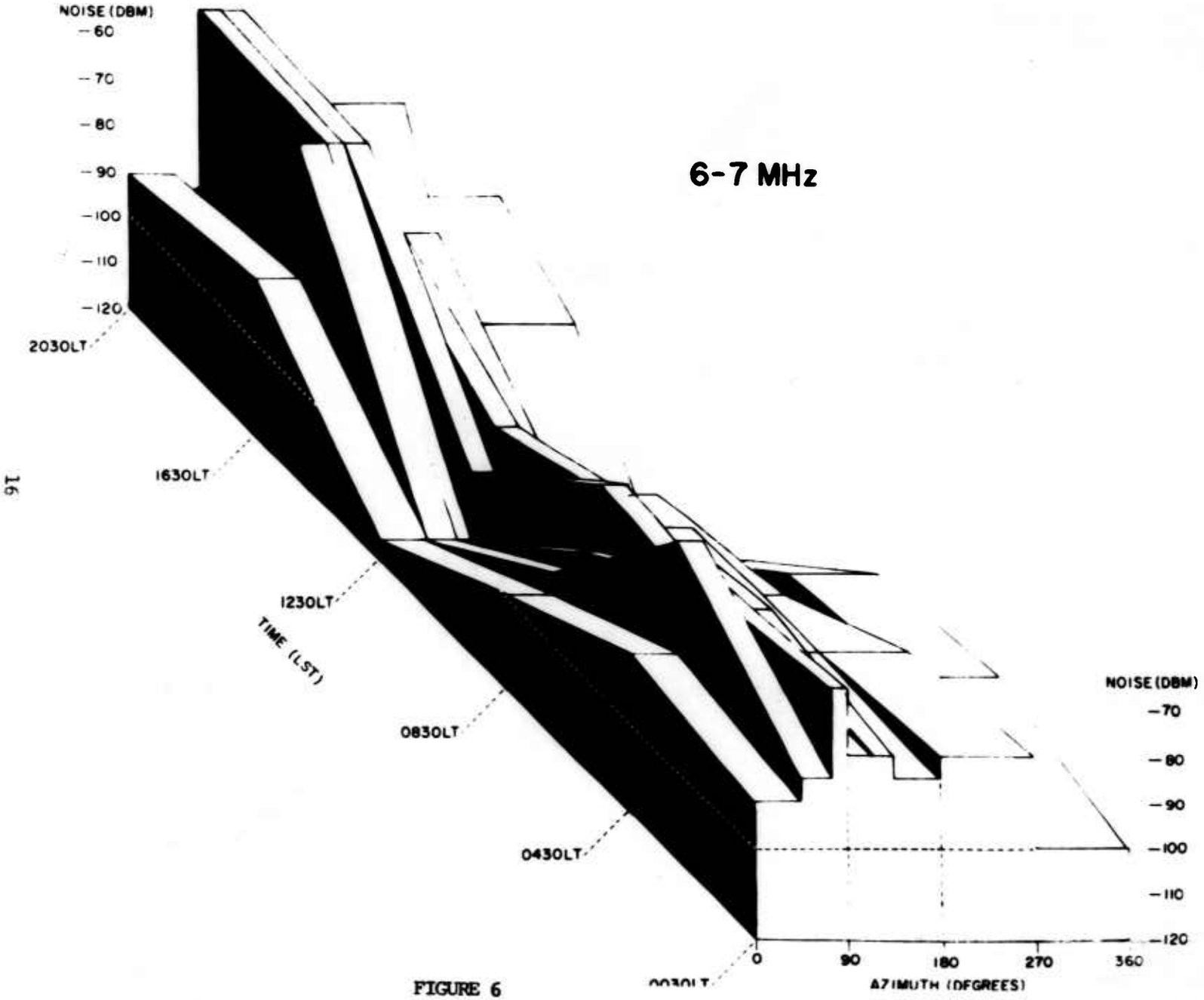
6-7 MHz
NOISE (DBM)
-60
-70
-80
-90
-100
-110
-120
2030LT
1630LT
1230LT
0830LT
0430LT
0030LT
TIME (LST)
NOISE (DBM)
-70
-80
-90
-100
-110
-120
0
90
180
270
360
AZIMUTH (DEGREES)

FIGURE 6

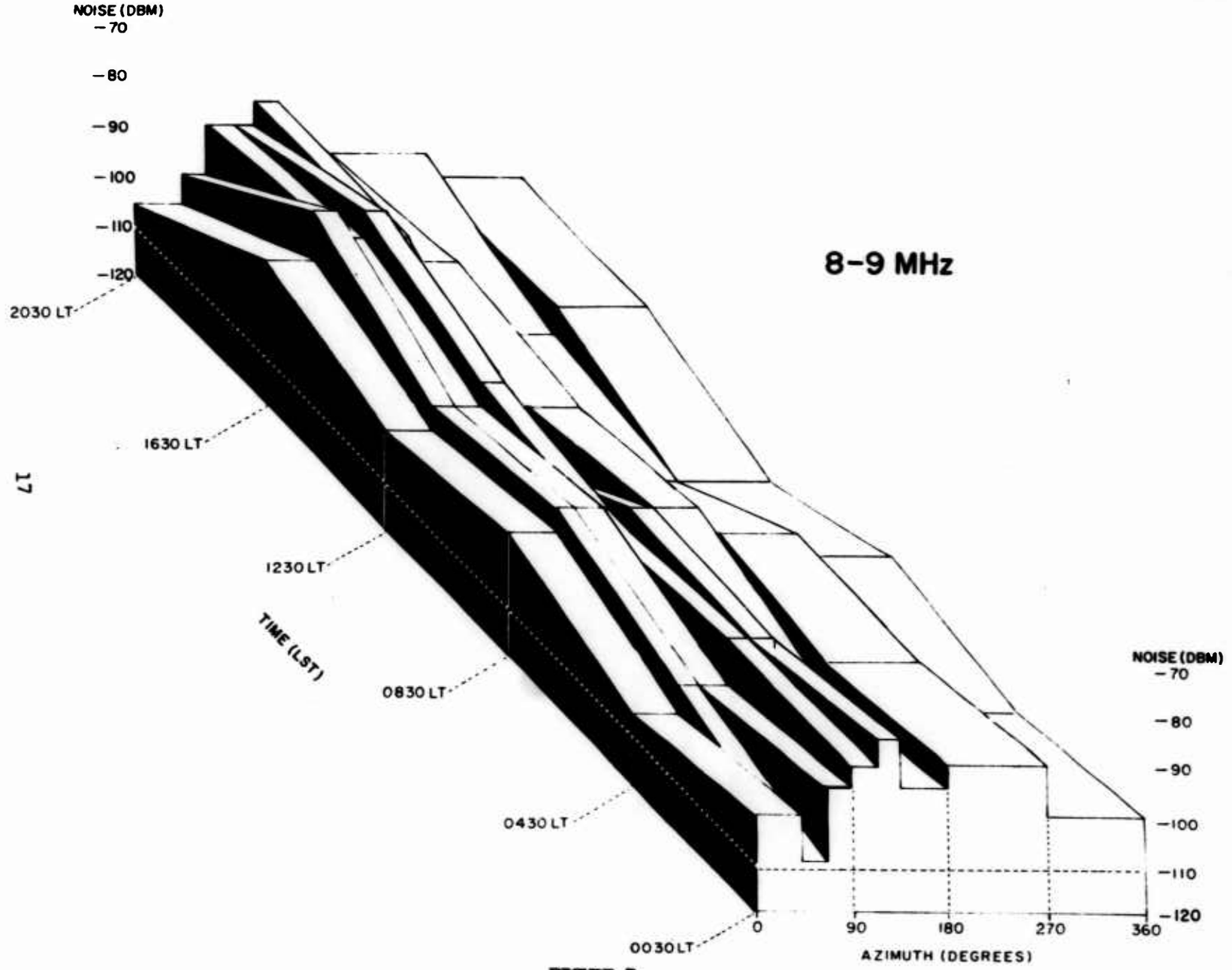
NOISE (DBM)
-70
-80
-90
-100
-110
-120
2030 LT
1630 LT
1230 LT
0830 LT
0430 LT
0030 LT
LT
TIME (LST)
8-9 MHz
NOISE (DBM)
-70
-80
-90
-100
-110
-120
0
90
180
270
360
AZIMUTH (DEGREES)

FIGURE 7

with time in (a) the number of noise emissions, (b) the location of the sources and (c) the propagation characteristics of the ionosphere. The general behavior of the ionosphere is such as to favor propagation of the lower frequencies ($\leq$ 8 MHz) over nocturnal paths, and of the higher frequencies ($\geq$ 15 MHz) over daytime paths. This selectivity results from the greater absorption of the lower frequencies in the sunlit ionosphere and the lack of support of the higher frequencies by the dark ionosphere. Diurnally, the radiated output of the semi-permanent noise sources maximizes in late afternoon and minimizes between 0200-0600, LST. The behavior stems directly from the diurnal variation in thunderstorm activity (see Figure 1). It is assumed that the spectral power density of the noise output is constant. Although the observations were made in winter, continental thunderstorm activity at lower latitudes of Europe constituted another, but rather minor, source of natural noise.

For the computations, the area within 4200 km of the receiving site was divided into equal angular sectors of fixed range; i.e., Δr-$\Delta\theta$ sectors where $\Delta r = 700$km and $\Delta\theta = 22.5^{\circ}$, as measured from the receiving antenna. This division provided 16 azimuthal sectors beginning at 0° and 6 annuli each 700 km in thickness. The corresponding ground locations of each $\Delta r - \Delta\theta$ segment were obtained from the usual equations of spherical trigonometry, and plotted on the set of hourly maps of thunderstorm activity.

The relative power emitted from any given $\Delta r - \Delta\theta$ segment was assumed to be proportional to the thunderstorm activity within the area; i.e.,

$$N_i = a \int p_i \, dS_i \qquad (1)$$

where

N_i = noise power emitted from area S_i

p_i = probability of thunderstorm occurence within the area S_i

$\int dS_i = \iint dr_i d\theta_i$ = elemental area contained with $\Delta r_i \, \Delta \theta_i$

and, a = constant of proportionality.

The value (ap_i) was scaled directly from the world maps of thunderstorm activity (e.g., see figure 1) for each hour of the day.

The ITS Ionospheric Prediction Program was utilized to compute the path loss (for the frequencies of interest) from the center of the segment $\Delta r_i \, \Delta \, \theta_i$ to the receiver. The power arriving from each segment within a given azimuthal sector was summed to provide the relative noise power for that sector. The predicted noise as a function of frequency, hour and azimuth is shown in Figures 8-11. It displays distinct diurnal and azimuthal variations.

The Figures reveal that for a given frequency the azimuth of peak intensity shifts with time of day. Since both thunderstorm activity and the frequency support of the ionosphere vary with hour, this result is not suprising. The highest amplitude tends to shift clockwise with hour, and the extent of the azimuthal differences in intensity increases with frequency. As noted above, the diurnal noise variation for the lower and higher frequencies is out of phase.

VI. COMPARISON: MEASUREMENTS VS MODEL

A comparison of the measured and calculated results may be undertaken by comparing Figures 4 and 8, 5 and 9, etc. For the lower frequencies lowest

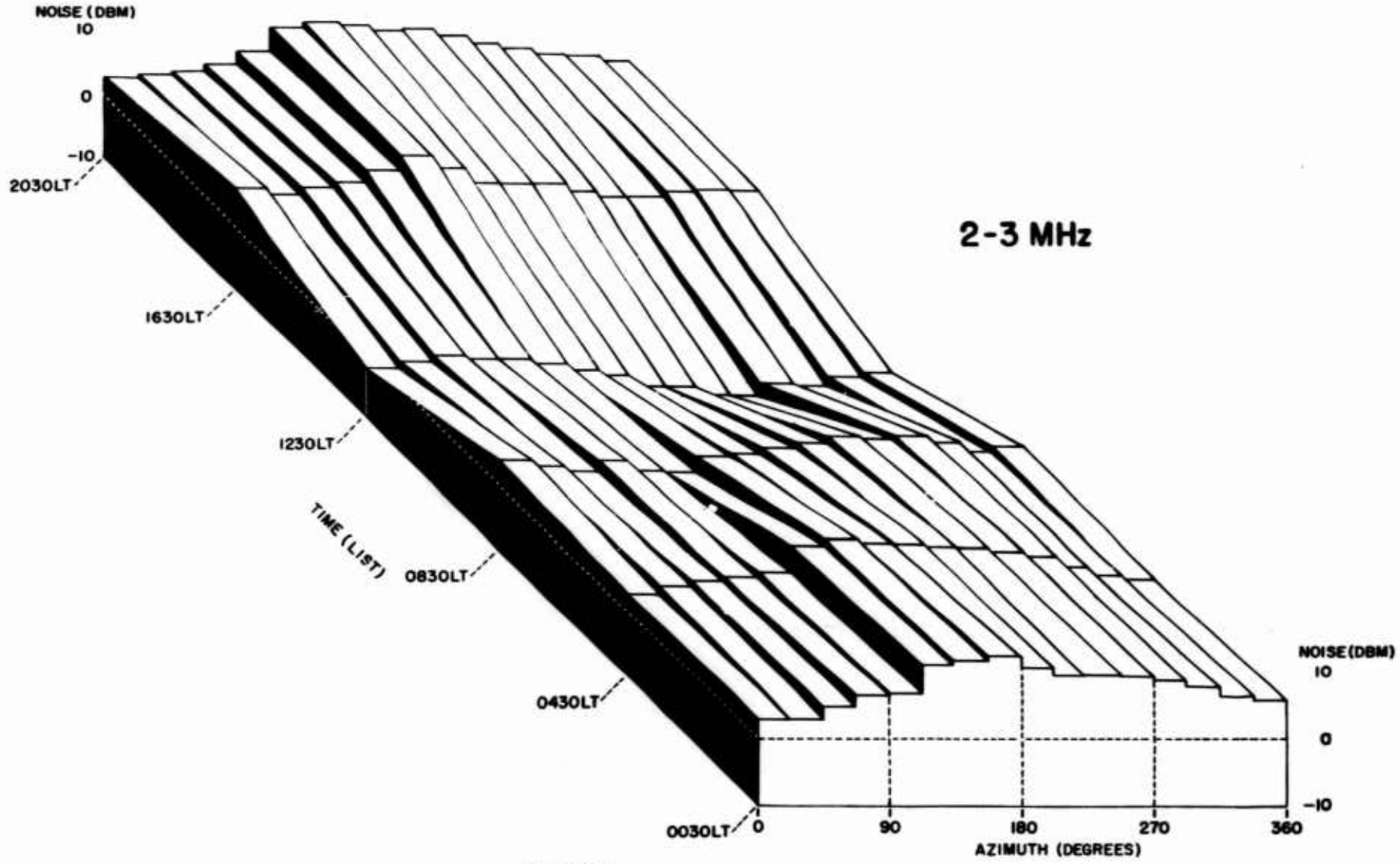
NOISE (DBM)
10
0
-10
2030LT
1630LT
1230LT
TIME (LIST)
0830LT
0430LT
0030LT
2-3 MHz
NOISE (DBM)
10
0
-10
0
90
180
270
360
AZIMUTH (DEGREES)

FIGURE 8

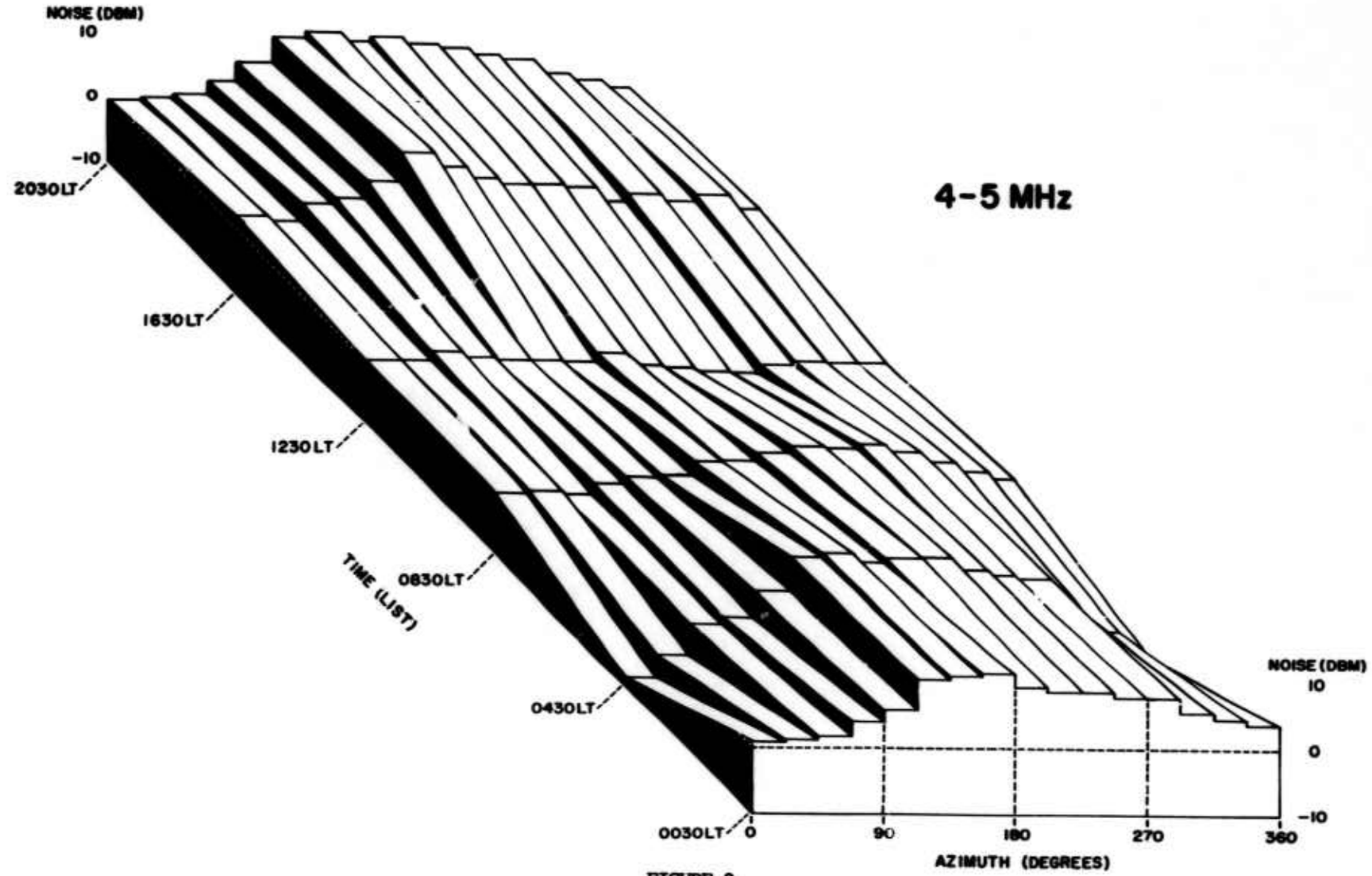
NOISE (DBM)
10
0
-10
2030LT
4-5 MHz
1630LT
1230LT
TIME (LIST)
0830LT
0430LT
0030LT
NOISE (DBM)
10
0
-10
0
90
180
270
360
AZIMUTH (DEGREES)

FIGURE 9

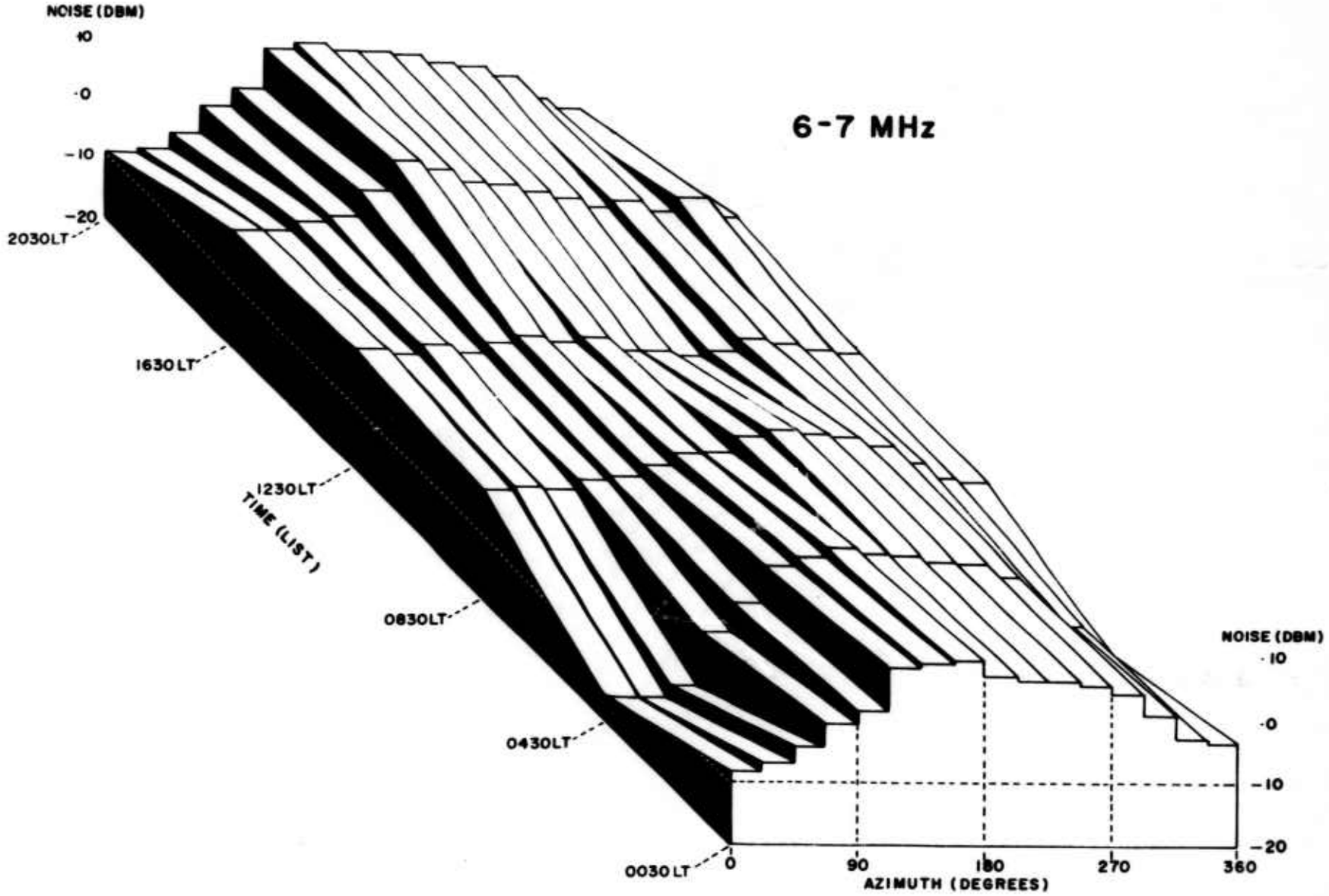
NOISE (DBM)
+10
-0
-10
-20
2030LT
1630LT
1230LT
TIME (LIST)
0830LT
0430LT
0030LT
6-7 MHz
NOISE (DBM)
-10
-0
-10
-20
0
90
180
270
360
AZIMUTH (DEGREES)

FIGURE 10

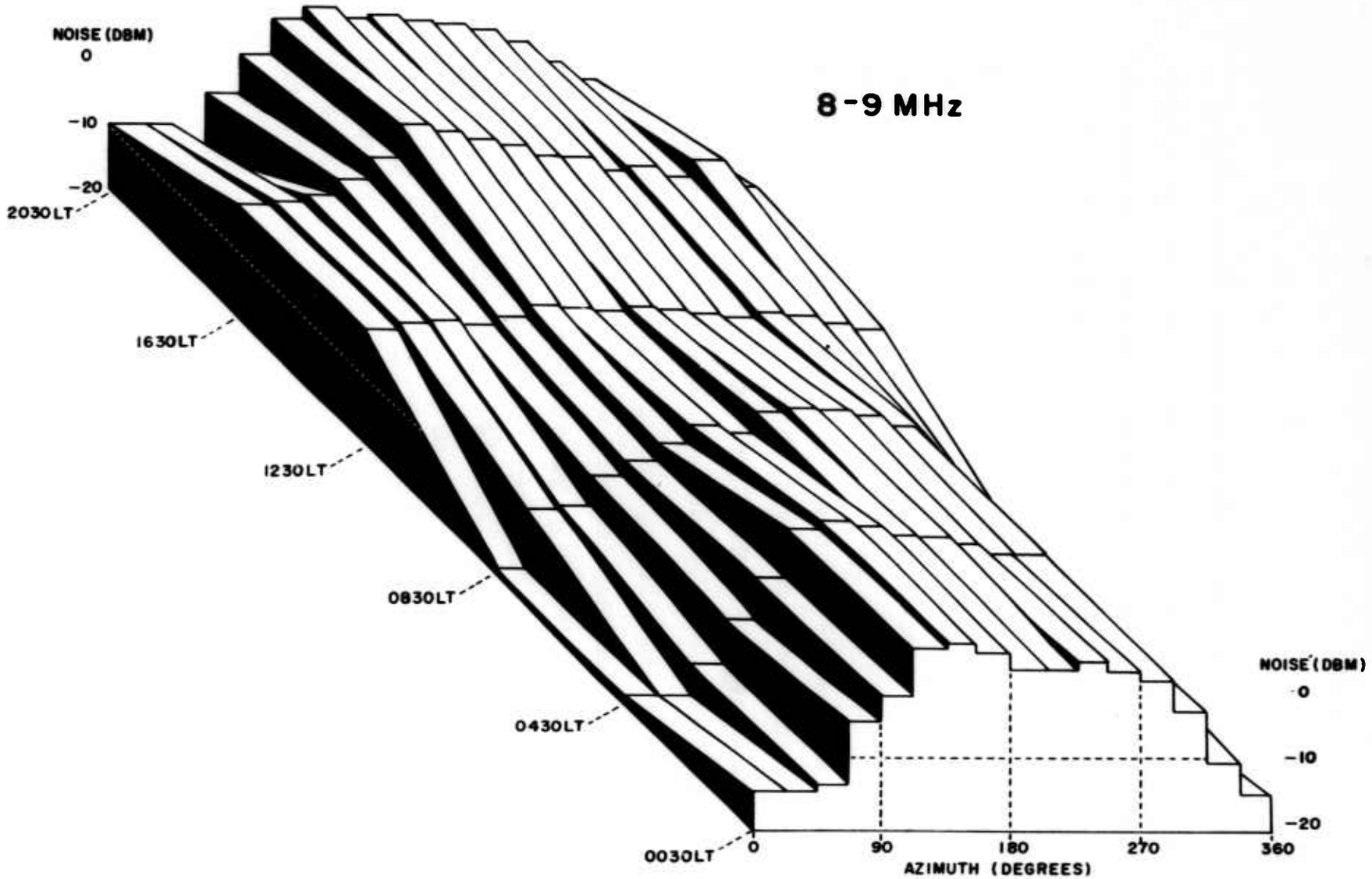
8-9 MHz
NOISE (DBM)
0
-10
-20
2030LT
1630LT
1230LT
0830LT
0430LT
0030LT
NOISE (DBM)
0
-10
-20
0
90
180
270
360
AZIMUTH (DEGREES)

FIGURE 11

amplitudes occur, as expected, during midday and highest during darkness (2030-0030 UT). In general, for a given frequency a shift in peak amplitude occurs with azimuth, but the shift is more clearly defined in the calculated than measured curves. The range of amplitudes in the observed data exceeds that found for the model.

The discrepancy between the measured and calculated values may arise from several sources. For example, the model was based on long term averages of thunderstorm activity, whereas during any particular month or day wide departures from the average may occur. The possibility of local thunderstorms in winter is small, but nontheless some may have been present within 4200 km of the receiving site. A strong possible source for the disagreement may arise from the neglect of man-made noise. The extent of this source may be visualized by examining Figure 12, which indicates the population density over Europe. To a first approximation the industrial growth of Europe may be considered to be directly related to the population density.

A factor of importance, which may be appreciable on some occasions, is the entry of noise into the receiving system through an antenna side lobe. Thus, a local storm, local man-made noise or propagated man-made noise occurring within a given sector may greatly increase the noise input into the receiver. It is believed that all the above factors in combination contributed to the disagreement between the predicted and observed azimuthal noise distributions.

On an overall basis the calculated results compare favorably with the experimental data during darkness and at the lower frequencies. Less favorable agreement is found at the higher frequencies.

VII. EFFECT OF ANTENNA

It should be noted that the azimuthal distribution of noise as measured has been influenced by the antenna pattern. The antenna utilized in the measurement,

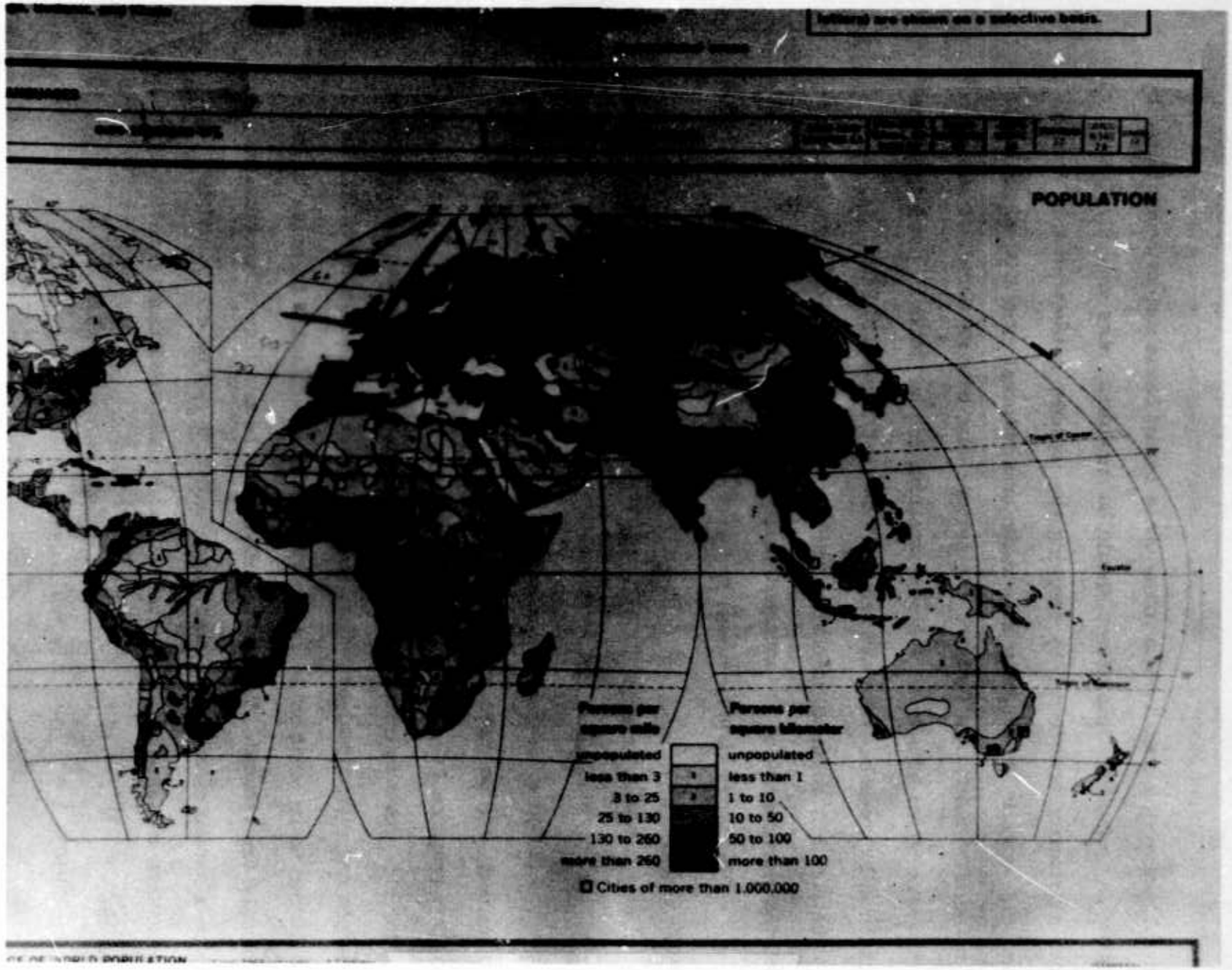
POPULATION
Persons per square mile
unpopulated
less than 3
3 to 25
25 to 130
130 to 260
more than 260
Persons per square kilometer
unpopulated
less than 1
1 to 10
10 to 50
50 to 100
more than 100
Cities of more than 1,000,000

FIGURE 12

was a Circular Disposed Antenna Array whose formed beams can be approximated by a (sinx)/x pattern. This effect should be considered more carefully, especially since all data were obtained by sampling the incident noise with this formed beam. In essence, to properly assess the true external azimuthal distribution of noise the smoothing effects of the antenna must be considered. Discussions on the theory and effects of antenna smoothing can be found in the literature particularly those on radio astronomy (Pawsey - Bracewell, 1955)

The incident noise distribution may be approximated as follows. Assume that the measurement of the external noise may be described as,

$$P(\theta,\phi) = (1/b) \iint h(\bar{\theta},\bar{\phi})\, n\,(\theta,\bar{\theta};\phi,\bar{\phi})\; d\bar{\theta}\; d\bar{\phi} \qquad (2)$$

where

θ = azimuth

ϕ = elevation

$n(\theta,\phi)$ = desired input spatial distribution of noise . The latter is assumed to be convolved with the spatial filter $h(\theta,\phi)$ to yield the measured response $P(\theta,\phi)$.

For the present discussion the above equation will be examined in terms of a simple one dimensional azimuthal model. The azimuthal variation will be considered to be periodic in 2π and the vertical variation of noise to be uniformly distributed. The spatial filter may be a (sinx)/x function, or may be a series of arbitrary step functions which may be considered to approximate the antenna lobe pattern. Under these conditions equation (2) becomes:

$$P(\theta) = \int h(\bar{\theta})\; n(\theta - \bar{\theta})\; d\bar{\theta} \qquad (3)$$

If equation (3) can be written as a Fourier Series:

$$P(\theta) = C_o + \sum_{n=1}^{\infty} (C_n \cos n\theta + d_n \sin n\theta) \tag{4}$$

$$n(\theta) = e_o + \sum_{m=1}^{\infty} (a_m \cos m\theta + b_m \sin m\theta) \tag{5}$$

$$h(\theta) = e_o + \sum_{q=1}^{\infty} e_q \cos q\theta \tag{6}$$

Assume further that $h(\theta)$ is symmetrical. Insert equations (5) and (6) into equation (3), yielding

$$P(\theta) = \int_{-\pi}^{\pi} \left(e_o + \Sigma\, e_q \cos \theta \{ a_o + \Sigma \left[a_m \cos m(\theta - \bar{\theta}) + \right. \right.$$

$$\left. \left. + b_m \sin m(\theta - \bar{\theta}) \right] \} \right) d\bar{\theta}$$

Performing the integration gives

$$P(\theta) = 2\pi e_o a_o + \pi \sum_{n=1}^{\infty} (e_n a_n \cos n\theta + e_n b_n \sin n\theta). \tag{7}$$

Equating equation (7) to equation (4) and equating coefficients yields:

$$a_o = C_o / 2\pi e_o, \tag{8}$$

$$a_m = C_n / \pi e_n,$$

$$b_n = d_n / \pi e_n.$$

Inserting the coefficients given in (8) into equation (5) provides a Fourier Series representation of the desired distribution $n(\theta)$. It should be noted that this representation is not unique and that the procedure is valid only for those values of $e_n = d$. This is analogous to the response of a low pass filter in which an infinite number of inputs having frequency components greater than the cutoff frequency of the filter can yield the same response (Pawsey and Bracewell, 1955)

VIII. CONCLUSIONS

All useful reception depends upon the value of the ratio signal/noise. Since the incident noise intensity varies spatially, the magnitude of the ratio may be increased by a suitable choice of receiving site vis-a-vis a given transmitter, other factors remaining equal.

REFERENCES

CCIR, 1963, World Distribution and Characteristic of Atmospheric Noise, Xth Plenary, Assembly, Consultive Comm Int Radio, Rept No. 322, Geneva.

Gerson, N.C., 1964, Polar Noise, J Atmo Terr Phys.

Materrazzi, D. J., 1968, HF Azimuthal Noise Variations, MS thesis in EE, Catholic University, Washington.

Pawsey, J. and Braceswell, R., 1955, Radio Astronomy, Oxford University, Press, NY, NY.

9.2 Unusual Radio Noise Sources in Direction Finding and High Frequency Receiving Systems

Calvin R. Graf
USAF SS
San Antonio, Texas

Abstract

Radiation from high power HF transmitters can be reradiated as noise due to diode rectifier action in lossy grounds or loose connections of a receiving or direction finding antenna system. Reradiation of strong signals as noise from lossy metallic objects due to diode action is believed to take place in most transmitting and receiving systems throughout the world. In sensitive HF receiving systems, this reradiated noise may actually limit the small signal sensitivity level, especially during the daytime hours when atmospheric noise levels are at a minimum. Unintended, spurious emissions from many HF stations, which raise the noise floor level, are discussed. An audio tape recording of representative types of signals and noise will be played.

AZIMUTHAL DISTRIBUTION AND CHARACTERISTIC PROPERTIES OF AMBIENT NOISE AT HF

A. S. Weeks*

AVCO SYSTEMS DIVISION
Lowell, Massachusetts 01851

ABSTRACT

Azimuthal measurements of noise in the HF band have been conducted using the Wullenweber array at the University of Illinois. The data has been analyzed to illustrate the following; the amplitude distribution as a function of direction, the effect of averaging the data, and the amplitude variation as a function of time. The effects of the ionosphere on HF propagation have been employed to explain both temporal and spatial variations in the noise data.

---

*Formerly with the University of Illinois Radiolocation Research Laboratory, Urbana, Illinois

1.0 INTRODUCTION

This paper reports on preliminary efforts to use a Wullenweber array in a study of the directional characteristics of received noise in the HF band. The work was done at the University of Illinois. A limited amount of data has been analyzed to show the importance of investigating azimuthal properties of the noise and to account for certain variations of the data as a function of time and/or direction.

Investigations of noise in the HF band have been conducted for some time. The most notable being work done by W. Crichlow and R. Disney who reported their findings in CCIR322. Equipment constraints and lack of a real need for directional studies have led previous investigators to make omnidirectional measurements (as was the study ending in CCIR322). Omnidirectional measurements, by their nature, integrate over any directional effects tending to eliminate them. Also, it has been the practice of most investigations to use time averaging techniques further reducing the effect of directional properties. The application of the results of a study such as CCIR322 in designing HF communications systems seem to be adequate. It is the purpose of this study to show that for HF systems using highly directional antennas, measurements of the azimuthal characteristics of noise are required to fully understand the interaction between noise and the HF system. The purpose of this paper is to illustrate the nature of the noise on an azimuthal basis and to compare the results of averaging the data and the results before averaging.

2.0 DATA ACQUISITION

To measure background noise, time and frequency slots in the high frequency spectrum had to be found that did not contain transmitted signals. This could be done for short periods and only with an observer available. But, with the volume of data needed, this was not practical. An obvious solution was to conduct the experiment on an automatic basis in slots of the spectrum that were reliably free of transmitted signals. The WWV transmissions on 5, 10, 15 and 20 MHz are off four minutes each hour beginning at 45:15 after the hour. Using the guard bands and off times of WWV noise measurements were made in twelve sectors spaced 30° apart and each sector sampled for sixteen seconds. The sector width is determined by the 3db beamwidth of the array. For the frequencies of interest here, this is approximately 6-8 degrees. Figure 1 is a block diagram of the data collection system. Digital conversion of the data was performed and computer methods used to analyze and reduce the data.

The frequency used in the experimental results presented in this paper was 10.004 MHz and the time was from 1645 (CST) 11 December 1970 to 0745 on 13 December 1970.

3.0 DATA ANALYSIS

The average noise amplitude was determined from the data collected for each hour. Following the lines of previous investigators the data were grouped into six time blocks per diurnal period and a composite average over two diurnal periods for each block was obtained. The results are given in Figure 2. Note that the azimuthal distribution of the amplitude

does not vary significantly by more than 6 db. This 6 db figure was predicted by CCIR322. Figure 3a and 3b present the hourly distribution of noise. The average hourly value for each sector has been plotted versus the corresponding sector. From these it can be seen that the variation in amplitude is significantly greater than what would be expected from average values.

Figure 4 is a plot of the average amplitude versus time. Variations in the hourly amplitudes require a departure from the usual averaging techniques and to consider the amplitude on an instantaneous basis to explain the characteristic seen in Figure 4. Since the noise may come from any part of the sector being observed, consider the noise sources as being distributed throughout the sector. If the noise sources are uncorrelated the amplitude observed will be the sum of the amplitude of the individual sources. Therefore, a decrease in the measured noise amplitude may be the result of a decrease in sources (i.e., thunderstorms) or the result of the ionosphere no longer supporting propagation from part of the sector. The question of which of the two choices is correct is a fundamental one if a predictive model of expected noise for a sector is to be generated. The latter choice was pursued in further analysis of the data. In this pursuit skip distance, MUF, and absorption effects were considered in an effort to determine if areas of the sector under observation were not able to contribute to the recorded noise level.

The analysis considered each sector as encompassing an area

determined by the beamwidth mentioned above and having an 8000 km two hop length. Using the ESSA predicted mean value of MUF for a 4000 km path during December 1970, the minimum MUF for each sector was determined at two hour intervals and plotted on the same time scale as the average hourly noise amplitude. Also, using vertical ionograms made at the receiver site during the time of the experiment and assuming a plane earth plane ionosphere approximation, the skip distance was determined as a function of time and plotted on the same scale as the average amplitude and minimum MUF. Figure 5 gives the results for four of the twelve sectors. The decrease in noise amplitude at approximately 2300 is seen to correspond to periods when the minimum MUF is at or below 10 MHz. That the curves do not match exactly may be the result of using median values rathen than actual values of the minimum MUF. This decrease in amplitude is characteristic of all twelve sectors as shown in Figure 4. The skip distance effect can be seen in Figure 5 as a continued decrease in noise amplitude after the minimum MUF has increased above 10MHz near 0300, 13 December in sectors 1 and 4. Sectors 7 and 10 indicate that an increase in skip distance does not cause a corresponding decrease in amplitude, possibly due to the major sources being located outside of the skip distance. All of the sectors indicate no relationship between skip distance and amplitude on December 12. This may be the result of a local disturbance. The significant decrease in noise during the day can be attributed to non-deviative absorption in the D layer. Careful analysis of Figure 4 indicates a more rapid decrease

in amplitude for sectors to the sunrise side of the receiving site than for sectors 180 degrees away. Recombination in the D region is rapid, therefore, the ionization density and the resulting absorption varies in synchronism with the elevation of the sun.

In the preceding analysis only ionospheric effects were considered in explaining the variations in noise level as a function of time. A complete analysis of the noise data would require a knowledge of source variation with time and direction. Figures 3a and 3b indicate significant difference in noise amplitude for the early evening hours of 11 December and late morning hours of 12 December and to a lesser extreme in the evening hours of 12 December and morning hours of 13 December. The reason for this may be ionospheric effects and/or source conditions. For a complete understanding of the noise characteristics both will have to be considered.

4.0 SUMMARY

For the limited amount of data analyzed here averaging techniques are not sufficient to allow an understanding of the noise properties. It is realized that with the analysis of a larger amount of data the characteristics of the noise may become more evident. The results of this analysis indicate a dependency on ionosphere conditions.

In designing HF communication system using directive antennas either an actual knowledge of the noise environment at the site is needed or some predictive model be employed to determine the design

constraints. Further, if the system already exists, then it may be desirable to make short-term predictions of direction and times for optimum efficiency. From the limited amount of data analyzed here, it seems evident that a thorough knowledge of noise sources and ionospheric effects are required for a predictive model. For short-term predictions (hours) knowledge of the ionosphere may be sufficient while for long-term predictions (months) knowledge of source variations and ionosphere characteristic may be required.

LIST OF ILLUSTRATIONS

Figure 1. Data Collection System

Figure 2. Average Distribution

Figure 3a. Hourly Distribution, 1645, 11 December 1970 - 1545, 12 December 1970

Figure 3b. Hourly Distribution, 1645, 12 December 1970 - 0745, 13 December 1970

Figure 4. Hourly Amplitude

Figure 5. Skip Distance and Minimum MUF

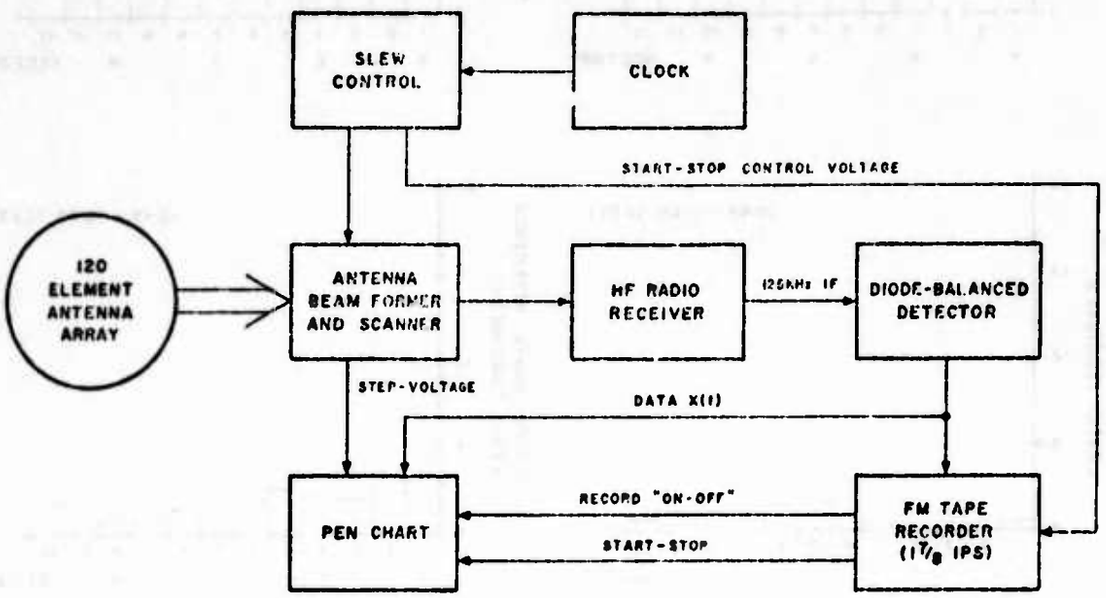

FICURE 1. DATA COLLECTION SYSTEM

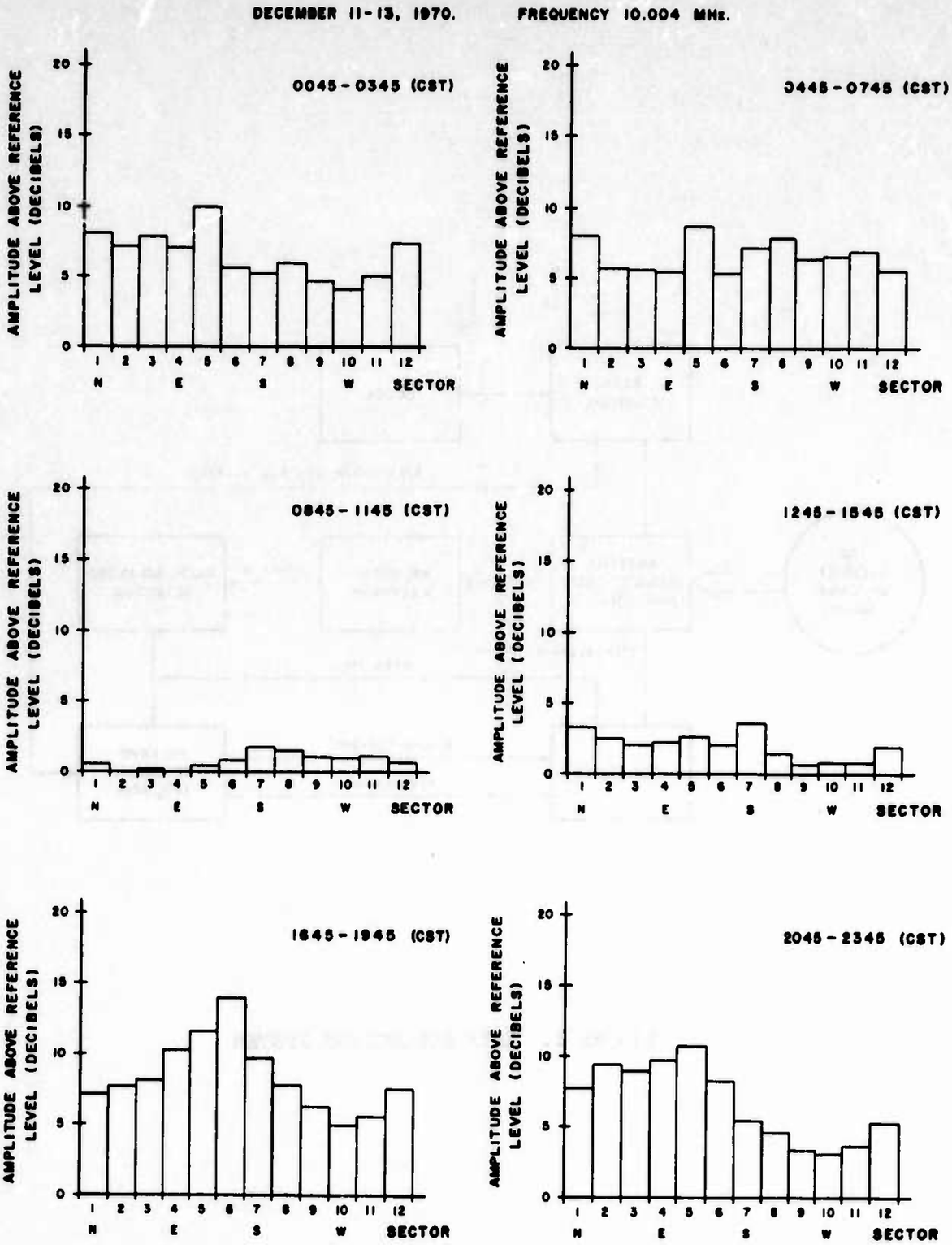

FIGURE 2. SECTOR AVERAGE AMPLITUDE

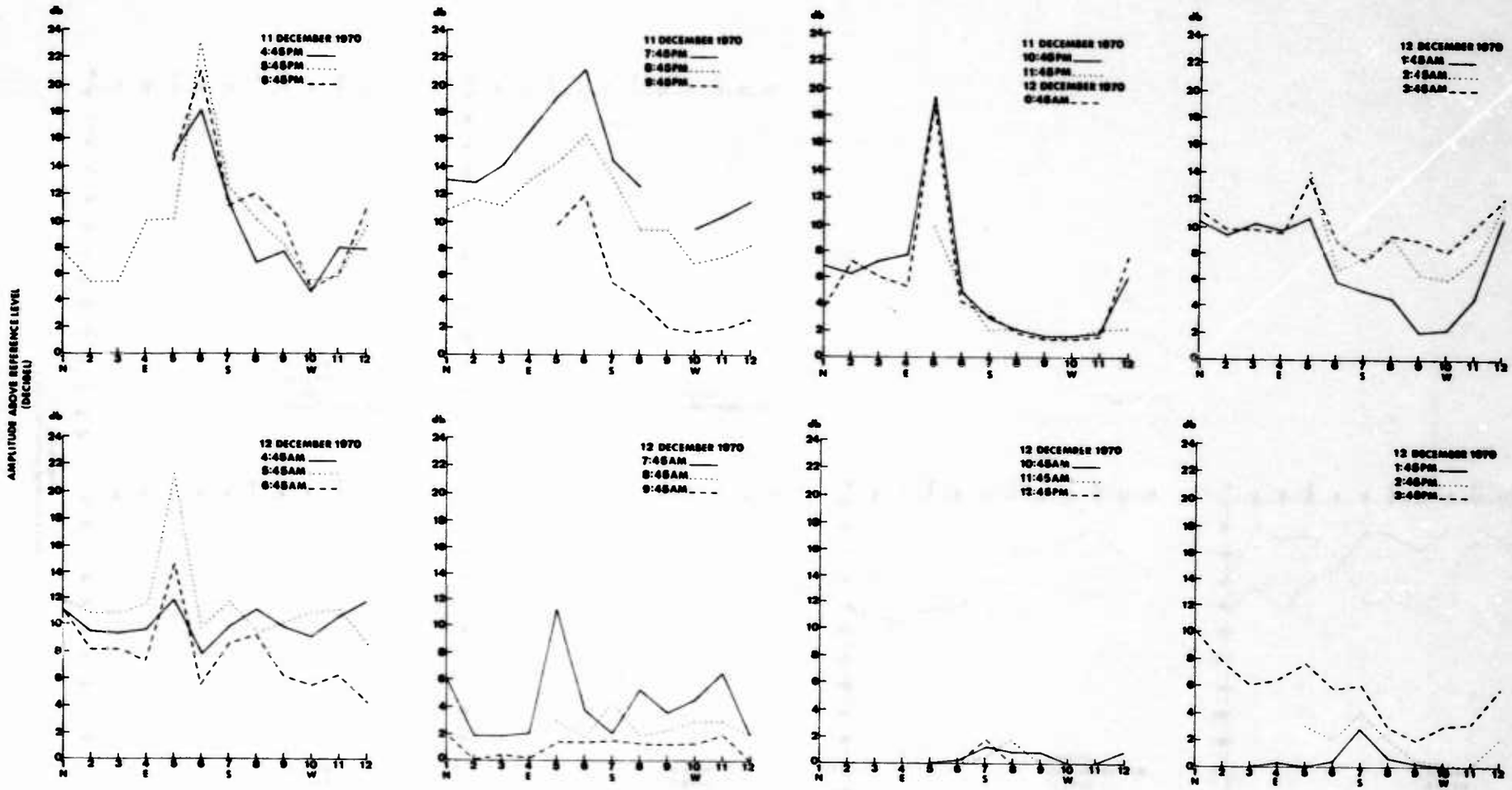

FIGURE 3a. HOURLY DISTRIBUTION
1645 11 DEC. 1970–
1545 12 DEC. 1970

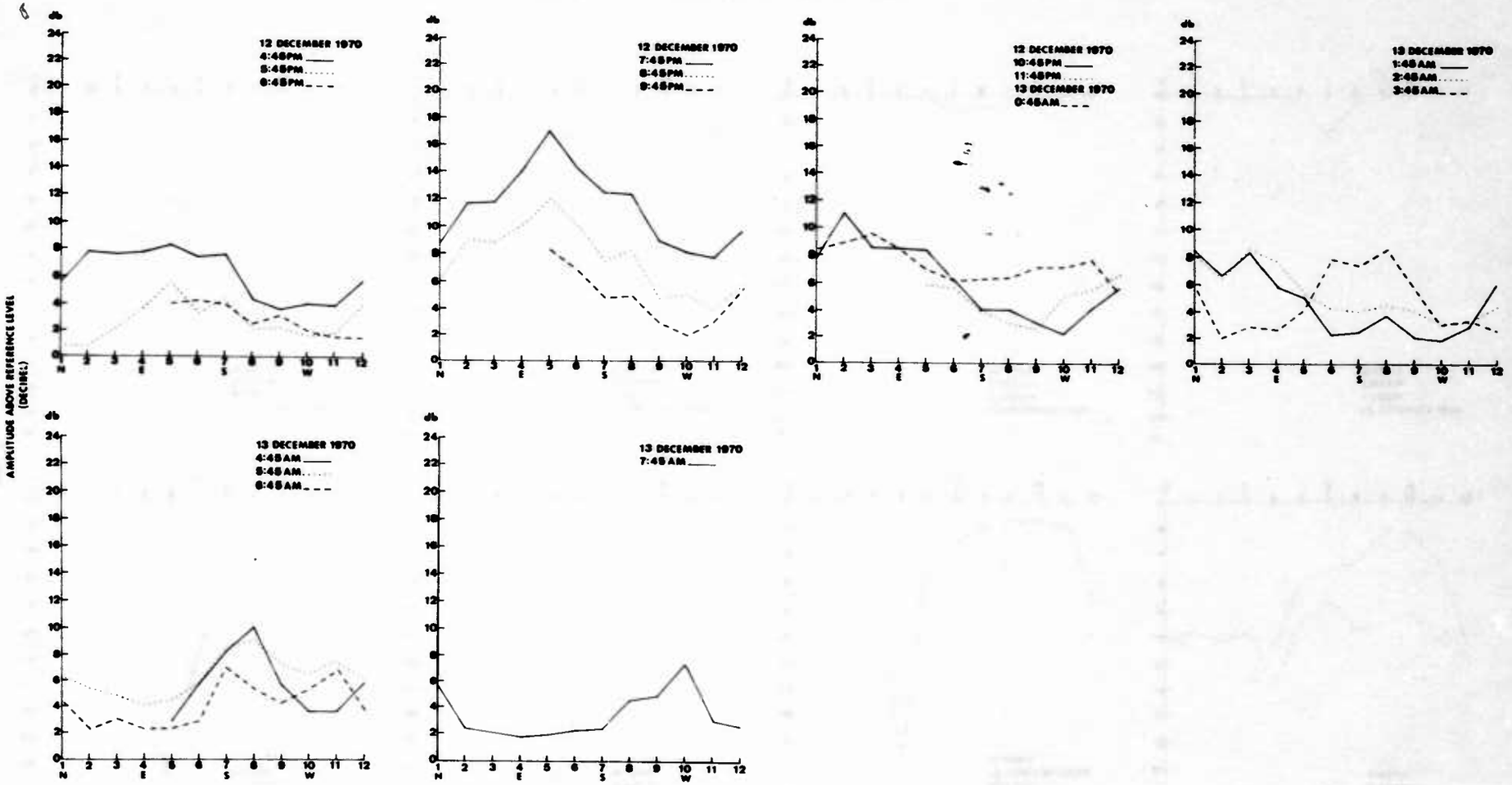

FIGURE 3b. HOURLY DISTRIBUTION
1645 12 DEC. 1970–
0745 13 DEC. 1970

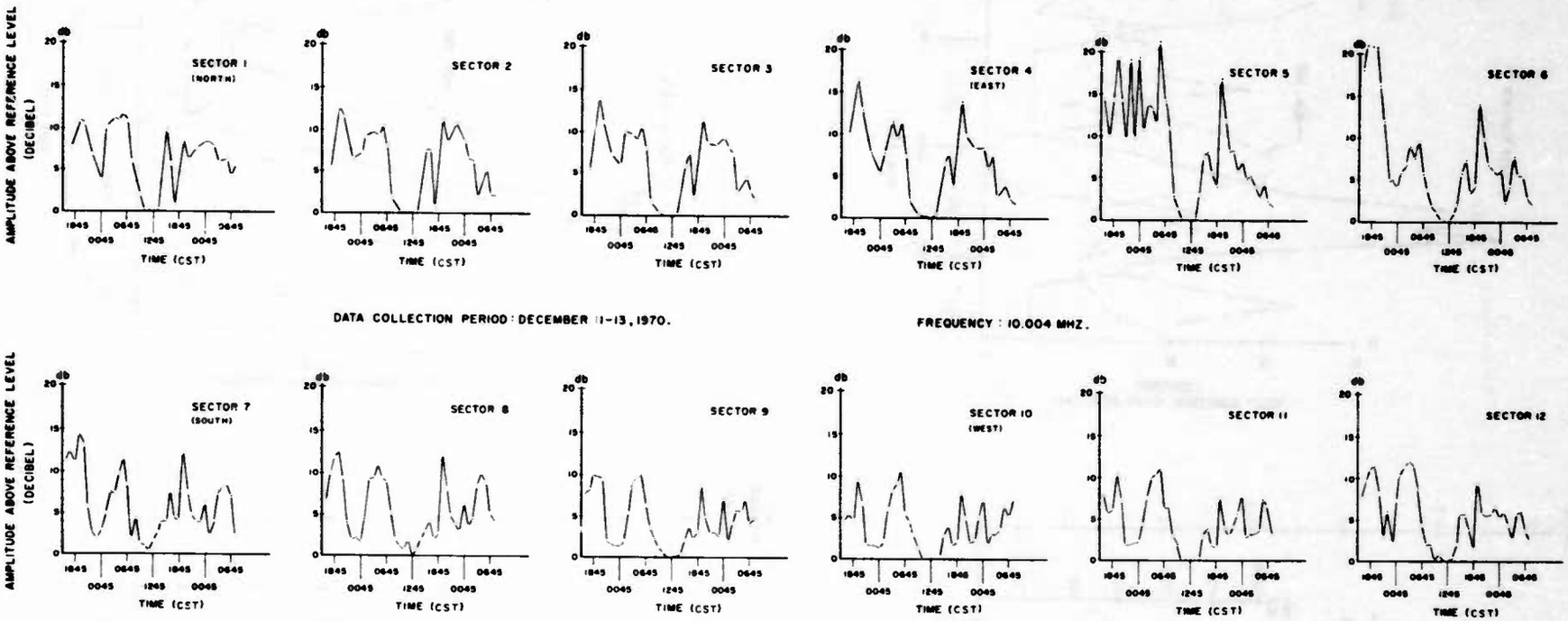

FIGURE 4. SECTOR HOURLY AMPLITUDE

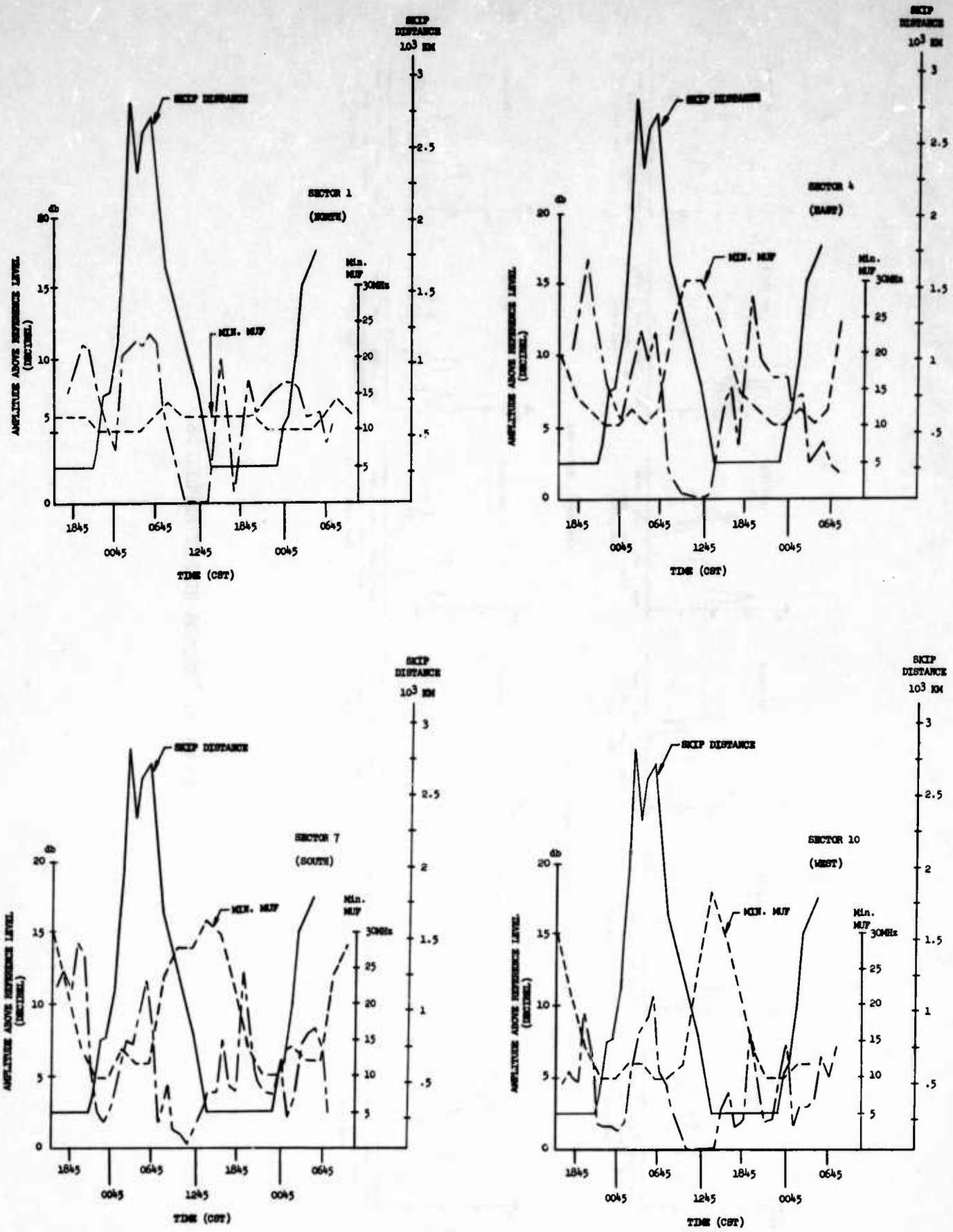
SKIP DISTANCE
SECTOR 1
(NORTH)
SECTOR 4
(EAST)
SECTOR 7
(SOUTH)
SECTOR 10
(WEST)
MIN. MUF
Min. MUF 30MHz
db
SKIP DISTANCE 10³ KM
AMPLITUDE ABOVE REFERENCE LEVEL (DECIBEL)
TIME (CST)
1845
0045
0645
1245

FIGURE 5 .

Paper 10.1

THE NAVY'S SATELLITE SOLAR ACTIVITY MONITORING AND FORECASTING SYSTEM

by

E. W. Peterkin, Technical Project Manager
SOLRAD Project
Naval Research Laboratory
Washington, D.C. 20390

FOURTH ALLERTON HOUSE CONFERENCE
ON RADIOLOCATION RESEARCH
UNIVERSITY OF ILLINOIS, MONTICELLO, ILLINOIS

History of Solar Monitoring at the Naval Research Laboratory

The solar monitoring program (SOLRAD) at the Naval Research Laboratory has developed as an outgrowth of studies of the upper air begun at NRL in 1946 when V-2 rockets were first made available for high atmosphere investigations. Measurements were made of the radiation incident on the upper air that could not be studied from below the earth's absorbing atmosphere. By recording the solar spectrum below the ozone cut-off of 3000Å the sun was shown by 1949 to be an emitter of energy in the far-ultraviolet and X-ray wavelengths.

During the 1950's, continued studies with rocket-borne sensors showed that the intensity of solar X-ray activity varied with the solar cycle. In 1956 a rocket flight during a solar flare found that X-rays were enhanced rather than ultraviolet. Because rocket flights have a useful trajectory of only a few minutes duration, a satellite solar monitoring program, under the sponsorship of the Naval Air Systems Command, was begun in 1960 with the launching of SOLRAD I, Fig. 1. Although data could be obtained only when the satellite was in range of the ground station, several flares were observed. Data recorded on 6 August 1960, shown in Fig. 2, resulted from a bright limb flare on the sun and indicates a strong increase in X-ray radiation at 1510Z in coincidence with optical observations. The ultraviolet flux, however, remains almost constant. Although the event was only a Class 1 flare, the X-rays were intense enough to produce a short wave radio fade out. SOLRAD I showed clearly that X-rays and not ultraviolet radiation were the cause of geophysically significant solar flare effects on earth.

Subsequently, seven improved SOLRAD satellites have been built and orbited at 300 to 500 nautical mile altitudes with additional detectors, orbital memory, and command and automatic control of the orientation of the spacecraft spin axis.

Current Operations

The SOLRAD 9 Satellite, Fig. 3, was launched in March, 1968 into a 270 by 420 n.mi. orbit carrying X-ray detectors measuring 0.1 to 60Å in five bands and ultraviolet emission from 1080 to 1350Å in two bands. The satellite, spinning at 60 rpm, maintains its spin axis perpendicular to the sun line to keep the sun in the plane of the detectors which are mounted in the equatorial section of the satellite. Each detector measures the incident, solar radiation in sequence once a second as it scans the sun. The data are broadcast immediately and continuously over two

136 MHz FM/AM telemetry systems. In addition, the readings of three, standard X-ray sensors are stored once a minute in the satellite on-board storage system. The satellite memory has a capacity to store data over a 14-hour period.

The satellite passes over the NRL Satellite Tracking Facility at Blossom Point, Maryland, as shown in Fig. 4, three to eight times a day. The ten to fifteen minute transmission from each pass is recorded and relayed in real-time over telephone lines to the SOLRAD Data Operations Center at NRL where the decommutated data are displayed on moving chart recorders. Operators convert the telemetry signals to flux units in ergs/cm^2/sec., prepare a computer-coded paper tape message representing the average value of the radiation levels of the various sensors, and release the data to the USAF Astrogeophysical Teletype Network (formerly, SOFNET) approximately five minutes after the end of the pass. Whenever the real-time X-ray data exceed an established level, a standard flare warning teletype message is released immediately. The primary customers for this real-time data are the USAF Aerospace Environmental Support Center (AESC) at NORAD, Cheyenne Mountain Complex and the NOAA Space Environment Forecast Center (SEFC) at Boulder, Colorado. Twice a day the satellite tracking station commands the satellite PCM telemetry system to "dump" the contents of the on-board memory. The data are formatted and processed by an off-line computer to produce a minute-by-minute printout and plot of the 0.5-3, 1-8, and 8-20Å X-ray sensors. These plots are produced in about one hour for routine transmission by facsimile to the SEFC at Boulder and relay to the AESC at NORAD. The plots are also reformatted by NRL to span 0-24 hours UT and are sent to Boulder for inclusion in the World Data Center records. SOLRAD 9 data are also included in the monthly NOAA publication, "Solar-Geophysical Data".

A statistical study of the frequency of solar X-ray and optical flares has been conducted at NRL and indices of X-ray activity have been established for the prediction of four to five-day periods of solar activity that may result in disturbances to high frequency radio communication. The probability of solar X-ray flares occurring will be four times greater when the indices of solar X-rays activity are met than when they are not. Approximately 50 such alerts have been sent to the Naval Communications Command since the launch of SOLRAD 9. As with previous SOLRAD satellites, the international scientific community, through the cooperation of the Committee on Space Research, is provided with information that enables them to track and make independent studies of the SOLRAD satellite outputs. At present, 15 world-wide observatories are participating.

Operational Implications

SOLRAD 9 is now entering into its fourth year of operation and we have been able to keep the sun under continuous observation during this period except for short transits through the Earth's shadow. As a result, no major solar event lasting more than 20 minutes has failed to be observed since March 1968. This continuous coverage and rapid dissemination of data has been an important feature of the SOLRAD Program and has demonstrated its potential as an operational system. The intermittent availability of real-time coverage (totalling only 6% of the day) and the inherent delay in preparing solar activity records from stored data are inconsistent with a truly operational system and for these reasons a decision was made four years ago to develop a satellite system that could provide continuous, real-time monitoring of solar activity. Real-time monitoring of solar activity will enable us to provide warnings and forecasts of solar-induced disturbances that may affect the performance of military systems employing the ionosphere.

If we look at a 24-hour period on 20 July 1969, as shown in Fig. 5, (which happens to be the day the APOLLO astronauts made their first landing on the moon) we see that the solar X-ray activity in the 8-20, 1-8 and 0.3-5Å bands is essentially quiet and probably caused very little disturbance to the expected variations of the ionosphere. However, if we look at 21 October 1968, Fig. 6, we see an almost continuous sequence of solar flares. The flare peaking at 0620 UT reaches about 0.3 ergs/cm^2/sec in the 1-8Å band. One of the effects of a solar X-ray flare of such intensity can be seen in Fig. 7. This figure represents the response of an 80-channel HF sounder operating between Hawaii and California on 1 November 1968 from 1900 to 2120 UT. The vertical "ridges" represent the relative amplitude of signal strength at the receiver. The normal ionosphere for this path and period of the day is limiting transmission to frequencies above 12 MHz. At 2000 UT a solar X-ray flare commences and rises from a "quiet sun" background level in the 1-8Å band to 0.3 ergs/cm^2/sec in 15 minutes. The concurrent loss of signal in the region between 12 to 32 MHz is essentially a direct image of the profile of the solar flare, disrupting the band for almost 60 minutes. X-ray flares also produce enhancement of the lower levels of the ionosphere and result in phase anomalies in VLF transmissions proportional to the intensity and duration of the flare.

Emissions of the sun that are enhanced during periods of flare activity are shown in Fig. 8. The electromagnetic radiations travel at the speed of light and arrive at the earth in about 8.3 minutes. These radiations cover the entire electromagnetic spectrum, but it is primarily

the enhancement of ultraviolet and X-ray radiation that cause radio wave absorption in the ionosphere or changes in the reflection height of radio wave signals. Radio bursts are also emitted that produce jamming-like environments for some radar systems. A few solar flares, usually of high intensity, may also produce proton flares that will intercept the earth if they are ejected to travel along the appropriate trajectory. High energy protons and alpha particles arrive 15 minutes to several hours after the initiation of the flare on the sun. Much of the earth's environment is shielded from these particles by the earth's magnetic field and as a result they penetrate at the polar cap regions where their production of enhanced ionization causes radar and communication blackouts and severe scintillations of satellite signals. Low energy protons and electrons are also produced during the proton flares and cause geomagnetic storms that result in world-wide disturbances to many communication systems. They can also cause heating of the outer atmosphere and thereby perturb the orbital motion of near-earth satellites.

SOLRAD High System

The NRL plan for a satellite system capable of providing continuous, real-time data has been named "SOLRAD HIGH" and the concept is shown in Fig. 9. Three satellites will be placed in a near-equatorial, circular orbit at a distance from the earth of 70,000 nautical miles (20 earth radii) and will be spaced 120° apart. Each satellite will monitor the sun's emission and will transmit telemetry signals continuously. With this arrangement at least one of the three satellites will always be in view of the NRL tracking station at Blossom Point, Md., thereby providing a constant, real-time monitoring capability. At this distance, the satellites will be orbiting in a path that is generally beyond the earth's magnetosphere and will make possible the measurement of the true values of solar proton emission and solar wind fluxes outside the disturbing influence of the earth's magnetic field.

The SOLRAD HIGH concept has involved some changes in the usual satellite instrumentation techniques. The long-range communication problem has dictated a low bit-rate telemetry link with data formatted to interface with real-time computer processing. Consequently, the on-board data processing system must be independent of the spin rate of the satellite. This has been accomplished by changing the spin axis of the satellite from being held perpendicular to the sun line to pointing directly at the sun. This change in spin axis orientation has resulted in a major configuration change in the SOLRAD HIGH satellites as shown in Fig. 10. The solar sensors, located in the top plate of the satellite, will observe the sun continuously and permit the use of slower, lower noise electronics

with greater dynamic ranges and detectors with narrow fields of view. The solar cell panels will also act as antenna dipoles. Tentative plans for these satellites include 26 detectors measuring solar, stellar, and auroral X-rays; solar ultraviolet emission; protons and electrons; and earth infrared and visible albedo as shown in Fig. 11, 12, and 13. Plans approved by DOD set a goal for launch of the SOLRAD HIGH satellites in March 1974. Solar emission data and flare warnings would be made available in real-time to operational users through a Naval Weather Service distribution system, as shown in Fig. 14.

SOLRAD 10

The SOLRAD 10 satellite is the next low-altitude satellite and is shown in Fig. 15. This satellite is scheduled for launch in July 1971 and will serve as a prototype and proof test for the major changes planned for SOLRAD HIGH. It will be the first of SOLRAD satellites operating with its spin axis oriented to point at the sun. An experimental hydrazine propulsion system and a high-powered RF transmitter will be flight tested also. Some 13 sensors are being carried, broadening our coverage in the X-ray and ultraviolet spectrum.

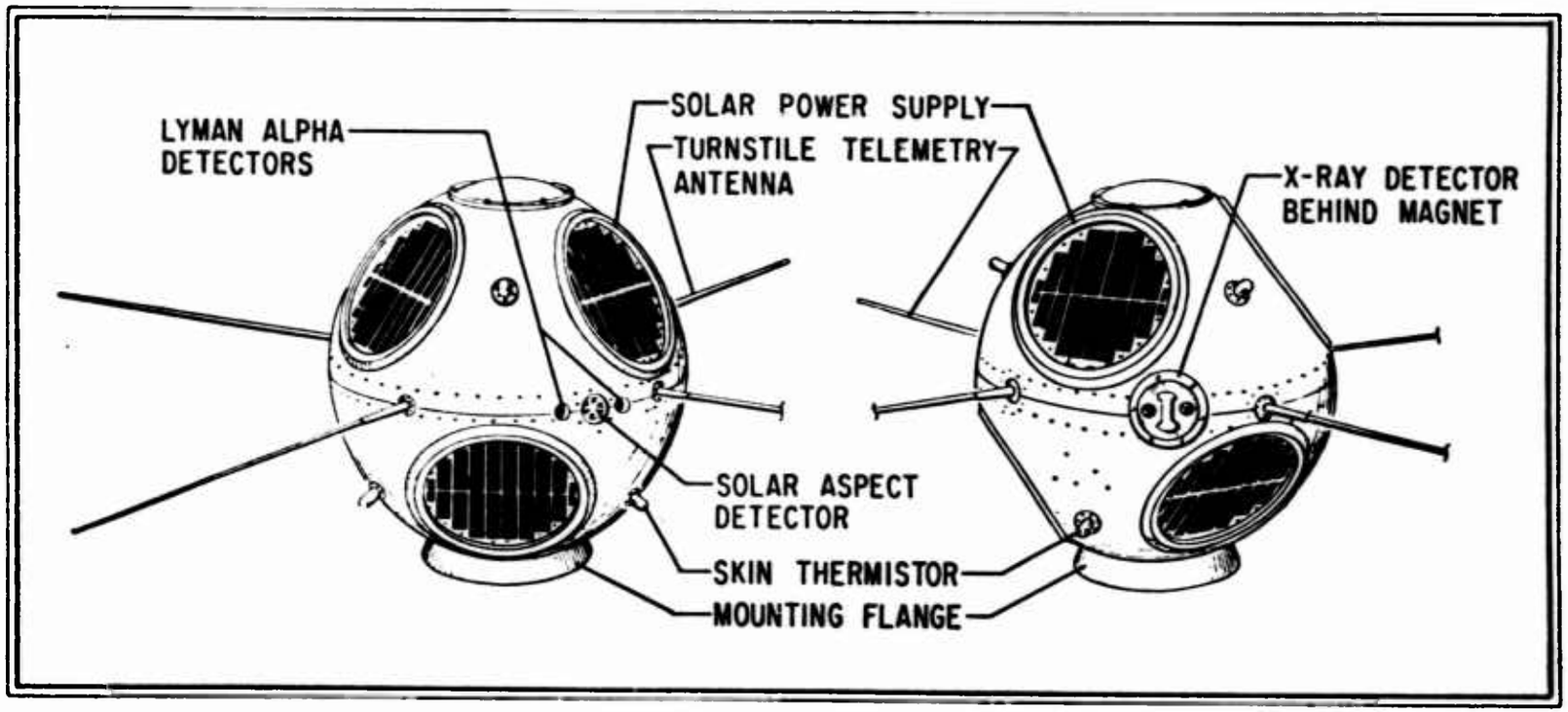

Fig. 1 - SOLRAD I

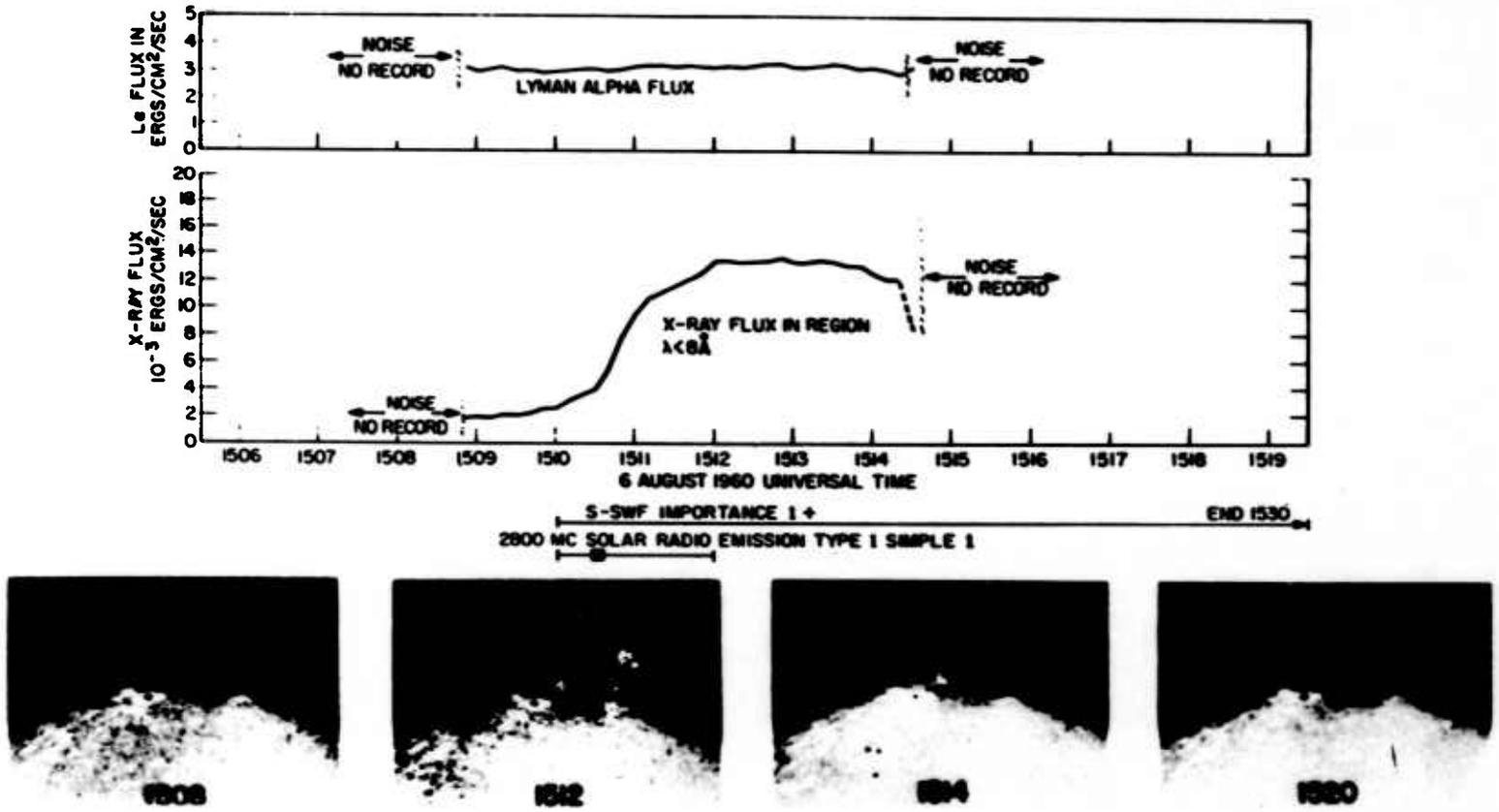

Fig. 2 - Evidence of Solar X-ray Enhancement Causing Short Wave Radio Fade Out

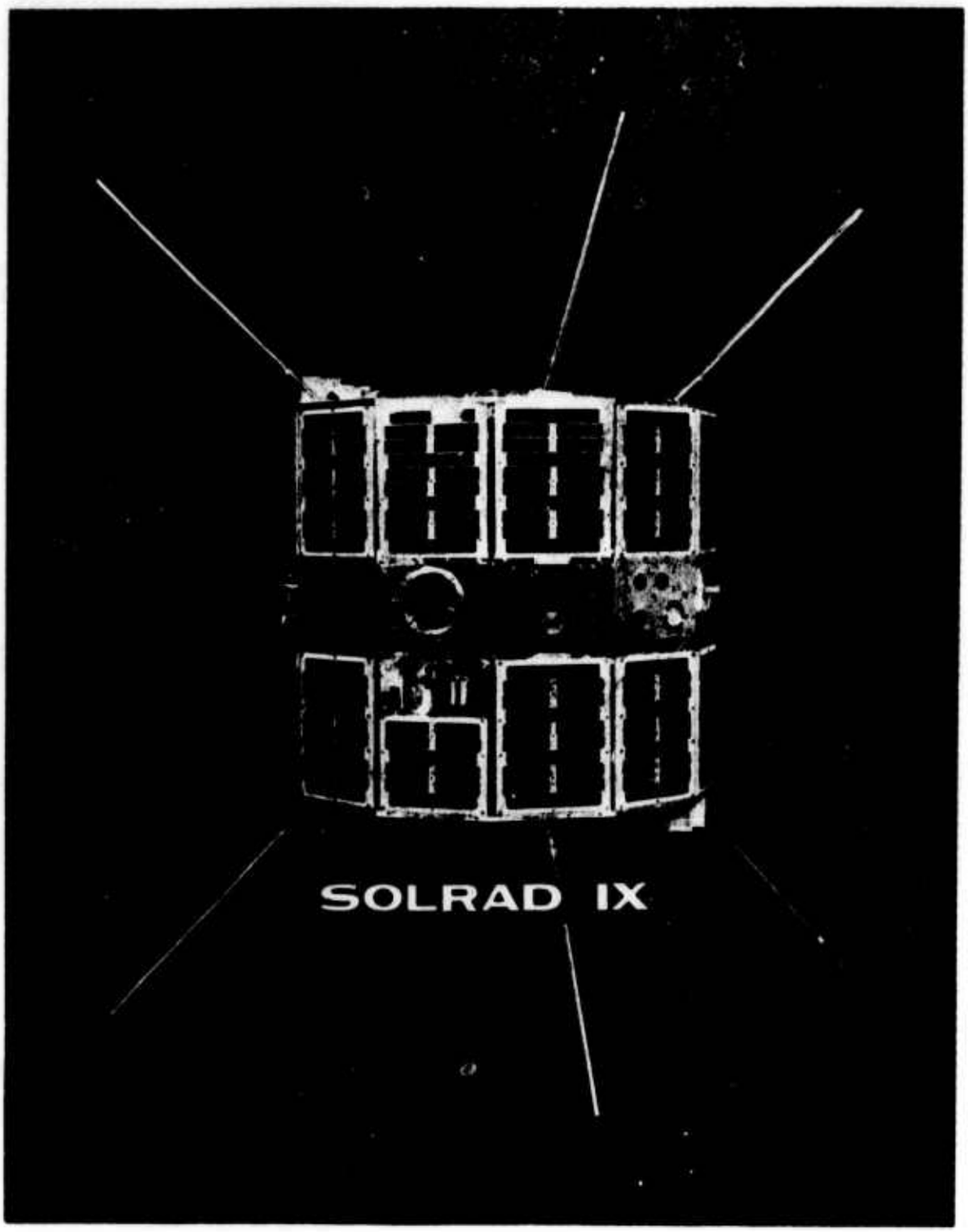

Figure 3

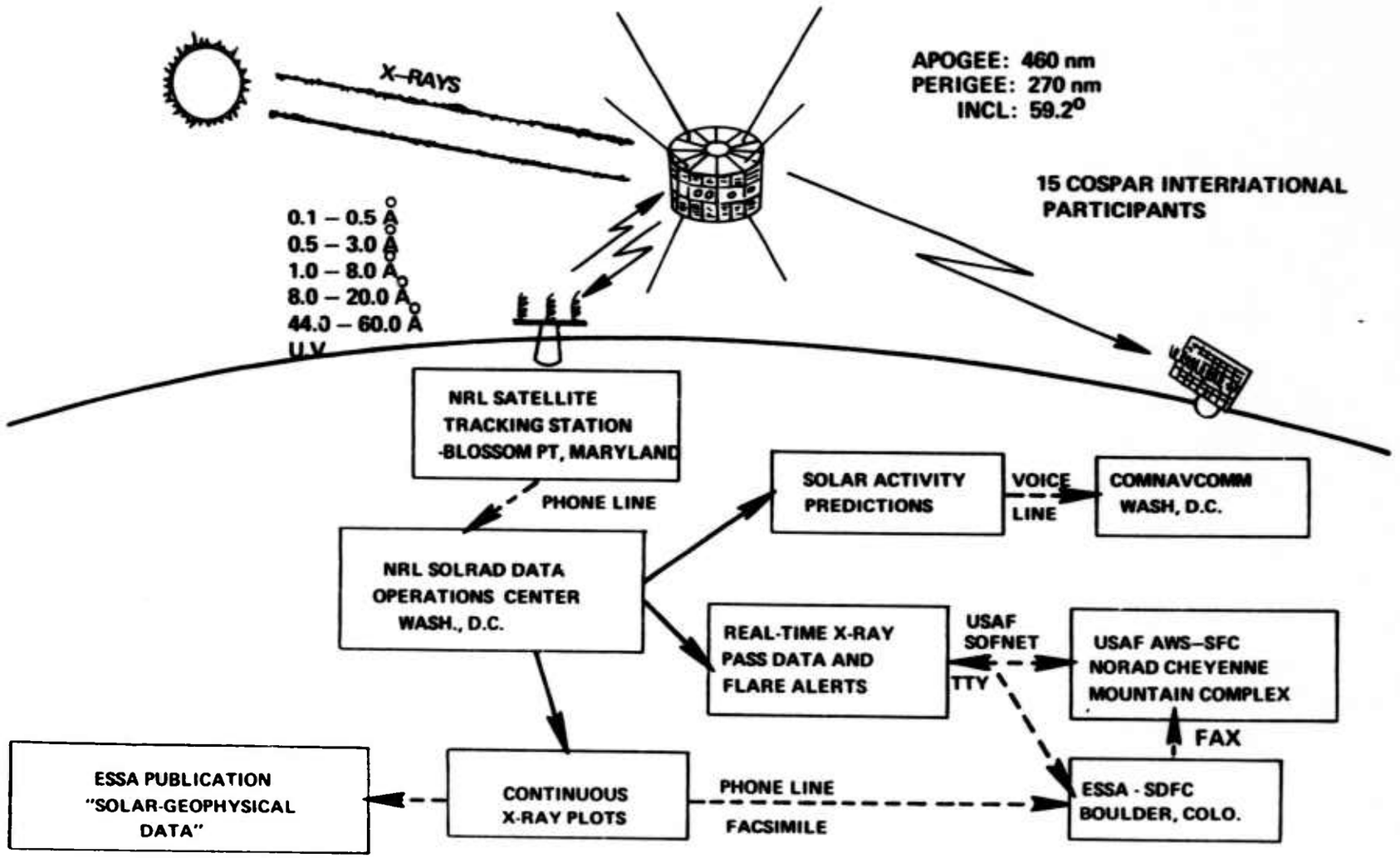

Fig. 4 - Current SOLRAD Operations

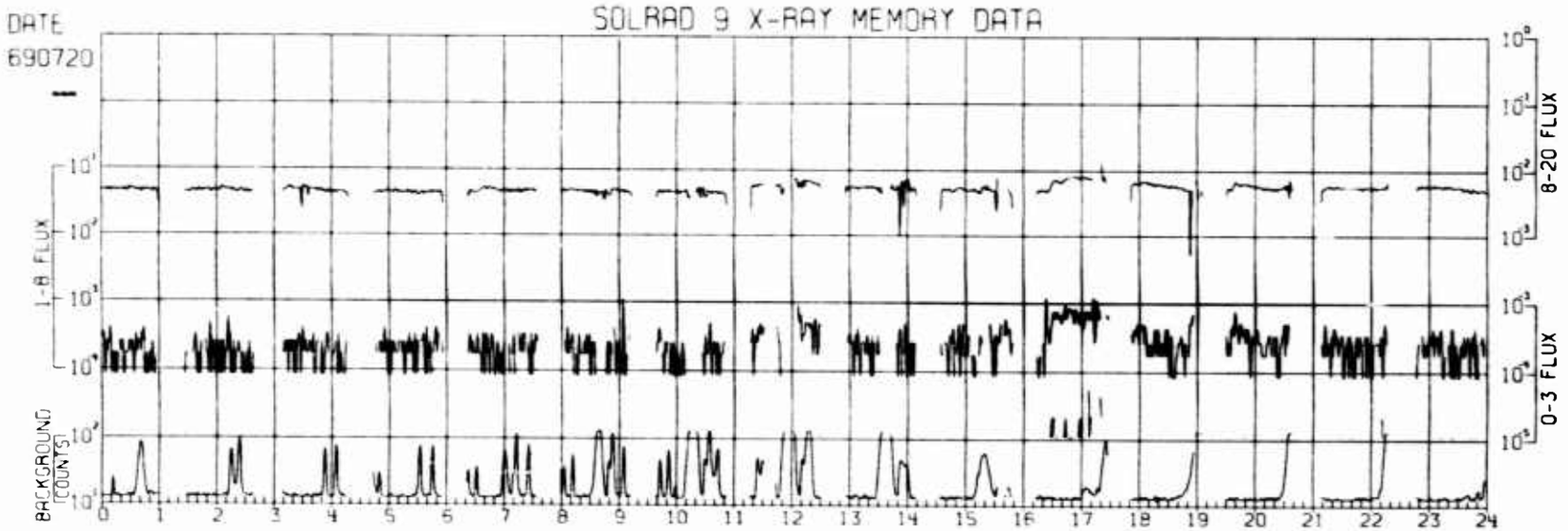

Fig. 5 – A Day of Quiet Solar Activity, 20 July 1969 (The Day APOLLO Astronauts First Landed on the Moon)

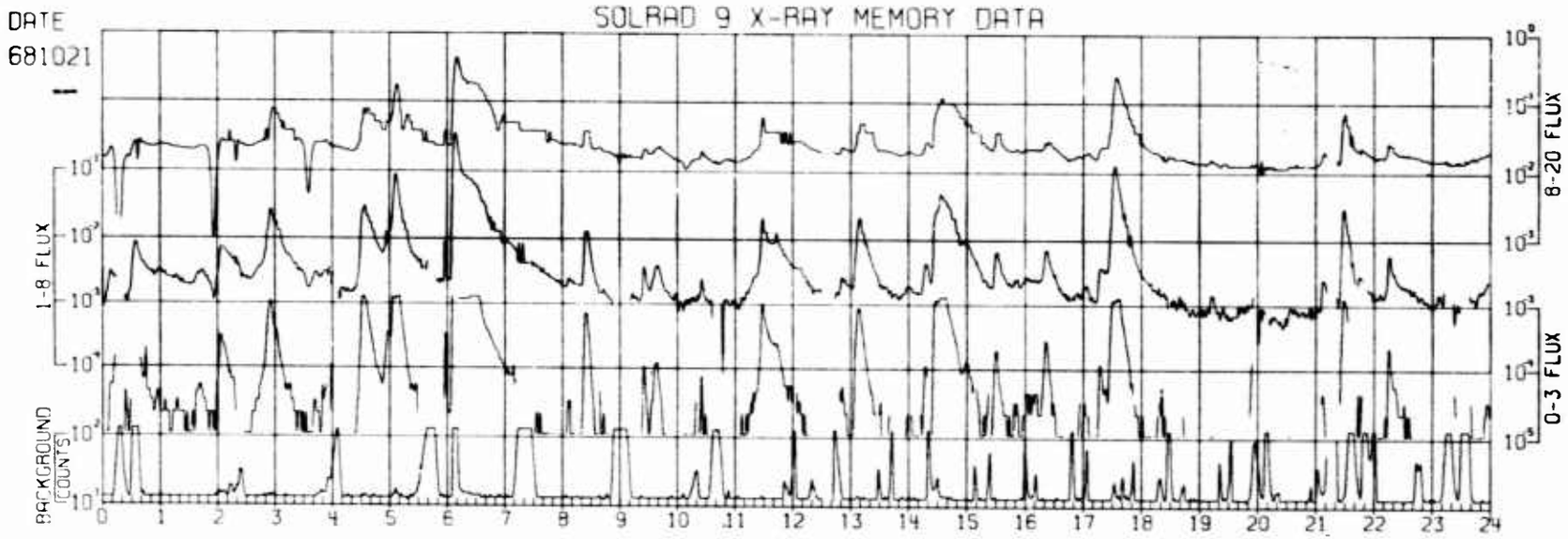

Fig. 6 - The Active Sun on 21 October 1968

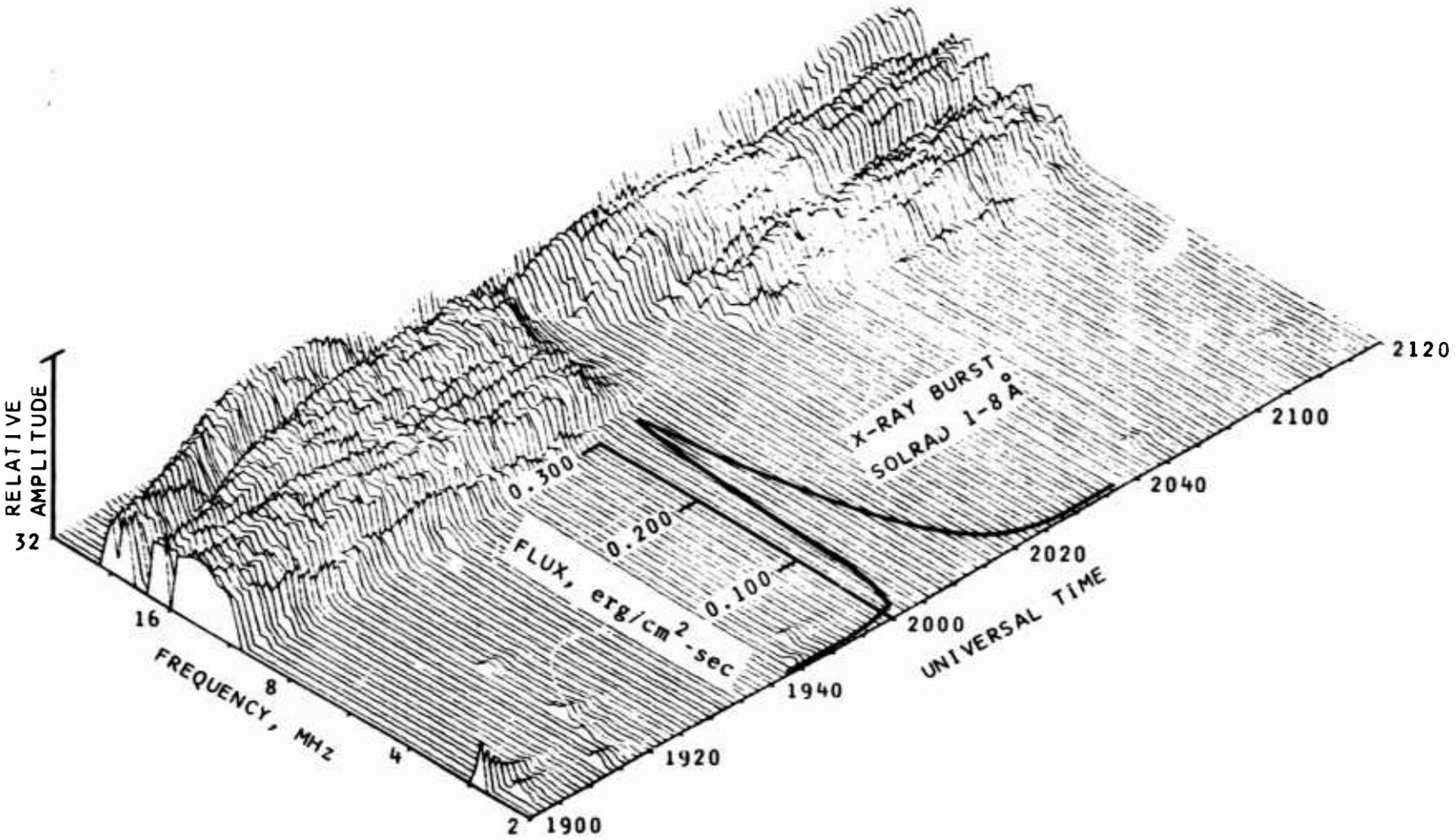

Fig. 7 - A Solar X-ray Flare Effect on the HF Band

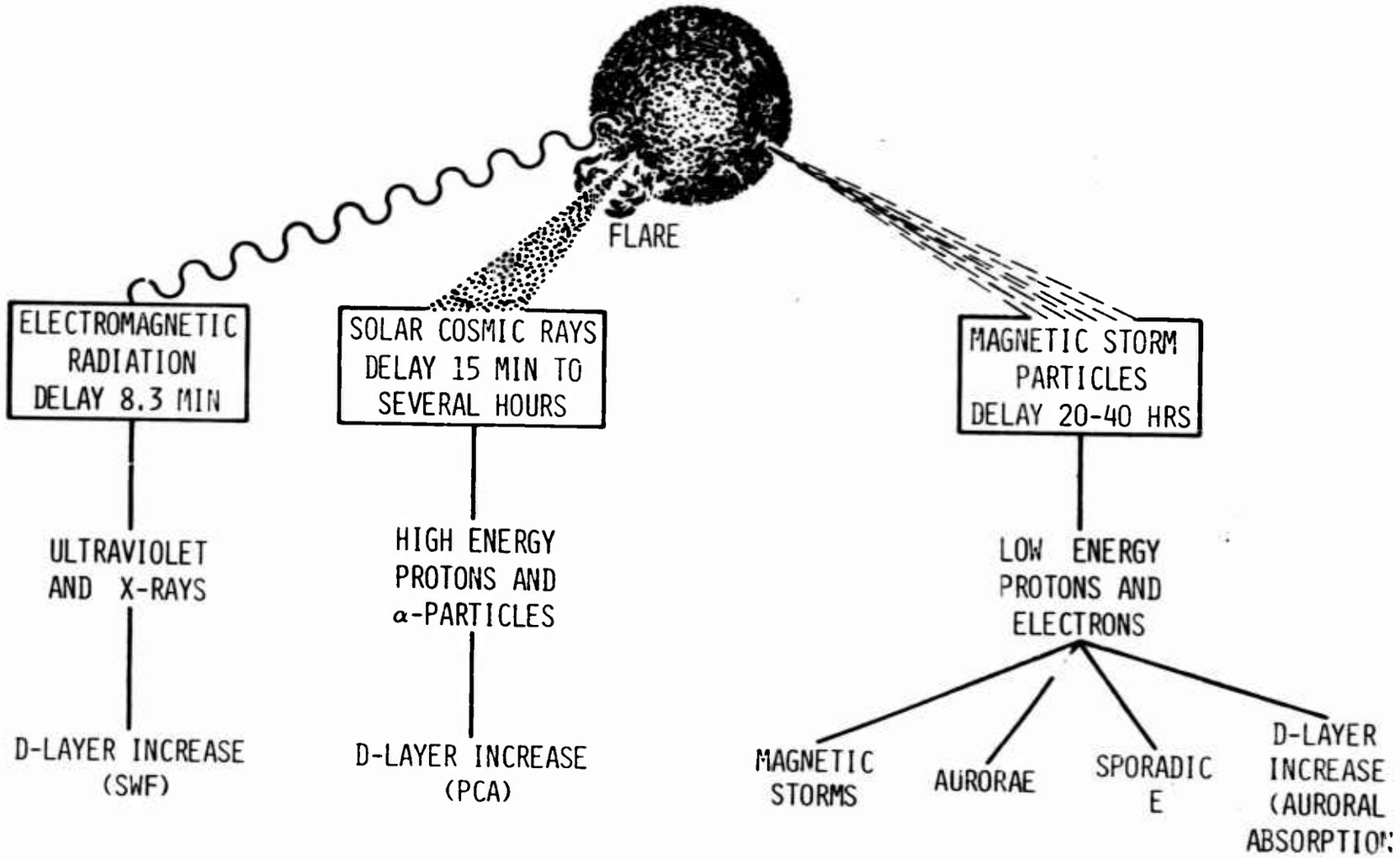

Fig. 8 - Solar Flare Emissions and Their Effects on the Ionosphere

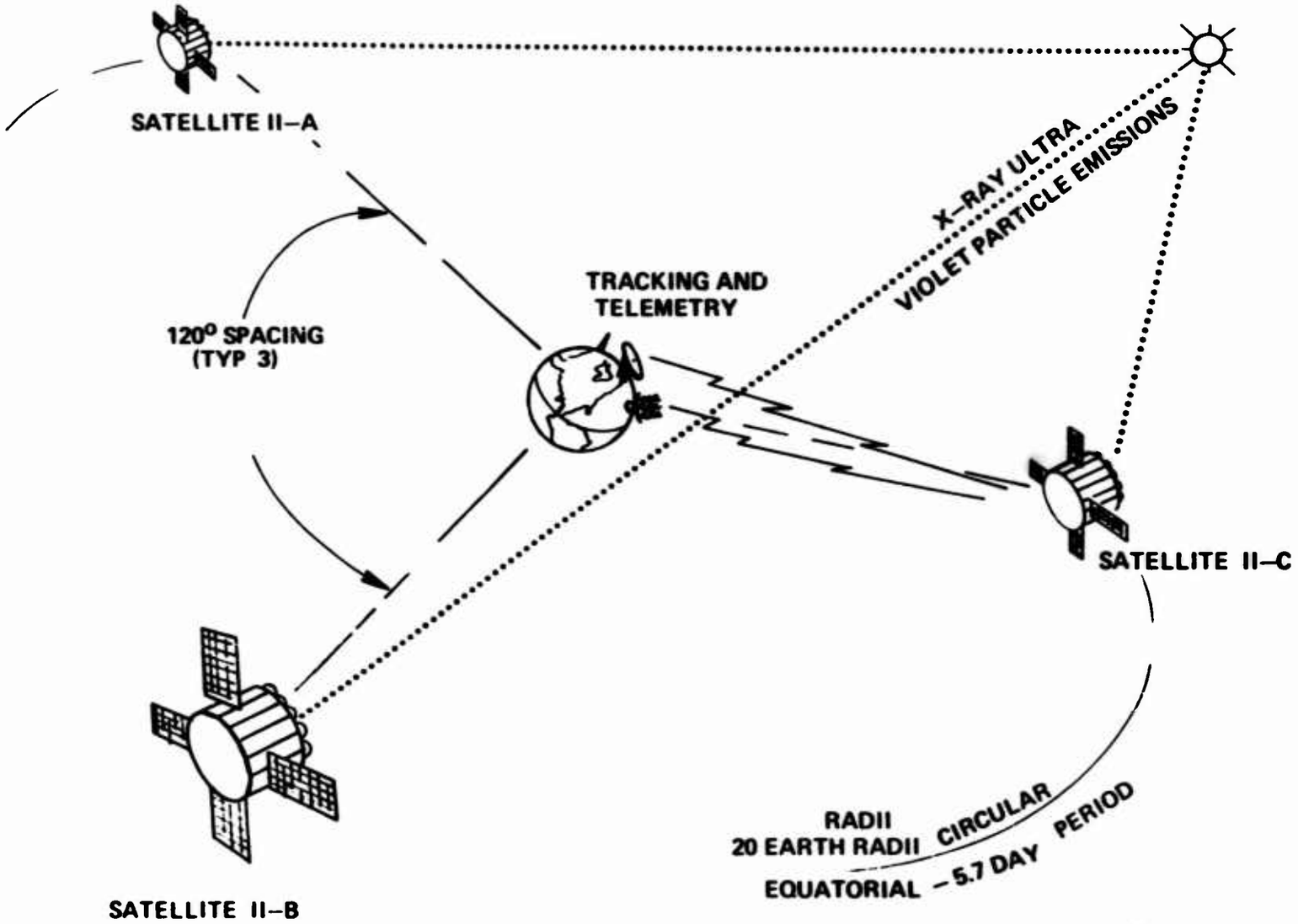

Fig. 9 - SOLRAD HIGH SYSTEM CONCEPT

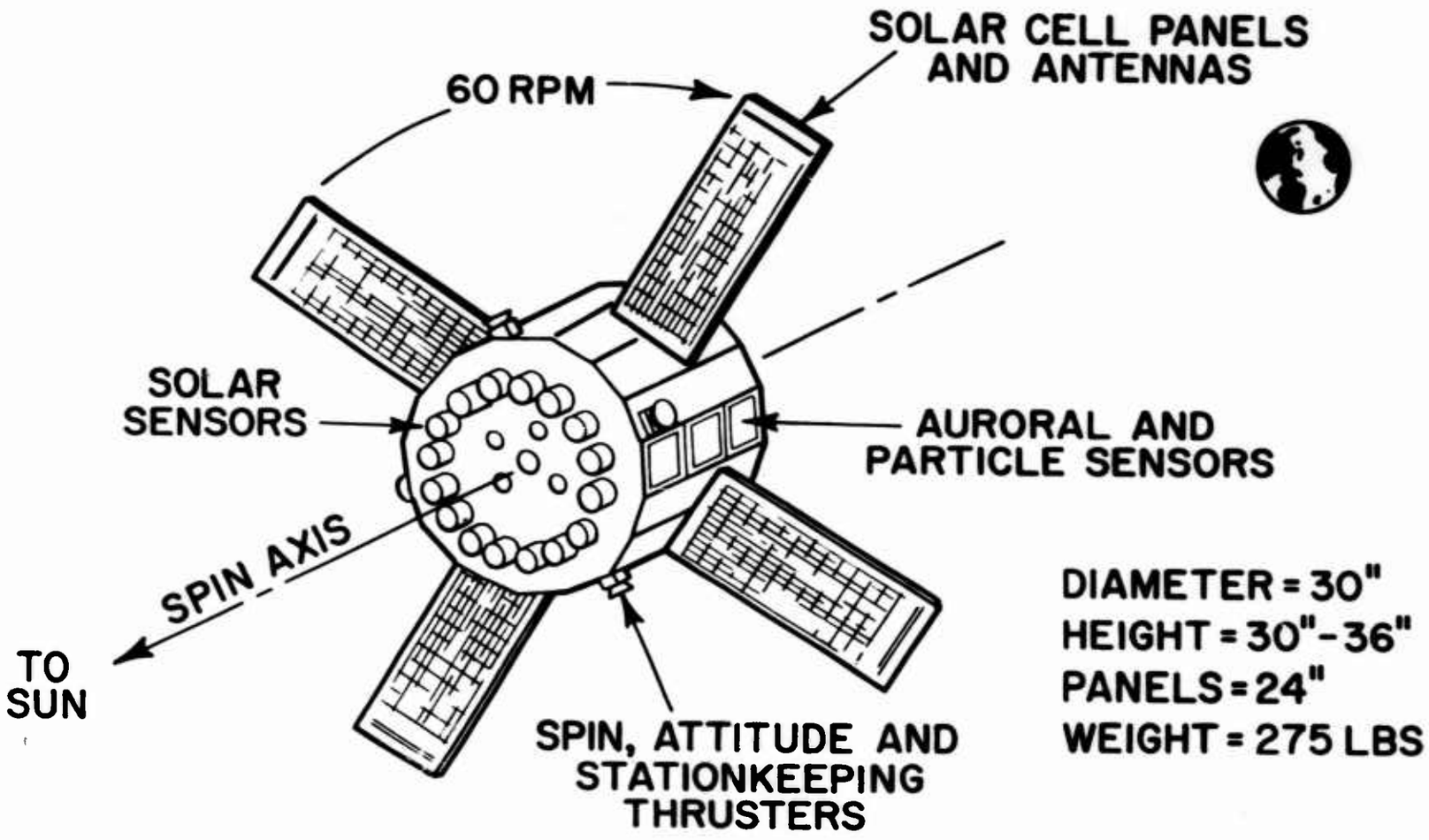

Fig. 10 - Preliminary Configuration of the SOLRAD HIGH Satillite

SOLRAD XI TENTATIVE EXPERIMENTS

FACING SUN

SOLAR X-RAYS:	ULTRA-VIOLET:
20 - 320 KEV	170 - 600 A
0.1 - 1.6 A	1080 - 1350 A
0.5 - 3 A	1225 - 1350 A
1 - 5 A	1350 - 1550 A
1 - 8 A	FLARE DETECTOR
8 - 20 A	
44 - 60 A	

BRAGG CRYSTAL SPECTROMETER (MG XI, XII)

SOLAR WIND (CURRENT, ENERGY, TEMPERATURE)

> 10 MEV PROTONS

ATMOSPHERIC SIMULATORS

Figure 11

SOLRAD XI TENTATIVE EXPERIMENTS

FACING SIDE

STELLAR OR AURORAL X-RAYS (1-8A)

NON-SOLAR LINE EMISSION (1216A, 304A)

PROTONS (OMNI-DIRECTIONAL)

> 0.5 MEV	> 10.0 MEV
> 1.0 MEV	> 20.0 MEV
> 2.0 MEV	> 50.0 MEV
> 5.0 MEV	> 100.0 MEV

AFCRL PROPOSED EXPERIMENTS

PROTON ALPHA TELESCOPE (P > 200 MEV; α: 50-100 MEV)

LOW ENERGY PROTON SPECTROMETER (0.1 - 1.0 MEV)

MAGNETIC ANALYSER (P: 0.020 - 0.250 MEV, E: 0.015 - 1.5 MEV)

Figure 12

SOLRAD XI TENTATIVE EXPERIMENTS

FACING BACK

> 10 MEV PROTONS

> 1 MEV ELECTRONS

VISIBLE EARTH ALBEDO

IR EARTH ALBEDO

Figure 13

SOLRAD HI OPERATIONAL DATA FLOW

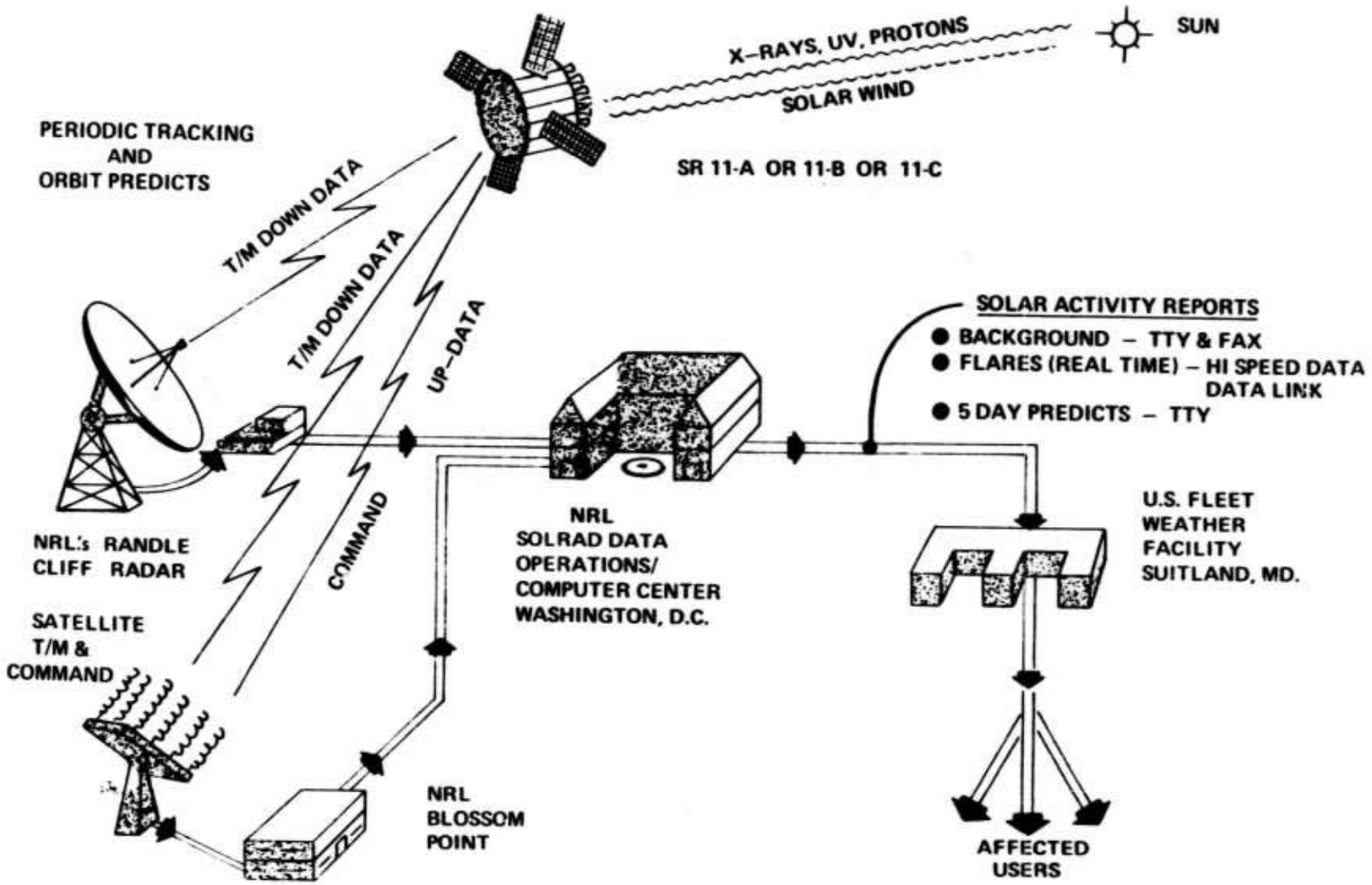

Figure 14

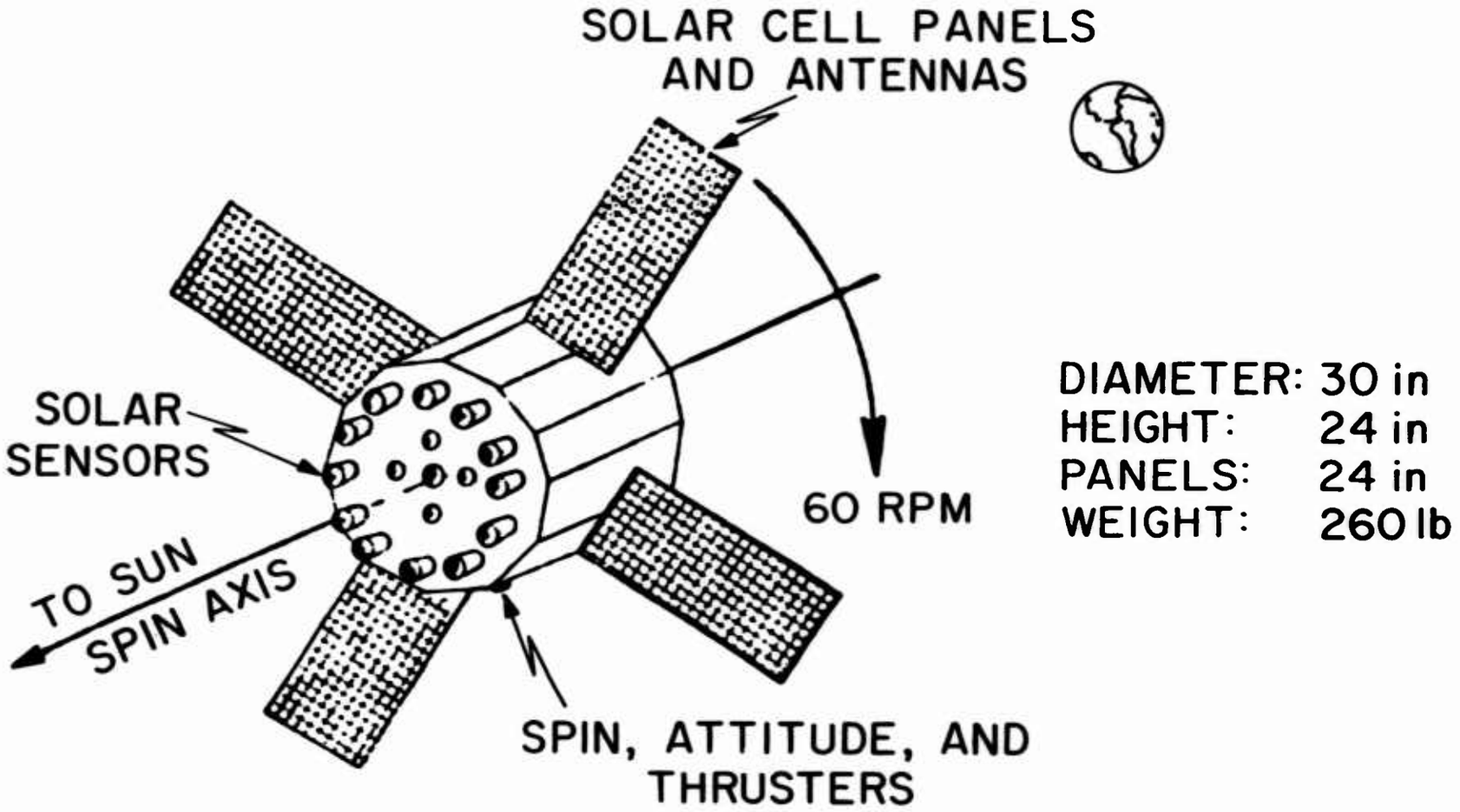

Fig. 15 - The NRL/NASA SOLRAD 10 Satillite to be Launched in Summer 1971 into a 350 Nautical Mile, 51 Inclination Orbit

W.M. SHERRILL, D.N. TRAVERS, P.E. MARTIN

Southwest Research Institute, San Antonio, Texas

ADVANCED RADIOLOCATION INTERFEROMETRY

ABSTRACT

The computer instrumented phase interferometer provides a highly flexible direction finding instrument for radiolocation and ionospheric propagation studies. Techniques for providing directive interferometers and mode analysis including azimuth/elevation polarization, coherence ratio, and angular width without wave interference are described. Techniques for eliminating the twin channel receiver are summarized including phase sweep interferometry and the use of an atomic frequency standard for temporal phase reference.

I. INTRODUCTION

The early application of the interferometer direction finder to sporadic E and other ionospheric studies utilized the amplitude null method of azimuth measurement. Eckersley's spaced loop interferometer of the mid-1930s (1) used two meter square loops on a 20-meter baseline and was mechanically rotated to locate the null. In addition to azimuth direction finding, Eckersley also exploited the fringe visibility of the interference pattern to provide an estimate of angular width. The amplitude interferometer in adcock and electrically small spaced loop versions has become a familiar direction finder over the years.

Other ionosphere studies have used the phase measuring interferometer with analog phase measurement and crossed baselines such as the Ross, Bramley, and Ashwell instrument (2) and the interferometers constructed by Burtynk, et al (3). The single site location interferometer used by Treharne et al (4) used phase nomograms while the University of Illinois (5) design has used both analog computation and off-line processing by digital computer for direction finding results.

II. COMPUTER INSTRUMENTED INTERFEROMETERS

The computer instrumented phase interferometer employing crossed baselines and a system computer operating in real time for azimuth and elevation computation has become conventional over the past five years (6).

Figure 1 shows a block diagram of the fully computer instrumented interferometer system now under development for the U.S. Army. A sequencer switches the array elements by pairs through a twin channel phase and gain matched receiver to the phasemeter. Amplitude threshhold and other data editing circuits are employed to cope with HF fading and other real world complications to data acquisition. The phasemeter output is digitized and fed through an A/D converter and multiplexer to the real time computer which computes data frames at the rate of 10 to 40 azimuth/elevation samples per second. Time averaging is used to resolve the strongest mode. Algorithms are under development in several laboratories for the resolution of multiple modes.

Figure 2 shows the planned system configuration. In order to perform the location functions for which it is designed, this system includes an FM/CW sounder also monitored in real time by the computer system and DF array which provides virtual height and effective ionospheric tilt and tilt compensation to the observed azimuth/elevation measurements. The operator's control panel is organized so that the operator concentrates on data acquisition and target identification while the computer instrumented system provides data reduction and signal analysis capability. The measured data is displayed on the graphic terminal including text (azimuth/elevation cut and location information) and real-time azimuth/elevation histograms of the frame data obtained during data acquisition. Figure 3 shows the control console and display in more detail.

The design aspect emphasized here is the integration of the system computer into an HF interferometer system and the division of labor between the operator and the computer so that each provides the functions for which he has maximum capability.

Figure 4 shows essentially the same computer instrumented interferometer concept using directive antenna elements. It should be emphasized that phase interferometry using appropriate directive elements such as, for example, Beverage sector arrays offers the capability for directive gain which excludes unwanted azimuth sectors, combined with high precision azimuth/elevation interferometric direction finding. The entire spectrum analyzer and phase measuring system can be implemented with identically the same hardware as used for the single site system but using different antenna elements.

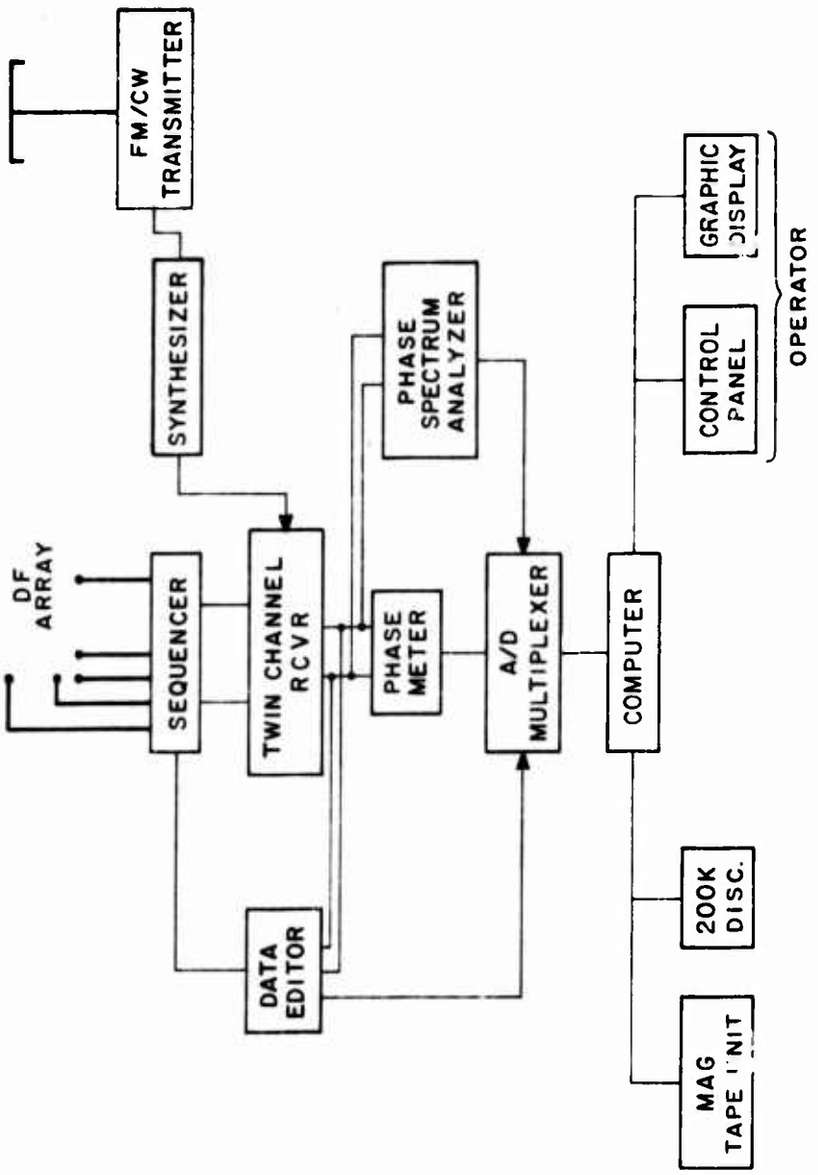

FIGURE 1

COMPUTER INSTRUMENTED INTERFEROMETER

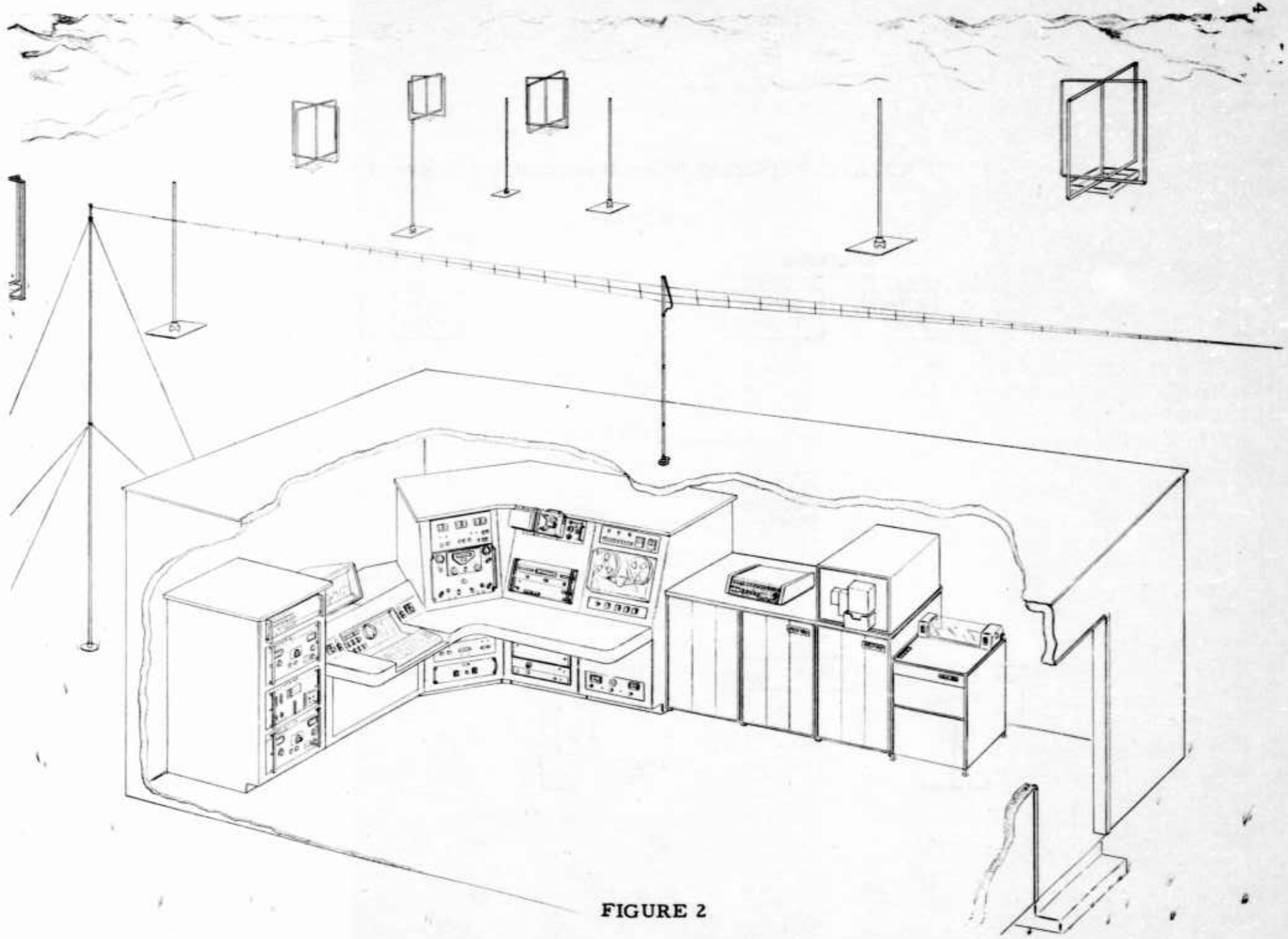

FIGURE 2

COMPUTER INSTRUMENTED INTERFEROMETER INSTALLATIONS

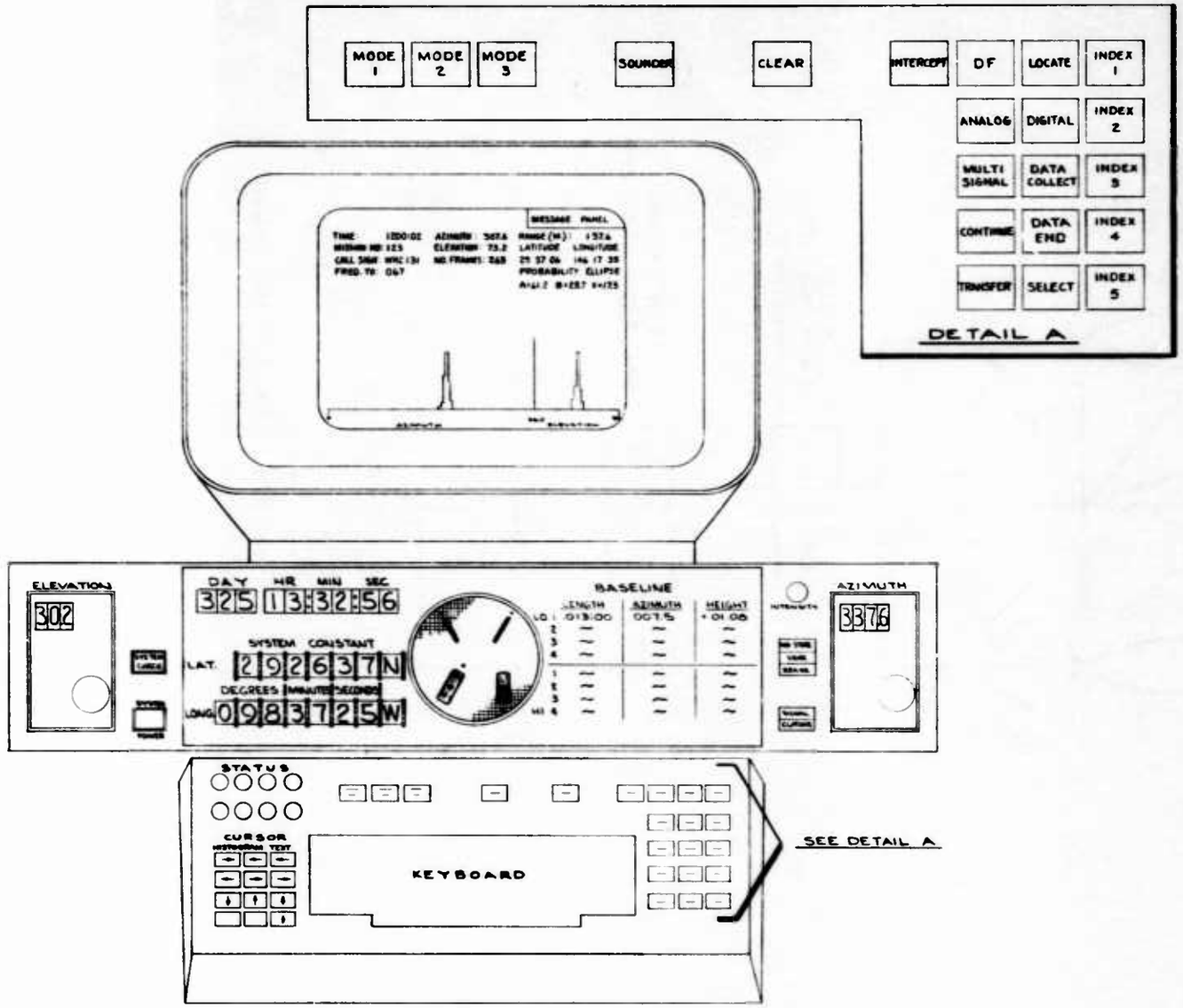

FIGURE 3

CONTROL AND DISPLAY CONSOLE

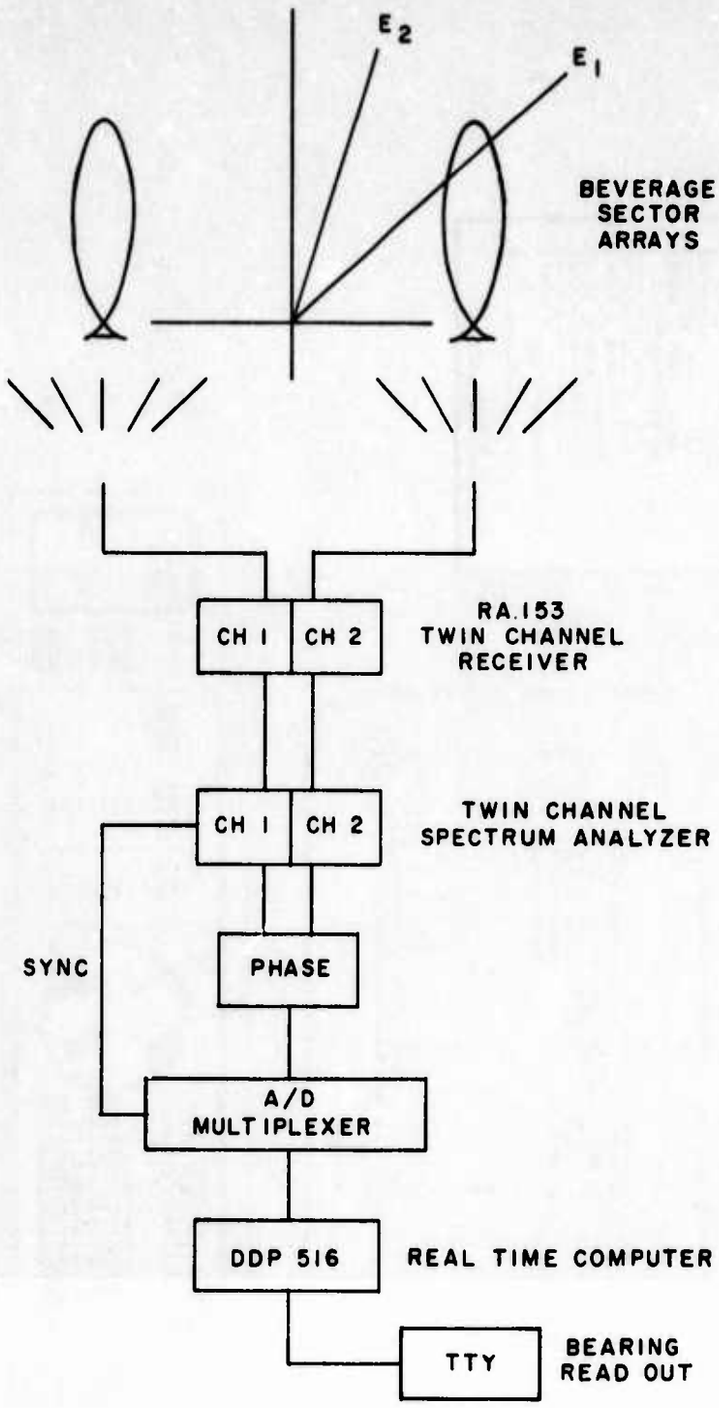

FIGURE 4

PROPOSED INSTRUMENTATION

Figure 5 shows another instrumentation arrangement for the phase interferometer once again using essentially the same hardware, including twin channel receiver, phasemeter, data editing circuits, and on-line computer. In this array the element is polarization selectable providing the capability summarized in Figure 6. By using the cross polarized antenna element, the measuring system can provide polarization measurement in real time, for example, on each mode of an oblique ionogram using FM/CW sounding technique. Also the direction finding capability demonstrated previously (7) can be employed for azimuth/elevation DF measurements on each resolved propagation mode of the ionogram without the presence of wave interference error. Finally, phase difference statistics data along the baselines can be analyzed for coherence ratio and angular width. The sum of these measurements can provide exhaustive propagation mode analysis for all modes present in the oblique ionogram by full exploitation of computer instrumentation capability.

Another important advantage of the computer instrumented interferometer is the ease with which the propagation model or the data processing method may be changed to suit specific requirements. Most past DF equipments have been designed to process data on the assumption that the received signal is to be interpreted as if it were a single plane wave. In the computer interferometer one may change to some other interpretation by replacing software as required.

As an example the data displayed in Figure 7 was obtained from a simulation corresponding to an interferometer similar to the one described above. A bearing computation program was used which interprets the received signal as two plane waves having arbitrary directions and amplitudes and randomly changing relative phase. In Figure 7 the behavior of the elevation angle is displayed as a time series. For this example three plane wave components having the amplitudes and directions shown were used for the test signal. The elevation angle displayed is that of either a single plane wave model or the stronger of the two components for a two plane wave model. The data processing method combines the results of two successive frames of data to obtain the solutions to the two plane waves. It is evident that variations in the stronger component elevation angle are less than those observed using a single plane wave model even when a two point sliding average is used.

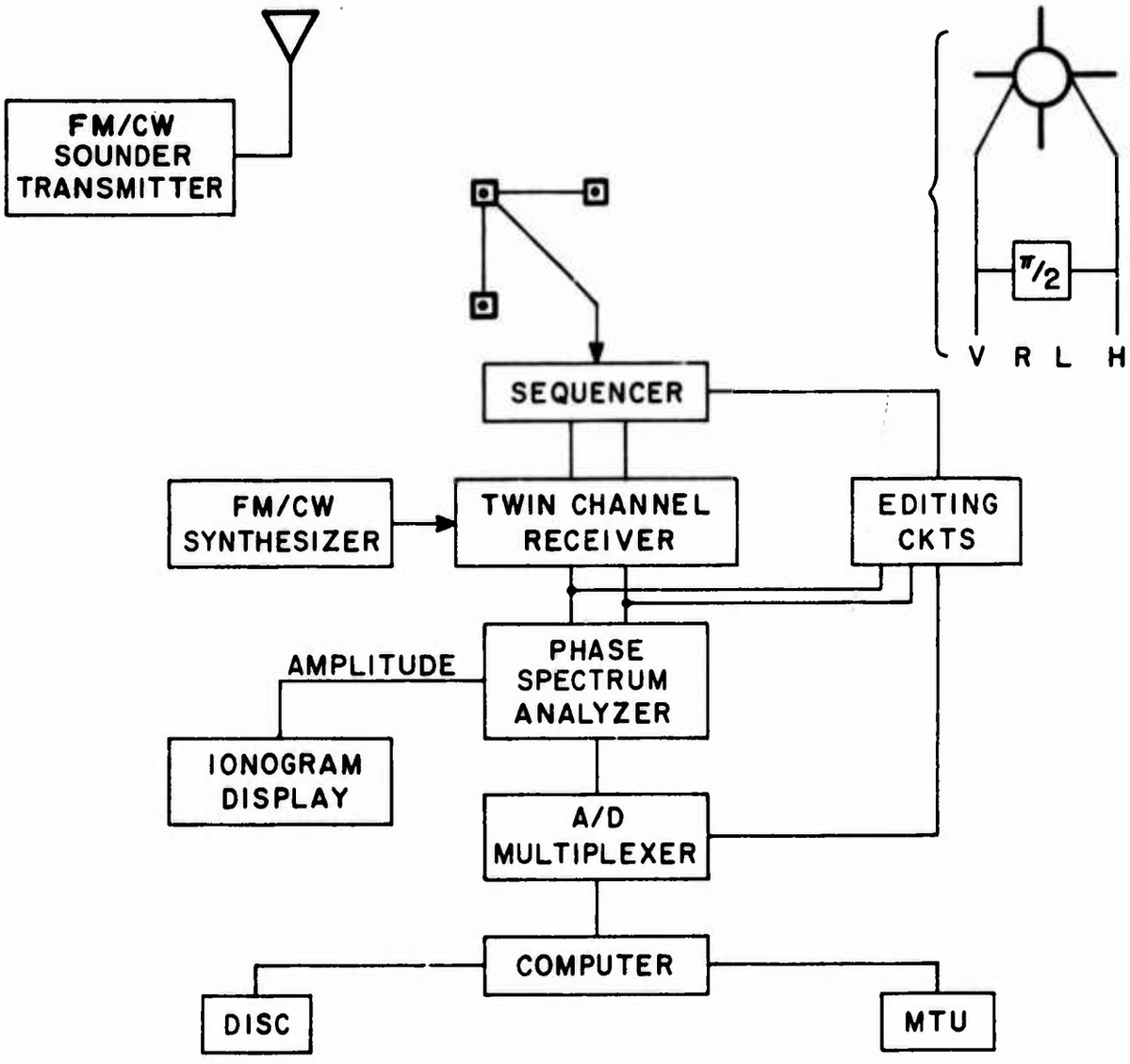

FIGURE 5

DF IONOSONDE

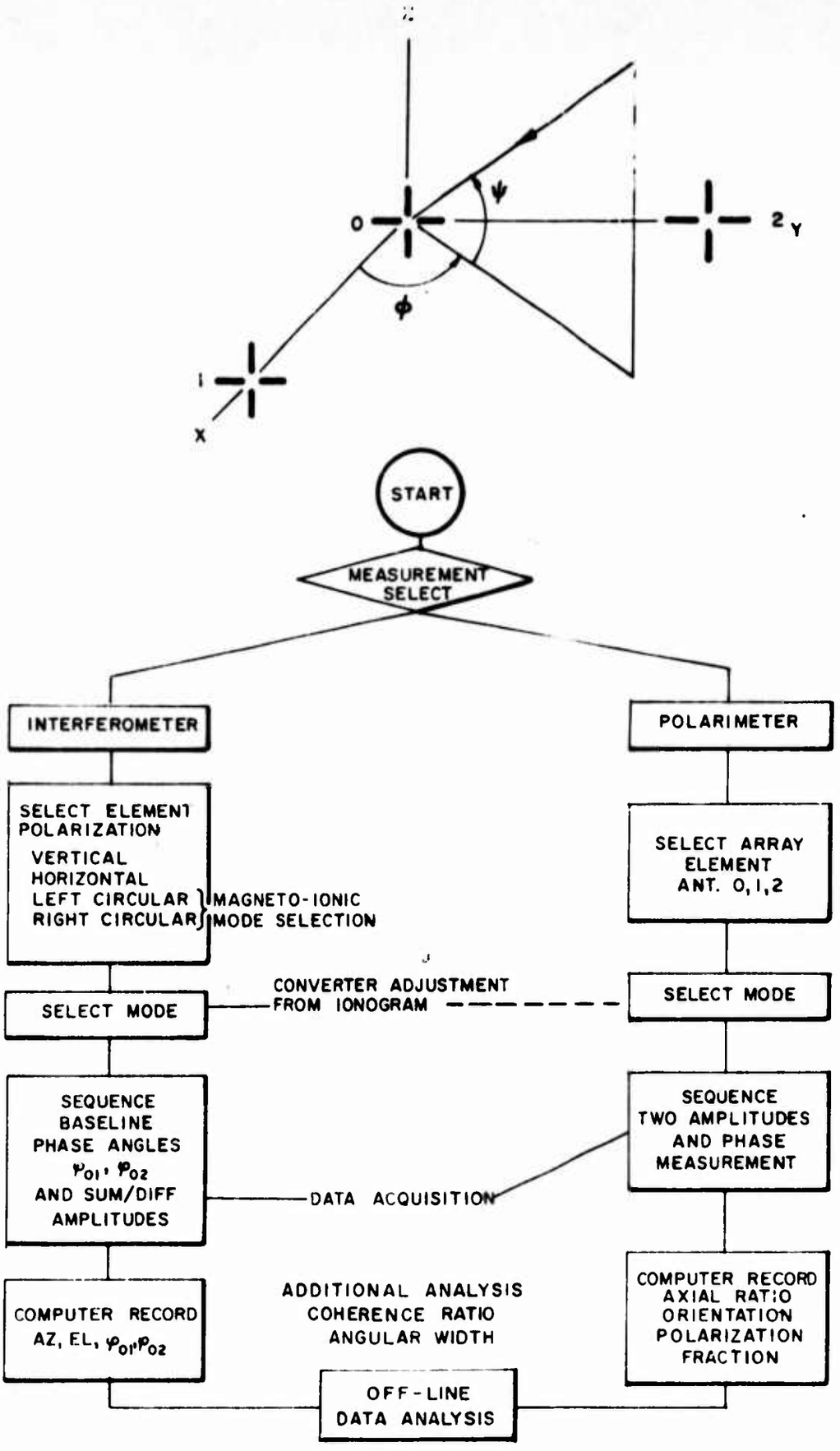

FIGURE 6

POLARIMETER INTERFEROMETER OPERATION

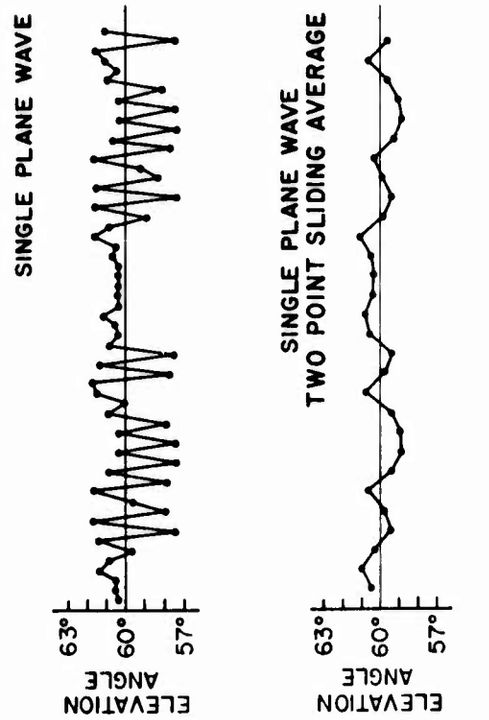

FREQUENCY 3 MHz			
COMPONENT	1	2	3
AMPLITUDE	1.00	.60	.36
AZIMUTH	30°	32°	28°
ELEVATION	60°	62°	58°

FIGURE 7

COMPARISON OF ONE AND TWO PLANE WAVE PROPAGATION MODELS

III. SINGLE CHANNEL PHASE INTERFEROMETERS

Another technique which has been developed during the past two years employs the principle of single channel phase interferometry developed by the Naval Research Laboratory for the minitrack satellite network (8) originally set up for the Vanguard and Mercury programs. Figure 8 shows a phase measuring interferometer which does not use a twin channel receiver but rather a conventional single channel communications receiver. This technique is analogous to the phase sweep interferometer used in radio astronomy where a continuous phase sweep in one element is introduced by off setting the local oscillator at first conversion for one element relative to the other element. After superheterodyne reception and detection at the offset frequency, the offset signal phase through the receiver with respect to the reference offset oscillator is a measure of the space phase difference between the antennas. Figure 9 shows a data logging system employing three such single channel systems in a simple azimuth radiolocation net designed for the wildlife tracking for the Department of the Interior (9). Figure 10 shows equipment photographs.

This technique offers the capability for phase interferometric direction finding including azimuth and elevation computation from crossed baselines where it is not expedient to use a phase and gain matched twin channel receiver.

In another technique for eliminating the twin channel receiver, a stable frequency standard is used as the phase reference as shown in Figure 11. This technique in its simplest form is a temporal reference interferometer compared to the spatial reference.interferometer described in the systems above. With the fixed antenna array, the phase on each element of the array is measured against the time standard and the spatial phase difference is derived by the phase subtraction and phase ambiguity resolution techniques used in the other space reference systems. Alternatively, a mobile moving probe approach can be used and a continuous phase function measured by continuous phase difference measurement with respect to an atomic frequency standard.

Where target transmitter drift and various modulations are employed it is necessary to modify the moving probe technique by the addition of a fixed reference channel which records the intrinsic drift of the target transmitter used to correct the measurements of the other direction finding antennas. This in effect re-establishes the twin channel spatial reference system but permits the antenna elements to be independent, as an extension of the very long baseline

a) BASIC PHASE DIFFERENCE UNIT

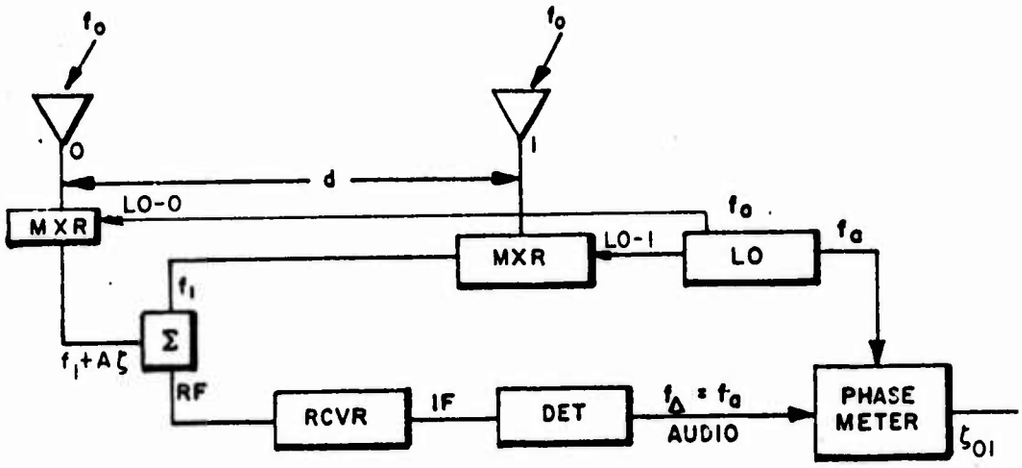

FIGURE 8

CONCEPTUAL BLOCK DIAGRAM

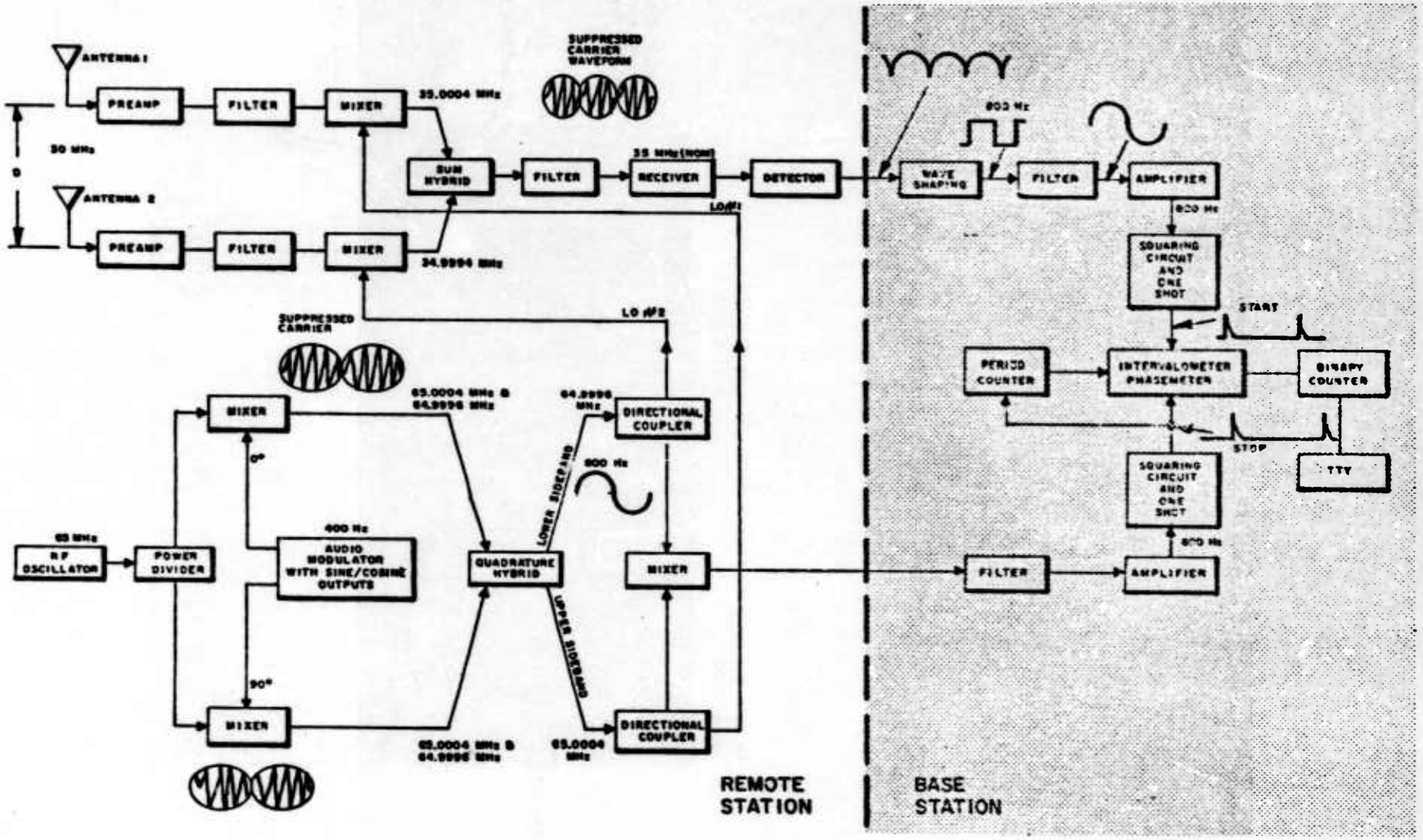

FIGURE 9

SINGLE CHANNEL INTERFEROMETER BLOCK DIAGRAM

a.) CASE CLOSED

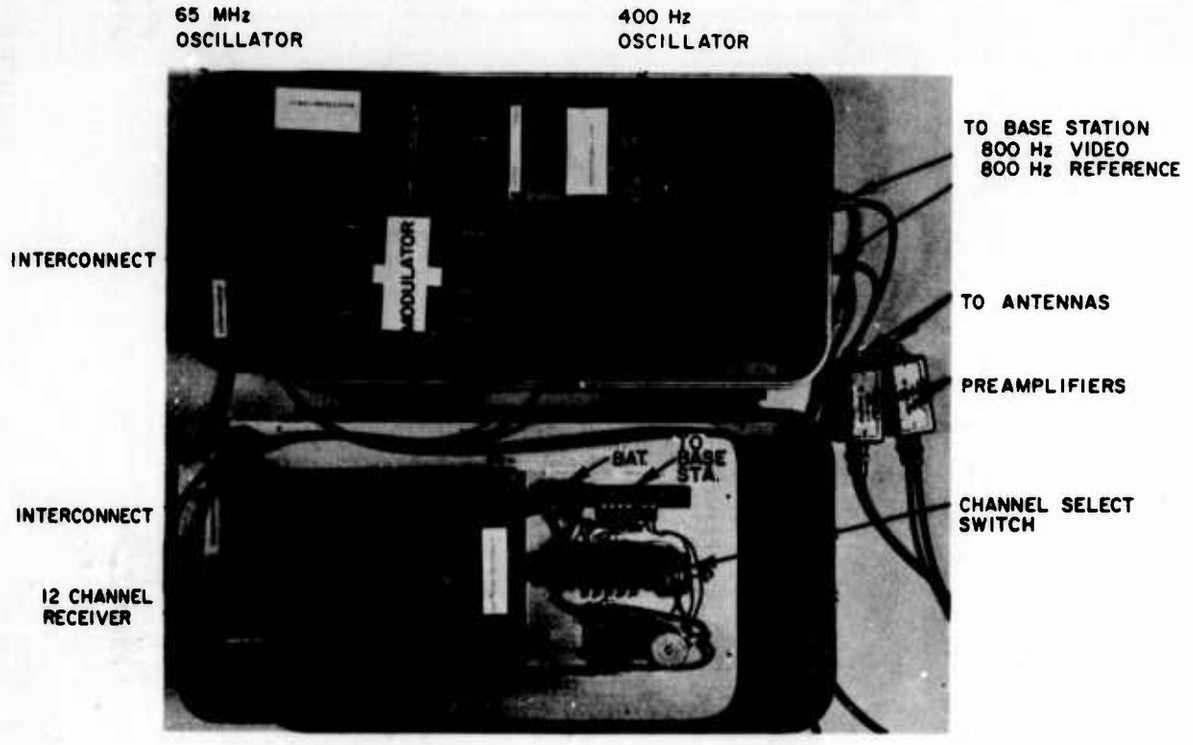

b.) CASE OPEN

FIGURE 10a

REMOTE INTERFEROMETER UNIT

a.). FRONT

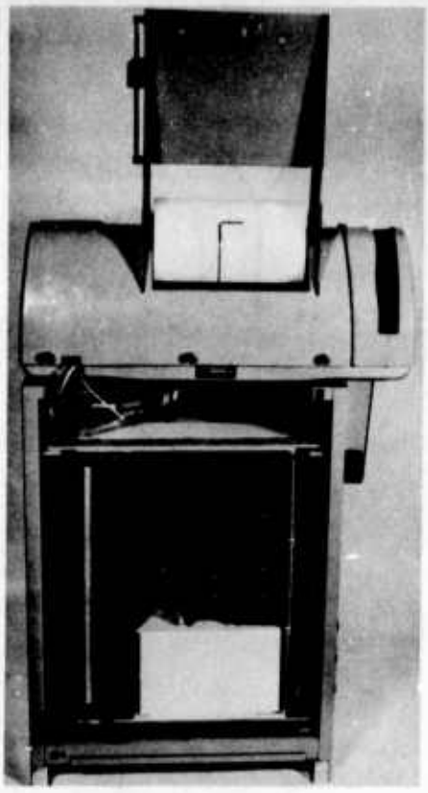

b.) BACK

c.) FOLD-OUT ELECTRONICS DRAWER

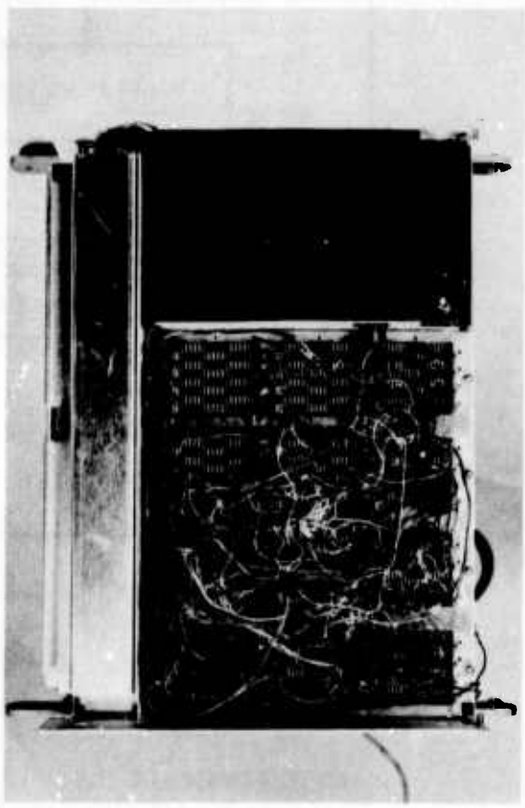

d.) ELECTRONIC DETAIL

FIGURE 10b

INTERFEROMETER BASE STATION AND
DATA LOGGING UNIT

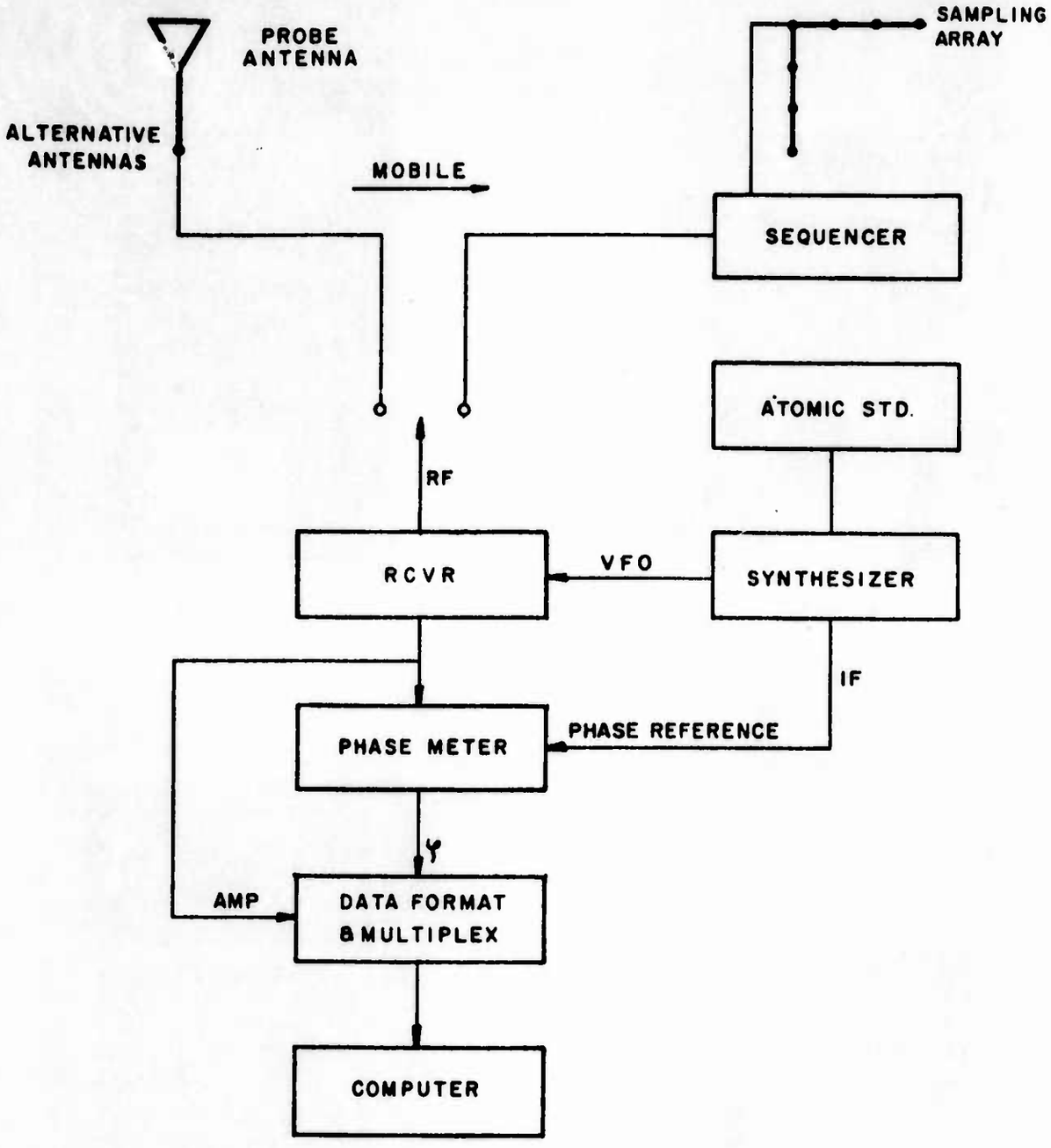

FIGURE 11

CONTINUOUS BASELINE INTERFEROMETER

Michaelson interferometer technique developed for radio astronomy where interferometer baselines stretch to intercontinental distances (10).

IV. SUMMARY

The advent of the computer and related HF component technologies has made practical the development of sophisticated interferometric analysis systems. The full generality of the interference measurement may be used in propagation experiments where coherence ratio, angular width, direction of arrival, and polarization for all modes of an oblique ionogram, can be derived. Alternatively, either single channel spatial reference, single channel temporal reference, or twin channel spatial reference systems may be erected for various radiolocation tasks which provide highly flexible and precise skywave and groundwave direction finding and at the same time are highly adaptable to the various locations and sites imposed by operational constraints.

REFERENCES

1. Eckersley, T. L., "Scattering, Polarization Errors, and the Accuracy of Short Wave Direction Finding," The Marconi Review, 20, 53, 1935.

2. Ross, W., E. N. Bramley, and G. E. Ashwell, "A Phase-Comparison Method of Measuring the Direction of Arrival of Ionospheric Radio Waves," JIEE, (III), 98, 294, 1951.

3. Burtynyk, N., C. W. McLeish, and J. Wolfe, "Performance of an Interferometer Direction Finder for the H. F. Band," Proc. IEE, 112, 2055, 1965.

4. Treharne, R. F., C. G. McCue, Z. R. Jeffrey, B. S. Hewett, "Some Characteristics of the Propagation of Skywaves Over Short Ionospheric Paths," Proc. IREE Australia, 245-254, 1965.

5. Bailey, A. D. and W. C. McClurg, "A Sum-and-Difference Interferometer System for HF Radio Direction Finding," IEEE Trans., ANE-10, 65, 1963.

6. Smith, G.A., P.E. Martin, and W.M. Sherrill, "HF Interferometer and SSL System," Southwest Research Institute, Final Report Draft for U.S. Army Contract DAAB07-69-C-0113, December 1970.

7. Johnson, R.L., P.E. Martin, and T.C. Green, "Short Time Scale Ionospheric Tilt Measurements for Lateral Deviation Compensation," paper presented at the University of Illinois DF Symposium, June 1971.

8. Berbert, J.H., "Effect of Tracking Accuracy Requirements on Design of Minitrack Satellite Tracking System," Trans. IRE, Vol. I-9, No. 2, pp. 84-88, September 1960.

9. Martin, P.E., L.G. Hickman, W.M. Sherrill, "An Interferometer Radiolocation System for Free Ranging Animals, Southwest Research Institute, Final Report for Department of the Interior Contract 14-16-008-510, 30 January 1971.

10. Papers presented at the Very Long Baseline Interferometry Conference, Charlottesville, Virginia, April 1970 and referenced in Radio Science, Volume 5, No. 10, October 1970.

FEEDBACK AND FEEDFORWARD

Albert D. Bailey
Radiolocation Research Laboratory
Department of Electrical Engineering
University of Illinois
Urbana, Illinois 61801

In recent years it has been my special privilege, opportunity and responsibility to travel to different parts of the world of radio direction finding in order to observe, hear, tell, relate, demonstrate, and otherwise interact as best I could with the disciplines and the state of the art and science. I would like to openly express my appreciation to each of you who had a part in making this happen for me. Possessed of all of this knowledge, I feel that I will have done less than my best if I do not make a few pertinent observations about what is becoming very clear to me.

Speaking not as an oracle, nor a prophet, but rather as one voice crying in the noisy wilderness, I respectfully invite your attention to the following:

1. The RDF site is all important.

The site on which the RDF wave collector is placed has been, is now, and always will be very important in connection with any meaningful interpretations. In fact any site, passive or active, is extremely important in any sense of interpretation. Ignore it and it may smite you mightily. After WWII the Marconi Company was able to improve on the classical Adcock RDF and was able to bring its systematic error down to approximately $\pm 1°$ on a good site. In use it had a standard deviation of 3 to 4 degrees and this was attributed to propagation errors. The teaching here is that low systematic error can be had on good sites with a minimum system. What are the compelling reasons that force us to do less than this with our up-and-coming systems? I would also remind you that there are DF Standards and Siting Criteria Requirements that exist and represent reference levels of attainment. It would seem to me that we are being naive if we ignore the standards.

2. Symmetry must be observed.

An omnidirectional RDF array is designed to look equally well in all directions; it should have as many planes of symmetry as possible. On the other hand, sector-type arrays require only symmetry about the boresight. The presence of asymmetries may require that one pays a very high price on occasion. I have been asked about what will happen if subject array is placed on a tilted or sloping site, such as the side of a hill or a mountain. Also, what will happen if an A-type direction finder is placed in close proximity to a B-type direction finder. My first reply is, "Don't do it." But then I hasten to add, "But if you must do it be prepared to pay a penalty... ." Now this is not what you would like to hear, but the weight of evidence that has been stored up in the written experiences of many, many experimenters and set down in the standards teaches that one avoid siting problems and watch symmetry. Now it may be

that we want to change the rules, rewrite the standards and toss the old sets of constraints out of the window and break these "damnable bounds." In the event of this latter I have some ideas and there is always hope in the sense of some "optimum policy." We all know it will be an optimum solution subject to the constraints, but it is just these constraints that siting criteria try to avoid.

3. Concentrated Complexity - is it a wave of the future?

In our own discipline one sees pressures building up due to new vectors - a convergence of solutions looking for problems. Let me illustrate the situation in two specific cases.

Ionospheric propagation and computers are receiving much attention these days and appear to be the waves of the future that are cresting now and, to all indications, will only increase. As far as we are concerned, I believe that each of these must be taken in stride and in proper perspective. But one cannot lose sight of the importance of the primary element - the wave collector. It really is the sine qua non element! I recall arguments that were presented by colleagues to the effect that in an RDF system one needs a certain amount of complexity and one may distribute it around as one sees fit. For example, if one puts a lot of complexity into one's directive array then one doesn't need much of an indicator. Again, if one puts a lot of complexity into a sophisticated computer one shouldn't need much of an antenna. The argument sounds good on the surface and one can cite cases where this does appear to be a fact of experience. It suggests the loosely stuffed sausage.

I would like to propose "Bailey's uncertainty principle" (with apologies to Werner Heisenberg). The idea is to the effect that there is a limiting or minimal complexity ΔC in any essential element of the RDF system that must be exceeded! To make it more quantitative, let ΔV_i be the volume of the ith element (which we want to control in one way or another) then $\Delta V_i \cdot \Delta C_j > h_B >> 0$ where ΔC_j is a measure of the complexity of the jth element that will compensate for the limitation of the ith element.

Computers are having their impact but they should be good and faithful servants and cooperative members of the team. They cannot grow to the complete exclusion of the other system elements. The same can be said for ionospheric propagation information. Up to a point, it is needed. In either case the old established economic principle of diminishing returns will be the deciding factor.

4. You really must make a sufficient number of measurements.

One hears the term "frame of data" or "data vector" being used in connection with our discipline. I believe the term means "a near instantaneous but complete set of measured data which will permit one to uniquely solve the set of simultaneous equations that describes our problem at that instant." There is a minimum set of antennas that would be needed in a wave collector to uniquely measure the single "frame" or "vector." I

believe that the number of antenna elements needed to specify a single frame of data is more than 5 and probably as large as 8 per mode!

Some recent work by P. A. Gothing on vertically stacked antenna element arrays has shown that for a single frame of data a minimum number of antenna elements is needed. Even if this number is as large as 6, it cannot solve many problems on a single-frame basis. Of course we all know that if one is given sufficient time in which to obtain many frames of data, the situation is far different and fewer antenna elements will suffice. This is an application of the classic ergodic theorem on stationary statistical processes wherein a long-time average over one member of an ensemble is equivalent to a large ensemble average obtained at any instant. The implication here is that some rethinking is needed.

5. The noise level is coming up.

Signal-to-noise ratio is a fact that will become more critical in any of our systems and very dramatically so! Recent theoretical work done at the Radiolocation Research Laboratory and reported at the last previous conference has become better appreciated here. I think its implications are inescapable. It was shown that in differential-phase type RDF systems the signal-to-noise ratio limits the minimum aperture of the array. Apertures approaching a wavelength, or more, are indicated as being very desirable. We are aware of the many other facets of the noise problem.

6. HF Receivers need to receive more for less.

Matched in gain and phase N-channel receivers are urgently needed to solve the new sets of problems that are being posed by both passive and active radiolocation systems at HF. But they must be relatively inexpensive. Something of the order of one "kilobuck" per channel would make them very attractive; the present cost per channel appears to be almost ten times this figure. Given this capability, multielement sampling arrays immediately become feasible and practical and new disciplines can evolve.

7. How much should one pay for a whistle?

The last point that I would like to address is concerned with the question of "what minimum ancillaries are needed for adequate probing of the ionosphere overhead and in the near neighborhood to help us solve our problems?"

I have seen the Buckland Park array near Adelaide. It has an aperture of approximately one kilometer consisting of a hundred or so elements. Evidently it permits one to get a good handle on the drifts and traveling disturbances in the ionosphere overhead. The frequency of the experiment was approximately 2MHz. I heard a report recently at URSI on a 32-element circular array having a diameter of 2km which was able to provide a raster-type display of the traveling features overhead. The work of Jones and Davies on Doppler Effect Techniques with special transmitters has been very successful with spacings of the order of 50 kilometers.

Our own work with spaced CW transmitters has demonstrated good results with spacings of 30 kilometers. Our hope, of course, is that one can glean all of this information from one complementary, collocated and compatible RDF-Ionosonde system. The RDF would be of the wide-base differential-phase type of system which has the capability of measuring both components of the angle of arrival of a radio signal. I feel inclined to believe that the success achieved by the very wide-base experiments points the way in which we must go if we want to realize the potential of these techniques. The other point I'd like to make is that whatever we do must be complementary, collocated and compatible and must not cost too much. It should not be another source of noise pollution.

DISTRIBUTION LIST

1 Scientific Officer

1 Cognizant ONR Branch Office

1 Administrative Contracting Officer

Director, Naval Research Laboratory
Washington, D. C. 20390
6 Attention: Library, Code 2029 (ONRL)

Director, Naval Research Laboratory
Washington, D. C. 20390
6 Attention: Technical Information Division

Defense Documentation Center, Building 5,
20 Cameron Station, Alexandria, Virginia 22314

Additional copies to be Distributed in accordance with
15 instructions furnished by the Scientific Officer

Unclassified
Security Classification

DOCUMENT CONTROL DATA - R&D

(Security classification of title, body of abstract and indexing annotation must be entered when the overall report is classified)

1. ORIGINATING ACTIVITY *(Corporate author)*
Department of Electrical Engineering
University of Illinois
Urbana, Illinois

2a. REPORT SECURITY CLASSIFICATION

2b. GROUP

3. REPORT TITLE
Proceedings of the Fourth Allerton-House Conference on HF Radio Direction Finding and Radiolocation Research

4. DESCRIPTIVE NOTES *(Type of report and inclusive dates)*
Final Report

5. AUTHOR(S) *(Last name, first name, initial)*
Bailey, A. D., Editor

6. REPORT DATE
September 1971

7a. TOTAL NO. OF PAGES
435

7b. NO. OF REFS

8a. CONTRACT OR GRANT NO.
N00014-71-C-0221

b. PROJECT AND TASK NO.

c. 371/167

d.

9a. ORIGINATOR'S REPORT NUMBER(S)
RRL No. 392

9b. OTHER REPORT NO(S) *(Any other numbers that may be assigned this report)*
UILU-ENG-71-2542

10. AVAILABILITY/LIMITATION NOTICES
"EACH TRANSMITTAL OF THIS DOCUMENT OUTSIDE OF THE DEPARTMENT OF DEFENSE MUST HAVE PRIOR APPROVAL OF THE OFFICE OF NAVAL RESEARCH (CODE 427) DEPARTMENT OF THE NAVY, ARLINGTON, VIRGINIA 22217"

11. SUPPLEMENTARY NOTES
Item A 001 AD

12. SPONSORING MILITARY ACTIVITY
Office of Naval Research and the Naval Electronics Systems Command
Arlington, Virginia 22217

13. ABSTRACT

The purpose of this conference is to promote discussion between Governmental, Educational and Industrial Groups on the "State-of-the-Art" and Science of Radio Direction Finding, Radio Position Finding, Directional Radio Propagation; and to explore, where possible, the future direction of these research efforts, based on user requirements.

The General Theme of this Conference:

"D/F IN THE '70'S"

with subtopics

1. RDF Systems,
2. Radiolocation Systems,
3. Modeling and Simulation Studies,
4. HF Directional Propagation Research,
5. Instrumentation.

DD FORM 1 JAN 64 1473

Unclassified
Security Classification

Unclassified
Security Classification

14. KEY WORDS	LINK A		LINK B		LINK C	
	ROLE	WT	ROLE	WT	ROLE	WT
Antennas						
Receivers						
Computers						
RDF Systems						
Measurements						
Potpourri						
Measurements						
Disturbances						
Ionosphere						
Noise						
Research						

INSTRUCTIONS

1. ORIGINATING ACTIVITY: Enter the name and address of the contractor, subcontractor, grantee, Department of Defense activity or other organization *(corporate author)* issuing the report.

2a. REPORT SECURITY CLASSIFICATION: Enter the overall security classification of the report. Indicate whether "Restricted Data" is included. Marking is to be in accordance with appropriate security regulations.

2b. GROUP: Automatic downgrading is specified in DoD Directive 5200.10 and Armed Forces Industrial Manual. Enter the group number. Also, when applicable, show that optional markings have been used for Group 3 and Group 4 as authorized.

3. REPORT TITLE: Enter the complete report title in all capital letters. Titles in all cases should be unclassified. If a meaningful title cannot be selected without classification, show title classification in all capitals in parenthesis immediately following the title.

4. DESCRIPTIVE NOTES: If appropriate, enter the type of report, e.g., interim, progress, summary, annual, or final. Give the inclusive dates when a specific reporting period is covered.

5. AUTHOR(S): Enter the name(s) of author(s) as shown on or in the report. Enter last name, first name, middle initial. If military, show rank and branch of service. The name of the principal author is an absolute minimum requirement.

6. REPORT DATE: Enter the date of the report as day, month, year, or month, year. If more than one date appears on the report, use date of publication.

7a. TOTAL NUMBER OF PAGES: The total page count should follow normal pagination procedures, i.e., enter the number of pages containing information.

7b. NUMBER OF REFERENCES: Enter the total number of references cited in the report.

8a. CONTRACT OR GRANT NUMBER: If appropriate, enter the applicable number of the contract or grant under which the report was written.

8b, 8c, & 8d. PROJECT NUMBER: Enter the appropriate military department identification, such as project number, subproject number, system numbers, task number, etc.

9a. ORIGINATOR'S REPORT NUMBER(S): Enter the official report number by which the document will be identified and controlled by the originating activity. This number must be unique to this report.

9b. OTHER REPORT NUMBER(S): If the report has been assigned any other report numbers *(either by the originator or by the sponsor)*, also enter this number(s).

10. AVAILABILITY/LIMITATION NOTICES: Enter any limitations on further dissemination of the report, other than those imposed by security classification, using standard statements such as:

(1) "Qualified requesters may obtain copies of this report from DDC."

(2) "Foreign announcement and dissemination of this report by DDC is not authorized."

(3) "U. S. Government agencies may obtain copies of this report directly from DDC. Other qualified DDC users shall request through _____."

(4) "U. S. military agencies may obtain copies of this report directly from DDC. Other qualified users shall request through _____."

(5) "All distribution of this report is controlled. Qualified DDC users shall request through _____."

If the report has been furnished to the Office of Technical Services, Department of Commerce, for sale to the public, indicate this fact and enter the price, if known.

11. SUPPLEMENTARY NOTES: Use for additional explanatory notes.

12. SPONSORING MILITARY ACTIVITY: Enter the name of the departmental project office or laboratory sponsoring *(paying for)* the research and development. Include address.

13. ABSTRACT: Enter an abstract giving a brief and factual summary of the document indicative of the report, even though it may also appear elsewhere in the body of the technical report. If additional space is required, a continuation sheet shall be attached.

It is highly desirable that the abstract of classified reports be unclassified. Each paragraph of the abstract shall end with an indication of the military security classification of the information in the paragraph, represented as *(TS), (S), (C), or (U).*

There is no limitation on the length of the abstract. However, the suggested length is from 150 to 225 words.

14. KEY WORDS: Key words are technically meaningful terms or short phrases that characterize a report and may be used as index entries for cataloging the report. Key words must be selected so that no security classification is required. Identifiers, such as equipment model designation, trade name, military project code name, geographic location, may be used as key words but will be followed by an indication of technical context. The assignment of links, rules, and weights is optional.

Unclassified
Security Classification